

# Potential biomarkers in neurovascular disorders

## volume II

**Edited by**

Wen-Jun Tu and Shenfeng Qiu

**Published in**

Frontiers in Neurology



## FRONTIERS EBOOK COPYRIGHT STATEMENT

The copyright in the text of individual articles in this ebook is the property of their respective authors or their respective institutions or funders. The copyright in graphics and images within each article may be subject to copyright of other parties. In both cases this is subject to a license granted to Frontiers.

The compilation of articles constituting this ebook is the property of Frontiers.

Each article within this ebook, and the ebook itself, are published under the most recent version of the Creative Commons CC-BY licence. The version current at the date of publication of this ebook is CC-BY 4.0. If the CC-BY licence is updated, the licence granted by Frontiers is automatically updated to the new version.

When exercising any right under the CC-BY licence, Frontiers must be attributed as the original publisher of the article or ebook, as applicable.

Authors have the responsibility of ensuring that any graphics or other materials which are the property of others may be included in the CC-BY licence, but this should be checked before relying on the CC-BY licence to reproduce those materials. Any copyright notices relating to those materials must be complied with.

Copyright and source acknowledgement notices may not be removed and must be displayed in any copy, derivative work or partial copy which includes the elements in question.

All copyright, and all rights therein, are protected by national and international copyright laws. The above represents a summary only. For further information please read Frontiers' Conditions for Website Use and Copyright Statement, and the applicable CC-BY licence.

ISSN 1664-8714  
ISBN 978-2-8325-3302-4  
DOI 10.3389/978-2-8325-3302-4

## About Frontiers

Frontiers is more than just an open access publisher of scholarly articles: it is a pioneering approach to the world of academia, radically improving the way scholarly research is managed. The grand vision of Frontiers is a world where all people have an equal opportunity to seek, share and generate knowledge. Frontiers provides immediate and permanent online open access to all its publications, but this alone is not enough to realize our grand goals.

## Frontiers journal series

The Frontiers journal series is a multi-tier and interdisciplinary set of open-access, online journals, promising a paradigm shift from the current review, selection and dissemination processes in academic publishing. All Frontiers journals are driven by researchers for researchers; therefore, they constitute a service to the scholarly community. At the same time, the *Frontiers journal series* operates on a revolutionary invention, the tiered publishing system, initially addressing specific communities of scholars, and gradually climbing up to broader public understanding, thus serving the interests of the lay society, too.

## Dedication to quality

Each Frontiers article is a landmark of the highest quality, thanks to genuinely collaborative interactions between authors and review editors, who include some of the world's best academicians. Research must be certified by peers before entering a stream of knowledge that may eventually reach the public - and shape society; therefore, Frontiers only applies the most rigorous and unbiased reviews. Frontiers revolutionizes research publishing by freely delivering the most outstanding research, evaluated with no bias from both the academic and social point of view. By applying the most advanced information technologies, Frontiers is catapulting scholarly publishing into a new generation.

## What are Frontiers Research Topics?

Frontiers Research Topics are very popular trademarks of the *Frontiers journals series*: they are collections of at least ten articles, all centered on a particular subject. With their unique mix of varied contributions from Original Research to Review Articles, Frontiers Research Topics unify the most influential researchers, the latest key findings and historical advances in a hot research area.

Find out more on how to host your own Frontiers Research Topic or contribute to one as an author by contacting the Frontiers editorial office: [frontiersin.org/about/contact](https://frontiersin.org/about/contact)



# Potential biomarkers in neurovascular disorders volume II

## Topic editors

Wen-Jun Tu — Chinese Academy of Medical Sciences and Peking Union Medical College, China

Shenfeng Qiu — University of Arizona, United States

## Citation

Tu, W.-J., Qiu, S., eds. (2023). *Potential biomarkers in neurovascular disorders volume II*. Lausanne: Frontiers Media SA. doi: 10.3389/978-2-8325-3302-4

# Table of contents

- 05 **Children with strabismus and amblyopia presented abnormal spontaneous brain activities measured through fractional amplitude of low-frequency fluctuation (fALFF)**  
Xiao-Qin Hu, Yi-Dan Shi, Jun Chen, Zhipeng You, Yi-Cong Pan, Qian Ling, Hong Wei, Jie Zou, Ping Ying, Xu-Lin Liao, Ting Su, Yi-Xin Wang and Yi Shao
- 16 **The predictive value of neutrophil to lymphocyte ratio on 30-day outcomes in spontaneous intracerebral hemorrhage patients after surgical treatment: A retrospective analysis of 128 patients**  
Yiqin Zhao, Yanfeng Xie, Shengjie Li and Mingliang Hu
- 24 **Biomarkers involved in the pathogenesis of cerebral small-vessel disease**  
Xiaolu Liu, Pei Sun, Jing Yang and Yuhua Fan
- 34 **Alzheimer's disease-associated inflammatory pathways might contribute to osteoporosis through the interaction between *PROK2* and *CSF3***  
Wenzheng Zhang, Ya Zhang, Naixia Hu and Anying Wang
- 46 **Impact of improved stroke green channel process on the delay of intravenous thrombolysis in patients with acute cerebral infarction during the COVID-19 pandemic: An observational study**  
Qiwei Wang, Yan Wang, Yongpeng Wang, Qianqian Bi, Quanbin Zhang and Feng Wang
- 55 **Potential mechanism of the Shunaoxin pill for preventing cognitive impairment in type 2 diabetes mellitus**  
Yuejie Guo, Ning Luo and Xueran Kang
- 69 **Hippocampal gene expression patterns in Sevoflurane anesthesia associated neurocognitive disorders: A bioinformatic analysis**  
Weiwei Li, Qijun Yi and Huijian Shi
- 85 **Analysis of co-expression gene network associated with intracranial aneurysm and type 2 diabetes mellitus**  
Tian Tian, Wenhao Sun, Jia Du and Yafei Sun
- 98 **Postoperative red blood cell distribution width predicts functional outcome in aneurysmal subarachnoid hemorrhage after surgical clipping: A single-center retrospective study**  
Long Zhao, Yi Zhang, Ping Lin, Weida Li, Xingyuan Huang, Hangyang Li, Mingkai Xia, Xinlong Chen, Xi Zhu and Xiaoping Tang
- 108 **An analysis of neurovascular disease markers in the hippocampus of *Tupaia chinensis* at different growth stages**  
Yiqiang Ouyang, Ying Zhang, Xiaoping Guo, Jiafu Li, Qingqing Ao, Songchao Guo, Mingyuan Zhang and Junming Sun

- 123 **High-fiber-diet-related metabolites improve neurodegenerative symptoms in patients with obesity with diabetes mellitus by modulating the hippocampal–hypothalamic endocrine axis**  
Ning Luo, Yuejie Guo, Lihua Peng and Fangli Deng
- 138 **Decreased degree centrality values as a potential neuroimaging biomarker for migraine: A resting-state functional magnetic resonance imaging study and support vector machine analysis**  
Qian Wang, Yujun Gao, Yuandong Zhang, Xi Wang, Xuying Li, Hang Lin, Ling Xiong and Chunyan Huang
- 145 **Research progress on the protective mechanism of a novel soluble epoxide hydrolase inhibitor TPPU on ischemic stroke**  
Pan Huang
- 151 **Prognostic models for survival and consciousness in patients with primary brainstem hemorrhage**  
Jingyi Zhou, Rui Wang, Jizhong Mao, Yichen Gu, Anwen Shao, Fengqiang Liu and Jianmin Zhang
- 162 **Identification of co-expressed central genes and transcription factors in atherosclerosis-related intracranial aneurysm**  
Quan Zhang, Hengfang Liu, Min Zhang, Fang Liu and Tiantian Liu
- 176 **Serum neutrophil gelatinase-associated lipocalin as a potential biomarker for cognitive decline in spinal cord injury**  
Qinghao Zhang, Ziteng Li, Liangyu Xie, Shengnan Cao, Zhonghao Cui, Bin Shi and Yuanzhen Chen
- 182 **Metabolomic analysis of vascular cognitive impairment due to hepatocellular carcinoma**  
Dan Zhu, Yamei Zhu, Lin Liu, Xiaoxue He and Shizhong Fu
- 198 **Alteration of neurofilament heavy chain and its phosphoforms reveals early subcellular damage beyond the optic nerve head in glaucoma**  
Lan Zhou, Dongyue Lin, Guihua Xu, Xiaoyi Wang, Zilin Chen, Dingding Wang and Huiya Fan
- 214 **Transcriptomic analysis reveals the potential biological mechanism of AIS and lung adenocarcinoma**  
Rong-Xing Qin, Yue Yang, Jia-Feng Chen, Li-Juan Huang, Wei Xu, Qing-Chun Qin, Xiao-Jun Liang, Xin-Yu Lai, Xiao-Ying Huang, Min-Shan Xie and Li Chen



## OPEN ACCESS

EDITED BY  
Yuzhen Xu,  
Tongji University, China

REVIEWED BY  
Ke Ning,  
Stanford University, United States  
Sanming Li,  
University of Texas Health Science  
Center at Houston, United States

\*CORRESPONDENCE  
Yi Shao  
freebee99@163.com  
Zhipeng You  
myscholar@163.com

†These authors have contributed  
equally to this work

SPECIALTY SECTION  
This article was submitted to  
Neurological Biomarkers,  
a section of the journal  
Frontiers in Neurology

RECEIVED 13 June 2022  
ACCEPTED 18 July 2022  
PUBLISHED 12 August 2022

CITATION  
Hu X-Q, Shi Y-D, Chen J, You Z, Pan  
Y-C, Ling Q, Wei H, Zou J, Ying P, Liao  
X-L, Su T, Wang Y-X and Shao Y (2022)  
Children with strabismus and  
amblyopia presented abnormal  
spontaneous brain activities measured  
through fractional amplitude of  
low-frequency fluctuation (fALFF).  
*Front. Neurol.* 13:967794.  
doi: 10.3389/fneur.2022.967794

COPYRIGHT  
© 2022 Hu, Shi, Chen, You, Pan, Ling,  
Wei, Zou, Ying, Liao, Su, Wang and  
Shao. This is an open-access article  
distributed under the terms of the  
[Creative Commons Attribution License](https://creativecommons.org/licenses/by/4.0/)  
(CC BY). The use, distribution or  
reproduction in other forums is  
permitted, provided the original  
author(s) and the copyright owner(s)  
are credited and that the original  
publication in this journal is cited, in  
accordance with accepted academic  
practice. No use, distribution or  
reproduction is permitted which does  
not comply with these terms.

# Children with strabismus and amblyopia presented abnormal spontaneous brain activities measured through fractional amplitude of low-frequency fluctuation (fALFF)

Xiao-Qin Hu<sup>1†</sup>, Yi-Dan Shi<sup>2†</sup>, Jun Chen<sup>3†</sup>, Zhipeng You<sup>1\*</sup>,  
Yi-Cong Pan<sup>2</sup>, Qian Ling<sup>2</sup>, Hong Wei<sup>2</sup>, Jie Zou<sup>2</sup>, Ping Ying<sup>2</sup>,  
Xu-Lin Liao<sup>4</sup>, Ting Su<sup>5</sup>, Yi-Xin Wang<sup>6</sup> and Yi Shao<sup>2\*</sup>

<sup>1</sup>Department of Strabismus and Amblyopia, Affiliated Eye Hospital of Nanchang University, Nanchang, China, <sup>2</sup>Department of Ophthalmology, Jiangxi Branch of National Clinical Research Center for Ocular Disease, The First Affiliated Hospital of Nanchang University, Nanchang, China, <sup>3</sup>Department of Ophthalmology, The First Affiliated Hospital of Nanchang University, Jiangxi Branch of National Clinical Research Center for Ocular Disease, Nanchang, China, <sup>4</sup>Department of Ophthalmology and Visual Sciences, The Chinese University of Hong Kong, Shatin, Hong Kong SAR, China, <sup>5</sup>Department of Ophthalmology, Massachusetts Eye and Ear, Harvard Medical School, Boston, MA, United States, <sup>6</sup>School of Optometry and Vision Sciences, College of Biomedical and Life Sciences, Cardiff University, Cardiff, United Kingdom

**Purpose:** Based on fMRI technology, we explored whether children with strabismus and amblyopia (SA) showed significant change in fractional amplitude of low-frequency fluctuation (fALFF) values in specific brain regions compared with healthy controls and whether this change could point to the clinical manifestations and pathogenesis of children with strabismus to a certain extent.

**Methods:** We enrolled 23 children with SA and the same number matched healthy controls in the ophthalmology department of the First Affiliated Hospital of Nanchang University, and the whole brain was scanned by rs-fMRI. The fALFF value of each brain area was derived to examine whether there is a statistical difference between the two groups. Meanwhile, the ROC curve was made in a view to evaluate whether this difference proves useful as a diagnostic index. Finally, we analyzed whether changes in the fALFF value of some specific brain regions are related to clinical manifestations.

**Results:** Compared with HCs, children with SA presented decreased fALFF values in the left temporal pole: the superior temporal gyrus, right middle temporal gyrus, right superior frontal gyrus, and right supplementary motor area. Meanwhile, they also showed higher fALFF values in specific brain areas, which included the left precentral gyrus, left inferior parietal, and left precuneus.

**Conclusion:** Children with SA showed abnormal fALFF values in different brain regions. Most of these regions were allocated to the visual formation pathway, the eye movement-related pathway, or other visual-related pathways, suggesting the pathological mechanism of the patient.

## KEYWORDS

amblyopia, fALFF, visual pathway, strabismus, children



## Introduction

Strabismus links to improper eye position, including esotropia and exotropia (1). The prevalence of strabismus varies in different regions or nations, but what is in common is the case that its incidence is increasing year by year (2). Refractive differences between the eyes, hyperopia, related family history, and improper behaviors during the gestation period (drinking, smoking, or drug dependence) are all clear risk factors for strabismus. Infants with congenital squint are often associated with the possibility of amblyopia, and the contemporary mainstream views are increasingly emphasizing the correction of amblyopia in children with strabismus. At the same time, strabismus constitutes one of the important reasons for the occurrence of amblyopia. The preferred practice pattern (PPP) (3) also pointed out that the correction of strabismus can promote the treatment of amblyopia. The increasing number of children with strabismus and amblyopia (SA) has grown up as a serious public health problem. Eyes are an imperative tool for directly perceiving the world. Ophthalmic abnormalities and obstacles have a profound influence on the growth process of children, and this impact is reflected in both physical development and mental development (4). Therefore, a comprehensive understanding of strabismus and amblyopia is very eminent.

Traditionally, the examinations prescribed for the diagnosis of SA were limited to optical function and acuity examinations, but a large number of studies have shown that patients with SA still have changes in the structure and function of the nervous system (5–7). However, the evaluation of this part rarely participants in clinical studies. The rapid development of the field of medical imaging in recent years suggests that we may take advantage of it to take a more intuitive and comprehensive view of SA. Among them, fMRI has become an important examination method to study the pathogenesis of SA patients at the neurological level and predict possible complications because it can evaluate the brain from many aspects such as morphology, metabolism, blood perfusion, and functional changes at the same time.

The fMRI is a noninvasive post-processing imaging technology for functional brain areas. Blood-oxygen level-dependent (BOLD) signals are obtained as being dependent upon the differences in the metabolic levels of discrete brain regions. Among them, the rs-fMRI examination is performed when the subject is awake, with closed eyes, resting, and shielded from external stimuli. The result of rs-fMRI can determine the spontaneous neural activity of the subject's brain (8).

Low-frequency oscillations (LFOs) are deemed to be caused by the spontaneous activity of brain neurons (9). When a person is in a resting state and not stimulated by the peripheral environment, there will be synchronous low-frequency vibrations in specific brain areas. This vibration can be considered by the BOLD signal, and moreover, it can be

detected, recorded, and presented by rs-fMRI. On this basis, ALFF was proposed as an index of rs-fMRI. ALFF is defined as the disparity between low-frequency oscillation of BOLD signal and average fluctuation amplitude of the spontaneous brain neuron activity baseline in a specific time (10), which can be helpful to some researchers to reprocess the rs-fMRI result data for the spontaneous activity of functional brain areas (11, 12). However, in practical applications, the interference of physiological noise on the consequences of ALFF increases the uncertainty of the research results, and the improved fALFF based on ALFF can deal with this issue and remove the signal artifacts caused by non-specific brain neuronal activities.

Due to its unique advantages, fALFF has been widely used in the research of many diseases, including pure major depression disorder (13), migraine (14), post-stroke depression (15), Parkinson's disease (16), and premenstrual syndrome (17).

This study adopted rs-fMRI to detect aberrant autogenic activities in specific brain areas of patients through fALFF to explore the possible neural mechanisms and potential pathological changes in the disease. To the best of our knowledge, this is the first time that this method has been used to study SA in children.

## Materials and methods

### Subjects

The study included 23 patients (no more than 18 years of age) who were diagnosed with strabismus and amblyopia and 23 healthy controls (HCs). All participants came from the Ophthalmology Department of the First Affiliated Hospital of Nanchang University.

The inclusion criteria of patients (PAT) were as follows: (1) under 18 years old; (2) being diagnosed with strabismus and amblyopia by a doctor who has obtained medical practitioner qualification strictly in accordance with the PPP diagnosis of strabismus and amblyopia (no distinction between monocular or binocular, esotropia and exotropia); (3) ophthalmoscopy showing the suppression of the macular center; and (4) lack of stereopsis.

The inclusion criteria of the healthy controls (HCs) were as follows: (1) under 18 years old; (2) non-conforming to the diagnostic criteria of strabismus and/or amblyopia; (3) could cooperate with MRI examination; (4) no history of other ophthalmic diseases; and (5) head MRI scanning showing no abnormality.

The exclusion criteria for all participants were as follows: (1) having a history of surgery, especially eye surgery; (2) having a history of eye trauma or brain trauma; (3) being born with abnormal neurological development; (4) having diseases that cannot cooperate with MRI examinations (from wearing a heart

pacemaker or severe mental illness; and (5) having a history of using medications that can impact the central nervous system.

The procedure for this study was approved by the Ethics Committee of the First Affiliated Hospital of Nanchang University. All participants had known the purpose, content, and risks of this research, and written informed consent was obtained from all participants before the start of the experiment.

## MRI parameters

The MRI scan was taken using a 3.0T Siemens Trio Tim MRI Scanner (Siemens, Munich, Germany). During scanning, all participants kept their eyes closed and awake with relaxed breathing and refraining from thinking on purpose or receiving external stimulation. The supine position was maintained throughout the scan. Scanning technical parameters were as presented: repetition time (TR) = 2,000 ms, echo time (TE) = 40 ms, flip angle = 90°, acquisition matrix = 240 × 240, thickness = 4 mm, and field of view (FOV) = 240 × 240. Finally, 240 functional images were generated. The entire scanning time went on for 8 min. The scanning range covered the entire brain.

## fMRI data analysis

The MRICro software was adopted to classify, identify, and delete incomplete data from the MRI scan for the integrity and validity of the data. The utilization of Statistical Parametric Mapping software8 (SPM8) was used for data preprocessing, which includes (1) abandon the first 15 functional images, convert the remaining data to the NIFTI format, and perform time layer correction and head movement correction (retaining the data with head movement  $\leq 1.5$  mm and head rotation  $\leq 2^\circ$ ); (2) taking into account the difference in brain volume of different subjects, standardize and resemble the fMRI images using echo plane imaging templates [using the Montreal Institute of Neurology (MNI) spatial standard; voxel = 3 mm × 3 mm × 3 mm]; (3) eliminate the linear trend of the time series and perform low-frequency filtering (0.01–0.08 Hz) on it to reduce low-frequency drift and high-frequency noise; and (4) use full width and half height (FWHM: 6 × 6 × 6 mm) to smooth the image.

The covariance referenced in the regression analysis contains the 6 parameters of head movement, the average frame displacement [FD], the overall brain signal, and the average signal of white matter and cerebrospinal fluid.

## Calculation of fALFF values

The value of fALFF is equal to the ratio of the power spectrum in a specific low-frequency range of a certain brain

area to the power spectrum of the entire frequency range, which can reduce the interference caused by the normal physiological activities of other brain areas to a certain extent. The REST software was selected for the calculation, conversion of time series data and a restricted frequency range, and calculation of the power spectrum. The specific low-frequency range is set to 0.01–0.08 Hz, and the entire frequency range is set to 0–0.25 Hz.

## Correlation analysis

Correlation analysis was carried out to evaluate the relationship between typical autonomous activities and clinical performance. Indexes we adopted included the minimum resolution angle logarithmic vision (LogMAR), which is based on the value of best-corrected visual acuity (BCVA); and the hospital anxiety and depression scale (HADS), which could quantify and evaluate the level of anxiety. With the application of the REST software, we defined brain regions in PAT with different fALFF values as regions of interest (ROI) and analyzed the correlation between mean fALFF values of ROI and one of the indexes through linear correlation analysis ( $\alpha = 0.05$ ,  $p < \alpha$  is statistically significant).

## Statistical analysis

The statistical analysis involved in the experiment was carried out using SPSS 20.0 (SPSS, IBM Corp, USA). General information and clinical characteristics of the subjects were statistically tested by independent sample *t*-test and chi-square test ( $\alpha = 0.05$ ,  $p < \alpha$  suggests that the difference is statistically significant). The difference of fALFF between PAT and HCs was verified by two independent sample *t*-tests to determine if it is statistically significant, and the value of this difference as a diagnostic indicator was analyzed by the ROC curve. The correlation analysis between the fALFF value and clinical manifestations of specific brain areas in the PAT group was performed by Pearson's correlation analysis ( $\alpha = 0.05$ ,  $p < \alpha$  is statistically significant).

## Results

### Demographics and visual measurements

There was no significant difference in gender ( $p > 0.99$ ), age ( $p = 0.322$ ), and BCVA ( $p = 0.276$  for domain eyes and  $P = 0.295$  for the fellow eye). More details are given in [Table 1](#).

TABLE 1 The conditions of participants included in the study.

| Condition                | SA           | HCS          | <i>t</i> -value | <i>P</i> -value* |
|--------------------------|--------------|--------------|-----------------|------------------|
| Male/female              | 15/8         | 15/8         | N/A             | >0.99            |
| Age (years)              | 10.46 ± 1.29 | 11.61 ± 1.32 | −1.056          | 0.322            |
| Weight (kg)              | 28.53 ± 3.64 | 29.64 ± 3.54 | −0.784          | 0.595            |
| Handedness               | 23R          | 23R          | N/A             | >0.99            |
| Best-corrected VA-DE     | 1.15 ± 0.15  | 1.10 ± 0.10  | 1.875           | 0.276            |
| Best-corrected VA-FE     | 1.10 ± 0.15  | 1.15 ± 0.10  | 1.864           | 0.295            |
| Duration of SA (years)   | 10.46 ± 1.29 | N/A          | N/A             | N/A              |
| Esotropia/exotropia      | 13/10        | N/A          | N/A             | N/A              |
| Angle of strabismus (PD) | 37.39 ± 9.24 | N/A          | N/A             | N/A              |

Independent *t*-tests comparing two groups ( $p < 0.05$  represented statistically significant differences).

DE, dominant eye; FE, fellow eye; HCs, healthy controls; N/A, not applicable; PD, prism diopter; SA, strabismus and amblyopia; VA, visual acuity.

## fALFF differences

Children with SA had decreased fALFF values in Temporal-Pole-Sup-L, Temporal-Mid-R, Frontal-Sup-R, and Supp-Motor-Area-R. Moreover, they also presented higher fALFF values in specific brain areas, which included Precentral-L, Precentral gyrus, Parietal\_Inf-L, and Precuneus-L. More detailed information is shown in Figure 1 and Table 2. In the meantime, Figure 2 depicts the mean of changed spontaneous brain activity between PAT and HCs.

## ROC analysis

Due to the difference in fALFF values in some brain regions between PAT and SA, we wonder whether this discrepancy could be considered as a diagnostic criterion for SA, and thus we chose the receiver operating characteristic (ROC) curve as a common method to explore the diagnostic value of this difference. We focused on the area under the curve (AUC) of the ROC curve, because this indicator can simultaneously take sensitivity and specificity into account. We divided the accuracy into low (AUC0.5–0.7) and high (AUC0.7–0.9) levels to evaluate its diagnostic value more accurately. The AUC value is 0.745 for Temporal-Pole-Sup-L ( $p = 0.005$ ); 0.755 for Temporal-Mid-R ( $p = 0.003$ ); 0.887 for Frontal-Sup-R ( $p < 0.001$ ); 0.773 for Supp-Motor-Area-R ( $p = 0.002$ ); 0.69 for Precentral-L ( $p = 0.001$ ); 0.68 for Parietal-L ( $p < 0.001$ ); and 0.73 for Precuneus-L ( $P = 0.003$ ) (Figure 3).

## Correlation analysis

Mean fALFF values of temporal-pole-sup-L showed a negative correlation with log MAR ( $r = -0.665$ ,  $p = 0.001$ ). Meanwhile, a familiar correlation was found between temporal-mid-R and HADS ( $r = -0.535$ ,  $p = 0.009$ ) (Figure 4).

## Discussion

### Analysis of the increased fALFF in children with SA

The superior temporal gyrus is associated with language comprehension (18), visual search (19), and other functions. The bilateral superior temporal gyrus and middle temporal gyrus are also known as the V5/MT area (visual area 5/middle temporal gyrus), and the functional connections in the hippocampus play an important role in visual memory (20). The V5/MT area is also the core area of the global motion perception (GMP) (21), that is, in a specific visual scene, the motion trajectory of a single element is integrated to form a comprehensive three-dimensional stimulus. In many diseases, there are certain pathological changes in the superior temporal gyrus, including schizophrenia (22), Alzheimer's disease (23), adult common exotropia (24) and unilateral acute open eye injury (25). Wang et al. (26) found that the thickness of the intra cellular in the V5/MT area of patients with high intraocular pressure glaucoma was reduced, which may be related to the decrease in the high intraocular pressure and visual stimulation caused by the disease (27, 28). The study of Cai et al. (29) showed that the stimulation of the V5/MT area may cause the subjects to discriminate the overall direction of movement. Like this result, the increase in the fALFF value in this experiment indicates that the V5/MT area of SA patients is overactive, which may be related to the compensatory overestimation of this area caused by the obstacle of SA patients' judgment of spatial location.

The frontal lobe is one of the main functional areas of the cerebral hemisphere, and there are aberrant immunological changes in the superior frontal gyrus in many ophthalmological diseases. Huang et al. (30) showed that the ALFF value of the superior frontal gyrus of patients with primary angle-closure glaucoma (POAG) decreased, and the increase in the ALFF value of the superior frontal gyrus was also discovered in

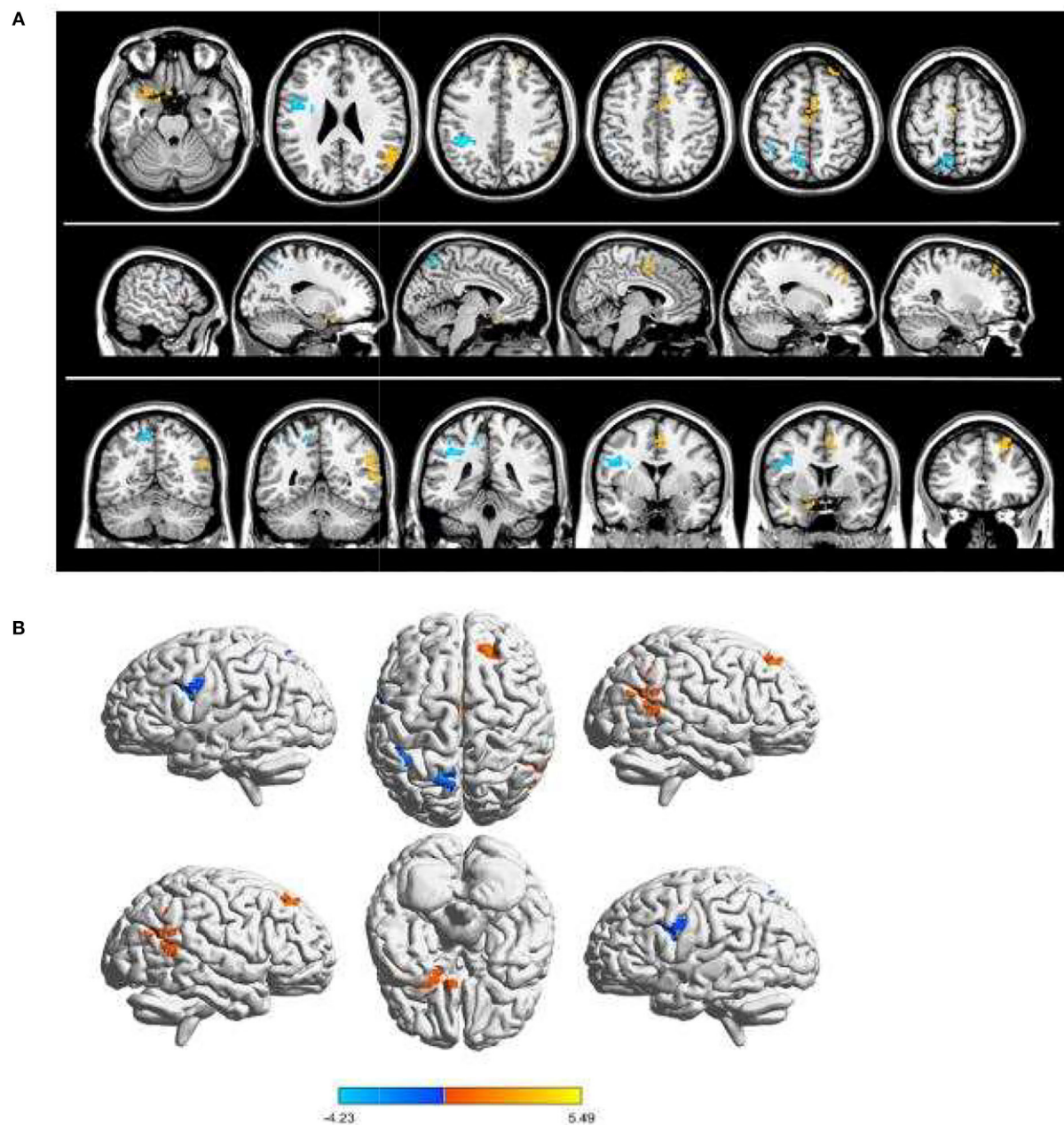


**FIGURE 1**  
Spontaneous brain activity in children and HCs. **(A)** The brain regions presented sensible differences in fALFF values between SA and HCs. **(B)** Children with SA would be observed some abnormal brain activities in specific regions. Compared with HCs, red regions trend to mean higher fALFF values. Regions marked by blue presented delegated regions presenting decreased fALFF values. fALFF, fractional amplitude of low-frequency fluctuation; HCs, healthy controls; SA, strabismus and amblyopia.

patients with corneal ulcer (31). Adults with SA also showed that the ALFF on the right forehead is worth increasing (6). This phenomenon may be due to the frontal eye field (FEF) (23, 32) formed by the autophagy of the frontal gyrus, which is related to saccade movement, visual perception (32),

and pain (33). In this study, children with strabismus and amblyopia also showed an increase in the fALFF value of the right superior frontal gyrus, suggesting that compared with HCs, the spontaneous activities of the right superior frontal gyrus of PAT were more active and caused eye



TABLE 2 Brain regions with significant differences in fALFF between PAT and HC groups.

| Brain areas         | MNI coordinates |     |     | fALFF |             |         | ROI sequence |
|---------------------|-----------------|-----|-----|-------|-------------|---------|--------------|
|                     | X               | Y   | Z   | BA    | Peak voxels | t-value |              |
| HCs>PAT             |                 |     |     |       |             |         |              |
| Temporal_Pole_Sup_L | −15             | 9   | −24 | 47    | 77          | 3.28    | Cluster 1    |
| Temporal_Mid_R      | 60              | −51 | 9   | 22    | 89          | 3.54    | Cluster 3    |
| Frontal_Sup_R       | 21              | 33  | 45  | 8     | 65          | 5.49    | Cluster 5    |
| Supp_Motor_Area_R   | 3               | 0   | 54  | 6     | 59          | 3.37    | Cluster 6    |
| HCs<PAT             |                 |     |     |       |             |         |              |
| Precentral_L        | −30             | −3  | 21  | 6     | 99          | −4.23   | Cluster 2    |
| Parietal_Inf_L      | −39             | −39 | 39  | 40    | 64          | −4.16   | Cluster 4    |
| Precuneus_L         | −9              | −60 | 60  | 7     | 66          | −3.2    | Cluster 7    |

$\alpha = 0.05$  for multiple comparisons through Gaussian random field theory ( $z > 2.3$ ,  $p < 0.01$ , cluster size  $> 40$  voxels, alphasim corrected).

PAT, patients; HCs, healthy controls; MNI, Montreal Neurological Institute; BA, Brodmann area; ROI, region of interest; L, left; R, right; Temporal-Pole-Sup, Temporal pole: superior temporal gyrus; Temporal-Mid, middle temporal gyrus; Frontal-Sup, superior frontal gyrus; Supp-Motor-Area, supplementary motor area; Precentral, precentral gyrus; Parietal\_Inf, inferior parietal, but supramarginal and angular gyri.

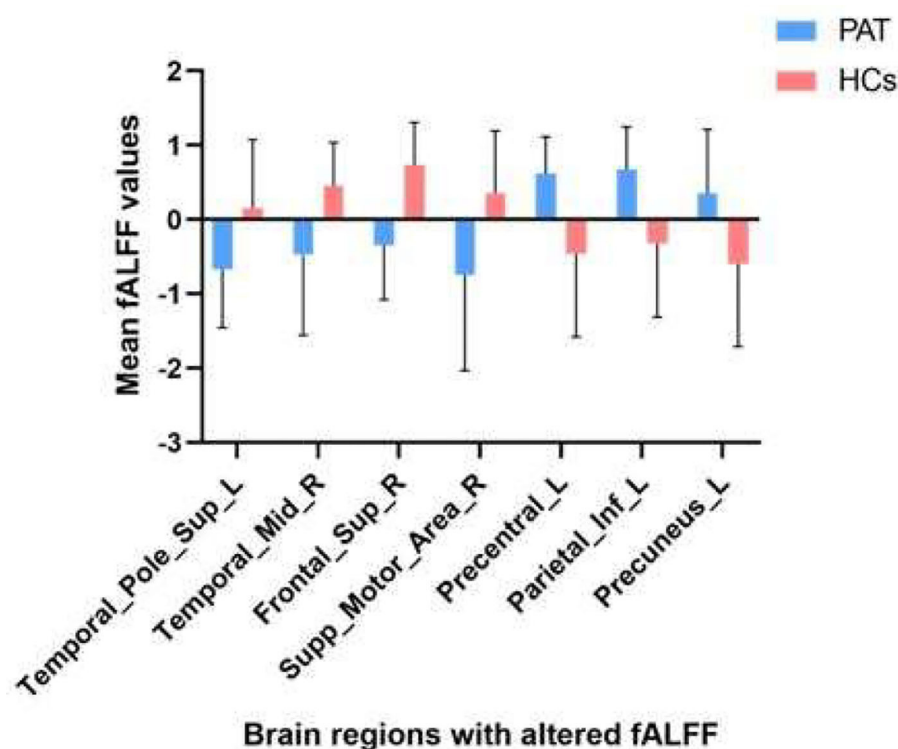


FIGURE 2  
The mean fALFF values between children with SA and HCs.

movement disorders and vision problems in patients with SA. The ability to receive and integrate stimuli decreases as the outcome of compensatory hyperfunction of the superior frontal gyrus.

The supplementary motor area (SMA) includes a part of the side of Brodmann 6 and 8. The anterior extremity is the

supplementary eye-field (SEF) and is next to the supplementary sensory area. Stimulating SEF under laboratory conditions could cause eye movement and combined eye movement (34). It shows that spontaneous brain activities of SEF could be detected before the movement of the unilateral eyeball (35), and there will be SMA activation after showing the intention to

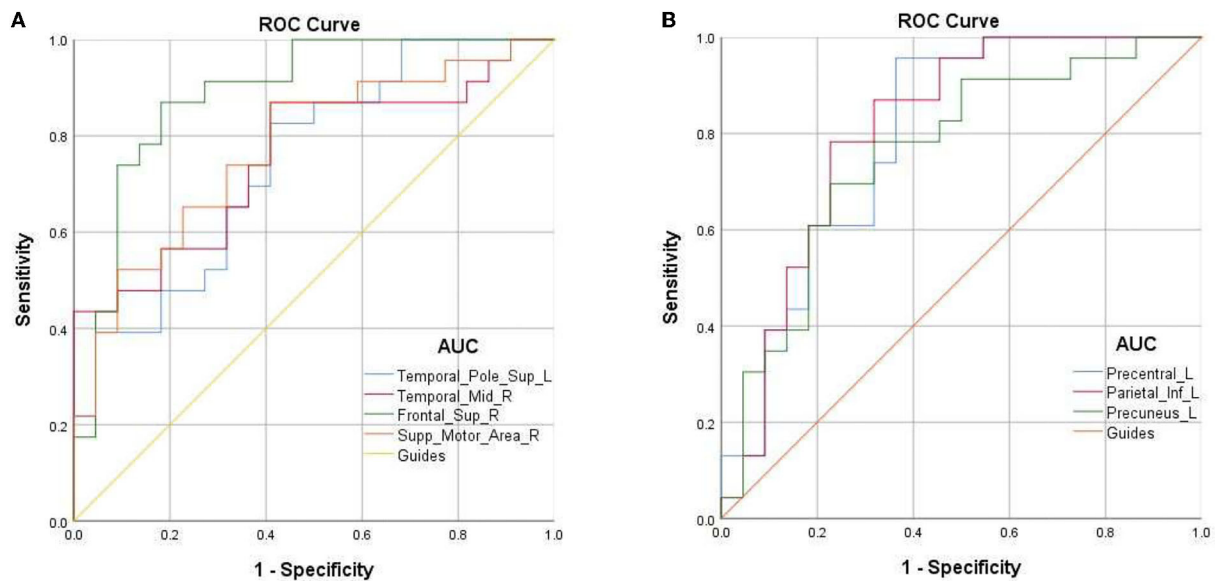


FIGURE 3

ROC curve analysis for the mean fALFF values of altered brain regions. (A) The area under ROC curve was 0.745 for Temporal-Pole-Sup-L ( $p = 0.005$ , 95%CI:0.603–0.887); 0.755 for Temporal-Mid-R ( $p = 0.003$ , 95%CI:0.621–0.898); 0.887 for Frontal-Sup-R ( $p < 0.001$ , 95%CI: 0.787–0.988); 0.773 for Supp-Motor-Area-R ( $p = 0.002$ , 95%CI: 0.635–0.910). (B) The area under ROC curve was 0.69 for Precentral-L ( $p = 0.001$ , 95%CI:0.659–0.930); 0.68 for Parietal-L ( $p < 0.001$ , 95%CI: 0.675–0.941); 0.73 for Precuneus-L ( $p = 0.003$ , 95%CI: 0.616–0.902).

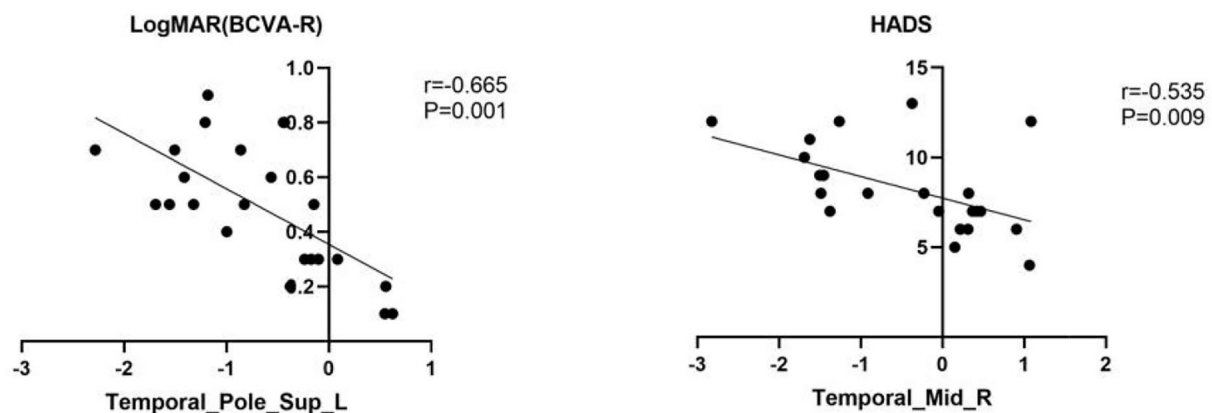


FIGURE 4

The result of correlation analysis. The values of LogMAR(BCVA-R) of PAT presented a significant correlation with the fALFF values of Temporal-Pole-Sup-L. The scores of HADS showed a negative correlation with fALFF values of temporal\_mid\_R ( $r = -0.535$ ,  $p = 0.009$ ).

change the existing combined eye movement state (36). Discrete lesions of SEF and SMA can cause abnormal eye movements in patients (37). In addition, activation of SMA can also be observed in sequence learning (38). Studies believe that this activation is explained by the visual cues and responses required during the learning process (39). At present, it is believed that the post-spinal inhibition of the supplemental exercise

area involved in exercise is closely connected with diseases such as Parkinson's disease (40). The SMA area, especially the SEF area, is closely connected with the movement of the eyeball. In this study, we found that there is a decrease in fALFF value in the SMA area in children with SA, which may indicate that in the early stages of the course of strabismus in children, there is a functional compensation in

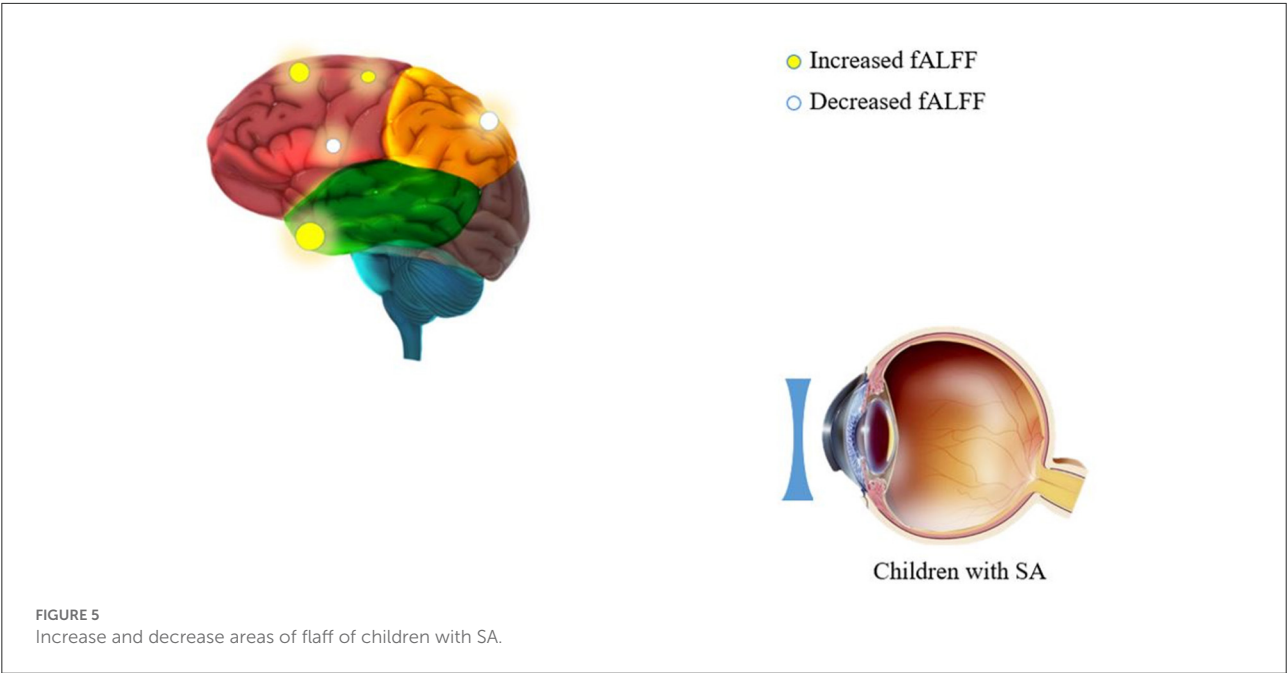


TABLE 3 The function of brain regions with altered fALFF values and its clinical significance.

| Brain region        | Experiment result | Function  | Anticipated results   |
|---------------------|-------------------|---|---|
| Temporal-Pole-Sup-L | HC>PAT            | Auditognosis; Language; emotion processing  | Depression; anxiety; visual impairment                      |
| Temporal-Mid-R      | HC>PAT            | Forming DMN; recognition and processing of color and shape                              | Depression; anxiety   |
| Frontal-Sup-R       | HC>PAT            | Memory; processing of cognitive information   | Damaged spatial cognitive ability and eye-hand coordination |
| Supp-Motor-Area-R   | HC>PAT            | Action inhibition; modulating interhemispheric interactions                             | Epilepsy; depression; motor neglect                         |
| Precentral-L        | HC<PAT            | Somatic movement controlling  | Damaged visual function                                     |
| Parietal-Inf-L      | HC<PAT            | Part of DMN; Advanced cognitive function  | Depression; anxiety   |
| Precuneus-L         | HC<PAT            | Visuospatial imagery; attention; episodic memory; Functional core of DMN; consciousness | Pain felling; dysfunction of spatial orientation            |

PAT, patient; HC, healthy controls; DMN, default-mode network.

this brain area due to abnormal eye movements, thus showing unusually active.

Analysis of the decreased fALFF in PAT

The precentral gyrus is part of the primary motor cortex (41), which receives proprioception and regulates autonomous movement. Studies have found that in many ophthalmological diseases, changes in the structure and function of the precentral can be observed. Huang et al. (30) found that the ALFF value of

precentral in PACG patients decreased, and analogously, Chan et al. (42) showed that the gray matter volume (GMV) of the right precentral gyrus was increased in patients with strabismus. The study by Lin et al. (43) observed more active spontaneous brain activities in the precentral gyrus in anisometropia patients. Those conclusions are in agreement with the results of our study, suggesting that children with SA have spontaneous eye movement disorders.

The parietal lobe is related to higher cognitive functions and thinking processing (44), while the inferior parietal lobules are thought to be related to the oculomotor

nerve, the forming and maintaining of attention, hand-eye coordination recalibration (45), and language learning in real life (46). Meanwhile, it was also reported to be greatly helpful to choose information, which is related to visual space (47). In this study, the fALFF value of the inferior parietal reduced, which may be related to the abnormal ocular function increasing the obstacles of language learning in children, leading to the lack of reading and spelling ability.

The default mode network (DMN) refers to a functional network composed of brain regions that are spatially separated but show a high degree of temporal correlation at rest. DMN involves numerous brain regions, including the subcortical region of the parietal lobe, middle frontal gyrus, frontal gyrus, and precuneus (48).

The precuneus plays an essential role in DMN and participates in the formation of optical network pathways. It also plays an irreplaceable role in the visual spatial imaging (49), self-processing (50), episodic memory extraction (51), spatial position coding (52), etc. We reviewed the studies of other researchers and found that many eye diseases have been observed to change the structure or connection function and spontaneous activity of the precuneus. In patients with binocular blindness, the volume of local gray matter in the precuneus boils down (17). Further studies have shown that in normal-tension glaucoma (53), diabetic retinopathy (54), primary angle-closure glaucoma (30), and other diseases, the precuneus shows spontaneous reduction of brain activity, which is consistent with our research. The conclusions are the same, and the results of the study are also consistent with the clinical manifestations of SA children with eye movement disorders and abnormal visual spatial imaging. However, Tan et al. (55) found that with withdrawnness lobe injury (OGI), the ALFF value associated with recuneus was increased, which was negatively related to the duration of OGI. This result strongly suggested that in the primary stage of eye injury, the damage will be compensated by more vigorous spontaneous brain activities of the precuneus. However, as the course of the disease continues, this compensatory effect may be lowered. This hypothesis can also explain the consequences of some parallel studies that are contrary to the results of our study (30).

In addition, due to the superficial anatomical position of the eyes, it is not difficult to notice in daily life and interpersonal communication. Therefore, some scholars believe that strabismus is actually a cosmetic disease (4), and childhood is an important period of character formation and interpersonal communication. Therefore, congenital SA may influence the physical and mental health of children. Studies have proved that SA may cause patients to feel destructive emotions such as low self-esteem and anxiety (56). In our study, the HADS was used for evaluating the anxiety of children, and it was found that the HADS score of SA patients was negatively correlated

with the spontaneous brain activity of the middle temporal gyrus. This anxiety may be secondary to the decreased activity of the middle temporal gyrus area in SA disease, or it may be attributable to the disease making children become unconfident and anxious in everyday life and social activities (Figure 3 and Table 3).

It should be noted in particular that there are still some limitations in this study, including (1) samples included in the study are not adequate; (2) the subjects were younger, and there may be a low degree of coordination in the process of fMRI examination; and (3) mixed bias is unavoidable.

## Conclusion

In this study, we found that children with SA presented abnormal spontaneous brain activities in the visual pathway or visual-related brain regions. These abnormal spontaneous activities may impact on the patient's clinical manifestations or be attributed to compensatory eye movement dysfunction. Besides, correlation analysis also showed that SA in childhood may cause undesirable emotions in patients.

## Data availability statement

The raw data supporting the conclusions of this article will be made available by the authors, without undue reservation.

## Ethics statement

The studies involving human participants were reviewed and approved by the committee of the medical ethics of the First Affiliated Hospital of Nanchang University. The patients/participants provided their written informed consent to participate in this study.

## Author contributions

X-QH, Y-DS, and JC were major contributors, conceived and designed the experiments, analyzed the data, and wrote and revised the manuscript. ZY, Y-CP, QL, HW, and JZ recruited the patients and healthy controls for the study and performed the MRI experiments. PY, X-LL, TS, and Y-XW collected and treated the data. YS designed the study and obtained financial support. All the authors read and approved the final manuscript.

## Funding

National Natural Science Foundation (No: 82160195); Central Government Guides Local Science and Technology



Development Foundation (No: 20211ZDG02003); Key Research Foundation of Jiangxi Province (Nos: 20181BBG70004 and 20203BBG73059).

## Conflict of interest

The authors declare that the research was conducted in the absence of any commercial or financial relationships that could be construed as a potential conflict of interest.

## References

- Sloper J. The other side of amblyopia. *JAAPOS*. (2016) 20:1. doi: 10.1016/j.jaaapos.2015.09.013
- Roider L, Ungerer G, Shock L, Aldridge K, Al-Samarraie M, Tanaka T, et al. Increased incidence of ophthalmologic findings in children with concurrent isolated non-syndromic metopic suture abnormalities and deformational cranial vault asymmetry. *Cleft Palate Craniofac J*. (2021) 58:497–504. doi: 10.1177/1055665620954739
- Wallace DK, Christiansen SP, Sprunger DT, Melia M, Lee KA, Morse CL, et al. Esotropia and exotropia preferred practice pattern(R). *Ophthalmology*. (2018) 125:P143–83. doi: 10.1016/j.ophtha.2017.10.007
- Menon V, Saha J, Tandon R, Mehta M, Khokhar S. Study of the psychosocial aspects of strabismus. *J Pediatr Ophthalmol Strabismus*. (2002) 39:203–8. doi: 10.3928/0191-3913-20020701-07
- Shao Y, Li QH, Li B, Lin Q, Su T, Shi WQ, et al. Altered brain activity in patients with strabismus and amblyopia detected by analysis of regional homogeneity: a resting state functional magnetic resonance imaging study. *Mol Med Rep*. (2019) 19:4832–40. doi: 10.3892/mmr.2019.10147
- Min YL, Su T, Shu YQ, Liu WF, Chen LL, Shi WQ, et al. Altered spontaneous brain activity patterns in strabismus with amblyopia patients using amplitude of low-frequency fluctuation: a resting-state fMRI study. *Neuropsychiatr Dis Treat*. (2018) 14:2351–2359. doi: 10.2147/NDT.S171462
- Joly O, Franko E. Neuroimaging of amblyopia and binocular vision: a review. *Front Integr Neurosci*. (2014) 8:62. doi: 10.3389/fnint.2014.00062
- Bullmore E, Sporns O. Complex brain networks: graph theoretical analysis of structural and functional systems. *Nat Rev Neurosci*. (2009) 10:186–198. doi: 10.1038/nrn2575
- Maknojia S, Churchill NW, Schweizer TA, Graham SJ. Resting state fMRI: going through the motions. *Front Neurosci*. (2019) 13:825. doi: 10.3389/fnins.2019.00825
- Zang YF, He Y, Zhu CZ, Cao QJ, Sui MQ, Liang M, et al. Altered baseline brain activity in children with ADHD revealed by resting-state functional MRI. *Brain Dev*. (2007) 29:83–91. doi: 10.1016/j.braindev.2006.07.002
- Shmuel A, Leopold DA. Neuronal correlates of spontaneous fluctuations in fMRI signals in monkey visual cortex: implications for functional connectivity at rest. *Hum Brain Mapp*. (2008) 29:751–761. doi: 10.1002/hbm.20580
- Jiang GH, Qiu YW, Zhang XL, Han LJ, Lv XF, Li LM, et al. Amplitude low-frequency oscillation abnormalities in the heroin users: a resting state fMRI study. *Neuroimage*. (2011) 57:149–154. doi: 10.1016/j.neuroimage.2011.04.004
- Wang ZL, Zou L, Lu ZW, Xie XQ, Jia ZZ, Pan CJ, et al. Abnormal spontaneous brain activity in type 2 diabetic retinopathy revealed by amplitude of low-frequency fluctuations: a resting-state fMRI study. *Clin Radiol*. (2017) 72:340–341. doi: 10.1016/j.crad.2016.11.012
- Bruner E, Preuss TM, Chen X, Rilling JK. Evidence for expansion of the precuneus in human evolution. *Brain Struct Funct*. (2017) 222:1053–1060. doi: 10.1007/s00429-015-1172-y
- Ye Q, Zou F, Lau H, Hu Y, Kwok SC. Causal evidence for mnemonic metacognition in human precuneus. *J Neurosci*. (2018) 38:6379–6387. doi: 10.1523/JNEUROSCI.0660-18.2018
- Cavanna AE. The precuneus and consciousness. *CNS Spectr*. (2007) 12:545–552. doi: 10.1017/s1092852900021295
- Wan CY, Wood AG, Chen J, Wilson SJ, Reutens DC. The influence of preterm birth on structural alterations of the vision-deprived brain. *Cortex*. (2013) 49:1100–9. doi: 10.1016/j.cortex.2012.03.013
- Bigler ED, Mortensen S, Neeley ES, Ozonoff S, Krasny L, Johnson M, et al. Superior temporal gyrus, language function, and autism. *Dev Neuropsychol*. (2007) 31:217–238. doi: 10.1080/87565640701190841
- Gharabaghi A, Fruhmman BM, Tatagiba M, Karnath HO. The role of the right superior temporal gyrus in visual search—insights from intraoperative electrical stimulation. *Neuropsychologia*. (2006) 44:2578–81. doi: 10.1016/j.neuropsychologia.2006.04.006
- Murray EA, Mishkin M. Severe tactual as well as visual memory deficits follow combined removal of the amygdala and hippocampus in monkeys. *J Neurosci*. (1984) 4:2565–80. doi: 10.1523/JNEUROSCI.04-10-02565.1984
- Chen N, Cai P, Zhou T, Thompson B, Fang F. Perceptual learning modifies the functional specializations of visual cortical areas. *Proc Natl Acad Sci U S A*. (2016) 113:5724–9. doi: 10.1073/pnas.1524160113
- Kasai K, Shenton ME, Salisbury DF, Hirayasu Y, Onitsuka T, Spencer MH, et al. Progressive decrease of left Heschl gyrus and planum temporale gray matter volume in first-episode schizophrenia: a longitudinal magnetic resonance imaging study. *Arch Gen Psychiatry*. (2003) 60:766–75. doi: 10.1001/archpsyc.60.8.766
- Watson CT, Roussos P, Garg P, Ho DJ, Azam N, Katsel PL, et al. Genome-wide DNA methylation profiling in the superior temporal gyrus reveals epigenetic signatures associated with Alzheimer's disease. *Genome Med*. (2016) 8:5. doi: 10.1186/s13073-015-0258-8
- Tan G, Dan ZR, Zhang Y, Huang X, Zhong YL, Ye LH, et al. Altered brain network centrality in patients with adult comitant exotropia strabismus: a resting-state fMRI study. *J Int Med Res*. (2018) 46:392–402. doi: 10.1177/0300060517715340
- Huang X, Li HJ, Ye L, Zhang Y, Wei R, Zhong YL, et al. Altered regional homogeneity in patients with unilateral acute open-globe injury: a resting-state functional MRI study. *Neuropsychiatr Dis Treat*. (2016) 12:1901–6. doi: 10.2147/NDT.S110541
- Wang Y, Wang X, Zhou J, Qiu J, Yan T, Xie Y, et al. Brain morphological alterations of cerebral cortex and subcortical nuclei in high-tension glaucoma brain and its associations with intraocular pressure. *Neuroradiology*. (2020) 62:495–502. doi: 10.1007/s00234-019-02347-1
- Li C, Cai P, Shi L, Lin Y, Zhang J, Liu S, et al. Voxel-based morphometry of the visual-related cortex in primary open angle glaucoma. *Curr Eye Res*. (2012) 37:794–802. doi: 10.3109/02713683.2012.683506
- Yu L, Xie B, Yin X, Liang M, Evans AC, Wang J, et al. Reduced cortical thickness in primary open-angle glaucoma and its relationship to the retinal nerve fiber layer thickness. *PLoS ONE*. (2013) 8:e73208. doi: 10.1371/journal.pone.0073208
- Cai P, Chen N, Zhou T, Thompson B, Fang F. Global versus local: double dissociation between MT+ and V3A in motion processing revealed using continuous theta burst transcranial magnetic stimulation. *Exp Brain Res*. (2014) 232:4035–41. doi: 10.1007/s00221-014-4084-9
- Huang X, Zhong YL, Zeng XJ, Zhou F, Liu XH, Hu PH, et al. Disturbed spontaneous brain activity pattern in patients with primary angle-closure glaucoma using amplitude of low-frequency fluctuation: a fMRI study. *Neuropsychiatr Dis Treat*. (2015) 11:1877–83. doi: 10.2147/NDT.S87596

## Publisher's note

All claims expressed in this article are solely those of the authors and do not necessarily represent those of their affiliated organizations, or those of the publisher, the editors and the reviewers. Any product that may be evaluated in this article, or claim that may be made by its manufacturer, is not guaranteed or endorsed by the publisher.

31. Shi WQ, Wu W, Ye L, Jiang N, Liu WF, Shu YQ, et al. Altered spontaneous brain activity patterns in patients with corneal ulcer using amplitude of low-frequency fluctuation: an fMRI study. *Exp Ther Med.* (2019) 18:125–132. doi: 10.3892/etm.2019.7550
32. Paus T. Location and function of the human frontal eye-field: a selective review. *Neuropsychologia.* (1996) 34:475–83. doi: 10.1016/0028-3932(95)00134-4
33. Obermann M, Rodriguez-Raecke R, Naegel S, Holle D, Mueller D, Yoon MS, et al. Gray matter volume reduction reflects chronic pain in trigeminal neuralgia. *Neuroimage.* (2013) 74:352–358. doi: 10.1016/j.neuroimage.2013.02.029
34. Martinez-Trujillo JC, Medendorp WP, Wang H, Crawford JD. Frames of reference for eye-head gaze commands in primate supplementary eye fields. *Neuron.* (2004) 44:1057–66. doi: 10.1016/j.neuron.2004.12.004
35. Schlag J, Schlag-Rey M. Evidence for a supplementary eye field. *J Neurophysiol.* (1987) 57:179–200. doi: 10.1152/jn.1987.57.1.179
36. Li CS, Huang C, Constable RT, Sinha R. Imaging response inhibition in a stop-signal task: neural correlates independent of signal monitoring and post-response processing. *J Neurosci.* (2006) 26:186–192. doi: 10.1523/JNEUROSCI.3741-05.2006
37. Nachev P, Kennard C, Husain M. Functional role of the supplementary and pre-supplementary motor areas. *Nat Rev Neurosci.* (2008) 9:856–69. doi: 10.1038/nrn2478
38. Hikosaka O, Sakai K, Miyauchi S, Takino R, Sasaki Y, Putz B. Activation of human pre-supplementary motor area in learning of sequential procedures: a functional MRI study. *J Neurophysiol.* (1996) 76:617–621. doi: 10.1152/jn.1996.76.1.617
39. Sakai K, Hikosaka O, Miyauchi S, Sasaki Y, Fujimaki N, Putz B. Presupplementary motor area activation during sequence learning reflects visuo-motor association. *J Neurosci.* (1999) 19:C1.
40. Botzel K, Schulze S. Self-initiated versus externally triggered movements. I. An investigation using measurement of regional cerebral blood flow with PET and movement-related potentials in normal and Parkinson's disease subjects. *Brain.* (1996) 119 (Pt 3):1045–8. doi: 10.1093/brain/119.3.1045
41. Binkofski F, Fink GR, Geyer S, Buccino G, Gruber O, Shah NJ, et al. Neural activity in human primary motor cortex areas 4a and 4p is modulated differentially by attention to action. *J Neurophysiol.* (2002) 88:514–9. doi: 10.1152/jn.2002.88.1.514
42. Chan ST, Tang KW, Lam KC, Chan LK, Mendola JD, Kwong KK. Neuroanatomy of adult strabismus: a voxel-based morphometric analysis of magnetic resonance structural scans. *Neuroimage.* (2004) 22:986–994. doi: 10.1016/j.neuroimage.2004.02.021
43. Lin X, Ding K, Liu Y, Yan X, Song S, Jiang T. Altered spontaneous activity in an isometric amblyopia subjects: revealed by resting-state FMRI. *PLoS ONE.* (2012) 7:e43373. doi: 10.1371/journal.pone.0043373
44. Catani M, Robertsson N, Beyh A, Huynh V, de Santiago RF, Howells H, et al. Short parietal lobe connections of the human and monkey brain. *Cortex.* (2017) 97:339–357. doi: 10.1016/j.cortex.2017.10.022
45. Clower DM, West RA, Lynch JC, Strick PL. The inferior parietal lobule is the target of output from the superior colliculus, hippocampus, and cerebellum. *J Neurosci.* (2001) 21:6283–91. doi: 10.1523/JNEUROSCI.21-16-06283.2001
46. Sliwinska MW, James A, Devlin JT. Inferior parietal lobule contributions to visual word recognition. *J Cogn Neurosci.* (2015) 27:593–604. doi: 10.1162/jocn\_a\_00721
47. Egnér T, Monti JM, Trittschuh EH, Wieneke CA, Hirsch J, Mesulam MM. Neural integration of top-down spatial and feature-based information in visual search. *J Neurosci.* (2008) 28:6141–6151. doi: 10.1523/JNEUROSCI.1262-08.2008
48. Liu Y, Li L, Li B, Feng N, Li L, Zhang X, et al. Decreased triple network connectivity in patients with recent onset post-traumatic stress disorder after a single prolonged trauma exposure. *Sci Rep.* (2017) 7:12625. doi: 10.1038/s41598-017-12964-6
49. Cavanna AE, Trimble MR. The precuneus: a review of its functional anatomy and behavioral correlates. *Brain.* (2006) 129:564–83. doi: 10.1093/brain/awl004
50. Nagahama Y, Okada T, Katsumi Y, Hayashi T, Yamauchi H, Sawamoto N, et al. Transient neural activity in the medial superior frontal gyrus and precuneus time locked with attention shift between object features. *Neuroimage.* (1999) 10:193–9. doi: 10.1006/nimg.1999.0451
51. Lundström BN, Ingvar M, Petersson KM. The role of precuneus and left inferior frontal cortex during source memory episodic retrieval. *Neuroimage.* (2005) 27:824–34. doi: 10.1016/j.neuroimage.2005.05.008
52. Frings L, Wagner K, Quiske A, Schwarzwald R, Spreer J, Halsband U, et al. Precuneus is involved in allocentric spatial location encoding and recognition. *Exp Brain Res.* (2006) 173:661–72. doi: 10.1007/s00221-006-0408-8
53. Li HL, Chou XM, Liang Y, Pan T, Zhou Q, Pei CG, et al. Use of rsfMRI-fALFF for the detection of changes in brain activity in patients with normal-tension glaucoma. *Acta Radiol.* (2021) 62:414–22. doi: 10.1177/0284185120926901
54. Wang Y, Shao Y, Shi WQ, Jiang L, Wang XY, Zhu PW, et al. The predictive potential of altered spontaneous brain activity patterns in diabetic retinopathy and nephropathy. *EPMA J.* (2019) 10:249–59. doi: 10.1007/s13167-019-00171-4
55. Tan G, Huang X, Ye L, Wu AH, He LX, Zhong YL, et al. Altered spontaneous brain activity patterns in patients with unilateral acute open globe injury using amplitude of low-frequency fluctuation: a functional magnetic resonance imaging study. *Neuropsychiatr Dis Treat.* (2016) 12:2015–20. doi: 10.2147/NDT.S110539
56. Wang CW, Chan CL, Jin HY. Psychometric properties of the Chinese version of the 25-item national eye institute visual function questionnaire. *Optom Vis Sci.* (2008) 85:1091–9. doi: 10.1097/OPX.0b013e31818b9f23
57. Buffenn AN. The impact of strabismus on psychosocial health and quality of life: A systematic review. *Surv Ophthalmol.* (2021) 66:1051–64. doi: 10.1016/j.survophthal.2021.03.005



## OPEN ACCESS

## EDITED BY

Yuzhen Xu,  
Tongji University, China

## REVIEWED BY

Xiang Xiang,  
Chongqing Three Gorges Central  
Hospital, China  
Beike Chen,  
Army Medical University, China  
Yuqi Chen,  
958 Hospital of the People's Liberation  
Army, China  
Ajay Hegde,  
NHS Greater Glasgow and Clyde,  
United Kingdom

## \*CORRESPONDENCE

Mingliang Hu  
humingliang100@163.com

## SPECIALTY SECTION

This article was submitted to  
Neurological Biomarkers,  
a section of the journal  
Frontiers in Neurology

RECEIVED 07 June 2022

ACCEPTED 25 July 2022

PUBLISHED 22 August 2022

## CITATION

Zhao Y, Xie Y, Li S and Hu M (2022) The  
predictive value of neutrophil to  
lymphocyte ratio on 30-day outcomes  
in spontaneous intracerebral  
hemorrhage patients after surgical  
treatment: A retrospective analysis of  
128 patients. *Front. Neurol.* 13:963397.  
doi: 10.3389/fneur.2022.963397

## COPYRIGHT

© 2022 Zhao, Xie, Li and Hu. This is an  
open-access article distributed under  
the terms of the [Creative Commons  
Attribution License \(CC BY\)](#). The use,  
distribution or reproduction in other  
forums is permitted, provided the  
original author(s) and the copyright  
owner(s) are credited and that the  
original publication in this journal is  
cited, in accordance with accepted  
academic practice. No use, distribution  
or reproduction is permitted which  
does not comply with these terms.

# The predictive value of neutrophil to lymphocyte ratio on 30-day outcomes in spontaneous intracerebral hemorrhage patients after surgical treatment: A retrospective analysis of 128 patients

Yiqin Zhao<sup>1,2,3</sup>, Yanfeng Xie<sup>2</sup>, Shengjie Li<sup>3</sup> and Mingliang Hu<sup>1,3\*</sup>

<sup>1</sup>The First Clinical Medical School, Chongqing Medical University, Chongqing, China, <sup>2</sup>Department of Neurosurgery, The First Affiliated Hospital of Chongqing Medical University, Chongqing, China, <sup>3</sup>Department of Neurosurgery, Dianjiang People's Hospital of Chongqing, Chongqing, China

**Objective:** The purpose of this study was to explore the predictive value of the neutrophil-to-lymphocyte ratio (NLR) on 30-day outcomes in patients with spontaneous intracerebral hemorrhage (ICH) after surgical treatment.

**Methods:** This retrospective study utilized data from patients with ICH who underwent craniotomy or minimally invasive puncture and drainage (MIPD) between January 2015 and June 2021. The patients meeting the inclusion criteria were divided into two groups according to 30-day outcomes, namely, the favorable outcome group and the poor outcome group. Sex, age, time from onset to admission, vital signs at admission, admission Glasgow Coma Scale (GCS) score, diabetes mellitus, hypertension, hematoma volume, hematoma location, surgical approach, and NLR at different time points were all recorded and analyzed.

**Results:** A total of 128 patients were finally enrolled in this study, including 32 and 96 patients in the favorable outcome group and the poor outcome group, respectively. During the course of ICH, the changing trend of NLR was to increase first and then decrease and peaked within 48 h after surgery. In the univariate analysis, systolic blood pressure, admission GCS score, hematoma volume, surgical approach, and NLR within 48 h after surgery were statistically significant. In the multivariable analysis, NLR within 48 h after surgery (odds ratio [OR] = 1.342,  $p < 0.001$ ) was an independent risk factor of the 30-day outcomes in patients with ICH after surgical treatment. The receiver operating characteristic (ROC) analysis showed that the best predictive cut-off value for NLR within 48 h after surgery was 12.35 [sensitivity 82.9%, specificity 81.8%, and area under the curve (AUC) 0.877] and 14.46 (sensitivity 55.1%, specificity 87.5%, and area under the curve 0.731) for the MIPD group and the craniotomy group, respectively.

**Conclusions:** In the process of ICH, the value of NLR was increased first and then decreased and peaked within 48 h after surgery. NLR within 48 h after surgery was an independent risk factor of the 30-day outcomes in patients with ICH. The peak NLR >12.35 or 14.46 in patients receiving MIPD or craniotomy reflected a poor prognosis, respectively.

#### KEYWORDS

neutrophil-to-lymphocyte ratio, spontaneous intracerebral hemorrhage, craniotomy, minimally invasive puncture and drainage, prognosis

## Introduction

Spontaneous (non-traumatic) intracranial hemorrhage (ICH) is a fatal illness with a high risk of morbidity and mortality of global importance, which affects approximately 2 million people in the world each year (1). Some of these patients require timely surgical management and the prognosis of patients with ICH after a surgery is of great concern for both neurosurgeons and patients. However, there are several different shortcomings in the current prognostic indicators for patients with ICH who have received surgery (2).

The neutrophil-to-lymphocyte ratio (NLR) has emerged as a potential and readily available inflammation indicator and has played an increasingly important role in many clinical contexts, such as glioma, infective endocarditis, colorectal cancer, and acute ischemic stroke (3–6). Since the inflammatory response is involved in the secondary brain injury following ICH (7), NLR, a marker of inflammation, may be an indicator of prognosis for patients with ICH. Recent evidence suggested that NLR is a more convincing indicator of inflammation than other markers (8) and is closely associated with 30 and 90-day outcomes in patients with ICH (9, 10). However, as an important part of treatment, surgery was not considered in these studies. Surgical treatment may prevent hematoma expansion, block the release of inflammatory products from hematomas, and thus intervene in the pathological processes after disease onset (11). Several studies reported that NLR was independently associated with a 90-day poor outcome and 30-day mortality of patients with ICH after hematoma evacuation (12, 13). However, these studies neglected the severity of the brain tissue damage caused by different surgical. The prognostic value and trend of NLR in different surgical methods are also not clear.

The aim of this study was to analyze the variation rule of NLR and evaluate the relationship between NLR and short-term prognosis of patients with ICH undergoing craniotomy and minimally invasive puncture and drainage (MIPD).

## Materials and methods

This study was approved by the Medical Ethics Review Committee of the First Affiliated Hospital of Chongqing Medical University and the Dianjiang People's Hospital of Chongqing. All participants provided written informed consent. The work has been reported in line with the Standards for Reporting of Diagnostic Accuracy Studies (STARD) criteria.

### Patient selection

This current retrospective study collected data from 128 patients with ICH treated with craniotomy or minimally invasive surgery at the First Affiliated Hospital of Chongqing Medical University and the Dianjiang People's Hospital of Chongqing from January 2015 to June 2021. Among them, 83 patients were from the First Affiliated Hospital of Chongqing Medical University and 45 patients were from the Dianjiang People's Hospital of Chongqing.

Inclusion criteria: (1) Patients over the age of 18 years; (2) patients diagnosed with spontaneous ICH confirmed by computed tomography (CT) scan within 24 h from symptoms ictus; and (3) patients who underwent either craniotomy or MIPD within 24 h of admission.

Exclusion criteria: (1) Patients who had an infection for 2 weeks; (2) patients who had comorbidity that might affect the value of NLR, such as cancer, autoimmune disease, hematological disease, chronic heart disease, and renal or liver diseases; (3) patients who had been treated with immunomodulatory treatments; (4) patients who had been evaluated as Glasgow Coma Scale (GCS) score  $\leq 5$  at admission, or disability before disease onset; (5) patients who had incomplete follow-up data; and (6) patients who

---

Abbreviations: NLR, neutrophil-to-lymphocyte ratio; ICH, spontaneous intracerebral hemorrhage; MIPD, minimally invasive puncture and drainage; GCS, Glasgow Coma Scale; ANC, absolute neutrophil count; ALC, absolute lymphocyte count; CT, computed tomography scan; ROC, receiver operating characteristic analysis; mRS, modified Rankin Scale score; IQR, interquartile range.



had the dissatisfied effect of the evacuation of hematoma or received re-operation.

## Preoperative management

All patients enrolled in the study were treated according to the guidelines of management from the American Heart Association/American Stroke and were divided into the craniotomy group and the MIPD group. When the patients arrived at the hospital, emergency CT was performed immediately to evaluate the size and location of the hematoma, diagnosing the level of consciousness was performed using GCS, and peripheral blood was collected for examination. The neurosurgical procedure for each patient was customized by experienced neurosurgeons based on the clinical conditions of patients with ICH at admission, including entry point, surgical approach, and bone window size.

## Surgery

### Craniotomy group

The patients in the craniotomy group underwent conventional craniotomy operations to clear the hematoma. The location of the bone window was determined according to the site of hematoma reflected by brain CT of the patient's preoperative condition. Once entering the hematoma cavity, suction and bipolar cautery were used to eliminate the hematoma as much as possible. A drainage tube was inserted into the hematoma cavity to prevent residual hematoma. Retaining bone flap or not for the craniotomy group was depended on the judgement of the neurosurgeon according to the intraoperative situation.

### MIPD group

According to the preoperative CT image, the puncture point was marked on the scalp and the puncture angle and catheter depth were planned. About 2% lidocaine was injected to anesthetize the skin around the puncture point. After the scalp was cut open with the puncture point as the center, the bone foramen was formed with an electric drill, and the stereotactic apparatus was installed and debugged. According to the puncture target, the hematoma was pricked by the used drainage tube according to the pre-designed direction and depth. After the bloody fluid flowed out, drainage gently with a syringe, the drainage tube was fixed and then connected with the drainage bag. After the patients of the MIPD group returned to the ward, they were injected with 10,000–20,000 units of urokinase/2–5 ml of saline solution to liquefy the hematoma for 1–2 times/day for 2–3 h.

## Postoperative care

The evacuation effect of hematoma was evaluated by brain CT every day after surgery. When the hematoma vanished or the remaining volume was <10 ml, the drainage tube was closed. After 24 h, the drainage tube was removed if the vital signs of the patient were steady and no increased intracranial pressure were observed. Peripheral blood samples were collected for examination at 7 a.m. every day after surgery. Follow-ups in the outpatient department or by telephone were performed at the 30-day functional outcome after diagnosis. The functional status at 30-days was evaluated for prognostic outcomes. A modified Rankin Scale score (mRS) was used to assess the prognosis of patients.

## Outcomes

We retrospectively collected demographic and clinical information of all patients enrolled in the current study from electronic medical records, such as demographic characteristics, vital signs at admission, Glasgow Coma Scale (GCS) score at admission, medical history of hypertension and diabetes, lifestyle history of smoking and/or drinking, hematoma volume, hematoma location (supratentorial or infratentorial hematoma), surgical approach (craniotomy or MIPD), and clinical laboratory tests.

Clinical laboratory tests included absolute neutrophil count (ANC) and absolute lymphocyte count (ALC) at admission, within 48 h after surgery and at 3–7 days after surgery. The NLR was calculated by the ratio of ANC to ALC at different time points. The hematoma characteristics were recorded within 24 h after admission based on brain CT, such as hemorrhage location (supratentorial or infratentorial hemorrhage) and volume [calculated using the ABC/2 software (14)], intraventricular hemorrhage, and subarachnoid hemorrhage.

The appearance of functional independence was defined as favorable outcome (mRS < 3), whereas dead or severely disabled were defined as a poor outcome (mRS ≥ 3) (15).

## Statistical analysis

The SPSS 25.0 (IBM Corporation, Armonk, New York, USA) and GraphPad Prism 9 (GraphPad Software, San Diego, California, USA) were used for statistical analysis and graph plotting, respectively. All continuous data are presented as median (interquartile range, IQR) and were analyzed using Student's *t*-test or the Mann–Whitney test, as appropriate. Categorical variables were expressed as frequency (percentage) and were analyzed using the chi-squared test. Baseline variables considered clinically relevant or showed a univariate

TABLE 1 Baseline characteristics related to the 30-day outcome in surgical patients with ICH.

| Characteristic                       | Total, (n = 128) | Favorable Outcome (n = 32) | Poor Outcome (n = 96) | P      |
|--------------------------------------|------------------|----------------------------|-----------------------|--------|
| Demographics                         |                  |                            |                       |        |
| Male, n (%)                          | 88(68.8%)        | 23(71.9%)                  | 65(67.7%)             | 0.660  |
| Age, IQR, Y                          | 60(50.0–67.0)    | 52(47.3–66.5)              | 62.5(51.3–67)         | 0.056  |
| Time from onset to admission, IQR, h | 3(2.0–8.75)      | 3.5(2–8)                   | 3(2–8.5)              | 0.958  |
| Vital signs at admission             |                  |                            |                       |        |
| Temperature, IQR, °C                 | 36.6(36.4–36.8)  | 36.6(36.3–36.7)            | 36.6(36.4–36.8)       | 0.571  |
| Heart rate, IQR, bpm                 | 80(71–90)        | 80(70–92)                  | 80(71–88)             | 0.643  |
| Respiratory rate, IQR, bpm           | 20(18–21)        | 20(18–21)                  | 20(18–21)             | 0.806  |
| Systolic blood pressure, IQR, mmHg   | 169(151–191)     | 161(143–177)               | 172(153–198)          | 0.032* |
| Diastolic blood pressure, IQR, mmHg  | 99(89–110)       | 96(90–110)                 | 99(88–110)            | 0.934  |
| Admission GCS score, IQR,            | 10(7–12)         | 10.5(9–13)                 | 9(7–11)               | 0.002* |
| Diabetes mellitus, n (%)             | 19(14.8%)        | 3(9.4%)                    | 16(16.7%)             | 0.315  |
| Hypertension, n (%)                  | 95(74.2%)        | 22(68.8%)                  | 73(76.0%)             | 0.414  |
| Alcohol use, n (%)                   | 29(22.7%)        | 8(25.0%)                   | 21(21.9%)             | 0.715  |
| Current smoking, n (%)               | 37(28.9%)        | 10(31.3%)                  | 27(28.1%)             | 0.736  |
| Hematoma volume, IQR, mL             | 35.9(26.0–48.5)  | 29.4(19.7–41.6)            | 36.3(29–63.4)         | 0.006* |
| Hematoma location                    |                  |                            |                       | 0.328  |
| Supratentorial                       |                  |                            |                       |        |
| Lobar, n (%)                         | 33(25.8%)        | 10(31.2%)                  | 23(24.0%)             |        |
| Deep, n (%)                          | 88(68.7%)        | 19(59.4%)                  | 69(71.9%)             |        |
| Infratentorial                       |                  |                            |                       |        |
| Cerebellum, n (%)                    | 7(5.5%)          | 3(9.4%)                    | 4(4.1%)               |        |
| Intraventricular hemorrhage, n (%)   | 47(36.7%)        | 11(34.4%)                  | 36(37.5%)             | 0.751  |
| Surgical approach                    |                  |                            |                       | 0.010* |
| Craniotomy n (%)                     | 57(44.5%)        | 8(25.0%)                   | 49(51.0%)             |        |
| MIPD, n (%)                          | 71(55.5%)        | 24(75.0%)                  | 47(49.0%)             |        |
| NLR1, IQR                            | 13.7(10.2–16.9)  | 8.8(7.3–13.0)              | 14.8(12.8–19.6)       | 0.001* |

GCS, Glasgow coma scale; MIPD, minimally invasive puncture and drainage; NLR1, neutrophil-to-lymphocyte ratio within 48 h after surgery; IQR, interquartile range; n, number; \* $P < 0.05$ .

relationship with the outcome ( $P < 0.1$ ) were included in a multivariate logistic regression to determine independent variables associated with a 30-day unfavorable outcome. The receiver operating characteristic analysis (ROC) was used to evaluate the threshold values for NLR in different surgical groups. The value of  $p < 0.05$  was considered as statistically significant.

## Results

In the current study, a total of 128 patients (88 men and 40 women) with a median age of 60 years (IQR: 50–67 years) were enrolled (Table 1). In the overall participants, the median time from onset to admission was 3 h (IQR: 2–8.75 h). The admission GCS score was 10 (IQR: 7–12). The hematoma volume was 35.9 ml (IQR: 26.0–48.5 ml). The proportion of 94.5% patients for the hematoma location was supratentorial. In addition, 57

(44.5%) patients with ICH were treated with craniotomy and 71 (55.5%) were treated with MIPD.

According to Figure 1A, the changing trend of NLR was to increase first and then decrease and peaked within 48 h after surgery (T1). When grouped by surgery (Figures 1B,C), the same trend emerged both in the MIPD group and the craniotomy group. NLR1 (NLR within 48 h after surgery) in the craniotomy group was higher than in the MIPD group ( $p < 0.05$ ) (Figure 1D).

A univariate analysis showed that age, systolic blood pressure, admission GCS score, hematoma volume, surgical approach, and NLR1 were all risk factors for 30-day outcomes (Table 1). In the multivariate logistic analysis (Table 2), baseline variables included the risk factors considered clinically relevant (16–18) and the above significant characteristics. NLR1 was an independent risk factor of the 30-day outcomes in patients with ICH after surgical treatment.

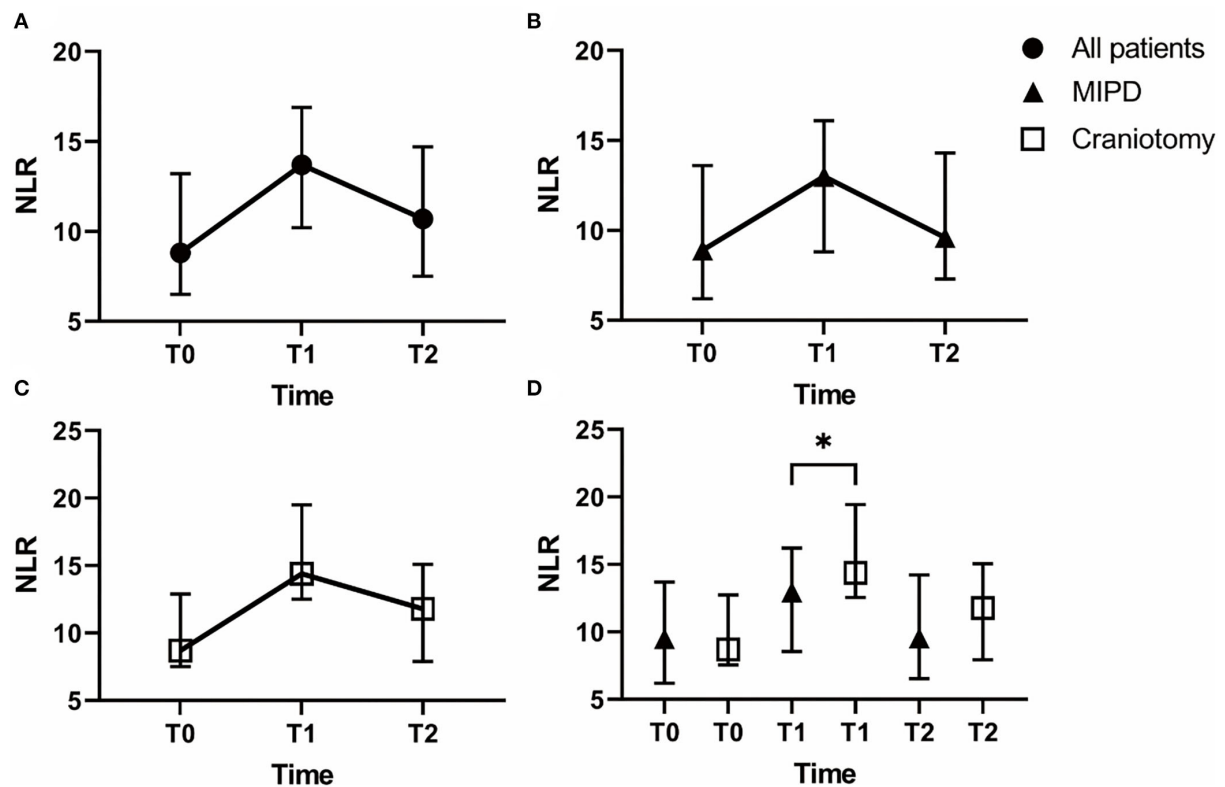


FIGURE 1

The median neutrophil-to-lymphocyte ratio (NLR) value over time between patients with a different surgical approach. The NLR of different time points in all patients (A), in the MIPD group (B) and in the craniotomy group (C). The difference of NLR between the MIPD group and the craniotomy group (D) (NLR, neutrophil-to-lymphocyte ratio; T0, at admission; T1, within 48 h after surgery; T2, at 3–7 days after surgery; \*  $p < 0.05$ ).

TABLE 2 The multivariate logistic regression analysis of variables associated with the 30-day poor outcome.

| Characteristic          | OR    | 95%CI       | P       |
|-------------------------|-------|-------------|---------|
| Male                    | 0.603 | 0.174–2.087 | 0.425   |
| Age                     | 1.049 | 0.999–1.102 | 0.057   |
| Systolic blood pressure | 1.012 | 0.992–1.033 | 0.243   |
| Admission GCS score     | 0.866 | 0.683–1.096 | 0.231   |
| Hematoma volume         | 1.025 | 0.984–1.068 | 0.242   |
| Hematoma location       | 0.370 | 0.034–4.034 | 0.414   |
| IVH                     | 0.711 | 0.206–2.459 | 0.590   |
| Surgical approach       | 1.816 | 0.538–6.344 | 0.329   |
| NLR1                    | 1.342 | 1.156–1.558 | <0.001* |

GCS, Glasgow coma scale; IVH, Intraventricular hemorrhage; NLR1, neutrophil-to-lymphocyte ratio within 48 h after surgery; OR, odds ratio; CI, confidence interval; \* $P < 0.05$ .

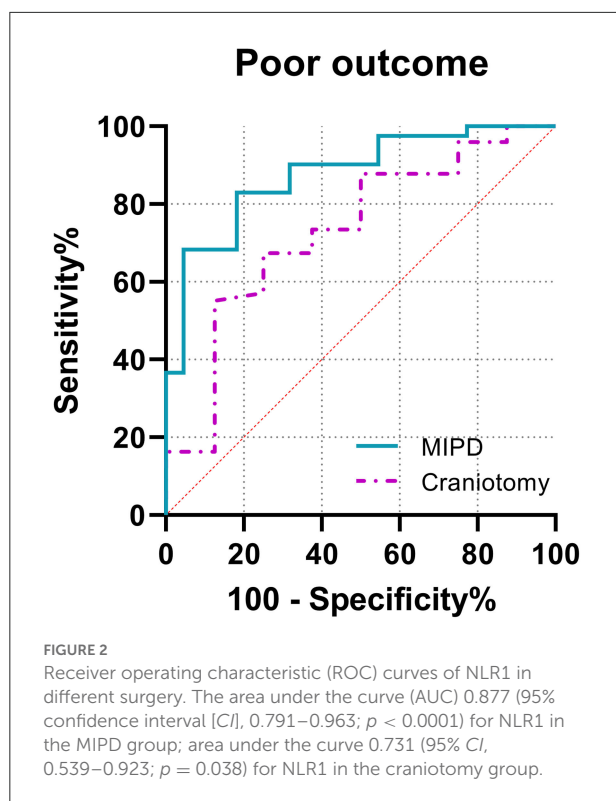
From the results of ROC (Figure 2), the best predictive cut-off value was 12.35 (sensitivity 82.9%, specificity 81.8%, positive predictive value, 4.55; and negative predictive value, 0.21) in the MIPD group and 14.46

(sensitivity 55.1%, specificity 87.5%, positive predictive value, 4.41; and negative predictive value, 0.51) in the craniotomy group.

## Discussion

In this study, the dynamic trend of NLR was to increase first and then decrease and peaked within 48 h after surgery. Moreover, NLR within 48 h after surgery was an independent risk factor of the 30-day outcomes in patients with ICH after surgical treatment. We also detected that the peak NLR > 12.35 or 14.46 in patients receiving MIPD or craniotomy suggested a poor prognosis, respectively.

The inflammatory response starts immediately after hematoma formation in the brain. Microglia are stimulated by hematoma components and promote peripheral inflammatory cell infiltration through the release of pro-inflammatory cytokines and chemokines (19, 20). Neutrophils are the earliest subtypes of leukocytes that infiltrate the hemorrhagic brain by the blood-brain barrier (21). In a study of patients with



ICH, the surrounding tissue of brain hematoma in patients confirmed that leukocyte infiltration occurred within 8 h after intracerebral hemorrhage and further increased within 1 day after onset (22). Another study showed that the number of neutrophils increased in peripheral blood may lead to central neutrophils infiltration, which may cause adverse outcomes (23). In addition, lymphocytes are apoptotic and deactivated by overactivation of the sympathetic nervous system and the hypothalamic-pituitary-adrenal axis in the immunodepression induced by stroke (24). Moreover, lymphocyte is a major component of the cellular immune system, and the decrease of lymphocyte is considered a marker of brain damage within 12 h after injury (24). Since inflammation is closely related to ICH pathophysiology, NLR, which reflects the information on both the innate and adaptive compartments of the immunity, may reasonably represent a surrogate biomarker of the likelihood of secondary brain injury and vulnerability to post-stroke complications (25). From the clinical perspective, although there was no evidence of infection, a significant proportion of patients with ICH in the acute stage is often observed to display an increase in peripheral white blood cells. At this moment, the local and systemic inflammatory response and the level of patients with acute ICH may be reflected by NLR (26).

The main finding of the present study was that the dynamic change of NLR in patients with ICH who underwent surgery was to increase first and then decrease, and reached a peak value within 48 h. A similar trend of NLR in patients with

ICH undergoing surgery had not been reported in the previous study, but was observed in patients with severe traumatic brain injury who underwent surgery (27). This change may be caused by many underlying factors. It is speculated that the process of the occurrence and progression of ICH, the inflammatory response was intense gradually, and the NLR value increased accordingly. As the disease improves, the inflammatory response fades away, and the NLR decreases accordingly (18, 27). In addition, surgical treatment may prevent hematoma expansion, block the release of inflammatory products from hematomas, and thus intervene the pathological processes after disease onset (11). Those may result in the peak NLR within 48 h after surgery. Considering secondary damage to brain tissue and the influence of inflammatory response caused by surgery (28), our study suggested that the NLR within 48 h after the surgery has more predictive value for the prognosis of patients with ICH who have undergone surgery than the NLR at other time points.

Our univariate analysis showed that the admission GCS score, hematoma volume, and NLR1 were correlated with 30-day outcomes of surgically treated patients. After multivariate logistic analysis, only NLR1 was found to be associated with prognosis. In previous studies, the admission GCS score and hematoma volume have been considered the predictors of prognosis in patients with ICH (16, 18). However, they are not completely satisfactory, and NLR may be used as a supplementary indicator. From a clinical perspective, the standardization for assessment of the admission GCS score is difficult to achieve and the accuracy of the GCS score is often affected by various factors, such as intubation (2). As for hematoma volume, it is not possible to follow-up frequently due to the exorbitant cost and radioactivity of CT. In comparison, NLR is cheaper and relatively easy to obtain from blood samples and more easily to observe dynamically. In addition, the peak NLR reflects the changes in inflammatory response in patients with ICH, which is helpful to timely adjust the treatment regimens. Therefore, NLR, especially the peak value of NLR, should be paid more attention during treatment. However, inconsistent with the previous study (12), the admission GCS score and hematoma volume were not associated with poor outcomes of patients with ICH in our study. The admission GCS score is highly subjective, which may be the reason for the different correlation between GCS score and prognosis in different studies. Since the hematoma volume is one of the bases to determine the surgical method, patients with different hematoma volumes have received appropriate treatment. Therefore, the influence of hematoma volume on prognosis may be relatively weak in this study.

In this study, the peak NLR >12.35 or 14.46 in patients treated with MIPD or craniotomy suggested a poor prognosis, respectively. The cut-off values in our study were similar to previous studies, which reported that range from 4.58 to 12.97 in previous studies (8, 13). The area under the curve (0.877 and 0.731) also suggested a satisfactory predictive power for the cut-off values of NLR in this study. Clinically, patients with

ICH in the acute stage often need a dynamic routine blood examination, so it is convenient to obtain the peak value of NLR without additional costs. The treatment of patients with ICH at the acute stage is of great significance for prognosis, and the occurrence of peak NLR can help clinicians to judge the therapeutic effect of intervention measures, so as to formulate a more beneficial treatment plan for patients. Early measures to reduce the inflammatory response may be helpful to improve prognosis, such as therapeutic hypothermia (29). More than that, the current prognostic evaluation model of patients with ICH, such as ICH score, is mainly based on clinical information and lacks corresponding attention to laboratory biomarkers. Our study on the prognostic value of NLR provided new ideas for exploring new prognostic indicators with clinical significance (30).

Several limitations in the study should be taken into account. First, this was a retrospective study with a small sample. Second, the follow-up time was short. Third, although those known factors related to prognosis were concerned in the multivariate logistic regression analysis, other potential confounding factors might be ignored in the current study.

## Conclusion

The dynamic trend of the NLR of patients with ICH was to increase first and then decrease and peaked within 48 h after surgery. The peak NLR was an independent risk factor of the 30-day outcomes in patients with ICH after surgical treatment. The peak NLR >12.35 or 14.46 in patients receiving MIPD or craniotomy represented a poor prognosis, respectively. Further high-quality studies with large samples and multicenter are needed to verify the above results in the future.

## Data availability statement

The raw data supporting the conclusions of this article will be made available by the authors, without undue reservation.

## References

1. Cordonnier C, Demchuk A, Ziai W, Anderson CS. Intracerebral haemorrhage: current approaches to acute management. *Lancet*. (2018) 392:1257–68. doi: 10.1016/S0140-6736(18)31878-6
2. Reith FC, Van den Brande R, Synnot A, Gruen R, Maas AI. The reliability of the Glasgow Coma Scale: a systematic review. *Intensive Care Med*. (2016) 42:3–15. doi: 10.1007/s00134-015-4124-3
3. Turak O, Özcan F, İşleyen A, Başar FN, Gül M, Yilmaz S, et al. Usefulness of neutrophil-to-lymphocyte ratio to predict in-hospital outcomes in infective endocarditis. *Can J Cardiol*. (2013) 29:1672–8. doi: 10.1016/j.cjca.2013.05.005
4. Guo D, Han A, Jing W, Chen D, Jin F, Li M, et al. Preoperative to postoperative change in neutrophil-to-lymphocyte ratio predict survival in colorectal cancer patients. *Future Oncol*. (2018) 14:1187–96. doi: 10.2217/fon-2017-0659
5. Wang L, Song Q, Wang C, Wu S, Deng L, Li Y, et al. Neutrophil to lymphocyte ratio predicts poor outcomes after acute ischemic stroke: a cohort study and systematic review. *J Neurol Sci*. (2019) 406:116445. doi: 10.1016/j.jns.2019.116445
6. Wang J, Xiao W, Chen W, Hu Y. Prognostic significance of preoperative neutrophil-to-lymphocyte ratio and platelet-to-lymphocyte ratio in patients with glioma. *EXCLI J*. (2018) 17:505–12.
7. Zhu H, Wang Z, Yu J, Yang X, He F, Liu Z, et al. Role and mechanisms of cytokines in the secondary brain injury after intracerebral hemorrhage. *Prog Neurobiol*. (2019) 178:101610. doi: 10.1016/j.pneurobio.2019.03.003
8. Lattanzi S, Cagnetti C, Provinciali L, Silvestrini M. Neutrophil-to-lymphocyte ratio predicts the outcome of acute intracerebral hemorrhage. *Stroke*. (2016) 47:1654–7. doi: 10.1161/STROKEAHA.116.013627

## Ethics statement

The studies involving human participants were reviewed and approved by the Medical Ethics Review Committee of the First Affiliated Hospital of Chongqing Medical University and the Dianjiang People's Hospital of Chongqing. The Ethics Committee waived the requirement of written informed consent for participation.

## Author contributions

YZ: conceptualization, data curation, formal analysis, methodology, writing-original draft, writing, reviewing, and editing the manuscript. YX: data curation, formal analysis, methodology, resources, writing, reviewing, and editing the manuscript. SL: formal analysis, software, writing, reviewing, and editing the manuscript. MH: conceptualization, methodology, resources, supervision, validation, writing, reviewing, and editing the manuscript. All authors contributed to the article and approved the submitted version.

## Conflict of interest

The authors declare that the research was conducted in the absence of any commercial or financial relationships that could be construed as a potential conflict of interest.

## Publisher's note

All claims expressed in this article are solely those of the authors and do not necessarily represent those of their affiliated organizations, or those of the publisher, the editors and the reviewers. Any product that may be evaluated in this article, or claim that may be made by its manufacturer, is not guaranteed or endorsed by the publisher.

9. Zhang F, Ren Y, Shi Y, Fu W, Tao C, Li X, et al. Predictive ability of admission neutrophil to lymphocyte ratio on short-term outcome in patients with spontaneous cerebellar hemorrhage. *Medicine (Baltimore)*. (2019) 98:e16120. doi: 10.1097/MD.00000000000016120
10. Tao C, Hu X, Wang J, Ma J, Li H, You C, et al. Admission neutrophil count and neutrophil to lymphocyte ratio predict 90-day outcome in intracerebral hemorrhage. *Biomark Med*. (2017) 11:33–42. doi: 10.2217/bmm-2016-0187
11. Qureshi AI, Mendelow AD, Hanley DF. Intracerebral haemorrhage. *Lancet*. (2009) 373:1632–44. doi: 10.1016/S0140-6736(09)60371-8
12. Zhang F, Tao C, Hu X, Qian J, Li X, You C, et al. Association of neutrophil to lymphocyte ratio on 90-day functional outcome in patients with intracerebral hemorrhage undergoing surgical treatment. *World Neurosurg*. (2018) 119:e956–61. doi: 10.1016/j.wneu.2018.08.010
13. Chen W, Wang X, Liu F, Tian Y, Chen J, Li G, et al. The predictive role of postoperative neutrophil to lymphocyte ratio for 30-day mortality after intracerebral hematoma evacuation. *World Neurosurg*. (2020) 134:e631–5. doi: 10.1016/j.wneu.2019.10.154
14. Kothari RU, Brott T, Broderick JP, Barsan WG, Sauerbeck LR, Zuccarello M, et al. The ABCs of measuring intracerebral hemorrhage volumes. *Stroke*. (1996) 27:1304–5. doi: 10.1161/01.STR.27.8.1304
15. Banks JL, Marotta CA. Outcomes validity and reliability of the modified Rankin scale: implications for stroke clinical trials: a literature review and synthesis. *Stroke*. (2007) 38:1091–6. doi: 10.1161/01.STR.0000258355.23810.c6
16. Qin J, Li Z, Gong G, Li H, Chen L, Song B, et al. Early increased neutrophil-to-lymphocyte ratio is associated with poor 3-month outcomes in spontaneous intracerebral hemorrhage. *PLoS ONE*. (2019) 14:e0211833. doi: 10.1371/journal.pone.0211833
17. Lattanzi S, Cagnetti C, Rinaldi C, Angelocola S, Provinciali L, Silvestrini M, et al. Neutrophil-to-lymphocyte ratio improves outcome prediction of acute intracerebral hemorrhage. *J Neurol Sci*. (2018) 387:98–102. doi: 10.1016/j.jns.2018.01.038
18. Wang F, Xu F, Quan Y, Wang L, Xia JJ, Jiang TT, et al. Early increase of neutrophil-to-lymphocyte ratio predicts 30-day mortality in patients with spontaneous intracerebral hemorrhage. *CNS Neurosci Ther*. (2019) 25:30–5. doi: 10.1111/cns.12977
19. Wang J, Doré S. Inflammation after intracerebral hemorrhage. *J Cereb Blood Flow Metab*. (2007) 27:894–908. doi: 10.1038/sj.jcbfm.9600403
20. Zhou Y, Wang Y, Wang J, Anne Stetler R, Yang QW. Inflammation in intracerebral hemorrhage: from mechanisms to clinical translation. *Prog Neurobiol*. (2014) 115:25–44. doi: 10.1016/j.pneurobio.2013.11.003
21. Wang J. Preclinical and clinical research on inflammation after intracerebral hemorrhage. *Prog Neurobiol*. (2010) 92:463–77. doi: 10.1016/j.pneurobio.2010.08.001
22. Mackenzie JM, Clayton JA. Early cellular events in the penumbra of human spontaneous intracerebral hemorrhage. *J Stroke Cerebrovasc Dis*. (1999) 8:1–8. doi: 10.1016/S1052-3057(99)80032-9
23. Hanhai Z, Bin Q, Shengjun Z, Jingbo L, Yinghan G, Lingxin C, et al. Neutrophil extracellular traps, released from neutrophil, promote microglia inflammation and contribute to poor outcome in subarachnoid hemorrhage. *Aging (Albany NY)*. (2021) 13:13108–23. doi: 10.18632/aging.202993
24. Meisel C, Schwab JM, Prass K, Meisel A, Dirnagl U. Central nervous system injury-induced immune deficiency syndrome. *Nat Rev Neurosci*. (2005) 6:775–86. doi: 10.1038/nrn1765
25. Lattanzi S, Brigo F, Trinka E, Cagnetti C, Napoli MDi, Silvestrini M, et al. Neutrophil-to-lymphocyte ratio in acute cerebral hemorrhage: a system review. *Transl Stroke Res*. (2019) 10:137–45. doi: 10.1007/s12975-018-0649-4
26. Du Y, Wang A, Zhang J, Zhang X, Li N, Liu X, et al. Association between the neutrophil-to-lymphocyte ratio and adverse clinical prognosis in patients with spontaneous intracerebral hemorrhage. *Neuropsychiatr Dis Treat*. (2022) 18:985–93. doi: 10.2147/NDT.S358078
27. Chen J, Qu X, Li Z, Zhang D, Hou L. Peak neutrophil-to-lymphocyte ratio correlates with clinical outcomes in patients with severe traumatic brain injury. *Neurocrit Care*. (2019) 30:334–9. doi: 10.1007/s12028-018-0622-9
28. Zhang F, Ren Y, Fu W, Yang Z, Wen D, Hu X, et al. Predictive accuracy of neutrophil-to-lymphocyte ratio on long-term outcome in patients with spontaneous intracerebral hemorrhage. *World Neurosurg*. (2019) 125:e651–7. doi: 10.1016/j.wneu.2019.01.143
29. Fischer M, Schiefecker A, Lackner P, Frank F, Helbok R, Beer R, et al. Targeted temperature management in spontaneous intracerebral hemorrhage: a systematic review. *Curr Drug Targets*. (2017) 18:1430–40. doi: 10.2174/1389450117666160703161511
30. Shi M, Li XF, Zhang TB, Tang QW, Peng M, Zhao WY, et al. Prognostic role of the neutrophil-to-lymphocyte ratio in intracerebral hemorrhage: a systematic review and meta-analysis. *Front Neurosci*. (2022) 16:825859. doi: 10.3389/fnins.2022.825859





## OPEN ACCESS

## EDITED BY

Yuzhen Xu,  
Tongji University, China

## REVIEWED BY

Yucheng Gu,  
Nanjing Medical University, China  
Brady Williamson,  
University of Cincinnati, United States

## \*CORRESPONDENCE

Yuhua Fan  
fanyuhua@mail.sysu.edu.cn

## SPECIALTY SECTION

This article was submitted to  
Neurological Biomarkers,  
a section of the journal  
Frontiers in Neurology

RECEIVED 14 June 2022

ACCEPTED 09 August 2022

PUBLISHED 01 September 2022

## CITATION

Liu X, Sun P, Yang J and Fan Y (2022)  
Biomarkers involved in the  
pathogenesis of cerebral small-vessel  
disease. *Front. Neurol.* 13:969185.  
doi: 10.3389/fneur.2022.969185

## COPYRIGHT

© 2022 Liu, Sun, Yang and Fan. This is  
an open-access article distributed  
under the terms of the [Creative  
Commons Attribution License \(CC BY\)](#).  
The use, distribution or reproduction  
in other forums is permitted, provided  
the original author(s) and the copyright  
owner(s) are credited and that the  
original publication in this journal is  
cited, in accordance with accepted  
academic practice. No use, distribution  
or reproduction is permitted which  
does not comply with these terms.

# Biomarkers involved in the pathogenesis of cerebral small-vessel disease

Xiaolu Liu, Pei Sun, Jing Yang and Yuhua Fan\*

Department of Neurology, The First Affiliated Hospital, Sun Yat-sen University, Guangdong Provincial Key Laboratory of Diagnosis and Treatment of Major Neurological Diseases, National Key Clinical Department and Key Discipline of Neurology, Guangzhou, China

Cerebral small-vessel disease (CSVD) has been found to have a strong association with vascular cognitive impairment (VCI) and functional loss in elderly patients. At present, the diagnosis of CSVD mainly relies on brain neuroimaging markers, but they cannot fully reflect the overall picture of the disease. Currently, some biomarkers were found to be related to CSVD, but the underlying mechanisms remain unclear. We aimed to systematically review and summarize studies on the progress of biomarkers related to the pathogenesis of CSVD, which is mainly the relationship between these indicators and neuroimaging markers of CSVD. Concerning the pathophysiological mechanism of CSVD, the biomarkers of CSVD have been described as several categories related to sporadic and genetic factors. Monitoring of biomarkers might contribute to the early diagnosis and progression prediction of CSVD, thus providing ideas for better diagnosis and treatment of CSVD.

## KEYWORDS

cerebral small-vessel disease, biomarker, blood-brain barrier, white matter hyperintensities, lacunes, enlarged perivascular spaces, cerebral microbleeds

## Introduction

Cerebral small-vessel disease (CSVD) is a series of clinical, imaging, and pathological syndromes resulting from the injury of cerebral microvessels, such as 2–5 mm cerebral parenchyma around small vessels and vascular structures in the subarachnoid space (1). As a highly age-related disease, CSVD is not only closely related to vascular cognitive impairment (VCI), but also a common risk factor for depression, neurological impairment such as gait disorder, and stroke recurrence.

At present, the diagnosis of CSVD mainly depends on neuroimaging. The neuroimaging features of CSVD include recent small subcortical infarcts, lacunes, white matter hyperintensities (WMH), enlarged perivascular spaces (EPVS), cerebral microbleeds (CMB), and brain atrophy (2). Studies have shown that subcortical WMH and paraventricular WMH are present in 100 and 95%, respectively, of the elderly older than 80 years. Moreover, advanced imaging modalities, such as 7-T MRI, additional metrics, and amyloid PET provide new insights into the diagnosis and study of CSVD (3–5).



Despite the advances in neuroimaging and biological detection in recent years, the pathogenesis of CSVD remains unsolved. Blood–brain barrier (BBB) injury seems to be one of the recognized pathogenesis of sporadic CSVD (6–8), and with the discovery of genetic factors, CSVD is thought to be divided into common sporadic and rare familial forms, there are still amyloidal and non-amyloidal subtypes among sporadic forms. The amyloidal form includes cerebral amyloid angiopathy (CAA), which is considered a chronic degenerative disease characterized by multiple microbleeds (9), while the non-amyloidal is often associated with common vascular risk factors, such as hypertension. Concerning familial forms, cerebral autosomal-dominant arteriopathy with subcortical infarcts and leukoencephalopathy (CADASIL), for example, has been widely recognized. Therefore, studies on the pathological mechanism of CSVD mainly focus on sporadic and genetic types.

Based on the ongoing exploration of the pathogenesis of CSVD, related biomarkers have attracted attention, especially their role in the early stage of CSVD. Thus, we mainly reviewed and discussed the biomarkers involved in the pathogenesis of CSVD and their association with neuroimaging markers (Figure 1).

## Sporadic cerebral small-vessel disease

Sporadic CSVD is divided into two main forms. One of them, CAA, is a chronic degenerative disease and another one is the non-amyloid form, which is often associated with common vascular risk factors, such as old age, hypertension, diabetes, and many other vascular risk factors.

## Cerebral amyloid angiopathy

The main pathological changes of CAA are vascular destruction, bleeding, and product deposition caused by the deposition of  $\beta$ -amyloid protein on small arteries. Moreover, amyloid infiltration of cerebrovascular may also lead to luminal stenosis, hyaline of arterioles, intimal hyperplasia of stenosis, fibrinoid degeneration, and fibrous obstruction, resulting in focal cerebral ischemia, infarction, and softening.

Apolipoprotein E (APOE) genotype, especially APOE- $\epsilon$ 4, a genetic marker for sporadic CAA, has been used as a genetic risk factor for CAA and Alzheimer disease (AD). APOE- $\epsilon$ 4 was found to be associated with a high burden of EPVS in the centrum semiovale (10). While the APOE- $\epsilon$ 2 allele appears to be more prevalent in patients with CAA-associated intracerebral hemorrhage (11).

## Non-amyloid cerebral small-vessel disease

Non-amyloid CSVD is less specific and usually refers to hypertensive CSVD, although it may be associated with a variety of vascular risk factors, such as diabetes. The pathological changes are mainly atherosclerosis, arteriolosclerosis, and lipohyalinosis. The exact pathogenesis remains unclear. Increased BBB permeability and endothelial dysfunction are important pathological features of sporadic CSVD. Therefore, related circulatory biomarkers may play a crucial role in the diagnosis and treatment of CSVD.

## Biomarkers of BBB and endothelial dysfunction

The BBB, which consists of endothelium, pericytes, basement membrane, and astrocytes, plays a complex and crucial role in maintaining material transport and fluid balance. In this process, at the cellular level, the endothelium is crucially important. In addition, damaged endothelial cells have been found to inhibit oligodendrocyte precursor cell maturation, which then affects the production of oligodendrocytes, leading to myelination impairment (12, 13). Dysfunction of endothelial and BBB function is usually due to chronic ischemia, inflammation, oxidative stress-induced lipid peroxidation, matrix metalloproteinase (MMP) activation, and DNA damage, and is reflected in an increase in related metabolites in blood or cerebrospinal fluid (CSF) (14). There has been a lot of evidence that these biomarkers are associated with CSVD neuroimaging markers.

## White matter hyperintensities

### Inflammatory biomarkers

C-reactive protein (CRP) has previously been associated with neurodegenerative diseases and poor cognitive outcomes in normal aging (15). In recent years, CRP has been found to be related to WMH severity and brain atrophy, and higher CRP levels were significantly associated with greater cognitive impairment (16–19). And in a study of 130 patients with CSVD, IL-1 $\alpha$  and IL-6 was found a significant association with recurrent stroke and other vascular events, and there was a correlation between IL-6 and deep WMH (19, 20). Moreover, as an early marker of inflammation, procalcitonin (PCT) has previously been considered a prognostic biomarker for cardiovascular diseases (21). In recent years, Li et al. found that higher levels of PCT were closely associated with WMH (22), suggesting a monitoring role of PCT for CSVD. For vascular inflammation/endothelial dysfunction, homocysteine (HCY) has been proposed to be a risk factor, most widely investigated in conjunction with imaging burden, including

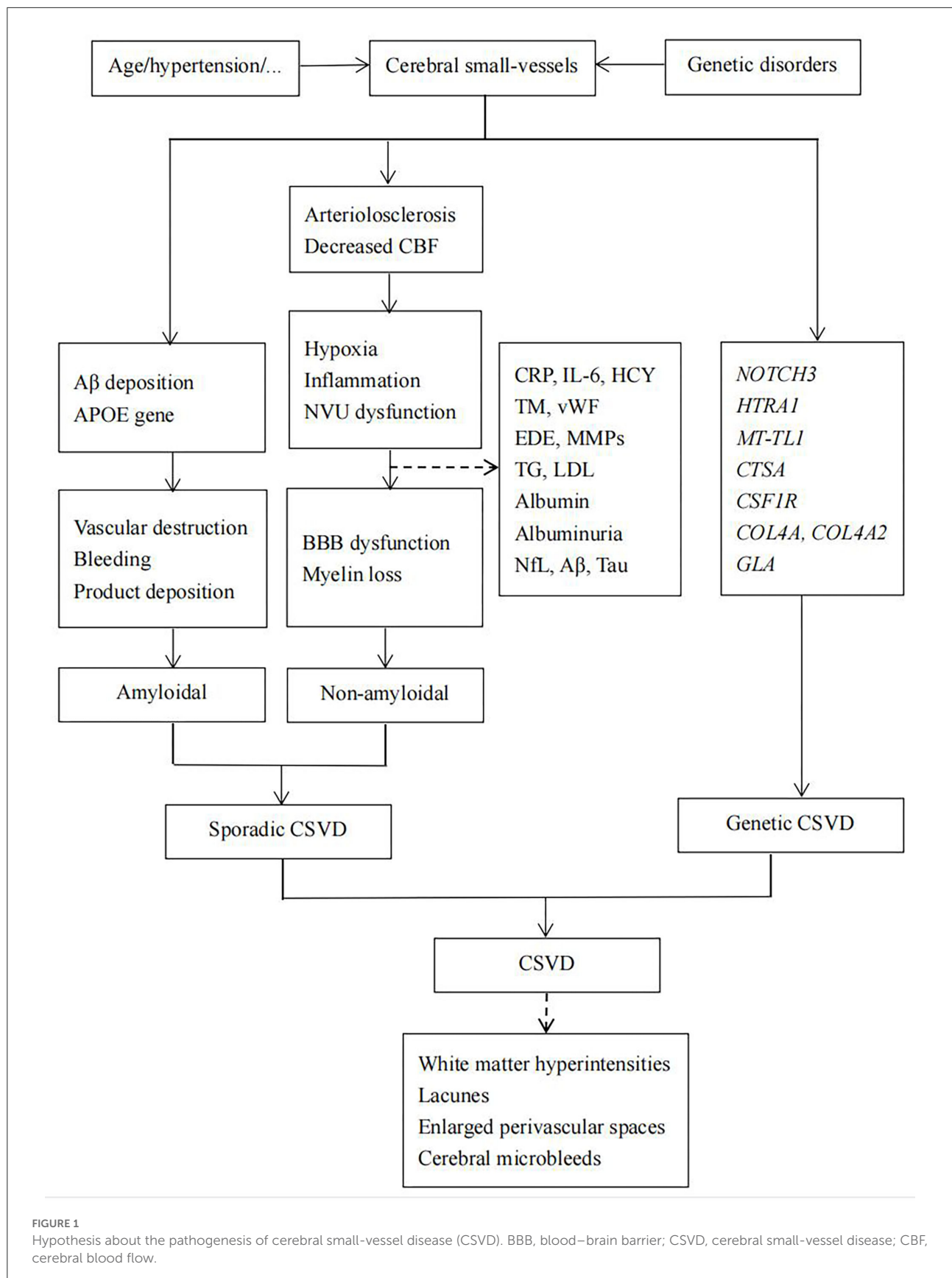


FIGURE 1

Hypothesis about the pathogenesis of cerebral small-vessel disease (CSVD). BBB, blood–brain barrier; CSVD, cerebral small-vessel disease; CBF, cerebral blood flow.

WMH in patients with CSVD (23–26). Also, studies on VCAM-1 and von Willebrand factor (vWF) revealed their prominent associations with WMH (27–30).

### Coagulation markers

It is well-known that prothrombotic status is associated with vascular risk events, and the role of coagulation biomarkers in CSVD has been increasingly discovered. A strong correlation between higher levels of thrombomodulin (TM) and WMH was found especially in the patients with microalbuminuria (31). Similarly, it was reported that higher thrombin–antithrombin values and D-dimer were associated with the presence of WMH in the previous studies (20). Moreover, vWF, synthesized by endothelial cells, was found to be related to periventricular WMH and WMH burden (32).

### BBB integrity-related metabolites

Endothelial-derived exosomes (EDE) play a significant role in maintaining endothelial function and inflammatory regulation (33). It has been reported that plasma levels of EDE cargo proteins GLUT1, LAT1, P-GP, and NOSTRIN were significantly higher in patients with WMH, especially AD patients with WMH (34). EDE may be suggested as a biomarker associated with cerebral endothelial pathogenesis, which contributes to BBB dysfunction and degenerative changes, such as CSVD. Matrix metalloproteinases (MMPs) are involved in sustaining neuronal remodeling, BBB integrity, and have been found to be related to higher WMH grades and vascular dementia (35, 36). Among MMPs, detectable plasma matrix metalloproteinase-9 (MMP-9) is associated with the severity of CSVD and WMH (37, 38). In addition, high-density lipoprotein and triglyceride (TG) levels were found to be risk factors for new lacunes in a 3-year follow-up study (39). There were also studies that suggested that increasing triglycerides levels were associated with larger WMH volume, and increasing low-density lipoprotein (LDL) cholesterol tended to be associated with a decreased frequency and severity of MRI markers of CSVD (40). Moreover, lipoprotein-associated phospholipase A2 (LP-PLA2) was reported to be an independent risk factor associated with WMH and cognitive impairment in CSVD (41).

### CSF and serum albumin

Elevated CSF and serum albumin that reflect albumin extravasation and BBB leakage have been found in patients with vascular dementia (42). Increased albumin CSF/serum ratio, a marker of BBB breakdown, has also been reported in patients with vascular dementia and WMH on neuroimaging (43).

### Lacunes

A higher level of HCY has been proposed to be a risk factor most widely investigated in conjunction with the imaging burden of progression of lacunes in patients with CSVD (23–26). Li et al. also found that higher levels of PCT were closely

associated with silent lacunar infarctions (22). However, no relationship was found between lacunes and CRP (24, 44). TM and fibrinogen were significantly associated with the risk of lacunes (31, 45). In addition, as the natural inhibitor of the exogenous coagulation pathway and the marker of endothelial activation, elevated factor pathway inhibitor (TFPI) were found in lacunar stroke patients than in controls, supporting the hypothesis that endothelial dysfunction is involved in the pathogenesis of lacunar stroke (46). Finally, high-density lipoprotein and triglyceride (TG) levels were found to be risk factors for new lacunes in a 3-year follow-up study (39).

### Enlarged perivascular spaces

High levels of CRP and PCT have been reported to be associated with EPVS (22, 47, 48), and plasma HCY level was correlated with EPVS in basal ganglia (49). There is also a significant association between neutrophil count and EPVS in basal ganglia in a community-based study (50), neutrophil-to-lymphocyte ratio (NLR), and EPVS in a patient study (51). Furthermore, serum cortisol levels were found to be independent predictors of moderate-to-severe EPVS and cognitive dysfunction (52).

### Cerebral microbleeds

Elevated levels of CRP and interleukin-6 were associated with an increased CMB burden in the stroke cohorts and more pronounced in APOE-ε4 carriers (53). Besides, higher HCY levels may result in the accumulation of amyloid protein because HCY impedes the clearance of amyloid protein through the glymphatic pathway (54), which may be the cause of its association with lobar CMB. Evidence of the studies on vascular endothelial growth factor (VEGF) also provides support for vascular inflammatory involvement in CMB formation in AD and stroke patients (55, 56).

## Genetic cerebral small-vessel disease

The discovery of genetic factors revealed a considerable impact of them on CSVD although CSVD is more often a sporadic disease. The estimated heritability for WMH as a biomarker of CSVD ranged between 50 and 80% (57). There are several hereditary forms of CSVD that have been identified, including CADASIL, cerebral autosomal recessive arteriopathy with subcortical infarcts and leukoencephalopathy (CARASIL), cathepsin A-related arteriopathy with strokes and leukoencephalopathy (CARASAL), hereditary diffuse leukoencephalopathy with spheroids (HDLS), COL4A1/2-related disorders, and Fabry disease. The numbers and in-depth investigations on the genetic loci are growing in recent years

to achieve the improved diagnosis and treatment of these rare single-gene disorders, as well as sporadic CSVD (58).

Cerebral autosomal-dominant arteriopathy with subcortical infarcts and leukoencephalopathy is the most common hereditary CSVD, which is caused by a mutation of cysteine-altering in the NOTCH3 gene on chromosome 19, mainly due to mutations in the NOTCH3 extracellular domain (NOTCH3 ECD). The NOTCH3 gene encodes the key molecular of transmembrane receptor protein during notch signaling and embryonal development (59), and NOTCH3 plays an essential role in the development of the vascular system in adults. There were also several reports that have described non-cysteine-related mutations and a single-particle *in vitro* aggregation assay might evaluate the clinical significance of the non-cysteine variants, but it was still a debatable point (60).

The next known rare hereditary CSVD is CARASIL, which pathogenic gene is HTRA1, located on chromosome 10q (10q25.3-q26.2). The mutation could result in the loss of HTRA1 protease activity, leading to the upregulation of TGF- $\beta$  family signaling (61), resulting in the degeneration of smooth muscle cells in the cerebral small vessels.

There are several other rare hereditary forms of CSVD as follows: colony-stimulating factor 1 receptor [CSF1R, MIM\*164770] mutations cause HDLS (62); CTSA mutations are the cause of CARASIL through the degradation of endothelin-1 and downregulation of oligodendrocyte (13); and Fabry disease is caused by the genetic mutations in the alpha-galactosidase-A gene (GLA-gene), located on the long arm of the X-chromosome (Xq22.1) (63). There is still COL4A1/2-related CSVD.

Furthermore, genome-wide association studies (GWAS) found several possible genetic factors that might be related to WMH, such as NEURL1, PDCD11, and SH3PXD2A. Mutations in TREX1, FOXC1, and PITX2 were also related to dysfunction of the vascular system, and usually present with WMH on MRI, lacunar infarctions, and EPVS (64). Hence, the genetic factors play a vital role in terms of revealing the molecular mechanism of CSVD and may also bring new ideas for the prevention and treatment of CSVD.

Besides, as mentioned above, APOE- $\epsilon$ 4 allele is associated with increased amyloid  $\beta$ -protein (A $\beta$ ) deposition and may lead to the formation and progression of WMH, especially in the frontal lobe. There is not only an increased risk of developing AD but also the prevalence of CAA in APOE- $\epsilon$ 4 carriers (65). Besides, Luo et al. found significantly more frontal WMH burden and basal ganglia EPVS at baseline and greater cognitive progression in APOE- $\epsilon$ 4 carriers (66).

## Cerebral small-vessel disease associated diseases

Some of the biomarkers of CSVD are also risk factors for other diseases, including cerebral and

non-cerebral diseases. Cerebral diseases are mainly neurodegenerative diseases, and non-cerebral diseases mainly include chronic kidney disease and retinal disease. They are directly or indirectly related to the pathogenesis of CSVD.

## Relationship between cerebral small-vessel disease and neurodegenerative diseases

### White matter hyperintensities

As the significant component of the neuronal cytoskeleton, neurofilament (NfL) provides structural support for axons (67). Thus, higher serum and CSF NfL levels could be a more direct biomarker to reflect neuronal damage and neurodegeneration diseases (68), such as AD (69). CSF NfL light polypeptide was thought to be involved in increased WMH volume in dementia-free, AD, subcortical ischemic disease, and mild cognitive impairment (MCI) patients (70, 71). As the extraction of CSF is invasive, plasma NfL is more often used to evaluate the neuroaxonal damage, and serum NfL is associated with baseline WMH volume in patients with CSVD (72, 73).

CSF and plasma A $\beta$  levels are usually used as the biomarkers of AD, and the toxic effects of A $\beta$  on blood vessel walls are also causing concern. There have been several studies investigated the association between A $\beta$  and WMH (74) in which Gurol et al. reported an association between WMH and plasma A $\beta$ 40 and A $\beta$ 42 (75), while Kester et al. found a negative correlation between CSF A $\beta$ 42 and WMH in a normal population (76), indicating A $\beta$  a potential risk factor for CSVD. Similarly, some studies also found the relationship between WMH and CSF total tau (t-tau) and phosphorylated tau (p-tau) (76–78).

### Lacunes

Serum NfL is found to be associated with the baseline presence of lacunes in CSVD patients (72, 73). In CSVD patients with higher levels of A $\beta$ 1-42, CRP was strongly associated with lacunes (47).

### Enlarged perivascular spaces

Higher levels of P-Tau, T-Tau, and neurogranin in A $\beta$ -positive individuals were significantly associated with EPVS in centrum semiovale (79). And CRP was strongly associated with EPVS in CSVD patients with higher A $\beta$ 1-42 (47).

### Cerebral microbleeds

The previous studies have found that the CMB is related to low CSF A $\beta$ 42, but there were also studies found that there

was no correlation between CSF A $\beta$ 42 and deep CMB (80, 81). It's worth noting that Kester et al. found that CMB was related to CSF A $\beta$ 42 only in the presence of APOE  $\epsilon$ 4 in AD and normal elderly (76). And there is a significant association between CMB and tau pathology that is lower tau and p-tau 181 in APOE  $\epsilon$ 4 non-carriers, but not in carriers (76, 82, 83).

## Relationship between cerebral small-vessel disease and non-cerebral diseases

Some extracranial diseases have also been found to have vascular lesions similar to those in CSVD, such as arteriosclerosis and endothelial dysfunction. The most common is chronic kidney disease (CKD). It has been reported that patients with CKD are more likely to develop CSVD and more severe WMH, but the pathological mechanism of CKD-related CSVD remains unclear and might be related to uremic toxins and chronic inflammation (84–86). As the main feature of CKD, albuminuria has been proposed as an independent biomarker for systemic endothelial dysfunction (87). There is also evidence suggesting an association between albuminuria and WMH burden (88), and another indicator of kidney function, lower GFR, could also reflect the advanced stage of microvascular disease (89). In addition, hyperphosphatemia was found to be significantly associated with vascular risk events (90, 91). In recent years, Chung et al. reported that higher circulatory phosphate levels were associated with severe WMH and downregulating tight junction proteins in human brain microvascular endothelial cells (92), suggesting that hyperphosphatemia might be a novel risk factor for CSVD and might be involved in BBB impairment. As the early marker of kidney disease, albuminuria has been proposed as an independent biomarker for systemic endothelial dysfunction (87). It's pretty clear that worse kidney function, associated with peripheral systemic microvascular disease, has been the biomarker that could be useful in the evaluation of brain microvascular damage.

On the other hand, the vascular network of the retina is physiologically similar to the corresponding cerebral neurovascular units (93). Therefore, non-invasive evaluation of retinal neurons and blood vessels may provide new biomarkers for the diagnosis and evaluation of CSVD (94, 95). Optical coherence tomography (OCT) showed a significant correlation between the Wall to Lumen Ratio (WLR) and WMH (96), and OCT angiography (OCTA) showed that retinal hypoperfusion was related to MRI markers, such as WMH and lacunes in CSVD patients (97), suggesting the potential value that these parameters as biomarkers for early CSVD.

## Other biomarkers

**Renin–angiotensin–aldosterone System:** The renin–angiotensin–aldosterone system previously has been studied as a potential marker in CSVD because it works in the regulation of vascular smooth muscle constriction and hypertension (98). And angiotensin-II, the key molecular related to hypertension, is found to be involved in BBB damage in CSVD (99–101). Specifically, increased angiotensin-converting enzyme (ACE) levels have been found in the patients with greater progression of deep WMH volume but less progression of cortical atrophy, suggesting a complex role of ACE in the brain (102).

**Plasma Brain Natriuretic Peptide (BNP) and NT-proBNP:** BNP and NT-proBNP are considered the diagnostic markers of cardiovascular diseases and have been linked to cerebrovascular diseases in recent years (103). Increased levels of plasma BNP are associated with WMHs and lacunar infarcts, but there was a negative correlation between BNP and CMB (104), thus it could be a useful biomarker for identifying ischemic CSVD in patients with hypertension. In addition, Vilar-Bergua et al. also found a higher level of NT-proBNP was independently associated with silent brain infarcts, CMB, EPVS, and WMHs volumes (103). The possible mechanism is that BNP reduces local blood flow and blood pressure, thereby reducing cerebral blood flow and causing ischemic injury.

## Conclusion

Despite the severe disease burden of CSVD, its pathologic mechanisms are not fully understood by clinicians. The basis for diagnosis and treatment of CSVD is mainly derived from neuroimaging, such as diffusion tensor imaging, imaging of the BBB, cerebrovascular reactivity, and cerebral blood flow, which partly reflect the pathological mechanisms of sporadic CSVD, such as BBB damage, reduced blood flow, and increased intracranial vascular pulsation (4, 105). And the advancement of molecular genetic tests improves diagnostic accuracy in patients with potential CSVD. Therefore, most studies focus on the sporadic and genetic types of CSVD.

Study on biomarkers of CSVD has become a promising field in disease diagnosis and monitoring. Numerous studies have suggested that APOE genotype is associated with amyloid angiopathy in sporadic CSVD, and biomarkers suggesting BBB damage, such as inflammatory factors and coagulation factors, are closely related to non-amyloidosis subtypes, especially their close association with neuroimaging markers. In addition, molecular testing helps us to improve the detection rate of hereditary CSVD. Moreover, there are also some diseases with pathological changes similar to CSVD, such as neurodegenerative diseases and renal diseases. These known biomarkers reflect the involvement of several interrelated pathways including but not limited



to endothelial and BBB dysfunction and genetic factors, showing the strong association between the possible biomarkers and CSVD. But their predictive or discriminative ability regarding diagnosis remains to be established perfectly during clinical research.

In summary, although the diagnosis of CSVD is still mainly relied on neuroimaging, the study of biomarkers, especially their association with neuroimaging markers, can help us better early identification, prediction, and evaluation of the development of CSVD, and may find new therapeutic targets.

## Author contributions

XL and YF designed the study. XL, PS, and JY collected the data. XL drafted the manuscript. All authors approved the final version of the manuscript.

## Funding

This study was supported by grants from the National Natural Science Foundation of China (No. 82071294), Guangdong Provincial Key Laboratory of Diagnosis and Treatment of Major Neurological Diseases (2020B1212060017), Guangdong Provincial Clinical Research Center for

Neurological Diseases (2020B1111170002), the Southern China International Cooperation Base for Early Intervention and Functional Rehabilitation of Neurological Diseases (2015B050501003 and 2020A0505020004), and Guangdong Provincial Engineering Center for Major Neurological Disease Treatment, Guangdong Provincial Translational Medicine Innovation Platform for Diagnosis and Treatment of Major Neurological Disease.

## Conflict of interest

The authors declare that the research was conducted in the absence of any commercial or financial relationships that could be construed as a potential conflict of interest.

## Publisher's note

All claims expressed in this article are solely those of the authors and do not necessarily represent those of their affiliated organizations, or those of the publisher, the editors and the reviewers. Any product that may be evaluated in this article, or claim that may be made by its manufacturer, is not guaranteed or endorsed by the publisher.

## References

- Pantoni L. Cerebral small vessel disease: from pathogenesis and clinical characteristics to therapeutic challenges. *Lancet Neurol.* (2010) 9:689–701. doi: 10.1016/S1474-4422(10)70104-6
- van Veluw SJ, Shih AY, Smith EE, Chen C, Schneider JA, Wardlaw JM, et al. Detection, risk factors, and functional consequences of cerebral microinfarcts. *Lancet Neurol.* (2017) 16:730–40. doi: 10.1016/S1474-4422(17)30196-5
- Saridin FN, Hilal S, Villaraza SG, Reilhac A, Gyanwali B, Tanaka T, et al. Brain amyloid  $\beta$ , cerebral small vessel disease, and cognition: a memory clinic study. *Neurology.* (2020) 95:e2845–53. doi: 10.1212/WNL.00000000000011029
- Ji F, Pasternak O, Liu S, Loke YM, Choo BL, Hilal S, et al. Distinct white matter microstructural abnormalities and extracellular water increases relate to cognitive impairment in Alzheimer's disease with and without cerebrovascular disease. *Alzheimer Res Ther.* (2017) 9:63. doi: 10.1186/s13195-017-0292-4
- Farid K, Charidimou A, Baron JC. Amyloid positron emission tomography in sporadic cerebral amyloid angiopathy: a systematic critical update. *NeuroImage Clin.* (2017) 15:247–63. doi: 10.1016/j.nicl.2017.05.002
- Petersen MA, Ryu JK, Akassoglou K. Fibrinogen in neurological diseases: mechanisms, imaging and therapeutics. *Nat Rev Neurosci.* (2018) 19:283–301. doi: 10.1038/nrn.2018.13
- Iadecola C. The neurovascular unit coming of age: a journey through neurovascular coupling in health and disease. *Neuron.* (2017) 96:17–42. doi: 10.1016/j.neuron.2017.07.030
- Wardlaw JM, Smith C, Dichgans M. Mechanisms of sporadic cerebral small vessel disease: insights from neuroimaging. *Lancet Neurol.* (2013) 12:483–97. doi: 10.1016/S1474-4422(13)70060-7
- Vinters HV, Zarow C, Borys E, Whitman JD, Tung S, Ellis WG, et al. Review: vascular dementia: clinicopathologic and genetic considerations. *Neuropathol Appl Neurobiol.* (2018) 44:247–66. doi: 10.1111/nan.12472
- Pinheiro A, Demissie S, Scruton A, Charidimou A, Parva P, DeCarli C, et al. Association of apolipoprotein E  $\epsilon$ 4 allele with enlarged perivascular spaces. *Ann Neurol.* (2022) 92:23–31. doi: 10.1002/ana.26364
- Camacho J, Moliné T, Bonaterra-Pastra A, Ramón YCS, Martínez-Sáez E, Hernández-Guillamón M. Brain ApoA-I, ApoJ and ApoE immunodetection in cerebral amyloid angiopathy. *Front Neurol.* (2019) 10:187. doi: 10.3389/fneur.2019.00187
- Rajani RM, Quick S, Ruigrok SR, Graham D, Harris SE, Verhaaren BFJ, et al. Reversal of endothelial dysfunction reduces white matter vulnerability in cerebral small vessel disease in rats. *Sci Transl Med.* (2018) 10:eam9507. doi: 10.1126/scitranslmed.aam9507
- Bugiani M, Kevelam SH, Bakels HS, Waisfisz Q, Ceuterick-de Groote C, Niessen HW, et al. Cathepsin A-related arteriopathy with strokes and leukoencephalopathy (CARASAL). *Neurology.* (2016) 87:1777–86. doi: 10.1212/WNL.0000000000003251
- Deanfield JE, Halcox JP, Rabelink TJ. Endothelial function and dysfunction: testing and clinical relevance. *Circulation.* (2007) 115:1285–95. doi: 10.1161/CIRCULATIONAHA.106.652859
- Noble JM, Manly JJ, Schupf N, Tang MX, Mayeux R, Luchsinger JA. Association of C-reactive protein with cognitive impairment. *Arch Neurol.* (2010) 67:87–92. doi: 10.1001/archneurol.2009.308
- Xin Y, Zhang L, Hu J, Gao H, Zhang B. Correlation of early cognitive dysfunction with inflammatory factors and metabolic indicators in patients with Alzheimer's disease. *Am J Transl Res.* (2021) 13:9208–15. doi: 10.3389/fneur.2022.944205
- Wersching H, Duning T, Lohmann H, Mohammadi S, Stehling C, Fobker M, et al. Serum C-reactive protein is linked to cerebral microstructural integrity and cognitive function. *Neurology.* (2010) 74:1022–9. doi: 10.1212/WNL.0b013e3181d7b45b

18. Gu Y, Gutierrez J, Meier IB, Guzman VA, Manly JJ, Schupf N, et al. Circulating inflammatory biomarkers are related to cerebrovascular disease in older adults. *Neurol Neuroimmunol Neuroinflamm.* (2019) 6:e521. doi: 10.1212/NXI.0000000000000521
19. Satizabal CL, Zhu YC, Mazoyer B, Dufouil C, Tzourio C. Circulating IL-6 and CRP are associated with MRI findings in the elderly: the 3C-Dijon Study. *Neurology.* (2012) 78:720–7. doi: 10.1212/WNL.0b013e318248e50f
20. Staszewski J, Skrobowska E, Piusińska-Macoch R, Brodacki B, Stepień A. IL-1 $\alpha$  and IL-6 predict vascular events or death in patients with cerebral small vessel disease—Data from the SHEF-CSVD study. *Adv Med Sci.* (2019) 64:258–66. doi: 10.1016/j.advms.2019.02.003
21. Ertem AG, Efe TH, Yayla Ç, Akboga MK, Açar B, Ünal S, et al. The association between serum procalcitonin levels and severity of coronary artery disease assessed by SYNTAX score in patients with acute coronary syndrome. *Angiology.* (2017) 68:40–5. doi: 10.1177/0003319716638239
22. Li G, Zhu C, Li J, Wang X, Zhang Q, Zheng H, et al. Increased level of procalcitonin is associated with total MRI burden of cerebral small vessel disease in patients with ischemic stroke. *Neurosci Lett.* (2018) 662:242–6. doi: 10.1016/j.neulet.2017.10.040
23. Arba F, Giannini A, Piccardi B, Biagini S, Palumbo V, Giusti B, et al. Small vessel disease and biomarkers of endothelial dysfunction after ischaemic stroke. *Euro Stroke J.* (2019) 4:119–26. doi: 10.1177/2396987318805905
24. Walker KA, Power MC, Hoogeveen RC, Folsom AR, Ballantyne CM, Knopman DS, et al. Midlife systemic inflammation, late-life white matter integrity, and cerebral small vessel disease: the atherosclerosis risk in communities study. *Stroke.* (2017) 48:3196–202. doi: 10.1161/STROKEAHA.117.018675
25. Rouhl RP, Damoiseaux JG, Lodder J, Theunissen RO, Knottnerus IL, Staals J, et al. Vascular inflammation in cerebral small vessel disease. *Neurobiol Aging.* (2012) 33:1800–6. doi: 10.1016/j.neurobiolaging.2011.04.008
26. Cao Y, Su N, Zhang D, Zhou L, Yao M, Zhang S, et al. Correlation between total homocysteine and cerebral small vessel disease: a Mendelian randomization study. *Euro J Neurol.* (2021) 28:1931–8. doi: 10.1111/ene.14708
27. El Hussein N, Bushnell C, Brown CM, Attix D, Rost NS, Samsa GP, et al. Vascular cellular adhesion molecule-1 (VCAM-1) and memory impairment in African-Americans after small vessel-type stroke. *J Stroke Cerebrovasc Dis.* (2020) 29:104646. doi: 10.1016/j.jstrokecerebrovasdis.2020.104646
28. Tchalla AE, Wellenius GA, Trivison TG, Gagnon M, Iloputaife I, Dantoine T, et al. Circulating vascular cell adhesion molecule-1 is associated with cerebral blood flow dysregulation, mobility impairment, and falls in older adults. *Hypertension.* (2015) 66:340–6. doi: 10.1161/HYPERTENSIONAHA.115.05180
29. Sun W, Luo Y, Zhang S, Lu W, Liu L, Yang X, et al. The relationship between ADAMTS13 activity and overall cerebral small vessel disease burden: a cross-sectional study based on CSVD. *Front Aging Neurosci.* (2021) 13:738359. doi: 10.3389/fnagi.2021.738359
30. Wang X, Chappell FM, Valdes Hernandez M, Lowe G, Rumley A, Shuler K, et al. Endothelial function, inflammation, thrombosis, and basal ganglia perivascular spaces in patients with stroke. *J Stroke Cerebrovasc Dis.* (2016) 25:2925–31. doi: 10.1016/j.jstrokecerebrovasdis.2016.08.007
31. Wada M, Nagasawa H, Kurita K, Koyama S, Arawaka S, Kawanami T, et al. Microalbuminuria is a risk factor for cerebral small vessel disease in community-based elderly subjects. *J Neurol Sci.* (2007) 255:27–34. doi: 10.1016/j.jns.2007.01.066
32. Nagai M, Hoshida S, Kario K. Association of prothrombotic status with markers of cerebral small vessel disease in elderly hypertensive patients. *Am J Hypertens.* (2012) 25:1088–94. doi: 10.1038/ajh.2012.85
33. Roig-Charles D, Willms E, Fontijn RD, Martinez-Pacheco S, Mäger I, de Vries HE, et al. Endothelial-derived extracellular vesicles induce cerebrovascular dysfunction in inflammation. *Pharmaceutics.* (2021) 13. doi: 10.3390/pharmaceutics13091525
34. Abner EL, Elahi FM, Jicha GA, Mustapic M, Al-Janabi O, Kramer JH, et al. Endothelial-derived plasma exosome proteins in Alzheimer's disease angiopathy. *FASEB J.* (2020) 34:5967–74. doi: 10.1096/fj.202000034R
35. Zhang DP, Peng YF, Zhang HL, Ma JG, Zhao M, Yin S, et al. Basilar artery tortuosity is associated with white matter hyperintensities by T1MP-1. *Front Neurosci.* (2019) 13:836. doi: 10.3389/fnins.2019.00836
36. Candelario-Jalil E, Thompson J, Taheri S, Grossetete M, Adair JC, Edmonds E, et al. Matrix metalloproteinases are associated with increased blood-brain barrier opening in vascular cognitive impairment. *Stroke.* (2011) 42:1345–50. doi: 10.1161/STROKEAHA.110.600825
37. Li M, Sun H, Shen T, Xue S, Zhao Y, Leng B, et al. Increased serum levels of cyclophilin a and matrix metalloproteinase-9 are associated with cognitive impairment in patients with obstructive sleep apnea. *Sleep Med.* (2021). doi: 10.1016/j.sleep.2021.10.009 [Epub ahead of print].
38. Romero JR, Vasan RS, Beiser AS, Au R, Benjamin EJ, DeCarli C, et al. Association of matrix metalloproteinases with MRI indices of brain ischemia and aging. *Neurobiol Aging.* (2010) 31:2128–35. doi: 10.1016/j.neurobiolaging.2008.11.004
39. Gouw AA, van der Flier WM, Fazekas F, van Straaten EC, Pantoni L, Poggesi A, et al. Progression of white matter hyperintensities and incidence of new lacunes over a 3-year period: the Leukoaraiosis and Disability study. *Stroke.* (2008) 39:1414–20. doi: 10.1161/STROKEAHA.107.498535
40. Schilling S, Tzourio C, Dufouil C, Zhu Y, Berr C, Alperovitch A, et al. Plasma lipids and cerebral small vessel disease. *Neurology.* (2014) 83:1844–52. doi: 10.1212/WNL.0000000000000980
41. Zhu S, Wei X, Yang X, Huang Z, Chang Z, Xie F, et al. Plasma lipoprotein-associated phospholipase A2 and superoxide dismutase are independent predictors of cognitive impairment in cerebral small vessel disease patients: diagnosis and assessment. *Aging Dis.* (2019) 10:834–46. doi: 10.14336/AD.2019.0304
42. Farrall AJ, Wardlaw JM. Blood-brain barrier: ageing and microvascular disease—systematic review and meta-analysis. *Neurobiol Aging.* (2009) 30:337–52. doi: 10.1016/j.neurobiolaging.2007.07.015
43. Wallin A, Sjögren M, Edman A, Blennow K, Regland B. Symptoms, vascular risk factors and blood-brain barrier function in relation to CT white-matter changes in dementia. *Euro Neurol.* (2000) 44:229–35. doi: 10.1159/00008242
44. Nylander R, Lind L, Wikström J, Lindahl B, Venge P, Larsson A, et al. Relation between cardiovascular disease risk markers and brain infarcts detected by magnetic resonance imaging in an elderly population. *J Stroke Cerebrovasc Dis.* (2015) 24:312–8. doi: 10.1016/j.jstrokecerebrovasdis.2014.08.027
45. Staszewski J, Piusińska-Macoch R, Brodacki B, Skrobowska E, Stepień A. Association between hemostatic markers, serum lipid fractions and progression of cerebral small vessel disease: a 2-year follow-up study. *Neurologia i neurochirurgia polska.* (2018) 52:54–63. doi: 10.1016/j.pjnns.2017.11.005
46. Knottnerus IL, Winkers K, Ten Cate H, Hackeng TM, Lodder J, Rouhl RP, et al. Levels of heparin-releasable TFPI are increased in first-ever lacunar stroke patients. *Neurology.* (2012) 78:493–8. doi: 10.1212/WNL.0b013e318246d6b7
47. Hilal S, Ikram MA, Verbeek MM, Franco OH, Stoops E, Vanderstichele H, et al. C-reactive protein, plasma amyloid- $\beta$  levels, and their interaction with magnetic resonance imaging markers. *Stroke.* (2018) 49:2692–8. doi: 10.1161/STROKEAHA.118.022317
48. Aribisala BS, Wiseman S, Morris Z, Valdés-Hernández MC, Royle NA, Maniega SM, et al. Circulating inflammatory markers are associated with magnetic resonance imaging-visible perivascular spaces but not directly with white matter hyperintensities. *Stroke.* (2014) 45:605–7. doi: 10.1161/STROKEAHA.113.004059
49. Ji Y, Li X, Teng Z, Li X, Jin W, Lv PY. Homocysteine is associated with the development of cerebral small vessel disease: retrospective analyses from neuroimaging and cognitive outcomes. *J Stroke Cerebrovasc Dis.* (2020) 29:105393. doi: 10.1016/j.jstrokecerebrovasdis.2020.105393
50. Jiang L, Cai X, Yao D, Jing J, Mei L, Yang Y, et al. Association of inflammatory markers with cerebral small vessel disease in community-based population. *J Neuroinflamm.* (2022) 19:106. doi: 10.1186/s12974-022-02468-0
51. Wang Y, Ma L, Zhang M, Wei J, Li X, Pan X, et al. Blood neutrophil-to-lymphocyte ratio as a predictor of cerebral small-vessel disease. *Med Sci Monitor.* (2022) 28:e935516. doi: 10.12659/MSM.935516
52. Qiu Q, Zhou X, Wu L, Zhang Y, Yu Z, Wang M, et al. Serum cortisol is associated with cerebral small vessel disease-related brain changes and cognitive impairment. *Front Aging Neurosci.* (2021) 13:809684. doi: 10.3389/fnagi.2021.809684
53. Low A, Su L, Stefaniak JD, Mak E, Dounavi ME, Muniz-Terrera G, et al. Inherited risk of dementia and the progression of cerebral small vessel disease and inflammatory markers in cognitively healthy midlife adults: the PREVENT-Dementia study. *Neurobiol Aging.* (2021) 98:124–33. doi: 10.1016/j.neurobiolaging.2020.10.029
54. Zhuo JM, Portugal GS, Kruger WD, Wang H, Gould TJ, Pratico D. Diet-induced hyperhomocysteinemia increases amyloid-beta formation and deposition in a mouse model of Alzheimer's disease. *Curr Alzheimer Res.* (2010) 7:140–9. doi: 10.2174/156720510790691326
55. Zhang JB, Li MF, Zhang HX, Li ZG, Sun HR, Zhang JS, et al. Association of serum vascular endothelial growth factor levels and cerebral microbleeds in patients with Alzheimer's disease. *Euro J Neurol.* (2016) 23:1337–42. doi: 10.1111/ene.13030
56. Dassan P, Brown MM, Gregoire SM, Keir G, Werring DJ. Association of cerebral microbleeds in acute ischemic stroke with high

- serum levels of vascular endothelial growth factor. *Arch Neurol.* (2012) 69:1186–9. doi: 10.1001/archneurol.2012.459
57. Dichgans M. Genetics of ischaemic stroke. *Lancet Neurol.* (2007) 6:149–61. doi: 10.1016/S1474-4422(07)70028-5
58. Choi JC. Genetics of cerebral small vessel disease. *J Stroke.* (2015) 17:7–16. doi: 10.5853/jos.2015.17.1.7
59. Bianchi S, Dotti MT, Federico A. Physiology and pathology of notch signalling system. *J Cell Physiol.* (2006) 207:300–8. doi: 10.1002/jcp.20542
60. Wollenweber FA, Hanecker P, Bayer-Karpinska A, Malik R, Bäßner H, Moreton F, et al. Cysteine-sparing CADASIL mutations in NOTCH3 show proaggregatory properties *in vitro*. *Stroke.* (2015) 46:786–92. doi: 10.1161/STROKEAHA.114.007472
61. Hara K, Shiga A, Fukutake T, Nozaki H, Miyashita A, Yokoseki A, et al. Association of HTRA1 mutations and familial ischemic cerebral small-vessel disease. *N Engl J Med.* (2009) 360:1729–39. doi: 10.1056/NEJMoa0801560
62. Rademakers R, Baker M, Nicholson AM, Rutherford NJ, Finch N, Soto-Ortolaza A, et al. Mutations in the colony stimulating factor 1 receptor (CSF1R) gene cause hereditary diffuse leukoencephalopathy with spheroids. *Nat Genet.* (2011) 44:200–5. doi: 10.1038/ng.1027
63. Revesz T, Holton JL, Lashley T, Plant G, Frangione B, Rostagno A, et al. Genetics and molecular pathogenesis of sporadic and hereditary cerebral amyloid angiopathies. *Acta Neuropathol.* (2009) 118:115–30. doi: 10.1007/s00401-009-0501-8
64. French CR, Seshadri S, Destefano AL, Fornage M, Arnold CR, Gage PJ, et al. Mutation of FOXC1 and PITX2 induces cerebral small-vessel disease. *J Clin Invest.* (2014) 124:4877–81. doi: 10.1172/JCI75109
65. Yu L, Boyle PA, Nag S, Leurgans S, Buchman AS, Wilson RS, et al. APOE and cerebral amyloid angiopathy in community-dwelling older persons. *Neurobiol Aging.* (2015) 36:2946–53. doi: 10.1016/j.neurobiolaging.2015.08.008
66. Luo X, Jiaerken Y, Yu X, Huang P, Qiu T, Jia Y, et al. Associations between APOE genotype and cerebral small-vessel disease: a longitudinal study. *Oncotarget.* (2017) 8:44477–89. doi: 10.18632/oncotarget.17724
67. Yuan A, Rao MV, Veeranna, Nixon RA. Neurofilaments and neurofilament proteins in health and disease. *Cold Spring Harbor Perspect Biol.* (2017) 9. doi: 10.1101/cshperspect.a018309
68. Khalil M, Teunissen CE, Otto M, Piehl F, Sormani MP, Gatteringer T, et al. Neurofilaments as biomarkers in neurological disorders. *Nature reviews Neurology.* (2018) 14:577–89. doi: 10.1038/s41582-018-0058-z
69. Mattsson N, Andreasson U, Zetterberg H, Blennow K. Association of plasma neurofilament light with neurodegeneration in patients with alzheimer disease. *JAMA Neurol.* (2017) 74:557–66. doi: 10.1001/jamaneurol.2016.6117
70. Jonsson M, Zetterberg H, van Straaten E, Lind K, Syversen S, Edman A, et al. Cerebrospinal fluid biomarkers of white matter lesions - cross-sectional results from the LADIS study. *Euro J Neurol.* (2010) 17:377–82. doi: 10.1111/j.1468-1331.2009.02808.x
71. Meeker KL, Butt OH, Gordon BA, Fagan AM, Schindler SE, Morris JC, et al. Cerebrospinal fluid neurofilament light chain is a marker of aging and white matter damage. *Neurobiol Dis.* (2022) 166:105662. doi: 10.1016/j.nbd.2022.105662
72. Peters N, van Leijzen E, Tuladhar AM, Barro C, Konieczny MJ, Ewers M, et al. Serum neurofilament light chain is associated with incident lacunes in progressive cerebral small vessel disease. *J Stroke.* (2020) 22:369–76. doi: 10.5853/jos.2019.02845
73. Qu Y, Tan CC, Shen XN, Li HQ, Cui M, Tan L, et al. Association of plasma neurofilament light with small vessel disease burden in nondemented elderly: a longitudinal study. *Stroke.* (2021) 52:896–904. doi: 10.1161/STROKEAHA.120.030302
74. Hedden T, Mormino EC, Amariglio RE, Younger AP, Schultz AP, Becker JA, et al. Cognitive profile of amyloid burden and white matter hyperintensities in cognitively normal older adults. *J Neurosci.* (2012) 32:16233–42. doi: 10.1523/JNEUROSCI.2462-12.2012
75. Gurol ME, Irizarry MC, Smith EE, Raju S, Diaz-Arrastia R, Bottiglieri T, et al. Plasma beta-amyloid and white matter lesions in AD, MCI, and cerebral amyloid angiopathy. *Neurology.* (2006) 66:23–9. doi: 10.1212/01.wnl.0000191403.95453.6a
76. Kester MI, Goos JD, Teunissen CE, Benedictus MR, Bouwman FH, Wattjes MP, et al. Associations between cerebral small-vessel disease and Alzheimer disease pathology as measured by cerebrospinal fluid biomarkers. *JAMA Neurol.* (2014) 71:855–62. doi: 10.1001/jamaneurol.2014.754
77. McAleese KE, Firbank M, Dey M, Colloby SJ, Walker L, Johnson M, et al. Cortical tau load is associated with white matter hyperintensities. *Acta neuropathologica communications.* (2015) 3:60. doi: 10.1186/s40478-015-0240-0
78. Tosto G, Zimmerman ME, Hamilton JL, Carmichael OT, Brickman AM. The effect of white matter hyperintensities on neurodegeneration in mild cognitive impairment. *Alzheimer Dement.* (2015) 11:1510–9. doi: 10.1016/j.jalz.2015.05.014
79. Vilor-Tejedor N, Ciampa I, Operto G, Falcón C, Suárez-Calvet M, Crous-Bou M, et al. Perivascular spaces are associated with tau pathophysiology and synaptic dysfunction in early Alzheimer's continuum. *Alzheimer Res Ther.* (2021) 13:135. doi: 10.1186/s13195-021-00878-5
80. Shams S, Granberg T, Martola J, Li X, Shams M, Fereshtehnejad SM, et al. Cerebrospinal fluid profiles with increasing number of cerebral microbleeds in a continuum of cognitive impairment. *J Cereb Blood Flow Metab.* (2016) 36:621–8. doi: 10.1177/0271678X15606141
81. Chiang GC, Cruz Hernandez JC, Kantarci K, Jack CR, Jr., Weiner MW. Cerebral microbleeds, CSF p-tau, and cognitive decline: significance of anatomic distribution. *AJNR Am J Neuroradiol.* (2015) 36:1635–41. doi: 10.3174/ajnr.A4351
82. Sparacia G, Agnello F, La Tona G, Iaia A, Midiri F, Sparacia B. Assessment of cerebral microbleeds by susceptibility-weighted imaging in Alzheimer's disease patients: a neuroimaging biomarker of the disease. *Neuroradiol J.* (2017) 30:330–5. doi: 10.1177/1971400916689483
83. Poliakova T, Levin O, Arablinskiy A, Vasenina E, Zerr I. Cerebral microbleeds in early Alzheimer's disease. *J Neurol.* (2016) 263:1961–8. doi: 10.1007/s00415-016-8220-2
84. Yao T, Song G, Li Y, Wang D. Chronic kidney disease correlates with MRI findings of cerebral small vessel disease. *Renal Failure.* (2021) 43:255–63. doi: 10.1080/0886022X.2021.1873804
85. Jiménez-Balado J, Riba-Llena I, Pizarro J, Palasí A, Penalba A, Ramírez C, et al. Kidney function changes and their relation with the progression of cerebral small vessel disease and cognitive decline. *J Neurol Sci.* (2020) 409:116635. doi: 10.1016/j.jns.2019.116635
86. Bugnicourt JM, Godefroy O, Chillon JM, Choukroun G, Massy ZA. Cognitive disorders and dementia in CKD: the neglected kidney-brain axis. *J Am Soc Nephrol.* (2013) 24:353–63. doi: 10.1681/ASN.2012050536
87. Georgakis MK, Chatzopoulou D, Tsigoulis G, Petridou ET. Albuminuria and cerebral small vessel disease: a systematic review and meta-analysis. *J Am Geriatrics Soc.* (2018) 66:509–17. doi: 10.1111/jgs.15240
88. Akoudad S, Sedaghat S, Hofman A, Koudstaal PJ, van der Lugt A, Ikram MA, et al. Kidney function and cerebral small vessel disease in the general population. *Int J Stroke.* (2015) 10:603–8. doi: 10.1111/ijvs.12465
89. van Dinther M, Schram MT, Jansen JFA, Backes WH, Houben A, Berendschot T, et al. Extracerebral microvascular dysfunction is related to brain MRI markers of cerebral small vessel disease: The Maastricht Study. *GeroScience.* (2021). doi: 10.1007/s11357-021-00493-0 [Epub ahead of print].
90. McGovern AP, de Lusignan S, van Vlymen J, Liyanage H, Tomson CR, Gallagher H, et al. Serum phosphate as a risk factor for cardiovascular events in people with and without chronic kidney disease: a large community based cohort study. *PLoS ONE.* (2013) 8:e74996. doi: 10.1371/journal.pone.0074996
91. Gross P, Six I, Kamel S, Massy ZA. Vascular toxicity of phosphate in chronic kidney disease: beyond vascular calcification. *Circul J.* (2014) 78:2339–46. doi: 10.1253/circj.CJ-14-0735
92. Chung CR, Peng LN, Chou KH, Liu LK, Lee WJ, Lin CP, et al. High circulatory phosphate level is associated with cerebral small-vessel diseases. *Transl Stroke Res.* (2019) 10:265–72. doi: 10.1007/s12975-018-0639-6
93. Kashani AH, Asanad S, Chan JW, Singer MB, Zhang J, Sharifi M, et al. Past, present and future role of retinal imaging in neurodegenerative disease. *Progress Retinal Eye Res.* (2021) 83:100938. doi: 10.1016/j.preteyeres.2020.100938
94. Liao H, Zhu Z, Peng Y. Potential utility of retinal imaging for Alzheimer's disease: a review. *Front Aging Neurosci.* (2018) 10:188. doi: 10.3389/fnagi.2018.00188
95. London A, Benhar I, Schwartz M. The retina as a window to the brain-from eye research to CNS disorders. *Nat Rev Neurol.* (2013) 9:44–53. doi: 10.1038/nrneurol.2012.227
96. Abdelhak A, Huss A, Brück A, Sebert U, Mayer B, Müller HP, et al. Optical coherence tomography-based assessment of retinal vascular pathology in cerebral small vessel disease. *Neurol Res Pract.* (2020) 2:13. doi: 10.1186/s42466-020-00062-4
97. Wang X, Wei Q, Wu X, Cao S, Chen C, Zhang J, et al. The vessel density of the superficial retinal capillary plexus as a new biomarker in cerebral small vessel disease: an optical coherence tomography angiography study. *Neurol Sci.* (2021) 42:3615–24. doi: 10.1007/s10072-021-05038-z
98. Chapman FA, Nyimamu D, Maguire JJ, Davenport AP, Newby DE, Dhaun N. The therapeutic potential of apelin in kidney disease. *Nat Rev Nephrol.* (2021) 17:840–53. doi: 10.1038/s41581-021-00461-z

99. Foulquier S, Namsolleck P, Van Hagen BT, Milanova I, Post MJ, Blankestijn WM, et al. Hypertension-induced cognitive impairment: insights from prolonged angiotensin II infusion in mice. *Hypertens Res.* (2018) 41:817–27. doi: 10.1038/s41440-018-0090-9
100. Lu YW, Hao RJ, Wei YY, Yu GR. The protective effect of harpagoside on angiotensin II (Ang II)-induced blood-brain barrier leakage *in vitro*. *Phytother Res.* (2021) 35:6241–54. doi: 10.1002/ptr.7269
101. Giani JF, Janjulia T, Taylor B, Bernstein EA, Shah K, Shen XZ, et al. Renal generation of angiotensin II and the pathogenesis of hypertension. *Curr Hypertens Rep.* (2014) 16:477. doi: 10.1007/s11906-014-0477-1
102. Jochemsen HM, Geerlings MI, Grool AM, Vincken KL, Mali WP, van der Graaf Y, et al. Angiotensin-converting enzyme and progression of white matter lesions and brain atrophy—the SMART-MR study. *J Alzheimer Dis.* (2012) 29:39–49. doi: 10.3233/JAD-2012-111772
103. Vilar-Bergua A, Riba-Llena I, Penalba A, Cruz LM, Jiménez-Balado J, Montaner J, et al. N-terminal pro-brain natriuretic peptide and subclinical brain small vessel disease. *Neurology.* (2016) 87:2533–9. doi: 10.1212/WNL.0000000000003423
104. Wei W, Chen Y, Lei D, Zhang Y, Weng X, Zhou Y, et al. Plasma brain natriuretic peptide is a biomarker for screening ischemic cerebral small vessel disease in patients with hypertension. *Medicine.* (2018) 97:e12088. doi: 10.1097/MD.00000000000012088
105. Zhang CE, Wong SM, van de Haar HJ, Staals J, Jansen JF, Jeukens CR, et al. Blood-brain barrier leakage is more widespread in patients with cerebral small vessel disease. *Neurology.* (2017) 88:426–32. doi: 10.1212/WNL.0000000000003556



## OPEN ACCESS

## EDITED BY

Jun Xu,  
Capital Medical University, China

## REVIEWED BY

Xiaofan Jiang,  
Fourth Military Medical  
University, China  
Jin Huang,  
Aviation General Hospital of China  
Medical University, China  
Chen Chen,  
The First Affiliated Hospital of  
Soochow University, China

## \*CORRESPONDENCE

Anying Wang  
wanganying008@163.com

## SPECIALTY SECTION

This article was submitted to  
Neurological Biomarkers,  
a section of the journal  
Frontiers in Neurology

RECEIVED 10 July 2022

ACCEPTED 03 August 2022

PUBLISHED 20 September 2022

## CITATION

Zhang W, Zhang Y, Hu N and Wang A  
(2022) Alzheimer's disease-associated  
inflammatory pathways might  
contribute to osteoporosis through  
the interaction between *PROK2* and  
*CSF3*. *Front. Neurol.* 13:990779.  
doi: 10.3389/fneur.2022.990779

## COPYRIGHT

© 2022 Zhang, Zhang, Hu and Wang.  
This is an open-access article  
distributed under the terms of the  
[Creative Commons Attribution License](#)  
(CC BY). The use, distribution or  
reproduction in other forums is  
permitted, provided the original  
author(s) and the copyright owner(s)  
are credited and that the original  
publication in this journal is cited, in  
accordance with accepted academic  
practice. No use, distribution or  
reproduction is permitted which does  
not comply with these terms.

# Alzheimer's disease-associated inflammatory pathways might contribute to osteoporosis through the interaction between *PROK2* and *CSF3*

Wenzheng Zhang<sup>1</sup>, Ya Zhang<sup>2</sup>, Naixia Hu<sup>3</sup> and Anying Wang<sup>4\*</sup>

<sup>1</sup>Department of Joint Sports Medicine, The Affiliated Taian City Central Hospital of Qingdao University, Taian, China, <sup>2</sup>Department of Pathology, The Second Affiliated Hospital of Shandong First Medical University, Taian, China, <sup>3</sup>Neurointensive Care Unit, The Second Affiliated Hospital of Shandong First Medical University, Taian, China, <sup>4</sup>Department of Orthopedics, The Second Affiliated Hospital of Shandong First Medical University, Taian, China

This study aimed to explore the potential molecular pathways and targets of Alzheimer's disease leading to osteoporosis using bioinformatics tools. The Alzheimer's and osteoporosis microarray gene expression data were retrieved from the Gene Expression Omnibus, and differentially expressed genes in the blood microenvironment related to Alzheimer's disease and osteoporosis were identified. The intersection of the three datasets (GSE97760, GSE168813, and GSE62402) was used to obtain 21 co-expressed targets in the peripheral blood samples in patients with Alzheimer's disease and osteoporosis. Based on the degree algorithm, the top 10 potential core target genes related to these diseases were identified, which included *CLEC4D*, *PROK2*, *SIGLEC7*, *PDGFB*, *PTCRA*, *ECH1*, etc. Two differentially expressed mRNAs, Prokineticin 2 (*PROK2*) and three colony-stimulating factor 3 (*CSF3*), were screened in the GSE62402 dataset associated with osteoporosis. Protein-protein rigid docking with ZDOCK revealed that *PROK2* and *CSF3* could form a stable protein docking model. The interaction of *PROK2* and *CSF3*, core genes related to osteoporosis inflammation, plays an important role in the mechanism of osteoporosis in patients with Alzheimer's. Therefore, abnormalities or alterations in the inflammatory pathways in the peripheral blood samples of Alzheimer's patients may affect the course of osteoporosis.

## KEYWORDS

Alzheimer's disease, osteoporosis, *PROK2*, *CSF3*, bio-informatics analysis, biomarkers, neurovascular

## Introduction

Osteoporosis (OP) is a bone metabolic disease that is common and highly prevalent in the elderly population (1). The prevalence of OP in the elderly increases with age (2). OP reduces bone strength and increases the risk of fracture in these patients (3, 4). Globally, osteoporotic fractures are an economic burden on society and the patients'



families. They are also associated with high disability and mortality rates in elderly patients, which raise serious concerns about their health in today's aging society (5–8).

Alzheimer's disease (AD), which is yet another concern in the elderly, has been found to have a high incidence in the elderly along with OP. Previous studies have shown a prevalence of osteoporosis of 27% in patients with Alzheimer's disease, compared to 16% in residents without dementia (9). Beta-amyloid, *APOE4*, vitamin K, and vitamin D may be important proteins that interconnect AD and OP (10). Vitamin deficiency significantly increases AD risk. Interestingly, vitamin levels within a certain range positively correlate with cognitive performance (11–13). Also, alterations in vitamin D levels in the serum in middle-aged and elderly populations are associated with decreased bone mineral density (14). The AD mouse model, APP/PS1 transgenic mice, had significantly different bone microarchitecture and bone density parameters compared to wild-type mice and was more susceptible to OP (15). *In vitro* and *in vivo* studies in AD transgenic mouse models showed an enhanced amyloid beta (A $\beta$ ) peptide expression in bone tissue. Furthermore, an increase in A $\beta$  peptide levels induces changes in bone mineral density, affecting the balance between bone formation and bone resorption, leading to OP (16). In addition, the Wnt/ $\beta$ -catenin signaling pathway plays an important role in AD and OP pathogenesis due to its role in inflammation (17, 18). Therefore, it is tempting to postulate a correlation between AD and OP. Patients with AD are cognitively impaired and prone to physical injuries. It is important to understand how AD regulates OP in patients to prevent OP occurrence and its treatment in patients with AD.

With the advancement in bioinformatics and high-throughput sequencing, it is now possible to screen the differentially expressed genes (DEGs) using microarray gene expression profiling (19–23). Publicly available databases and repositories that store information on gene expression, microarrays, and clinical samples can help understand the underlying mechanism of the disease and screen potential molecular targets quickly and efficiently before their use in clinical settings (24–26). This study aimed to investigate the molecular mechanism of OP in patients with AD using data retrieved from the Gene Expression Omnibus (GEO) database. The potential molecular pathways and biological processes associated with OP in patients with AD were explored using bioinformatics tools. Finally, we identified key targets for preventing and treating OP in patients with AD. This will provide valuable insights into understanding the pathogenesis and progression of OP in patients with AD.

---

Abbreviations: AD, Alzheimer's disease; OP, Osteoporosis; PPI, Protein–protein interaction; GO, Gene Ontology; KEGG, Kyoto Encyclopedia of Genes and Genomes; DEGs, Differentially expressed genes.

## Materials and methods

### Target gene identification

The gene expression microarray data on “Alzheimer's disease” and “osteoporosis” were retrieved from the GEO database (<https://www.ncbi.nlm.nih.gov/geo/>). The data were screened using the following criteria: (i) keywords “Alzheimer's disease,” “osteoporosis,” (ii) peripheral blood, and (iii) human. The expression matrix data were corrected and normalized using the Bioconductor R package (R version 4.0.4). The differentially expressed mRNAs in the peripheral blood samples of patients with “AD” and “OP,” that is, the differentially expressed genes (DEGs) associated with AD and OP, were found in compared to normal healthy adults. The DEGs between the two groups were calculated using the linear models for the microarray data (limma package), with the screening criteria of  $P < 0.05$  and absolute value of fold change  $\geq 1.41$  ( $|\log_2 \text{FC}| \geq 0.50$ ). We used the statistical tests built into the ggpubr package for statistical testing.

### Screening and co-expression of differential genes in AD and OP and PPI network construction

Using the Venn R package, Venn graphs were created by intersecting AD-related and OP-related DEGs. The Search Tool for the Retrieval of Interacting Genes/Proteins database (<https://string-db.org/>) was used to construct the protein–protein interaction (PPI) network and generate PPI relationship data. The PPI network model was further visualized by Cytoscape 3.7.2. The PPI network was topologically analyzed according to degree values to screen for the core target proteins.

### Gene ontology functional analysis and KEGG pathway enrichment

The clusterProfiler, an R package, was used to perform Gene Ontology (GO) and Kyoto Encyclopedia of Genes and Genomes (KEGG) enrichment analysis on AD-OP-related DEGs. The species was set to human for this analysis. The signaling pathways were mapped using the “Pathview: an R/Bioconductor package.”

### Establishment of OP-inflammatory-related gene expression matrix

The gene expression matrix of the OP transcriptome profile was established with the inflammatory response-related genes

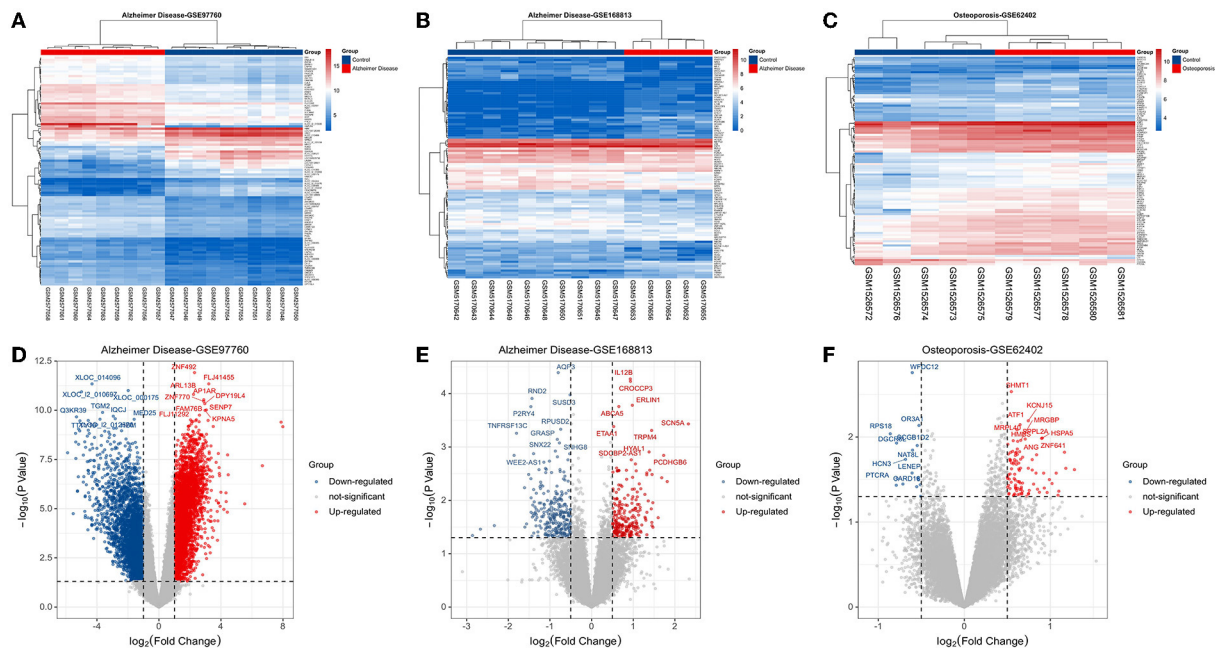


**FIGURE 1**  
Disease target screening. (A) Heat map of differentially expressed genes in GSE97760; (B) heat map of differentially expressed genes in GSE168813; (C) heat map of differentially expressed genes in GSE62402; (D) volcano map of differentially expressed genes in GSE97760; (E) volcano map of differentially expressed genes in GSE168813; (F) volcano map of differentially expressed genes in GSE62402.

extracted from the Gene Set Enrichment Analysis (GSEA) database as previous researches (27–29). The differentially expressed mRNAs between the OP group and normal healthy groups were calculated using the limma package. The “heatmap” package was used to construct maps of gene expression and cluster the DEGs.

## Relative expression of core target genes

The microarray data of the OP-related gene expression matrix were retrieved from GEO, and the expression of core DEGs in each sample was derived based on the core targets obtained from the pre-screening. The “ggpubr package” was used to analyze the relative expression of the core targets in the OP expression data.  $P < 0.05$  was considered statistically significant. A box plot of the relative expression of the core targets was plotted (R version 4.0.4).

## GO and KEGG enrichment analysis of OP-inflammation-related genes

GO and KEGG pathway enrichment analysis of OP-inflammation-related genes were done using the Scatterplot3d: 3D graphics, clusterProfiler in R package software, and Perl software package.

## Molecular docking to validate the interactions between inflammatory proteins

Rigid protein–protein docking (ZDOCK) was performed between inflammatory proteins to study the reciprocal relationships. The PDB format of the protein structural domain was downloaded from the Protein Data Bank PDB database (<http://www.rcsb.org/>). The protein structure was imported into Discovery Studio 2019 software to dehydrate and dephosphorylate the proteins. The upstream protein of the inflammatory pathway was set as the receptor protein, and the downstream protein was selected as the ligand–protein. The angular step size was set to  $15^\circ$ . The ZDOCK module was run to identify the docking site and calculate the ZDOCK Score. When molecular dynamics simulation (MDS) finds the docking site, the two form a stable docking (30–33). The results of protein–protein molecular docking are shown in 2D format.

## Results

### Screening for disease targets

Based on the keywords used and screening criteria set, nine patients with AD and 10 normal healthy individuals from the GSE97760 dataset retrieved from GEO were included in

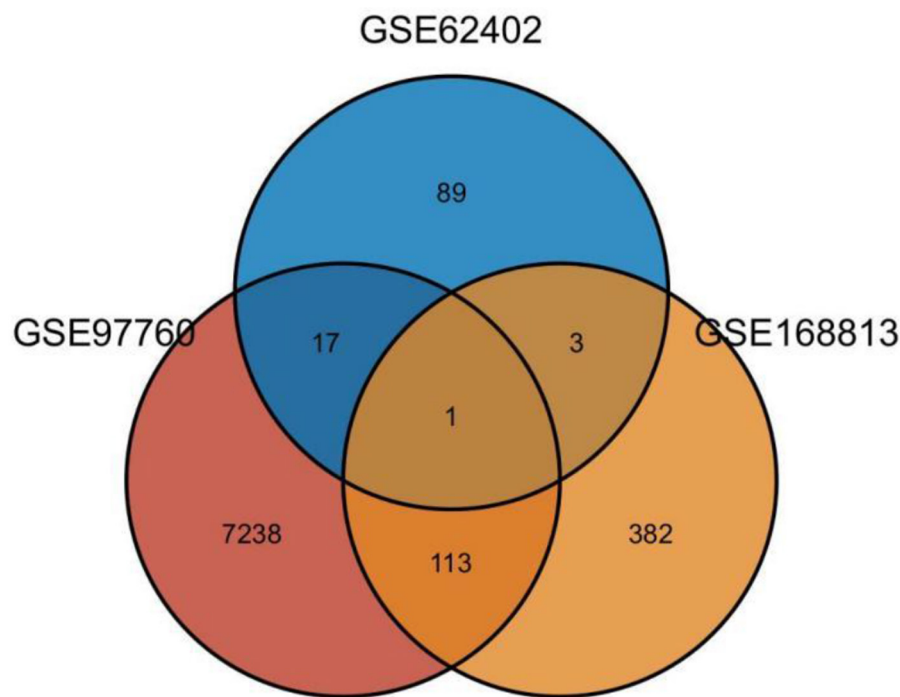


FIGURE 2

Venn diagram of differential co-expressed genes in Alzheimer's disease and osteoporosis in the blood microenvironment.

the study. A total of 7,370 differentially expressed mRNAs, of which 4,003 upregulated and 3,367 downregulated mRNAs, were obtained. In the GSE168813 dataset, five patients with AD and 10 normal healthy individuals were included in the study. In this dataset, 499 differentially expressed mRNAs were identified, of which 236 mRNAs were upregulated, and 263 mRNAs were downregulated. In the GSE62402 dataset, five OP patients and five normal healthy individuals were included in the study, and 110 differentially expressed mRNAs (94 upregulated and 16 downregulated mRNAs) were obtained. The heat map generated is shown in [Figures 1A–C](#). The transcriptome differential expression data were represented by constructing a volcano map, as shown in [Figures 1D–F](#).

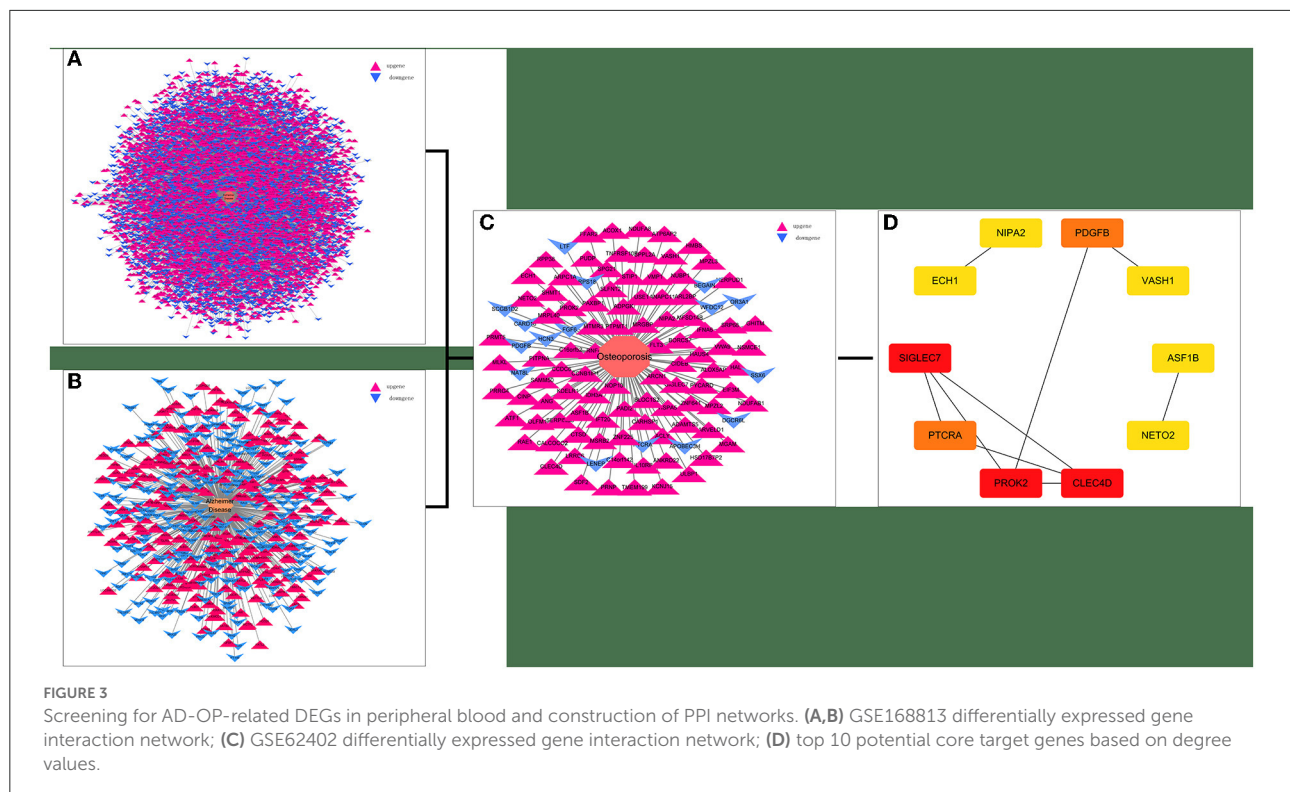
## Detection of AD-OP-related DEGs in peripheral blood and construction of PPI networks

Twenty-one AD-OP-related DEGs were obtained from the intersection of the DEGs of the three microarray datasets ([Figure 2](#)). The AD-OP-target gene network was constructed by Cytoscape software ([Figures 3A–C](#)). Protein–protein interaction of the AD-OP-related DEGs was constructed using Cytoscape software. The top 10 potential core target proteins ([Figure 3D](#)), including *CLEC4D*, *PROK2*, *SIGLEC7*,

*PDGFB*, *PTCRA*, and *ECH1*, were obtained using the CytoHubba plugin in Cytoscape software based on degree size screening ([34](#)).

## Results of the GO and KEGG enrichment analysis

The biological processes (BP) associated with the 21 AD-OP-related DEGs were regulation of calcium ion import, endothelial cell proliferation, and inositol phosphate-mediated signaling ([Figure 4A](#)). The related cell compositions (CC) mainly included BLOC-1 complex, eukaryotic 48S preinitiation complex, and eukaryotic translation initiation factor 3 complex ([Figure 4B](#)). The related molecular functions (MF) mainly enriched were glutamate receptor binding, superoxide-generating NADPH oxidase activator, and G protein-coupled glutamate receptor binding ([Figure 4C](#)). [Figure 4D](#) shows the GO enrichment features. KEGG pathway enrichment analysis shows that pathways like transcriptional dysregulation in cancer, ferroptosis, porphyrin metabolism, and other immune-related signaling pathways ([Figure 5A](#)) were associated with 21 AD-OP-related DEGs in peripheral blood. Furthermore, AD-OP-related DEGs in peripheral blood function were closely related to the ferroptosis signaling pathway ([Figure 5B](#)).



## Establishment of OP-inflammatory response-related gene expression matrix

The gene set related to the inflammatory response was downloaded from GSEA. The OP-related GSE62402 dataset was retrieved from GEO based on the pre-set filters. R software was used to organize and analyze the metabolomics-related expression matrix. According to the screening criteria set earlier, two differentially expressed mRNAs were identified, *PROK2* was upregulated, and *CSF3* was downregulated. Figure 6 shows a heat map of the OP-inflammatory response-related gene expression matrix.

## Relative expression of the core target genes associated with OP inflammation

The core OP-inflammation-related genes *PROK2* and *CSF3* were obtained by comprehensive differential expression analysis. The relative expression of *PROK2* and *CSF3* in OP was analyzed. The relevant expression profile of *PROK2* and *CSF3* in OP patients was downloaded from GEO, analyzed by the ggpvr package, and visualized using the box expression map (Figures 7A,B). The results showed that *PROK2* was highly expressed in peripheral blood OP patients compared to normal healthy individuals and the difference was statistically

significant ( $P < 0.01$ ). Furthermore, compared to normal healthy individuals, there was a significant reduction in *CSF3* expression in peripheral blood of OP patients ( $P < 0.01$ ).

## GO and KEGG enrichment analysis results of OP-inflammation-related genes

Enrichment analysis of the two OP-inflammatory response-related genes enriched BP, such as the regulation of actin cytoskeleton reorganization, smooth muscle contraction, and granulocyte differentiation. Their molecular functions enriched were growth factor receptor binding, growth factor activity, and cytokine activity (Figures 8A–D). The KEGG pathway enrichment analysis found that their functions are mainly associated with malaria, IL-17 signaling pathway, hematopoietic cell lineage, JAK-STAT signaling pathway, and COVID-19 (Figures 8E,F).

## Molecular docking of inflammatory proteins

The 3D structures of the 11MT structural domain of *PROK2* protein and the 2D9Q structural domain of *CSF3* protein were downloaded from the PDB database



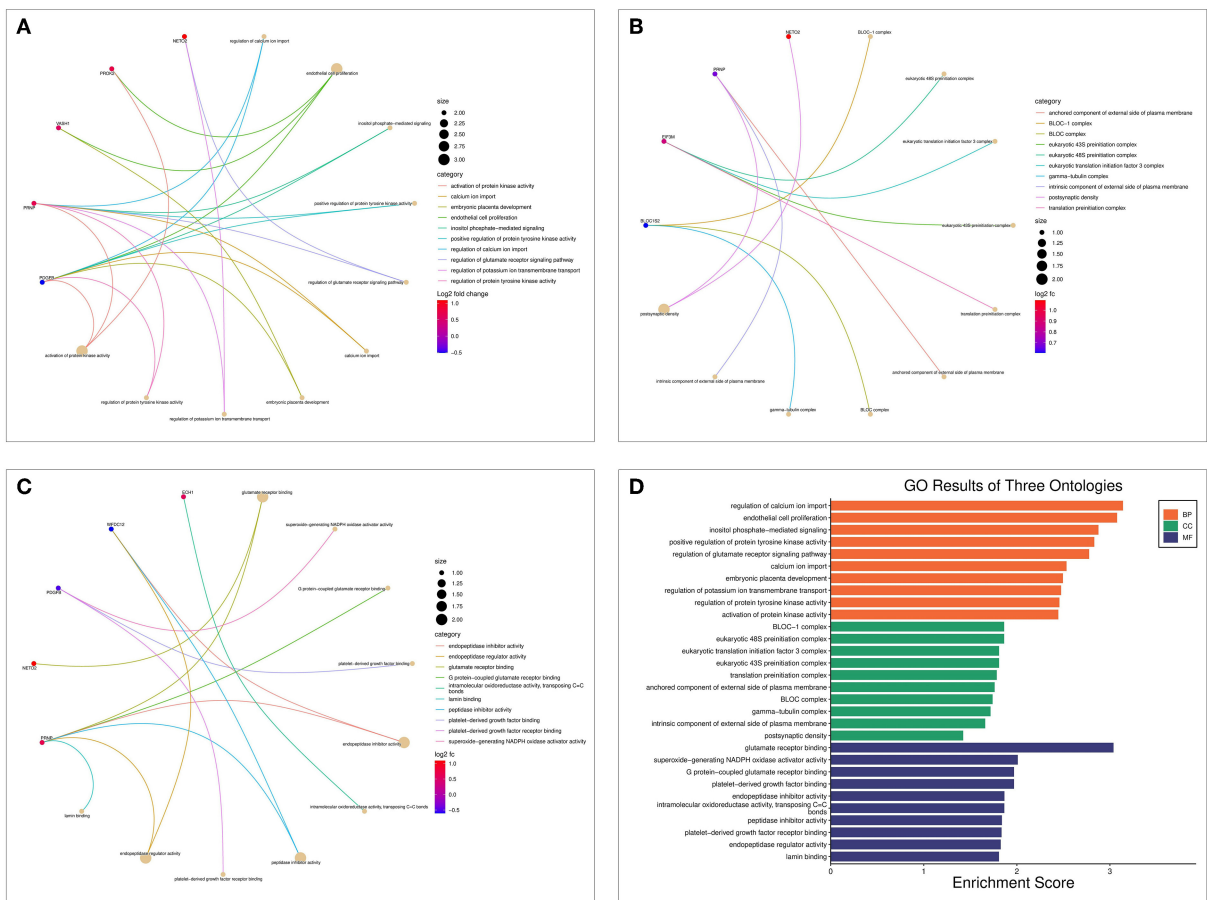


**FIGURE 4** Results of the GO enrichment analysis for AD-OP-related DEGs. (A) Chord diagram of biological processes functional analysis; (B) chord diagram of cell component functional analysis; (C) chord diagram of molecular function functional analysis; (D) histogram of GO enrichment analysis.

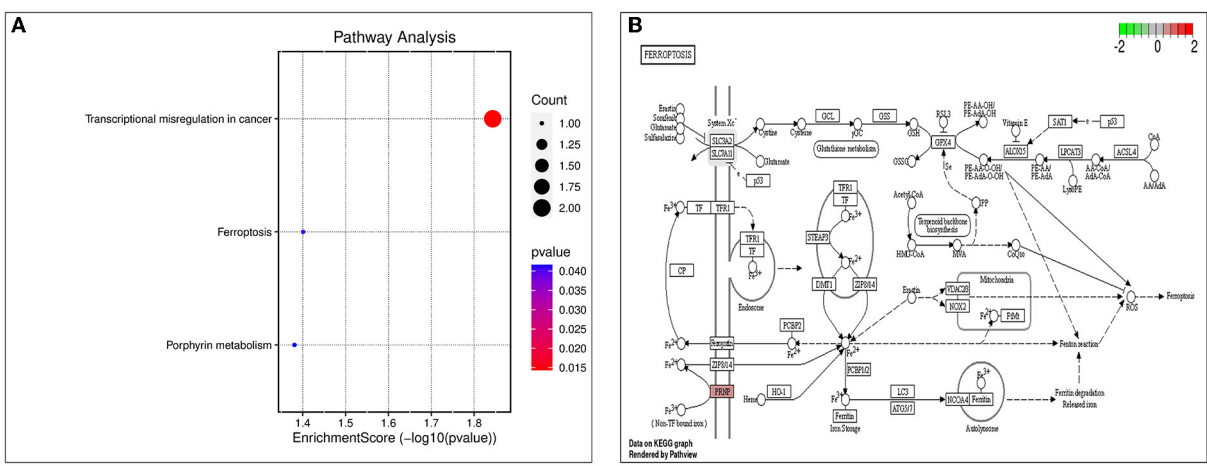
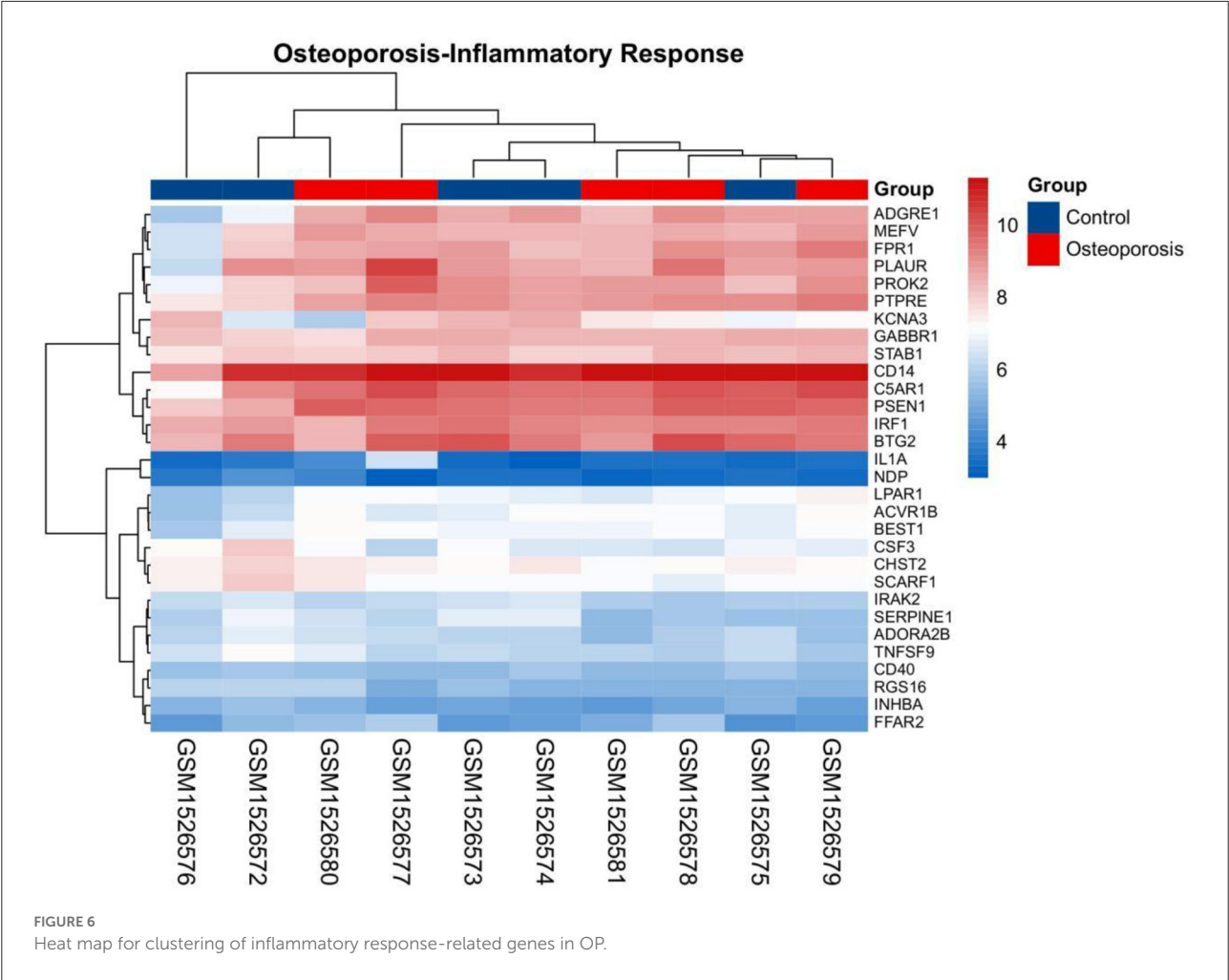


**FIGURE 5** Results of KEGG enrichment analysis. (A) KEGG enrichment analysis bubble chart; (B) ferroptosis signaling pathway.





and exported in PDB format. The ZDOCK module of Discovery Studio 2019 software was used to rigidly dock *PROK2* protein to *CSF3* protein. The ZDOCK Score values and their best pose interaction were calculated, as shown in Table 1. The ZDOCK Score of the 1IMT domain of *PROK2* protein and the 2D9Q docking model of *CSF3* protein was  $-85.085$ . The 1IMT domain of *PROK2* proteins forms hydrogen bond links with amino acid sites such as B:ARG167:NH1—A:ASP109:OD1, B:ARG167:NH2—A:ASP112:OD1, B:ARG288:NH2—A:GLU19:OE1, A:HOH177:O—A:PRO65:O, and other amino acid sites, whereas A:LYS16:NZ—B:ASP197:O D1, A:LYS16:NZ—B:ASP200:OD1, B:ARG167:NH1—A:ASP112:OD2, B:ARG288:NH1—A:GLU19:OE2, A:LEU15—B:LEU291, and other amino acid sites form electrostatic interactions and water transport bonds. Comprehensive analysis revealed that proteins *PROK2* and *CSF3* formed a stable protein docking model. Figure 9 demonstrates two-dimensional molecular docking constructed using Discovery Studio 2019 software.

## Discussion

Gene expression microarray datasets on Alzheimer's disease and osteoporosis patients' peripheral blood samples were retrieved from the GEO database. The results revealed that two dysregulated proteins, *PROK2* and *CSF3*, were associated with the occurrence of OP in patients with AD. Using rigid protein-protein docking by ZDOCK confirmed that the two proteins form a stable protein docking model, suggesting that the interaction between the two proteins plays an important role in the occurrence of OP in patients with AD.

Prokineticin 2 (*PROK2*) is expressed throughout the central nervous system (35). As a new family of chemokine-like molecules, they are involved in various physiological and pathological processes, including nerve and blood vessel regeneration, pain, inflammation, and neuroinflammation (36–38). A study confirmed that *PROK2* mediates harmful brain injuries (39). In AD, *PROK2* maintains a state of neuroinflammation and

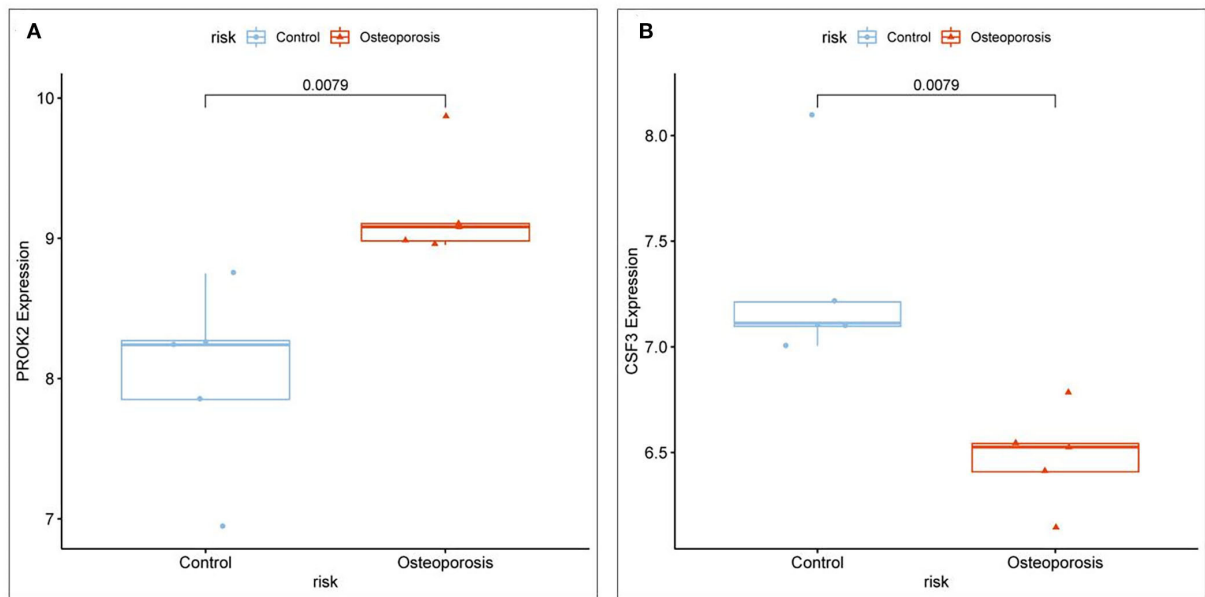


FIGURE 7  
Relative expression levels of core targets involved in OP inflammation. (A) *PROK2* relative expression; (B) *CSF3* relative expression.

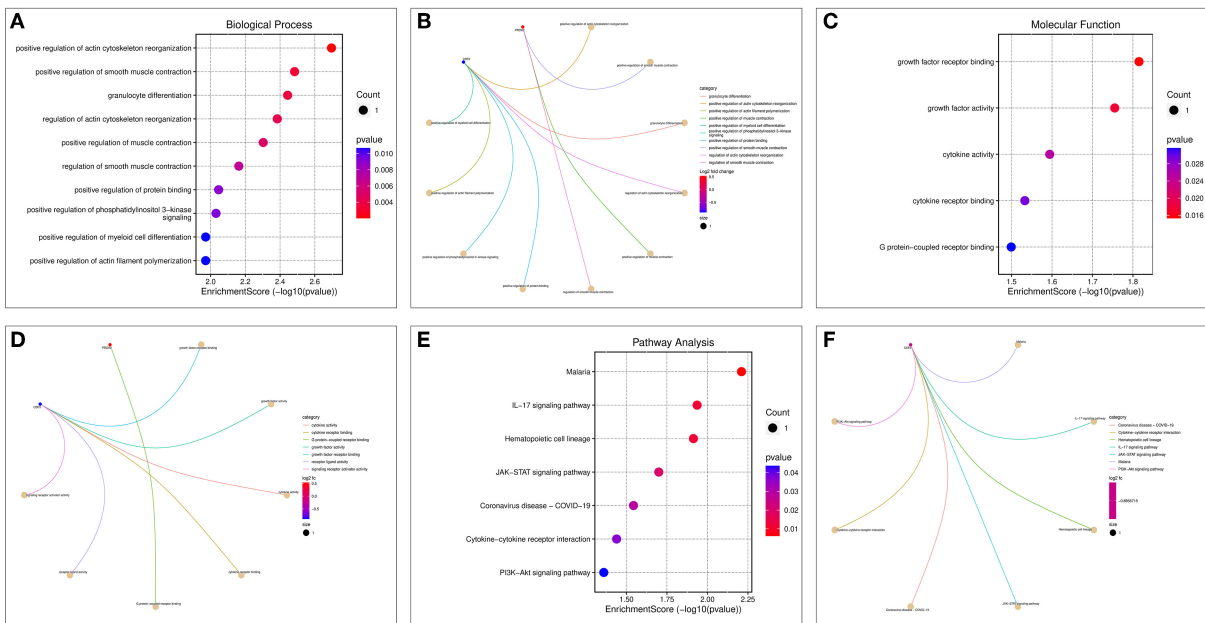


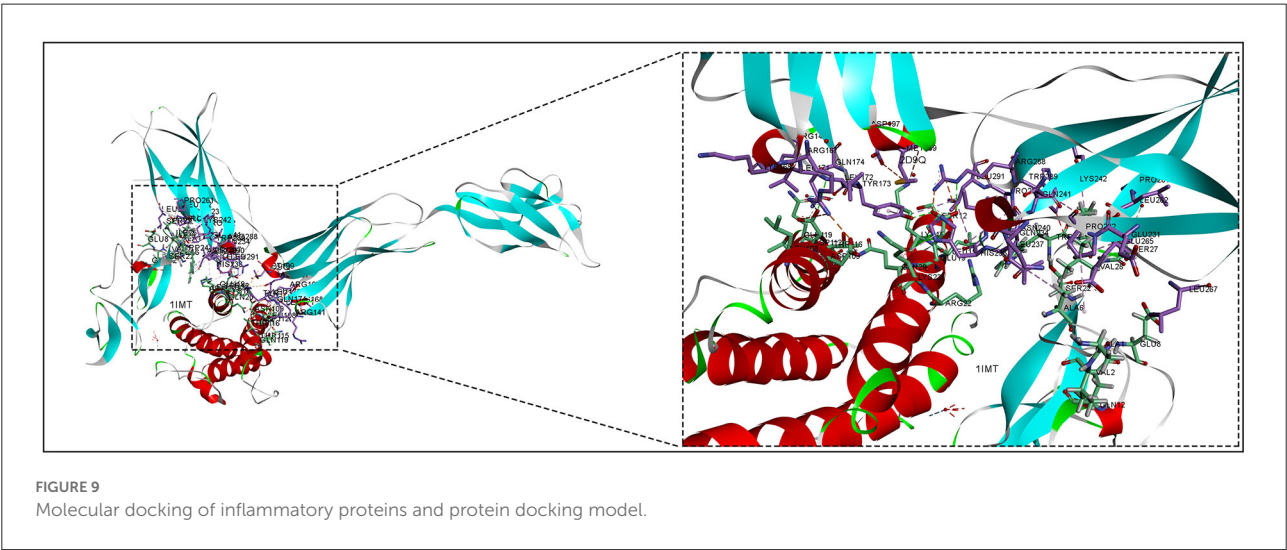
FIGURE 8  
GO and KEGG enrichment analysis of OP-inflammation-related genes. (A) BP enrichment bubble diagram; (B) BP enrichment arc diagram; (C) MF enrichment bubble diagram; (D) MF enrichment arc diagram; (E) KEGG enrichment bubble diagram; (F) KEGG enrichment arc diagram.

causes neurotoxicity (35). Studies show the involvement of *PROK2* in A $\beta$ -induced toxicity, as A $\beta$  peptides increase *PROK2* expression in AD, representing a new class of pathological markers in AD animal models (40–42). Consistent with the previous studies, our results show

that *PROK2* expression was upregulated in patients with AD. Furthermore, the *PROK2* expression was not only associated with inflammatory responses in the blood samples of patients with AD but also was a core gene associated with inflammation in OP.

TABLE 1 Results of molecular docking vina, discovery studio 2019.

| Receptor            | Ligand             | ZDOCK score | Hydrogen bond interaction  | Electrostatic interaction   |
|---------------------|--------------------|-------------|--|---|
| <i>PROK2</i> (1IMT) | <i>CSF3</i> (2D9Q) | −85.085     | B:ARG167:NH1—A:ASP109:OD1,<br>B:ARG167:NH2—A:ASP112:OD1,<br>B:ARG288:NH2—A:GLU19:OE1,<br>A:HOH177:O—A:PRO65:O... | A:LYS16:NZ—B:ASP197:OD1,<br>A:LYS16:NZ—B:ASP200:OD1,<br>B:ARG167:NH1—A:ASP112:OD2,<br>B:ARG288:NH1—A:GLU19:OE2,<br>A:LEU15—B:LEU291 |



Few studies have shown the *PROK2* expression and functions in OP. Interestingly, previous studies have demonstrated the involvement of *PROK2* in A $\beta$ -mediated toxicity and have a positive correlation with A $\beta$  peptides. It also alters the bone mineral density, which may affect the bone formation and resorption balance, leading to the development of OP (16, 42). Prokineticin receptor 2 (*PROKR2*) is the *PROK2* and G protein-coupled receptor (GPCR). In addition, GPCRs affect bone metabolism by influencing the cytokines and signaling pathways that regulate osteoblasts (OB) and osteoclasts (OC) (43). In addition, *PROK2* is also closely associated with gastrointestinal (GI) function and GI diseases (44). Previous studies have also shown that the OP incidences were significantly higher in patients with GI diseases (45, 46). Hence, we hypothesized that *PROK2* plays an important role in the development of OP. In this study, we show for the first time the upregulation of *PROK2* expression in OP. Furthermore, *PROK2* was a core gene associated with OP inflammation and a common gene differentially expressed between AD and OP patients. Hence, *PROK2* could be potentially used as a molecular marker for predicting the occurrence of OP in patients with AD.

*CSF3* is a member of the colony-stimulating factor family. Together with its receptor *CSF3R*, *CSF3* is involved in regulating

sarcomere cell production, neutrophil function, etc. (47). A study has reported that neutrophil/lymphocyte ratio could be used in predicting the occurrence of OP (48). Zhang et al. demonstrated the expression of RANKL, the osteoclast differentiation factor on the surface of neutrophils. RANKL binds to the osteoclast differentiation factor receptor, RANK, which mediates osteoclast differentiation, thereby enhancing the osteoclast activity. This disrupts bone metabolism, which reduces bone mass (49). However, the relationship between *CSF3* and OP has not been established.

In this study, the expression of *CSF3* was downregulated in OP as a core gene related to OP inflammation. Bone resorption is enhanced during the chronic inflammatory response, reducing the bone formation and promoting OP (50). Previous studies show that *CSF3* is an anti-inflammatory cytokine that clears bacterial pathogens and modulates the inflammatory response (51). Therefore, we postulate the involvement of *CSF3* in inflammation-related biological processes in the progression of OP.

The core inflammation-related genes *PROK2* and *CSF3* involved in OP, identified in this study, were associated with the signal transducer and activator of the transcription (STAT) pathway. The STAT pathway induces astrocyte proliferation

and is activated in AD animal models and humans. Previous studies have demonstrated that reactive astrocyte proliferation is a hallmark of the AD signaling pathway (52). STAT3 induces astrocyte proliferation and is activated in human AD and animal models, and reactive astrocyte proliferation is a hallmark of AD (52). During acute inflammation and septic inflammatory conditions, *CSF3* mediates STAT3-dependent upregulation of neutrophil IL-4R (53). Interestingly, an increase in *STAT3* phosphorylation was observed in cells stably expressing *PROKR2*, which is the receptor for *PROK2* (54). In addition, the STAT signaling pathway plays an important role in the pathogenesis of OP and AD. Inhibiting *STAT3* phosphorylation attenuates learning and causes memory deficits in AD animal models (55). Furthermore, the *STAT3* signaling pathway is involved in the progression of OP by altering osteoblast bone metabolism (43, 56). Consistent with the previous studies, the KEGG pathway enrichment analysis revealed that both genes enriched the JAK-STAT signaling pathway and pathways associated with malaria, IL-17 signaling pathway, hematopoietic cell lineage, and COVID-19. GeneCards database (<https://ga.genecards.org/#results>) shows that both *PROK2* and *CSF3* were associated with the extracellular region. Furthermore, GO analysis revealed the involvement of *PROK2* and *CSF3* in protein binding and their association with VEGF. In this study, we identified the combined role of *PROK2* and *CSF3* in the pathogenesis of AD and OP. Our results reveal those alterations in the inflammatory response pathway in the peripheral blood of patients with AD may affect the occurrence and progression of OP. The docking results show that proteins *PROK2* and *CSF3* could form a stable protein docking model, thus confirming the previous bioinformatics results that the interaction between the *PROK2* and *CSF3* could be involved in the inflammatory-related response to OP in patients with AD.

In this study, using bioinformatics analysis, we demonstrated that the proteins *PROK2* and *CSF3* may be involved in inflammation-related processes in the development of OP in patients with AD and confirmed stable protein interactions between them by docking, thereby verifying the reliability of predictions made by bioinformatics analysis. However, the study has a few shortcomings. The primary technique used in this study was bioinformatics analysis. Hence, further experiments validating the interaction between *PROK2* and *CSF3* proteins are required. The results of our study predict the role of *PROK2* and *CSF3* protein binding in the pathogenesis of OP in patients with AD. However, the mechanism is still unclear and needs further exploration using appropriate experiments.

## Conclusion

AD-related OP may be caused by the interaction between *PROK2* and *CSF3*, two proteins related to OP inflammation. Accordingly, abnormalities/alterations in the inflammatory response in the peripheral blood of patients with AD could influence the progression of OP. Further exploration of targets for treating OP in patients with AD will be facilitated by our study.

## Data availability statement

Publicly available datasets were analyzed in this study. This data can be found at: The gene micro-array data related to Alzheimer's disease and osteoporosis were downloaded from the GEO (gene expression omnibus) database (<https://www.ncbi.nlm.nih.gov/geo/>): GSE97760, GSE168813, and GSE62402 dataset.

## Author contributions

AW, WZ, YZ, and NH: conceptualization, methodology, software, data curation, writing the original draft preparation, and validation. AW and WZ: visualization, investigation, writing, reviewing, and editing. AW: supervision. All authors contributed to the article and approved the submitted version.

## Conflict of interest

The authors declare that the research was conducted in the absence of any commercial or financial relationships that could be construed as a potential conflict of interest.

## Publisher's note

All claims expressed in this article are solely those of the authors and do not necessarily represent those of their affiliated organizations, or those of the publisher, the editors and the reviewers. Any product that may be evaluated in this article, or claim that may be made by its manufacturer, is not guaranteed or endorsed by the publisher.

## References

- Li G, Thabane L, Papaioannou A, Ioannidis G, Levine MAH, Adachi JD. An overview of osteoporosis and frailty in the elderly. *BMC Musculoskelet Disord.* (2017) 18:46. doi: 10.1186/s12891-017-1403-x
- Vandenbroucke A-M, Luyten F, Flamaing J, Gielen E. Pharmacological treatment of osteoporosis in the oldest old. *CIA.* (2017) 12:1065–77. doi: 10.2147/CIA.S131023
- Li W, Zhang S, Liu J, Liu Y, Liang Q. Vitamin K2 stimulates Mc3T3-E1 osteoblast differentiation and mineralization through autophagy induction. *Mol Med Report.* (2019) 19:3676–84. doi: 10.3892/mmr.2019.10040
- Agnew AM, Dominguez VM, Sciulli PW, Stout SD. Variability of *in vivo* linear microcrack accumulation in the cortex of elderly human ribs. *Bone Rep.* (2017) 6:60–3. doi: 10.1016/j.bonr.2017.02.004
- Tella SH, Gallagher JC. Prevention and treatment of postmenopausal osteoporosis. *J Steroid Biochem Mol Biol.* (2014) 142:155–70. doi: 10.1016/j.jsbmb.2013.09.008
- Hongo M, Miyakoshi N, Shimada Y, Sinaki M. Association of spinal curve deformity and back extensor strength in elderly women with osteoporosis in Japan and the United States. *Osteoporos Int.* (2012) 23:1029–34. doi: 10.1007/s00198-011-1624-z
- Snellman G, Byberg L, Lemming EW, Melhus H, Gedeberg R, Mallmin H, et al. Long-term dietary vitamin D intake and risk of fracture and osteoporosis: a longitudinal cohort study of Swedish middle-aged and elderly women. *J Clin Endocrinol Metab.* (2014) 99:781–90. doi: 10.1210/jc.2013-1738
- Yoo JE, Shin DW, Han K, Kim D, Yoon JW, Lee D-Y. Association of female reproductive factors with incidence of fracture among postmenopausal women in Korea. *J Am Med Assoc Netw Open.* (2021) 4:e2030405. doi: 10.1001/jamanetworkopen.2020.30405
- Weller I. Hip fractures and Alzheimer's disease in elderly institutionalized Canadians. *Ann Epidemiol.* (2004) 14:319–24. doi: 10.1016/j.annepidem.2003.08.005
- Frame G, Bretland KA, Dengler-Criss CM. Mechanistic complexities of bone loss in Alzheimer's disease: a review. *Connect Tissue Res.* (2020) 61:4–18. doi: 10.1080/03008207.2019.1624734
- Balton C, Griffith LE, Striffler L, Henderson M, Patterson C, Heckman G, et al. Vitamin D, cognition, and dementia: a systematic review and meta-analysis. *Neurology.* (2012) 79:1397–405. doi: 10.1212/WNL.0b013e31826c197f
- Littlejohns TJ, Henley WE, Lang IA, Annweiler C, Beauchet O, Chaves PHM, et al. Vitamin D and the risk of dementia and Alzheimer disease. *Neurology.* (2014) 83:920–8. doi: 10.1212/WNL.0000000000000755
- Shen L, Ji H-F. Vitamin D deficiency is associated with increased risk of Alzheimer's disease and dementia: evidence from meta-analysis. *Nutr J.* (2015) 14:76. doi: 10.1186/s12937-015-0063-7
- Wei Q, Chen Z, Tan X, Su H, Chen X, He W, et al. Relation of age, sex and bone mineral density to serum 25-hydroxyvitamin D levels in Chinese women and men: 25(OH)D in healthy adults. *Orthop Surg.* (2015) 7:343–9. doi: 10.1111/os.12206
- Panaro MA, Corrado A, Benamer T, Paolo CF, Cici D, Porro C. The emerging role of curcumin in the modulation of TLR-4 signaling pathway: focus on neuroprotective and anti-rheumatic properties. *Int J Mol Sci.* (2020) 21:2299. doi: 10.3390/ijms21072299
- Kelly RR, Sidles SJ, LaRue AC. Effects of neurological disorders on bone health. *Front Psychol.* (2020) 11:612366. doi: 10.3389/fpsyg.2020.612366
- Jia L, Piña-Crespo J, Li Y. Restoring Wnt/ $\beta$ -catenin signaling is a promising therapeutic strategy for Alzheimer's disease. *Mol Brain.* (2019) 12:104. doi: 10.1186/s13041-019-0525-5
- Wang F, Li C, Shao J, Ma J. Sevoflurane induces inflammation of microglia in hippocampus of neonatal rats by inhibiting Wnt/ $\beta$ -Catenin/CaMKIV pathway. *J Pharmacol Sci.* (2021) 146:105–15. doi: 10.1016/j.jphs.2021.02.004
- Feng X, Ding Y, Zhou M, Song N, Ding Y. Integrative analysis of exosomal miR-452 and miR-4713 downregulating NPY1R for the prevention of childhood obesity. *Dis Markers.* (2022) 2022:1–12. doi: 10.1155/2022/2843353
- Huang H, Jiang H, Liu J, Chen J, Qiu L, Wang J, et al. Facial nerve monitoring under different levels of neuromuscular blockade with *Cisatracurium besilate* in parotid tumour surgery. *Biomed Res Int.* (2021) 2021:5655061. doi: 10.1155/2021/5655061
- Won H-H, Kim SR, Bang OY, Lee S-C, Huh W, Ko J-W, et al. Differentially expressed genes in human peripheral blood as potential markers for statin response. *J Mol Med.* (2012) 90:201–11. doi: 10.1007/s00109-011-0818-3
- Kleinrouweler CE, Van Uitert M, Moerland PD, Ris-Stalpers C, Van Der Post JAM, Afink GB. Differentially expressed genes in the pre-eclamptic placenta: a systematic review and meta-analysis. *PLoS ONE.* (2013) 8:e68991. doi: 10.1371/journal.pone.0068991
- Chen Y, Sun Y, Luo Z, Chen X, Wang Y, Qi B, et al. Exercise Modifies the Transcriptional regulatory features of monocytes in Alzheimer's patients: a multi-omics integration analysis based on single cell technology. *Front Aging Neurosci.* (2022) 14:881488. doi: 10.3389/fnagi.2022.881488
- Andreu-Perez J, Poon CCY, Merrifield RD, Wong STC, Yang G-Z. Big data for health. *IEEE J Biomed Health Inform.* (2015) 19:1193–208. doi: 10.1109/JBHI.2015.2450362
- Dong S, Huang F, Zhang H, Chen Q. Overexpression of BUB1B, CCNA2, CDC20, and CDK1 in tumor tissues predicts poor survival in pancreatic ductal adenocarcinoma. *Biosci Rep.* (2019) 39:BSR20182306. doi: 10.1042/BSR20182306
- Chen L, Yuan L, Wang Y, Wang G, Zhu Y, Cao R, et al. Co-expression network analysis identified FCER1G in association with progression and prognosis in human clear cell renal cell carcinoma. *Int J Biol Sci.* (2017) 13:1361–72. doi: 10.7150/ijbs.21657
- Wu L, Su C, Yang C, Liu J, Ye Y. TBX3 regulates the transcription of VEGFA to promote osteoblasts proliferation and microvascular regeneration. *PeerJ.* (2022) 10:e13722. doi: 10.7717/peerj.13722
- Xu K, Wu C, Wang Z, Wang H, Yin F, Li W, et al. Family gene expression as prognostic biomarkers for Alzheimer's disease and primary liver cancer. *Comput Math Methods Med.* (2021) 2021:1–15. doi: 10.1155/2021/3422393
- Subramanian A, Tamayo P, Mootha VK, Mukherjee S, Ebert BL, Gillette MA, et al. Gene set enrichment analysis: a knowledge-based approach for interpreting genome-wide expression profiles. *Proc Natl Acad Sci USA.* (2005) 102:15545–50. doi: 10.1073/pnas.0506580102
- Hildebrand PW, Rose AS, Tiemann JKS. Bringing molecular dynamics simulation data into view. *Trends Biochem Sci.* (2019) 44:902–13. doi: 10.1016/j.tibs.2019.06.004
- Lu L, Kang X, Yi B, Jiang C, Yan X, Chen B, et al. Exploring the mechanism of Yiqi Qingre Ziyin method in regulating neuropeptide expression for the treatment of atrophic rhinitis. *Dis Markers.* (2022) 2022:1–12. doi: 10.1155/2022/4416637
- Chen Y, Luo Z, Lin J, Qi B, Sun Y, Li F, et al. Exploring the potential mechanisms of melilots officinalis (l) pall in chronic muscle repair patterns using single cell receptor-ligand marker analysis and molecular dynamics simulations. *Dis Markers.* (2022) 2022:1–11. doi: 10.1155/2022/9082576
- Hollingsworth SA, Dror RO. Molecular dynamics simulation for all. *Neuron.* (2018) 99:1129–43. doi: 10.1016/j.neuron.2018.08.011
- Chin C-H, Chen S-H, Wu H-H, Ho C-W, Ko M-T, Lin C-Y. cytoHubba: identifying hub objects and sub-networks from complex interactome. *BMC Syst Biol.* (2014) 8:S11. doi: 10.1186/1752-0509-8-S4-S11
- Zuena AR, Casolini P, Lattanzi R, Maftei D. Chemokines in Alzheimer's disease: new insights into prokineticins, chemokine-like proteins. *Front Pharmacol.* (2019) 10:622. doi: 10.3389/fphar.2019.00622
- Zinni M, Zuena AR, Marconi V, Petrella C, Fusco I, Giuli C, et al. Maternal exposure to low levels of corticosterone during lactation protects adult rat progeny against TNBS-induced colitis: a study on GR-mediated anti-inflammatory effect and prokineticin system. *PLoS ONE.* (2017) 12:e0173484. doi: 10.1371/journal.pone.0173484
- Negri L, Ferrara N. The prokineticins: neuromodulators and mediators of inflammation and myeloid cell-dependent angiogenesis. *Physiol Rev.* (2018) 98:1055–82. doi: 10.1152/physrev.00012.2017
- Negri L, Maftei D. Targeting the prokineticin system to control chronic pain and inflammation. *Curr Med Chem.* (2018) 25:3883–94. doi: 10.2174/0929867324666170713102514
- Cheng MY, Lee AG, Culbertson C, Sun G, Talati RK, Manley NC, et al. Prokineticin 2 is an endangering mediator of cerebral ischemic injury. *Proc Natl Acad Sci USA.* (2012) 109:5475–80. doi: 10.1073/pnas.1113363109
- Severini C, Lattanzi R, Maftei D, Marconi V, Ciotti MT, Petrocchi Passeri P, et al. Bv8/prokineticin 2 is involved in A $\beta$ -induced neurotoxicity. *Sci Rep.* (2015) 5:15301. doi: 10.1038/srep15301



41. Caioli S, Severini C, Ciotti T, Florenzano F, Pimpinella D, Petrocchi Passeri P, et al. Prokineticin system modulation as a new target to counteract the amyloid beta toxicity induced by glutamatergic alterations in an *in vitro* model of Alzheimer's disease. *Neuropharmacology*. (2017) 116:82–97. doi: 10.1016/j.neuropharm.2016.12.012
42. Maftei D, Ratano P, Fusco I, Marconi V, Squillace S, Negri L, et al. The prokineticin receptor antagonist PC1 rescues memory impairment induced by  $\beta$  amyloid administration through the modulation of prokineticin system. *Neuropharmacology*. (2019) 158:107739. doi: 10.1016/j.neuropharm.2019.107739
43. Luo J, Sun P, Siwko S, Liu M, Xiao J. The role of GPCRs in bone diseases and dysfunctions. *Bone Res*. (2019) 7:19. doi: 10.1038/s41413-019-0059-6
44. Kurebayashi H, Goi T, Shimada M, Tagai N, Naruse T, Nakazawa T, et al. Prokineticin 2 (*PROK2*) is an important factor for angiogenesis in colorectal cancer. *Oncotarget*. (2015) 6:26242–51. doi: 10.18632/oncotarget.4385
45. Locantore P, Del Gatto V, Gelli S, Paragliola RM, Pontecorvi A. The interplay between immune system and microbiota in osteoporosis. *Mediators Inflamm*. (2020) 2020:1–8. doi: 10.1155/2020/3686749
46. Stuckey BGA, Mahoney LA, Dragovic S, Brown SJ. Celiac disease and bone health: is there a gap in the management of postmenopausal osteoporosis? *Climacteric*. (2020) 23:559–65. doi: 10.1080/13697137.2020.1816957
47. Zhang H, Coblenz C, Watanabe-Smith K, Means S, Means J, Maxson JE, et al. Gain-of-function mutations in granulocyte colony-stimulating factor receptor (*CSF3R*) reveal distinct mechanisms of *CSF3R* activation. *J Biol Chem*. (2018) 293:7387–96. doi: 10.1074/jbc.RA118.002417
48. Gao K, Zhu W, Liu W, Ma D, Li H, Yu W, et al. The predictive role of monocyte-to-lymphocyte ratio in osteoporosis patient. *Medicine*. (2019) 98:e16793. doi: 10.1097/MD.00000000000016793
49. Zhang P, Pan L, Luo Z, Zhao H, Cai S. Interrelationship of circulating matrix metalloproteinase-9, TNF- $\alpha$ , and OPG/RANK/RANKL systems in COPD patients with osteoporosis. *J Chronic Obst Pulmonary Dis*. (2013) 10:650–6. doi: 10.3109/15412555.2013.813928
50. Sato K, Suematsu A, Okamoto K, Yamaguchi A, Morishita Y, Kadono Y, et al. Th17 functions as an osteoclastogenic helper T cell subset that links T cell activation and bone destruction. *J Exp Med*. (2006) 203:2673–82. doi: 10.1084/jem.20061775
51. Yeganegi M, Leung CG, Martins A, Kim SO, Reid G, Challis JRG, et al. *Lactobacillus rhamnosus* GR-1 stimulates colony-stimulating factor 3 (Granulocyte) (*CSF3*) output in placental trophoblast cells in a fetal sex-dependent manner. *Biol Reprod*. (2011) 84:18–25. doi: 10.1095/biolreprod.110.085167
52. Reichenbach N, Delekate A, Plescher M, Schmitt F, Krauss S, Blank N, et al. Inhibition of Stat3-mediated astrogliosis ameliorates pathology in an Alzheimer's disease model. *EMBO Mol Med*. (2019) 11:e9665. doi: 10.15252/emmm.201809665
53. Panda SK, Wigerblad G, Jiang L, Jiménez-Andrade Y, Iyer VS, Shen Y, et al. IL-4 controls activated neutrophil Fc $\gamma$ R2b expression and migration into inflamed joints. *Proc Natl Acad Sci USA*. (2020) 117:3103–13. doi: 10.1073/pnas.1914186117
54. Lattanzi R, Maftei D, Vincenzi M, Fullone MR, Miele R. Identification and characterization of a new splicing variant of prokineticin 2. *Life*. (2022) 12:248. doi: 10.3390/life12020248
55. Choi M, Kim H, Yang E-J, Kim H-S. Inhibition of STAT3 phosphorylation attenuates impairments in learning and memory in 5XFAD mice, an animal model of Alzheimer's disease. *J Pharmacol Sci*. (2020) 143:290–9. doi: 10.1016/j.jphs.2020.05.009
56. Seeliger C, Schyschka L, Kronbach Z, Wottge A, van Griensven M, Wildemann B, et al. Signaling pathway STAT1 is strongly activated by IFN- $\beta$  in the pathogenesis of osteoporosis. *Eur J Med Res*. (2015) 20:1. doi: 10.1186/s40001-014-0074-4



## OPEN ACCESS

## EDITED BY

Yuzhen Xu,  
Tongji University, China

## REVIEWED BY

Paolo Candelaesi,  
Ospedale Antonio Cardarelli, Italy  
Yi Sui,  
Shenyang Medical College Affiliated  
Brain Hospital, China

## \*CORRESPONDENCE

Feng Wang  
13816566556@163.com  
Quanbin Zhang  
quanbinzhang@aliyun.com

<sup>†</sup>These authors have contributed  
equally to this work and share first  
authorship

<sup>†</sup>These authors have contributed  
equally to this work

## SPECIALTY SECTION

This article was submitted to  
Neurological Biomarkers,  
a section of the journal  
Frontiers in Neurology

RECEIVED 19 July 2022

ACCEPTED 06 September 2022

PUBLISHED 26 September 2022

## CITATION

Wang Q, Wang Y, Wang Y, Bi Q,  
Zhang Q and Wang F (2022) Impact of  
improved stroke green channel  
process on the delay of intravenous  
thrombolysis in patients with acute  
cerebral infarction during the  
COVID-19 pandemic: An observational  
study. *Front. Neurol.* 13:998134.  
doi: 10.3389/fneur.2022.998134

## COPYRIGHT

© 2022 Wang, Wang, Wang, Bi, Zhang  
and Wang. This is an open-access  
article distributed under the terms of  
the [Creative Commons Attribution  
License \(CC BY\)](#). The use, distribution  
or reproduction in other forums is  
permitted, provided the original  
author(s) and the copyright owner(s)  
are credited and that the original  
publication in this journal is cited, in  
accordance with accepted academic  
practice. No use, distribution or  
reproduction is permitted which does  
not comply with these terms.

# Impact of improved stroke green channel process on the delay of intravenous thrombolysis in patients with acute cerebral infarction during the COVID-19 pandemic: An observational study

Qiwei Wang<sup>1†</sup>, Yan Wang<sup>2†</sup>, Yongpeng Wang<sup>1</sup>, Qianqian Bi<sup>1</sup>,  
Quanbin Zhang<sup>3\*\*</sup> and Feng Wang<sup>1\*\*</sup>

<sup>1</sup>Departments of Neurology, Seventh People's Hospital of Shanghai University of Traditional Chinese Medicine, Shanghai, China, <sup>2</sup>Department of Neurology, Shanghai General Hospital of Shanghai Jiao Tong University School of Medicine, Shanghai, China, <sup>3</sup>Department of Neurosurgery, Shanghai Tenth People's Hospital, Tongji University School of Medicine, Shanghai, China

**Objective:** This study analyzed the impact of the improved stroke green channel process on the delay of intravenous thrombolysis in patients with acute cerebral infarction under coronavirus disease 2019 (COVID-19) prevention and control measures.

**Methods:** We included 57 patients from the stroke center of the Seventh People's Hospital of Shanghai University of Traditional Chinese Medicine before the improvement of the stroke green channel process (March–July 2019), as well as 94 patients during the severe acute respiratory syndrome coronavirus 2 (SARS-CoV-2) outbreak (March–July 2020) and 68 patients during the Omicron variant outbreak (March–July 2022) after the improvement of stroke green channel process. The door-to-needle time (DNT), door-to-imaging time (DIT), and door-to-test completion time were compared among the three groups. We analyzed the impact of this process improvement in the emergency green channel during the pandemic on the delay of intravenous thrombolysis.

**Results:** This study included a total of 229 patients with acute cerebral infarction who went through the green channel for intravenous thrombolysis (57 in the pre-pandemic group, 94 in the SARS-CoV-2 outbreak group, and 68 in the Omicron outbreak group). The percentages of patients undergoing intravenous thrombolysis in the pre-pandemic, SARS-CoV-2 outbreak, and Omicron outbreak groups differed significantly (19.32%, 22.27%, and 28.94%, respectively,  $P = 0.029$ ). Compared to the pre-pandemic group, the National Institutes of Health Stroke Scale (NIHSS) score at admission was significantly higher in the Omicron outbreak group ( $7.71 \pm 7.36$  in the Omicron outbreak group vs.  $5.00 \pm 4.52$  in the pre-pandemic group) ( $P = 0.026$ ) but not in the SARS-CoV-2 outbreak group ( $4.79 \pm 5.94$  in the SARS-CoV-2 outbreak group vs.  $5.00 \pm 4.52$  in the pre-pandemic group,  $P = 0.970$ ). Significantly higher

proportions of patients undergoing emergency intravenous thrombolysis came to the hospital by ambulance in the SARS-CoV-2 and Omicron outbreak groups compared to the pre-pandemic group (38.6% in the pre-pandemic group, 51.1% in the SARS-CoV-2 outbreak group, and 82.4% in the Omicron outbreak group,  $P < 0.001$ ). Compared to the pre-pandemic group, the DIT was significantly higher in the SARS-CoV-2 outbreak group ( $22.42 \pm 7.62$  min in the SARS-CoV-2 outbreak group vs.  $18.91 \pm 8.23$  min in the pre-pandemic group,  $P = 0.031$ ) but not the Omicron outbreak group ( $20.35 \pm 10.38$  min in the Omicron outbreak group vs.  $18.91 \pm 8.23$  min in the pre-pandemic group,  $P = 0.543$ ). The door-to-test completion time was significantly longer in the SARS-CoV-2 and Omicron outbreak groups compared to that in the pre-pandemic group ( $78.37 \pm 25.17$  min in the SARS-CoV-2 outbreak group,  $92.60 \pm 25.82$  min in the Omicron outbreak group vs.  $65.11 \pm 22.35$  min in the pre-pandemic group,  $P < 0.001$ ); however, the DNT in the SARS-CoV-2 and Omicron outbreak groups did not differ significantly from those in the pre-pandemic group (both  $P > 0.05$ ).

**Conclusion:** During the two periods of the COVID-19 outbreak (SARS-CoV-2 and Omicron), after the improvement of the green channel for intravenous thrombolysis, there might be some delay in in-hospital DIT during the SARS-CoV-2 outbreak, however, the in-hospital delay indicator DNT for intravenous thrombolysis were not affected.

#### KEYWORDS

acute cerebral infarction, COVID-19, improved green channel for intravenous thrombolysis, intravenous thrombolysis, time delay

## Introduction

Acute cerebral infarction is characterized by high incidence, disability, and mortality rates. Patients are often left with motor-sensory, language function, and cognitive impairments, which not only significantly reduce their quality of life but also impose great burdens on families and society. Currently, intravenous thrombolytic therapy is the most effective treatment for early-stage cerebral infarction. This therapy recanalizes the occluded blood vessels and restores cerebral blood flow, helping to save damaged neurons in the brain, thus minimizing the degree of patient disability. However, the administration of intravenous thrombolytic therapy has a strict time window of 4.5 h after disease onset, which can be extended to 9 h for patients who pass a strict screening process (1). Thrombolysis beyond this time window not only fails to improve neurological function but also may induce serious complications such as reperfusion injury. The prognosis of patients with acute cerebral infarction is closely related to the timing of thrombolysis (2, 3). The construction of the stroke green channel aims to shorten the time delay for the administration of intravenous thrombolysis and to achieve a good patient prognosis.

In December 2019, a pneumonia outbreak caused by a novel coronavirus occurred in Wuhan City, Hubei Province, China,

and surrounding areas. The World Health Organization (WHO) announced the name of the novel coronavirus pneumonia, coronavirus disease 2019 (COVID-19), on February 11, 2020. At the same time, the International Committee on Taxonomy of Viruses declared that the novel coronavirus was named severe acute respiratory syndrome coronavirus 2 (SARS-CoV-2). The COVID-19 outbreak spread rapidly across the country, and Shanghai launched a Level 1 response to major public health emergencies to control the spread of the virus. After the WHO announced on November 25, 2021, that the Omicron (B.1.1.529) variant of SARS-CoV-2 was detected for the first time in South Africa, this variant has led to a global surge of newly diagnosed cases of COVID-19. An outbreak of the Omicron variant occurred in Shanghai in March 2022. To prevent viral spread within healthcare facilities and ensure that patients with acute stroke were treated effectively and in promptly, new requirements were introduced for stroke green channel management (4). Considering the need for pandemic prevention and control, our hospital has improved and optimized the emergency stroke green channel accordingly since March 2020. Further improvement was implemented in March 2022 to address the Omicron variant. The present study explored whether the improvement and optimization of the stroke green channel process under the prevention and control of the

COVID-19 pandemic would affect the timing for intravenous thrombolysis in patients with acute cerebral infarction.

## Materials and methods

### Subjects

The data of 219 patients with acute ischemic stroke who were sequentially admitted to the stroke center of the Seventh People's Hospital of Shanghai University of Traditional Chinese Medicine through the stroke green channel process from March 1 to July 31, 2019 (pre-pandemic group), March 1 to July 31, 2020 (SARS-CoV-2 outbreak group), and March 1 to July 31, 2022 (Omicron outbreak group) were included in this study.

The SARS-CoV-2 outbreak group adopted the initial improved stroke green channel process, while the Omicron outbreak group adopted the advanced improved stroke green channel process. The pre-hospital and in-hospital delays of the patients in these two groups were compared to those of patients in the pre-pandemic group.

## Methods

### Inclusion criteria

The inclusion criteria were as follows: acute ischemic stroke diagnosed by head computed tomography (CT); within 4.5 h of symptom onset; age  $\geq 18$  years; informed consent signed by family members; patients who met the diagnostic criteria of the "Chinese Guidelines for Diagnosis and Treatment of Acute Ischemic Stroke 2018; and underwent intravenous thrombolysis. The exclusion criteria were patients with acute cerebral infarction who did not undergo intravenous thrombolysis.

### Emergency stroke green channel process

#### Before green channel improvement

The stroke center was established in 2015. Before the COVID-19 outbreak, no epidemic prevention measures had been adopted for the emergency stroke green channel. Upon patient arrival at the emergency room, the nurse at the reception desk triaged the patient according to the symptoms, and patients with suspected stroke were directed into the emergency room. The emergency physician in the stroke center recorded the patient medical history and conducted physical examinations and then prescribed assessments, including head CT scan, hematology tests, electrocardiogram (ECG), etc. Subsequently, the emergency physician analyzed the examination results and confirmed the diagnosis of acute ischemic stroke. In patients who did not exceed the time window for intravenous thrombolysis, the current condition was explained in detail to the patient's family members, and informed consent for

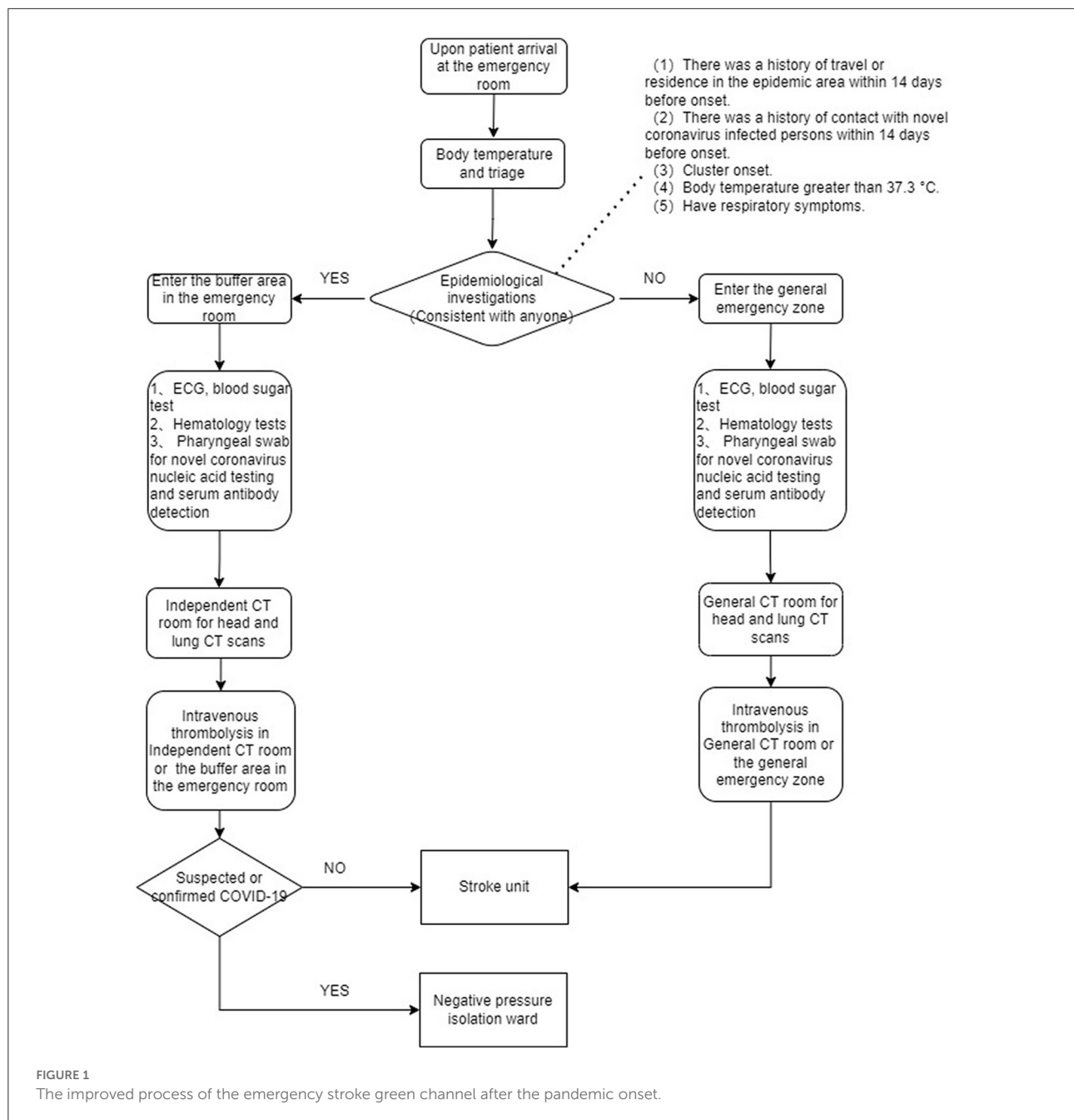
intravenous thrombolysis was requested. The patients received thrombolytic therapy in the emergency room under ECG monitoring and were then admitted to the stroke unit for further diagnosis and treatment.

#### After green channel improvement

COVID-19 first emerged in China in November 2019 and gradually spread across the entire country. On February 20, 2020, we improved the green channel process to prevent the spread of the virus and to minimize the impact on in-hospital delays. The improved green channel process was adopted at the hospital from February 20, 2020 to February 28, 2022. Upon patient arrival at the emergency room, additional full-time nurses performed epidemiological investigations, body temperature measurements, and triage. Patients with suspected stroke with no travel history to high-risk epidemic areas and no fever followed the previous stroke green channel process, with the addition of lung CT scan, novel coronavirus nucleic acid testing *via* pharyngeal swab, and serum antibody detection. Patients with a travel history to epidemic areas or fever were first admitted to the buffer area in the emergency room. The buffer area was relatively isolated, with independent nurses and the medical staff wearing level two protection to enter the buffer area (work clothes, work cap, medical protective mask, goggles or face shield, and disposable isolation gown). The emergency physician in the stroke center recorded the patient's medical history and performed physical examinations in the buffer area, while ECG, blood pressure, pulse, respiration, and blood oxygen saturation (SPO<sub>2</sub>) were monitored. ECG, blood sugar test, hematology tests, pharyngeal swab for novel coronavirus nucleic acid testing and serum antibody detection were performed at the bedside. The buffer area could directly access an independent CT room for head and lung CT scans. Patients eligible for thrombolysis after examination were returned to the buffer area. The emergency physician in the stroke center talked with the patient and family members and requested informed consent for thrombolysis. The patient then received intravenous thrombolysis and was observed. Patients diagnosed with or with suspected COVID-19 based on follow-up findings were admitted to the negative pressure isolation unit after intravenous thrombolysis. Patients in whom COVID-19 was excluded were admitted to the stroke unit for further treatment (Figure 1).

#### Advanced improvement of the green channel

The Omicron variant outbreak occurred in Shanghai in March 2022. To address the issues of faster transmission and higher vaccine resistance associated with the Omicron variant, further improvement was made to the green channel on March 1, 2022. Based on the original pandemic prevention measures, the COVID-19 antigen detection was added upon patient admission to the hospital. Four physicians from the stroke center were stationed in the emergency room, all of whom were



required to see patients while wearing level two protection in shifts every 8 h; the other procedures were consistent with the improved green channel process in 2.2.2.

## Observation indicators

In this study, the door-to-needle time (DNT), door-to-imaging time (DIT), and door-to-test completion time were used as the main time indicators of in-hospital delay of the

stroke green channel. The Modified Rankin Scale (mRS) score at 30 days, incidence of spontaneous intracerebral hemorrhage (sCIH) and 30-day mortality were adopted as indicators for the observation of patient outcomes. Indicator variables subjected to statistical analysis in this study included demographic data (age and sex); presence or absence of history of hypertension, diabetes, coronary heart disease, atrial fibrillation, and stroke; mode of hospital arrival (*via* the emergency medical service or other methods); and stroke severity assessed using the National Institutes of Health Stroke Scale (NIHSS). The main time



indicators were defined according to international standards as follows: (1) onset time: time of onset of the current stroke symptoms of the patient (for patients with an unclear onset time, the last-known normal time was used); (2) door time: time at which the patient arrived at the emergency room for registration; (3) head imaging time: time at which the plain CT scan of the head had been completed and the images had been obtained; (4) test completion time: time at which the laboratory provided all test reports; and (5) intravenous thrombolysis time: time of initiation of intravenous thrombolytic therapy.

## Date collection and patient follow

During the hospital stay of each patient, the following data were recorded by a neurologist: patient age, sex, past histories, mode of transportation to the hospital, NIHSS score at admission, NIHSS score at discharge, DNT, DIT, door-to-test completion time, and whether sCIH had occurred. For each patient or patient's surrogate, reliable contact information was obtained to assess outcome in person (eg., clinic follow-up) or by telephone between 30 days from the incident stroke. The mRS score was obtained at 30 days (+7 days allowed to establish contact). Patients who were lost to follow-up received the last recorded mRS or an mRS derived from the last documented neurological evaluation as their final score.

## Statistical analysis

Statistical analysis was performed using IBM SPSS Statistics for Windows, version 25.0. The quantitative data were expressed as  $\bar{x} \pm s$ , and  $\chi^2$  tests were used for comparisons among the three groups. Qualitative data were expressed as frequencies,

and comparisons among the three groups were performed using Fisher's exact tests. Pairwise comparisons among the three groups were performed using Dunnett's tests.  $P < 0.05$  indicated statistical significance.

## Ethics statement

The studies involving human participants were reviewed and approved by Seventh People's Hospital of Shanghai University of Traditional Chinese Medicine. The patients/participants provided their written informed consent to participate in this study.

## Results

### Basic clinical data of the three patient groups

A total of 295 patients with acute cerebral infarction were admitted to our hospital between March and July 2019, before the pandemic onset. Of these, 57 patients (19.32%) underwent intravenous thrombolysis in the emergency room. A total of 422 patients with acute cerebral infarction were admitted between March and July, during the SARS-CoV-2 outbreak. Of these, 94 patients (22.27%) underwent intravenous thrombolysis in the emergency room. A total of 235 patients with acute cerebral infarction were admitted between March and July, during the Omicron outbreak. Of these, 68 patients (28.94%) underwent intravenous thrombolysis in the emergency room ( $P = 0.029$ ).

The baseline data of the three groups of patients are shown in Table 1. Patient age; sex; and histories of hypertension, diabetes, coronary heart disease, atrial fibrillation, and stroke did not differ significantly among the groups (all  $P > 0.05$ ). The NIHSS

TABLE 1 Baseline information of three patients groups undergoing intravenous thrombolysis.

|                                     | Pre-pandemic group<br><i>N</i> = 57 | SARS-CoV-2 outbreak group<br><i>N</i> = 94 | Omicron outbreak group<br><i>N</i> = 68 | P value |
|-------------------------------------|-------------------------------------|--|---|---------|
| Age (years)                         | 65.84 ± 14.35                       | 66.98 ± 14.21                              | 66.41 ± 13.70                           | 0.889   |
| Male sex                            | 36 (63.2%)                          | 52 (55.3%)                                 | 49 (72.1%)                              | 0.094   |
| History of hypertension             | 39 (68.4%)                          | 56 (59.6%)                                 | 51 (75.0%)                              | 0.115   |
| History of diabetes                 | 13 (22.8%)                          | 20 (21.3%)                                 | 15 (22.1%)                              | 0.975   |
| History of coronary heart disease   | 10 (17.5%)                          | 18 (19.1%)                                 | 15 (22.1%)                              | 0.808   |
| History of atrial fibrillation      | 2 (3.5%)                            | 10 (10.6%)                                 | 8 (11.8%)                               | 0.223   |
| History of cerebral infarction      | 12 (21.1%)                          | 13 (13.8%)                                 | 13 (19.1%)                              | 0.471   |
| NIHSS score at admission            | 5.00 ± 4.52                         | 4.79 ± 5.94                                | 7.71 ± 7.36                             | 0.007   |
| NIHSS score at discharge            | 3.84 ± 4.57                         | 4.73 ± 7.20                                | 5.22 ± 7.07                             | 0.501   |
| Taking an ambulance to the hospital | 22 (38.6%)                          | 48 (51.1%)                                 | 56 (82.4%)                              | <0.001  |

NIHSS, the National Institute of Health Scale Score.

scores at admission did not differ significantly between the SARS-CoV-2 outbreak group and the pre-pandemic group, but was significantly higher in the Omicron outbreak group than that in the pre-pandemic group ( $7.71 \pm 7.36$  vs.  $5.00 \pm 4.52$ ,  $P = 0.026$ ). The NIHSS scores did not differ significantly among the three patient groups at discharge (pre-pandemic group  $3.84 \pm 4.57$ , SARS-CoV-2 outbreak group  $4.73 \pm 7.20$ , Omicron outbreak group  $5.22 \pm 7.07$ ,  $P = 0.501$ ). The proportions of patients undergoing emergency intravenous thrombolysis who came to the hospital by ambulance were significantly higher during the COVID-19 pandemic (pre-pandemic group 38.6%, SARS-CoV-2 outbreak group 51.1%, Omicron outbreak group 82.4%,  $P < 0.001$ ).

### Comparison of the delay indicators for intravenous thrombolysis in the three patient groups

The DNT did not differ significantly among the three patient groups ( $39.96 \pm 10.75$  min in the pre-pandemic group,  $46.07 \pm 22.83$  min in the SARS-CoV-2 outbreak group, and  $39.92 \pm 17.12$  min in the Omicron outbreak group,  $P = 0.064$ ).

The DIT in the SARS-CoV-2 outbreak group was significantly longer than that in the pre-pandemic group ( $22.42 \pm 7.62$  vs.  $18.91 \pm 8.23$  min,  $P = 0.031$ ), but did not differ significantly between the Omicron outbreak group and pre-pandemic group ( $20.35 \pm 10.38$  min vs.  $18.91 \pm 8.23$  min,  $P = 0.543$ ).

The door-to-test completion time in the Omicron outbreak group was significantly longer than that in the pre-pandemic group ( $92.60 \pm 25.82$  min vs.  $65.11 \pm 22.35$  min,  $P < 0.001$ ) and also visible between the SARS-CoV-2 outbreak group and the pre-pandemic group ( $78.37 \pm 25.17$  min vs.  $65.11 \pm 22.35$  min,  $P = 0.003$ ) (Tables 2, 3).

### Comparison of outcome indicators of the three groups

At the 1-month follow-up, the proportion of patients with mRS scores of 0–2 did not differ significantly among the

three groups (82.5% in the pre-pandemic group, 76.6% in the SARS-CoV-2 outbreak group, and 73.5% in the Omicron outbreak group,  $P = 0.488$ ). The incidence of sICH was not significantly different among the three groups (1.8% in the pre-pandemic group, 2.7% in the SARS-CoV-2 outbreak group, and 3.2% in the Omicron outbreak group,  $P = 0.151$ ). Significant differences in 30-day mortality were also absent among the three groups (1.8% in the pre-pandemic group, 2.1% in the SARS-CoV-2 outbreak group, and 2.9% in the Omicron outbreak group,  $P = 0.899$ ) (Table 4).

## Discussion

The COVID-19 pandemic is the largest public health crisis in a century, with an estimated 541 million infections and 6.33 million deaths as of June 28, 2022 (5). The novel coronavirus pneumonia caused by SARS-CoV-2 infection appeared in December 2019, with its widespread dissemination of SARS-CoV-2 and the large number of infected patients attracting global attention. At present, SARS-CoV-2 has evolved into multiple variants, including  $\alpha$  (B.1.1.7), Beta (B.1.351), Gamma (P.1), Delta (B.1.617.2), and the currently dominant variant Omicron (B.1.1.529). Due to the global spread of the Omicron variant, the cumulative number of infections in Shanghai from March to July 2022 exceeded 600,000. Compared with the other variants, the Omicron variant is the most highly mutated variant, spreads faster than the original virus strain and other VOCs, and poses a higher risk of reinfection than the other variants (6, 7), thus posing a greater challenge for outbreak prevention and control.

Emergency medical service resources were heavily utilized during the COVID-19 pandemic, with a 330% increase in the number of calls to the emergency medical system in some places (8). The results of the present study showed an increased proportion of patients with acute cerebral infarction who visited the clinic by ambulance during the SARS-CoV-2 outbreak. It was also observed that the proportion of patients with acute cerebral infarction who arrived at the hospital via emergency medical services increased further during the Omicron outbreak, which may be due to the strict traffic control measures and movement restrictions imposed in Shanghai during this period.

TABLE 2 Comparisons of in-hospital delay indicators in the three groups of patients undergoing intravenous thrombolysis.

|                                    | Pre-pandemic group<br>N = 57 | SARS-CoV-2 outbreak<br>group N = 94 | Omicron outbreak<br>group N = 68 | P value |
|------------------------------------|------------------------------|-------------------------------------|----------------------------------|---------|
| DIT (min)                          | $18.91 \pm 8.23$             | $22.42 \pm 7.62$                    | $20.35 \pm 10.38$                | 0.049   |
| DNT (min)                          | $39.96 \pm 10.75$            | $46.07 \pm 22.83$                   | $39.92 \pm 17.12$                | 0.064   |
| DNT < 60 min                       | 54 (94.7%)                   | 80 (85.1%)                          | 62 (91.2%)                       | 0.150   |
| Door-to-test completion time (min) | $65.11 \pm 22.35$            | $78.37 \pm 25.17$                   | $92.60 \pm 25.82$                | <0.001  |

NIHSS, the National Institute of Health Scale Score; DNT, door-to-needle time; DIT, door-to-imaging time.

TABLE 3 Further comparisons by Dunnett's test.

|                              | Group                     | Group              | P-value |
|------------------------------|---------------------------|--------------------|---------|
| NIHSS score at admission     | SARS-CoV-2 outbreak group | Pre-pandemic group | 0.970   |
|                              | Omicron outbreak group    | Pre-pandemic group | 0.026   |
| DIT                          | SARS-CoV-2 outbreak group | Pre-pandemic group | 0.031   |
|                              | Omicron outbreak group    | Pre-pandemic group | 0.543   |
| Door-to-test completion time | SARS-CoV-2 outbreak group | Pre-pandemic group | 0.003   |
|                              | Omicron outbreak group    | Pre-pandemic group | <0.001  |

NIHSS, the National Institute of Health Scale Score; DIT, door-to-imaging time.

TABLE 4 Comparisons of outcome indicators in the three groups of patients undergoing intravenous thrombolysis.

|                   | Pre-pandemic group<br>N = 57 | SARS-CoV-2 outbreak group<br>N = 94 | Omicron outbreak group N = 68 | P-value |
|-------------------|------------------------------|-------------------------------------|-------------------------------|---------|
| MRS 0-2           | 47 (82.5%)                   | 72 (76.6%)                          | 50 (73.5%)                    | 0.488   |
| sICH              | 1 (1.8%)                     | 6 (2.7%)                            | 7 (3.2%)                      | 0.151   |
| 30 days mortality | 1 (1.8%)                     | 2 (2.1%)                            | 2 (2.9%)                      | 0.899   |

MRS, Modified Rankin Scale; sICH, symptomatic Intracranial Hemorrhage.

The COVID-19 pandemic has an inevitable impact on the management of stroke patients. Some studies have shown a decreased rate of stroke patients intravenous thrombolysis during the pandemic, which might be related to the delayed access or even reluctance of stroke patients to seek medical care during this time (9). However, some studies also showed that the reperfusion therapy rate was not greatly affected during the pandemic (10). Our study indicates that the number of patients with acute cerebral infarction and proportion of acute cerebral infarction patients who received intravenous thrombolytic therapy were increased during the SARS-CoV-2 outbreak compared with the pre-pandemic period. Previous studies have shown that first-line neurologist decision, Laboratory and neuroimaging in nearest Location can increase the rate of intravenous thrombolysis (11). In our process improvement, we set up a separate CT room and access, and arranged a separate neurologist in the emergency department, which may have played a role. During the Omicron outbreak, the number of patients with acute cerebral infarction decreased significantly compared with the previous period, although the number of patients who underwent intravenous thrombolysis did not show a corresponding decrease, resulting in an increase in the proportion of intravenous thrombolysis. A possible explanation for this phenomenon is that the number of COVID-19 cases during the SARS-CoV-2 outbreak period was relatively low, which did not affect the healthcare seeking behavior of patients. In addition, health education related to stroke has been ongoing; previous research has shown that public health education

promotes an increase in the intravenous thrombolysis rate (12). However, the number of COVID-19 cases in Shanghai showed a huge surge during the Omicron outbreak period, prompting the adoption of traffic control measures and movement restrictions by the Shanghai government. Consequently, some patients, especially those with mild symptoms and slow progression who were less likely to experience obstruction of large blood vessels, avoided seeking medical care due to fear of being infected. This resulted in a decrease in the number of acute cerebral infarction patients who sought medical attention, although those with a more severe condition, who were in genuine need of emergency intravenous thrombolysis, were still transported to the hospital via emergency medical services.

SARS-CoV-2 is transmitted primarily through respiratory and contact transmission. The safe distance between people is inevitably reduced in a medical setting, which increases the risk of infection. During the COVID-19 pandemic, the optimization of the stroke green channel played a great role in protecting the health environment of medical institutions and the safety of relevant medical personnel, preventing the spread of SARS-CoV-2 in medical institutions, and ensuring that patients with acute stroke received timely and effective treatment. During the SARS-CoV-2 outbreak, we: (1) arranged for trained full-time nurses in the stroke green channel to conduct epidemiological investigations, body temperature measurements, and screening of stroke patients to screen for patients at risk of COVID-19 infection while performing triage; (2) required all medical staff working in the stroke green channel to implement level 2 or

higher protection in the emergency room (wearing work clothes, a disposable cap, a medical protective mask [N95 or above], goggles or face shield, a medical protective gown, disposable gloves, and disposable shoe covers) and also required patients and their family members to wear a mask throughout the whole process; (3) set up an independent buffer area in the emergency room to isolate suspected infected patients from non-infected patients and reduce transmission; (4) set up an independent CT room near the emergency buffer area equipped with radiologists. Lung CT scans were performed in patients with suspected infection, who reached the independent CT room through an independent channel; (5) performed pharyngeal swabs for novel coronavirus nucleic acid testing and serum antibody detection. During the Omicron outbreak in 2022, we further optimized the stroke green channel given the highly infectious and insidious characteristics of this variant: (1) Novel coronavirus antigen detection was performed additionally in patients at admission to provide rapid results; (2) a biometric door reader with body temperature detection was set up to facilitate the detection of febrile patients at admission; (3) several doctors stationed in the stroke green channel in shifts were relatively isolated from other areas of the hospital to reduce the risk of transmission. These additional protocols were designed to prevent the spread of the virus inside the hospital and they worked accordingly. During the pandemic, no patients with acute cerebral infarction in the stroke green channel were cross-infected in our hospital. Studies have shown that patients presenting to the hospital with acute neurological symptoms during the COVID-19 pandemic may experience delayed treatment due to in-hospital delays (13, 14). In this study, while the DIT time during the SARS-CoV-2 outbreak increased, the DIT time during the Omicron outbreak did not differ significantly from that before the pandemic, which might be related to the additional COVID-19 screening measures at the beginning of the pandemic. However, with the continuous improvement of the stroke green channel after the normalized prevention and control of the pandemic, and the continuous familiarity of nurses, doctors from the stroke center, and radiologists with the improved process, the impact continued to decrease over time. Moreover, the DNT for intravenous thrombolysis and proportion of DNT < 60 min in the new process for the stroke green channel was not affected by the pandemic, during either the SARS-CoV-2 or Omicron outbreaks. This result indicates that the optimization of the green channel process to reduce in-hospital virus transmission did not affect the in-hospital delay of intravenous thrombolysis.

In this study, the door-to-test completion time was prolonged in patients with acute cerebral infarction during the SARS-CoV-2 outbreak and the Omicron outbreak compared to that before the pandemic, a further increase occurred during the Omicron outbreak compared with the SARS-CoV-2 outbreak, which may be due to the increase in antigen and antibody testing for outbreak prevention and control during the SARS-CoV-2 outbreak period. This might be related to the demand

for medical resources during the Omicron outbreak and the participation of laboratory physicians in nucleic acid screening in the community, resulting in a decreased number of laboratory physicians in the hospital. Although the door-to-test completion time did not affect the in-hospital delay in intravenous thrombolysis, reduced platelet count and abnormal coagulation function are contraindications to intravenous thrombolysis in some patients (15). Thus, it was necessary to wait for the laboratory test results before starting intravenous thrombolysis, which may have affected the thrombolysis timing.

Our results showed that the incidence of sICH after intravenous thrombolysis and 30-day mortality did not differ significantly among the three groups of patients and were not affected by adjustments made to the green channel process during the pandemic period. To investigate the short-term outcomes of the patients, we performed a 30-day follow-up of the mRS scores of patients. It was found that the good outcome rate (proportion of patients with mRS scores of 0–2) was also not significantly different among the three groups.

This study has certain limitations. First, this was a single-center study with a relatively small sample size, which may not comprehensively reflect the effects of the COVID-19 pandemic on stroke green channels in high-risk areas. However, the hospital had experienced the SARS-CoV-2 and Omicron outbreak stages of the COVID-19 pandemic and implemented corresponding pandemic prevention and control measures according to the different virus transmission characteristics of the two stages. Therefore, our results possess certain reference value, and it is not limited to the COVID-19 virus. Second, there are certain inherent limitations due to the retrospective nature of the study, any observed changes may have been subject to general trends or interventions targeting public health or individual behavior changing. We hope that future prospective studies will be conducted to understand the role of green channel adjustment in epidemic prevention and control. Last, since arterial thrombectomy was not performed in our hospital before 2020, there is a lack of impact of improved green access on in-hospital time delays for arterial thrombectomy during the pandemic.

In conclusion, the results of this study showed that during the two outbreaks of the COVID-19 pandemic (SARS-CoV-2 and Omicron), improvement of the green channel for intravenous thrombolysis might have caused some delay in the in-hospital DIT during the SARS-CoV-2 outbreak, however, it did not affect the in-hospital delay indicator DNT for intravenous thrombolysis during the pandemic.

## Data availability statement

The original contributions presented in the study are included in the article/[Supplementary material](#), further inquiries can be directed to the corresponding author/s.

## Ethics statement

The studies involving human participants were reviewed and approved by Seventh People's Hospital of Shanghai University of Traditional Chinese Medicine. The patients/participants provided their written informed consent to participate in this study.

## Author contributions

QW and YaW wrote the manuscript. YoW and QB completed data collection. FW and QZ designed and supervised the study. All authors contributed to the article and approved the submitted version.

## Funding

This study was supported by the grants from 2020 Health Science and Technology Project of Pudong New Area Health Commission (PW2020D-5), 2021 Scientific Research Project of Shanghai Municipal Commission of Health and Family Planning (No. 202140282), 2020 Science and Technology Development Fund of Pudong New Area Special Fund for People's Livelihood Scientific Research (PKJ2020-Y-15), and 2019 Scientific Research Project of Shanghai Science and Technology Commission (No. 19401972803).

## References

- Ma H, Campbell BC, Parsons MW, Churilov L, Levi CR, Hsu C. Thrombolysis guided by perfusion imaging up to 9 hours after onset of stroke. *N Engl J Med*. (2019) 380:1795–803. doi: 10.1056/NEJMoa1813046
- Demel SL, Stanton R, Aziz YN, Adeoye O, Khatri P. Reflection on the past, present, and future of thrombolytic therapy for acute ischemic stroke. *Neurology*. (2021) 97(20 Suppl 2):S170–S7. doi: 10.1212/WNL.00000000000012806
- Fonarow GC, Smith EE, Saver JL. Timeliness of tissue-type plasminogen activator therapy in acute ischemic stroke: patient characteristics, hospital factors, and outcomes associated with door-to-needle times within 60 min. *Circulation*. (2011) 123:750–8. doi: 10.1161/CIRCULATIONAHA.110.974675
- Expert Committee of Stroke Prevention and Treatment Project of National Health Commission. *Expert consensus on green Channel management of stroke during COVID-19* (2020).
- World Health Organization. *WHO. Coronavirus (COVID-19) dashboard*. (2022). Available online at: <https://covid19who.int/> (accessed Jun 28, 2022).
- Wolter N, Jassat W, Walaza S, Welch R, Moultrie H, Groome M. Early assessment of the clinical severity of the SARS-CoV-2 omicron variant in South Africa: a data linkage study. *Lancet*. (2022) 399:437–46. doi: 10.1016/S0140-6736(22)00017-4
- Tian D, Sun Y, Xu H, Ye Q. The emergence and epidemic characteristics of the highly mutated SARS-CoV-2 Omicron variant. *J Med Virol*. (2022) 94:2376–83. doi: 10.1002/jmv.27643
- Morelli N, Immoivili P, Guidetti D. Letter by Morelli et al. regarding article, "Acute stroke care is at risk in the era of COVID-19: experience at a comprehensive stroke center in Barcelona". *Stroke*. (2020) 51:e322–3. doi: 10.1161/STROKEAHA.120.031124
- Hsiao J, Sayles E, Antzoulatos E, Stanton RJ, Sucharew H, Broderick JP, et al. Effect of COVID-19 on emergent stroke care: a regional experience. *Stroke*. (2020) 51:e2111–4. doi: 10.1161/STROKEAHA.120.030499
- Hoyer C, Ebert A, Huttner HB, Puetz V, Kallmünzer B, Barlann K, et al. Acute stroke in times of the COVID-19 pandemic: a multicenter study. *Stroke*. (2020) 51:2224–7. doi: 10.1161/STROKEAHA.120.030395
- Sui Y, Luo J, Dong C, Zheng L, Zhao W, Zhang Y, et al. Implementation of regional Acute stroke care map increases thrombolysis rates for acute ischaemic stroke in Chinese urban area in only 3 months. *Stroke Vasc Neurol*. (2021) 6:87–94. doi: 10.1136/svn-2020-000332
- Fassbender K, Balucani C, Walter S, et al. Streamlining of prehospital stroke management: the golden h. *Lancet Neurol*. (2013) 12:585–96. doi: 10.1016/S1474-4422(13)70100-5
- Siegler JE, Zha AM, Czup AL, Ortega-Gutierrez S, Farooqui M, Liebeskind DS. Influence of the COVID-19 pandemic on treatment times for acute ischemic stroke: the society of vascular and interventional neurology multicenter collaboration. *Stroke*. (2021) 52:e104. doi: 10.1161/STROKEAHA.120.032789
- Candelaresi P, Manzo V, Servillo G, Muto M, Barone P, Napoletano R, et al. The impact of COVID-19 lockdown on stroke admissions and treatments in Campania. *J Stroke Cerebrovasc Dis*. (2021) 30:105448. doi: 10.1016/j.jstrokecerebrovasdis.2020.105448
- Powers WJ, Rabinstein AA, Ackerson T, Adeoye OM, Bambakidis NC, Becker K, American Heart Association Stroke Council. 2018 guidelines for the early management of patients with acute ischemic stroke: a guideline for healthcare professionals from the American Heart Association/American Stroke Association. *Stroke*. (2018) 49:e46–e110. doi: 10.1161/STR.0000000000000158

## Acknowledgments

We would like to thank Editage ([www.editage.com](http://www.editage.com)) for English language editing.

## Conflict of interest

The authors declare that the research was conducted in the absence of any commercial or financial relationships that could be construed as a potential conflict of interest.

The handling editor declared a shared parent affiliation with the author QZ at the time of review.

## Publisher's note

All claims expressed in this article are solely those of the authors and do not necessarily represent those of their affiliated organizations, or those of the publisher, the editors and the reviewers. Any product that may be evaluated in this article, or claim that may be made by its manufacturer, is not guaranteed or endorsed by the publisher.

## Supplementary material

The Supplementary Material for this article can be found online at: <https://www.frontiersin.org/articles/10.3389/fneur.2022.998134/full#supplementary-material>





## OPEN ACCESS

## EDITED BY

Jun Xu,  
Capital Medical University, China

## REVIEWED BY

Jiang-Hua Le,  
Affiliated Hospital of Guilin Medical  
University, China  
Xiaoyu Zhao,  
Shandong University of Traditional  
Chinese Medicine, China

## \*CORRESPONDENCE

Yuejie Guo  
yugou7451@163.com

<sup>†</sup>These authors have contributed  
equally to this work

## SPECIALTY SECTION

This article was submitted to  
Neurological Biomarkers,  
a section of the journal  
Frontiers in Neurology

RECEIVED 25 June 2022

ACCEPTED 26 September 2022

PUBLISHED 21 October 2022

## CITATION

Guo Y, Luo N and Kang X (2022)  
Potential mechanism of the Shunaixin  
pill for preventing cognitive  
impairment in type 2 diabetes mellitus.  
*Front. Neurol.* 13:977953.  
doi: 10.3389/fneur.2022.977953

## COPYRIGHT

© 2022 Guo, Luo and Kang. This is an  
open-access article distributed under  
the terms of the [Creative Commons  
Attribution License \(CC BY\)](#). The use,  
distribution or reproduction in other  
forums is permitted, provided the  
original author(s) and the copyright  
owner(s) are credited and that the  
original publication in this journal is  
cited, in accordance with accepted  
academic practice. No use, distribution  
or reproduction is permitted which  
does not comply with these terms.

# Potential mechanism of the Shunaixin pill for preventing cognitive impairment in type 2 diabetes mellitus

Yuejie Guo<sup>1\*†</sup>, Ning Luo<sup>2†</sup> and Xueran Kang<sup>3</sup>

<sup>1</sup>Department of Geriatrics, The First People's Hospital of Chenzhou, Chenzhou, China, <sup>2</sup>Department of Endocrinology, The First People's Hospital of Chenzhou, Chenzhou, China, <sup>3</sup>Shanghai Jiao Tong University College of Basic Sciences, Shanghai, China

**Objective:** This study aims to analyze the efficacy and mechanism of action of the Shunaixin pill in preventing cognitive impairment in diabetic patients using network pharmacology.

**Methods:** The main active compounds of the Shunaixin pills and their action targets were identified *via* the TCMSP and Batman-TCM databases. The GEO database was used to identify the genes in type 2 diabetic individuals associated with cognitive impairment. Subsequently, a common target protein-protein interaction (PPI) network was constructed using the STRING database, and targets associated with diabetes and cognitive impairment were screened by performing a topological analysis of the PPI network. The AutoDock Vina software was used for molecular docking to evaluate the reliability of the bioinformatic analysis predictions and validate the interactions between the active ingredients of the Shunaixin pill and proteins associated with diabetes and cognitive impairment.

**Results:** Based on the TCMSP and Batman-Tcm platform, 48 active ingredients of the Shunaixin pill were identified, corresponding to 222 potential action targets. Further analysis revealed that 18 active components of the Shunaixin pill might contribute to cognitive impairment in type 2 diabetic patients. Molecular docking simulations demonstrated that the active ingredients of the Shunaixin pill (hexadecanoic acid, stigmasterol, beta-sitosterol, and angelicin) targeted four core proteins: OPRK1, GABRA5, GABRP, and SCN3B.

**Conclusion:** Active ingredients of the Shunaixin pill may alleviate cognitive impairment in diabetic patients by targeting the proteins OPRK1, GABRA5, GABRP, and SCN3B.

## KEYWORDS

Shunaixin pill, diabetes, cognitive impairment, network pharmacology, molecular docking

## Introduction

Diabetes mellitus (DM) is a metabolic disorder characterized by hyperglycemia caused by genetic and environmental factors and is the third most common non-communicable disease (1–4). DM has become a major health problem worldwide owing to its increasing prevalence and associated disability and mortality (5–7). The

global prevalence of diabetes is expected to increase to 7.7% by 2030 (8, 9), and ~592 million people are expected to suffer from diabetes by 2035 (10). Furthermore, diabetic complications also increase dramatically as the incidence of diabetes increases (11). Due to inadequate insulin secretion or insulin resistance, T2DM patients experience hyperglycemia, leading to chronic damage to blood vessels, neurons, brains, and other organs (12, 13). Moreover, diabetes may also cause nervous system complications, such as cognitive impairment (14, 15). Mild cognitive impairment is estimated to affect 45% of type 2 diabetes patients (16). Learning and memory impairment are the most distinctive features of cognitive impairment in DM (17, 18). Diabetic patients may suffer from cognitive impairment, leading to abnormalities in brain neuroplasticity and energy metabolism (19). DM is associated with cognitive impairment in the elderly, a risk factor for dementia, including Alzheimer's disease (AD) (20, 21). Cognitive impairment may also result in brain deterioration or neurodegenerative diseases (16, 22). In addition, it is estimated that diabetes causes ~10–15% of dementia cases, with patients demonstrating poorer self-management skills and glycemic control (16, 23). The healthcare costs for dementia patients are 1.5 times higher than control subjects of the same age group without dementia (24), and the financial figures indicate a significant burden for patients with cognitive impairment and society. However, the pathophysiology of diabetes-induced cognitive impairment remains poorly understood, and timely and adequate diagnostic and therapeutic tools are still lacking.

Chinese medicines have multi-faceted and multi-channel effects (25–28). Network pharmacology enables the exploration of the active ingredients and potential targets of Chinese medicine by providing a holistic view of complex systems interacting with multiple disease targets (29, 30). As a result, network pharmacology has gained popularity for studying key disease-related targets and biological functions and predicting potential synergistic mechanisms against complex diseases (31, 32). Shunaoxin pills, a drug with significant therapeutic potential, have been shown to be able to dilate the thoracic aorta of isolated rats (33). A clinical study investigating the effects of the Shunaoxin pill has reported an alleviation in diabetes-induced cognitive decline (34). The Shunaoxin pill consists of two herbs, Chuanxiong and Angelica, both of which can improve chronic cerebral ischemia (35). Researchers have found that the chemical components of the Shunaoxin pill, including ferulic acid and ligustilide, possess hypoglycemic, antioxidant, and anti-inflammatory properties

(36–38). Furthermore, the Shunaoxin pill can be used to treat a variety of cardiovascular and cerebrovascular diseases, such as cerebral ischemia and inadequate blood supply to the vertebral basilar artery (39). The mechanisms of cognitive impairment vary across different types of diabetes. Cognitive impairment in type 1 diabetes is associated with persistent hyperglycemic states, diabetic ketoacidosis, and hypoglycemic episodes (40, 41). On imaging, type 2 diabetes mellitus (T2DM) patients with cognitive impairment often exhibit cerebral vasculopathy, cortical atrophy, and hippocampal volume reduction (18, 42). In addition, neuroinflammation and oxidative stress are often observed in diabetes-related cognitive impairment (43–47). Therefore, the Shunaoxin pill can somewhat alleviate diabetes-related cognitive impairment. However, it is still unclear how the Shunaoxin pill prevents cognitive impairment in diabetics.

This study applied network pharmacology and molecular docking techniques to determine Shunaoxin's mechanism of action in improving cognitive impairment in diabetic patients. The study aimed to provide scientific support for traditional Chinese medicine as a treatment for cognitive impairment in diabetics from a modern medical perspective.

## Materials and methods

### Screening of active ingredients and drugs' targets

The active ingredients of Chuanxiong Rhizoma, Angelica Sinensis Radix, and the drug composition of the Shunaoxin pill were searched on the TCMSP with the following screening conditions: oral bioavailability (OB)  $\geq 30\%$ , drug-likeness (DL)  $\geq 0.18$ , and half-life (HL)  $\geq 4$ . The active ingredients of Chuanxiong Rhizoma and Angelica Sinensis Radix were searched in the Batman-Tcm database (<http://bionet.ncpsb.org.cn/batman-tcm/>) to obtain potential targets. The score cutoff was set to 100, and the adjusted  $P$ -value cutoff was set to 0.05. Subsequently, the Uniprot database (<https://www.uniprot.org/>) was used to identify the gene names of the matching targets (48, 49).

### Disease target acquisition

The gene microarray data related to “cognitive impairment in type 2 diabetes” was downloaded from the GEO (gene expression omnibus) database (<https://www.ncbi.nlm.nih.gov/geo/>). The study data were obtained from 19 healthy adults and 17 patients with type 2 diabetes from the microarray dataset GSE138260, 15 patients with Alzheimer's disease, and 18 patients with Alzheimer's disease combined with type 2 diabetes from the microarray dataset GSE161355. Microarray data background correction, normalization, and expression

Abbreviations: DM, diabetes mellitus; T2DM, type 2 diabetes mellitus; SNX, Shunaoxin dropping pills; OPRK1, opioid receptor kappa 1; GABA, gamma-aminobutyric acid; GABRA5, gamma-aminobutyric acid type A receptor subunit alpha5; GABRP, gamma-aminobutyric acid type A receptor subunit pi; SCN3B, sodium voltage-gated channel beta subunit 3.

value calculation were performed using the Bioconductor R package in R software. The limma package was used to calculate the differentially expressed mRNAs between the two groups. The screening criteria for differential genes were set as  $P < 0.05$  and expression change  $\geq 1.5$ -fold ( $|\log_2 \text{FC}| \geq 0.58$ ). Upregulated mRNA expression was defined as  $\log_2 \text{FC} \geq 0.58$ , and down-regulated mRNA expression was defined as  $\log_2 \text{FC} \leq -0.58$ . Finally, the differentially expressed genes (DEGs) for cognitive impairment in type 2 diabetic patients were finally derived. The heatmap package was used for cluster analysis of the screened DEGs, and the  $P$  of the differentially expressed data were transformed to  $-\log_{10}$ , which was grouped according to  $\log_2 \text{FC}$ .

## Common target screening of active ingredients and diseases and PPI network construction

The R software (<https://www.r-project.org/>) and Perl programs were used to identify the intersection between disease targets and drug targets, and the Venn diagram was generated by the Venny 2.1 software (<http://bioinfo.cnb.csic.es/tools/venny/index.html>). The protein-protein interaction (PPI) was constructed using the STRING database (<https://string-db.org/>). The protein species was set to “Homo sapiens,” medium confidence was set to 0.4, and other parameters were kept to the default settings. The potential protein-protein interaction network (PPI network) was obtained by Cytoscape 3.7.2 software (<https://cytoscape.org/>), and topological analysis of the PPI network was performed to screen the key targets.

## Gene ontology biofunctional analysis and Kyoto encyclopedia of genes and genomes pathway enrichment

The clusterProfilerGO R package was used to analyze the common targets of the Shunaoxin pill active ingredients (50). Gene ontology (GO) analysis is mainly used to characterize the functions of gene products, including cellular components (CC), molecular functions (MF), and biological processes (BP). The Kyoto encyclopedia of genes and genomes (KEGG) pathway enrichment analysis was also performed by applying the clusterProfilerKEGG package, while the corresponding signaling pathways were mapped using the path view package. Moreover, the degree of core pathway enrichment was analyzed to investigate the possible biological functions and signaling pathway mechanisms of the active ingredients of the Shunaoxin pill in the treatment of cognitive impairment in type 2 diabetic patients based on the enrichment factor values.

## Molecular docking verification

The interactions between the top four core active ingredients and the core proteins obtained from the preliminary network pharmacology screening were validated by molecular screening. The structural formula of the active ingredient was downloaded from the PubChem database (<https://pubchem.ncbi.nlm.nih.gov/>), and the corresponding 3D structure was produced with Chem3D software (51). The PDB format of the core protein structural domain was then downloaded from the PDB database (<http://www.rcsb.org/>), and protein dehydration and dephosphorylation were performed by PyMOL software. The active drug ingredient and core protein gene file were converted from PDB format to PDBQT format by the AutoDockTools 1.5.6 software, and the active pockets were identified. Finally, the Vina script was run to calculate the molecular binding energy and molecular docking results, while docking sites were identified with Discovery Studio 2019, and the LibDockScore was calculated for flexible binding. The molecular docking results were imported into PyMOL software for molecular docking conformation display. The binding energy of  $<0$  indicates spontaneous binding of the ligand and the receptor. For the results showing Vina binding energy  $\leq -5.0$  kcal/mol and LibDockScore  $>100$ , the ligand-receptor complexes were examined in 3D and 2D to evaluate the reliability of the bioinformatics predictions as per previous research (52–55).

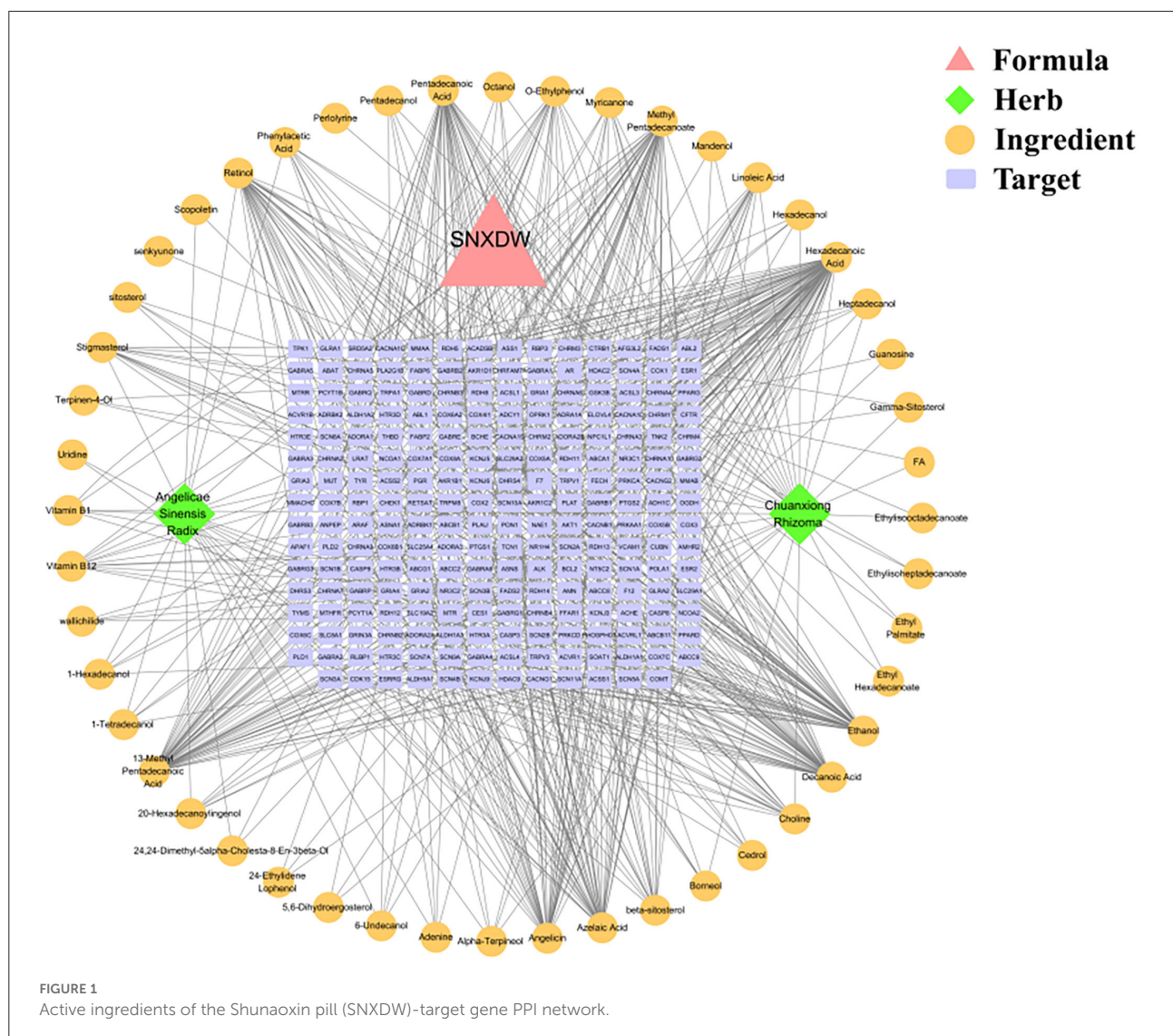
## Results

### Active drug ingredients and corresponding targets

The relevant action targets of the Shunaoxin pill active ingredients were obtained from the TCMSP database, and the Uniprot database (<https://www.uniprot.org/>) was used to correct the matching target gene names. Finally, 48 active ingredients were obtained, corresponding to 222 potential targets. Cytoscape 3.7.2 software was used to construct the topology of the Shunaoxin pill active ingredient target network (Figure 1). Eight active ingredients were identified, namely hexadecanoic acid, ethanol, 13-methyl pentadecanoic acid, methyl pentadecanoate, pentadecanoic acid, azelaic acid, decanoic acid, angelicin. These may be the main active ingredients in Shunaoxin pills.

### Screening for disease targets

To screen for protein targets associated with diabetes and cognitive impairment, 993 differentially expressed mRNAs were screened in the GSE138260 dataset, including 652 upregulated and 341 downregulated mRNAs. The GSE161355 dataset screened 196 differentially expressed mRNAs, including



145 upregulated and 51 downregulated mRNAs. Figures 2A,B display the heat maps based on the  $p$ -value screening of the top 100 most significant DEGs. Those processed data were imported into R to generate volcano plots, as shown in Figures 2C,D. Diabetes and cognitive impairment may be associated with these differential mRNAs.

## Common target screening and interaction network construction

All active ingredient targets of the Shunaoxin pill, the GSE138260 dataset, and the GSE161355 dataset were imported into the online Venn diagram production site jvenn, and 18 intersecting potential targets of action were obtained (Figure 3). Cytoscape 3.7.2 was used to construct the target network for

cognitive impairment in type 2 diabetics (Figures 4A,B). The intersecting target genes were imported into the STRING online analysis website (<https://string-db.org/>), and the protein-protein interaction results were exported (Figure 4C). After that, the CytoHubba plugin was used to obtain the core 16 potential target genes based on the degree algorithm as in previous research (Figure 4D) (56). Therefore, the Shunaoxin pill may target proteins that have been identified as targets as a result of these screenings.

## GO and KEGG enrichment analysis results

The Bioconductor package and cluster profile package in R were used to analyze GO and KEGG pathway enrichment analysis of Shunaoxin pill target proteins. GO analysis revealed



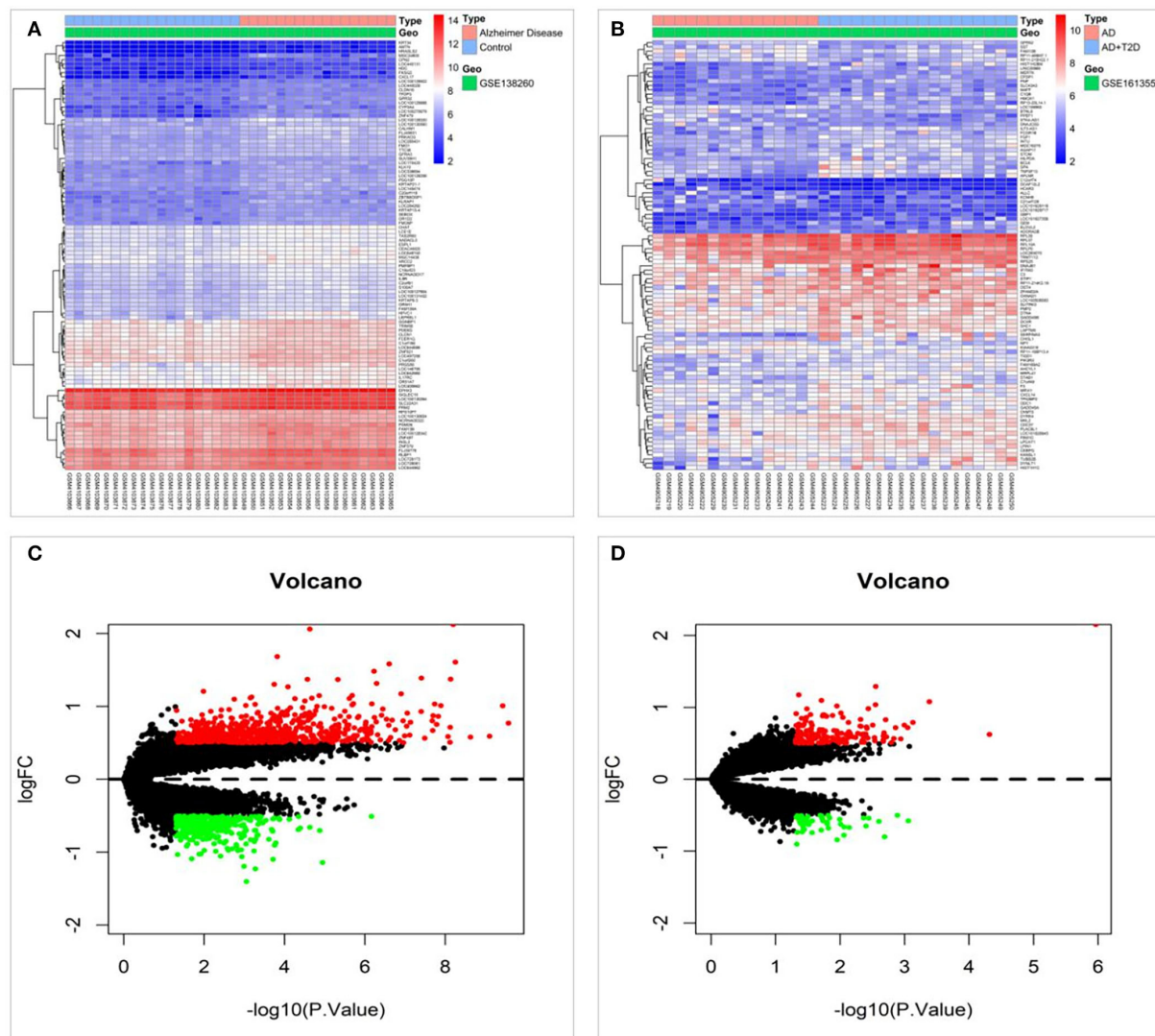


FIGURE 2

Differentially expressed mRNAs were screened in the GSE138260 and GSE161355 datasets. (A) Heat map of differentially expressed genes in the GSE138260 dataset. (B) Heat map of differentially expressed genes in the GSE161355 dataset. (C) Volcano plot of differentially expressed genes in the GSE138260 dataset. (D) Volcano plot of differentially expressed genes in the GSE161355 dataset.

that the 18 potential targets were mainly enriched in the biological processes of membrane potential regulation, chloride transmembrane transport, chloride transport, etc (Figure 5A). In addition, cell composition (CC) was mainly enriched in ion channel complexes, transmembrane transporter complexes, transporter complexes, etc (Figure 5B); molecular function (MF) was enriched primarily in neurotransmitter receptor activity, gated channel activity, extracellular ligand-gated ion channel activity, etc (Figure 5C). These GO enrichment pathways are shown in Figure 5D.

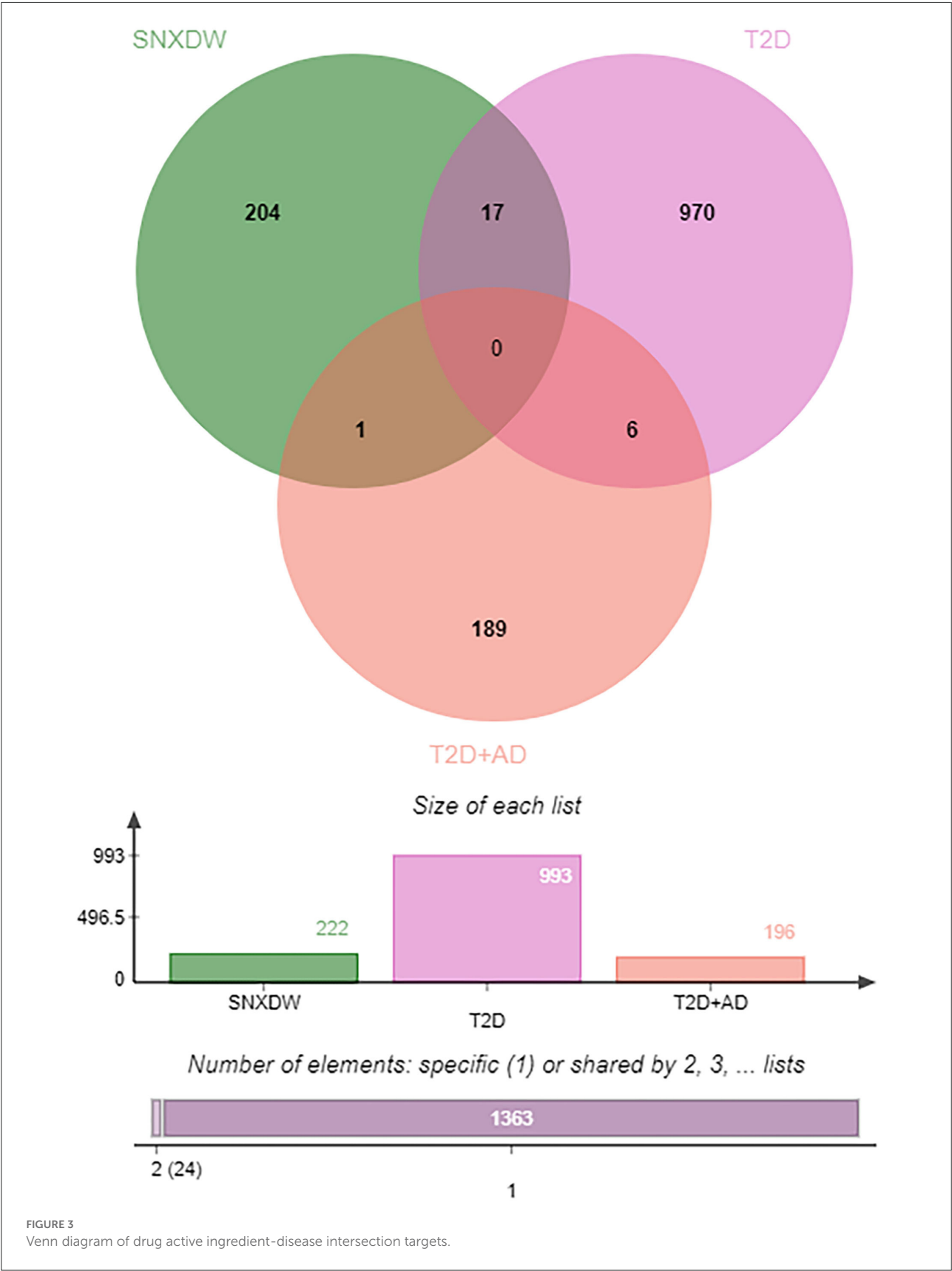
KEGG pathway enrichment analysis revealed that it was mainly concentrated in inflammatory signaling pathways such as neuroactive ligand-receptor interaction, nicotine addiction,

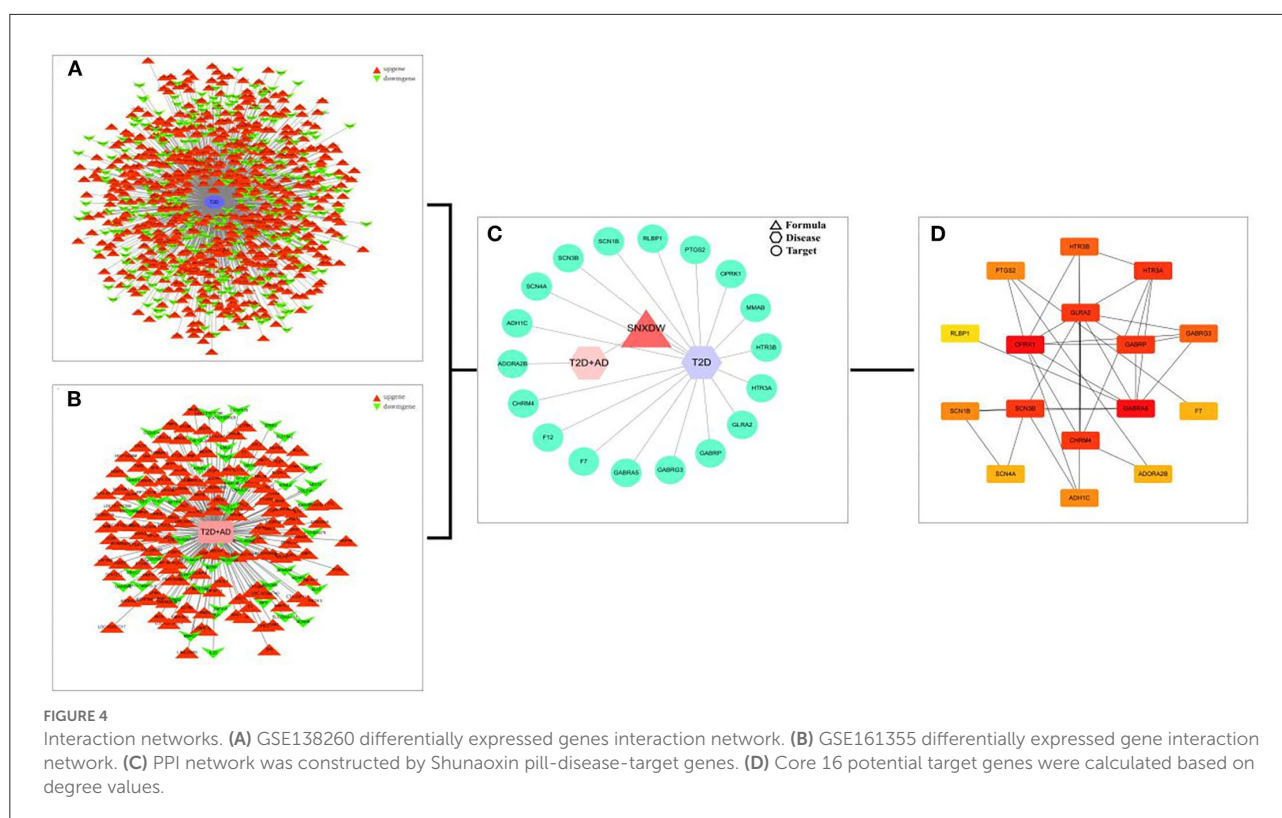
retrograde endocannabinoid signaling, taste transduction, and GABAergic synapse (Figure 6A). The path view package in R software was used to display the signaling pathway map associated with cognitive impairment in Shunaoxin pill-treated patients with type 2 diabetes (Figure 6B). The neuroactive ligand-receptor interaction signaling pathway was found to be enriched in the potential target proteins of the Shunaoxin pill.

## Results of molecular docking

The 3D structures of hexadecanoic acid, stigmasterol, beta-sitosterol, and angelicin were drawn based on their structural







formulae using Chem3D software. The 3D structures of the core proteins OPRK1, GABRA5, GABRP, and SCN3B were downloaded from the PDB database and exported to PDB format. The Vina script was used to calculate the binding energy of ligands and receptors, as shown in Table 1. GABRA5, GABRP, and SCN3B were all unable to form a stable docking model with hexadecanoic acid due to binding energies  $> -5.0$  kcal/mol. However, the binding energies of the remaining dockers were all lower than  $-5.0$  kcal/mol, indicating stable docking. In addition, the active molecules and corresponding target proteins were docked using the Discovery Studio 2019 software, and the LibDockScore was calculated, as shown in Table 1. The results suggested that the active ingredients hexadecanoic acid, stigmaterol, beta-sitosterol, and angelicin were able to dock semi-flexibly with the core proteins OPRK1, GABRA5, GABRP, and SCN3B, revealing the docking sites. The docking model LibDockScore of core protein OPRK1 with active ingredients hexadecanoic acid, stigmaterol, and beta-sitosterol, core protein GABRA5 with active ingredient beta-sitosterol, and core protein SCN3B with active ingredients stigmaterol and beta-sitosterol were all  $> 100$  (Figures 7, 8). The dimer formed by active ingredient stigmaterol and core protein OPRK1 was the most stable in terms of Root Mean Square Deviation (RMSD), chemical energy, and docking fraction, while the dimer formed by active ingredient beta-sitosterol and core protein SCN3B was the second most stable. Finally, the results of the

compounds exported by Vina and the three-dimensional and 2-dimensional molecular docking presentations with protein ligands were imported into Pymol using Discovery Studio 2019 software (Figures 7, 8). In this study, it was demonstrated that the beneficial effects of Shunaoxin pill on diabetic cognitive impairment are mediated by the active ingredients hexadecanoic acid, stigmaterol, beta-sitosterol, and angelicin on the diabetic cognitive impairment-related proteins OPRK1, GABRA5, GABRP, and SCN3B.

## Discussion

In this study, 18 potential targets of the Shunaoxin pill were obtained, and 16 potential core target genes were identified. Subsequently, a Shunaoxin pill-disease-target gene PPI network was constructed. The core proteins identified in PPI were OPRK1, GABRA5, GABRP, and SCN3B.

The OPRK1 gene encodes an opioid receptor, and methylation of the gene has been linked to the development of Alzheimer's disease. It is considered a drug target for the treatment of neurological diseases, playing an essential role in the development of cognitive impairment (57). The opioid receptors are mainly located in the hippocampal region, where neuroprotective effects reduce beta-amyloid production (58–60). Hiramatsu et al. reported that in a mouse model, OPRK1

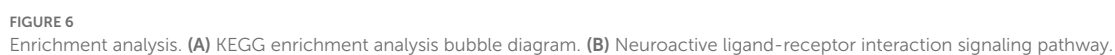
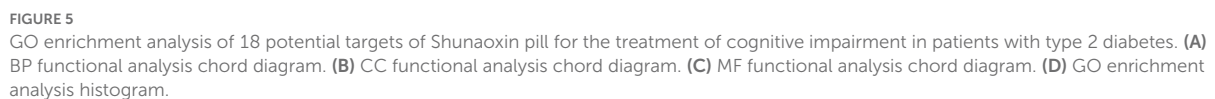


TABLE 1 Results of simulated molecular docking by Autodock-Vina, Discovery Studio 2019.

| Protein          | Compound          | Free energy of Vina<br>(kcal·mol <sup>-1</sup> ) | RMSD   | DS(LibDockScore) | Hydrogen bond interaction | Hydrophobic interaction   |
|------------------|-------------------|--|--------|------------------|---------------------------|---|
| OPRK1<br>(4DJH)  | Hexadecanoic acid | -5.0   | 2.040  | 107.731          | HIS:291, PHE:231          | VAL:134   |
| OPRK1<br>(4DJH)  | Stigmasterol      | -9.0   | 2.295  | 120.908          | THR:111                   | TRP:287, ILE:316,<br>VAL:108, TYR:320,<br>VAL:134, HIS:291, ILE:294,<br>ILE:290, MET:142                      |
| OPRK1<br>(4DJH)  | Beta-sitosterol   | -8.1   | 2.378  | 118.529          | TYR:320                   | VAL:108, ILE:316, ILE:294,<br>LYS:227, LEU:295,<br>PHE:231, HIS:291,<br>MET:142, ILE:290,<br>VAL:230, TRP:287 |
| OPRK1<br>(4DJH)  | Angelicin         | -6.9   | 2.207  | 87.6618          | HIS:291, PHE:231          | MET:142, ILE:290,<br>ILE:291, VAL:230, LYS:227  |
| GABRA5<br>(5O8F) | Hexadecanoic acid | -2.9   | 2.157  | 88.3026          | -                         | MET:49  |
| GABRA5<br>(5O8F) | Stigmasterol      | -5.7   | 3.447  | 96.615           | -                         | MET:49, LYS:103,<br>PHE:105, LYS:102  |
| GABRA5<br>(5O8F) | beta-sitosterol   | -5.0   | 3.624  | 102.021          | -                         | PHE:105, MET:49,<br>LYS:102, LYS:103  |
| GABRA5<br>(5O8F) | Angelicin         | -5.5   | 1.056  | 68.2034          | LYS:103                   | PHE:105, LYS:102, LYS:103   |
| GABRP<br>(4COF)  | Hexadecanoic acid | -4.9   | 1.288  | 71.5379          | GLU:52, VAL:53,<br>SER:51 | HIS:267, LEU:268  |
| GABRP<br>(4COF)  | Stigmasterol      | -7.9   | 28.196 | 34.1934          | -                         | MET:49  |
| GABRP<br>(4COF)  | Beta-sitosterol   | -5.8   | 2.202  | 44.4127          | -                         | LYS:102, MET:49   |
| GABRP<br>(4COF)  | Angelicin         | -8.0   | 1.509  | 57.8331          | ARG:68, CYS37             | VAL:36  |
| SCN3B<br>(7TJ8)  | Hexadecanoic acid | -4.6   | 1.587  | 90.199           | TRP:144                   | ASP:1437  |
| SCN3B<br>(7TJ8)  | Stigmasterol      | -8.9   | 1.844  | 111.354          | PHE:1433,<br>THR:1140     | PHE:1141, TRP:689,<br>ALA:351, PHE:347,<br>ILE:713, MET:350   |
| SCN3B<br>(7TJ8)  | Beta-sitosterol   | -9.5   | 2.334  | 110.397          | GLN:352                   | ALA:1434, PRO:355,<br>TRP:1144, ILE:1145  |
| SCN3B<br>(7TJ8)  | Angelicin         | -6.9   | 13.405 | 64.1714          | GLU:356, ASP:353          | GLU:688, PRO:355  |

agonists slowed the progression of cognitive dysfunction due to Aβ deposition (61). Diabetes can lead to massive production of islet amyloid polypeptide (IAPP), which crosses the blood-brain barrier and is deposited in the brain (hippocampus), further causing misfolding and aggregation of β-amyloid, resulting in cognitive impairment (62, 63). Hippocampal volume atrophy is observed in patients with type 2 diabetes who develop cognitive

impairment (18, 42). Thus, the OPRK1 gene may be involved in the development of cognitive impairment in diabetes by affecting β-amyloid. In the present study, the Shunaoxin pill active ingredient stigmasterol was found to bind the most stably with the core protein OPRK1 in T2DM-induced cognitive impairment. This further confirms that OPRK1 plays a vital role in diabetic cognitive impairment.



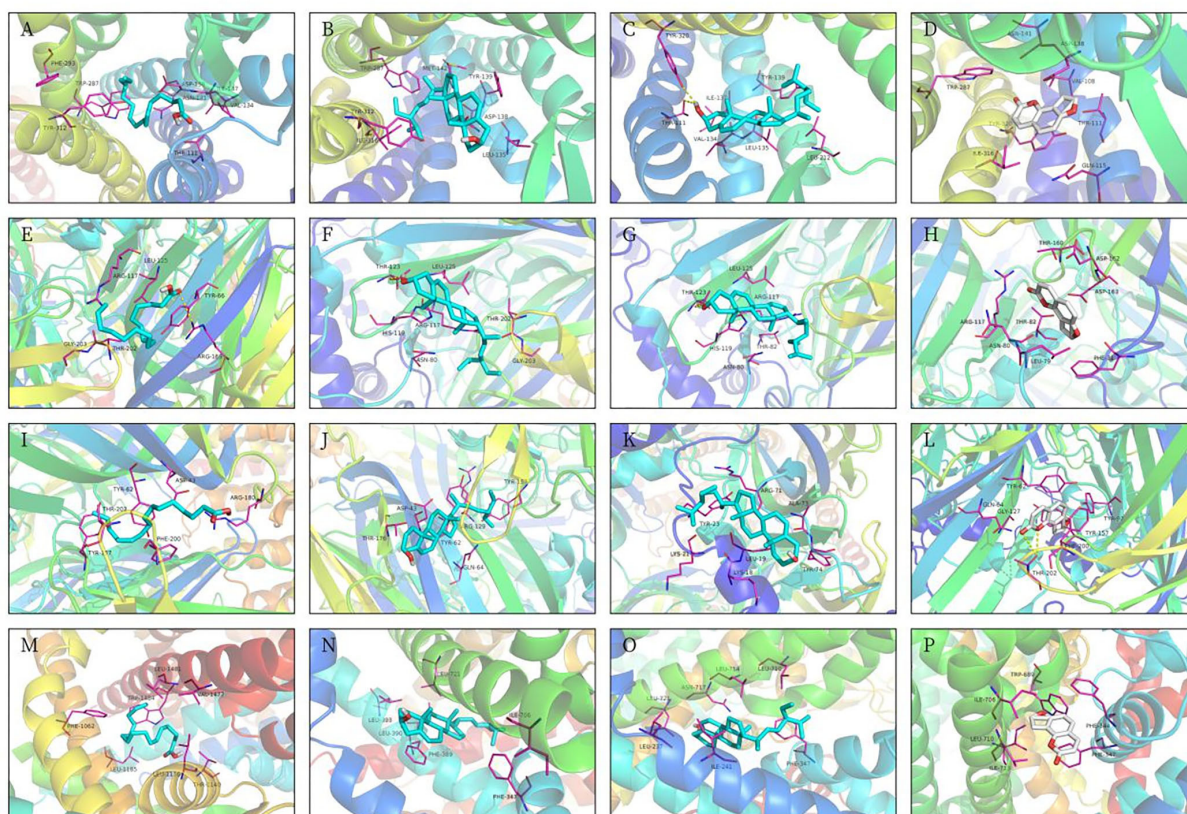


FIGURE 7

Molecular docking 3D models. (A) OPRK1-hexadecanoic acid complex. (B) OPRK1-stigmasterol complex. (C) OPRK1-beta-sitosterol complex. (D) OPRK1-angelicin complex. (E) GABRA5-Hexadecanoic acid complex. (F) GABRA5-stigmasterol complex. (G) GABRA5-beta-sitosterol complex. (H) GABRA5-angelicin complex. (I) GABRP-hexadecanoic acid complex. (J) GABRP-stigmasterol complex. (K) GABRP-beta-sitosterol complex. (L) GABRP-angelicin complex. (M) SCN3B-Hexadecanoic acid complex. (N) SCN3B-stigmasterol complex. (O) SCN3B-beta-sitosterol complex. (P) SCN3B-angelicin complex.

GABRA5 encodes a receptor for the  $\alpha 5$  subunit of GABA and is highly expressed in pyramidal neurons of the hippocampus (64). Furthermore, GABRA5 gene expression levels were correlated with memory function and learning index (65). In aged rats, GABRA5-encoded receptor protein expression was also associated with cognitive performance, spatial working memory, and neuronal apoptosis in aged rats (66). Moreover, it is involved in the neurophysiological features of cognitive decline in rats and humans (65). Although the exact mechanism is unknown, cognitive deficits are mainly associated with hippocampal damage in T2DM (67). In this study, GABRA5 was found to be involved in diabetes-related cognitive impairment as one of the core target proteins of the Shunaoxin pill, which may be related to its high expression in the hippocampus.

GABRP is the  $\pi$ -subunit of the amino acid-like inhibitory neurotransmitter gamma-aminobutyric acid (GABA) A receptor (68). GABRP was found to improve glucose tolerance and increase insulin sensitivity in the peripheral

tissues of diabetic mice, interacting with GABA to maintain normal metabolism and blood glucose stability (69, 70). This study identified GABRP as one of the core target proteins of the Shunaoxin pill for preventing diabetes-related cognitive impairment. Brain insulin resistance and disorders of intracellular glucose metabolism are associated with abnormal glucose transport in diabetes (71). Brain insulin resistance in the brain may fail to stimulate the clearance of A $\beta$ . Accumulating A $\beta$  in neurons leads to neurodegeneration or neuronal loss, which causes cognitive impairment (72). According to previous studies, GABRP may protect against diabetes-related cognitive impairment by maintaining normal metabolism and glucose stability.

The sodium channel  $\beta 3$  subunit (SCN3B) is an ion channel gene that is upregulated in the dorsal root ganglion during nerve injury, suggesting neuropathic injury (73). Stimulation of peripheral nerves in diabetic peripheral neuropathy (DPN) patients was demonstrated to activate cognitive-related areas of the brain, such as the temporal lobe and hippocampus (74).



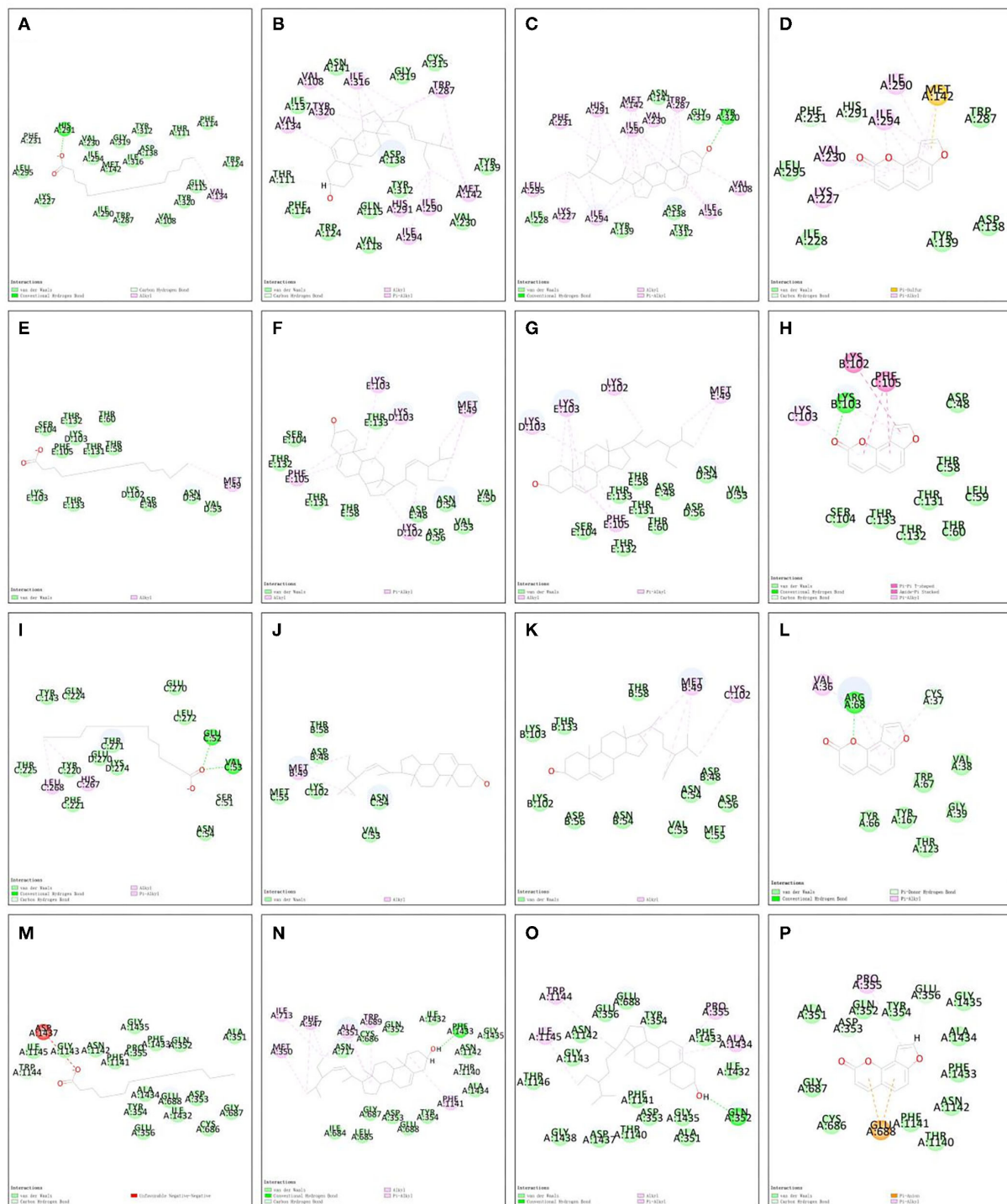


FIGURE 8

Molecular docking 2D models. (A) OPRK1-hexadecanoic acid complex. (B) OPRK1-stigmasterol complex. (C) OPRK1-beta-sitosterol complex. (D) OPRK1-angelicin complex. (E) GABRA5-hexadecanoic acid complex. (F) GABRA5-stigmasterol complex. (G) GABRA5-beta-sitosterol complex. (H) GABRA5-angelicin complex. (I) GABRP-hexadecanoic acid complex. (J) GABRP-stigmasterol complex. (K) GABRP-beta-sitosterol complex. (L) GABRP-angelicin complex. (M) SCN3B-hexadecanoic acid complex. (N) SCN3B-stigmasterol complex. (O) SCN3B-beta-sitosterol complex. (P) SCN3B-angelicin complex.

Furthermore, the reduced sensory conduction velocity of the peroneal nerve is often seen in DPN. In the present study, beta-sitosterol, an active ingredient in the Shunaoxin pill, was shown to bind stably to SCN3B, thus possibly playing a role in the development of diabetes-induced cognitive impairment. Therefore, we hypothesize that its mechanism of action on cognition may involve neurotransmission sodium channels.

The findings of this study provide a foundation for further exploration of TCM therapeutic targets for diabetic cognitive impairment. Network pharmacology revealed that the active ingredients in the Shunaoxin pill—hexadecanoic acid, stigmasterol, beta-sitosterol, and angelicin—could be semi-flexibly docked to the receptor-ligands of their respective core proteins, OPRK1, GABRA5, GABRP, and SCN3B. The active ingredient stigmasterol formed the most stable dimer with the core protein OPRK1, and the active ingredient beta-sitosterol formed the second most stable dimer with the core protein SCN3B. The present study illustrates the action of the active ingredients—hexadecanoic acid, stigmasterol, beta-sitosterol, and angelicin—on the diabetic cognitive impairment-related proteins OPRK1, GABRA5, GABRP, and SCN3B that are responsible for the beneficial properties of the Shunaoxin pill on cognitive impairment in diabetic patients.

However, this study also has some limitations. This study is based on network pharmacology and lacks experiments exploring the specific mechanism of the Shunaoxin pill's active ingredients targeting core proteins in diabetic cognitive impairment. Further validation of core proteins in clinical samples of the disease should be performed. Since cognitive impairment includes multiple disorders, this study focused only on AD-related datasets; future studies should explore more cognitive impairment-related datasets.

## Conclusion

This study demonstrated that the Shunaoxin pill is pharmacologically effective for cognitive impairment in diabetic

patients. Its active ingredients, hexadecanoic acid, stigmasterol, beta-sitosterol, and angelicin, target the proteins OPRK1, GABRA5, GABRP, and SCN3B associated with diabetic cognitive impairment. This research provides a foundation for further exploration of TCM therapeutic targets for cognitive impairment in diabetic patients.

## Data availability statement

The original contributions presented in the study are included in the article/supplementary materials, further inquiries can be directed to the corresponding author.

## Author contributions

YG and NL proposed and designed the study and collected and analyzed the data. YG provided the analysis tools and performed quality control. YG, NL, and XK wrote the manuscript. All authors contributed to the article and approved the submitted version.

## Conflict of interest

The authors declare that the research was conducted in the absence of any commercial or financial relationships that could be construed as a potential conflict of interest.

## Publisher's note

All claims expressed in this article are solely those of the authors and do not necessarily represent those of their affiliated organizations, or those of the publisher, the editors and the reviewers. Any product that may be evaluated in this article, or claim that may be made by its manufacturer, is not guaranteed or endorsed by the publisher.

## References

1. Makar AB, McMartin KE, Palese M, Tephly TR. Formate assay in body fluids: application in methanol poisoning. *Biochem Med.* (1975) 13:117–26. doi: 10.1016/0006-2944(75)90147-7
2. Wang J, Xiao M, Wang J, Wang S, Zhang J, Guo Y, et al. NRF2-related epigenetic modifications in cardiac and vascular complications of diabetes mellitus. *Front Endocrinol.* (2021) 12:598005. doi: 10.3389/fendo.2021.598005
3. Evans JL, Goldfine ID. A new Road for treating the vascular complications of diabetes: so let's step on the gas. *Diabetes.* (2016) 65:346–8. doi: 10.2337/dbi15-0029
4. Zhou Q, Ge Q, Ding Y, Qu H, Wei H, Wu R, et al. Relationship between serum adipon and the first phase of glucose-stimulated insulin secretion in individuals with different glucose tolerance. *J Diabetes Investig.* (2018) 9:1128–34. doi: 10.1111/jdi.12819
5. Li Y, Teng D, Shi X, Qin G, Qin Y, Quan H, et al. Prevalence of diabetes recorded in mainland China using 2018 diagnostic criteria from the American Diabetes Association: national cross sectional study. *BMJ.* (2020) 2020:m997. doi: 10.1136/bmj.m997
6. Vos T, Abajobir AA, Abate KH, Abbafati C, Abbas KM, Abd-Allah F, et al. Global, regional, and national incidence, prevalence, and years lived with disability for 328 diseases and injuries for 195 countries, 1990–2016: a systematic analysis for the Global Burden of Disease Study 2016. *Lancet.* (2017) 390:1211–59. doi: 10.1016/S0140-6736(17)32154-2
7. Suviranta T, Timonen J, Martikainen J, Aarnio E. The effects of reimbursement reform of antidiabetic medicines from the patients' perspective—a survey among patients with type 2 diabetes in Finland. *BMC Health Serv Res.* (2019) 19:769. doi: 10.1186/s12913-019-4633-9

8. Shaw JE, Sicree RA, Zimmet PZ. Global estimates of the prevalence of diabetes for 2010 and 2030. *Diabetes Res Clin Pract.* (2010) 87:4–14. doi: 10.1016/j.diabres.2009.10.007
9. Xu X, Pan X, Li S. Prospective analysis of the efficacy of beraprost sodium combined with alprostadil on diabetic nephropathy and influence on renninangiotensin system and TNF- $\alpha$ . *Exp Ther Med.* (2020) 19:639–45. doi: 10.3892/etm.2019.8265
10. Guariguata L, Whiting DR, Hambleton I, Beagley J, Linnenkamp U, Shaw JE. Global estimates of diabetes prevalence for 2013 and projections for 2035. *Diabetes Res Clin Pract.* (2014) 103:137–49. doi: 10.1016/j.diabres.2013.11.002
11. Mayer-Davis EJ, Lawrence JM, Dabelea D, Divers J, Isom S, Dolan L, et al. Incidence trends of type 1 and type 2 diabetes among youths, 2002–2012. *N Engl J Med.* (2017) 376:1419–29. doi: 10.1056/NEJMoa1610187
12. Geijselaers SLC, Sep SJS, Stehouwer CDA, Biessels GJ. Glucose regulation, cognition, and brain MRI in type 2 diabetes: a systematic review. *Lancet Diabetes Endocrinol.* (2015) 3:75–89. doi: 10.1016/S2213-8587(14)70148-2
13. Koekkoek PS, Kappelle LJ, van den Berg E, Rutten GEHM, Biessels GJ. Cognitive function in patients with diabetes mellitus: guidance for daily care. *Lancet Neurol.* (2015) 14:329–40. doi: 10.1016/S1474-4422(14)70249-2
14. Ahtiluoto S, Polvikoski T, Peltonen M, Solomon A, Tuomilehto J, Winblad B, et al. Diabetes, Alzheimer disease, and vascular dementia: a population-based neuropathologic study. *Neurology.* (2010) 75:1195–202. doi: 10.1212/WNL.0b013e3181f4d7f8
15. Zhu L, Li C, Du G, Pan M, Liu G, Pan W, Li X. High glucose upregulates myosin light chain kinase to induce microfilament cytoskeleton rearrangement in hippocampal neurons. *Mol Med Rep.* (2018) 18:216–22. doi: 10.3892/mmr.2018.8960
16. You Y, Liu Z, Chen Y, Xu Y, Qin J, Guo S, et al. The prevalence of mild cognitive impairment in type 2 diabetes mellitus patients: a systematic review and meta-analysis. *Acta Diabetol.* (2021) 58:671–85. doi: 10.1007/s00592-020-01648-9
17. Kessels RPC, Kappelle LJ, Biessels GJ. A 4-year follow-up study of cognitive functioning in patients with type 2 diabetes mellitus. *Diabetologia.* (2010) 53:58–65. doi: 10.1007/s00125-009-1571-9
18. McCrimmon RJ, Ryan CM, Frier BM. Diabetes and cognitive dysfunction. *Lancet.* (2012) 379:2291–9. doi: 10.1016/S0140-6736(12)60360-2
19. Lei H, Hu R, Luo G, Yang T, Shen H, Deng H, et al. Altered structural and functional MRI connectivity in type 2 diabetes mellitus related cognitive impairment: a review. *Front Hum Neurosci.* (2022) 15:755017. doi: 10.3389/fnhum.2021.755017
20. Strachan MWJ, Reynolds RM, Frier BM, Mitchell RJ, Price JF. The relationship between type 2 diabetes and dementia. *Br Med Bull.* (2008) 88:131–46. doi: 10.1093/bmb/ldn042
21. Bohnen NI, Kotagal V, Müller MLTM, Koeppe RA, Scott PJH, Albin RL, et al. Diabetes mellitus is independently associated with more severe cognitive impairment in Parkinson's disease. *Parkinsonism Relat Disord.* (2014) 20:1394–8. doi: 10.1016/j.parkreldis.2014.10.008
22. Cheong JLY, de Pablo-Fernandez E, Foltynie T, Noyce AJ. The association between type 2 diabetes mellitus and Parkinson's disease. *JPD.* (2020) 10:775–89. doi: 10.3233/JPD-191900
23. Biessels GJ, Reagan LP. Hippocampal insulin resistance and cognitive dysfunction. *Nat Rev Neurosci.* (2015) 16:660–71. doi: 10.1038/nrn4019
24. Vagelatos NT, Eslick GD. Type 2 diabetes as a risk factor for Alzheimer's disease: the confounders, interactions, and neuropathology associated with this relationship. *Epidemiol Rev.* (2013) 35:152–60. doi: 10.1093/epirev/mxs012
25. Song Y, Yang J, Jing W, Wang Q, Liu Y, Cheng X, et al. Systemic elucidation on the potential bioactive compounds and hypoglycemic mechanism of *Polygonum multiflorum* based on network pharmacology. *Chin Med.* (2020) 15:121. doi: 10.1186/s13020-020-00401-2
26. Tao P, Ji J, Gu S, Wang Q, Xu Y. Progress in the mechanism of autophagy and traditional Chinese medicine herb involved in dementia. *Front Pharmacol.* (2022) 12:825330. doi: 10.3389/fphar.2021.825330
27. Chen Y, Luo Z, Lin J, Qi B, Sun Y, Li F, et al. Exploring the potential mechanisms of *Melilotus officinalis* (L) Pall in chronic muscle repair patterns using single cell receptor-ligand marker analysis and molecular dynamics simulations. *Disease Markers.* (2022) 2022:1–11. doi: 10.1155/2022/9082576
28. Chen Y, Luo Z, Sun Y, Li F, Han Z, Qi B, et al. Exercise improves choroid plexus epithelial cells metabolism to prevent glial cell-associated neurodegeneration. *Front Pharmacol.* (2022) 13:1010785. doi: 10.3389/fphar.2022.1010785
29. Poornima P, Kumar JD, Zhao Q, Blunder M, Efferth T. Network pharmacology of cancer: understanding complex interactomes to designing multi-target specific therapeutics from nature. *Pharmacol Res.* (2016) 111:290–302. doi: 10.1016/j.phrs.2016.06.018
30. Lee H-S, Lee I-H, Park S-I, Lee D-Y. Network pharmacology-based investigation of the system-level molecular mechanisms of the hematopoietic activity of Samul-Tang, a traditional Korean herbal formula. *Evid Based Complement Altern Med.* (2020) 2020:1–17. doi: 10.1155/2020/9048089
31. Zhang R, Zhu X, Bai H, Ning K. Network pharmacology databases for traditional Chinese medicine: review and assessment. *Front Pharmacol.* (2019) 10:123. doi: 10.3389/fphar.2019.00123
32. Li S, Zhang B. Traditional Chinese medicine network pharmacology: theory, methodology, and application: traditional Chinese medicine network pharmacology: theory, methodology, and application. *Chin J Nat Med.* (2014) 11:110–20. doi: 10.3724/SP.J.1009.2013.00110
33. Huo L, Zhang J, Qu Z, Chen H, Li Y, Gao W. Vasorelaxant effects of Shunaoxin pill are mediated by NO/cGMP pathway, HO/CO pathway, and calcium channel blockade in isolated rat thoracic aorta. *J Ethnopharmacol.* (2015) 173:352–60. doi: 10.1016/j.jep.2015.07.048
34. Zhou H, Qu Z, Zhang J, Liu Y, Yang H, Chen H, et al. Antidiabetic effect of ligustilide-rich total lactones derived from Shunaoxin dropping pills on mice with type 2 diabetes induced by a high-fat diet and streptozotocin. *RSC Adv.* (2016) 6:109132–42. doi: 10.1039/C6RA24274J
35. Shi J, Li R, Yang S, Phang Y, Zheng C, Zhang H. The protective effects and potential mechanisms of *Ligusticum chuanxiong*: focus on anti-inflammatory, antioxidant, and antiapoptotic activities. *Evid Based Complement Altern Med.* (2020) 2020:1–9. doi: 10.1155/2020/8205983
36. Choi HG, Tran PT, Lee J-H, Min BS, Kim JA. Anti-inflammatory activity of caffeic acid derivatives isolated from the roots of *Salvia miltiorrhiza* Bunge. *Arch Pharm Res.* (2018) 41:64–70. doi: 10.1007/s12272-017-0983-1
37. Schwager J, Gagno L, Richard N, Simon W, Weber P, Bendik I. Z-ligustilide and anti-inflammatory prostaglandins have common biological properties in macrophages and leukocytes. *Nutr Metab (Lond).* (2018) 15:4. doi: 10.1186/s12986-018-0239-1
38. Mitra S, Tareq AM, Das R, Emran TB, Nainu F, Chakraborty AJ, et al. Polyphenols: a first evidence in the synergism and bioactivities. *Food Rev Int.* (2022) 2022:1–23. doi: 10.1080/87559129.2022.2026376
39. Wu K, Wang Z-Z, Liu D, Qi X-R. Pharmacokinetics, brain distribution, release, and blood-brain barrier transport of Shunaoxin pills. *J Ethnopharmacol.* (2014) 151:1133–40. doi: 10.1016/j.jep.2013.12.027
40. Semenkovich K, Bischoff A, Doty T, Nelson S, Siller AF, Hershey T, et al. Clinical presentation and memory function in youth with type 1 diabetes: Memory Effects of DKA and Hyperglycemia. *Pediatr Diabetes.* (2016) 17:492–9. doi: 10.1111/pedi.12314
41. Li W, Huang E, Gao S. Type 1 diabetes mellitus and cognitive impairments: a systematic review. *JAD.* (2017) 57:29–36. doi: 10.3233/JAD-161250
42. Brundel M, Kappelle LJ, Biessels GJ. Brain imaging in type 2 diabetes. *Eur Neuropsychopharmacol.* (2014) 24:1967–81. doi: 10.1016/j.euroneuro.2014.01.023
43. Hsieh C-F, Liu C-K, Lee C-T, Yu L-E, Wang J-Y. Acute glucose fluctuation impacts microglial activity, leading to inflammatory activation or self-degradation. *Sci Rep.* (2019) 9:840. doi: 10.1038/s41598-018-37215-0
44. Cervellati C, Trentini A, Pecorelli A, Valacchi G. Inflammation in neurological disorders: the thin boundary between brain and periphery. *Antioxid Redox Signal.* (2020) 33:191–210. doi: 10.1089/ars.2020.8076
45. Mao X-Y, Cao D-F, Li X, Yin J-Y, Wang Z-B, Zhang Y, et al. Huperzine A ameliorates cognitive deficits in streptozotocin-induced diabetic rats. *IJMS.* (2014) 15:7667–83. doi: 10.3390/ijms15057667
46. Farbood Y, Ghaderi S, Rashno M, Khoshnam SE, Khorsandi L, Sarkaki A, et al. Sesamin: a promising protective agent against diabetes-associated cognitive decline in rats. *Life Sci.* (2019) 230:169–77. doi: 10.1016/j.lfs.2019.05.071
47. Liu C, Cui G, Zhu M, Kang X, Guo H. Neuroinflammation in Alzheimer's disease: chemokines produced by astrocytes and chemokine receptors. *Int J Clin Exp Pathol.* (2014) 7:8342–55.
48. Xu X, Zhang W, Huang C, Li Y, Yu H, Wang Y, et al. Novel chemometric method for the prediction of human oral bioavailability. *IJMS.* (2012) 13:6964–82. doi: 10.3390/ijms13066964
49. Wan Y, Xu L, Liu Z, Yang M, Jiang X, Zhang Q, et al. Utilising network pharmacology to explore the underlying mechanism of Wumei Pill in treating pancreatic neoplasms. *BMC Complement Altern Med.* (2019) 19:158. doi: 10.1186/s12906-019-2580-y

50. Luo W, Brouwer C. Pathview: a R/Bioconductor package for pathway-based data integration and visualization. *Bioinformatics*. (2013) 29:1830–1. doi: 10.1093/bioinformatics/btt285
51. Kim S, Chen J, Cheng T, Gindulyte A, He J, He S, et al. PubChem in 2021: new data content and improved web interfaces. *Nucleic Acids Res.* (2021) 49:D1388–95. doi: 10.1093/nar/gkaa971
52. Veber DF, Johnson SR, Cheng H-Y, Smith BR, Ward KW, Kopple KD. Molecular properties that influence the oral bioavailability of drug candidates. *J Med Chem.* (2002) 45:2615–23. doi: 10.1021/jm020017n
53. Zhang Q, Yang J, Yang C, Yang X, Chen Y. Eucommia ulmoides olivertribulus terrestris l. drug pair regulates ferroptosis by mediating the neurovascular-related ligand-receptor interaction pathway- a potential drug pair for treatment hypertension and prevention ischemic stroke. *Front Neurol.* (2022) 13:833922. doi: 10.3389/fneur.2022.833922
54. Kang X, Sun Y, Yi B, Jiang C, Yan X, Chen B, et al. Based on network pharmacology and molecular dynamics simulations, baicalein, an active ingredient of Yiqi Qingre Ziyin method, potentially protects patients with atrophic rhinitis from cognitive impairment. *Front Aging Neurosci.* (2022) 14:880794. doi: 10.3389/fnagi.2022.880794
55. Lu L, Kang X, Yi B, Jiang C, Yan X, Chen B, et al. Exploring the Mechanism of Yiqi Qingre Ziyin method in regulating neuropeptide expression for the treatment of atrophic rhinitis. *Dis Markers.* (2022) 2022:1–12. doi: 10.1155/2022/4416637
56. Chin C-H, Chen S-H, Wu H-H, Ho C-W, Ko M-T, Lin C-Y. cytoHubba: identifying hub objects and sub-networks from complex interactome. *BMC Syst Biol.* (2014) 8:S11. doi: 10.1186/1752-0509-8-S4-S11
57. Liu G, Ji H, Liu J, Xu C, Chang L, Cui W, et al. Association of OPRK1 and OPRM1 methylation with mild cognitive impairment in Xinjiang Han and Uygur populations. *Neuroscience Letters.* (2017) 636:170–6. doi: 10.1016/j.neulet.2016.11.018
58. Daumas S, Betourne A, Halley H, Wolfer DP, Lipp H-P, Lassalle J-M, et al. Transient activation of the CA3 Kappa opioid system in the dorsal hippocampus modulates complex memory processing in mice. *Neurobiol Learn Mem.* (2007) 88:94–103. doi: 10.1016/j.nlm.2007.02.001
59. Cai Z, Ratka A. Opioid system, and Alzheimer's disease. *Neuromol Med.* (2012) 14:91–111. doi: 10.1007/s12017-012-8180-3
60. Wang Y, Wang Y-X, Liu T, Law P-Y, Loh HH, Qiu Y, et al.  $\mu$ -Opioid receptor attenuates a  $\beta$  oligomers-induced neurotoxicity through mTOR signaling. *CNS Neurosci Ther.* (2015) 21:8–14. doi: 10.1111/cns.12316
61. Hiramatsu M, Inoue K, Kameyama T. Dynorphin A-(1-13) and (2-13) improve  $\beta$ -amyloid peptide-induced amnesia in mice. *NeuroReport.* (2000) 11:431–5. doi: 10.1097/00001756-200002280-00001
62. Ferreira S, Raimundo A, Menezes R, Martins I. Islet amyloid polypeptide and amyloid beta peptide roles in Alzheimer's disease: two triggers, one disease. *Neural Regen Res.* (2021) 16:1127. doi: 10.4103/1673-5374.300323
63. Wang Y, Westermark GT. The amyloid forming peptides islet amyloid polypeptide and amyloid  $\beta$  interact at the molecular level. *IJMS.* (2021) 22:11153. doi: 10.3390/ijms222011153
64. Jacob TC. Neurobiology and therapeutic potential of  $\alpha$ 5-GABA type A receptors. *Front Mol Neurosci.* (2019) 12:179. doi: 10.3389/fnmol.2019.00179
65. Haberman R, Quigley C, Gallagher M. Characterization of CpG island DNA methylation of impairment-related genes in a rat model of cognitive aging. *Epigenetics.* (2012) 7:1008–19. doi: 10.4161/epi.21291
66. Shan L, Ma D, Zhang C, Xiong W, Zhang Y. miRNAs may regulate GABAergic transmission associated genes in aged rats with anesthetics-induced recognition and working memory dysfunction. *Brain Res.* (2017) 1670:191–200. doi: 10.1016/j.brainres.2017.06.027
67. Bonds JA, Shetti A, Stephen TKL, Bonini MG, Minshall RD, Lazarov O. Deficits in hippocampal neurogenesis in obesity-dependent and -independent type-2 diabetes mellitus mouse models. *Sci Rep.* (2020) 10:16368. doi: 10.1038/s41598-020-73401-9
68. Söderhielm PC, Klein AB, Bomholtz SH, Jensen AA. Profiling of GABAA and GABAB receptor expression in the myometrium of the human uterus. *Life Sci.* (2018) 214:145–52. doi: 10.1016/j.lfs.2018.10.033
69. Purwana I, Zheng J, Li X, Deurloo M, Son DO, Zhang Z, et al. GABA promotes human  $\beta$ -cell proliferation and modulates glucose homeostasis. *Diabetes.* (2014) 63:4197–205. doi: 10.2337/db14-0153
70. Reetz A, Solimena M, Matteoli M, Folli F, Takei K, De Camilli P, et al. and pancreatic beta-cells: colocalization of glutamic acid decarboxylase (GAD) and GABA with synaptic-like microvesicles suggests their role in GABA storage and secretion. *EMBO J.* (1991) 10:1275–84. doi: 10.1002/j.1460-2075.1991.tb08069.x
71. Nguyen TT, Ta QTH, Nguyen TKO, Nguyen TTD, Van Giau V. Type 3 diabetes and its role implications in Alzheimer's disease. *IJMS.* (2020) 21:3165. doi: 10.3390/ijms21093165
72. Nguyen TT, Ta QTH, Nguyen TTD, Le TT, Vo VG. Role of insulin resistance in the Alzheimer's disease progression. *Neurochem Res.* (2020) 45:1481–91. doi: 10.1007/s11064-020-03031-0
73. Dong Y, Chen Y, Yao B, Song P, Xu R, Li R, et al. Neuropathologic damage induced by radiofrequency ablation at different temperatures. *Clinics.* (2022) 77:100033. doi: 10.1016/j.clinsp.2022.100033
74. Li J, Zhang W, Wang X, Yuan T, Liu P, Wang T, et al. Functional magnetic resonance imaging reveals differences in brain activation in response to thermal stimuli in diabetic patients with and without diabetic peripheral neuropathy. *PLoS ONE.* (2018) 13:e0190699. doi: 10.1371/journal.pone.0190699





## OPEN ACCESS

## EDITED BY

Jun Xu,  
Capital Medical University, China

## REVIEWED BY

Xiangqiong Liu,  
China Tibetology Research  
Center, China  
Aneesha Acharya,  
Dr. D. Y. Patil Dental College &  
Hospital, India

## \*CORRESPONDENCE

Huijian Shi  
shihuijian@asdfmu.edu.cn

†These authors have contributed  
equally to this work and share first  
authorship

## SPECIALTY SECTION

This article was submitted to  
Neurological Biomarkers,  
a section of the journal  
Frontiers in Neurology

RECEIVED 31 October 2022

ACCEPTED 21 November 2022

PUBLISHED 06 December 2022

## CITATION

Li W, Yi Q and Shi H (2022)  
Hippocampal gene expression  
patterns in Sevoflurane anesthesia  
associated neurocognitive disorders: A  
bioinformatic analysis.  
*Front. Neurol.* 13:1084874.  
doi: 10.3389/fneur.2022.1084874

## COPYRIGHT

© 2022 Li, Yi and Shi. This is an  
open-access article distributed under  
the terms of the [Creative Commons  
Attribution License \(CC BY\)](#). The use,  
distribution or reproduction in other  
forums is permitted, provided the  
original author(s) and the copyright  
owner(s) are credited and that the  
original publication in this journal is  
cited, in accordance with accepted  
academic practice. No use, distribution  
or reproduction is permitted which  
does not comply with these terms.

# Hippocampal gene expression patterns in Sevoflurane anesthesia associated neurocognitive disorders: A bioinformatic analysis

Weiwei Li<sup>1†</sup>, Qijun Yi<sup>2†</sup> and Huijian Shi<sup>1\*</sup>

<sup>1</sup>Department of Anesthesiology, The Second Affiliated Hospital of the Shandong First Medical University, Taian, China, <sup>2</sup>Department of Oncology, The Second Affiliated Hospital of the Shandong First Medical University, Taian, China

**Background:** Several studies indicate general anesthetics can produce lasting effects on cognitive function. The commonly utilized anesthetic agent Sevoflurane has been implicated in neurodegenerative processes. The present study aimed to identify molecular underpinnings of Sevoflurane anesthesia linked neurocognitive changes by leveraging publically available datasets for bioinformatics analysis.

**Methods:** A Sevoflurane anesthesia related gene expression dataset was obtained. Sevoflurane related genes were obtained from the CTD database. Neurocognitive disorders (NCD) related genes were downloaded from DisGeNET and CTD. Intersecting differentially expressed genes between Sevoflurane and NCD were identified as cross-talk genes. A protein-protein interaction (PPI) network was constructed. Hub genes were selected using LASSO regression. Single sample gene set enrichment analysis; functional network analysis, pathway correlations, composite network analysis and drug sensitivity analysis were performed.

**Results:** Fourteen intersecting cross-talk genes potentially were identified. These were mainly involved in biological processes including peptidyl-serine phosphorylation, cellular response to starvation, and response to gamma radiation, regulation of p53 signaling pathway, AGE-RAGE signaling pathway and FoxO signaling. Egr1 showed a central role in the PPI network. Cdkn1a, Egr1, Gadd45a, Slc2a1, and Slc3a2 were identified as important or hub cross-talk genes. Among the interacting pathways, Interleukin-10 signaling and NF-kappa B signaling enriched among Sevoflurane-related DEGs were highly correlated with HIF-1 signaling enriched in NCD-related genes. Composite network analysis showed Egr1 interacted with AGE-RAGE signaling and Apelin signaling pathways, Cdkn1a, and Gadd45a. Cdkn1a was implicated in FoxO signaling, PI3K-Akt signaling, ErbB signaling, and Oxytocin signaling pathways, and Gadd45a. Gadd45a was involved in NF-kappa B signaling and FoxO signaling pathways. Drug sensitivity analysis showed Egr1 was highly sensitive to GENIPIN.



**Conclusion:** A suite of bioinformatics analysis revealed several key candidate hippocampal genes and associated functional signaling pathways that could underlie Sevoflurane associated neurodegenerative processes.

#### KEYWORDS

Sevoflurane, anesthesia, neurocognitive disorders, molecular mechanisms, bioinformatics

## Background

Sevoflurane is currently one of the most commonly applied anesthetic agents with a high safety record of over two decades (1, 2). It is a volatile anesthetic, which have a low tissue and blood-gas solubility and partition coefficient as compared to traditional inhaled anesthetics (3). These support a fast uptake, control of depth, and fast elimination resulting in faster recovery time and shorter periods of respiratory depression (4, 5). Furthermore, it has also shown cardio protective effects when used in cardiac surgery and also in other organs (6, 7). Therefore it is frequently applied in both induction and maintenance of general anesthesia.

Cognitive deficits after general anesthesia and surgery have been observed since a long time (8, 9). Various forms of short and long-term cognitive disturbances after anesthesia and surgery have been extensively documented. These include postoperative delirium and postoperative cognitive dysfunction (9, 10). Postoperative cognitive dysfunction can lead to long-term impairments multiple domains including executive function, visual-spatial and verbal memory, processing speed (11).

Increasingly, research has shown that general anesthetics can induce long lasting brain changes marked by altered tissue morphology and function, with the elderly and pediatric groups being the most vulnerable. Experimental studies have revealed several mechanistic aspects, including apoptotic cell death, impairment of neurogenesis and synaptic loss (12). Multiple molecular mechanisms have been implicated in general anesthetic mediated neurotoxicity, among which the role of pro-BDNF/p75/RHOA axis leading to actin depolymerization, synapse loss and apoptosis has been highlighted (13). Additionally, the role of increased mitochondrial complex leading to reactive oxygen species production and caspase activation has been identified as a mechanism leading to neuronal apoptosis (14).

Repeated Sevoflurane anesthesia has been shown to induce increased neuroinflammation marked by rise IL-6 levels and aberrant AKT signaling (15). Sevoflurane anesthesia was also found to induce phosphorylation of the tau protein, causing activation of GSK3 $\beta$  signaling and cognitive damage (16). Other purported mechanisms include increased  $\alpha$ 5GABAAR activity

(17). Sevoflurane was found to induce higher neurotoxicity, caspase-mediated apoptosis and amyloid accumulation in Alzheimer's disease (AD) transgenic mice, suggesting higher susceptibility (18). Particularly, aberrant functioning of the hippocampus has been implicated in anesthesia induced cognitive dysfunction (19).

Despite available experimental data, many critical gaps remain in the understanding of general anesthetic induced neurocognitive disorders (NCD). Among these, specific differences between different anesthetic agents remain unclear. Molecular mechanisms and functional signaling pathway aberrations that can underlie Sevoflurane anesthesia linked effects on NCD have not been comprehensively and systematically investigated. Secondary integrative utilization of available gene expression and other bioinformatic data can allow exploratory analyses to reveal novel candidate mechanistic pathways which can direct translational research. Therefore, in the present bioinformatic study, we hypothesized that mechanisms implicated in Sevoflurane anesthesia associated cognitive impairment could be explored by leveraging gene expression data related to Sevoflurane anesthesia and NCD to identify shared features.

## Materials and methods

### Sevoflurane anesthesia related dataset

For the Sevoflurane anesthesia related dataset, we downloaded GSE139220 (PRJNA578770) (20) from NCBI GEO (<https://www.ncbi.nlm.nih.gov/geo/>), which described Sevoflurane anesthesia related gene expression in the hippocampus of aged rats. The dataset consists of 3 Cases and 3 Controls, and the species was *Rattus norvegicus*. In addition, we retrieved 314 differentially expressed genes related to Sevoflurane anesthesia (*Mus musculus*) through literature (21) (PRJNA556843). The screening criteria was  $FDR < 0.05$ ,  $|\log FC| > 0$  which identified 49 up-regulated and 265 down-regulated genes. We also obtained a Sevoflurane anesthesia-related gene expression dataset and Sevoflurane anesthesia-related pathway dataset from CTD (<http://ctdbase.org/>). Since human genes were obtained from the CTD

database whereas mouse data was mainly used in this study, the “biomaRt” package in R project was used to convert gene names between species.

## Neurocognitive disorders (NCD) related datasets

We downloaded genes associated with neurocognitive disorders (NCD) from the DisGeNET (<https://www.disgenet.org/>) database (selected diseases named Mild Neurocognitive Disorders and neurocognitive disorders). In addition, we also obtained NCD-related genes and pathways from CTD. Next, we combined the NCD-related genes obtained from the two databases for subsequent analysis. Since the human genes were obtained from the two databases, and mouse data was mainly used in this study, the “biomaRt” package in R project was used to convert gene names between species.

## Preprocessing and differential expression analysis of the Sevoflurane anesthesia dataset

For GSE139220, we converted the probe ids in the chip to gene symbol based on the platform information. In performing the transformation, we screened the NCBI refseq database for annotated genes. Then we filtered the dataset by genes applying filtering rules: (1) If the expression value of the gene in more than 50% of the samples was 0, then we removed the gene. (2) If the same gene had multiple expression values in a certain sample, we deduplicated based on the average.

Differential expression analysis compares the expression values of different groups of samples in the dataset, and predicts whether genes are differently expressed between different groups. For GSE139220, we used the “limma” package in R project for the differential expression analysis. The parameters used were Case vs. Control. Genes with  $P$  value  $< 0.05$  and  $|\log FC| > 0$  as were selected as differentially expressed genes (DEGs). A volcano plot depicted the distribution of differentially expressed genes.

## Cross-talk genes between Sevoflurane anesthesia and NCD

We merged the two sets of differentially expressed genes (DEGs) associated with Sevoflurane, and then intersected the merged DEGs with the Sevoflurane anesthesia-related genes obtained from CTD. The resultant overlapping genes were considered as the definitive Sevoflurane anesthesia-related DEGs. Next, we obtained

the intersection of Sevoflurane anesthesia-related DEGs and NCD-related genes, to identify common DEGs shared by Sevoflurane anesthesia and NCD, namely, the cross talk genes.

Functional enrichment analysis was conducted using the ‘clusterProfiler’ package in R to analyze enriched GO Biological process and KEGG pathways. At the same time, the human homologous genes corresponding to these cross-talk genes were extracted and functional enrichment analysis using GO Biological process and KEGG pathway was performed.

## Cross talk gene protein-protein interaction (PPI) network

To obtain the role of cross talk genes in protein networks, we extracted the interacting proteins of the cross talk genes from the STRING database (<https://cn.string-db.org/>). Among the proteins interacting with the cross talk genes, we further screened those that appeared in any two groups from the three datasets including Sevoflurane anesthesia related genes and the NCD genes. Next, we used Cytoscape (version 3.9.1) to construct a PPI network and explored the the topological properties of the network.

## Screening of hub cross-talk genes

We used LASSO (Least absolute shrinkage and selection operator) Logistic Regression to perform feature selection among the Cross talk genes. We first extracted the expression values of the cross-talk genes from GSE139220, and then based on the sample type, we used LASSO to build a model for feature screening. As these feature selected genes obtained by LASSO analysis could be considered to play important connecting roles between Sevoflurane anesthesia and NCD, they were considered as hub cross talk genes.

The expression values of the hub cross talk gene in GSE139220 were obtained and  $t$ -test was applied to verify significant group differences in the hub cross talk gene expression values. In addition, Pearson correlation coefficient was computed to analyze the correlation between the hub cross talk gene and other cross talk genes.

## Single sample gene set enrichment analysis (ssGSEA)

ssGSEA is a tool that calculates enrichment scores for pairing of each samples with a gene set and generates gene enrichment score for each sample. We obtained Sevoflurane anesthesia and

NCD-related pathways from the CTD database from KEGG (<https://www.kegg.jp/>) and Reactome (<https://reactome.org/>). We download all pathways for *Rattus norvegicus* and the genes under the pathways from the KEGG and Reactome. Based on the pathway-gene dataset, we obtained all genes under the pathways related to Sevoflurane anesthesia and NCD, each. Then we used the GSVA package in R project to perform ssGSEA analysis on GSE139220, and calculated the abundance scores of Sevoflurane anesthesia and NCD-related pathways, each. For the pathways related to Sevoflurane anesthesia, we used the limma package in R to perform differential expression analysis based on the ssGSEA scoring results, and considered the pathways with  $P$  value  $< 0.05$  as DE-pathways. For the NCD-related pathways, we performed correlation analysis between the NCD pathways and the DE-pathways of Sevoflurane anesthesia, and then screened the NCD pathway highly related to the DE-pathways (marked as NCD hub pathway).

## Hub cross talk gene and pathway correlation analysis

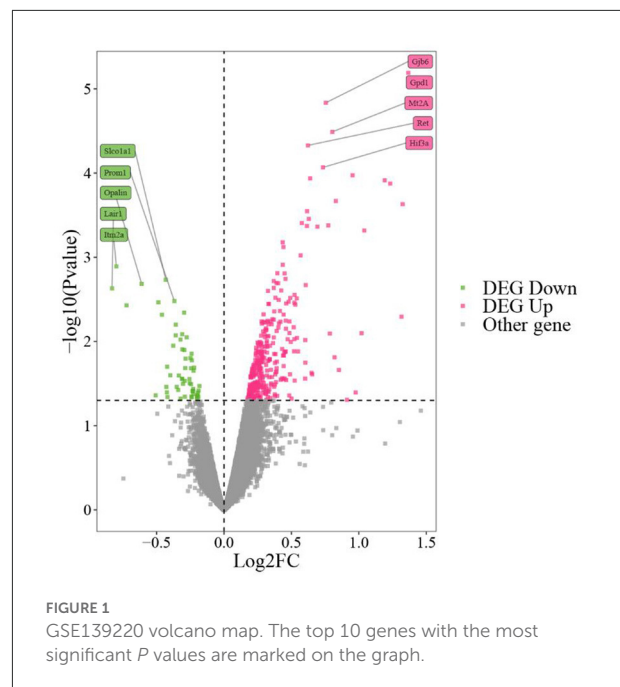
To further analyze the possible relationship and influence of Sevoflurane anesthesia on NCD in relation to gene transcriptome and function, we used Pearson correlation coefficient to analyze the relationship among hub cross talk gene, Sevoflurane anesthesia DE-pathways and NCD hub pathways.

## Hub cross talk gene and pathway complex functional network

We extracted genes (marked as Target genes) that interacted with the hub cross talk genes in the PPI network of the cross talk genes. Then, we extracted the Pathways related to hub cross talk genes and Target genes from the Pathways of Sevoflurane anesthesia and NCD. We integrated the relationship pairs composed of hub cross talk genes, Target genes and Pathways, and finally constructed a composite functional network with pathways and hub cross talk genes.

## Candidate drug prediction

We extracted the human homologous genes of the hub cross talk genes, and then downloaded drug-related genes (version 2022-Feb) from DGIdb (<https://dgidb.genome.wustl.edu/>). We screened the drugs targeting the hub cross talk genes and Target genes to identify the potentially useful candidate drugs for Sevoflurane associated cognitive impairment.



## Results

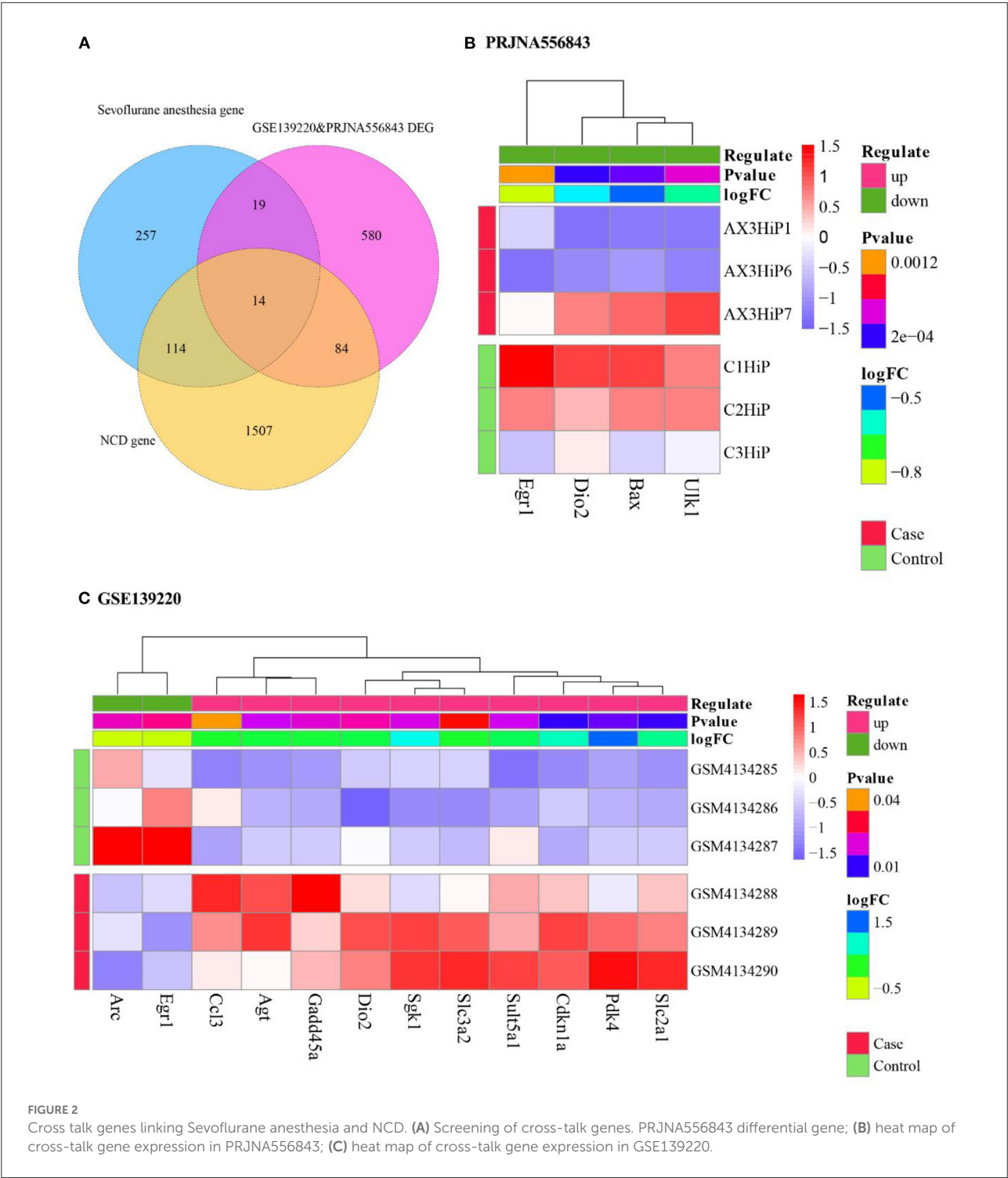
### Differential expression analysis

We performed differential expression analysis on GSE139220. We selected genes with  $P$  value  $< 0.05$  and  $|\log_2FC| > 0$  as DEGs, where  $\log_2FC > 0$  indicated an up-regulated gene, and  $\log_2FC < 0$  indicated a down-regulated gene. Thus, we obtained 392 differentially expressed genes, including 335 up-regulated genes and 57 down-regulated genes (Figure 1).

### Cross-talk genes of Sevoflurane anesthesia and NCD

We merged the 392 DEGs from GSE139220 (20) and the 314 DEGs from PRJNA556843 (21) and obtained 697 DEGs after deleting the duplicated genes. Next, we intersected the 697 DEG and Sevoflurane anesthesia-related genes from CTD databases to obtain 33 overlapping genes. Subsequently, from the intersection of 33 overlapping genes related to Sevoflurane anesthesia and NCD-related genes, we obtained 14 cross-talk genes (Figure 2A). The differential expression values of these 14 cross-talk genes are shown in Table 1.

Then we extracted the expression values of 14 cross-talk genes in GSE139220 and PRJNA556843. 12 genes were expressed in GSE139220, and 4 genes were expressed in PRJNA556843. We used R's pheatmap package to draw a heatmap of gene expression in GSE139220 and PRJNA556843 (Figures 2B,C).



## Functional enrichment of cross talk gene

We used the clusterProfiler package in R to analyze the GO Biological process and KEGG pathway of mice

for these 14 cross talk genes. We selected functions with  $P_{\text{adjust}} < 0.05$  as significant and displayed the Top 20 functions (Figures 3A,B). In addition, we also performed GO Biological process and KEGG pathway analysis on the

TABLE 1 Difference analysis results of 14 cross talk genes.

| Gene    | Data        | LogFC     | P value   | Regulate |
|---------|-------------|-----------|-----------|----------|
| Sult5a1 | GSE139220   | 0.38249   | 0.0140901 | Up       |
| Slc3a2  | GSE139220   | 0.2093867 | 0.0364218 | Up       |
| Slc2a1  | GSE139220   | 0.5686387 | 0.0009515 | Up       |
| Sgk1    | GSE139220   | 0.8205483 | 0.015407  | Up       |
| Pdk4    | GSE139220   | 1.316298  | 0.0050749 | Up       |
| Gadd45a | GSE139220   | 0.2703933 | 0.0171574 | Up       |
| Cdkn1a  | GSE139220   | 0.692644  | 0.0004328 | Up       |
| Ccl3    | GSE139220   | 0.221027  | 0.0476096 | Up       |
| Arc     | GSE139220   | -0.421316 | 0.0199493 | Down     |
| Agt     | GSE139220   | 0.2838157 | 0.0133006 | Up       |
| Egr1    | GSE139220   | -0.398263 | 0.0251983 | Down     |
|         | PRJNA556843 | -0.63057  | 0.0012029 | Down     |
| Dio2    | GSE139220   | 0.3196857 | 0.0221334 | Up       |
|         | PRJNA556843 | -0.436048 | 6.91E-05  | Down     |
| Ulk1    | PRJNA556843 | -0.4822   | 0.000481  | Down     |
| Bax     | PRJNA556843 | -0.376606 | 0.0001761 | Down     |

human homologous genes corresponding to the 14 cross talk genes, and selected  $P$ . adjust  $< 0.05$  as a significant function (Figures 3C,D).

The results showed that the cross-talk genes were mainly involved in biological processes including peptidyl-serine phosphorylation, cellular response to starvation, and response to gamma radiation. In addition, cross-talk genes were involved in the regulation of p53 signaling pathway, AGE-RAGE signaling pathway in diabetic complications and FoxO signaling pathway.

## Cross talk gene PPI network

We obtained a total of 231 genes at the intersection of any two datasets from Figure 2A. Based on the String database, we extracted the cross-talk genes and the PPIs between these 231 genes, and constructed a PPI network for these relationship pairs (Figure 4).

Next, we analyzed the topological properties of the network, and extracted the topological properties of 14 cross talk genes. The results indicated a dominant role of Egr1 in the network (Table 2).

## Screening of hub cross talk genes

We used LASSO to perform feature screening on the 14 Cross talk genes (Figures 5A,B), and obtained 5 hub cross talk genes (Cdkn1a, Egr1, Gadd45a, Slc2a1, and Slc3a2). Next, we extracted the expression values of these five hub cross talk genes in cases and controls, and performed  $t$ -test. The results showed

that the expression levels of Cdkn1a, Slc2a1 and Slc3a2 were significantly different between case and control (Figure 5C).

Then we used the Pearson correlation coefficient to analyze the correlation between the hub cross talk genes and the non-hub cross talk genes in gene expression. The gene pairs Slc3a2 and Sgk1, Slc2a1 and Cdkn1a were found highly positive correlated. Slc3a2 and Egr1, Cdkn1a and Arc were negatively correlated (Figure 5D).

## SsGSEA analysis

We obtained all genes under Sevoflurane anesthesia and NCD-related Pathways from KEGG and Reactome, and used ssGSEA to calculate the abundance scores of Sevoflurane anesthesia and NCD-related Pathways in GSE139220, respectively. For the pathways related to Sevoflurane anesthesia, we used the limma package to perform differential expression analysis on the pathway set after ssGSEA analysis, and thus obtained 11 DE-pathways (pathways with  $P$  value  $< 0.05$  were regarded as DE-PATHWAYS) (Table 3, Figure 6A).

For NCD-related Pathways, we used the Pearson correlation coefficient to analyze the correlation between Sevoflurane anesthesia DE-pathway and NCD Pathway. The 7 Sevoflurane anesthesia DE-pathways and 11 NCD pathways were found highly correlated (Table 4), and these 11 NCD pathways were marked as NCD hub pathways.

mTOR signaling pathway, Metabolism and PIP3 activates AKT signaling were highly expressed in NCD disease group (Figure 6B).

## Correlation analysis between hub cross talk genes and pathways

We calculated the correlation between the Sevoflurane anesthesia DE-pathway and the NCD hub Pathway using the Pearson correlation coefficient. The results showed that Interleukin-10 signaling and HIF-1 signaling pathway, NF-kappa B signaling pathway and HIF-1 signaling pathway, Biological oxidations and Metabolism were highly correlated (Figure 7A).

We analyzed the relationship among Sevoflurane anesthesia DE-pathways. The results showed that these pathway pairs were highly correlated: Frs2-mediated activation and Prolonged ERK activation events, ascorbate and aldarate metabolism and Biological oxidations, NF-kappa B signaling pathway and Interleukin-10 signaling, Prolonged ERK activation events ARMS and mediated activation (Figure 7B). At the same time, we analyzed the relationship between Sevoflurane anesthesia DE-pathway and hub cross talk genes. Results showed that Egr1 was highly correlated with Biological oxidations, Ascorbate



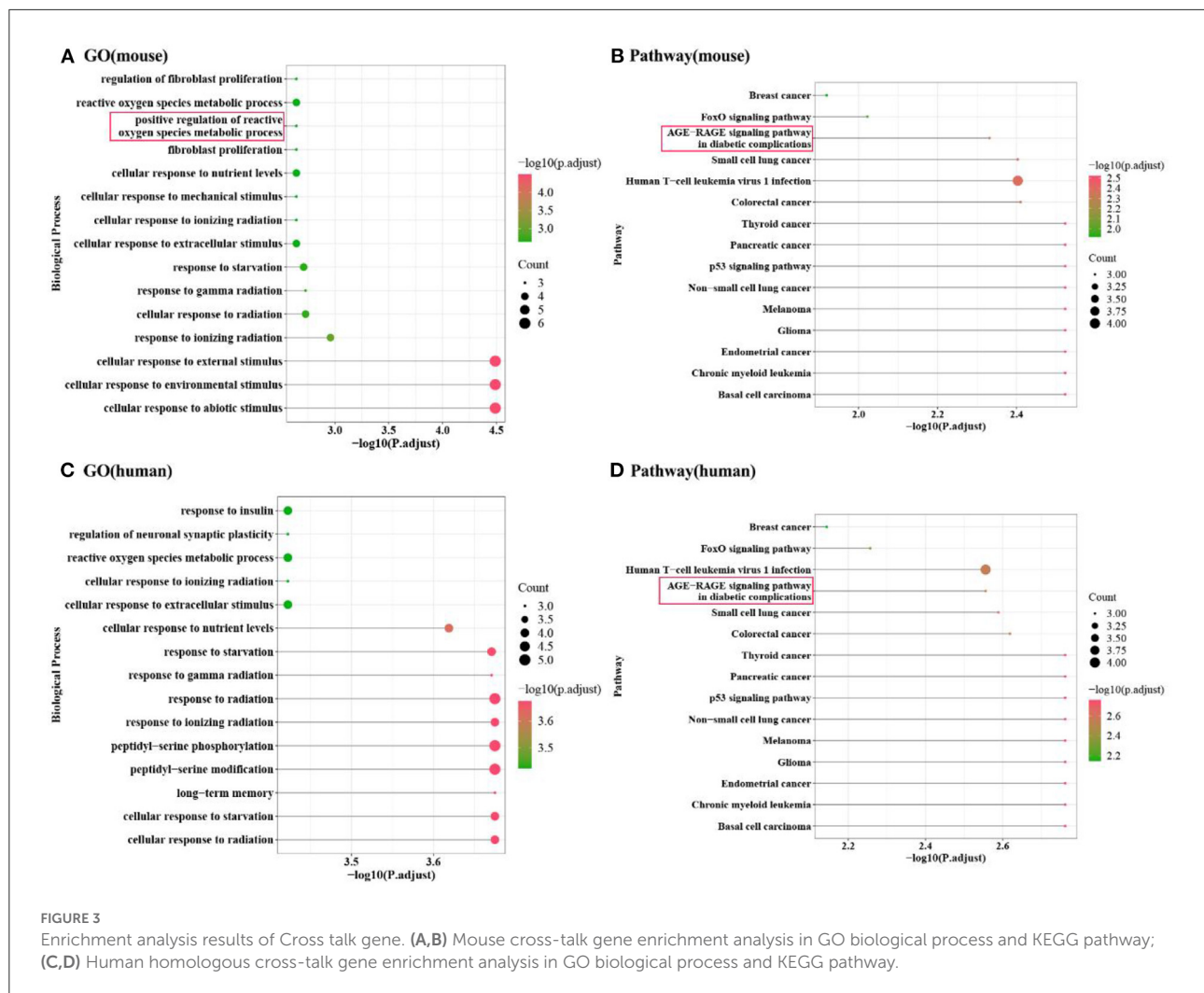


FIGURE 3

Enrichment analysis results of Cross talk gene. (A,B) Mouse cross-talk gene enrichment analysis in GO biological process and KEGG pathway; (C,D) Human homologous cross-talk gene enrichment analysis in GO biological process and KEGG pathway.

and aldarate metabolism, and NF-kappa B signaling pathway (Figure 7B).

Furthermore, we analyzed the relationship among NCD hub pathways. The results showed that Immune System and DAP12 interactions, Immune System and HIF-1 signaling pathway, Insulin resistance m and TOR signaling pathway were highly correlated (Figure 7C). Finally, we analyzed the relationship between these NCD hub pathways and hub cross talk genes, and obtained high correlation between Egr1 and Innate Immune System and Metabolism (Figure 7C).

## The relationships between hub cross talk genes, target genes and pathways

We obtained the target genes that interacted with the five hub cross talk genes from the PPI of the cross talk gene. Then we extracted the related pathways of hub cross talk gene and target gene in Sevoflurane anesthesia. In addition,

we extracted the related pathways of hub cross talk gene and target gene in NCD. Based on the above relationship pairs, we constructed the hub cross talk gene-target gene-pathway network (Figure 8).

The results showed that Egr1 interacted with AGE-RAGE signaling pathway in diabetic complications, Apelin signaling pathway, Cdkn1a and Gadd45a. Furthermore, Cdkn1a was involved in FoxO signaling pathway, PI3K-Akt signaling pathway, ErbB signaling pathway and Oxytocin signaling pathway. In addition, Cdkn1a interacted with Gadd45a. Moreover, Gadd45a was involved in the regulation of NF-kappa B signaling pathway and FoxO signaling pathway.

## Candidate drug prediction

We extracted the sensitive drugs of the hub cross talk gene from the DGIdb database, and obtained 4 hub cross talk genes

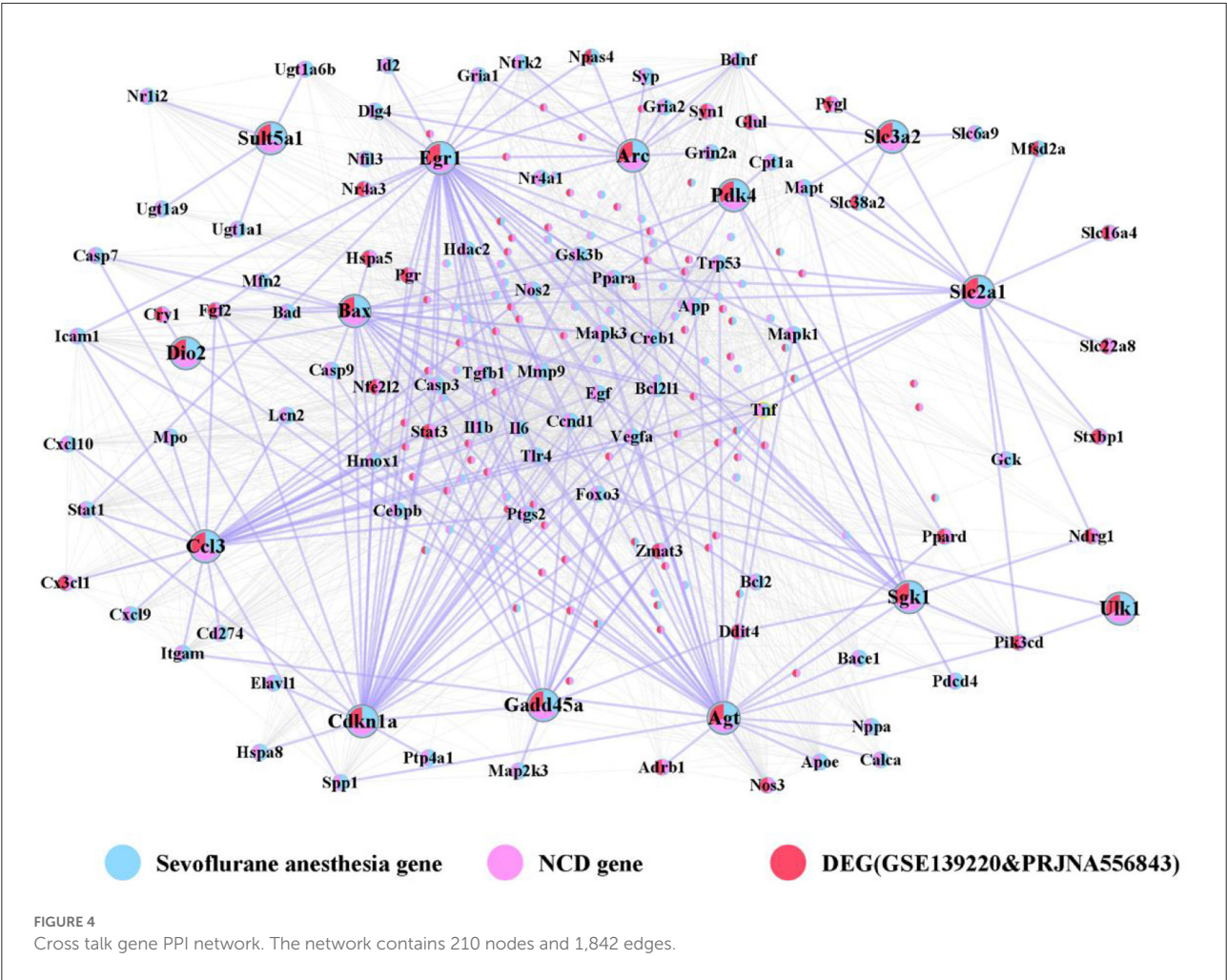


TABLE 2 The topology character of cross talk gene in PPI network.

| Gene    | Degree | Average shortest pathlength | Betweenness centrality | Closeness centrality | Topological coefficients |
|---------|--------|-----------------------------|------------------------|----------------------|--------------------------|
| Egr1    | 40     | 2                           | 0.009451               | 0.5                  | 0.25731                  |
| Agt     | 34     | 2.052632                    | 0.002564               | 0.487179             | 0.281965                 |
| Cdkn1a  | 33     | 2.105263                    | 0.011983               | 0.475                | 0.287495                 |
| Ccl3    | 26     | 2.287081                    | 3.08E-04               | 0.437238             | 0.354962                 |
| Bax     | 22     | 2.220096                    | 6.94E-04               | 0.450431             | 0.344156                 |
| Slc2a1  | 17     | 2.215311                    | 0.034202               | 0.451404             | 0.208267                 |
| Sgk1    | 16     | 2.311005                    | 0.00142                | 0.432712             | 0.283062                 |
| Arc     | 13     | 2.430622                    | 5.05E-04               | 0.411417             | 0.293956                 |
| Gadd45a | 13     | 2.430622                    | 6.61E-04               | 0.411417             | 0.367521                 |
| Pdk4    | 6      | 2.454545                    | 2.33E-04               | 0.407407             | 0.387464                 |
| Slc3a2  | 6      | 2.837321                    | 0.001168               | 0.352445             | 0.233974                 |
| Sult5a1 | 4      | 3.114833                    | 9.29E-06               | 0.321045             | 0.558333                 |
| Dio2    | 3      | 2.77512                     | 1.11E-05               | 0.360345             | 0.5                      |
| Ulk1    | 2      | 2.909091                    | 0                      | 0.34375              | 0.607843                 |

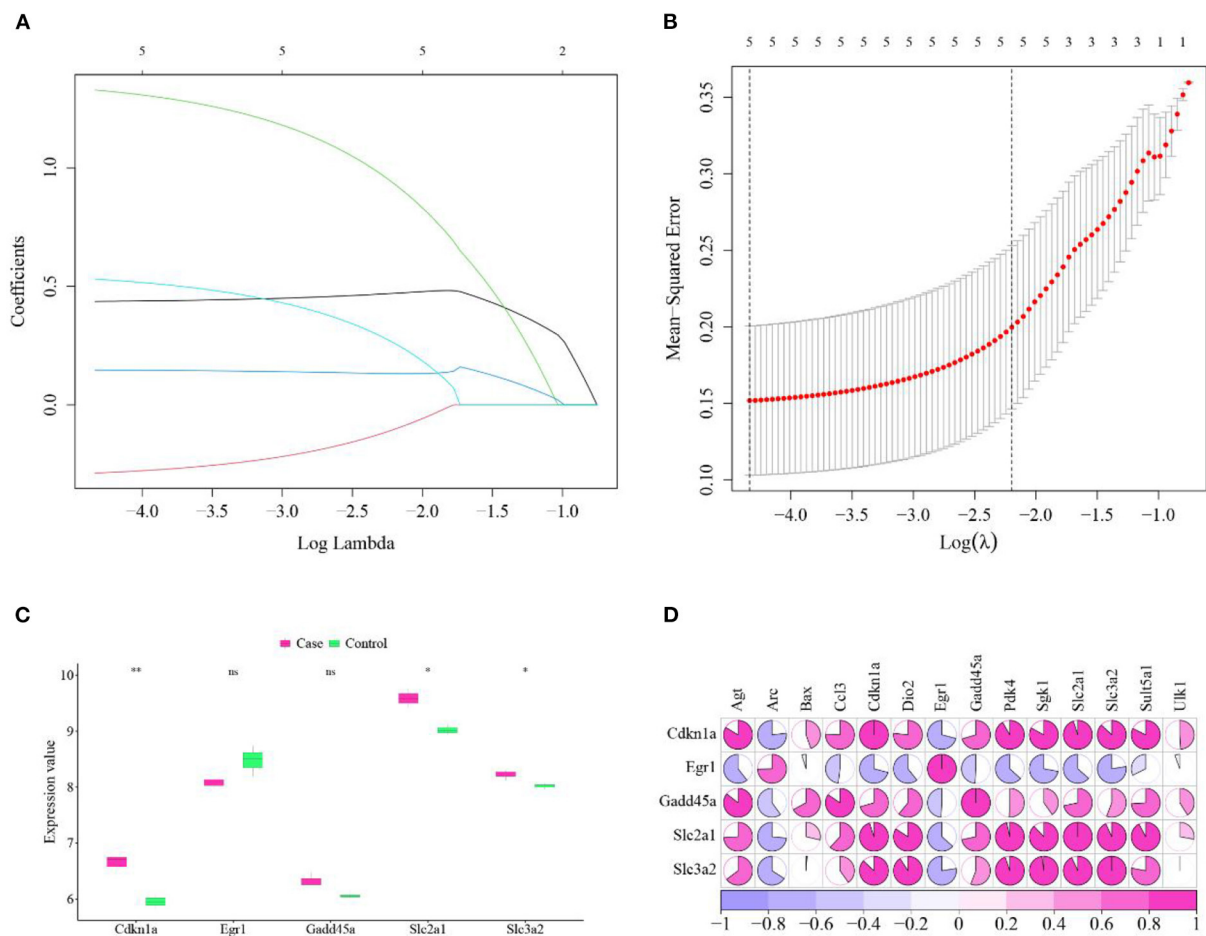


FIGURE 5

Hub cross talk gene screening and analysis. **(A)** LASSO analysis results, each line in the figure represents a gene. When a gene tends to 0, the larger the value of the abscissa (Log Lambda), the more critical the gene is. **(B)** Results of model cross-validation. There are two dashed lines in the figure, one is the  $\lambda$  value  $\lambda_{\min}$  when the mean square error is the smallest, and the other is the  $\lambda$  value  $\lambda_{1se}$  when the distance from the mean square error is the smallest one standard error, you can choose one of these two values, the dotted line. The corresponding number is the result of the number of screening genes, here we choose  $\lambda_{1se}$  as the screening condition for key genes. **(C)** Hub cross talk gene expression and *t*-test. The smaller the *P* value value of the test result, the more significant the sample difference results, and the more "\*" on the graph. The corresponding relationship between the *P* value and the "\*" sign is: ns:  $P > 0.05$ , \*:  $P \leq 0.05$ , \*\* $P \leq 0.01$ , \*\*\* $P \leq 0.001$ , \*\*\*\* $P \leq 0.0001$ . **(D)** Correlation between hub cross talk gene and non-hub cross talk gene.

that are sensitive to drugs. We constructed hub cross talk gene-Drug network for hub cross talk gene and drug (Figure 9). As a result, Egr1 and the drug GENIPIN were obtained with high sensitivity. In addition, Gadd45a and Cdkn1a are sensitive to various drugs.

## Discussion

We applied a series of bioinformatic analysis including feature selection among cross-talk genes and composite network analysis to identify candidate genes and functional pathways that might mediate Sevoflurane anesthesia associated cognitive

disturbance and neurological injury. 14 cross talk genes were identified, among which 5 genes, Cdkn1a, Egr1, Gadd45a, Slc2a1 and Slc3a2, emerged as 'hub' genes, suggesting highly relevant mechanistic roles. Egr 1 also showed a central role in the PPI network.

The Egr1 'Early Growth Response 1' gene is a transcriptional regulator, an 'early gene' induced rapidly in response to stimulus and Egr1 is widely documented in the nervous system as responsive to oxidative stress (22). The Egr1 gene is well established in playing a role in hippocampal functions including memory acquisition and potentiation (23). In the hippocampus, the GABA<sub>A</sub> receptor subunits are documented as transcriptional targets of Egr1, which regulates their composition (24), which is

consistent with our findings. Animal experiments have indicated a key role of Egr1 in Propofol anesthesia mediated cognitive dysfunction (25, 26). Sevoflurane has been shown to depress Egr1 expression during the anesthetic and post anesthetic period (27). Our results showed Egr1 was implicated in AGE RAGE signaling in context of Sevoflurane related neurotoxicity. The

TABLE 3 Sevoflurane anesthesia DE-pathway.

| Pathway  | LogFC    | P value  |
|--|----------|----------|
| Retinol metabolism                                   | 0.015774 | 0.002209 |
| AKT phosphorylates targets in the cytosol            | 0.013836 | 0.011622 |
| NF-kappa B signaling pathway                         | 0.012108 | 0.021568 |
| Ascorbate and aldarate metabolism                    | 0.010656 | 0.028185 |
| AGE-RAGE signaling pathway in diabetic complications | 0.010799 | 0.035033 |
| Biological oxidations                                | 0.011121 | 0.03941  |
| Adipocytokine signaling pathway                      | 0.006232 | 0.044233 |
| Interleukin-10 signaling                             | 0.022627 | 0.045018 |
| ARMS-mediated activation                             | −0.0185  | 0.025965 |
| Frs2-mediated activation                             | −0.01105 | 0.029621 |
| Prolonged ERK activation events                      | −0.0087  | 0.045874 |

role of RAGE (receptor for advanced glycation end-products) in regulating the blood brain barrier is established along with a protective role of anti-RAGE antibody in Isoflurane related cognitive dysfunction (28). Sevoflurane can disrupt the barrier by damage to brain vascular endothelial cells (29) but the specific role of AGE-RAGE signaling is yet to be comprehensively described. Egr1 was also implicated in Apelin signaling, Apelin being an orphan G-protein-coupled receptor APJ ligand with anti neuronal apoptotic and neuroprotective roles (30).

Cdkn1a is a cell cycle arrest and senescence marker gene targeted by the p53 gene (31). In Alzheimer’s disease Cdkn1a expression marks senescence like phenotype and inflammation (32). Sevoflurane anesthesia reportedly can increase p53 signaling along with rise in the apoptosis marker Caspase-3 (33). The solute carrier transporters (Slc), Slc2a1 and Slc3a2 comprised hub cross talk genes. Slc genes are regulators of the blood brain barrier (34). The potential mechanistic role of Sevoflurane in inducing Slc gene mediated disruption of the blood brain barrier remains to be well investigated. The hub gene Gadd45a was found involved in NF-kappa B signaling and FoxO signaling pathways. Gadd45a (growth arrest and DNA damage-inducible protein 45 alpha) has been found upregulated in response to Sevoflurane along with the corresponding long noncoding RNA (35) and also activates the p53 pathway. Gadd45a is implicated

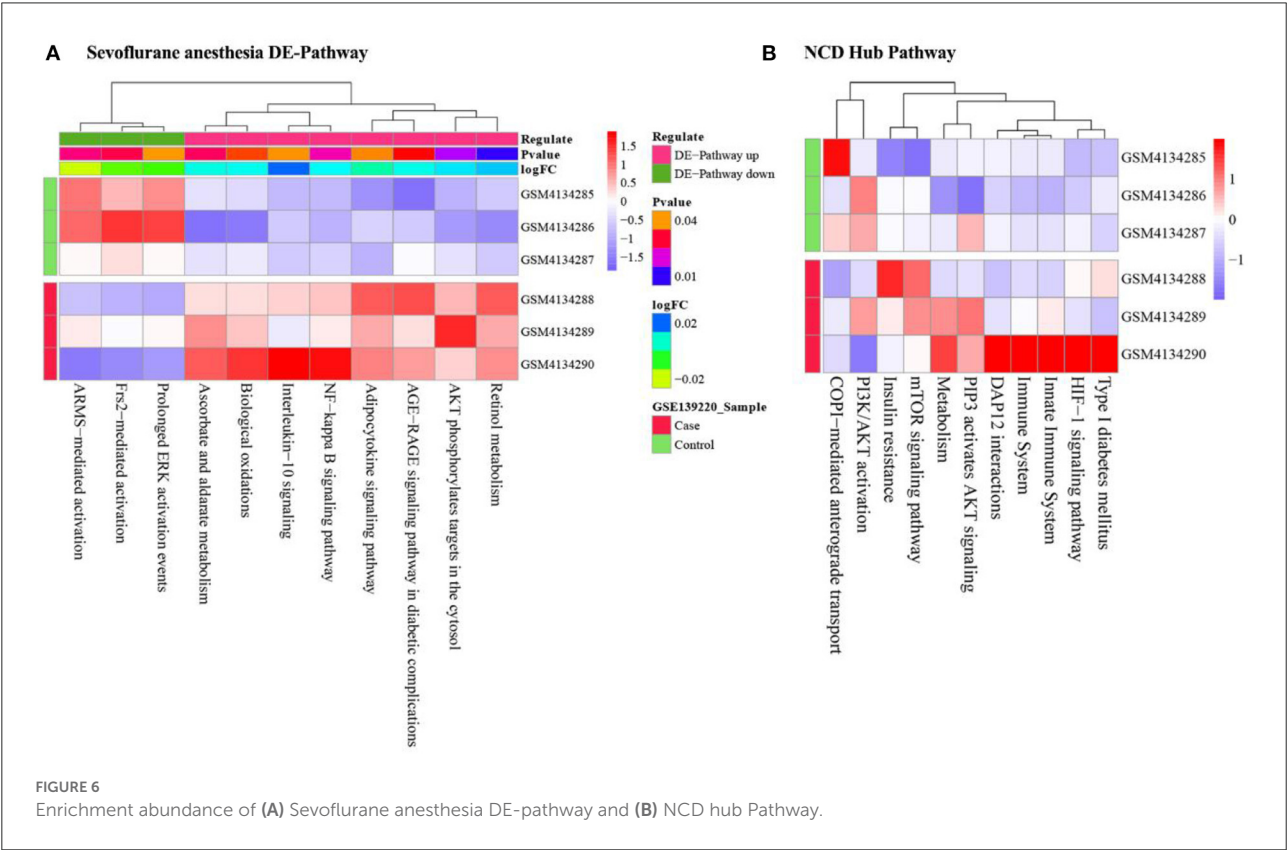




TABLE 4 Correlation of 7 Sevoflurane anesthesia DE-pathways and 11 NCD hub hub pathways.

| Sevoflurane anesthesia_pathway                       | NCD_pathway                         | Correlation |
|--|-------------------------------------|-------------|
| NF-kappa B signaling pathway                         | HIF-1 signaling pathway             | 0.935044    |
| Ascorbate and aldarate metabolism                    | Metabolism                          | 0.946657    |
| Biological oxidations                                | Metabolism                          | 0.940878    |
| Interleukin-10 signaling                             | HIF-1 signaling pathway             | 0.966138    |
| Interleukin-10 signaling                             | Type I diabetes mellitus            | 0.963346    |
| ARMS-mediated activation                             | HIF-1 signaling pathway             | -0.92007    |
| NF-kappa B signaling pathway                         | Immune system                       | 0.883918    |
| NF-kappa B signaling pathway                         | Innate immune system                | 0.862379    |
| NF-kappa B signaling pathway                         | Type I diabetes mellitus            | 0.876083    |
| Ascorbate and aldarate metabolism                    | PIP3 activates AKT signaling        | 0.850632    |
| AGE-RAGE signaling pathway in diabetic complications | COPI-mediated anterograde transport | -0.89447    |
| AGE-RAGE signaling pathway in diabetic complications | Insulin resistance                  | 0.877234    |
| AGE-RAGE signaling pathway in diabetic complications | mTOR signaling pathway              | 0.875509    |
| Biological oxidations                                | Immune system                       | 0.847582    |
| Biological oxidations                                | Innate immune system                | 0.869361    |
| Adipocytokine signaling pathway                      | COPI-mediated anterograde transport | -0.83779    |
| Interleukin-10 signaling                             | DAP12 interactions                  | 0.826367    |
| Interleukin-10 signaling                             | Immune system                       | 0.9008      |
| Interleukin-10 signaling                             | Innate immune system                | 0.858116    |
| Interleukin-10 signaling                             | PI3K/AKT activation                 | -0.84829    |
| ARMS-mediated activation                             | Type I diabetes mellitus            | -0.82896    |

in hippocampal memory and potentiation (36). Composite network analysis implicated Gadd45a, a DNA-damage-inducible gene, in modulating NF-kappa B signaling in Sevoflurane related cognitive damage. In cancer, Gadd45a was found induce Gadd45a-dependant apoptosis in response to NF-kappa B signaling (37) and serves as important links between NF-kappa B and MAPK signaling (38). Sevoflurane was found to impair the AMPK/FoxO3a signaling pathway activation leading to apoptosis of mouse hippocampal neurons (39) and in mouse cerebral cortex (40). FoxO signaling is implicated in increased M1 type polarization of macrophages in Sevoflurane related postoperative cognitive dysfunction (41). Sevoflurane and NCD related pathways were found highly correlated and largely supported by existing literature. NF-kappa B was highly correlated with HIF-1  $\alpha$  in context of Sevoflurane related NCD. HIF 1  $\alpha$  (Hypoxia-inducible factor-1 $\alpha$ ) can be activated by inhalational anesthetics and is implicated in the disruption of the blood brain barrier in postoperative cognitive dysfunction induced by Isoflurane (42). We also performed drug sensitivity analysis for the hub genes and found a number of candidate drugs. Genipin, a biological compound derived from *Gardenia jasminoides* was found to target Erg1, a key candidate gene. Earlier research has shown Genipin could modulate the levels of 5-HT genes and BDNF in the hippocampus (43). The present data

suggests the roles of Apexin and Genipin among others to counter Sevoflurane related cognitive dysfunction. Several drugs including dexmedetomidine, ketamine, other anti-inflammatory and anti-oxidant molecules (44, 45) have been documented for treatment of post-operative cognitive dysfunction. Our analysis identified several anti-diabetic drugs as candidates, which have shown potential in Alzheimer's disease (46) but are not documented for post-operative cognitive protection. In addition progesterone, which has been documented for post brain surgery cognitive dysfunction (47) was also identified as a candidate.

Overall the candidate genes and functional pathways implicated in Sevoflurane related postoperative cognitive dysfunction was supported by existing experimental data. Although earlier studies have utilized gene expression analysis for analysis of postoperative cognitive dysfunction (48, 49) no studies have focused on Sevoflurane to our knowledge. Furthermore, as many peri-operative factors can contribute to postoperative cognitive dysfunction, it is challenging in to isolate molecular mechanisms attributable to an anesthetic agent alone. By the *in-silico* approach adopted in this study, overlapping mechanisms were identified as candidates attributed to the anesthetic agent. Future studies should focus on verifying the roles of specific candidate gene-signaling axis pathways that might mediate Sevoflurane



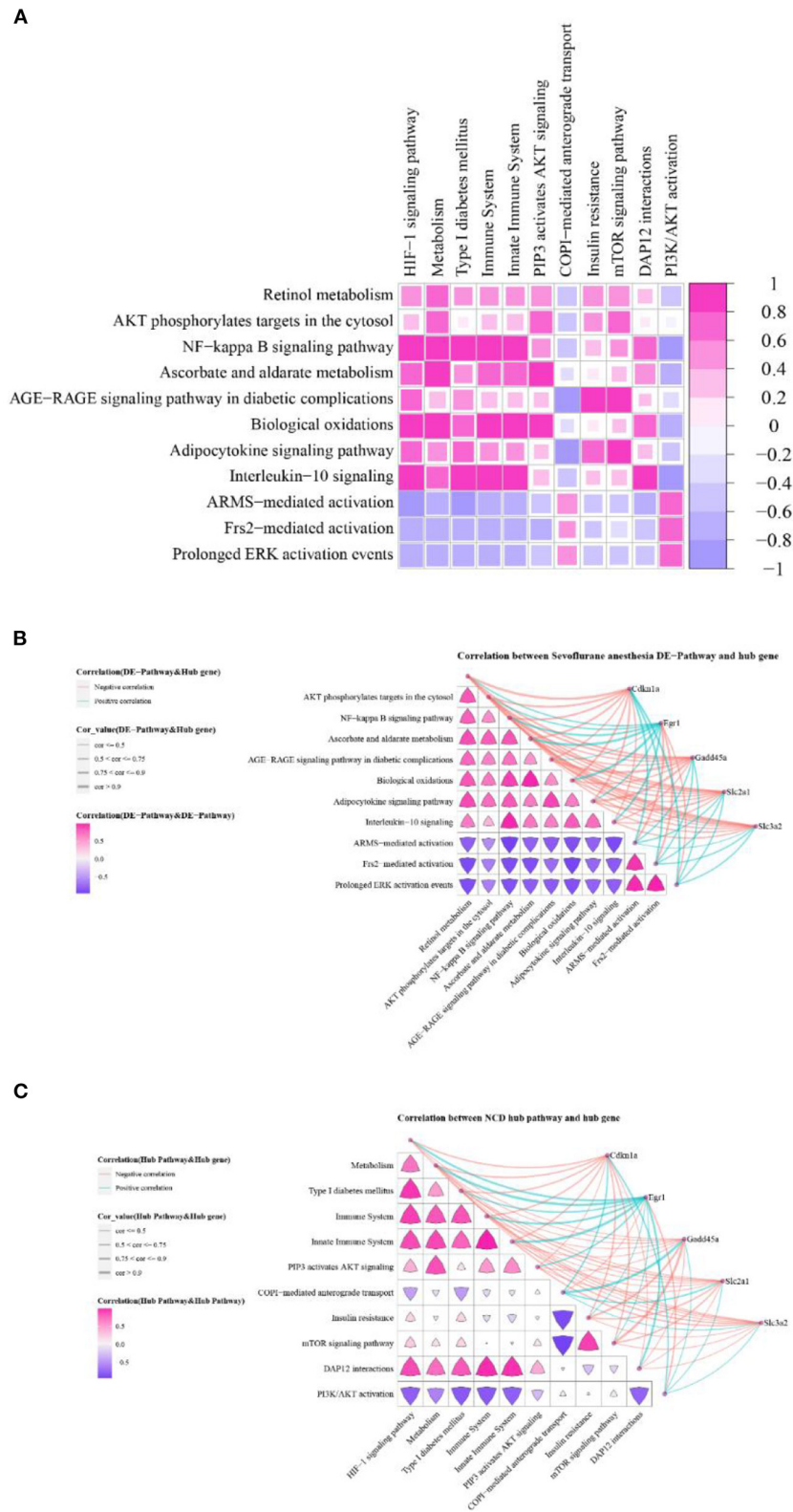
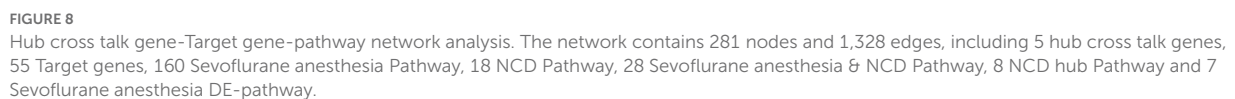


**FIGURE 7**  
Hub cross talk gene and pathway correlation. **(A)** Correlation of Sevoflurane anesthesia DE-pathway and NCD hub pathway. **(B)** Correlation between Sevoflurane anesthesia DE-pathway, and hub cross talk gene and Sevoflurane anesthesia DE-pathway. **(C)** The correlation between the NCD hub pathway and the hub cross talk gene and the NCD hub pathway.



## Conclusion

A suite of bioinformatics analysis revealed several key candidate hippocampal genes including Cdkn1a, Egr1, Gadd45a, Slc2a1 and Slc3a2 and multiple enriched functional signaling pathways that could underlie Sevoflurane induced neurodegenerative processes.

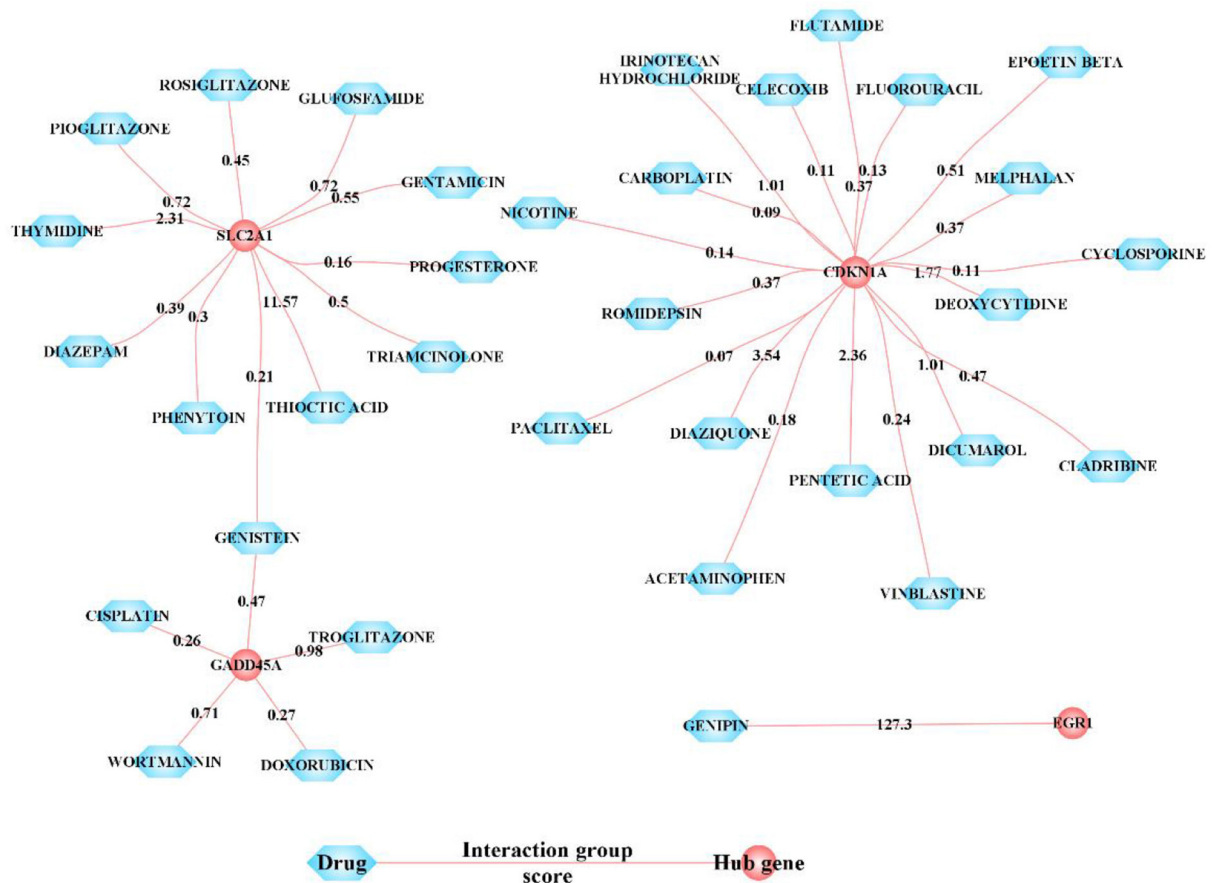


FIGURE 9

Sensitivity relationship between hub cross talk gene and Drug. In the network, nodes with interaction group score  $\geq 4$  are displayed, and other nodes are hidden. The interaction score is a static score and based on the evidence of an interaction.

## Data availability statement

The data presented in the study are deposited in the GEO dataset repository, accession number GSE139220 dataset (URL: <https://www.ncbi.nlm.nih.gov/geo/query/acc.cgi?acc=GSE139220>). The original contributions presented in the study are included in the article, further inquiries can be directed to the corresponding author.

## Ethics statement

Ethical review and approval was not required for the study on animals in accordance with the local legislation and institutional requirements. Ethical review and approval was not required for the study on human participants in accordance with the local legislation and institutional requirements. Written informed consent from the patients/participants' or patients/participants

legal guardian/next of kin was not required to participate in this study in accordance with the national legislation and the institutional requirements.

## Author contributions

WL and QY conceptualized the research idea, designed the workflow, carried out the computational biology analysis, interpreted the results, and wrote the draft of the manuscript. HS reviewed and edited the manuscript, as well as administrated and supervised the whole research project. All authors read and approved the final manuscript.

## Funding

We appreciate the research funding provided by the Science and Technology Innovation Development Project of Tai'an

(Grant No. 2021NS160), the Medical and Health Science and Technology Development Plan of Shandong Province (Grant No. 202102010647), the Traditional Chinese Medicine Science and Technology Project of Shandong Province (Grant No. 2021M190), and the Science and Technology Innovation Development Project of Tai'an (Grant Nos. 2020NS188 and 2020NS217).

## Conflict of interest

The authors declare that the research was conducted in the absence of any commercial or financial relationships

that could be construed as a potential conflict of interest.

## Publisher's note

All claims expressed in this article are solely those of the authors and do not necessarily represent those of their affiliated organizations, or those of the publisher, the editors and the reviewers. Any product that may be evaluated in this article, or claim that may be made by its manufacturer, is not guaranteed or endorsed by the publisher.

## References

- Juvin P, Frederique S, Giraud O, Desmonts JM. Emergence of elderly patients from prolonged desflurane, isoflurane, or propofol anesthesia. *Anesth Analg*. (1997) 3:647–51. doi: 10.1097/00005539-199709000-00029
- Joo HS, Perks WJ. Sevoflurane vs. propofol for anesthetic induction: a meta-analysis. *Anesth Analg*. (2000) 1:213–9. doi: 10.1097/00005539-200007000-00040
- Esper T, Wehner M, Meinecke CD, Rueffert H. Blood/gas partition coefficients for Isoflurane, Sevoflurane, and Desflurane in a clinically relevant patient population. *Anesth Analg*. (2015) 120:45–50. doi: 10.1213/ANE.0000000000000516
- Katoh T, Suguro Y, Nakajima R, Kazama T, Ikeda K. Blood concentrations of Sevoflurane and isoflurane on recovery from anaesthesia. *Br J Anaesth*. (1992) 3:259–62. doi: 10.1093/bja/69.3.259
- Ikeda K. Postanesthetic respiratory depression in humans: a comparison of Sevoflurane, isoflurane and halothane. *J Anesth*. (1987) 1:137–42. doi: 10.1007/s0054070010137
- De Hert SG, Van der Linden PJ, Cromheecke S, Meeus R, Nelis A, Van Reeth V. Cardioprotective properties of Sevoflurane in patients undergoing coronary surgery with cardiopulmonary bypass are related to the modalities of its administration. *J Am Soc Anesthesiol*. (2004) 101:299–310. doi: 10.1097/0000542-200408000-00009
- Lee HT, Kim M, Jan M, Emala CW, Emala. Anti-inflammatory and antinecrotic effects of the volatile anesthetic Sevoflurane in kidney proximal tubule cells. *Am J Physiol Renal Physiol*. (2006) 291:F67–78. doi: 10.1152/ajprenal.00412.2005
- Bedford PD. Adverse cerebral effects of anaesthesia on old people. *The Lancet*. (1955) 266, 6884:259–64. doi: 10.1016/S0140-6736(55)92689-1
- Rasmussen LS, Moller JT. Central nervous system dysfunction after anesthesia in the geriatric patient. *Anesthesiol Clin N Am*. (2000) 1:59–70. doi: 10.1016/S0889-8537(05)70149-8
- Monk TG, Price CC. Postoperative cognitive disorders. *Curr Opin Crit Care*. (2011) 17:4. doi: 10.1097/MCC.0b013e328328348bece
- Huang JM, Lv ZT, Zhang B, Jiang WX, Nie MB. Intravenous parecoxib for early postoperative cognitive dysfunction in elderly patients: evidence from a meta-analysis. *Expert Rev Clin Pharmacol*. (2020) 4:451–60. doi: 10.1080/17512433.2020.1732815
- Vutskits L, Xie Z. Lasting impact of general anaesthesia on the brain: mechanisms and relevance. *Nat Rev Neurosci*. (2016) 11:705–18. doi: 10.1038/nrn.2016.128
- Head BP, Patel HH, Niesman IR, Drummond JC, Roth DM, Patel PM. Inhibition of p75 neurotrophin receptor attenuates isoflurane-mediated neuronal apoptosis in the neonatal central nervous system. *J Am Soc. Anesthesiol*. 110, 813–825 (2009). doi: 10.1097/ALN.0b013e31819b602b
- Boscolo A, Milanovic D, Starr JA, Sanchez V, Oklopčić A, Moy L, Ori CC, Erisir A, Jevtic-Todorovic, V. Early exposure to general anesthesia disturbs mitochondrial fission and fusion in the developing rat brain. *Anesthesiology* (2013) 118:1086–97. doi: 10.1097/ALN.0b013e318289bc9b
- Zang L, Zhang J, Dong Y, Swain CA, Zhang Y, Xie Z. The potential dual effects of Sevoflurane on AKT/GSK3 $\beta$  signaling pathway. *Med Gas Res*. (2014) 4:5. doi: 10.1186/2045-9912-4-5
- Tao G, Zhang J, Zhang L, Dong Y, Yu B, Crosby G, Culley DJ, Zhang Y, Xie Z. Sevoflurane induces tau phosphorylation and glycogen synthase kinase 3 $\beta$  activation in young mice. *Anesthesiology*. (2014) 121:510–27. doi: 10.1097/ALN.0000000000000278
- Zurek AA, Bridgwater EM, and Orser BA. Inhibition of  $\alpha 5$   $\gamma$ -aminobutyric acid type A receptors restores recognition memory after general anesthesia. *Anesth. Analg*. (2012) 114:845–55. doi: 10.1213/ANE.0b013e31824720da
- Lu Y, Wu X, Dong Y, Xu Z, Zhang Y, Xie Z. Anesthetic Sevoflurane causes neurotoxicity differently in neonatal naive and Alzheimer disease transgenic mice. *J Am Soc Anesth*. (2010) 112:1404–16. doi: 10.1097/ALN.0b013e3181d94de1
- Meng B, Li X, Lu B, Liu R, Yuan H, Zhai X, et al. The investigation of hippocampus-dependent cognitive decline induced by anesthesia/surgery in mice through integrated behavioral Z-scoring. *Front Behav Neurosci*. (2020) 13:282. doi: 10.3389/fnbeh.2019.00282
- Qu Y, Li H, Shi C, Qian M, Yang N, Wang L, Gao X, Ni C. Incrns are involved in Sevoflurane anesthesia-related brain function modulation through affecting mitochondrial function and aging process. *BioMed Research International*. (2020) 2020. doi: 10.1155/2020/8841511
- Song SY, Meng XW, Xia Z, Liu H, Zhang J, Chen QC, et al. Cognitive impairment and transcriptomic profile in hippocampus of young mice after multiple neonatal exposures to Sevoflurane. *Aging*. (2019) 19:8386–417. doi: 10.18632/aging.102326
- Pagel JI, Deind E. Disease progression mediated by egr-1 associated signaling in response to oxidative stress. *Int J Mol Sci*. (2012) 10:13104–17. doi: 10.3390/ijms131013104
- Maddox SA, Melissa SM, Glenn E. Schafe. Early growth response gene 1 (Egr-1) is required for new and reactivated fear memories in the lateral amygdala. *Learn Memory*. (2011) 1:24–38. doi: 10.1101/lm.1980211
- Mo J, Kim CH, Lee D, Sun W, Lee HW, Kim H. Early growth response 1 (Egr-1) directly regulates GABAA receptor  $\alpha 2$ ,  $\alpha 4$ , and  $\theta$  subunits in the hippocampus. *J. Neurochem*. (2015) 133:489–500. doi: 10.1111/jnc.13077
- Kidambi S, Yarmush J, Berdichevsky Y, Kamath S, Fong W, SchianodiCola J. Propofol induces MAPK/ERK cascade dependant expression of cFos and Egr-1 in rat hippocampal slices. *BMC Res Notes*. (2010) 31:1–6. doi: 10.1186/1756-0500-3-201
- Zhang X, Yue Y, Wu A. Roles of c-Fos, EGR-1, PKA, and PKC in cognitive dysfunction in rats after propofol anesthesia. *Braz J Pharm Sci*. (2022) 66:58. doi: 10.1590/s2175-97902022e18807
- Kobayashi K, Takemori K, Sakamoto A. Circadian gene expression is suppressed during Sevoflurane anesthesia and the suppression persists after awakening. *Brain Res*. (2007) 1185:1–7. doi: 10.1016/j.brainres.2007.09.011
- Shi C, Yi D, Li Z, Zhou Y, Cao Y, Sun Y, et al. Anti-RAGE antibody attenuates isoflurane-induced cognitive dysfunction in aged rats. *Behav Brain Res*. (2017) 322:167–76. doi: 10.1016/j.bbr.2017.01.012



29. Acharya NK, Goldwaser EL, Forsberg MM, Godsey GA, Johnson CA, Sarkar A, et al. Sevoflurane and isoflurane induce structural changes in brain vascular endothelial cells and increase blood-brain barrier permeability: possible link to postoperative delirium and cognitive decline. *Brain Res.* (2015) 1620:29–41. doi: 10.1016/j.brainres.2015.04.054
30. Liu Y, Zhang T, Wang Y, Wu P, Li Y, Wang C, Xu S, Shi H. Apelin-13 attenuates early brain injury following subarachnoid hemorrhage via suppressing neuronal apoptosis through the GLP-1R/PI3K/Akt signaling. *Biochem Biophys Res Commun.* (2019) 513:105–11. doi: 10.1016/j.bbrc.2019.03.151
31. Cheng Z, Zheng YZ, Li YQ, Wong CS. Cellular senescence in mouse hippocampus after irradiation and the role of p53 and p21. *J Neuropathol Exp Neurol.* (2017) 4:260–9. doi: 10.1093/jnen/nlx006
32. Zhang P, Kishimoto Y, Grammatikakis I, Gottimukkala K, Cutler RG, Zhang S, et al. Senolytic therapy alleviates A $\beta$ -associated oligodendrocyte progenitor cell senescence and cognitive deficits in an Alzheimer's disease model. *Nat Neurosci.* (2019) 5:719–28. doi: 10.1038/s41593-019-0372-9
33. Zhou X, Xian D, Xia J, Tang Y, Li W, Chen X, et al. MicroRNA-34c is regulated by p53 and is involved in Sevoflurane-induced apoptosis in the developing rat brain potentially via the mitochondrial pathway. *Mol Med Rep.* (2017) 4:2204–12. doi: 10.3892/mmr.2017.6268
34. Geier EG, Chen EC, Webb A, Papp AC, Yee SW, Sadee W, et al. Profiling solute carrier transporters in the human blood-brain barrier. *Clin Pharmacol Therap.* (2013) 6:636–9. doi: 10.1038/clpt.2013.175
35. Lu G, Xu H, Zhao W, Zhang J, Rao D, Xu S. Upregulation of long noncoding RNA Gadd45a is associated with Sevoflurane-induced neurotoxicity in rat neural stem cells. *Neuroreport.* (2018) 8:605–14. doi: 10.1097/WNR.0000000000000980
36. Aparisi Rey A, Karaulanov E, Sharopov S, Arab K, Schäfer A, Gierl M, et al. Gadd45 $\alpha$  modulates aversive learning through post-transcriptional regulation of memory-related mRNA s. *EMBO Rep.* (2019) 6:e46022. doi: 10.15252/embr.201846022
37. Zerbini LF, Libermann TA. Life and death in cancer GADD45  $\alpha$  and  $\gamma$  are critical regulators of NF- $\kappa$ B mediated escape from programmed cell death. *Cell Cycle.* (2005) 4:18–20. doi: 10.4161/cc.4.1.1363
38. Yang Z, Song L, Huang C. Gadd45 proteins as critical signal transducers linking NF- $\kappa$ B to MAPK cascades. *Curr Cancer Drug Targets.* (2009) 9:915–30. doi: 10.2174/156800909790192383
39. Zhang H, Yan L. Solasonine relieves Sevoflurane-induced neurotoxicity via activating the AMP-activated protein kinase/FoxO3a pathway. *Hum Exp Toxicol.* (2022) 41:09603271211069984. doi: 10.1177/09603271211069984
40. Wang Q, Li Y, Tan H, Wang Y. Sevoflurane-induced apoptosis in the mouse cerebral cortex follows similar characteristics of physiological apoptosis. *Front Mol Neurosci.* (2022). doi: 10.3389/fnmol.2022.873658
41. Fu JB, Wang ZH, Ren YY. Forkhead box O1-p21 mediates macrophage polarization in postoperative cognitive dysfunction induced by Sevoflurane. *Curr Neurovasc Res.* (2020) 1:79–85. doi: 10.2174/1567202617666200128142728
42. Cao Y, Li Z, Li H, Ni C, Li L, Yang N, et al. Hypoxia-inducible factor-1 $\alpha$  is involved in isoflurane-induced blood-brain barrier disruption in aged rats model of POCD. *Behav Brain Res.* (2018) 339:39–46. doi: 10.1016/j.bbr.2017.09.004
43. Wang QS, Tian JS, Cui YL, Gao S. Genipin is active via modulating monoaminergic transmission and levels of brain-derived neurotrophic factor (BDNF) in rat model of depression. *Neuroscience.* (2014) 275:365–73. doi: 10.1016/j.neuroscience.2014.06.032
44. Safavynia SA, Goldstein PA. The role of neuroinflammation in postoperative cognitive dysfunction: moving from hypothesis to treatment. *Front Psychiatry.* (2019) 9:752. doi: 10.3389/fpsyt.2018.00752
45. Kotekar N, Anshul S, Ravishankar N. Postoperative cognitive dysfunction—current preventive strategies. *Clin Interv Aging.* (2018) 13:2267. doi: 10.2147/CIA.S133896
46. Alagiakrishnan K, Sankaralingam S, Ghosh M, Mereu L, Senior P. Antidiabetic drugs and their potential role in treating mild cognitive impairment and Alzheimer's disease. *Discov Med.* (2013) 90:277–86. doi: 10.3233/JAD-180121
47. Cheng SY, Gilberto KK. Can progesterone be a better alternative to dexamethasone for use in routine brain surgery? *Neural Regener Res.* (2015) 9:1379. doi: 10.4103/1673-5374.165221
48. Wu YQ, Liu Q, Wang HB, Chen C, Yi-Man Sun HH, Ma LH, et al. Microarray analysis identifies key differentially expressed circular RNAs in aged mice with postoperative cognitive dysfunction. *Front Aging Neurosci.* (2021) 66:526. doi: 10.3389/fnagi.2021.716383
49. Zhang Y, Liu YX, Xiao QX, Liu Q, Deng R, Bian J, et al. Microarray expression profiles of lncRNAs and mRNAs in postoperative cognitive dysfunction. *Front Neurosci.* (2018) 12:694. doi: 10.3389/fnins.2018.00694
50. Huang C, Mårtensson J, Gögenur I, Asghar MS. Exploring postoperative cognitive dysfunction and delirium in noncardiac surgery using MRI: a systematic review. *Neural Plast.* (2018) 2018. doi: 10.1155/2018/1281657





## OPEN ACCESS

## EDITED BY

Yuzhen Xu,  
Tongji University, China

## REVIEWED BY

Hanning Ma,  
General Hospital of Ningxia Medical  
University, China  
Weidong Wu,  
Shanxi Medical University, China

## \*CORRESPONDENCE

Yafei Sun  
shang96142407@163.com

## SPECIALTY SECTION

This article was submitted to  
Neurological Biomarkers,  
a section of the journal  
Frontiers in Neurology

RECEIVED 30 August 2022

ACCEPTED 14 November 2022

PUBLISHED 06 December 2022

## CITATION

Tian T, Sun W, Du J and Sun Y (2022)  
Analysis of co-expression gene  
network associated with intracranial  
aneurysm and type 2 diabetes mellitus.  
*Front. Neurol.* 13:1032038.  
doi: 10.3389/fneur.2022.1032038

## COPYRIGHT

© 2022 Tian, Sun, Du and Sun. This is  
an open-access article distributed  
under the terms of the [Creative  
Commons Attribution License \(CC BY\)](#).  
The use, distribution or reproduction  
in other forums is permitted, provided  
the original author(s) and the copyright  
owner(s) are credited and that the  
original publication in this journal is  
cited, in accordance with accepted  
academic practice. No use, distribution  
or reproduction is permitted which  
does not comply with these terms.

# Analysis of co-expression gene network associated with intracranial aneurysm and type 2 diabetes mellitus

Tian Tian<sup>1</sup>, Wenhao Sun<sup>1</sup>, Jia Du<sup>2</sup> and Yafei Sun<sup>3\*</sup>

<sup>1</sup>Department of Neurological Surgery, Chengde Medical University Affiliated Hospital, Chengde, China, <sup>2</sup>Department of Neurological Surgery, Cangzhou Center Hospital, Cangzhou, China,

<sup>3</sup>Department of Neurology, The Second Hospital of Hebei Medical University, Shijiazhuang, China

To screen for common target genes in intracranial aneurysms (IA) and type 2 diabetes mellitus (T2DM), construct a common transcriptional regulatory network to predict clusters of candidate genes involved in the pathogenesis of T2DM and IA, and identify the common neurovascular markers and pathways in T2DM causing IA. Microarray datasets (GSE55650, GSE25462, GSE26969, GSE75436, and GSE13353) from the GEO database were analyzed in this research. Screening of the IA and the T2DM datasets yielded a total of 126 DEGs, among which 78 were upregulated and 138 were downregulated. Functional enrichment analysis revealed that these DEGs were enriched for a total of 68 GO pathways, including extracellular matrix composition, coagulation regulation, hemostasis regulation, and collagen fiber composition pathways. We also constructed transcriptional regulatory networks, and identified key transcription factors involved in both the conditions. Univariate logistic regression analysis showed that ARNTL2 and STAT1 were significantly associated with the development of T2DM and IA, acting as the common neurovascular markers for both the diseases. In cellular experiments, hyperglycemic microenvironments exhibited upregulated STAT1 expression. STAT1 may be involved in the pathogenesis of IA in T2DM patients. Being the common neurovascular markers, STAT1 may acts as novel therapeutic targets for the treatment of IA and T2DM.

## KEYWORDS

intracranial aneurysm, T2DM, STAT1, neurovascular markers, ARNTL2

## Introduction

Diabetes mellitus (DM) is a clinical syndrome characterized by high blood glucose levels due to a combination of genetic and environmental factors. It is categorized as type 1 (T1DM) or type 2 (T2DM) depending on the underlying cause. T2DM is the more common type of DM, and it is primarily manifested by insulin resistance or relatively insufficient insulin secretion (1). Furthermore, T2DM is usually accompanied by micro and macroangiopathy, including diabetic eye disease, diabetic nephropathy, diabetic foot, cerebral infarction, myocardial infarction, and other manifestations, seriously affecting the quality of life and life expectancy of patients (2–4). However, effective intervention

in reducing blood glucose reduces the incidence of cardiovascular events. Daqing et al. found that a 6-year lifestyle intervention reduced the incidence of diabetes and cardiovascular events (heart attack, cerebral infarction, and heart failure) by 49 and 26% over 30 years, in people with impaired glucose tolerance (5).

The molecular mechanisms associated with the development of aneurysms are complex. Although the cause of intracranial aneurysms (IA) is still poorly understood, it is thought to be a result of a combination of factors, including hemodynamic, morphological, and clinical factors (6–8). Hemodynamic disorders can induce endothelial dysfunction, induce macrophages to release pro-inflammatory cytokines and matrix metalloproteinases (MMPs) to digest the extracellular matrix (ECM), and induce apoptosis of vascular smooth muscle cells (SMCs), resulting in the loss of vessel wall integrity and development of aneurysm (9–11). In addition, vascular morphological factors are also important in the development of aneurysm. High glucose-induced reactive oxygen species (ROS) may be involved in the activation of c-Jun N-terminal kinase (JNK) pathway, which in turn triggers caspase-3 and promotes apoptosis of vascular endothelial cells, leading to changes in the vascular structure (12). Additionally, ROS can induce vascular SMC senescence and aneurysm formation by activating nuclear factor kappa-light-chain-enhancer of activated B cells (NF- $\kappa$ B) (13). In contrast, immunosuppressants can limit aneurysm growth by reducing JNK activation, decreasing the inflammatory response, and reducing endothelial cell activation (14).

These studies suggest that T2DM can induce the development of IA; however, the underlying mechanism is unclear. The hemodynamic and vascular structural damage induced by T2DM is considered to be an important factor in the development of aneurysms. Free fatty acid (FA) concentrations are elevated in the blood of diabetic patients due to excessive release of adipose tissue and its reduced uptake by skeletal muscles (15–17). The liver increases very low density lipoproteins (VLDL) production and cholesteryl esters synthesis to eliminate the excess FA. Free cholesterol contributes to atherosclerosis by activating toll-like receptor proteins (TLRs) and prolonging the activation of p38 mitogen-activated protein kinase (MAPK), thereby causing degenerative variations in the arterial wall and promoting the development of aneurysms (18, 19). A few studies have shown that platelet reactivity is elevated in T2DM patients, leading to impaired coagulation regulation, increasing the risk of cardiovascular events (20). In addition, an increase in plasma coagulation factors (e.g., factor VII and thrombin) and a decrease in endogenous anticoagulants (e.g., thrombomodulin and protein C) in DM patients, increases the risk of thrombosis, which can cause altered hemodynamics and aneurysm development (21, 22). A decrease in the expression of MMP-2 and 3 and an increase in the expression of tissue inhibitor of metalloproteinases (TIMP),

in response to high glucose induction, can cause vascular lesions that induce aneurysm formation (23).

In previous studies, diabetes and IA prevalence and growth were paradoxically negatively associated, and this protective effect may have been attributed to diabetes drugs (24). As a result, the specific relationship between diabetes and IA remains unclear (25). Diabetes is a risk factor for vascular dysfunction (26). It is a consequence of vascular dysfunction that IA occurs (27, 28). Recent developments in bioinformatics have provided us with an effective method for establishing the link between diabetes and neurovascular diseases, including IA (29–36). Transcription factors (TFs) are an important breakthrough in the study of disease associations (37–40). Currently, it is unclear whether TFs in peripheral blood can serve as effective markers for T2DM and IA. Therefore, identifying TFs that are differentially expressed in peripheral blood of T2DM and IA patients may provide a new avenue for the prevention and diagnosis of T2DM and IA.

In order to further explore the association between T2DM and IA, we analyzed the correlation between the differentially expressed genes (DEGs) common to IA and T2DM through multi-omics analyses and constructed a transcriptional regulatory network by using logistic regression curve analysis. The results of this analysis provide a theoretical basis for IA pathogenesis in T2DM patients and provide theoretical support for its diagnosis and treatment.

## Methods

### Data acquisition and pre-processing

For the following keywords: diabetes mellitus, type 2 diabetes mellitus, or intracranial aneurysms, we searched the NCBI GEO database (<https://www.ncbi.nlm.nih.gov/geo/>). In order to screen the dataset and ensure that relevant data was recorded, the following criteria were used: (i) samples included both normal and disease samples; (ii) the dataset was capable of completing expression profiling based on the array method; (iii) the species was restricted to *Homo sapiens*; and (iv) raw data was available for analysis. The IA-associated gene expression microarray datasets (GSE26969, GSE75436, and GSE13353) and T2DM-associated gene expression microarray datasets (GSE55650 and GSE25462) were obtained via the Gene Expression Omnibus (GEO) database. GSE26969 dataset included three unruptured IA and the corresponding control samples, GSE75436 included 15 IA and the corresponding superficial temporal artery samples, and GSE13353 included eight unruptured IA samples. The GSE55650 dataset included 12 T2DM and 11 control samples with family history of DM, while the GSE25462 dataset included 10 T2DM and 25 control samples with family history of DM. Thus, we included a total of 26 disease and 18 control samples for

TABLE 1 Sources of data related to intracranial aneurysms and T2DM.

| ID | GSE number | Platform | Samples                  | Diseases                       |
|----|------------|----------|--------------------------|--------------------------------|
| 1  | GSE26969   | GPL570   | 3 patients, 3 controls   | Intracranial arterial aneurysm |
| 2  | GSE75436   | GPL570   | 15 patients, 15 controls | Intracranial arterial aneurysm |
| 3  | GSE13353   | GPL570   | 8 patients               | Intracranial arterial aneurysm |
| 4  | GSE55650   | GPL570   | 12 patients, 11 controls | Type 2 diabetes                |
| 5  | GSE25462   | GPL570   | 10 patients, 25 controls | Type 2 diabetes                |

IA and 22 disease and 36 control samples for T2DM as show in Table 1.

## Differential expression analysis

R software (version 4.0.2) was used to process the download matrix file and platform. Gene symbols were assigned to the probe names corresponding to the IDs. The mean value was chosen when multiple probes corresponded to one gene. In addition, for each of the two disease categories, we used the ComBat function in the sva (v3.40.0) package to eliminate batch effects between multiple datasets and retain the biological differences between the disease and control samples. Thereafter, we normalized the samples using the normalize Between Arrays function in the limma (v3.48.3) package (41). Differential expression analysis (DEA) was done individually for the IA and the T2DM datasets using the limma package, and the thresholds for DEGs were set as  $|\log_2FC| > 1$  and  $FDR < 0.05$ . Furthermore, the intersection analysis is integrated in the dataset using Venn Analytics (Venn).

## Weighted co-expression network construction and module identification

By analyzing gene expression data, WGCNA (Weighted Correlation Network Analysis) constructs gene co-expression networks (42). By analyzing association relationships between genes, WGCNA categorizes genes into modules. Finally, correlation analysis between these modules and sample phenotypes is used to examine molecular features of specific phenotypes. The expression profiles of the two disease categories were integrated and the expression distributions of all the samples were normalized using the normalizeBetweenArrays function in the limma (v 3.48.3), and the genes in the top 25% of the standard deviation ( $N_{\text{gene}} = 5,720$ ) were selected for subsequent analysis. Thereafter, we conducted weighted gene co-expression network analysis (WGCNA) using the WGCNA (v 1.70-3) package (43), and the strength of association between

the nodes was determined by using the adjacency matrix. The pickSoftThreshold function of WGCNA was used to calculate the scale free fit index ( $R^2$ ) corresponding to different soft thresholds, and the first soft threshold that marked the  $R^2 > 0.9$  was selected. The soft threshold  $\beta$  was set at 8. Subsequently, we transformed the adjacency matrix into a topological overlap matrix (TOM), to quantitatively describe the similarity of nodes by comparing the weighted correlation between two nodes and other nodes. Thereafter, we performed hierarchical clustering to identify co-expression modules, each containing at least 50 genes. Lastly, we computed module eigengene (ME) and merged the similar modules (abline = 0.1).

## Identification of significant co-expressed genes

Pearson correlations between ME and the disease types were calculated and their significance was calculated using the corPvalueStudent function. Finally, the intersections between the gene modules that were significantly associated with both the disease types and the common DEGs of the two disease types were taken as the target genes.

## Construction of transcriptional regulatory networks

We obtained 8,427 human-related transcriptional regulatory relationships, including 795 TFs from the TRRUST (v2) database, which collects a large number of manually-calibrated TF-target regulatory interactions (44). Subsequently, we extracted the transcriptional regulatory networks associated with the target genes and visualized them using cytoscape (v 3.8.0).

## Enrichment analyses

The enrichGO function in the clusterProfiler (v 4.2.2) package was used to enrich the set of genes of interest into GO

entries, and those with a  $p$ -value of  $<0.05$  were considered to be significantly enriched (45). The samples were divided into high and low expression groups based on STAT1 expression values. Then the GSEA function in the clusterProfiler package was used to screen for activated ( $p$ -value  $< 0.05$  and  $NES > 1$ ) or inhibited ( $p$ -value  $< 0.05$  and  $NES < 1$ ) biological process (BP) pathways in the different groups.

## Western blot and cell culture for detecting protein expression

The Shanghai Institute of Cell Biology, Chinese Academy of Sciences has provided us with human umbilical vein endothelial cell line (ECV-304). Cells were cultured in RPMI1640 medium containing 10% FBS at 37°C in a 5% CO<sub>2</sub> incubator. The cells were cultured in groups and given different concentrations of D-glucose to stimulate ECV-304 cell line for the same time (24 h), and the experiment was divided into two groups as follows: (i) control group: Glucose 5.5 mmol/L; (ii) diabetic group: Glucose 16.5 mmol/L. By using the BCA method, total protein was extracted from the cells and quantified. SDS-PAGE electrophoresis of 12% proteins was used for separation, PVDF membranes were sealed with 5% skimmed milk powder for 1 h at room temperature, rinsed three times with TBST, incubated overnight at 4°C with the primary antibody, rinsed with TBST three times, then incubated at room temperature for 1 h with the HRP-labeled secondary antibody, rinsed three times, and then ECL-illuminated for color development. The results were analyzed by chemiluminescence imaging system.

## ComPPI constructs protein interaction networks

The ComPPI database (version 2.1.1) is a comprehensive, open source database for analyzing experimental results in biochemistry, molecular biology, proteomics, as well as proteomic and interactomic research in bioinformatics and network science, contributing to cell biology, medicine, and drug design. STAT1 is the input gene and the result file of ComPPI is exported. R software imports the program file along with the input data file and annotates the file after defining the input parameters. Based on ComPPI, we obtained the STAT1 protein interactions network map.

## Statistical analysis

Each experiment was replicated at least three times. Means and standard deviations (SDs) are used to express quantitative data. All statistical tests and

graphs were generated using the Project R software (version 4.0.2). To detect differentially expressed genes (DEGs), Bayesian tests were used.  $P$ -values  $< 0.05$  were considered significant.

## Results

### Identification of genes co-expressed in IA and T2DM

We selected the GSE26969, GSE75436, GSE13353, GSE55650, and GSE25462 datasets from the GEO database for the analysis to include as many disease samples as possible, while minimizing the impact of batch effects on the analysis. The number of samples, disease types, and platform information included in each dataset are shown in Table 1.

DEGs were identified after removing batch effects between multiple datasets (Figures 1A,B). We screened 822 upregulated and 837 downregulated genes in IA and 1678 upregulated and 1474 downregulated genes in T2DM (Figures 1C,D).

### Screening for target genes

The expression profiles of IA and T2DM were integrated and normalized, and hierarchical clustering analyses of all the samples revealed that the different types of samples could be well distinguished (Figure 2A). We used WGCNA to identify the gene modules associated with disease types, and set the soft threshold ( $\beta$ ) at 8 for constructing the scale-free network (Figure 2B). Subsequently, we constructed the adjacency matrix and TOM to identify the co-expressed gene modules. A total of 12 gene modules were identified using mean hierarchical clustering and dynamic tree cropping methods (Figure 2C). The red and salmon modules were significantly associated with both IA and T2DM (Figure 2D) and were considered to be clinically significant for subsequent analysis. DEA demonstrated that, in both the diseases, 206 and 214 genes were downregulated and upregulated, respectively (Figure 2E). Furthermore, combined results of DEA and WGCNA revealed that 78 genes were downregulated and 138 genes were upregulated in both the diseases (Figure 2F). These 216 genes showed the same dysregulation pattern in both the diseases and were significantly associated with disease onset, suggesting a possible common pathogenic molecular mechanism between both the diseases; therefore, they were considered as the target genes for IA and T2DM. The target genes were significantly enriched to 68 GO pathways (Figure 3A), including ECM composition, coagulation regulation, hemostasis regulation, and collagen protofibril composition pathways.

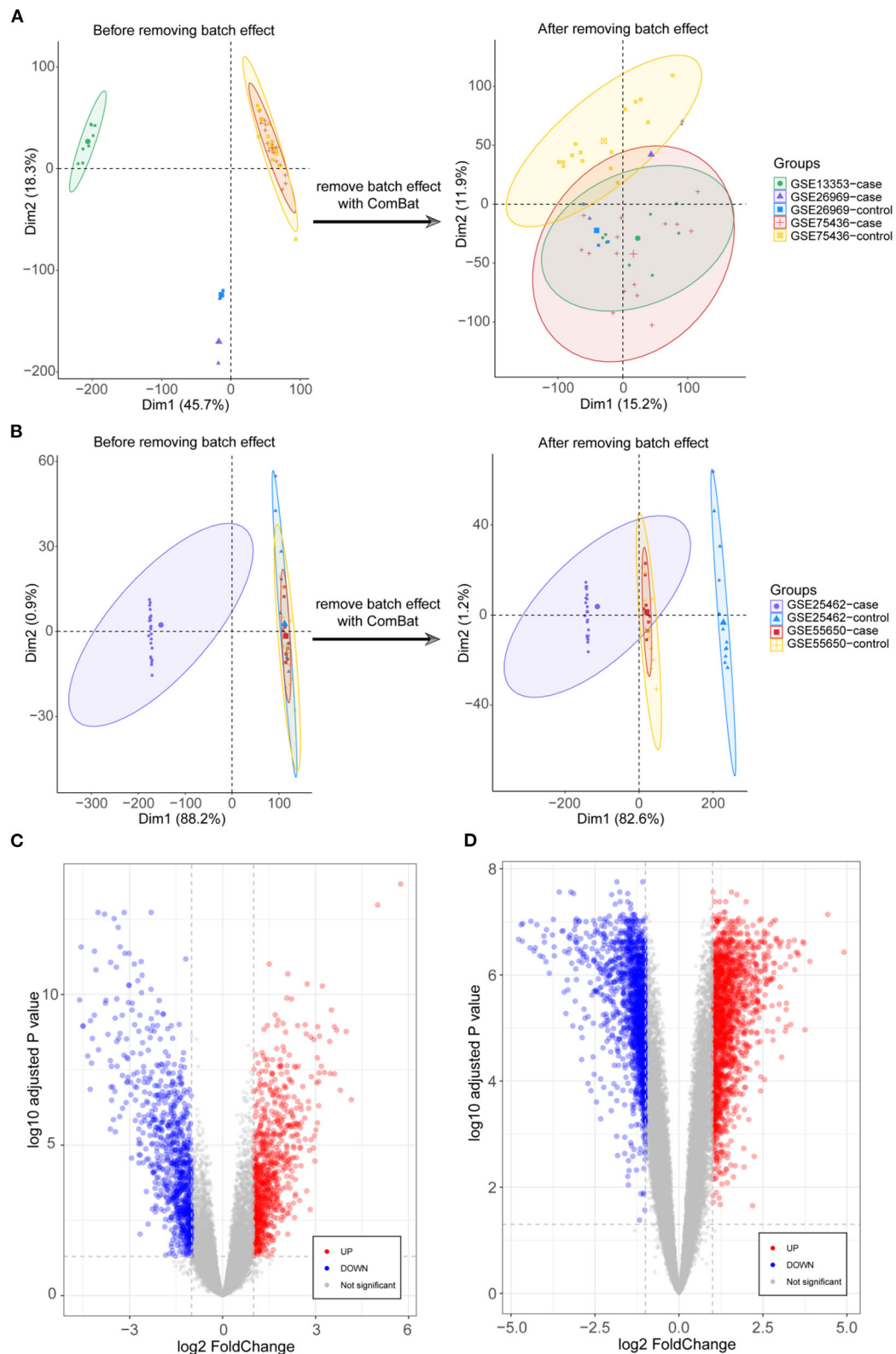


**FIGURE 1** Integration of datasets and differential expression analysis. **(A)** First and second principal components of the intracranial aneurysm (IA)—GSE13353, GSE26969, and GSE75436 datasets before and after eliminating the batch effects. **(B)** First and second principal components of the type 2 diabetes mellitus (T2DM)—GSE25462 and GSE55650 datasets before and after eliminating the batch effects. **(C)** Volcano plots of differentially expressed genes (DEGs) in IA and T2DM. **(D)** Volcano plots of DEGs in T2DM.



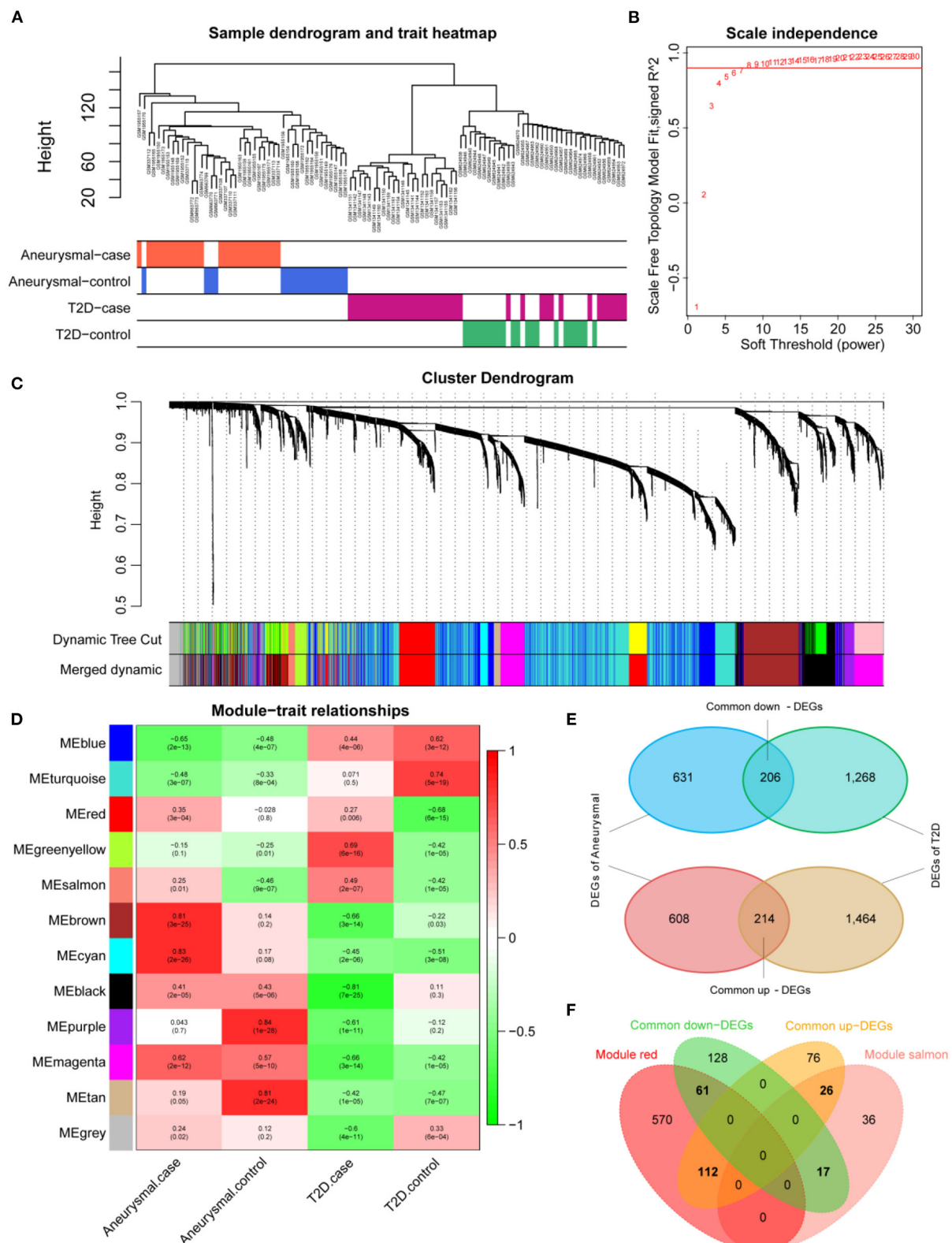


FIGURE 2

Screening of target genes. (A) Dendrogram of clusters for all the samples. (B)  $R^2$  of scale-free model fit analysis corresponding to different soft threshold values;  $R^2$  of the red horizontal line is 0.9. (C) Dendrogram of the genes in the top 25% of the standard deviation based on dissimilarity measure (1-TOM) clustering; color bars are used to mark different modules. (D) Heat map of correlation between module eigengenes (ME) and clinical phenotypes; red and salmon modules are significantly correlated with both intracranial aneurysm (IA) and type 2 diabetes mellitus (T2DM). (E) Venn diagram of differentially expressed genes (DEGs) for IA and T2DM. (F) Venn diagram of common DEGs for IA and T2DM with red and salmon modules, in which 216 genes were considered as significant target genes.

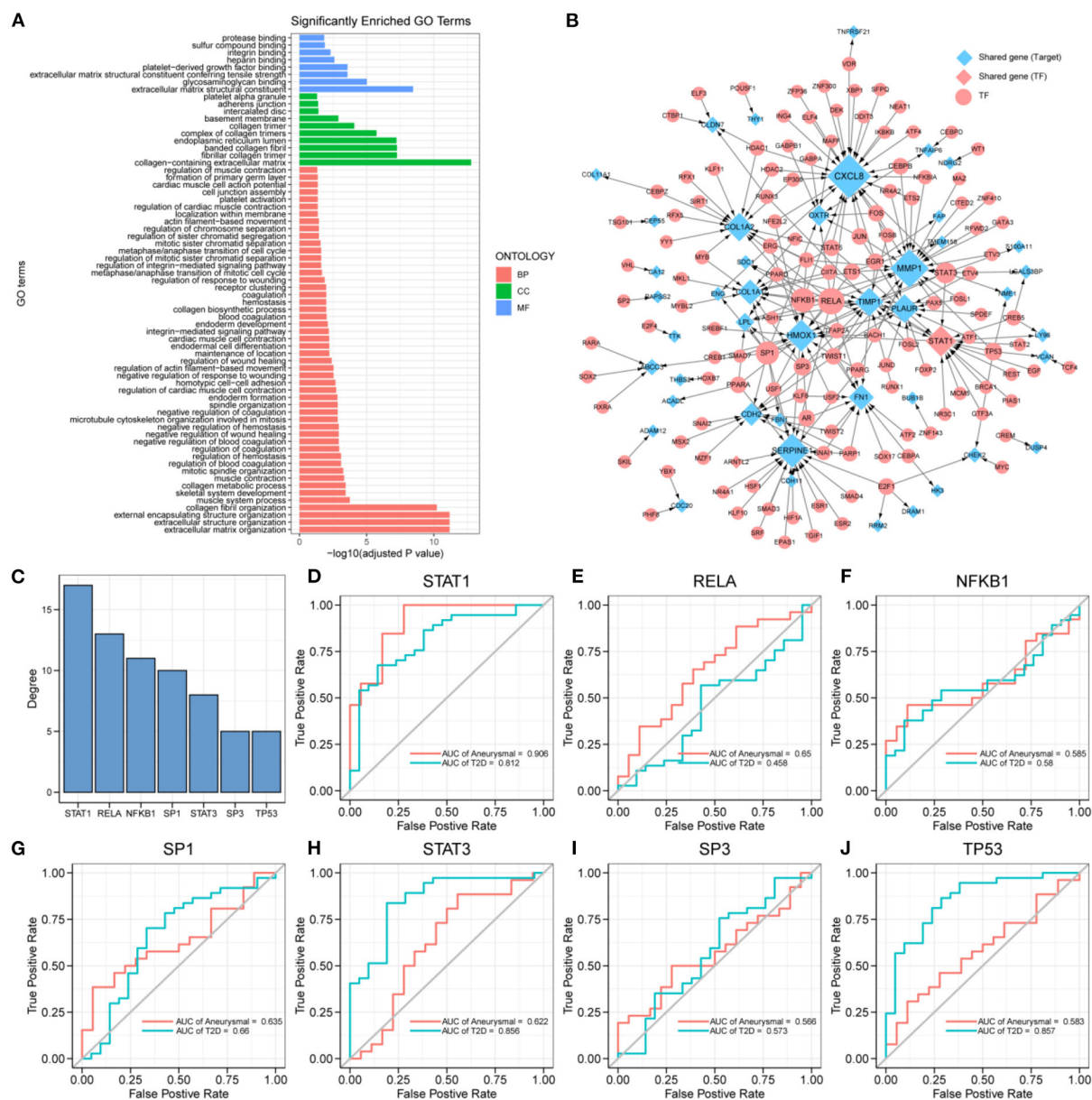


FIGURE 3

Key transcription factors associated with the target genes. (A) 216 target genes enriched to gene ontology (GO) pathways, including 8 molecular function (MF) pathways, 10 cellular component (CC) pathways, and 50 biological process (BP) pathways. (B) Transcriptional regulatory networks associated with target genes; the size of nodes is proportional to degree. (C) Transcription factors (TFs) with degree  $\geq 5$ , including: STAT1, RELA, NFKB1, SP1, STAT3, SP3, and TP53. (D–J) ROC curves of STAT1, RELA, NFKB1, SP1, STAT3, SP3, and TP53 in intracranial aneurysm (IA) and type 2 diabetes mellitus (T2DM) diagnosis.

## Construction of target genes-related transcriptional regulatory networks and identification of key TFs

The differential expression of target genes in IA and T2DM may be related to the regulation of TFs. To identify the key

TFs associated with the occurrence of IA and T2DM, we constructed a target genes-related transcriptional regulatory network (Figure 3B), including 130 TFs and 44 target genes, among which ARNTL2 and STAT1 were both the target genes as well as TFs. Seven TFs in the network had a degree value  $\geq 5$  (Figure 3C), and these TFs may play a key regulatory role

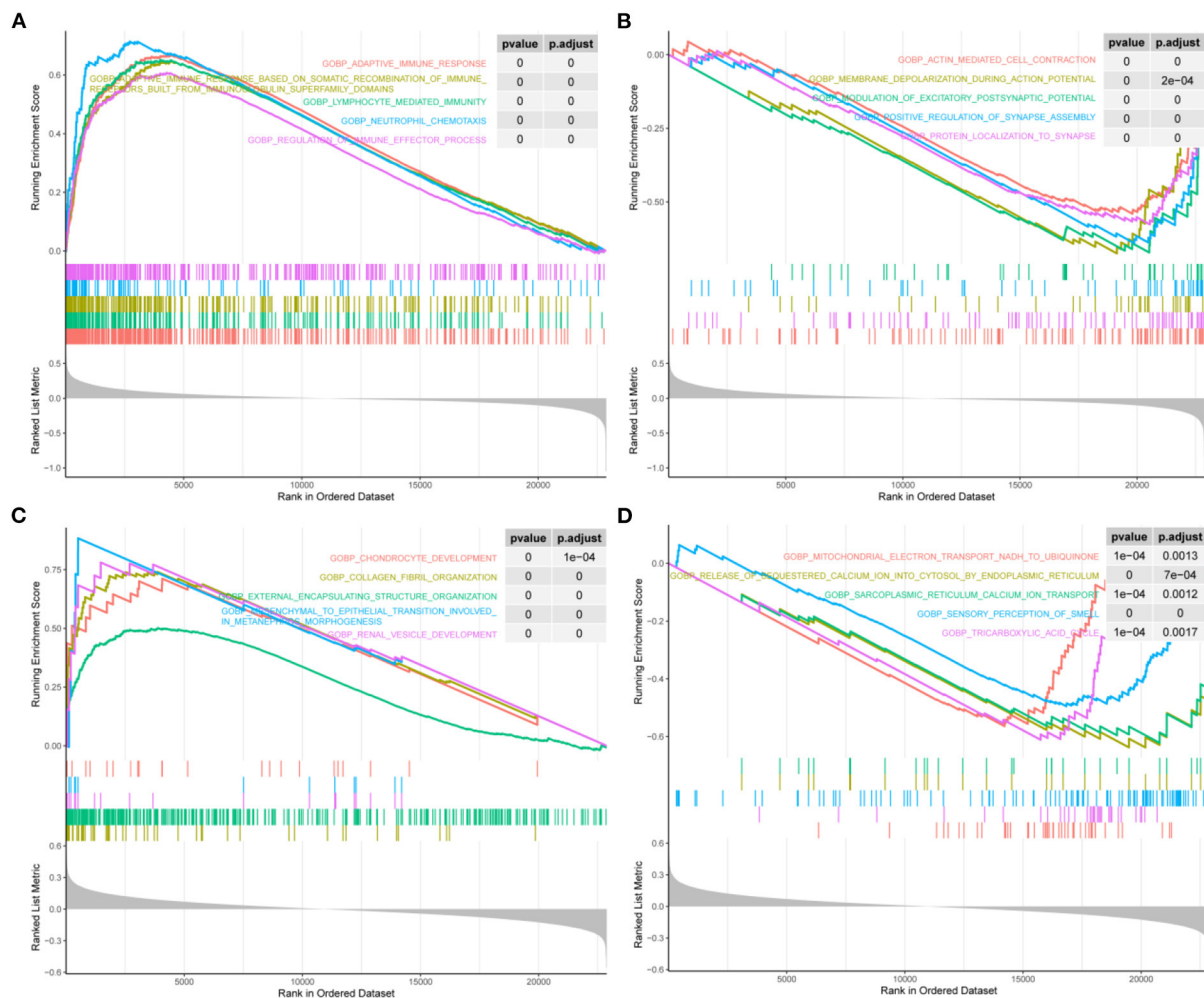


FIGURE 4

Biological process pathways associated with STAT1 in intracranial aneurysm and type 2 diabetes mellitus. (A) Top 5 biological process (BP) pathways (BP) that were significantly activated in patients with intracranial aneurysm (IA) and type 2 diabetes mellitus (T2DM) with high STAT1 expression. (B) Top 5 BPs that were significantly inhibited in patients with IA and T2DM with high STAT1 expression. (C) Top 5 BPs that were significantly activated in patients with T2DM with high STAT1 expression. (D) Top 5 BPs that were significantly inhibited in patients with T2DM with high STAT1 expression.

in the pathogenic mechanism of both the diseases. We further explored the potential clinical diagnostic value of these seven TFs (STAT1, RELA, NFKB1, SP1, STAT3, SP3, and TP53) by plotting their ROC curves based on univariate logistic regression in the diagnosis of the two diseases (Figures 3D–J). The results showed that the AUC values of STAT1 in both diseases were >0.8 indicating that it was significantly associated with the occurrence of both the diseases. Determining its biological functions in IA and T2DM will facilitate the understanding of the common pathogenic mechanisms between IA and T2DM. As a result, STAT1 was selected for further functional pathway analysis.

## Functional pathways involved in STAT1 in IA and T2DM

We screened for the BP pathways associated with STAT1 expression levels in IA and T2DM using gene pooling enrichment analysis. The results revealed that in both IA and T2DM, a large number of immune response-related pathways, including adaptive immune response, lymphocyte-mediated immunity, and neutrophil chemotaxis were activated in the high STAT1 expression group (Figure 4A), while the synaptic-related pathways were inhibited (Figure 4B). In T2DM, the renal vascular development and posterior

renal-associated epithelial mesenchymal transition pathways were activated in the high STAT1 expression group (Figure 4C), while the calcium transfer-related pathways were inhibited (Figure 4D). Therefore, STAT1 plays a key role in immune and vascular function-related pathways in IA and T2DM.

## Analysis of diabetes mellitus-related high STAT1 expression and its protein interactions

Experimental studies with WB demonstrated that ECV-304 cells exposed to high glucose expressed STAT1 ( $p < 0.05$ ) (Figure 5A). The hyperglycemic microenvironment may upregulate STAT1 in endothelial cells by upregulating STAT1. The CompPPI database was used to identify the proteins that interact with STAT1 at different cell sites (Figure 5B). GO functions enriched in these STAT1-interacting proteins include interferon- $\gamma$ -mediated signaling pathway, peptidyl-tyrosine modification, peptidyl-tyrosine phosphorylation, retromer complex, transcription factor complex, RNA polymerase II transcription factor complex, non-membrane spanning protein tyrosine kinase activity, ubiquitin-like protein ligase binding, and protein tyrosine kinase activity (Figure 5C). And the STAT1-interacting proteins are mainly found in the KEGG pathways of Th17 cell differentiation, JAK-STAT signaling pathway, and Kaposi sarcoma-associated herpesvirus infection (Figure 5C). In diabetes and IA, ISG15 was upregulated as a co-interacting protein of STAT1, while PTP4A3 was downregulated as a co-interacting protein of STAT1 (Figure 5D). Accordingly, ISG15 and PTP4A3 may interact with STAT1 to affect diabetes and IA, though more studies are needed (Table 2).

## Discussions

T2DM accounts >90% of DM cases globally, and it is characterized by hyperglycemia, low insulin production, and insulin resistance. Long-term hyperglycemia is likely to lead to poor blood flow to the extremities, resulting in reduced vascular elasticity and blood flow blockage. IA are abnormal bulges that occur in the walls of intracranial arteries. Although its etiology is unclear, it is believed that cerebral arteriosclerosis and rising vascular pressure are related to its development. Comparative analysis of the symptoms and causative factors of both the diseases suggested the existence of a common pathogenesis. Therefore, we used RNA-seq data from public databases to obtain genetic features as well as regulatory mechanisms that are common between IA and T2DM. In this study, a total of 216 DEGs were screened from 5 GSE datasets, among which 78 were upregulated and 138 were downregulated.

Additionally, 12 gene modules were identified using WGCNA, two of which were significantly associated with both IA and T2DM. Furthermore, in the transcriptional regulatory network constructed using the DEGs, ARNTL2 and STAT1 were identified to be the target genes as well as TFs in both the disease samples.

ARNTL2, also known as BMAL2, belongs to the PAS (Per-Arnt-Sim) superfamily. PAS proteins play an important role in adapting to the circadian oscillations, and disruption of circadian rhythms leads to predisposition to metabolic syndromes, such as obesity and diabetes (46–48). A cohort study showed that the A/G and A/A genotypes of BMAL2 rs7958822 showed a higher adjusted advantage ratio than the G/G genotype in obese men (OR = 2.2), suggesting a significant association between the BMAL2 rs7958822 genotype and T2DM in obese subjects (49). BMAL2 can regulate circadian rhythms, and interventions in the circadian patterns of activity and feeding can have significant effects on body weight and metabolism (47, 50). A study revealed that insulin resistance and blood glucose concentrations were improved after overexpression of BMAL2 (51).

STAT1 belongs to the STAT family and mediates the expression of a variety of genes (52–54). Several studies have reported that STAT1 gain-of-function mutations induce the diabetes and multiple autoimmune diseases (55–57). Furthermore, it has been shown that diabetes risk factors, such as hyperglycemia and hyperlipidemia can exacerbate diabetes symptoms by activating NF- $\kappa$ B and STAT1, which together reduce the number of B cells. Another study indicated that CD40L, the physiological ligand of TNFR-5, can activate NF- $\kappa$ B activity in pancreatic islet  $\beta$ -cells, thus inducing islet cell death (58). In addition, one study found that inhibition of the JAK1-STAT1 pathway could protect pancreatic  $\beta$ -cells from cytokine-induced cell death, and improving the T2DM symptoms (59). STAT1 can also be involved in interferon- $\gamma$  (IFN- $\gamma$ ), TLR4, and interleukin-6 (IL-6) activation pathways thereby amplifying pro-inflammatory signals, leading to increased SMC leukocyte migration, leukocyte adhesion to endothelial cells, and foam cell formation, thereby promoting atherosclerosis and atheroma formation (60).

Through the enrichment analysis of ARNTL2 and STAT1, target genes were enriched to 68 GO pathways, including ECM composition, coagulation regulation, hemostasis regulation, and collagen fiber composition pathways. Among these, BMAL2 regulates the transcription of anticoagulant thrombomodulin and PAI-1 by forming a heterodimer with CLOCK; therefore, abnormal expression of BMAL2 may cause coagulation disorders (61, 62). STAT1 inhibits thrombin-induced STAT-DNA binding activity and TIMP-1 mRNA expression, thereby inhibiting the coagulation process and promoting thrombosis (63). Furthermore, thrombosis can lead to hemodynamic changes that may promote the development of aneurysms. Therefore, it may be assumed that BMAL2 and STAT1



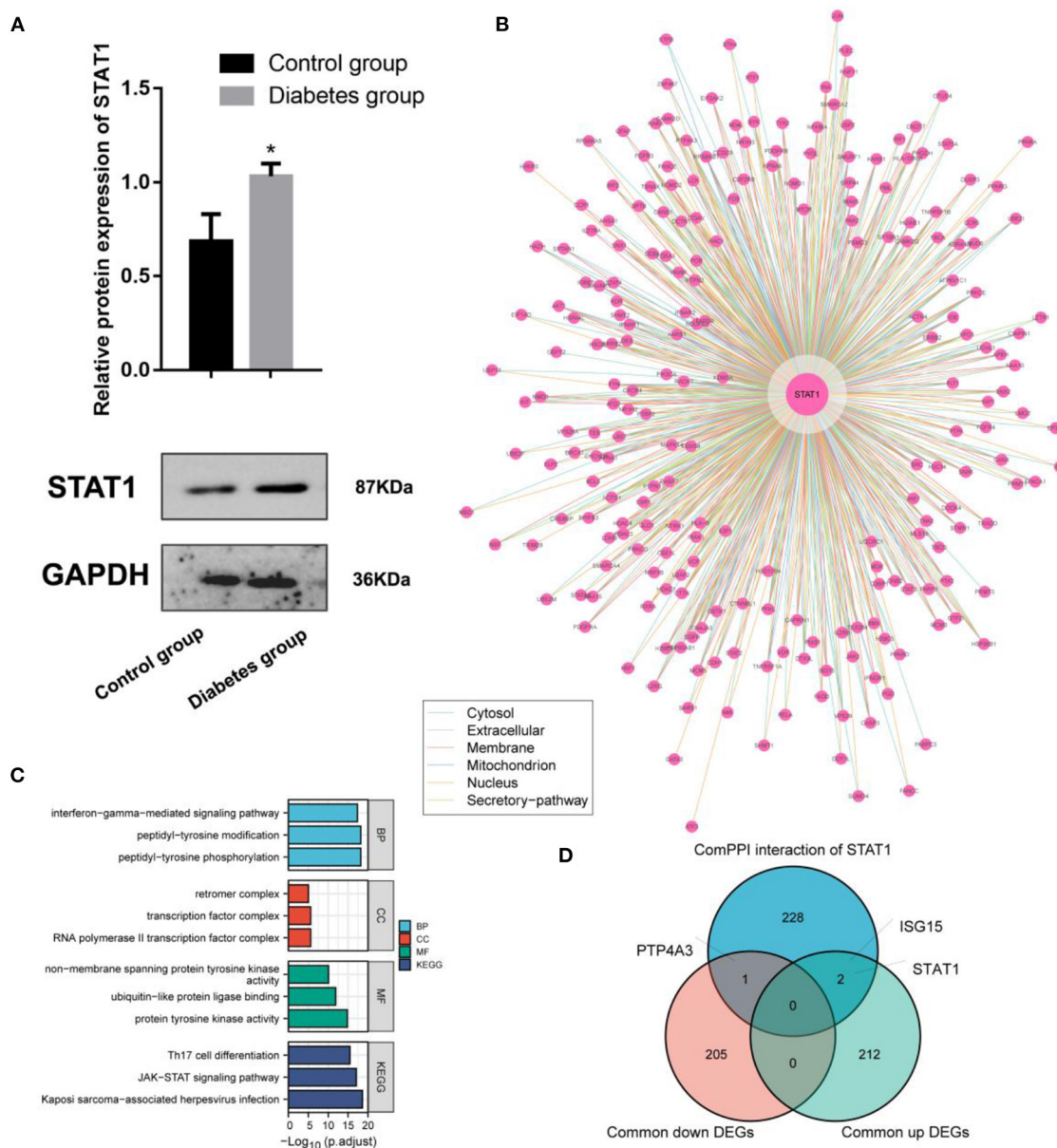


FIGURE 5

Interaction and functional analysis of the highly expressed STAT1 protein in diabetes mellitus. **(A)** WB experimental study to verify the differential expression of STAT1 in ECV-304 cell lines in the high glucose and control groups; **(B)** Analysis of STAT1 interaction proteins at different cell sites using the ComPPI database; **(C)** Protein interactions with STAT1 enrichment; **(D)** Relationships between proteins interacting with STAT1 and genes differentially expressed in diabetes and IA cross-tabulation analysis. \* $p < 0.05$ .

can influence the development of aneurysmal complications in T2DM.

In summary, we screened ARNTL2 and STAT1 by constructing a transcriptional regulatory network through multi-omics analyses, and the gene pathways were enriched for clotting regulation and ECM-related pathways. Therefore, it is important to investigate their role in the hemostatic regulatory pathways in T2DM, which can help in the diagnosis and treatment of future complications. However, our study is yet to

be validated by *in vitro* experiments to further clarify the specific molecular mechanisms.

## Conclusions

ARNTL2 and STAT1 are aberrantly expressed in T2DM and IA and act as common neurovascular markers for both the diseases. ARNTL2 and STAT1 are involved in hyperglycemic



TABLE 2 Protein information of PTP4A3 and ISG15 obtained from the ComPPI database.

| Source | Target | Location  | ComPPI score | Expression in diabetes and IA |
|--------|--------|---|--------------|-------------------------------|
| STAT1  | PTP4A3 | Cytosol/mitochondrion/nucleus/secretory-pathway/extracellular | 0.9974       | Common down                   |
|        | ISG15  | Cytosol/nucleus/extracellular/extracellular                   | 0.9600       | Common up                     |

metabolism and coagulation-related regulation of T2DM, causing aneurysms. The findings of this study provide novel diagnostic and therapeutic targets for T2DM complications.

## Data source

In the paper, microarray datasets (GSE55650, GSE25462, GSE26969, GSE75436, and GSE13353) from the GEO database were analyzed.

## Data availability statement

The original contributions presented in the study are included in the article/supplementary material, further inquiries can be directed to the corresponding author/s.

## Author contributions

TT and YS conceived and designed the analysis. TT, WS, and YS collected the data. TT, WS, JD, and

YS performed the analysis and wrote the paper. All authors contributed to the article and approved the submitted version.

## Conflict of interest

The authors declare that the research was conducted in the absence of any commercial or financial relationships that could be construed as a potential conflict of interest.

## Publisher's note

All claims expressed in this article are solely those of the authors and do not necessarily represent those of their affiliated organizations, or those of the publisher, the editors and the reviewers. Any product that may be evaluated in this article, or claim that may be made by its manufacturer, is not guaranteed or endorsed by the publisher.

## References

- DeFronzo RA, Ferrannini E, Groop L, Henry RR, Herman WH, Holst JJ, et al. Type 2 diabetes mellitus. *Nat Rev Dis Primers*. (2015) 1:15019. doi: 10.1038/nrdp.2015.19
- DeFronzo RA. From the triumvirate to the ominous octet: a new paradigm for the treatment of type 2 diabetes mellitus. *Diabetes*. (2009) 58:773–95. doi: 10.2337/db09-9028
- Fong DS, Aiello L, Gardner TW, King GL, Blankenship G, Cavallerano JD, et al. for the American Diabetes Association. Retinopathy in diabetes. *Diabetes Care*. (2004) 27:s84–7. doi: 10.2337/diacare.27.2007.S84
- Ho KKL, Pinsky JL, Kannel WB, Levy D. The epidemiology of heart failure: the Framingham study. *J Am College Cardiol*. (1993) 22:A6–A13. doi: 10.1016/0735-1097(93)90455-A
- Gong Q, Zhang P, Wang J, Ma J, An Y, Chen Y, et al. Morbidity and mortality after lifestyle intervention for people with impaired glucose tolerance: 30-year results of the Da Qing diabetes prevention outcome study. *Lancet Diabetes Endocrinol*. (2019) 7:452–61. doi: 10.1016/S2213-8587(19)30093-2
- Doddasomayajula R, Chung B, Hamzei-Sichani F, Putman CM, Cebra JR. Differences in hemodynamics and rupture rate of aneurysms at the bifurcation of the basilar and internal carotid arteries. *AJNR Am J Neuroradiol*. (2017) 38:570–6. doi: 10.3174/ajnr.A5088
- Wang G, Liu J, Chen Y, Wen L, Yang M, Gong M, et al. Morphological characteristics associated with the rupture risk of mirror posterior communicating artery aneurysms. *J NeuroIntervent Surg*. (2018) 10:995–8. doi: 10.1136/neurintsurg-2017-013553
- Zhang Y, Jing L, Liu J, Li C, Fan J, Wang S, et al. Clinical, morphological, and hemodynamic independent characteristic factors for rupture of posterior communicating artery aneurysms. *J NeuroIntervent Surg*. (2016) 8:808–12. doi: 10.1136/neurintsurg-2015-011865
- Chalouhi N, Ali MS, Jabbour PM, Tjoumakaris SI, Gonzalez LF, Rosenwasser RH, et al. Biology of intracranial aneurysms: role of inflammation. *J Cereb Blood Flow Metab*. (2012) 32:1659–76. doi: 10.1038/jcbfm.2012.84
- Starke R, Chalouhi N, Ali M, Jabbour P, Tjoumakaris S, Gonzalez L, et al. The role of oxidative stress in cerebral aneurysm formation and rupture. *CNR*. (2013) 10:247–55. doi: 10.2174/15672026113109990003
- Chalouhi N, Ali MS, Starke RM, Jabbour PM, Tjoumakaris SI, Gonzalez LF, et al. Cigarette Smoke and inflammation: role in cerebral aneurysm formation and rupture. *Mediat Inflamm*. (2012) 2012:1–12. doi: 10.1155/2012/21582
- Ho FM, Liu SH, Liau CS, Huang PJ, Lin-Shiau SY. High glucose-induced apoptosis in human endothelial cells is mediated by sequential activations of c-Jun NH<sub>2</sub> terminal kinase and caspase-3. *Circulation*. (2000) 101:2618–24. doi: 10.1161/01.CIR.101.22.2618

13. You W, Hong Y, He H, Huang X, Tao W, Liang X, et al. TGF- $\beta$  mediates aortic smooth muscle cell senescence in Marfan syndrome. *Aging*. (2019) 11:3574–84. doi: 10.18632/aging.101998
14. Marinković G, Hibender S, Hoogenboezem M, van Broekhoven A, Girigorie AF, Bleeker N, et al. Immunosuppressive drug azathioprine reduces aneurysm progression through inhibition of Rac1 and c-Jun-Terminal-N-Kinase in endothelial cells. *ATVB*. (2013) 33:2380–8. doi: 10.1161/ATVBAHA.113.301394
15. Boden G. Free fatty acids, insulin resistance, and type 2 diabetes mellitus. *PAAP*. (1999) 111:241–8. doi: 10.1046/j.1525-1381.1999.99220.x
16. Fujimoto WY. The importance of insulin resistance in the pathogenesis of type 2 diabetes mellitus. *Am J Med*. (2000) 108:9–14. doi: 10.1016/S0002-9343(00)00337-5
17. Kelley DE, Simoneau JA. Impaired free fatty acid utilization by skeletal muscle in non-insulin-dependent diabetes mellitus. *J Clin Invest*. (1994) 94:2349–56. doi: 10.1172/JCI117600
18. Sun Y, Ishibashi M, Seimon T, Lee M, Sharma SM, Fitzgerald KA, et al. Free cholesterol accumulation in macrophage membranes activates toll-like receptors and p38 mitogen-activated protein kinase and induces Cathepsin K. *Circul Res*. (2009) 104:455–65. doi: 10.1161/CIRCRESAHA.108.182568
19. Sniderman AD, Scantlebury T, Cianflone K. Hypertriglyceridemic HyperapoB: the unappreciated atherogenic dyslipoproteinemia in type 2 diabetes mellitus. *Ann Intern Med*. (2001) 135:447. doi: 10.7326/0003-4819-135-6-200109180-00014
20. Westein E, Hoefler T, Calkin AC. Thrombosis in diabetes: a shear flow effect? *Clin Sci*. (2017) 131:1245–60. doi: 10.1042/CS20160391
21. Hafer-Macko CE, Ivey FM, Gyure KA, Sorkin JD, Macko RF. Thrombomodulin deficiency in human diabetic nerve microvasculature. *Diabetes*. (2002) 51:1957–63. doi: 10.2337/diabetes.51.6.1957
22. Ceriello A, Giacomello R, Stel G, Motz E, Taboga C, Tonutti L, et al. Hyperglycemia-induced thrombin formation in diabetes: the possible role of oxidative stress. *Diabetes*. (1995) 44:924–8. doi: 10.2337/diab.44.8.924
23. Tsilibary EC. Microvascular basement membranes in diabetes mellitus: microvascular basement membranes in diabetes. *J Pathol*. (2003) 200:537–46. doi: 10.1002/path.1439
24. Ribeiro-Silva M, Oliveira-Pinto J, Mansilha A. Abdominal aortic aneurysm: a review on the role of oral antidiabetic drugs. *Int Angiol*. (2020) 39:4362. doi: 10.23736/S0392-9590.20.04362-X
25. Simmons RK, Echouffo-Tcheugui JB, Griffin SJ. Screening for type 2 diabetes: an update of the evidence. *Diabetes Obesity Metabol*. (2010) 12:838–44. doi: 10.1111/j.1463-1326.2010.01244.x
26. Queiroz M, Sena CM. Perivascular adipose tissue in age-related vascular disease. *Ageing Res Rev*. (2020) 59:101040. doi: 10.1016/j.arr.2020.101040
27. Xu Z, Rui Y-N, Hagan JP, Kim DH. Intracranial aneurysms: pathology, genetics, and molecular mechanisms. *Neuromol Med*. (2019) 21:325–43. doi: 10.1007/s12017-019-08537-7
28. Sheinberg DL, McCarthy DJ, Elwardany O, Bryant J-P, Luther E, Chen SH, et al. Endothelial dysfunction in cerebral aneurysms. *Neurosurg Focus*. (2019) 47:E3. doi: 10.3171/2019.4.FOCUS19221
29. Tamilnadu I, Mani V. Effect of  $\beta$ -Caryophyllene on insulin resistance in skeletal muscle of high fat diet and fructose-induced type-2 diabetic rats. *Bioinformation*. (2021) 17:741–7. doi: 10.6026/97320630017741
30. Wu J, Chen Z-J, Liang J, Lai C-S, Li X-Y, Yang Z-J. Identifying and validating key genes mediating intracranial aneurysm rupture using weighted correlation network analysis and exploration of personalized treatment. *Ann Transl Med*. (2022) 10:1057–1057. doi: 10.21037/atm-22-4068
31. Zhu H, Tan J, Wang Z, Wu Z, Zhou W, Zhang Z, et al. Bioinformatics analysis constructs potential ferroptosis-related ceRNA network involved in the formation of intracranial aneurysm. *Front Cell Neurosci*. (2022) 16:1016682. doi: 10.3389/fncel.2022.1016682
32. Turhon M, Maimaiti A, Gheyret D, Axier A, Rexiati N, Kadeer K, et al. An immunogenic cell death-related regulators classification patterns and immune microenvironment infiltration characterization in intracranial aneurysm based on machine learning. *Front Immunol*. (2022) 13:1001320. doi: 10.3389/fimmu.2022.1001320
33. Tang G-Y, Yu P, Zhang C, Deng H-Y, Lu M-X, Le J-H. The neuropeptide-related HERC5/TAC1 interactions may be associated with the dysregulation of lncRNA GAS5 expression in gestational diabetes mellitus exosomes. *Disease Mark*. (2022) 2022:1–12. doi: 10.1155/2022/8075285
34. Cao T, Hong J, Qi F, Zheng B, Chen G, Yu B, et al. Hyperglycemic microenvironment inhibits tendon-to-bone healing through the let-7b-5p/CFTR pathway. *Comput Math Methods Med*. (2022) 2022:1–10. doi: 10.1155/2022/8268067
35. Lin W-W, Xu L-T, Chen Y-S, Go K, Sun C, Zhu Y-J. Single-cell transcriptomics-based study of transcriptional regulatory features in the mouse brain vasculature. *BioMed Res Int*. (2021) 2021:1–15. doi: 10.1155/2021/7643209
36. Chen Y, Kang X, Zhou Z, Yang J, Xin Q, Ying C, et al. MiR-1908/EXO1 and MiR-203a/FOS, regulated by scd1, are associated with fracture risk and bone health in postmenopausal diabetic women. *Aging*. (2020) 12:9549–84. doi: 10.18632/aging.103227
37. Gómez-García EF, del Campo FM, Cortés-Sanabria L, Mendoza-Carrera F, Avesani CM, Stenvinkel P, et al. Transcription factor NRF2 as potential therapeutic target for preventing muscle wasting in aging chronic kidney disease patients. *J Nephrol*. (2022) doi: 10.1007/s40620-022-01484-w. [Epub ahead of print].
38. Chen Y, Sun Y, Xu Y, Lin W-W, Luo Z, Han Z, et al. Single-cell integration analysis of heterotopic ossification and fibrocartilage developmental lineage: endoplasmic reticulum stress effector Xbp1 transcriptionally regulates the notch signaling pathway to mediate fibrocartilage differentiation. *Oxidat Med Cell Long*. (2021) 2021:1–29. doi: 10.1155/2021/7663366
39. Chen Y, Sun Y, Luo Z, Chen X, Wang Y, Qi B, et al. Exercise modifies the transcriptional regulatory features of monocytes in Alzheimer's patients: a multi-omics integration analysis based on single cell technology. *Front Aging Neurosci*. (2022) 14:881488. doi: 10.3389/fnagi.2022.881488
40. Luo Z, Qi B, Sun Y, Chen Y, Lin J, Qin H, et al. Engineering bioactive M2 macrophage-polarized, anti-inflammatory, miRNA-based liposomes for functional muscle repair: from exosomal mechanisms to biomaterials. *Small*. (2022) 18:2201957. doi: 10.1002/smll.202201957
41. Ritchie ME, Phipson B, Wu D, Hu Y, Law CW, Shi W, et al. Limma powers differential expression analyses for RNA-sequencing and microarray studies. *Nucl Acids Res*. (2015) 43:e47. doi: 10.1093/nar/gkv007
42. Zhao W, Langfelder P, Fuller T, Dong J, Li A, Hovarth S. Weighted gene coexpression network analysis: state of the art. *J Biopharm Stat*. (2010) 20:281–300. doi: 10.1080/10543400903572753
43. Langfelder P, Horvath S. WGCNA. An R package for weighted correlation network analysis. *BMC Bioinform*. (2008) 9:559. doi: 10.1186/1471-2105-9-559
44. Han H, Cho J-W, Lee S, Yun A, Kim H, Bae D, et al. TRRUST v2: an expanded reference database of human and mouse transcriptional regulatory interactions. *Nucl Acids Res*. (2018) 46:D380–6. doi: 10.1093/nar/gkx1013
45. Wu T, Hu E, Xu S, Chen M, Guo P, Dai Z, et al. A clusterProfiler 40: a universal enrichment tool for interpreting omics data. *Innovation*. (2021) 2:100141. doi: 10.1016/j.xinn.2021.100141
46. Green CB, Takahashi JS, Bass J. The meter of metabolism. *Cell*. (2008) 134:728–42. doi: 10.1016/j.cell.2008.08.022
47. Scheer FAJL, Hilton MF, Mantzoros CS, Shea SA. Adverse metabolic and cardiovascular consequences of circadian misalignment. *Proc Natl Acad Sci USA*. (2009) 106:4453–8. doi: 10.1073/pnas.0808180106
48. Gimble JM, Sutton GM, Bunnell BA, Pttitsyn AA, Floyd ZE. Prospective influences of circadian clocks in adipose tissue and metabolism. *Nat Rev Endocrinol*. (2011) 7:98–107. doi: 10.1038/nrendo.2010.214
49. Yamaguchi M, Uemura H, Arisawa K, Katsuura-Kamano S, Hamajima N, Hishida A, et al. Association between brain-muscle-ARNT-like protein-2 (BMAL2) gene polymorphism and type 2 diabetes mellitus in obese Japanese individuals: a cross-sectional analysis of the Japan multi-institutional collaborative cohort study. *Diabet Res Clin Pract*. (2015) 110:301–8. doi: 10.1016/j.diabetes.2015.10.009
50. Buxton OM, Cain SW, O'Connor SP, Porter JH, Duffy JF, Wang W, et al. Adverse metabolic consequences in humans of prolonged sleep restriction combined with circadian disruption. *Sci Transl Med*. (2012) 4:3200. doi: 10.1126/scitranslmed.3003200
51. Shi S, Ansari TS, McGuinness OP, Wasserman DH, Johnson CH. Circadian disruption leads to insulin resistance and obesity. *Curr Biol*. (2013) 23:372–81. doi: 10.1016/j.cub.2013.01.048
52. Mogensen TH, IIR, and STAT transcription factors: from basic biology to roles in infection, protective immunity, and primary immunodeficiencies. *Front Immunol*. (2019) 9:3047. doi: 10.3389/fimmu.2018.03047
53. Okada S, Asano T, Moriya K, Boisson-Dupuis S, Kobayashi M, Casanova J-L, et al. Human STAT1 gain-of-function heterozygous mutations: chronic mucocutaneous candidiasis and type I interferonopathy. *J Clin Immunol*. (2020) 40:1065–81. doi: 10.1007/s10875-020-00847-x
54. Butturini E, Carcereri de Prati A, Mariotto S. Redox regulation of STAT1 and STAT3 signaling. *IJMS*. (2020) 21:7034. doi: 10.3390/ijms21197034

55. Forbes LR, Vogel TP, Cooper MA, Castro-Wagner J, Schussler E, Weinacht KG, et al. Jakinibs for the treatment of immune dysregulation in patients with gain-of-function signal transducer and activator of transcription 1 (STAT1) or STAT3 mutations. *J Allergy Clin Immunol.* (2018) 142:1665–9. doi: 10.1016/j.jaci.2018.07.020
56. Toubiana J, Okada S, Hiller J, Oleastro M, Lagos Gomez M, Aldave Becerra JC, et al. Heterozygous STAT1 gain-of-function mutations underlie an unexpectedly broad clinical phenotype. *Blood.* (2016) 127:3154–64. doi: 10.1182/blood-2015-11-679902
57. Vargas-Hernández A, Mace EM, Zimmerman O, Zerbe CS, Freeman AF, Rosenzweig S, et al. Ruxolitinib partially reverses functional natural killer cell deficiency in patients with signal transducer and activator of transcription 1 (STAT1) gain-of-function mutations. *J Allergy Clin Immunol.* (2018) 141:2142–55.e5. doi: 10.1016/j.jaci.2017.08.040
58. Bagnati M, Ogunkolade BW, Marshall C, Tucci C, Hanna K, Jones TA, et al. Glucolipotoxicity initiates pancreatic  $\beta$ -cell death through TNFR5/CD40-mediated STAT1 and NF- $\kappa$ B activation. *Cell Death Dis.* (2016) 7:e2329–e2329. doi: 10.1038/cddis.2016.203
59. Couto FM, Minn AH, Pise-Masison CA, Radonovich M, Brady JN, Hanson M, et al. Exenatide blocks JAK1-STAT1 in pancreatic beta cells. *Metabolism.* (2007) 56:915–8. doi: 10.1016/j.metabol.2007.02.004
60. Sikorski K, Czerwonec A, Bujnicki JM, Wesoly J, Bluysen HAR. STAT1 as a novel therapeutical target in pro-atherogenic signal integration of IFN $\gamma$ , TLR4 and IL-6 in vascular disease. *Cytokine Growth Factor Rev.* (2011) 22:211–9. doi: 10.1016/j.cytogfr.2011.06.003
61. Takeda N, Maemura K, Horie S, Oishi K, Imai Y, Harada T, et al. Thrombomodulin is a clock-controlled gene in vascular endothelial cells. *J Biol Chem.* (2007) 282:32561–7. doi: 10.1074/jbc.M705692200
62. Schoenhard J. Regulation of the PAI-1 promoter by circadian clock components: differential activation by BMAL1 and BMAL2. *J Mol Cell Cardiol.* (2003) 35:473–81. doi: 10.1016/S0022-2828(03)00051-8
63. Chen X, Liu W, Wang J, Wang X, Yu Z. STAT1 and STAT3 mediate thrombin-induced expression of TIMP-1 in human glomerular mesangial cells. *Kidney Int.* (2002) 61:1377–82. doi: 10.1046/j.1523-1755.2002.00283.x



## OPEN ACCESS

## EDITED BY

Jun Xu,  
Beijing Tiantan Hospital, Capital  
Medical University, China

## REVIEWED BY

Sebastian Major,  
Charité Universitätsmedizin  
Berlin, Germany  
Vasilis Kola,  
Charité University Medicine Berlin,  
Germany

## \*CORRESPONDENCE

Xi Zhu  
✉ nsmc\_zhuqian@163.com  
Xiaoping Tang  
✉ nsmc\_txping1971@163.com

<sup>†</sup>These authors have contributed  
equally to this work and share first  
authorship

## SPECIALTY SECTION

This article was submitted to  
Neurological Biomarkers,  
a section of the journal  
Frontiers in Neurology

RECEIVED 04 September 2022

ACCEPTED 30 November 2022

PUBLISHED 22 December 2022

## CITATION

Zhao L, Zhang Y, Lin P, Li W, Huang X,  
Li H, Xia M, Chen X, Zhu X and Tang X  
(2022) Postoperative red blood cell  
distribution width predicts functional  
outcome in aneurysmal subarachnoid  
hemorrhage after surgical clipping: A  
single-center retrospective study.  
*Front. Neurol.* 13:1036433.  
doi: 10.3389/fneur.2022.1036433

## COPYRIGHT

© 2022 Zhao, Zhang, Lin, Li, Huang, Li,  
Xia, Chen, Zhu and Tang. This is an  
open-access article distributed under  
the terms of the [Creative Commons  
Attribution License \(CC BY\)](#). The use,  
distribution or reproduction in other  
forums is permitted, provided the  
original author(s) and the copyright  
owner(s) are credited and that the  
original publication in this journal is  
cited, in accordance with accepted  
academic practice. No use, distribution  
or reproduction is permitted which  
does not comply with these terms.

# Postoperative red blood cell distribution width predicts functional outcome in aneurysmal subarachnoid hemorrhage after surgical clipping: A single-center retrospective study

Long Zhao<sup>1,2,3†</sup>, Yi Zhang<sup>2†</sup>, Ping Lin<sup>2</sup>, Weida Li<sup>2</sup>,  
Xingyuan Huang<sup>4</sup>, Hangyang Li<sup>2</sup>, Mingkai Xia<sup>5</sup>, Xinlong Chen<sup>2</sup>,  
Xi Zhu<sup>6\*</sup> and Xiaoping Tang<sup>1,3\*</sup>

<sup>1</sup>Department of Neurosurgery, Affiliated Hospital of North Sichuan Medical College, Nanchong, China, <sup>2</sup>School of Clinical Medicine, North Sichuan Medical College, Nanchong, China, <sup>3</sup>Neurosurgical Research Center, Affiliated Hospital of North Sichuan Medical College, Nanchong, China, <sup>4</sup>School of Psychiatry, North Sichuan Medical College, Nanchong, China, <sup>5</sup>School of Medical Imaging, North Sichuan Medical College, Nanchong, China, <sup>6</sup>Outpatient Department, Affiliated Hospital of North Sichuan Medical College, Nanchong, China

**Objective:** Red blood cell (RBC) parameters are associated with outcomes following aneurysmal subarachnoid hemorrhage (aSAH), but their predictive value remains uncertain. This study aimed to detect the association between RBC parameters and functional outcome in aSAH patients undergoing surgical clipping.

**Methods:** This retrospective observational study included aSAH patients who underwent surgical clipping at Affiliated Hospital of North Sichuan Medical College between August 2016 and September 2019. The functional outcome following aSAH was assessed by modified Rankin Scale (mRS), and mRS 3–6 was defined as poor functional outcome.

**Results:** Out of 187 aSAH patients included (62% female, 51–66 years old), 73 patients had poor functional outcome. Multivariate logistic regression of admission parameters showed that World Federation of Neurosurgical Societies (WFNS) grade (odds ratio [95% CI]: 1.322 [1.023–1.707],  $p = 0.033$ ) and white blood cell (WBC) (odds ratio [95% CI]: 1.136 [1.044–1.236],  $p = 0.003$ ) were independently associated with poor functional outcome. In postoperative parameters, RBC distribution width (RDW) (odds ratio [95% CI]: 1.411 [1.095–1.818],  $p = 0.008$ ), mean platelet volume (MPV, odds ratio [95% CI]: 1.253 [1.012–1.552],  $p = 0.039$ ) and admission WFNS grade (odds ratio [95% CI]: 1.439 [1.119–1.850],  $p = 0.005$ ) were independently associated with poor functional outcome. The predictive model including WFNS grade, admission WBC, and postoperative RDW and MPV had significantly higher predictive power compared to WFNS grade alone (0.787 [0.722–0.852] vs. 0.707 [0.630–0.784],  $p = 0.024$ ). The combination of WFNS grade and WBC on admission showed the highest positive predictive value (75.5%) and

postoperative RDW and MPV combined with admission WFNS grade and WBC showed the highest negative predictive value (83.7%).

**Conclusion:** Postoperative RDW is independently associated with poor functional outcome in aSAH patients undergoing surgical clipping. A combined model containing postoperative RDW may help predict good outcome in patients with aSAH after timely aneurysm clipping.

#### KEYWORDS

aneurysmal subarachnoid hemorrhage, red blood cell distribution width, surgical clipping, functional outcome, predictor

## 1. Introduction

Aneurysmal subarachnoid hemorrhage (aSAH), a severe type of hemorrhagic stroke, results from the rupture of intracranial aneurysms (1). With significant morbidity and mortality, such disease continues to be a clinical emergency despite advances in strategies of diagnosis, treatment, and neurocritical care (2). When a rupture occurs, guidelines recommend the repair be conducted as soon as possible (3, 4). Though endovascular coiling is widely performed, some forms of aSAH are suitable for surgical clipping. This requires complicated perioperative management and leads to clinical problems, such as the relationship between anemia, intraoperative blood loss and outcomes, which are still under investigation. Therefore, biomarkers predicting outcomes after surgical clipping are needed for advanced clinical care.

Red blood cell (RBC) parameters have been reported to predict poor outcomes after an aSAH event. Postoperative hemoglobin, an anemia biomarker, is observed to be an independent risk factor of poor neurological outcomes (5). Gong et al. found that mean corpuscular volume (MCV) and mean corpuscular hemoglobin (MCH) are predictors of cognitive impairment (6). Recent studies also have shown that RBC distribution width (RDW) is associated with outcome indicators such as functional outcome, mortality, delayed cerebral ischemia (DCI) and cerebral infarction following aSAH (7–9). Since the role of blood transfusion in the management of aSAH is still controversial and there is a lack of practical indicators for reference in the management of blood volume clinically, it is of great significance to continue evaluating the role of RBC parameters in aSAH.

Although several studies discussed the predictive value of RBC parameters, few considered the craniotomy performed in relation to the analysis, which may affect RBC parameters and outcome. Moreover, these studies have not been externally validated. It is unclear whether these results are broadly applicable and whether postoperative RBC parameters are associated with outcomes of aSAH patients after clipping. Therefore, this retrospective case-control study was conducted to comprehensively analyze the relationship between RBC parameters on admission and after surgical clipping and

functional outcome of aSAH patients, and to screen parameters with independent predictive value.

## 2. Materials and methods

### 2.1. Study design and patients

This retrospective observational study included consecutive patients with aSAH admitted to Affiliated Hospital of North Sichuan Medical College between August 2016 and September 2019. The inclusion criteria were: (1) age >18 years; (2) patients with aSAH confirmed by computed tomographic angiography or digital subtraction angiography; (3) admitted within 24 h of initial symptom onset; (4) undergoing surgical clipping within 72 h of the onset; (5) complete blood count (CBC) test was completed within 24 h after admission and within 6 h after surgery. The exclusion criteria were: (1) patients with a history of primary or secondary central nervous system diseases, acute or chronic infections, or systemic diseases; (2) patients with trauma, surgery, bleeding events or blood donation within 3 months; (3) patients with incomplete information. This study was performed according to the TRIPOD statement (10), followed the revised Declaration of Helsinki and was approved by the ethics committee of Affiliated Hospital of North Sichuan Medical College. Patients' consent was waived due to the retrospective nature of this study.

### 2.2. Data collection and definition

Data were collected from the electronic medical records, including demographics (age, gender), addictions (smoking and alcohol consumption), medical history (hypertension, diabetes mellitus), admission clinical grades, aneurysm characteristics, and admission and postoperative CBC parameters. Clinical grades included the World Federation of Neurosurgical Society (WFNS) grade and modified Fisher (mFisher) grade. Aneurysm characteristics included location and number. Location was divided into "anterior" and "posterior" circulation, and number was divided into "single" and

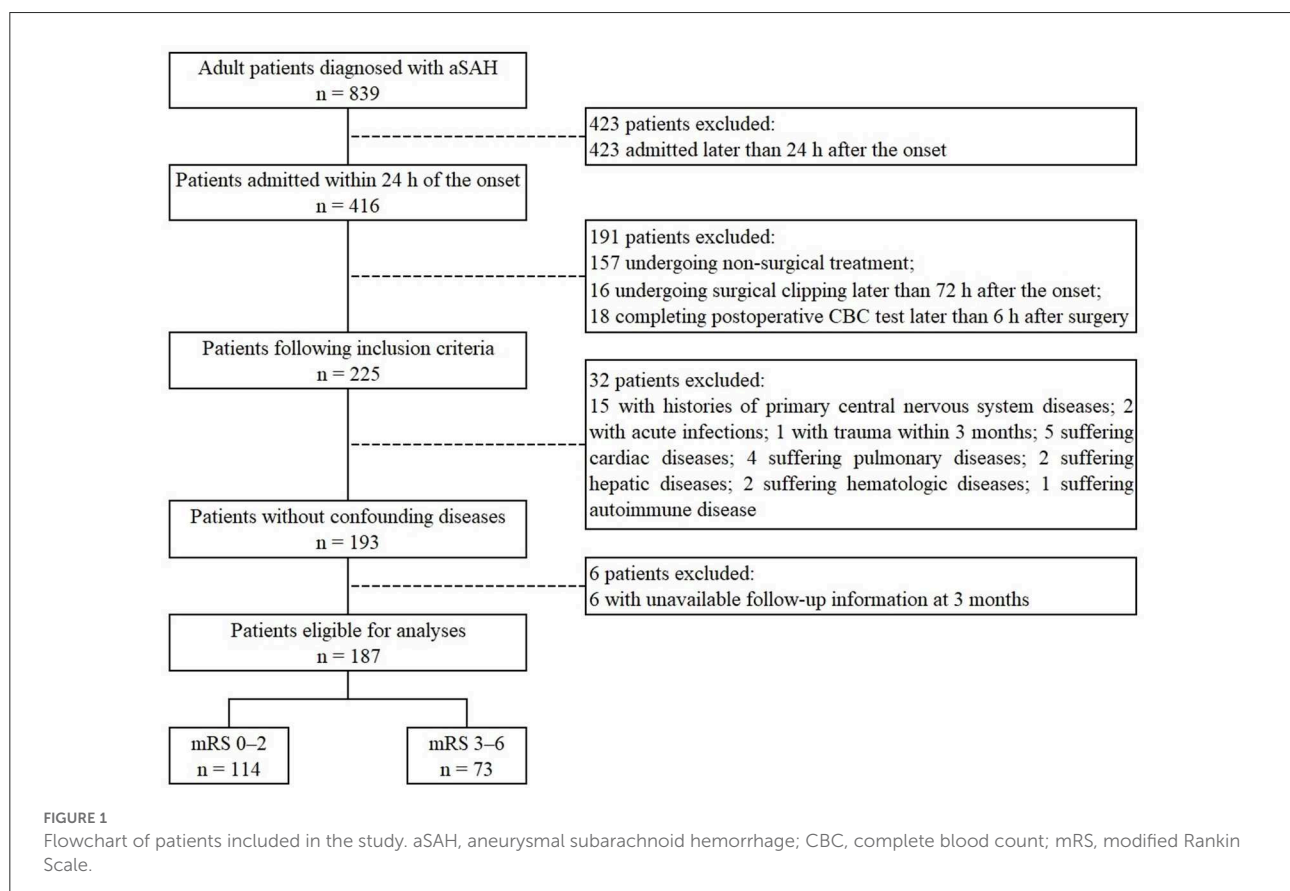


“multiple”. RBC parameters including hemoglobin, RBC, hematocrit, MCV, MCH, mean corpuscular hemoglobin concentration (MCHC), and RDW were collected on admission and postoperatively. Other CBC parameters reported as outcome predictors were also collected, including white blood cell (WBC), neutrophil, lymphocyte, monocyte, platelet and mean platelet volume (MPV) (11–13). Differences between admission and postoperative RBC parameters were calculated by subtracting the admission values from the postoperative values. For data accuracy and comparability, only the first CBC results after admission and surgery were collected separately.

Functional outcome was assessed through telephone interview or outpatient visit at 3 months by fixed staff who was blind to laboratory data of patients, following the modified Rankin scale (mRS) (14). The mRS is scored 0–6: 0 (no symptoms), 1 or 2 (functional independence), 3 (moderate handicap), 4 or 5 (moderate to severe handicap) and 6 (death). We defined good functional outcome as 3-month mRS between 0 and 2 and poor outcome as mRS between 3 and 6 (15). Patients were dichotomized into two groups (mRS 0–2 vs. mRS 3–6).

## 2.3. Statistical analysis

Statistical analysis was performed with SPSS Statistics 26 (IBM, Armonk, NY, USA), and  $p < 0.05$  was considered significant. Categorical variables were presented as number (percentage) and compared by Chi-square or Fisher’s exact test. Continuous variables that conformed to normal distribution were expressed as mean  $\pm$  standard deviation and compared by Student’s *t*-test. Continuous variables that conformed to skewed distribution were expressed as median with interquartile range (25th–75th percentile) and compared by the Mann-Whitney U test, which was also applied to rank variables. Multivariate logistic regression was performed to identify the independent predictors of poor functional outcome. Variables considered clinically relevant or with  $p < 0.05$  in univariate analyses were incorporated into multivariate logistic regression models. Receiver operating characteristic (ROC) analysis was conducted to evaluate the predictive value and to determine the cutoff value by calculating Youden’s index. Delong’s test compared areas under ROC curves (AUCs).



### 3. Results

#### 3.1. Baseline characteristics

A total of 187 patients were included in this study, of which 114 (61.0%) had good functional outcome while 73 (39.0%) had poor functional outcome, including 15 patients (8.0%) who died within 3 months of the onset (Figure 1). Of the included cases, 122 were included in a published article to establish an early predictive nomogram for DCI after aSAH (13). Parameters of demographics, addictions, medical history and aneurysm characteristics showed no significant differences between two groups. In contrast, parameters of admission clinical grades differed significantly between two groups (WFNS grade,  $p < 0.001$ ; mFisher grade,  $p = 0.011$ ; Table 1).

#### 3.2. Admission CBC parameters

Admission CBC parameters showed that WBC (11.46 [8.90–14.00] vs. 14.69 [11.81–17.90],  $p < 0.001$ ), neutrophil (10.30 [7.61–12.92] vs. 13.18 [10.38–15.88],  $p < 0.001$ ), monocyte (0.37 [0.23–0.51] vs. 0.60 [0.36–0.84],  $p < 0.001$ ) and RDW (13.1 [12.5–13.6] vs. 13.4 [12.8–14.2],  $p < 0.001$ ) in patients with poor functional outcome were significantly higher than those in patients with good functional outcome (Table 1). Patients with poor functional outcome also had significantly lower MCHC (328 [321–334] vs. 324 [318–331],  $p = 0.011$ ; Table 1). Multivariate logistic regression showed that WFNS grade (odds ratio [95% CI]: 1.322 [1.023–1.707],  $p = 0.033$ ) and WBC (odds ratio [95% CI]: 1.136 [1.044–1.236],  $p = 0.003$ ) predicted poor functional outcome independently (Table 2).

#### 3.3. Postoperative CBC parameters

In postoperative CBC parameters, WBC (10.82 [9.01–13.80] vs. 12.93 [10.29–16.86],  $p = 0.001$ ), neutrophil (8.89 [7.46–11.73] vs. 11.77 [8.56–14.72],  $p < 0.001$ ), monocyte (0.59 [0.41–0.88] vs. 0.69 [0.51–1.04],  $p = 0.041$ ), RDW (13.1 [12.6–13.6] vs. 13.9 [13.1–14.5],  $p < 0.001$ ) and MPV ( $11.3 \pm 1.6$  vs.  $12.0 \pm 1.5$ ,  $p = 0.004$ ) in patients with poor functional outcome were significantly higher than those with good functional outcome (Table 1). Results of multivariate logistic regression revealed that WFNS grade (odds ratio [95% CI]: 1.439 [1.119–1.850],  $p = 0.005$ ), MPV (odds ratio [95% CI]: 1.253 [1.012–1.552],  $p = 0.039$ ) and RDW (odds ratio [95% CI]: 1.411 [1.095–1.818],  $p = 0.008$ ) independently predicted poor functional outcome (Table 3).

#### 3.4. Differences between admission and postoperative RBC parameters

The variation of RBC parameters was analyzed and only RDW showed significant difference. The difference of RDW in patients with poor functional outcome was higher than those with good functional outcome (0.2 [−0.2 to 1.0] vs. 0.0 [−0.3 to 0.4],  $p = 0.010$ ).

#### 3.5. ROC analysis

The AUCs of WFNS grade, admission WBC and postoperative RDW and MPV were 0.670 (0.589–0.750), 0.704 (0.626–0.781), 0.707 (0.630–0.784) and 0.623 (0.542–0.704), respectively (Figure 2). The best cutoff point of WFNS grade predicting poor functional outcome (Youden's index = 0.286) was 2.5, where the sensitivity was 57.5% and the specificity was 71.1%. The positive predictive value (PPV) was 56.0% and the negative predictive value (NPV) was 72.3%. The best cutoff point of admission WBC predicting poor functional outcome (Youden's index = 0.383) was  $12.875 \times 10^9/L$ , where the sensitivity was 69.9% and the specificity was 68.4%. The PPV was 58.6% and the NPV was 78.0%. The best cutoff point of postoperative RDW predicting poor functional outcome (Youden's index = 0.383) was 13.65%, where the sensitivity was 60.3% and the specificity was 78.1%. The PPV was 63.8% and the NPV was 75.4%. The best cutoff point of postoperative MPV predicting poor functional outcome (Youden's index = 0.247) was 11.25 fL, where the sensitivity was 71.2% and the specificity was 53.5%. The PPV was 49.5% and the NPV was 74.4%. There was no significant difference between the AUCs of the four ROC curves (WFNS grade vs. admission WBC,  $p = 0.462$ ; WFNS grade vs. postoperative RDW,  $p = 0.477$ ; WFNS grade vs. postoperative MPV,  $p = 0.419$ ; admission WBC vs. postoperative RDW,  $p = 0.949$ ; admission WBC vs. postoperative MPV,  $p = 0.182$ ; postoperative RDW vs. postoperative MPV,  $p = 0.112$ ). The AUC of postoperative RDW was significantly larger than the difference of RDW ( $p = 0.020$ ).

Three combined diagnostic models based on WFNS grade, admission WBC and postoperative RDW and MPV were established and evaluated to achieve better predictive value. The AUC of parameter combination A (WFNS grade and admission WBC) and B (WFNS grade and postoperative RDW and MPV) was 0.734 (0.657–0.811) and 0.753 (0.685–0.822), respectively (Figure 3). The sensitivity was 54.8% and the specificity was 88.6% at the best cutoff point of parameter combination A (Youden's index = 0.434). The PPV was 75.5% and the NPV was 75.4%. The sensitivity was 50.7% and the specificity was 86.8% at the best cutoff point of

TABLE 1 Univariate analysis of baseline characteristics and CBC parameters associated with poor functional outcome at 3 months.

| Characteristics                | Total<br>( <i>n</i> = 187) | mRS at 3 Months       |                      | <i>p</i> -value |
|--------------------------------|----------------------------|-----------------------|----------------------|-----------------|
|                                |                            | 0–2 ( <i>n</i> = 114) | 3–6 ( <i>n</i> = 73) |                 |
| Demographics                   |                            |                       |                      |                 |
| Female                         | 116 (62.0%)                | 72 (63.2%)            | 44 (60.3%)           | 0.692           |
| Age (year)                     | 59 (51–66)                 | 55 (50–67)            | 62 (53–66)           | 0.080           |
| Addictions                     |                            |                       |                      |                 |
| Smoking                        | 35 (18.7%)                 | 21 (18.4%)            | 14 (19.2%)           | 0.897           |
| Alcohol consumption            | 28 (15.0%)                 | 17 (14.9%)            | 11 (15.1%)           | 0.977           |
| Medical history                |                            |                       |                      |                 |
| Hypertension                   | 101 (54.0%)                | 59 (51.8%)            | 42 (57.5%)           | 0.439           |
| Diabetes mellitus              | 4 (2.1%)                   | 1 (0.9%)              | 3 (4.1%)             | 0.331           |
| Clinical grades                |                            |                       |                      |                 |
| WFNS grade                     | 2 (1–4)                    | 1 (1–3)               | 3 (1–4)              | <0.001          |
| mFisher grade                  | 3 (3–4)                    | 3 (2–4)               | 3 (3–4)              | 0.011           |
| Aneurysm characteristics       |                            |                       |                      |                 |
| Location                       |                            |                       |                      | 0.780           |
| Anterior                       | 179 (95.7%)                | 110 (96.5%)           | 69 (94.5%)           |                 |
| Posterior                      | 8 (4.3%)                   | 4 (3.5%)              | 4 (5.5%)             |                 |
| Number                         |                            |                       |                      | 0.984           |
| Single                         | 151 (80.7%)                | 92 (80.7%)            | 59 (80.8%)           |                 |
| Multiple                       | 36 (19.3%)                 | 22 (19.3%)            | 14 (19.2%)           |                 |
| Admission CBC                  |                            |                       |                      |                 |
| WBC ( $\times 10^9$ /L)        | 12.54 (9.64–15.74)         | 11.46 (8.90–14.00)    | 14.69 (11.81–17.90)  | <0.001          |
| Neutrophil ( $\times 10^9$ /L) | 11.32 (8.53–14.49)         | 10.30 (7.61–12.92)    | 13.18 (10.38–15.88)  | <0.001          |
| Lymphocyte ( $\times 10^9$ /L) | 0.81 (0.59–1.16)           | 0.81 (0.58–1.20)      | 0.81 (0.62–1.11)     | 0.812           |
| Monocyte ( $\times 10^9$ /L)   | 0.42 (0.28–0.65)           | 0.37 (0.23–0.51)      | 0.60 (0.36–0.84)     | <0.001          |
| Hemoglobin (g/L)               | 128 $\pm$ 17               | 130 $\pm$ 14          | 125 $\pm$ 19         | 0.069           |
| RBC ( $10^{12}$ /L)            | 4.30 (3.89–4.57)           | 4.31 (3.96–4.56)      | 4.30 (3.83–4.59)     | 0.546           |
| Hematocrit                     | 0.389 (0.358–0.423)        | 0.392 (0.364–0.423)   | 0.383 (0.348–0.423)  | 0.210           |
| MCV (fL)                       | 92.0 (89.8–96.0)           | 92.0 (89.9–96.1)      | 93.1 (89.8–95.5)     | 0.803           |
| MCH (pg)                       | 30.2 (29.1–31.4)           | 30.5 (29.3–31.5)      | 30.0 (28.8–31.1)     | 0.103           |
| MCHC (g/L)                     | 326 (320–333)              | 328 (321–334)         | 324 (318–331)        | 0.011           |
| RDW (%)                        | 13.2 (12.6–13.7)           | 13.1 (12.5–13.6)      | 13.4 (12.8–14.2)     | <0.001          |
| Platelet ( $\times 10^9$ /L)   | 186.8 $\pm$ 51.6           | 186.2 $\pm$ 46.7      | 187.8 $\pm$ 58.7     | 0.841           |
| MPV (fL)                       | 11.5 $\pm$ 1.7             | 11.3 $\pm$ 1.8        | 11.9 $\pm$ 1.6       | 0.039           |
| Postoperative CBC              |                            |                       |                      |                 |
| WBC ( $\times 10^9$ /L)        | 11.72 (9.43–14.77)         | 10.82 (9.01–13.80)    | 12.93 (10.29–16.86)  | 0.001           |
| Neutrophil ( $\times 10^9$ /L) | 9.80 (7.79–13.01)          | 8.89 (7.46–11.73)     | 11.77 (8.56–14.72)   | <0.001          |
| Lymphocyte ( $\times 10^9$ /L) | 0.85 (0.59–1.23)           | 0.88 (0.59–1.32)      | 0.85 (0.59–1.15)     | 0.655           |
| Monocyte ( $\times 10^9$ /L)   | 0.63 (0.45–0.95)           | 0.59 (0.41–0.88)      | 0.69 (0.51–1.04)     | 0.041           |

(Continued)

TABLE 1 (Continued)

| Characteristics                 | Total<br>( <i>n</i> = 187) | mRS at 3 Months       |                      | <i>p</i> -value  |
|---------------------------------|----------------------------|-----------------------|----------------------|------------------|
|                                 |                            | 0–2 ( <i>n</i> = 114) | 3–6 ( <i>n</i> = 73) |                  |
| Hemoglobin (g/L)                | 110 (99–118)               | 111 (101–119)         | 108 (96–115)         | 0.081            |
| RBC (10 <sup>12</sup> /L)       | 3.66 ± 0.52                | 3.66 ± 0.44           | 3.66 ± 0.63          | 0.941            |
| Hematocrit                      | 0.339 (0.310–0.367)        | 0.340 (0.314–0.367)   | 0.335 (0.299–0.367)  | 0.261            |
| MCV (fL)                        | 93.6 (90.6–96.9)           | 93.7 (91.1–96.8)      | 92.6 (90.1–96.9)     | 0.254            |
| MCH (pg)                        | 30.3 (29.2–31.1)           | 30.3 (29.3–31.3)      | 30.0 (29.0–30.8)     | 0.097            |
| MCHC (g/L)                      | 322 (315–328)              | 324 (316–328)         | 321 (314–328)        | 0.116            |
| RDW (%)                         | 13.3 (12.8–14.1)           | 13.1 (12.6–13.6)      | 13.9 (13.2–14.5)     | <b>&lt;0.001</b> |
| Platelet (× 10 <sup>9</sup> /L) | 144 (115–172)              | 143 (118–168)         | 144 (112–177)        | 0.872            |
| MPV (fL)                        | 11.6 ± 1.6                 | 11.3 ± 1.6            | 12.0 ± 1.5           | <b>0.004</b>     |

Boldface type represents statistical significance.

Values are *n* (%), mean ± standard deviation or median (25–75%).

CBC, complete blood count; mRS, modified Rankin Scale; WFNS, World Federation of Neurosurgical Societies; mFisher, modified fisher; WBC, white blood cell; RBC, red blood cell; MCV, mean corpuscular volume; MCH, mean corpuscular hemoglobin; MCHC, mean corpuscular hemoglobin concentration; RDW, red blood cell distribution width; MPV, mean platelet volume.

TABLE 2 Multivariate logistic regression of baseline characteristics and admission CBC parameters associated with poor functional outcome at 3 months.

| Characteristics | OR    | 95% CI      | <i>p</i> -value |
|-----------------|-------|-------------|-----------------|
| WFNS grade      | 1.322 | 1.023–1.707 | <b>0.033</b>    |
| mFisher grade   | 1.165 | 0.796–1.706 | 0.432           |
| WBC             | 1.136 | 1.044–1.236 | <b>0.003</b>    |
| MCHC            | 0.975 | 0.939–1.013 | 0.196           |
| RDW             | 1.327 | 0.918–1.919 | 0.132           |
| MPV             | 1.199 | 0.982–1.462 | 0.074           |

Boldface type represents statistical significance.

CBC, complete blood count; OR, odds ratio; CI, confidence interval; WFNS, World Federation of Neurosurgical Societies; mFisher, modified fisher; WBC, white blood cell; MCHC, mean corpuscular hemoglobin concentration; RDW, red blood cell distribution width; MPV, mean platelet volume.

parameter combination B (Youden's index = 0.375). The PPV was 71.2% and the NPV was 73.3%. The AUC of parameter combination C (all four parameters) was 0.787 (0.722–0.852) (Figure 3). The sensitivity was 80.8% and the specificity was 63.2% at the best cutoff point of parameter combination C (Youden's index = 0.440). The PPV was 58.4% and the NPV was 83.7%. The AUC of parameter combination C was higher than parameter combination A and B with statistical significance (parameter combination A vs. parameter combination C, *p* = 0.029; parameter combination B vs. parameter combination C, *p* = 0.048). The AUC of parameter combination A was significantly higher than WFNS grade (*p* = 0.018). The AUC of parameter combination B was significantly higher than WFNS grade and postoperative

TABLE 3 Multivariate logistic regression of baseline characteristics and postoperative CBC parameters associated with poor functional outcome at 3 months.

| Characteristics | OR    | 95% CI      | <i>p</i> -value |
|-----------------|-------|-------------|-----------------|
| WFNS grade      | 1.439 | 1.119–1.850 | <b>0.005</b>    |
| mFisher grade   | 1.189 | 0.824–1.718 | 0.355           |
| WBC             | 1.083 | 0.993–1.182 | 0.073           |
| RDW             | 1.411 | 1.095–1.818 | <b>0.008</b>    |
| MPV             | 1.253 | 1.012–1.552 | <b>0.039</b>    |

Boldface type represents statistical significance.

CBC, complete blood count; OR, odds ratio; CI, confidence interval; WFNS, World Federation of Neurosurgical Societies; mFisher, modified fisher; WBC, white blood cell; RDW, red blood cell distribution width; MPV, mean platelet volume.

MPV (parameter combination B vs. WFNS grade, *p* = 0.005; parameter combination B vs. postoperative MPV, *p* = 0.001). The AUC of parameter combination C was higher than all four parameters alone (parameter combination C vs. WFNS grade, *p* < 0.001; parameter combination C vs. admission WBC, *p* = 0.009; parameter combination C vs. postoperative RDW, *p* = 0.024; parameter combination C vs. postoperative MPV, *p* < 0.001).

## 4. Discussion

This study showed that admission WBC and postoperative RDW and MPV were associated with poor functional outcome in aSAH patients undergoing surgical clipping, and combining them with WFNS grade could improve the predictive value. It also revealed that combining RBC

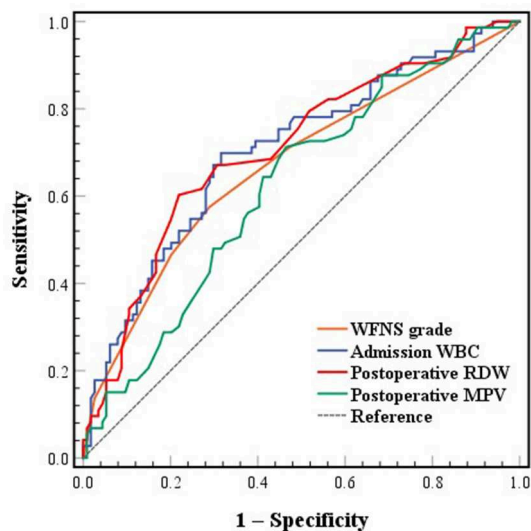


FIGURE 2

ROC curves of WFNS grade, admission WBC, postoperative RDW and MPV associated with poor functional outcome at 3 months. ROC, receiver operating characteristic; WFNS, World Federation of Neurological Societies; WBC, white blood cell; RDW, red blood cell distribution width; MPV, mean platelet volume.

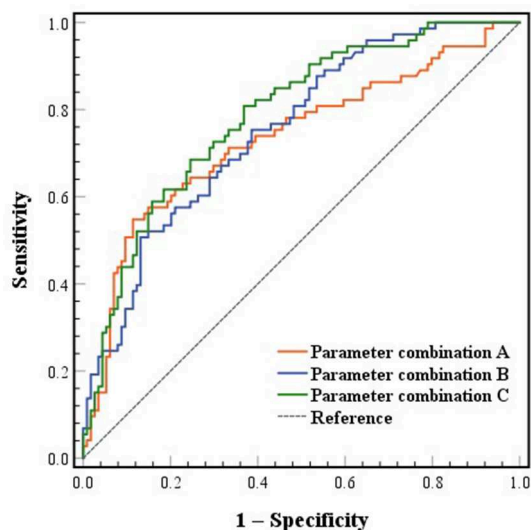


FIGURE 3

ROC curves of combined parameters predicting poor functional outcome at 3 months. ROC, receiver operating characteristic. Parameter combination A included World Federation of Neurological Societies (WFNS) grade and admission white blood cell (WBC). Parameter combination B included WFNS grade and postoperative red blood cell distribution width (RDW) and mean platelet volume (MPV). Parameter combination C included WFNS grade, admission WBC and postoperative RDW and MPV.

parameters could substantially increase the clinical prediction of functional outcome.

RDW changes dynamically with the development of aSAH. When an aSAH happens, body damage is inevitable. Clinicians and scientists have been investigated pathophysiological mechanisms following aSAH for decades. Several studies have found that the rupture of an aneurysm leads to a series of mechanisms such as cerebral edema, inflammation, oxidative stress and microthrombosis (16–18). A recent study has shown that the toll-like receptor (TLR) 4/myeloid differentiation primary response protein (MyD) 88/nuclear factor (NF)- $\kappa$ B pathway plays an essential role in the neuroinflammation following aSAH (19). After the activation of TLR4 by endogenous ligands with damage-associated molecular patterns produced after aSAH, the MyD88-dependent pathway activates the transcription factor NF- $\kappa$ B. It also produces pro-inflammatory cytokines such as tumor necrosis factor (TNF)- $\alpha$ , interleukins, intercellular adhesion molecule-1 (19), etc. According to the research by Wang et al. (20), RDW predicts significant inflammation in patients with autoimmune hepatitis. RDW is also associated with serum TLR4 and TNF- $\alpha$  (21, 22), both belonging to the TLR4/MyD88/NF- $\kappa$ B pathway. Therefore, it could be inferred that RDW is a biomarker of inflammation following aSAH. In an animal experiment by Zhao et al. (21), RDW is associated with serum superoxide dismutase and malondialdehyde, representing oxidative stress. Oxidative stress reduces the survival rate of RBCs, causing immature RBCs to increase in circulation, contributing to an increase in RDW. Furthermore, RDW is associated with stroke, cerebral infarction and cerebral vein thrombosis (23, 24). The release of internal organelles and the externalization of vesicular contents in the maturation process of the immature RBCs may lead to the activation of the coagulation system and thrombosis (25). Studies mentioned above suggest that inflammatory response, oxidative stress and microthrombosis are all related to RDW changes after aSAH. Although the admission RDW in the group of poor outcome was found to be significantly higher than the group of good outcome, admission RDW did not predict functional outcome independently in this study. In contrast, WFNS grade and admission WBC, which were deemed to be confounders, showed statistical significance in multivariate logistic regression. Additionally, RDW may not change in such a short amount of time, and factors like nutritional status can also affect the level of RDW, which could explain the results of multivariate logistic regression.

In this study, postoperative RDW was found to independently predict poor functional outcome at 3 months after surgical clipping in patients with aSAH, whereas admission RDW was not a predictor. The elevation of RDW on admission may reflect pathophysiological damage mediated by bleeding,



as it is generally known that RDW increases with blood loss. Since blood loss and occasional RBC transfusions are inevitable in craniotomy, an increase in RDW is likely to occur (26). Besides, inflammation, oxidative stress and a hypercoagulable state of blood are everyday events after craniotomy, all probably elevating the RDW level. Since these mechanisms also occur at the initial stage of aSAH, we infer that the disadvantages of surgical clipping may magnify the pathophysiological changes present on admission.

RDW has been widely used for the differential diagnosis of anemia over the past few decades (27, 28). Recent studies have shown that the function of RDW is mainly applied in cardiovascular and cerebrovascular diseases (29). In diagnosing acute myocardial infarction (AMI) among patients with chest pain and the discrimination of stroke subtypes in young patients, RDW demonstrates excellent diagnostic accuracy (30, 31). Other studies have suggested that RDW could also be a risk and outcome predictor. In patients with coronary artery diseases, RDW is associated with myocardial scar burden, impaired left ventricular function and postoperative cognitive dysfunction (32, 33). In patients suffering from atrial fibrillation, RDW enhances the risk of major adverse cardiovascular events, thromboembolic events and all-cause mortality (34–36). In patients undergoing ischemic stroke, RDW predicts worse neurological improvement and mortality (37, 38). RDW also shows predictive performance in hemorrhagic cerebrovascular diseases like spontaneous intracerebral hemorrhage (39) and aSAH (7–9), the latter of which our study focused on.

This study presents the first published analysis investigating the relationship between postoperative RDW and functional outcome in aSAH patients undergoing surgical clipping. Three previous studies performed dynamic monitoring of RDW. Fontana et al. monitored RDW daily from the day of admission for a maximum of 7 days during the intensive unit stay (7), and Siegler et al. (9) and Chugh et al. (15) collected RDW data continuously for up to 10 days or longer after aSAH onset. However, these studies did not mention whether patients received surgical treatment and when the surgical treatment was performed. As we explained above, admission and postoperative RDW are different, so evaluating RDW levels by calculating the maximum or mean throughout the aSAH course is likely to cause bias. In addition, high RDW levels at different periods will correspond to different strategies of clinical management. Hence, the separate assessment of admission and postoperative RDW may provide more practical guidance for the perioperative management of aSAH. Therefore, we selected patients who only underwent surgical clipping to reduce the confounding bias.

In addition to screening for independent predictors of poor functional outcome, we evaluated the differentiation and predictive potential of each predictor individually and in combination for functional outcome by comparing AUCs and calculating PPVs and NPVs. The result of AUC comparison showed that combined models had a higher degree of

differentiation than single predictors and the combined model of all four predictors was the highest. The PPVs indicated that the combination of WFNS grade and admission WBC appeared to provide the best predictive power of poor outcome. However, the combination of all parameters had the highest NPV, 83.7%, which could be used to predict good outcome. These results suggest that adding RDW to the predictive model improves the predictive power and has greater potential for predicting good outcome.

The RDW test is an excellent strategy of biomarker detection because it is easy to implement, inexpensive, and noninvasive. Since RDW is independently associated with functional outcome, it could guide clinical decisions in the perioperative management of aSAH, especially in the postoperative management. If the application of RDW is combined with demographics, medical history, clinical grades, radiological data and other laboratory data, it may contribute to better assessment, improve functional outcome and bring great benefit to patients. For example, RBC transfusion is usually given at the discretion of treating physicians when patients suffer blood loss in craniotomy or (and) anemia caused by other factors (40). However, the effect of RBC transfusion in aSAH can be detrimental. Several studies have shown that RBC transfusion is associated with unfavorable functional outcome indicators, such as poor functional outcome, mortality, acute lung injury, acute respiratory distress syndrome and thrombotic events (41–43). RDW is elevated during the regeneration of RBCs after blood loss and help diagnose some types of anemia. However, there is no specific guideline for RBC transfusion in aSAH. Thus, we hypothesize that combining hemoglobin and RDW to adjust transfusion practice may contribute to better functional outcome.

## 5. Limitations

This study has several limitations. First, it is a retrospective study performed at a single center with a small sample size, which is less persuasive than a large prospective study. Second, although baseline information regarding demographics, addictions, medical history, admission clinical grades and aneurysm characteristics was collected, some data like nutritional status, reticulocyte count and RBC transfusion records were not obtained. Third, other outcome indicators such as mortality, cerebral infarction, cognitive impairment, etc., were not collected. Finally, dynamic monitoring of RDW wasn't performed, which could provide more in-depth analysis.

## 6. Conclusion

Postoperative RDW is independently associated with poor functional outcome in aSAH patients undergoing surgical clipping. Combining postoperative RDW and MPV with WFNS

grade and WBC on admission may help predict good outcome more accurately. Further research is demanded to determine the clinical value and relevant mechanisms.

## Data availability statement

The raw data supporting the conclusions of this article will be made available by the authors, without undue reservation.

## Ethics statement

The studies involving human participants were reviewed and approved by Medical Ethics Committee of Affiliated Hospital of North Sichuan Medical College. The Ethics Committee waived the requirement of written informed consent for participation.

## Author contributions

This study was conceptualized and designed by LZ, YZ, XZ, and XT. Data collection and analysis were performed by LZ, YZ, PL, WL, XH, HL, MX, and XC. The original manuscript was written by LZ and YZ. Review and revision of the manuscript were performed by XZ and XT. All authors read and approved the final manuscript. All authors commented on previous versions of the manuscript.

## References

1. Tawk RG, Hasan TF, D'Souza CE, Peel JB, Freeman WD. Diagnosis and Treatment of Unruptured Intracranial Aneurysms and Aneurysmal Subarachnoid Hemorrhage. *Mayo Clin Proc.* (2021) 96:1970–2000. doi: 10.1016/j.mayocp.2021.01.005
2. Daou BJ, Koduri S, Thompson BG, Chaudhary N, Pandey AS. Clinical and experimental aspects of aneurysmal subarachnoid hemorrhage. *CNS Neurosci Ther.* (2019) 25:1096–112. doi: 10.1111/cns.13222
3. Diringer MN, Bleck TP, Claude Hemphill J. 3rd, Menon D, Shutter L, Vespa P, et al. Critical care management of patients following aneurysmal subarachnoid hemorrhage: recommendations from the neurocritical care society's multidisciplinary. *Consens Conferen Neurocrit Care.* (2011) 15:211–40. doi: 10.1007/s12028-011-9605-9
4. Connolly ES. Jr., Rabinstein AA, Carhuapoma JR, Derdeyn CP, Dion J, Higashida RT, et al. Guidelines for the management of aneurysmal subarachnoid hemorrhage: a guideline for healthcare professionals from the American Heart Association/American Stroke. *Assoc Stroke.* (2012) 43:1711–37. doi: 10.1161/STR.0b013e3182587839
5. Ayling OGS, Ibrahim GM, Alotaibi NM, Gooderham PA, Macdonald RL. Anemia after aneurysmal subarachnoid hemorrhage is associated with poor outcome and death. *Stroke.* (2018) 49:1859–65. doi: 10.1161/strokeaha.117.020260
6. Gong L, Gu Y, Dong Q, Zhang X, Wang H, Zhao Y, et al. A direct correlation between red blood cell indices and cognitive impairment after aneurysmal subarachnoid hemorrhage (Asah). *Curr Neurovasc Res.* (2019) 16:142–7. doi: 10.2174/1567202616666190412142718
7. Fontana V, Bond O, Spadaro S, Annoni F, Nobile L, Badenes R, et al. Red cell distribution width after subarachnoid hemorrhage. *J Neurosurg Anesthesiol.* (2018) 30:319–27. doi: 10.1097/ana.0000000000000459
8. Hong DY, Kim SY, Kim JY, Kim JW. Red blood cell distribution width is an independent predictor of mortality in patients with

## Funding

This study was supported by the Funds for Cooperation Project of Nanchong City and North Sichuan Medical College, Grant No. 20SXQT0317 (to LZ), Research and Development Project of Affiliated Hospital of North Sichuan Medical College, Grant No. 2022SK021 (to XZ), and Innovation and Entrepreneurship Training Program for College Students in Sichuan Province, Grant No. S202210634098 (to YZ).

## Conflict of interest

The authors declare that the research was conducted in the absence of any commercial or financial relationships that could be construed as a potential conflict of interest.

## Publisher's note

All claims expressed in this article are solely those of the authors and do not necessarily represent those of their affiliated organizations, or those of the publisher, the editors and the reviewers. Any product that may be evaluated in this article, or claim that may be made by its manufacturer, is not guaranteed or endorsed by the publisher.

- aneurysmal subarachnoid hemorrhage. *Clin Neurol Neurosurg.* (2018) 172:82–6. doi: 10.1016/j.clineuro.2018.06.044
9. Siegler JE, Marcaccio C, Nawalinski K, Quattrone F, Sandsmark DK, Maloney-Wilensky E, et al. Elevated red cell distribution width is associated with cerebral infarction in aneurysmal subarachnoid hemorrhage. *Neurocrit Care.* (2017) 26:26–33. doi: 10.1007/s12028-016-0306-2
10. Collins GS, Reitsma JB, Altman DG, Moons KG. Transparent reporting of a multivariable prediction model for individual prognosis or diagnosis (tripod): the tripod statement. *BMJ.* (2015) 350:g7594. doi: 10.1136/bmj.g7594
11. Tao C, Wang J, Hu X, Ma J, Li H, You C. Clinical value of neutrophil to lymphocyte and platelet to lymphocyte ratio after aneurysmal subarachnoid hemorrhage. *Neurocrit Care.* (2017) 26:393–401. doi: 10.1007/s12028-016-0332-0
12. Feghali J, Kim J, Gami A, Rapaport S, Caplan JM, McDougall CG, et al. Monocyte-based inflammatory indices predict outcomes following aneurysmal subarachnoid hemorrhage. *Neurosurg Rev.* (2021) 44:3499–507. doi: 10.1007/s10143-021-01525-1
13. Zhao L, Chen T, Yan HJ, Liu C, Cao Y, Zhang Y, et al. Development and validation of an early predictive nomogram for delayed cerebral ischemia after aneurysmal subarachnoid hemorrhage. *Ann Transl Med.* (2021) 9:1664. doi: 10.21037/atm-21-5200
14. Wolfe CD, Taub NA, Woodrow EJ, Burney PG. Assessment of scales of disability and handicap for stroke patients. *Stroke.* (1991) 22:1242–4. doi: 10.1161/01.str.22.10.1242
15. Chugh C, Nyirjesy SC, Nawalinski KP, Sandsmark DK, Frangos S, Maloney-Wilensky E, et al. Red blood cell distribution width is associated with poor clinical outcome after subarachnoid hemorrhage: a pilot study. *Neurocrit Care.* (2015) 23:217–24. doi: 10.1007/s12028-015-0117-x

16. van Lieshout JH, Dibué-Adjei M, Cornelius JF, Slotty PJ, Schneider T, Restin T, et al. An introduction to the pathophysiology of aneurysmal subarachnoid hemorrhage. *Neurosurg Rev.* (2018) 41:917–30. doi: 10.1007/s10143-017-0827-y
17. Hayman EG, Wessell A, Gerzanich V, Sheth KN, Simard JM. Mechanisms of global cerebral edema formation in aneurysmal subarachnoid hemorrhage. *Neurocrit Care.* (2017) 26:301–10. doi: 10.1007/s12028-016-0354-7
18. Wu F, Liu Z, Li G, Zhou L, Huang K, Wu Z, et al. Inflammation and oxidative stress: potential targets for improving prognosis after subarachnoid hemorrhage. *Front Cell Neurosci.* (2021) 15:739506. doi: 10.3389/fncel.2021.739506
19. Okada T, Suzuki H. Toll-like receptor 4 as a possible therapeutic target for delayed brain injuries after aneurysmal subarachnoid hemorrhage. *Neural Regen Res.* (2017) 12:193–6. doi: 10.4103/1673-5374.200795
20. Wang H, Wang J, Huang R, Xia J, Zuo L, Yan X, et al. Red blood cell distribution width for predicting significant liver inflammation in patients with autoimmune hepatitis. *Eur J Gastroenterol Hepatol.* (2019) 31:1527–32. doi: 10.1097/meg.0000000000001447
21. Zhao Z, Liu T, Li J, Yang W, Liu E, Li G. Elevated red cell distribution width level is associated with oxidative stress and inflammation in a canine model of rapid atrial pacing. *Int J Cardiol.* (2014) 174:174–6. doi: 10.1016/j.ijcard.2014.03.189
22. Lorente L, Martín MM, Abreu-González P, Solé-Violán J, Ferreres J, Labarta L, et al. Red blood cell distribution width during the first week is associated with severity and mortality in septic patients. *PLoS ONE.* (2014) 9:e105436. doi: 10.1371/journal.pone.0105436
23. Söderholm M, Borné Y, Hedblad B, Persson M, Engström G. Red cell distribution width in relation to incidence of stroke and carotid atherosclerosis: a population-based cohort study. *PLoS ONE.* (2015) 10:e0124957. doi: 10.1371/journal.pone.0124957
24. Maino A, Abbattista M, Bucciarelli P, Artoni A, Passamonti SM, Lanfranchi S, et al. Red cell distribution width and the risk of cerebral vein thrombosis: a case-control study. *Eur J Intern Med.* (2017) 38:46–51. doi: 10.1016/j.ejim.2016.10.017
25. Thachil J. Immature reticulocytes and its relevance to thrombosis. *Ann Hematol.* (2008) 87:1025–6. doi: 10.1007/s00277-008-0524-6
26. Spadaro S, Taccone FS, Fogagnolo A, Franchi F, Scolletta S, Ragazzi R, et al. The effects of blood transfusion on red blood cell distribution width in critically ill patients: a pilot study. *Transfusion.* (2018) 58:1863–9. doi: 10.1111/trf.14759
27. Salvagno GL, Sanchis-Gomar F, Picanza A, Lippi G. Red blood cell distribution width: a simple parameter with multiple clinical applications. *Crit Rev Clin Lab Sci.* (2015) 52:86–105. doi: 10.3109/10408363.2014.992064
28. Said AS, Spinella PC, Hartman ME, Steffen KM, Jackups R, Holubkov R, et al. RBC distribution width: biomarker for red cell dysfunction and critical illness outcome? *Pediatr Crit Care Med.* (2017) 18:134–42. doi: 10.1097/pcc.0000000000001017
29. Li N, Zhou H, Tang Q. Red blood cell distribution width: a novel predictive indicator for cardiovascular and cerebrovascular diseases. *Dis Markers.* (2017) 2017:7089493. doi: 10.1155/2017/7089493
30. Lippi G, Filippozzi L, Montagnana M, Salvagno GL, Franchini M, Guidi GC, et al. Clinical usefulness of measuring red blood cell distribution width on admission in patients with acute coronary syndromes. *Clin Chem Lab Med.* (2009) 47:353–7. doi: 10.1515/cclm.2009.066
31. Demir R, Saritemur M, Atis O, Ozel L, Kocaturk I, Emet M, et al. Can we distinguish stroke and stroke mimics via red cell distribution width in young patients? *Arch Med Sci.* (2015) 11:958–63. doi: 10.5114/aoms.2014.40995
32. Magri CJ, Tian TX, Camilleri L, Xuereb R, Galea J, Fava S. Red Blood cell distribution width and myocardial scar burden in coronary artery disease. *Postgrad Med J.* (2017) 93:607–12. doi: 10.1136/postgradmedj-2016-134781
33. Wan J, Luo P, Du X, Yan H. Preoperative red cell distribution width predicts postoperative cognitive dysfunction after coronary artery bypass grafting. *Biosci Rep.* (2020) 40:4. doi: 10.1042/bsr20194448
34. Wan H, Yang Y, Zhu J, Huang B, Wang J, Wu S, et al. The relationship between elevated red cell distribution width and long-term outcomes among patients with atrial fibrillation. *Clin Biochem.* (2015) 48:762–7. doi: 10.1016/j.clinbiochem.2015.06.001
35. Cha MJ, Lee HS, Kim HM, Jung JH, Choi EK, Oh S. Association between red cell distribution width and thromboembolic events in patients with atrial fibrillation. *Eur J Intern Med.* (2017) 46:41–6. doi: 10.1016/j.ejim.2017.07.028
36. Saliba W, Barnett-Griness O, Rennert G. Red cell distribution width and all-cause mortality in patients with atrial fibrillation: a cohort study. *J Arrhythm.* (2017) 33:56–62. doi: 10.1016/j.joa.2016.06.001
37. Turcato G, Cappellari M, Follador L, Dilda A, Bonora A, Zannoni M, et al. Red cell distribution width is an independent predictor of outcome in patients undergoing thrombolysis for ischemic stroke. *Semin Thromb Hemost.* (2017) 43:30–5. doi: 10.1055/s-0036-1592165
38. Wang L, Wang C, Wu S, Li Y, Guo W, Liu M. Red blood cell distribution width is associated with mortality after acute ischemic stroke: a cohort study and systematic review. *Ann Transl Med.* (2020) 8:81. doi: 10.21037/atm.2019.12.142
39. Pinho J, Silva L, Quintas-Neves M, Marques L, Amorim JM, Reich A, et al. Red cell distribution width is associated with 30-day mortality in patients with spontaneous intracerebral hemorrhage. *Neurocrit Care.* (2021) 34:825–32. doi: 10.1007/s12028-020-01103-1
40. Sampson TR, Dhar R, Diringner MN. Factors associated with the development of anemia after subarachnoid hemorrhage. *Neurocrit Care.* (2010) 12:4–9. doi: 10.1007/s12028-009-9273-1
41. Kumar MA, Levine J, Faerber J, Elliott JP, Winn HR, Doerfler S, et al. The effects of red blood cell transfusion on functional outcome after aneurysmal subarachnoid hemorrhage. *World Neurosurg.* (2017) 108:807–16. doi: 10.1016/j.wneu.2017.09.038
42. Festic E, Rabinstein AA, Freeman WD, Mauricio EA, Robinson MT, Mandrekar J, et al. Blood transfusion is an important predictor of hospital mortality among patients with aneurysmal subarachnoid hemorrhage. *Neurocrit Care.* (2013) 18:209–15. doi: 10.1007/s12028-012-9777-y
43. Kumar MA, Boland TA, Baiou M, Moussouttas M, Herman JH, Bell RD, et al. Red blood cell transfusion increases the risk of thrombotic events in patients with subarachnoid hemorrhage. *Neurocrit Care.* (2014) 20:84–90. doi: 10.1007/s12028-013-9819-0



## OPEN ACCESS

## EDITED BY

Jun Xu,  
Beijing Tiantan Hospital, Capital  
Medical University, China

## REVIEWED BY

Ke Ning,  
The University of Sheffield,  
United Kingdom  
Vaibhavi Vijay Peshattiwar,  
Institute of Chemical Technology, India

## \*CORRESPONDENCE

Junming Sun  
✉ sjm990205@163.com  
Mingyuan Zhang  
✉ Bio\_MYZhang@163.com

†These authors have contributed  
equally to this work

## SPECIALTY SECTION

This article was submitted to  
Neurological Biomarkers,  
a section of the journal  
Frontiers in Neurology

RECEIVED 28 October 2022

ACCEPTED 12 December 2022

PUBLISHED 17 January 2023

## CITATION

Ouyang Y, Zhang Y, Guo X, Li J, Ao Q,  
Guo S, Zhang M and Sun J (2023) An  
analysis of neurovascular disease  
markers in the hippocampus of *Tupaia  
chinensis* at different growth stages.  
*Front. Neurol.* 13:1083182.  
doi: 10.3389/fneur.2022.1083182

## COPYRIGHT

© 2023 Ouyang, Zhang, Guo, Li, Ao,  
Guo, Zhang and Sun. This is an  
open-access article distributed under  
the terms of the [Creative Commons  
Attribution License \(CC BY\)](#). The use,  
distribution or reproduction in other  
forums is permitted, provided the  
original author(s) and the copyright  
owner(s) are credited and that the  
original publication in this journal is  
cited, in accordance with accepted  
academic practice. No use, distribution  
or reproduction is permitted which  
does not comply with these terms.

# An analysis of neurovascular disease markers in the hippocampus of *Tupaia chinensis* at different growth stages

Yiqiang Ouyang<sup>1†</sup>, Ying Zhang<sup>1,2†</sup>, Xiaoping Guo<sup>1</sup>, Jiafu Li<sup>1</sup>,  
Qingqing Ao<sup>1</sup>, Songchao Guo<sup>1</sup>, Mingyuan Zhang<sup>1\*</sup> and  
Junming Sun<sup>1\*</sup>

<sup>1</sup>Laboratory Animal Center, Guangxi Medical University, Nanning, China, <sup>2</sup>Health and Regimen School, Guangxi Vocational and Technical College, School of Food and Biotechnology, Nanning, China

**Introduction:** It is considered that *Tupaia chinensis* can replace laboratory primates in the study of nervous system diseases. To date, however, protein expression in the brain of *Tupaia chinensis* has not been fully understood.

**Method:** Three age groups of *T. chinensis*—15 days, 3 months and 1.5 years—were selected to study their hippocampal protein expression profiles.

**Results:** A significant difference was observed between the 15-day group and the other two age groups, where as there were no significant differences between the 3-month and 1.5-year age groups. The Kyoto Encyclopedia of Genes and Genomes (KEGG) analysis found that differentially expressed proteins could be enriched in several pathways related to neurovascular diseases, such as metabolic pathways for Alzheimer's disease (AD), Huntington's disease, Parkinson's disease, and other diseases. The KEGG enrichment also showed that relevant protein involved in oxidative phosphorylation in the hippocampus of *T. chinensis* for 15days were downregulated, and ribosomal proteins (RPs) were upregulated, compared to those in the hippocampus of the other two age groups.

**Discussion:** It was suggested that when the hippocampus of *T. chinensis* developed from day 15 to 3 months, the expression of oxidatively phosphorylated proteins and RPs would vary over time. Meanwhile, the hippocampal protein expression profile of *T. chinensis* after 3 months had become stable. Moreover, the study underlines that, during the early development of the hippocampus of *T. chinensis*, energy demand increases while protein synthesis decreases. The mitochondria of *T. chinensis* changes with age, and the oxidative phosphorylation metabolic pathway of mitochondria is closely related to neurovascular diseases, such as stroke and cerebral ischemia.

## KEYWORDS

*Tupaia chinensis*, hippocampal proteomic analysis, different growth stages, neurovascular disease, neurovascular disease biomarkers

## Introduction

The hippocampus is a critical component of brain research and memory functions. An injury to the hippocampus is accompanied by many cognitive disorders, and morphological and functional changes in the hippocampus are also associated with pathological changes caused by many diseases of the nervous system (1–3). Animal brains continue to develop after birth, and there are certain differences in the growth characteristics of the hippocampus at different stages of development. These differences involve not only anatomy but also molecular biology, that is, gene protein expression (4–7). An oxidative damage to ribonucleic acid (RNA) increased significantly with age in all regions of the hippocampus (8). It could thus suggest some brain development characteristics and processes, and knowing more about these characteristics would help us understand the formation of brain research and memory functions. As neurovascular diseases are usually related to age, it is necessary to study how their markers change with age.

*Tupaia chinensis* is well suited for scientific study as a closely related phylogenetic primate due to its small size and short breeding cycle. *T. chinensis* has been found to have a larger brain than rodents and a more developed nervous system, making it having a higher application value in the study of neurovascular diseases (9). In recent years, many scholars have used *T. chinensis* to study the markers of neurovascular diseases such as stroke and cerebral ischemia (10–12). *T. chinensis* has a relatively longer life span, exceeding 10 years on average (9, 13). When considering the growth characteristics of *T. chinensis*, most *T. chinensis* used for laboratory experiments are aged between 3 months and 1.5 years, which corresponds to the human age of 10–20 years. Understanding the physiological features of the brain of *T. chinensis* at this growth stage facilitates its use in the study of neurovascular diseases. As tree shrews are more similar to humans than developing rodents and have a significantly higher brain-to-body weight ratio than rats, they are often used in animal models of diseases of the nervous system, such as cerebral ischemia, stroke, and depression.

Proteins are closely related to life and various forms of life activities. We expect to find clues concerning the biological functions of genes, which could be through the study of proteomes and then reveal their role in the whole functional network, thus understanding the phenomena and essence of life. Therefore, proteomics will play an extremely important role in discovering the mystery of life (14, 15). “Proteome” refers to the entire set of proteins expressed by the genome through transcription, translation, and post-translational modifications (16, 17).

Proteomics is a study of the dynamic changes of all proteins expressed by the genome of the cells of an organism in a specific time and space and analyzes the protein composition, the expression patterns, and the relationships among various components of the cell, enabling us to understand the unity of

the structure and function of proteins, to further regulate the vital activities of living organisms, and to reveal the nature of life phenomena (18). The present study compared hippocampal protein expression profiles of *T. chinensis* at three different age groups from the perspective of bioinformatics to find proteins that manifest a significant change in the process of neural development and better explain the role of proteins in the development of the nervous system. We also hope to find some age-related markers of neurovascular diseases through this research.

## Materials and methods

### Ethics statement

*Tupaia chinensis*, provided by the Kunming Institute of Zoology of the Chinese Academy of Sciences for this study, are standard laboratory animals artificially bred in captivity. Both the animal transport and the experiment were approved by the Laboratory Animal Ethics Committee of Guangxi Medical University and met the requirements of the national standard GB/T 35892-2018 “Laboratory Animal-Guideline for Ethical Review of Animal Welfare” of the People’s Republic of China.

### Animals

In total, nine male *T. chinensis* were purchased from the Kunming Institute of Zoology, Chinese Academy of Sciences and divided into three age groups: 15 days, 3 months, and 1.5 years. All were in good health with no abnormalities, and their microorganisms and parasites met the laboratory animal standards of Yunnan province. All *T. chinensis* were rapidly decapitated to obtain their tissue, and hippocampal tissues were promptly placed in liquid nitrogen for cryopreservation.

### Protein extraction

For protein extraction, hippocampal tissue samples from *T. chinensis* were combined with 1:50 (W:V) Lysis Buffer (8 M urea, 2 mM ethylenediaminetetraacetic acid (EDTA), 10 mM DTT, and 1% protease inhibitor cocktail) and thoroughly homogenized with a tissue grinder. Samples were sonicated for 3 min and centrifuged at  $13,000 \times g$  at  $4^{\circ}\text{C}$  for 10 min to remove debris, and then, protein in the supernatant was precipitated with cold acetone for 3 h at  $-2^{\circ}\text{C}$ . After centrifugation at  $4^{\circ}\text{C}$  at  $12,000 \times g$  for 10 min, the protein deposit was redissolved with urea buffer [8 M urea and 100 mM triethylammonium bicarbonate (TEAB)]. Protein concentration was determined using a Modified Bradford Protein Assay kit according to the instructions of the manufacturer, purchased from ABclonal



Technology Co., Ltd. Cat No of Antibodies: NDUFA9 Polyclonal Antibody A3196-50  $\mu$ l, ATP5F1 Polyclonal Antibody A7645-50  $\mu$ l, NDUFS3 Polyclonal Antibody A8013-50  $\mu$ l, RPS21 Polyclonal Antibody A18585-50  $\mu$ l, RPS18 Polyclonal Antibody 50  $\mu$ l A11687-50  $\mu$ l, NDUFS1 Polyclonal Antibody A2592-50  $\mu$ l, RPS23 Polyclonal Antibody A17528-50  $\mu$ l, NDUFA10 Polyclonal Antibody A10123-50  $\mu$ l, RPS13 Polyclonal Antibody A15720-50  $\mu$ l, SOD1 Polyclonal Antibody A0274-50  $\mu$ l, RPS2 Polyclonal Antibody 50  $\mu$ l A6728-50  $\mu$ l, and NDUFB9 A17454-50  $\mu$ l.

## Trypsin digestion

For digestion, 100  $\mu$ g of protein from each sample was first reduced with 10 mM DTT at 37°C for 60 min and then alkylated with 25 mM iodoacetamide (IAM) at room temperature for 30 min in the dark. The urea concentration of the protein samples was diluted to <2 M by adding 100 mM TEAB. The protein pool of each sample was digested with Sequencing Grade Modified Trypsin with the ratio of protein:trypsin = 50:1 mass ratio at 37°C overnight and 100:1 for the second digestion for 4 h.

## Peptide isobaric labeling

After trypsin digestion, the peptide was desalted *via* a Strata X SPE column and vacuum-dried. The peptide was reconstituted in 20  $\mu$ l of 500 mM TEAB and processed according to the protocol of the manufacturer for the 8-plex iTRAQ kit. Briefly, one unit of iTRAQ reagent was added to the peptide solution after it had been thawed and dissolved in 50  $\mu$ l of isopropanol. Peptide mixtures were incubated for 2 h at room temperature, pooled, and dried by vacuum centrifugation.

## High-performance liquid chromatography fractionation

Dried and labeled peptides were reconstituted with high-performance liquid chromatography (HPLC) solution A [2% acetonitrile (ACN), pH 10] and then fractionated into fractions by high-pH reversed-phase HPLC using Waters Bridge Peptide BEH C18 (130 Å, 3.5  $\mu$ m, 4.6 mm  $\times$  250 mm). Briefly, peptides were first separated with a gradient of 2–98% ACN with pH 10 at a speed of 0.5 ml/min over 88 min into 48 fractions. Then, the peptides were combined into 16 fractions and dried by vacuum centrifugation. Peptide fractions were desalted using ZipTip C18 according to the instructions of the manufacturer. Finally, the samples were dried under vacuum and kept at –20°C until mass spectrometer (MS) analysis could be performed.

## High-resolution liquid chromatography with tandem mass spectrometry analysis

Then, the experiment was performed by NanoLC 1000 liquid chromatography with tandem mass spectrometry (LC-MS/MS) using a Proxeon EASY-nLC 1000 coupled to Thermo Fisher Q Exactive. Trypsin digestion fractions were reconstituted in 0.1% formic acid (FA) and loaded directly onto a reverse phase precolumn (Acclaim PepMap<sup>®</sup> 100C18, 3  $\mu$ m, 100 Å, 75  $\mu$ m  $\times$  2 cm) at 5  $\mu$ l/min in 100% solvent A (0.1 M acetic acid in water). Furthermore, the peptides that eluted from the trap column were loaded onto a reverse phase analytical column (Acclaim PepMap<sup>®</sup> RSLC C18, 2  $\mu$ m, 100 Å, 50  $\mu$ m  $\times$  15 cm). The gradient was composed of an increase from 15 to 35% solvent B (0.1% FA in 98% ACN) over 30 min and from 35 to 98% solvent B for 5 min and kept in 98% ACN for 5 min at a constant flow rate of 300 nl/min on an EASY-nLC 1000 system. The eluent was sprayed *via* an NSI source at an electrospray voltage of 2.0 kV and then analyzed by tandem mass spectrometry (MS/MS) in Q Exactive. The MS was operated in data-dependent mode, automatically switching between MS and MS/MS. Full-scan MS spectra (from  $m/z$  350 to 1,800) were acquired on the Orbitrap with a resolution of 70,000. Ion fragments were detected in the Orbitrap at a resolution of 17,500, and the 20 most intense precursors were selected for subsequent decision tree-based ion trap HCD fragmentation with a collision energy of 27% in the MS survey scan with dynamic exclusion of 40.0 s.

## Data processing

The resulting MS/MS raw data were searched against the *T. chinensis* proteome database (Taxon identifier: 246,437 including 20,824 protein sequences; Proteome: UP000011518) downloaded from the UniProt database (<https://sparql.uniprot.org/>) using the SEQUEST software integration in Proteome Discoverer (version 1.3, Thermo Scientific). Trypsin was chosen as the enzyme, and two missed cleavages were allowed. Carbamidomethylation (C) was set as a fixed modification and oxidation (M), and N-terminal acetylation was set as a variable modification. Searches were performed using a peptide mass tolerance of 20 ppm and a product ion tolerance of 0.05 Da, resulting in a false discovery rate (FDR) of 5%.

## Protein functional annotation

Proteins were then classified using the gene ontology (GO) annotation based on three categories: biological processes, cellular components, and molecular functions. The

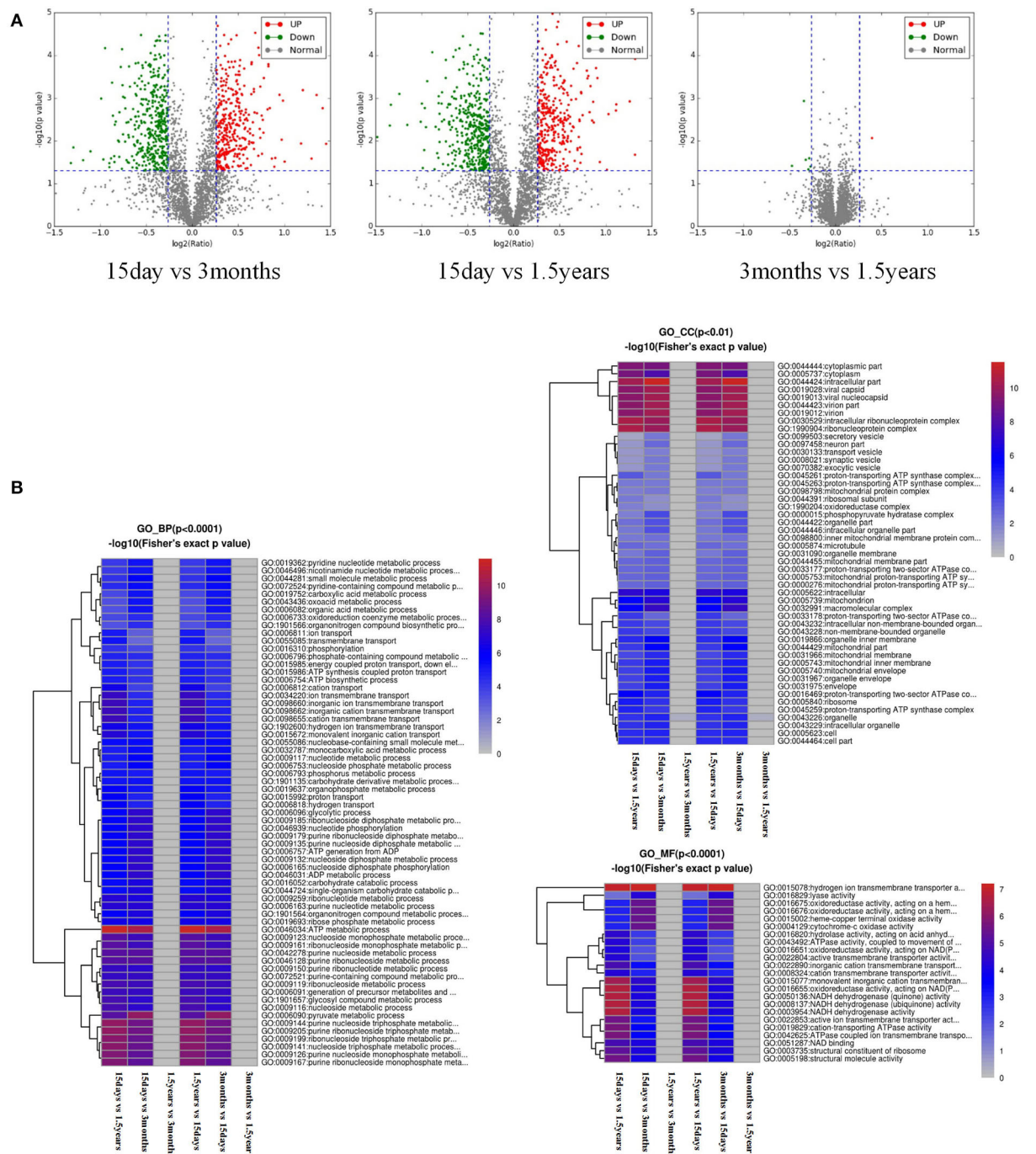


FIGURE 1

Analysis of a difference in protein expression difference and a functional cluster. **(A)** Differentially expressed proteins and a volcano map screened out with the differential multiple of 1.2 and the differential  $p$ -value of 0.05. The abscissa coordinate in the figure is the multiple variation values of a difference between the two samples, for which log<sub>2</sub> logization is performed. The ordinate is the statistical  $t$ -test  $p$ -value of the difference in protein expression, which is treated with  $-\log_{10}$ . The smaller the  $p$ -value is, the more significant the difference in expression is. Each dot represents a specific protein: green dots represent downregulated proteins, and red dots represent upregulated proteins. There were many different proteins between the 15-day age group and the other two age groups (3-month and 1.5-year age groups), whereas there were only a few different proteins between the 3-month and 1.5-year age groups. **(B)** Functional enrichment-based clustering for protein groups, and functional enrichment of the different proteins in the three biological processes, molecular functions, and cellular components. Reddish color indicates a significant difference; there were obvious differences between the 15-day age group and the other two age groups (3-month and 1.5-year age groups), whereas there was almost no difference between the 3-month and 1.5-year age groups.

TABLE 1 Quantity sheet of differential proteins between different groups at different multiples and *P* values.

| Multiples | <i>P</i> -value | 2&0.01 | 2&0.05 | 1.5&0.01 | 1.5&0.05 | 1.3&0.01 | 1.3&0.05 | 1.2&0.01 | 1.2&0.05 |
|-----------|-----------------|--------|--------|----------|----------|----------|----------|----------|----------|
| 15D/1.5Y  | Up              | 10     | 13     | 45       | 60       | 152      | 207      | 239      | 365      |
|           | Down            | 6      | 6      | 52       | 76       | 142      | 251      | 258      | 416      |
| 15D/3M    | Up              | 6      | 11     | 38       | 58       | 137      | 198      | 220      | 345      |
|           | Down            | 0      | 4      | 38       | 68       | 164      | 233      | 258      | 403      |
| 1.5Y/3M   | Up              | 0      | 0      | 0        | 0        | 0        | 1        | 2        | 7        |
|           | Down            | 0      | 0      | 0        | 0        | 1        | 1        | 1        | 1        |

GO annotation proteome was derived from the UniProt-GOA database (<http://www.ebi.ac.uk/GOA/>). The Kyoto Encyclopedia of Genes and Genomes (KEGG, <https://www.kegg.jp/>) database was used to annotate the protein pathway. First, KEGG online service tools KAAS (<https://www.genome.jp/tools/kaas/>) were used to annotate the protein description in the KEGG database. The annotation result was then mapped into the KEGG pathway database using the KEGG online service tools KEGG mapper.

## Functional enrichment

A two-tailed Fisher's exact test was employed to test GO (<http://geneontology.org/>), the KEGG pathway, and the domain enrichment of differentially expressed proteins against all identified proteins. Correction for multiple hypothesis tests was performed using standard FDR control methods, and a corrected  $p < 0.05$  was considered significant.

## Expression-based clustering and enrichment-based clustering for protein groups

Expression-based clustering and functional enrichment-based clustering for different protein groups were used to explore potential relationships between different protein groups at protein function (such as the KEGG pathway). We first collated all protein groups obtained after functional enrichment analysis along with their *p*-values and then filtered out those categories that were enriched for at least one of the protein groups with a  $p < 0.05$ . This filtered *p*-value matrix was transformed by the function  $x = -\log_{10}(p\text{-value})$ . Finally, these *x*-values were *z*-transformed for each functional category. These *z*-scores were then clustered using one-way hierarchical clustering (Euclidean distance, average link age clustering). Cluster membership was visualized *via* a heat map using the "Heat Map" function of the R-package.

## Western blot assays

Total proteins were extracted from the hippocampal samples of *T. chinensis* from different age groups. The concentration of the protein samples was determined using the BCA kit. Protein samples (25 µg/well) were separated by 8–12% sodium dodecyl sulfate–polyacrylamide gel electrophoresis (SDS-PAGE) and transferred to polyvinylidene fluoride (PVDF) membranes. These membranes were sealed at room temperature for 1 h in 5% blocking solution, incubated at 4°C overnight with diluted primary antibodies, then washed three times with TBST (10 min/time), incubated with a second antibody at room temperature for 2 h, washed in the same way as before, and developed by electrochemiluminescence (ECL). Except for anti-tubulin, which was purchased from Beyotime Biotechnology, all primary antibodies were purchased from ABClonal. Goat anti-rabbit IgG-HRP was purchased from ZSGB-BIO Co. Ltd.

## Results

### Screening of the hippocampal protein expression of *T. chinensis* at different growth stages

For samples from all three age groups, Identify Protein Num from the database of 27,080 proteins was 6,287, Quantify Protein Num with reliability  $q < 0.05$  was 5,952, Protein Num with FDR = 0.01 was 1,051, identifying the ratio of peptide fragments was 23.4%, and the average protein coverage was 13.2%.

The volcano plot showed a relatively significant difference in the hippocampal protein expression between the 15-day age group, the 3-month age group, and the 1.5-year age group and a few differentially expressed proteins between the 3-month and 1.5-year age groups (Figure 1A). Compared with the 1.5-year age group, there were 781 differentially expressed proteins in the 15-day age group, including 365 upregulated and 416 downregulated (Table 1). Compared with the 3-month age group, there were 748 differentially expressed proteins

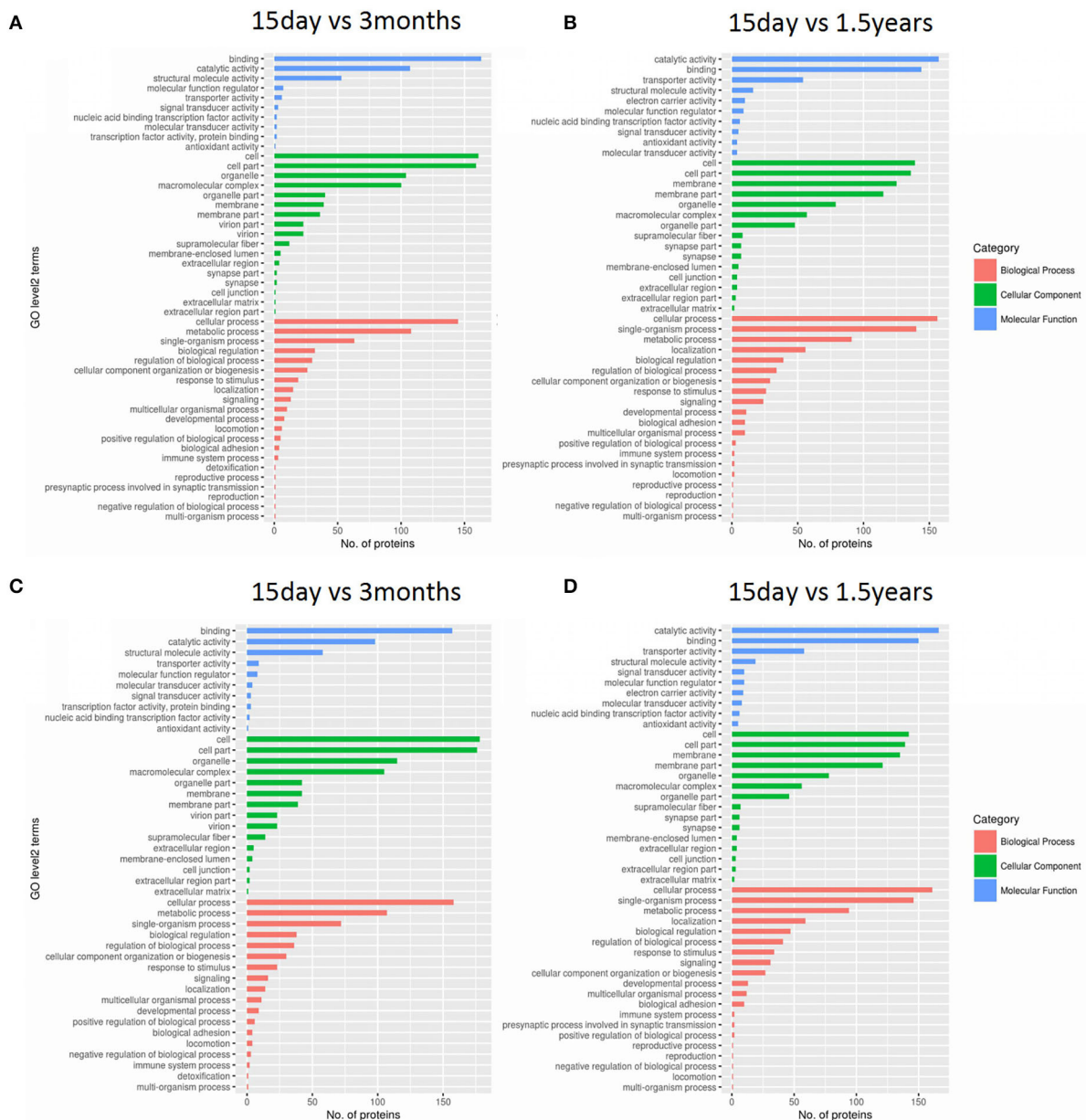


FIGURE 2

Gene ontology (GO) functional analysis of differentially expressed proteins. Enrichment classification at the second level of GO analysis. The length of the histogram indicates the number of functionally rich proteins, the red stripe represents biological processes, the green stripe represents cellular components, and the blue stripe represents molecular functions. (A) The upregulated protein functional enrichment in the 15-day and 1.5-year age groups, (B) the upregulated protein functional enrichment in the 15-day and 3-month age groups, (C) the downregulated protein functional enrichment in the 15-day and 1.5-year age groups, and (D) the downregulated protein functional enrichment in the 15-day and 3-month age groups.

in the 15-day age group, including 345 upregulated and 403 downregulated (when expression multiple  $> 1.2$ ,  $p < 0.05$ ).

After the functional enrichment-based clustering analysis, in the three categories of level 2: biological processes, cellular components, and molecular functions, there were certain differences in the hippocampal protein

function between the 15-day age group, the 3-month age group, and the 1.5-year age group, but there were no differences between the 3-month and 1.5-year age groups (Figure 1B).

Gene ontology functional significant enrichment analysis of differentially expressed proteins may explain their functional



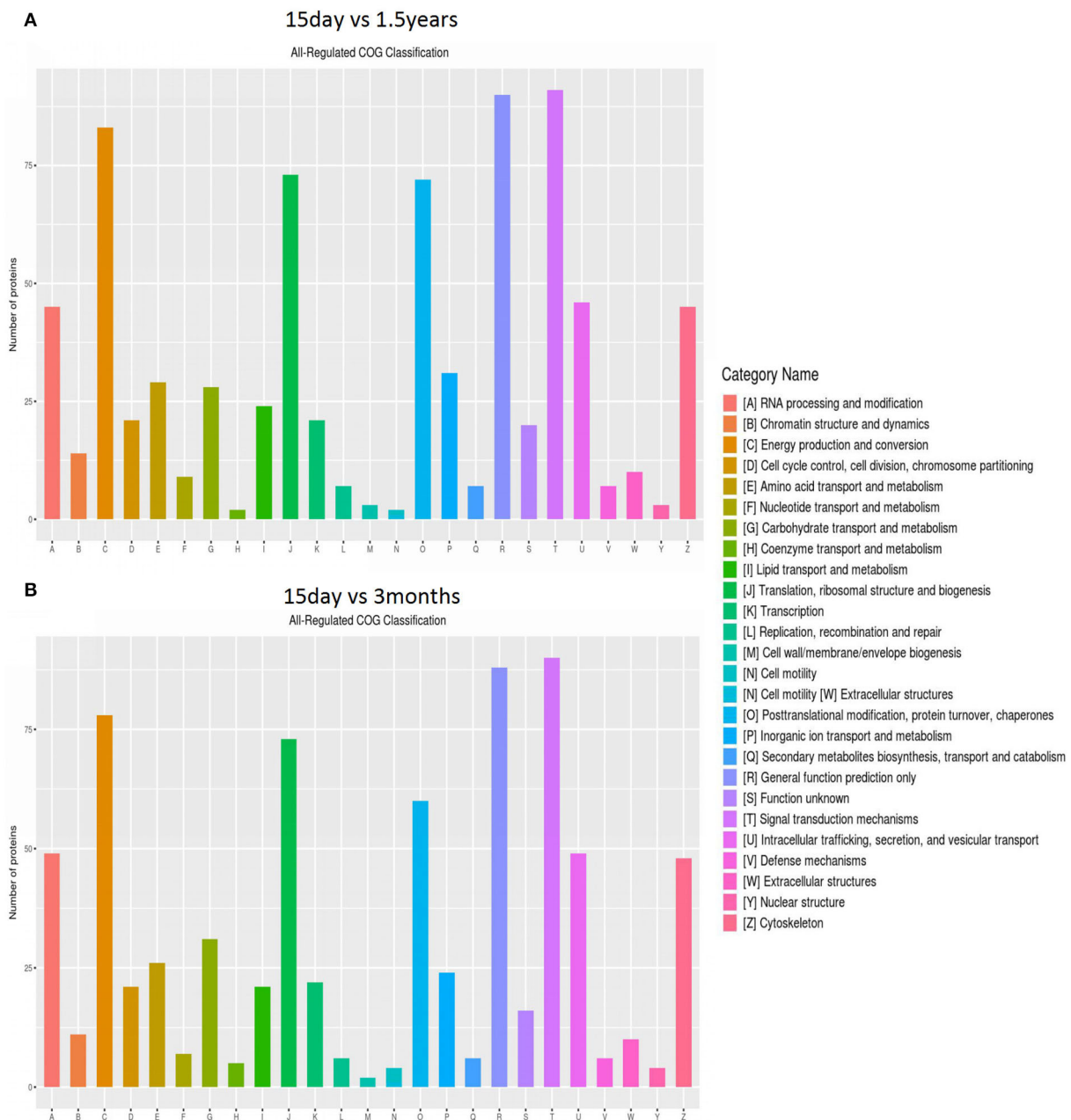


FIGURE 3

Clusters of orthologous genes (COG) enrichment analysis. The vertical axis represents the number of enriched proteins, and the horizontal axis is an enrichment function entry. (A) Functional enrichment of differentially expressed proteins in the 15-day and 1.5-year age groups, and (B) functional enrichment of differentially expressed proteins in the 15-day and 3-month age groups.

enrichment and illustrate the functional differences of the samples. This analysis used the DAVID software (<https://david-d.ncicrf.gov/>) and Fisher's exact test. The GO function was considered to be significantly enriched when the  $p \leq 0.05$ . The enrichment analysis figure (Figure 2) of hippocampal protein expression was obtained between the 15-day age group,

the 3-month age group, and the 1.5-year age group, and there was no functional enrichment of differentially expressed proteins in the 3-month and 1.5-year age groups. When comparing the 15-day age group with the 3-month age group, there were 65 upregulated and 133 downregulated proteins in biological processes, 29 upregulated and 74 downregulated



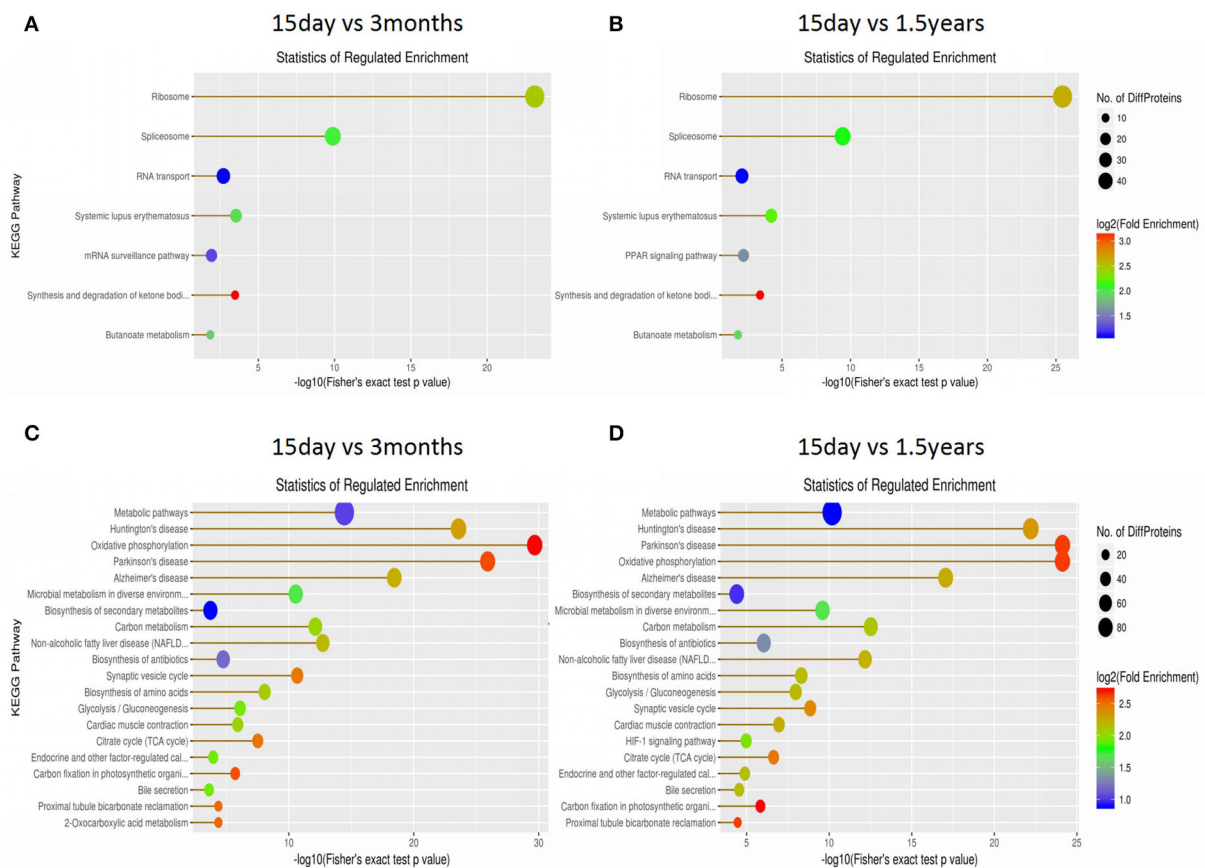


FIGURE 4

The Kyoto Encyclopedia of Genes and Genomes (KEGG) pathway enrichment analysis of differentially expressed proteins. Each solid circle in the figure is a KEGG pathway term. The horizontal axis represents a significant  $p$ -value of the KEGG pathway enrichment, which is  $-\log_{10}$ . The larger the value is, the greater the enrichment is. The ordinate represents the name of the KEGG pathway classification. The size of solid circles represents the number of different proteins under the KEGG pathway classification, and the larger circles represent a larger number of different proteins. The color of the solid circle represents the enrichment multiple of the KEGG pathway classification, and the redder the color is, the greater the enrichment multiple is. (A) The upregulated protein pathway enrichment in the 15-day and 3-year age groups. (B) The upregulated protein pathway enrichment in the 15-day and 1.5-year age groups. (C) The downregulated protein pathway enrichment in the 15-day and 3-year age groups. (D) The downregulated protein pathway enrichment in the 15-day and 1.5-year age groups.

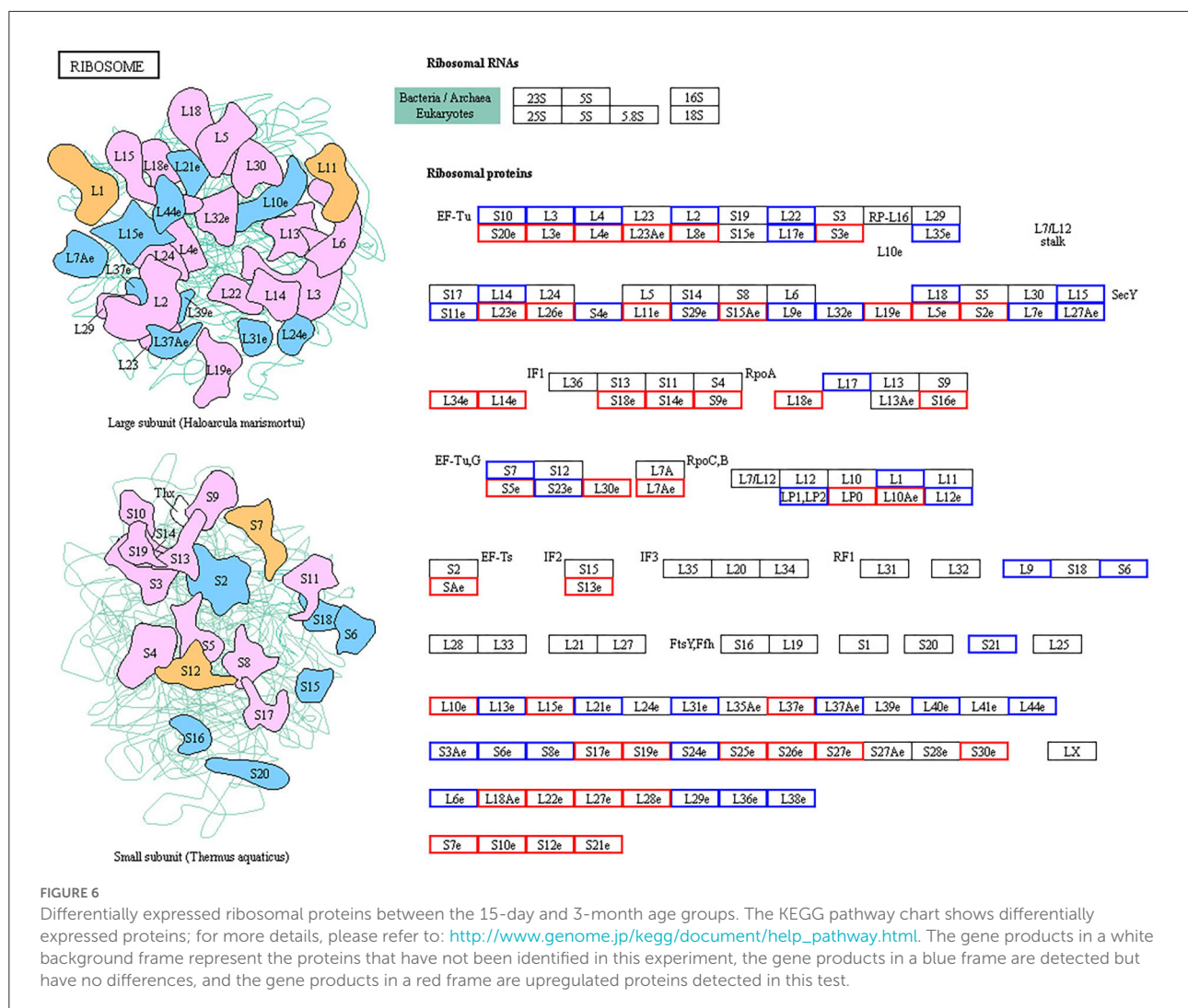
proteins in cellular components, and 21 upregulated and 98 downregulated proteins in molecular functions. When comparing the 15-day age group with the 1.5-year age group, there were 64 upregulated and 139 downregulated proteins in biological processes, 30 upregulated and 58 downregulated proteins in the cellular component analysis, and 11 upregulated and 100 downregulated proteins in molecular functions.

The distribution and amount of differentially expressed proteins in different clusters of orthologous genes (COG) categories are shown in Figure 3. When comparing the 15-day age group with the 3-month age group, 757 differentially expressed proteins were enriched in 26 COG categories, including 357 upregulated proteins and 400 downregulated proteins. When comparing the 15-day age group with the 1.5-year age group, 783 differentially expressed proteins, including

373 upregulated proteins and 410 downregulated proteins, were enriched in 26 COG categories.

The KEGG database was used to classify proteins according to their pathway or function, and an enrichment analysis was performed on the KEGG pathway of differentially expressed proteins in each pair within the three age groups. The enrichment of differentially expressed proteins between the 15-day age group, the 3-month age group, and the 1.5-year age group can be seen in Figure 4 and Supplementary Table S1. When comparing the 15-day age group with the 3-month age group, upregulated proteins were enriched on seven metabolic pathways, whereas downregulated proteins were enriched on 50 metabolic pathways. When comparing the 15-day age group with the 1.5-year age group, upregulated proteins were enriched on seven metabolic pathways, whereas downregulated proteins were enriched on 47





each subcellular localization and showed the result in a pie chart (Figure 8). When comparing the 15-day age group with the 3-month age group, differentially expressed proteins were concentrated in 11 subcellular locations, and the six locations with the highest distribution proportion were the cytosol (32.53%), nucleus (27.18%), mitochondria (13.65%), and plasma membrane (11.78%). When comparing the 15-day age group with the 1.5-year age group, differentially expressed proteins were concentrated in 12 subcellular locations, and the six locations with the highest distribution proportion were the cytosol (33.93%), nucleus (26.89%), mitochondria (13.96%), plasma membrane (11.65%), extracellular (7.17%), cytosol, nucleus (3.71%), extracellular (8.03%), and cytosol, nucleus (4.28%).

Western blot showed that the expressions of RPS2 and RPS18 in the ribosome pathway were upregulated at 15 days compared to 3 months and 1.5 years and that NDUFA9, NDUFA10, NDUFB9, ATP5F1, and SOD1 in the oxidative

phosphorylation pathway were downregulated at 15 days compared to 3 months and 1.5 years, which was consistent with the sequencing results (Figure 9).

## Discussion

It is very necessary to use animals at appropriate ages for relevant studies in scientific research. *T. chinensis* can live up to 10 years and grow quite rapidly, with sexual maturity at 3–4 months and body maturity at 5–6 months (9). Most *T. chinensis* used for experiment are older than 3 months, and older ones have a higher feeding cost, so older *T. chinensis* of greater months are not usually used unless special requirements are met. The study result indicates that the cerebral hippocampus growth of *T. chinensis* coincides with its stage of sexual maturity, and 3-month-old *T. chinensis* is very similar to mature in hippocampal protein expression, almost the same as 1.5-year-old *T. chinensis*.

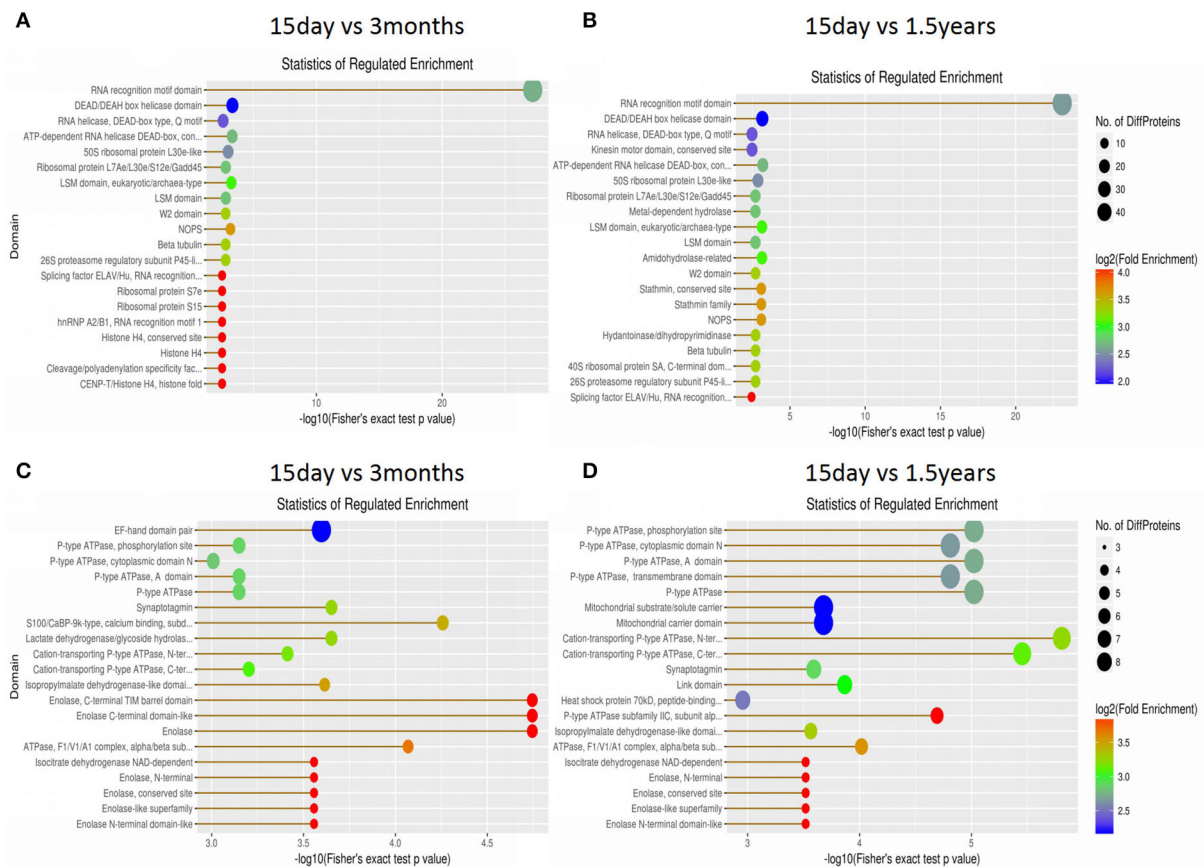


FIGURE 7

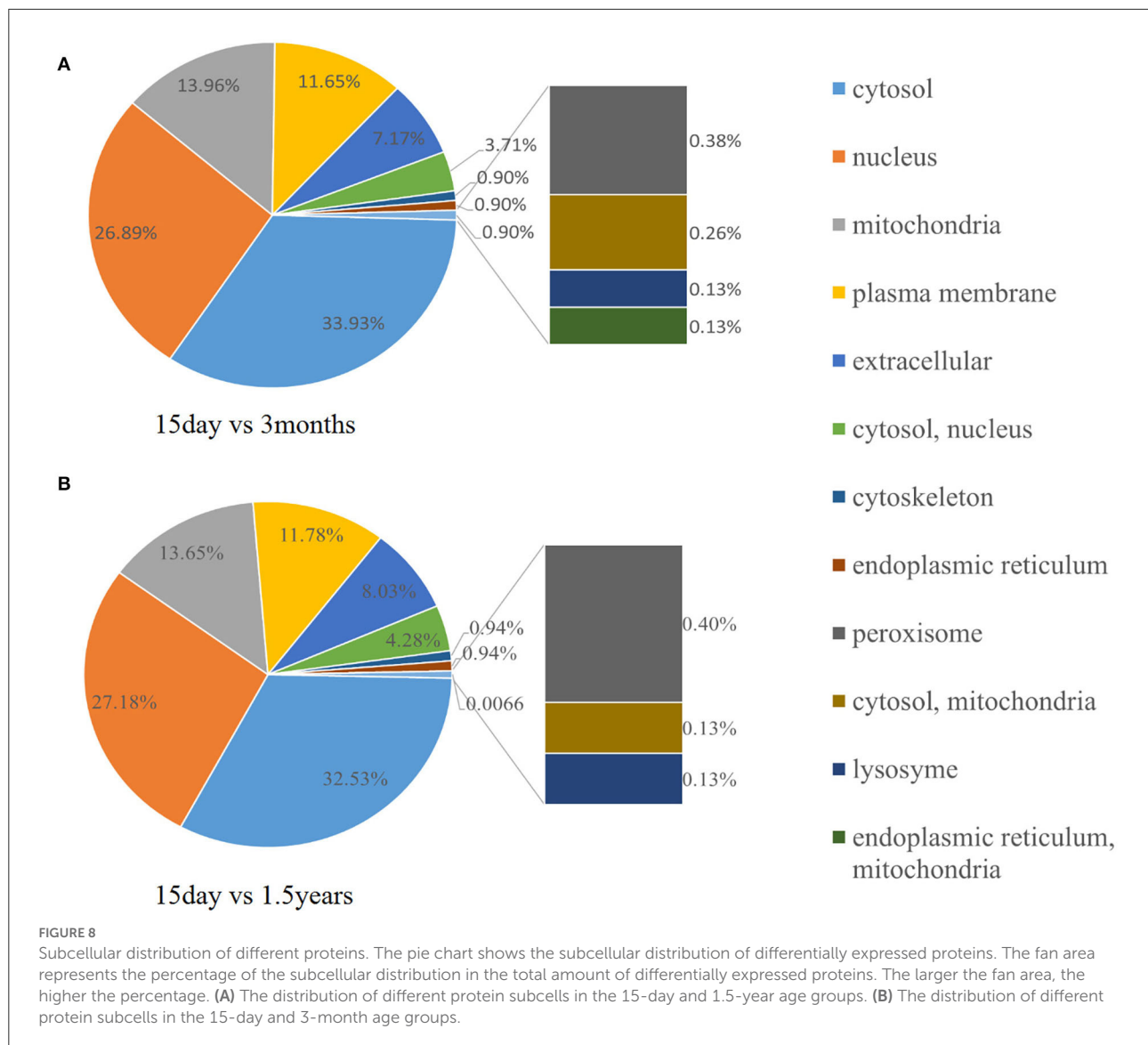
Domain enrichment analysis of differentially expressed proteins. Each solid circle is a domain, and a horizontal coordinate represents a significant  $p$ -value of domain enrichment, which is  $-\log_{10}$ . The larger the value is, the more enriched it is. The ordinate represents the name of the domain class. The size of the solid circle represents the number of different proteins under the domain classification, and the larger the circle is, the more different the proteins are. The color of the solid circle indicates the enrichment multiple of the domain classification, and the redder the color, the greater the enrichment multiple. (A) The upregulated protein domain enrichment in the 15-day and 3-month age groups. (B) The upregulated protein domain enrichment in the 15-day and 1.5-year age groups. (C) The downregulated protein domain enrichment in the 15-day and 3-month age groups. (D) The downregulated protein domain enrichment in the 15-day and 1.5-year age groups.

This will be helpful for the study of the nervous system of *T. chinensis*. The hippocampal protein content in infant *T. chinensis* differs from young and adult *T. chinensis*, which is manifested mainly by fewer oxidatively phosphorylated proteins and higher RPs in infants. There is little difference in the hippocampal protein content of young and adult *T. chinensis*.

Brain development includes not only the increase in the number of cells but also the differentiation and consumption of cells and tissues, as well as functional maturity or neurovascular diseases. It is also accompanied by changes in energy metabolism. Mitochondria, as the energy chamber of cells, generate a lot of energy through oxidative phosphorylation for tissue metabolism, which plays an important role in cell growth, proliferation, differentiation, neurovascular diseases, and other diseases. According to previous research, the functional status of mitochondria determines cell survival to

a large extent, and the quantity and quality of mitochondria directly influence the level of energy metabolism, with the former being closely related to the mitochondrial protein (19). Changes in brain mitochondrial protein are not only related to the mitochondrial global function but also related to aging and neurovascular diseases (e.g., Parkinson's disease and AD) (20, 21). Mitochondria, an organ of energy metabolism, provide energy for cell activities through oxidative phosphorylation. Ischemia causes tissue cells to be unable to obtain enough oxygen, meaning that mitochondria cannot effectively carry out oxidative phosphorylation, leading to the pH value falling in the cells and bringing about cellular acidosis and decreased mitochondrial membrane potential. Along with the time extension of ischemia, mitochondrial structure and function would be severely damaged, and cells would eventually die. Several dementia diseases have been related





to mitochondrial abnormalities, including AD, Huntington's disease, Parkinson's disease, and other diseases (20–24). Recent research suggested that mitochondria are considered a critical marker of neurovascular diseases such as cerebral ischemia and ischemia/reperfusion injury (25, 26).

Earlier studies determined the oxidase activity of brain, heart, and liver homogenates and cytochrome C in isolated mitochondria and also found that oxidase activity was inhibited in the aging process (27). The present study found that mitochondrial protein expression in the hippocampus of infant *T. chinensis* was lower, and oxidative phosphorylation-related proteins were downregulated at large levels, compared to adults. This, in turn, showed that the improvement of energy metabolism in the process of brain development was a gradual

process and that energy metabolism was the lowest in the hippocampus of young animals. It was suggested that damage to the mitochondria of young animals might be conducive to simulating disease models of nervous system abnormalities.

The KEGG pathway analysis showed that differentially expressed proteins were enriched in the pathways of Huntington's disease, oxidative phosphorylation, Parkinson's disease, AD, and other diseases. These genes may be further studied as markers of neurovascular diseases. The main reason for this is that there are many proteins related to oxidative phosphorylation in mitochondria, and the changes in oxidative phosphorylation-related proteins are closely related to the metabolic pathways for Huntington's disease, Parkinson's disease, and AD (28–32).



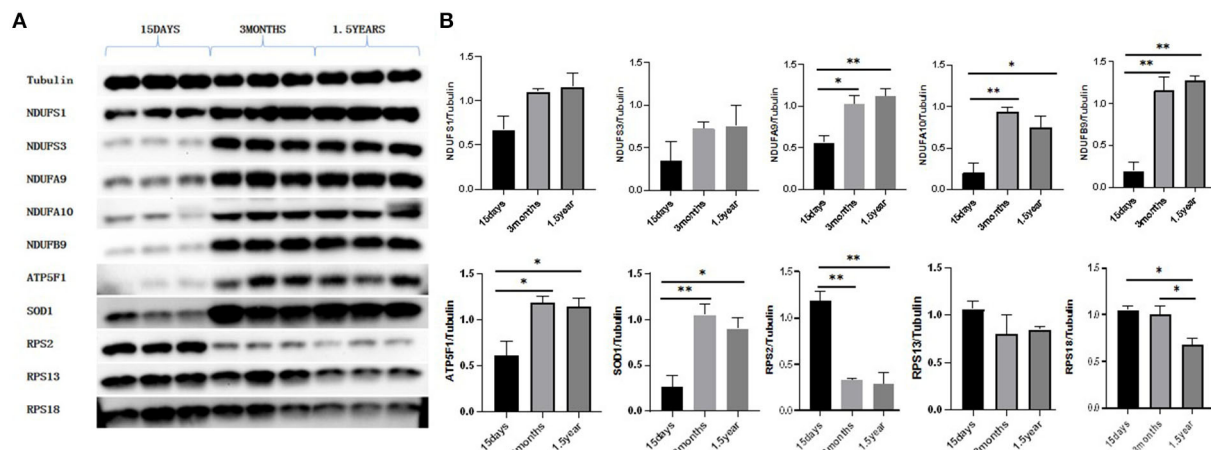


FIGURE 9

Western blot results. (A) Protein expression of NDUF51, NDUF53, NDUF9, NDUF10, NDUF9, ATP5F1, SOD1, RPS2, RPS13, and RPS18. (B) Gray value analysis results of Western blot. With Tubulin as an internal reference, the expression of proteins related to oxidative phosphorylation pathways, NDUF9, NDUF10, NDUF9, ATP5F1, and SOD1 were significantly lower in the 15-day age group than in the other two age groups. The expression of ribosome-related proteins RPS2 and RPS18 was significantly higher in the 15-day age group than in the other two age groups, which was consistent with the proteomic analysis. \* $P < 0.05$  compared with 15 days group, \*\* $P < 0.01$  compared with 15 days group.

Ribosomes are the sites of protein synthesis in biological cells. They are composed of RP and ribosomal RNA (rRNA) and are involved in deoxyribonucleic acid (DNA) and protein translation, processing and repair of transcribed and duplicated RNA, and cell proliferation and apoptosis. Ribosomes, as an important organelle in the cell, consist of a 40S small subunit and a 60S large subunit in a ratio of 1:1 in the eucell and have many varieties. Its name is based on the size of the ribosome subunit, where the large subunit RP is named as L1–L44 and the small subunit RP as S1–S31. In AD, the number of ribosomes in neuronal cells is significantly decreased, resulting in impaired protein synthesis, and the large subunit 60S RP L7 can promote apoptosis and regulate cellular transcription by interfering in the expression of cell cycle-related proteins (33, 34).

Mammalian cerebral proteins have a very high level of metabolism. Experiments have proven that more than 90% of rat cerebral proteins have a half-life of only 4–14 days, and some proteins even have a half-life of just several hours (35, 36). Studies showed that newly synthesized cerebral proteins every day during the fetal period account for approximately 47% of total brain proteins, and the rate of synthesis decreases rapidly after birth (37). The expanded repertoire of ribosome biogenesis factors is likely to enable multicellular organisms to coordinate multiple steps of ribosome production in response to different developmental and environmental stimuli (38). The present experiment indicated that the RP level in 15-day-old *T. chinensis* was evidently high compared to that of 3-month-old and 1.5-year-old *T. chinensis*. It has been suggested that *T. chinensis* in this period has a large number

of ribosomes in the hippocampus strong protein synthesis and is constantly growing and developing. The level of ribosomes in the hippocampus would gradually decrease with age. Mitochondria gradually increases during hippocampal development, suggesting that hippocampal energy demand increases with age. Ribosomes gradually decrease in the developmental process of the hippocampus, suggesting that some nerve cell proteins are synthesized in large amounts in the early stage of development, and the demand for protein synthesis is reduced after maturity. In the future, more studies on the protein expression profile of different regions of tree shrews, and single-cell sequencing of nerve cells in the brain should be carried out to provide more information for the study of diseases of the nervous system.

## Conclusion

In conclusion, the protein expression level in the hippocampus of 3-month-old *T. chinensis* begins to stabilize. When the hippocampus of *T. chinensis* develops from day 15 to 3 months, the expression levels of oxidatively phosphorylated proteins and RPs vary over time. Meanwhile, the protein expression profile in the hippocampus of *T. chinensis* has become stable within 3 months. In this research, some age-related neurovascular disease markers were found, and a change in their contents was observed in the hippocampus of tree shrews at different ages. Hence, our study provides further insights into animal models of neurovascular diseases in *T. chinensis*.

## Data availability statement

The data presented in the study are deposited in the <http://www.proteomexchange.org/> website, accession number PXD039177.

## Ethics statement

The animal study was reviewed and approved by the Experimental Animal Ethics Committee of Guangxi Medical University.

## Author contributions

YZ is responsible for all experimental operations, article writing, data collection, data sorting, statistical analysis, and picture production. MZ is responsible for the experimental operation, data sorting, and statistical analysis. XG is responsible for animal experiment, molecular experiment, and data analysis. QA is responsible for writing articles and sorting data. SG is responsible for guiding experimental ideas, article writing, and article submission. JS is responsible for animal experiments, data collation, and article submission. YO is responsible for guiding experimental ideas, article writing, data collection, data sorting, statistical analysis, picture production, and article submission. All authors contributed to the article and approved the submitted version.

## References

- Eichenbaum H. Memory: organization and control. *Annu Rev Psychol.* (2017) 68:19–45. doi: 10.1146/annurev-psych-010416-044131
- Bayley PJ, O'Reilly RC, Curran T, Squire LR. New semantic learning in patients with large medial temporal lobe lesions. *Hippocampus.* (2008) 18:575–83. doi: 10.1002/hipo.20417
- Manns JR, Eichenbaum H. A cognitive map for object memory in the hippocampus. *Learn Mem.* (2009) 16:616–24. doi: 10.1101/lm.1484509
- Uematsu A, Hata J, Komaki Y, Seki F, Yamada C, Okahara N, et al. Mapping orbitofrontal-limbic maturation in non-human primates: a longitudinal magnetic resonance imaging study. *Neuroimage.* (2017) 163:55–67. doi: 10.1016/j.neuroimage.2017.09.028
- Akers KG, Martinez-Canabal A, Restivo L, Yiu AP, De Cristofaro A, Hsiang HL, et al. Hippocampal neurogenesis regulates forgetting during adulthood and infancy. *Science.* (2014) 344:598–602. doi: 10.1126/science.1248903
- Mistry AM, Thompson CH, Miller AR, Vanoye CG, George AJ, Kearney JA. Strain- and age-dependent hippocampal neuron sodium currents correlate with epilepsy severity in dravet syndrome mice. *Neurobiol Dis.* (2014) 65:1–11. doi: 10.1016/j.nbd.2014.01.006
- Lu C, Sun X, Li N, Wang W, Kuang D, Tong P, et al. Circrnas in the tree shrew (*tupaia belangeri*) brain during postnatal development and aging. *Aging (Albany NY).* (2018) 10:833–52. doi: 10.18632/aging.101437
- Rodriguez-Callejas JD, Fuchs E, Perez-Cruz C. Increased oxidative stress, hyperphosphorylation of tau, and dystrophic microglia in the hippocampus of aged *tupaia belangeri*. *Glia.* (2020) 68:1775–93. doi: 10.1002/glia.23804
- Li B, Zhang R, Li J, He B, Zhen H, Wang L, et al. Measurement and analysis of anatomical parameter values in tree shrews. *Dong wu xue yan jiu.* (2013) 34:132–8. doi: 10.3724/SP.J.1141.2013.02132
- Ma KL, Gao JH, Huang ZQ, Zhang Y, Kuang DX, Jiang QF, et al. Motor function in mptp-treated tree shrews (*tupaia belangeri chinensis*). *Neurochem Res.* (2013). doi: 10.1007/s11064-013-1099-8
- Feng R, Li S, Li F. Toll-like receptor 4 is involved in ischemic tolerance of postconditioning in hippocampus of tree shrews to thrombotic cerebral ischemia. *Brain Res.* (2011) 1384:118–27. doi: 10.1016/j.brainres.2011.02.005
- Ouyang Y, Liang Z, Huang S, Zhang Y, Luo S, Liang J, et al. Preliminary behavioral, pathological and transcriptome studies of tree shrew: evidence for a complementary small-animal alzheimer's disease model. *Pak J Zool.* (2017) 49:1231–41. doi: 10.17582/journal.pjz/2017.49.4.1231.1241
- James KKK, Hubrecht RH. *The Ufaw Handbook on the Care and Management of Laboratory and Other Research Animals.* New York: Wiley-Blackwell. (2010). doi: 10.1002/9781444318777
- Pandey A, Mann M. Proteomics to study genes and genomes. *Nature.* (2000) 405:837–46. doi: 10.1038/35015709
- Rosamond J, Allsop A. Harnessing the power of the genome in the search for new antibiotics. *Science.* (2000) 287:1973–6. doi: 10.1126/science.287.5460.1973
- Wilkins MR, Sanchez JC, Gooley AA, Appel RD, Humphrey-Smith I, Hochstrasser DF, et al. Progress with proteome projects: why all proteins expressed by a genome should be identified and how to do it. *Biotechnol Genet Eng.* (1996) 13:19–50. doi: 10.1080/02648725.1996.10647923

## Funding

This study was funded by National Natural Science Foundation of China (31560612).

## Conflict of interest

The authors declare that the research was conducted in the absence of any commercial or financial relationships that could be construed as a potential conflict of interest.

## Publisher's note

All claims expressed in this article are solely those of the authors and do not necessarily represent those of their affiliated organizations, or those of the publisher, the editors and the reviewers. Any product that may be evaluated in this article, or claim that may be made by its manufacturer, is not guaranteed or endorsed by the publisher.

## Supplementary material

The Supplementary Material for this article can be found online at: <https://www.frontiersin.org/articles/10.3389/fneur.2022.1083182/full#supplementary-material>

17. Adhikari S, Nice EC, Deutsch EW, Lane L, Omenn GS, Pennington SR, et al. A high-stringency blueprint of the human proteome. *Nat Commun.* (2020) 11:5301. doi: 10.1038/s41467-020-19045-9
18. Liu Y, Tong C, Cong P, Liu Y, Shi X, Shi L, et al. Quantitative proteomic analysis and identification of differentially expressed proteins involved in blast exposure-induced inflammatory response. *research square.* (2020). doi: 10.21203/rs.3.rs-40702/v1
19. Sullivan EM, Pennington ER, Green WD, Beck MA, Brown DA, Shaikh SR. Mechanisms by which dietary fatty acids regulate mitochondrial structure-function in health and disease. *Adv Nutr.* (2018) 9:247–62. doi: 10.1093/advances/nmy007
20. Keating DJ. Mitochondrial dysfunction, oxidative stress, regulation of exocytosis and their relevance to neurodegenerative diseases. *J Neurochem.* (2008) 104:298–305.
21. Yang X, Wu J, Jing S, Forster MJ, Yan LJ. Mitochondrial protein sulfenation during aging in the rat brain. *Biophys Rep.* (2018) 4:104–13. doi: 10.1007/s41048-018-0053-3
22. Mancuso M, Calsolaro V, Orsucci D, Siciliano G, Murri L. Is there a primary role of the mitochondrial genome in Alzheimer's disease? *J Bioenerg Biomembr.* (2009) 41:411–6. doi: 10.1007/s10863-009-9239-1
23. Edison P, Ahmed I, Fan Z, Hinz R, Gelosa G, Ray CK, et al. Microglia, amyloid, and glucose metabolism in Parkinson's disease with and without dementia. *Neuropsychopharmacol.* (2013) 38:938–49. doi: 10.1038/npp.2012.255
24. Franco-Iborra S, Vila M, Perier C. The parkinson disease mitochondrial hypothesis. *The Neuroscientist.* (2016) 22:266–77. doi: 10.1177/1073858415574600
25. Christophe M, Nicolas S. Mitochondria: a target for neuroprotective interventions in cerebral ischemia-reperfusion. *Curr Pharm Des.* (2006) 12:739–57. doi: 10.2174/138161206775474242
26. Kašparová S, Brezová V, Valko M, Horecký J, Mlynárik V, Liptaj T, et al. Study of the oxidative stress in a rat model of chronic brain hypoperfusion. *Neurochem Int.* (2005) 46:601–11. doi: 10.1016/j.neuint.2005.02.006
27. Beckman KB, Ames BN. Endogenous oxidative damage of MTDNA. *Mutat Res.* (1999) 424:51–8. doi: 10.1016/S0027-5107(99)00007-X
28. Li XJ, Orr AL, Li S. Impaired mitochondrial trafficking in huntington's disease. *Biochim Biophys Acta.* (2010) 1802:62–5. doi: 10.1016/j.bbdis.2009.06.008
29. Ferreira IL, Nascimento MV, Ribeiro M, Almeida S, Cardoso SM, Grazina M, et al. Mitochondrial-dependent apoptosis in huntington's disease human cybrids. *Exp Neurol.* (2010) 222:243–55. doi: 10.1016/j.expneurol.2010.01.002
30. Abdullah R, Basak I, Patil KS, Alves G, Larsen JP, Moller SG. Parkinson's disease and age: the obvious but largely unexplored link. *Exp Gerontol.* (2015) 68:33–8. doi: 10.1016/j.exger.2014.09.014
31. Swerdlow RH, Burns JM, Khan SM. The Alzheimer's disease mitochondrial cascade hypothesis. *J Alzheimer's Disease.* (2010) 20:S265–79. doi: 10.3233/JAD-2010-100339
32. Torres AK, Rivera BI, Polanco CM, Jara C, Tapia-Rojas C. Phosphorylated tau as a toxic agent in synaptic mitochondria: implications in aging and Alzheimer's disease. *Neural Regen Res.* (2022) 17:1645–51. doi: 10.4103/1673-5374.332125
33. Lohrum M, Ludwig RL, Kubbutat M, Hanlon M, Vousden KH. Regulation of hdm2 activity by the ribosomal protein l11. *Cancer Cell.* (2003) 3:577–87. doi: 10.1016/S1535-6108(03)00134-X
34. Siniša Volarević MJSB. Proliferation, but not growth, blocked by conditional deletion of 40s ribosomal protein s6 author(s): siniša volarević, mary j. In: *Stewart, birgit ledermann, frederic zilberman, luigi terracciano, eugenio montini, markus grompe, sara c. Kozma and george thomas source: science, new series.* 288, 2045–2047. American Association for the Advancement of Science Stable. (2000). Available online at: <http://www.jstor.org/stable/3075543> (accessed September 19, 2016).
35. Seta K, Sansur M, Lajtha A. The rate of incorporation of amino acids into brain proteins during infusion in the rat. *Biochim Biophys Acta.* (1973) 294:472–80. doi: 10.1016/0005-2787(73)90103-2
36. Lajtha A, Latzkovits L, Toth J. Comparison of turnover rates of proteins of the brain, liver and kidney in mouse in vivo following long term labeling. *Biochim Biophys Acta.* (1976) 425:511–20. doi: 10.1016/0005-2787(76)90015-0
37. Lajtha A, Dunlop D. Turnover of protein in the nervous system. *Life Sci.* (1981) 29:755–67. doi: 10.1016/0024-3205(81)90030-8
38. Ni C, Schmitz DA, Lee J, Pawlowski K, Wu J, Buszczak M. Labeling of heterochronic ribosomes reveals clorf109 and spata5 control a late step in human ribosome assembly. *Cell Rep.* (2022) 38:110597. doi: 10.1016/j.celrep.2022.110597



## OPEN ACCESS

## EDITED BY

Jun Xu,  
Beijing Tiantan Hospital, Capital  
Medical University, China

## REVIEWED BY

Boyan Zhao,  
Fourth Military Medical  
University, China  
Jie Tao,  
Shanghai General Hospital, China  
Chao Xu,  
The Second Affiliated Hospital of  
Shaanxi University of Traditional  
Chinese Medicine, China

## \*CORRESPONDENCE

Ning Luo  
✉ ned8122@163.com

<sup>†</sup>These authors have contributed  
equally to this work

## SPECIALTY SECTION

This article was submitted to  
Neurological Biomarkers,  
a section of the journal  
Frontiers in Neurology

RECEIVED 24 August 2022

ACCEPTED 09 December 2022

PUBLISHED 17 January 2023

## CITATION

Luo N, Guo Y, Peng L and Deng F  
(2023) High-fiber-diet-related  
metabolites improve  
neurodegenerative symptoms in  
patients with obesity with diabetes  
mellitus by modulating the  
hippocampal–hypothalamic  
endocrine axis.  
*Front. Neurol.* 13:1026904.  
doi: 10.3389/fneur.2022.1026904

## COPYRIGHT

© 2023 Luo, Guo, Peng and Deng. This  
is an open-access article distributed  
under the terms of the [Creative  
Commons Attribution License \(CC BY\)](#).  
The use, distribution or reproduction  
in other forums is permitted, provided  
the original author(s) and the copyright  
owner(s) are credited and that the  
original publication in this journal is  
cited, in accordance with accepted  
academic practice. No use, distribution  
or reproduction is permitted which  
does not comply with these terms.

# High-fiber-diet-related metabolites improve neurodegenerative symptoms in patients with obesity with diabetes mellitus by modulating the hippocampal–hypothalamic endocrine axis

Ning Luo<sup>1\*†</sup>, Yuejie Guo<sup>2†</sup>, Lihua Peng<sup>3</sup> and Fangli Deng<sup>4</sup>

<sup>1</sup>Department of Endocrinology, Chenzhou No. 1 People's Hospital, Chenzhou, China, <sup>2</sup>Department of Geriatrics, Chenzhou No. 1 People's Hospital, Chenzhou, China, <sup>3</sup>Department of Clinical Laboratory, Chenzhou No. 4 People's Hospital, Chenzhou, China, <sup>4</sup>Breast Health Care Center, Chenzhou No. 1 People's Hospital, Chenzhou, China

**Objective:** Through transcriptomic and metabolomic analyses, this study examined the role of high-fiber diet in obesity complicated by diabetes and neurodegenerative symptoms.

**Method:** The expression matrix of high-fiber-diet-related metabolites, blood methylation profile associated with pre-symptomatic dementia in elderly patients with type 2 diabetes mellitus (T2DM), and high-throughput single-cell sequencing data of hippocampal samples from patients with Alzheimer's disease (AD) were retrieved from the Gene Expression Omnibus (GEO) database and through a literature search. Data were analyzed using principal component analysis (PCA) after quality control and data filtering to identify different cell clusters and candidate markers. A protein–protein interaction network was mapped using the STRING database. To further investigate the interaction among high-fiber-diet-related metabolites, methylation-related DEGs related to T2DM, and single-cell marker genes related to AD, AutoDock was used for semi-flexible molecular docking.

**Result:** Based on GEO database data and previous studies, 24 marker genes associated with high-fiber diet, T2DM, and AD were identified. Top 10 core genes include SYNE1, ANK2, SPEG, PDZD2, KALRN, PTPRM, PTPRK, BIN1, DOCK9, and NPNT, and their functions are primarily related to autophagy. According to molecular docking analysis, acetamidobenzoic acid, the most substantially altered metabolic marker associated with a high-fiber diet, had the strongest binding affinity for SPEG.

**Conclusion:** By targeting the SPEG protein in the hippocampus, acetamidobenzoic acid, a metabolite associated with high-fiber diet, may improve diabetic and neurodegenerative diseases in obese people.

## KEYWORDS

high-fiber diet, neurodegenerative diseases, obesity, neurovascular, SPEG, AD

## 1. Introduction

The incidence of obesity is increasing annually worldwide. According to the recent data published in NEJM, the incidence of obesity has been increasing at a high rate since the 1980s, with the incidence rate being 12 and 5% among adults and children, respectively. The number of individuals with obesity is highest in China (1, 2). Obesity and type 2 diabetes mellitus (T2DM) significantly increase the incidence of neurodegenerative diseases such as depression, dementia, stroke, and memory loss (3–8). Chronic systemic inflammation throughout the body is a common feature of obesity and diabetes and may be present in the central nervous system, suggesting an important relationship among obesity, diabetes, and neurodegenerative diseases (9). Therefore, examining the regulation of energy balance in obesity and identifying biomarkers are major research directions at present.

The central nervous system plays an important role in regulating energy balance in the body, energy metabolism is also linked to the health of the central nervous system (10–14). As the main appetite control center of the hypothalamus, the arcuate nucleus region (ARC) is one of the most studied neural circuits for energy balance (10). As the sensors of peripheral nutrients and hormones, AgRP and POMC neurons in the ARC are considered key neurons involved in sensing the global energy status of an organism and playing an important role in diet and weight regulation (15–18). In a state of energy surplus, POMC neurons release neuropeptides such as  $\alpha$ -MSH, which have appetite-suppressing effects, to reduce the energy intake of the body, thereby maintaining body weight (17). There are network loops in the hypothalamus that regulate feeding and are precisely interconnected (19). The hippocampus is part of the limbic nervous system. In addition to its relevance to cognition and learning, it has received increasing attention in the study of feeding and digestion; processing visceral sensory information and participating in the regulation of energy balance mainly through connections with the hypothalamus, amygdala and medulla (20, 21). This phenomenon may be attributed to the regulation of the hypothalamus *via* the hippocampal–hypothalamic neural loop. Direct neural projections from the ventral pole of hippocampal CA1 to hypothalamic loci are involved in the control of food intake (22). In a study, significant alterations in feeding behavior were observed in rats with a damaged hippocampus. The effects of nesfatin-1 on GD-responsive neurons in the ventral medial nucleus of the hypothalamus were significantly reduced after the hippocampal CA1 region of rats was electrically damaged, thereby affecting gastric motility (21). However, factors affecting hippocampal

function are intricate. Previous studies have found that many hormone receptors are related to feeding and energy regulation in the hippocampus, such as ghrelin, nesfatin-1, and insulin (21, 23). The hypothalamic–pituitary–adrenal (HPA) axis and its neuroendocrine hormones can mediate stressful effects in the hippocampus (24). In addition, various neurovascular markers can influence hippocampal function (25). Therefore, we hypothesized that modulation of hippocampal function can improve the energy homeostasis function of the hypothalamus by improving the hippocampal–hypothalamic neural circuit, thus suppressing obesity.

An increase in dietary fiber intake is associated with a reduced risk of obesity, and dietary fiber also plays a beneficial role in obesity-related metabolic diseases (26, 27). High-fiber and low-glycaemic-index diets with conventional T2DM treatment can improve the disorder of glucolipid metabolism and have certain hypoglycaemic effects in elderly patients with T2DM (28, 29). Consumption of whole grains may prevent the development of T2DM (30, 31). Consumption of almonds increases dietary fiber intake, which is beneficial for obesity, glycaemic control and lipid profile, probably owing to the presence of fiber, which promotes an antidiabetic microbiome by increasing the amount of short-chain fatty acids (32–34). Moreover, high-fiber diet is essentially a low-calorie diet and consuming foods rich in fiber increases satiety and hence reduces caloric intake (35). In addition, a high fiber intake is associated with a reduced risk of Alzheimer's disease (AD) (36). Metabolites associated with high-fiber diet are blood markers that target key genes and suppress obesity. Inulin, a type of soluble dietary fiber, promotes the production of glucagon-like peptide-1 (GLP-1) in enteroendocrine cells and suppresses postprandial blood glucose elevation and appetite through short-chain fatty acids (SCFAs) produced by the intestinal microbiota (37, 38). Kimura et al. reported that SCFA exerts an inhibitory effect on fat accumulation *via* GPR43 (39). Therefore, high-fiber diet improves metabolic status and prevents obesity. However, its effects on the hippocampal–hypothalamic functional axis remain unknown. Previous studies have reported that dietary fiber plays a role in improving insulin resistance (40). Adherence to high-fiber diet can decrease the plasma levels of ghrelin and GLP-1 (41). Many hormone receptors related to feeding and energy regulation are present in the hippocampus, such as ghrelin, nesfatin-1 and insulin (21, 23). Therefore, we speculate that metabolites from high-fiber diet might act on the hippocampus. In order to identify new treatment targets for obesity, it is important to investigate how high-fiber diet work in obesity and the corresponding complications.

This study examined high-fiber diet's ability to delay the progression of obesity complicated by diabetes type 2 and neurodegenerative symptoms using integrated scRNA transcriptomic and metabolomic analyses, providing new insights into obesity management.

Abbreviations: T2DM, Type 2 diabetes mellitus; AD, Alzheimer's disease; SPEG, Striated muscle preferentially expressed protein kinase; GO, Gene ontology; KEGG, Kyoto Encyclopedia of Genes and Genomes.



## 2. Materials and methods

### 2.1. Methylation genes in the peripheral blood of patients with T2DM–AD

Gene methylation signature matrix data associated with pre-dementia in elderly T2DM patients were downloaded from the GEO database. The following search strategy was used: keywords, “Type 2 diabetes” and “Alzheimer’s disease;” study subjects, “*Homo sapiens*,” study type, “Blood methylomic signatures.” Datasets were obtained using whole-genome RNA-expression microarrays, and human-derived whole blood was used for experiments. After fine data screening, the microarray dataset GSE62003 was eventually selected (Illumina HumanMethylation 450 BeadChip; HumanMethylation 450\_15017482) (42). The platform used for testing samples was GPL13534, and the dataset contained the expression data of methylation-related genes from 58 patients with T2DM. Firstly, samples with >10% missing methylation sites were excluded. Then, the R package “ChAMP” was used to perform a series of processes: the missing values were filled in using the ChAMP (43, 44). Data were extracted and screened for DEGs using the R package. The probe IDs were converted to standard gene symbols. Genes with  $P < 0.05$  and  $|\log_2FC| > 0.1$  were selected as methylation genes in peripheral blood of T2DM–AD patients.

### 2.2. Acquisition of metabolomics data for high-fiber diets

Metabolomic data of the high-fiber diet were obtained using the GEO database and a literature search, and metabolite expression matrices were created to screen and identify potential metabolic markers of serum endogenous origin based on differential expression multiplicity ( $|\log_2FC| > 1.00$ ) and  $t$ -test ( $P < 0.05$ ) results. The MetaboAnalyst 5.0 (<http://www.metaboanalyst.ca/>) database was further used to perform metabolic pathway analysis of the potential metabolic markers that were significantly back-regulated after the high-fiber diet intervention and to obtain metabolism related differentially expressed genes (DEGs) (45).

### 2.3. Downloading single-cell RNA sequencing data of hippocampal tissue from the AD patients

The high-throughput scRNA-seq data of the hippocampal samples associated with AD were downloaded from the GEO database with the following screening criteria: (i) Alzheimer’s disease; (ii) human; (iii) hippocampus; and (iv) single cell RNA-seq/scRNA-seq. The single-cell sequencing data of hippocampal

samples from patients with AD were extracted from the GEO database using “Alzheimer’s disease” as the search term, and the scRNA-seq dataset (GSE163577) was selected for further analysis (46). The single-cell sequencing data of nine patients with AD (AD group) and eight healthy individuals (control group) in the dataset were selected, and cells with gene counts of 200–10,000 and mitochondrial gene proportion of <5% were screened using the Seurat package as previous researches (47–52). Subsequently, the data were normalized using the “Normalizeddata” function of the Seurat package and the global scaling normalization method “LogNormalize.” To remove the batch effects of cells include in the analysis and maximize the preservation of the gene expression data of these cells, the “ScaleData” function of the Seurat package was used to regress the variances of “nCount/nFeature\_RNA” and “percent. Mt” (Supplementary Figure 2C). Subsequently, the “RunPCA” function of the Seurat package was used for dimensionality reduction and t-SNE clustering. The identified cells were subjected to top-down clustering analysis and annotated according to the known human gastric tissue cell marker genes.

### 2.4. Single cell sequencing quality control and data removal

For quality assessment, quality control processing of sequencing raw expression data, Limma, Seurat, Dplyr, and Magrittr packages were used. Seurat’s R package is used to generate objects, remove poor quality data, and calculate the percentages of gene counts, cell counts, and mitochondrial sequencing counts from the matrix data. For quality control, set Seurat’s screening criteria as follows: cells with <3 genes expressed and <50 genes were rejected. It was necessary to remove cells with more than 5% mitochondrial genes.

### 2.5. Cell annotation and screening of marker genes

In order to obtain the highest principal component in the cell population, further principal component analysis (PCA) was conducted after quality control of the sequencing data. The principal components were determined by  $P < 0.05$  screening and the t-SNE clustering algorithm was used to select the significant components. We used the Seurat package for the t-SNE analysis, and all the removed data was classified by setting the clustering parameter of the FindClusters function in Seurat to 0.5. The R package by limma was used to adjust  $P < 0.05$ , and the expression change was greater than or equal to twice the ( $|\log_2FC| \geq 1.00$ ) as the criteria to filter the marker genes.

In addition, candidate marker genes were found in different clusters of cells using the ggplot2 package.

## 2.6. GO/KEGG enrichment analysis of marker genes

The Gene Ontology (GO) and Kyoto Encyclopedia of Genes and Genomes (KEGG) signaling pathway analysis of the marker genes obtained in the previous step was performed in the R language to further explore the potential mechanisms of marker genes in specific cell clusters in Alzheimer's disease (53). Potential marker genes are categorized by Cellular Components (CC), Molecular Functions (MF), and Biological Processes (BP). Pathview is also used to map the corresponding signaling pathways. GO enrichment and KEGG pathway analyses were performed using the DAVID (<http://david.ncicrf.gov>) and Metascape databases, and the results were visualized using the R software (54–58). The DAVID online database was conducted on methylation genes associated with high-fiber diet, T2DM, and AD for GO and KEGG enrichment analysis. Based on the  $P$ -value of each item  $p < 0.05$ , the best biological process and enrichment pathway were selected.

## 2.7. Network involving high-fiber diet, T2DM, and AD in single cells

To illustrate the relevant target sets of the T2DM-AD-monocyte marker gene methylation network, the Venn R package was used to map hippocampus-associated marker genes in AD to DEGs in high-fiber diets and differentially methylated genes in T2DM patients, respectively. In order to map intersecting protein interaction networks and output protein-interaction relationship data, the STRING database (<https://string-db.org/>) was applied (59–63). By analyzing the topological structure of the protein-protein interaction network model with Cytohubba plugin of Cytoscape 3.7.2, the top-ranked core targets were selected, and their degree, closeness, and betweenness values were visualized (64, 65).

## 2.8. Molecular docking

The study used AutoDock 4 for semi-flexible molecular docking of ligands and receptors to investigate the interaction of differentially metabolized compounds of a high fiber diet with the T2DM-AD-monocyte marker methylation gene (66, 67). Small molecule ligands are flexible and changeable in semi-flexible docking, while receptors are robust and difficult to change. By downloading the 3D SDF file from PubChem, modifying the structure with Chem Bio3D Ultra 14.0, and saving it as mol2 format, the active ingredient was first processed. Our

next step was to download the 3D protein model of the core target from the PDB database, dehydrate, hydrogenate, extract the ligand, and save it as a PDB file using PyMOL. The files were then converted to pdbqt files using Auto Dock Tools-1.5.6. The docking results were visualized in PyMOL to map the “protein-molecule” docking interaction patterns. In addition, run Discovery Studio 2019 to find the docking site and calculate the LibDockScore. Analyze the chemical bonds formed between the docking model and the 2-dimensional image.

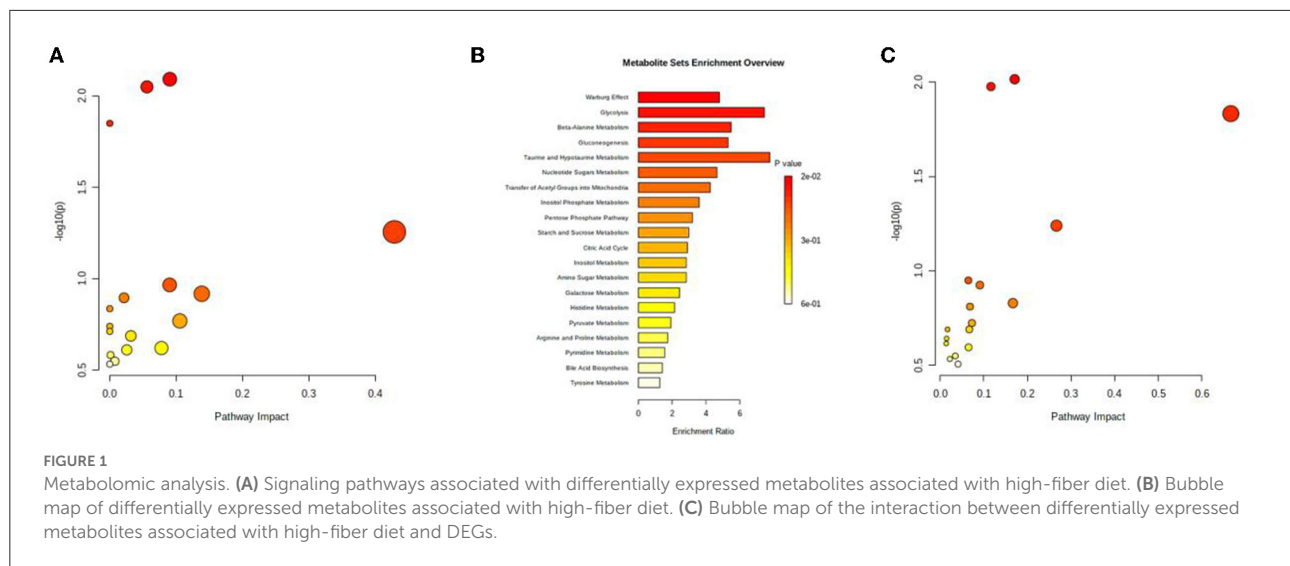
## 3. Results

### 3.1. Differential expression analysis of metabolites associated with high-fiber diet

Potential serum endogenous metabolic markers were identified *via* differential expression analysis ( $|\log_2FC| > 1$ ) and a  $t$ -test ( $P < 0.05$ ) using data from the GEO database and previous studies (68, 69). A total of nine upregulated and seven downregulated metabolites were identified. According to the MetaboAnalyst 5.0 database, the three most relevant pathways ( $P < 0.05$ ) were related to the citrate cycle (TCA cycle); beta-alanine metabolism and the biosynthesis of neomycin, kanamycin, and gentamicin (Figure 1A). In addition, the enrichment analysis of potential metabolic markers revealed that their functions were mainly related to the Warburg effect, glycolysis, and beta-alanine metabolism (Figure 1B). Furthermore, the combined multifunctional analysis of high-fiber-diet-related metabolic DEGs and differential metabolites revealed that these metabolites were mainly involved in the citrate cycle (TCA cycle), beta-alanine metabolism and the biosynthesis of neomycin, kanamycin, and gentamicin, which is consistent with the results of the previous pathway enrichment analysis (Figure 1C). As a result of the above analysis, we identified differential metabolites associated with high fiber diets.

### 3.2. Methylation genes in the peripheral blood of patients with T2DM-AD

The expression profiles of methylation-related genes in the peripheral blood of patients with T2DM-AD were obtained. And a total of 11 upregulated and 10 downregulated methylation-related genes were identified and visualized on a heat map (Supplementary Figure 1A). The transcriptomic data of these DEGs were imported into the R software to construct a volcano plot (Supplementary Figure 1B). The peripheral blood of T2DM-AD patients was analyzed for methylation-related genes.



### 3.3. Cellular distribution and characteristics in the hippocampal tissue of patients with AD

Hippocampal samples from patients with AD were extracted from the GEO database using “Alzheimer’s disease” as the search term, and the scRNA-seq dataset (GSE163577) was selected for further analysis. The single-cell sequencing data of nine patients with AD and eight healthy individuals in the dataset were selected, and cells with gene counts of 200–10,000 and mitochondrial gene proportion of <5% were screened using the Seurat package in R (Supplementary Figures 2A, B). To remove the batch effects of cells include in the analysis and maximize the preservation of the gene expression data of these cells, the “ScaleData” function of the Seurat package was used to regress the variances of “nCount/nFeature\_RNA” and “percent. Mt” (Supplementary Figure 2C). Subsequently, the “RunPCA” function of the Seurat package was used for dimensionality reduction and t-SNE clustering (Supplementary Figures 3A, B). A total of 182,056 cells and 27,005 associated genes were identified after quality control, integration and normalization of data and removal of batch effects from the single-cell sequencing data of patients with AD and healthy individuals. The identified cells were subjected to top-down clustering analysis and annotated according to the known human gastric tissue cell marker genes. A total of 27 cell types were identified (Supplementary Figure 3B), with uniform scattered distribution and good integration of batch effects. The expression of marker genes in each cell type was specific, indicating that the cell annotation results were accurate (Figure 2). Thus, hippocampal tissue of AD patients was examined with respect to its distribution and characteristics.

### 3.4. Screening and enrichment analysis of marker genes

Based on the results of cell annotation, different types of cell subpopulations were identified using the Seurat package, and DEGs in different cell subpopulations in the hippocampal tissue of patients with AD and healthy individuals were screened using the FindMarkers function. A total of 12,610 DEGs were identified and visualized on a heat map (Figure 3A). GO analysis revealed that the identified DEGs were mainly enriched in cellular responses to nitric oxide, muscle cell differentiation, and RNA polymerase II transcriptional regulation complex (Figure 3B). KEGG analysis revealed that the genes were mainly enriched in pathways associated with autophagy, cellular senescence, AGE–RAGE signaling in diabetic complications and NF–kappa B signaling (Figure 3C).

### 3.5. Interaction network of high-fiber-diet-related metabolites, methylation-related DEGs associated with T2DM–AD, and single-cell marker genes associated with AD

There were 24 high-fiber-diet–T2DM–AD marker genes identified by intersecting high-fiber-diet-related metabolites with methylation-related DEGs associated with T2DM (Figure 4A). The STRING (version 11.0) database was used to construct a gene interaction network for these marker genes. The species selected was “Homo sapiens.” To identify hub genes (Figures 4B–D), the cytoHubba plug-in in Cytoscape 3.7.2 software was used to construct a protein–protein interaction

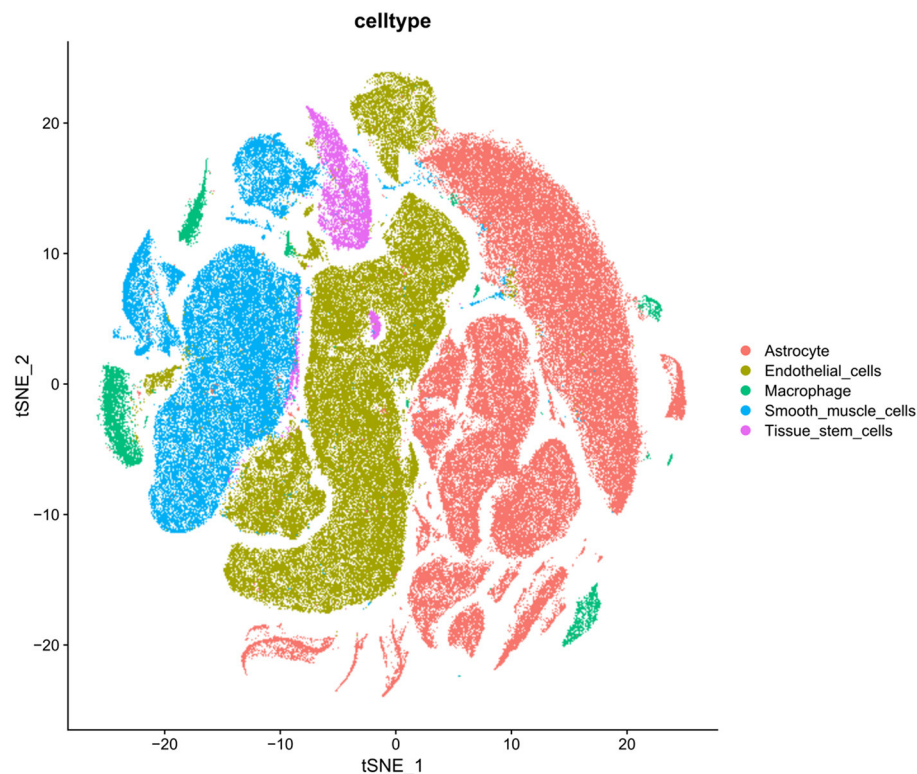


FIGURE 2  
Annotated distribution maps of cells in tSNE map.

network based on network topology, calculate degree, closeness, and betweenness values, and select the size of the values for ranking. Top hub genes included SYNE1, ANK2, SPEG, PDZD2, KALRN, PTPRM, PTPRK, BIN1, DOCK9, and NPNT. As a result, we constructed a network of interactions between high-fiber diet-associated metabolites, methylation-associated DEGs associated with T2DM-AD, and single-cell marker genes related to AD. Functional and pathway enrichment analyses of the 24 high-fiber-diet-T2DM-AD-related marker genes were performed using Metascape. GO enrichment analysis revealed a total of 245 biological processes (BPs), 33 cellular components (CCs), and 26 molecular functions (MFs). BPs included muscle cell differentiation, muscle cell development, cell-cell adhesion mediated by integrin, CC assembly involved in morphogenesis, and nephron development. MFs included transmembrane receptor protein tyrosine phosphatase activity, transmembrane receptor protein phosphatase activity, protein serine/threonine kinase activity, protein tyrosine phosphatase activity, and cysteine-type endopeptidase activity. CCs included contractile fibers, cell-cell junction, sarcomere, T-tubules, and myofibrils (Figures 5A–D). According to KEGG pathway enrichment analysis, the marker genes were enriched in two pathways (Figures 5E, F), of which autophagy was the pathway of interest in this study.

### 3.6. Molecular docking validation

The most significantly altered metabolic markers, including phosphoenolpyruvate and acetamidobenzoic acid, as well as the top three core proteins, SYNE1 (4DXR), ANK2 (5Y4E), and SPEG (6CY6) (the corresponding structural domains of the proteins are mentioned in parentheses) were analyzed with the AutoDock Tools (version 1.5.6) software. Smaller the binding energy, the stronger the binding capacity. Table 1 shows that phosphoenolpyruvate and acetamidobenzoic acid had adequate binding affinities for the core proteins SYNE1 (4DXR), ANK2 (5Y4E), and SPEG (6CY6). Acetamidobenzoic acid had the strongest binding affinity for the core protein SPEG (6CY6), with an RMSD value of <2.00 (Figure 6). Docking the active molecule with the corresponding target protein in Discovery Studio 2019 revealed that acetamidobenzoic acid binds *via* hydrogen and hydrophobic bonds to SPEG (6CY6). Acetamidobenzoic acid forms hydrogen bonds with amino acid residues at position 31 (ARG) and 123 (ILE) and hydrophobic bonds with amino acid residues at position 159 (ALA) and 150 (PHE) of the structural domain of SPEG (6CY6) (Figure 6). Acetamidobenzoic acid, a metabolite associated with high-fiber diet, may target SPEG in the hippocampus and affect autophagy related pathway.



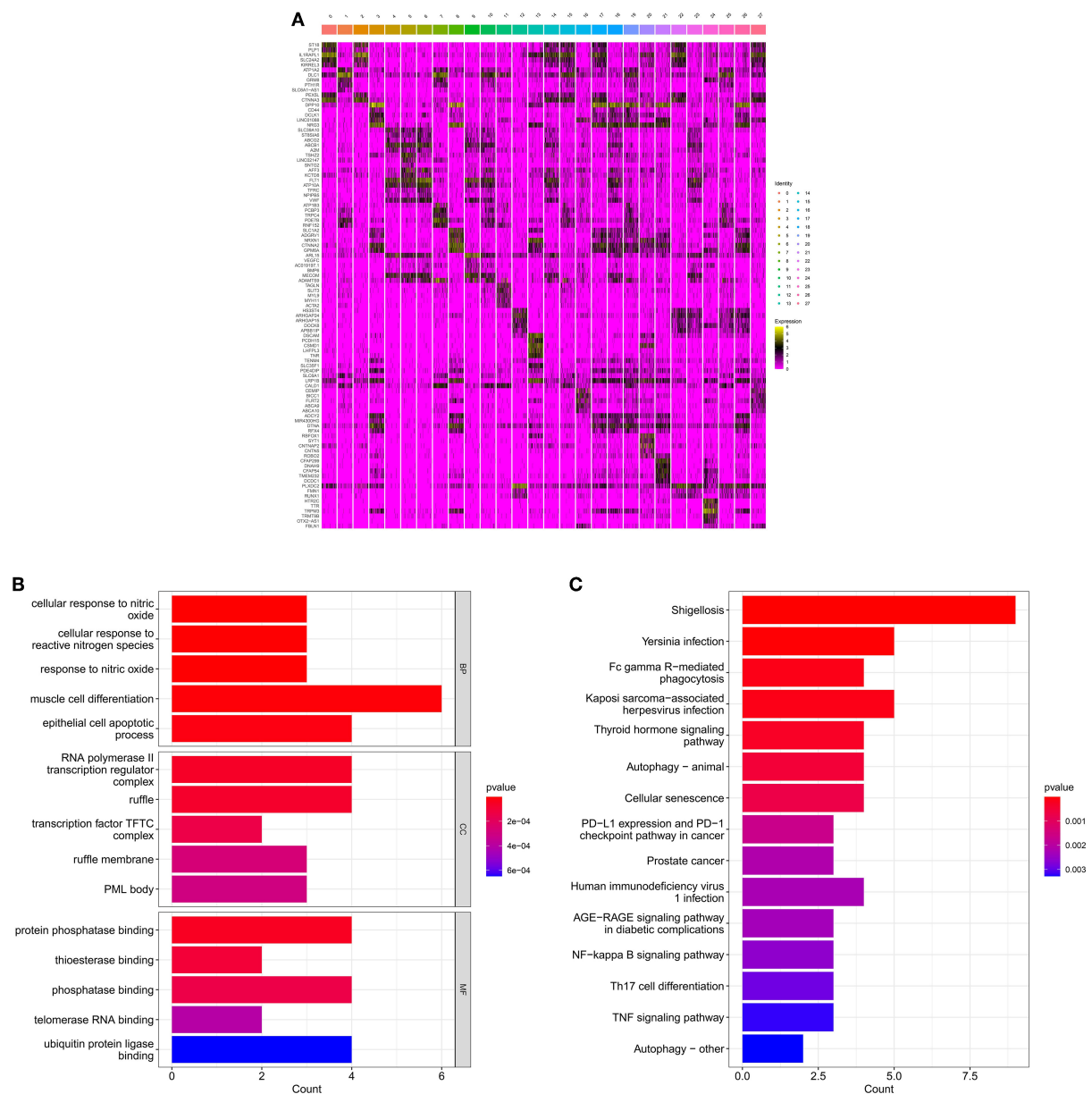


**FIGURE 3**  
Enrichment analysis for the identification of marker genes. **(A)** Heat map demonstrating the distribution of marker genes. **(B)** Histogram of GO enrichment analysis of marker genes. **(C)** Histogram of KEGG functional analysis of marker genes.

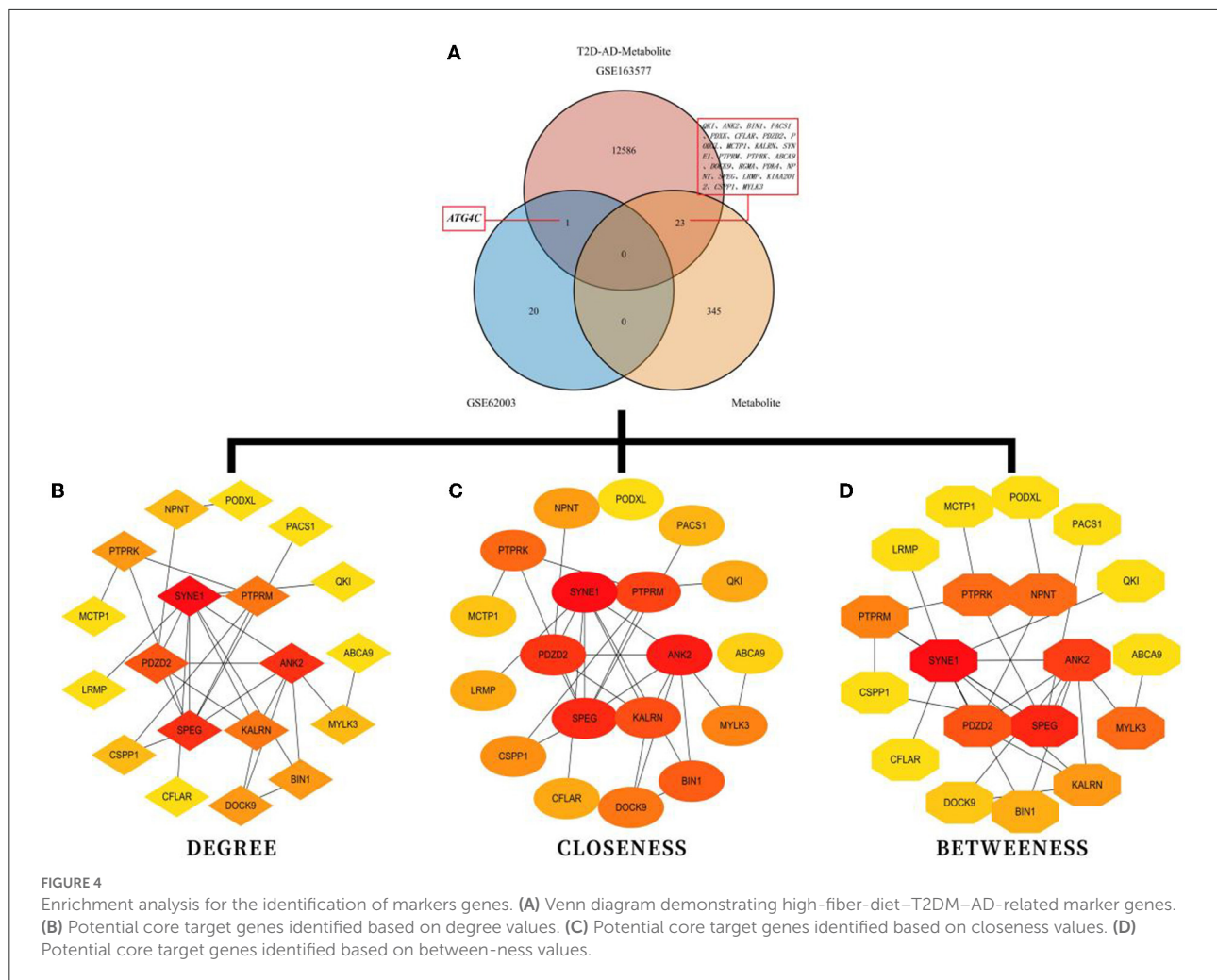
## Discussion

In this study, metabolites and signaling pathways associated with high-fiber diet were identified based on databases. The GEO database was used to identify 10 core high-fiber-diet-T2DM-AD-related marker genes, whose functions are mainly related to autophagy. The results of molecular docking suggested that high-fiber-diet-associated metabolites can stably bind to the core high-fiber diet-T2DM-AD-associated proteins, with

the most stable binding observed between SPEG (6CY6) and acetamidobenzoic acid. These results suggest that high-fiber diet influences autophagic homeostasis in the hippocampus through binding of the metabolite acetamidobenzoic acid to the SPEG (6CY6) protein and regulation of the hippocampal-hypothalamic endocrine axis, eventually improving the diabetic and neurodegenerative disease states of patients with obesity.

Autophagy is involved in the regulation of lipid metabolism, and its dysregulation in adipose tissue is associated with the

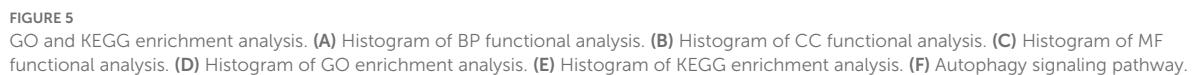




development of metabolic diseases (70, 71). Dysregulation of autophagy alters energy metabolism in hypothalamic neurons and white adipose tissue (WAT). Imbalance of autophagy in hypothalamic neurons can lead to increased caloric intake and weight gain, resulting in obesity and metabolic disorders (72). Mitochondrial autophagy is critical for protecting neurons in the hippocampal CA1 region from ischaemic stress injury (73). In addition to hippocampal CA1 neuronal deletion leading to cognitive impairment, direct neural projections from the ventral pole of hippocampal CA1 to hypothalamic loci are involved in the control of food intake (22, 74). Furthermore, the autophagic pathway is closely related to the pathogenic mechanism underlying the impairment of intestinal mucosal barrier function (75). Impairment of intestinal barrier structure and function is an important pathogenic process in T2DM (76). Autophagy is also involved in the pathological process of AD through several mechanisms, such as the removal of misfolded proteins, and is a novel therapeutic target for AD (77, 78). Therefore, autophagy is closely related to the pathogenesis of obesity and the associated metabolic diseases

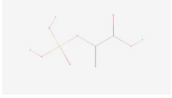
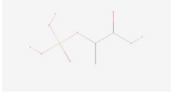
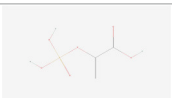
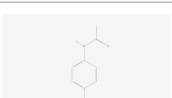
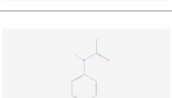
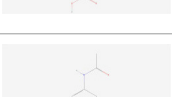
T2DM and neurodegenerative diseases and regulates the hippocampal-hypothalamic neuroendocrine axis. In the present study, KEGG pathway enrichment analysis strongly suggested that the function of high-fiber-diet-T2DM-AD-related DEGs was mainly related to autophagy, which is consistent with the results of previous similar studies (79–82). Therefore, metabolites associated with high-fiber diet may play a role in the pathological process of T2DM and AD among patients with obesity by affecting autophagy in the hippocampus and hypothalamus.

Furthermore, this study demonstrated that the high-fiber-diet-associated metabolite acetamidobenzoic acid can bind to the SPEG (6CY6) protein in the hippocampus and affect autophagic homeostasis in the hippocampus, thus improving the diabetic and neurodegenerative disease states of individuals with obesity. Acetamidobenzoic acid is a derivative of benzoic acid. Benzoic acid derivatives are involved in promoting the activity of the autophagy-lysosome pathway (83). Benzoic acid is involved in the composition of the compound Mn (III) tetrakis (4-benzoic acid) porphyrin chloride (MnTBAP), which reduces



the PPAR signaling pathway or inactivate the phospholipase D signaling pathway to exert an anti-T2DM effect (86). In addition, the bifunctional molecule BPBA synthesized using benzoic acid can target A $\beta$  and inhibit neuroinflammation, which plays a role

TABLE 1 Molecular docking and binding energy.

| Protein      | Compound              | Structure  | DS (LibDockScore) | Vina (kcal.mol <sup>-1</sup> ) | RMSD  |
|--------------|-----------------------|--|-------------------|--------------------------------|-------|
| SYNE1 (4DXR) | Phosphoenolpyruvate   |   | 67.3832           | −2.9                           | 1.276 |
| ANK2 (5Y4E)  | Phosphoenolpyruvate   |   | 44.551            | −3.5                           | 1.491 |
| SPEG (6CY6)  | Phosphoenolpyruvate   |   | 57.2527           | −4.5                           | 1.011 |
| SYNE1 (4DXR) | Acetamidobenzoic acid |   | 90.7005           | −4.9                           | 2.728 |
| ANK2 (5Y4E)  | Acetamidobenzoic acid |   | 56.6351           | −4.5                           | 1.450 |
| SPEG (6CY6)  | Acetamidobenzoic acid |  | 75.5652           | −6.0                           | 1.719 |

in AD (87). To the best of our knowledge, this study is the first to identify the potential role of acetamidobenzoic acid in the pathogenesis of obesity–T2DM–AD, thus laying a foundation for the subsequent development of new drugs.

Striated muscle preferentially expressed protein kinase (SPEG) is a myosin light-chain kinase containing a double serine/threonine kinase domain and multiple immunoglobulin (Ig)-like and proline-rich regions involved in protein–protein interactions (88). SPEG as a single gene can be alternatively spliced into several tissue-specific isoforms, including BPEG (the brain) and SPEG $\alpha$  (skeletal muscle) and SPEG $\beta$  (cardiac muscle) (89–91). Patients with neurodegenerative diseases had significantly lower levels of SPEG methylation, which is strongly associated with obesity. The m6A demethylase FTO may regulate adipocyte differentiation and adipogenesis by regulating the expression of proteins such as gastric starvation hormone, pro-adipogenic factors and peroxisome proliferator-activated receptor, thereby affecting the development of obesity (92). Furthermore, FTO plays a major role in the development of T2DM, as m6A methyltransferases can inhibit adipogenesis, delay the onset and progression of obesity by inhibiting autophagosome formation, blocking mitotic clone expansion, and controlling adipogenic differentiation in mesenchymal stem cells (93). And missense mutations in SPEG are also closely associated with the development of T2DM in GK rats (94). Therefore, acetaminobenzoic acid may target SPEG in the

hippocampus, thereby affecting the autophagic balance of the hippocampus and regulating the hippocampal-hypothalamic endocrine axis, improving diabetic and neurodegenerative disease states.

To the best of our knowledge, this study is the first to report that the SPEG protein in the hippocampus, a peripheral blood biomarker in patients with obesity with concomitant T2DM and neurodegenerative diseases, can bind to acetamidobenzoic acid, a high-fiber-diet-related metabolite, and plays an important role in the development of T2DM and neurodegenerative diseases in patients with obesity. In addition to acetamidobenzoic acid and SPEG, the metabolite phosphoenolpyruvate, which is significantly altered by high-fiber diet, was found to have a strong binding affinity for the core proteins SYNE1 and ANK2, suggesting that high-fiber diet can benefit individuals with obesity through multiple targets and pathways.

However, this study has some limitations. This study was mainly based on bioinformatic analysis of data extracted from databases and lacks relevant experimental validation. Further research is needed to determine exactly how acetamidobenzoic acid binds to hippocampal SPEG proteins.

## 5. Conclusion

Acetamidobenzoic acid, a metabolite associated with high-fiber diet, can target SPEG (6CY6) protein in the

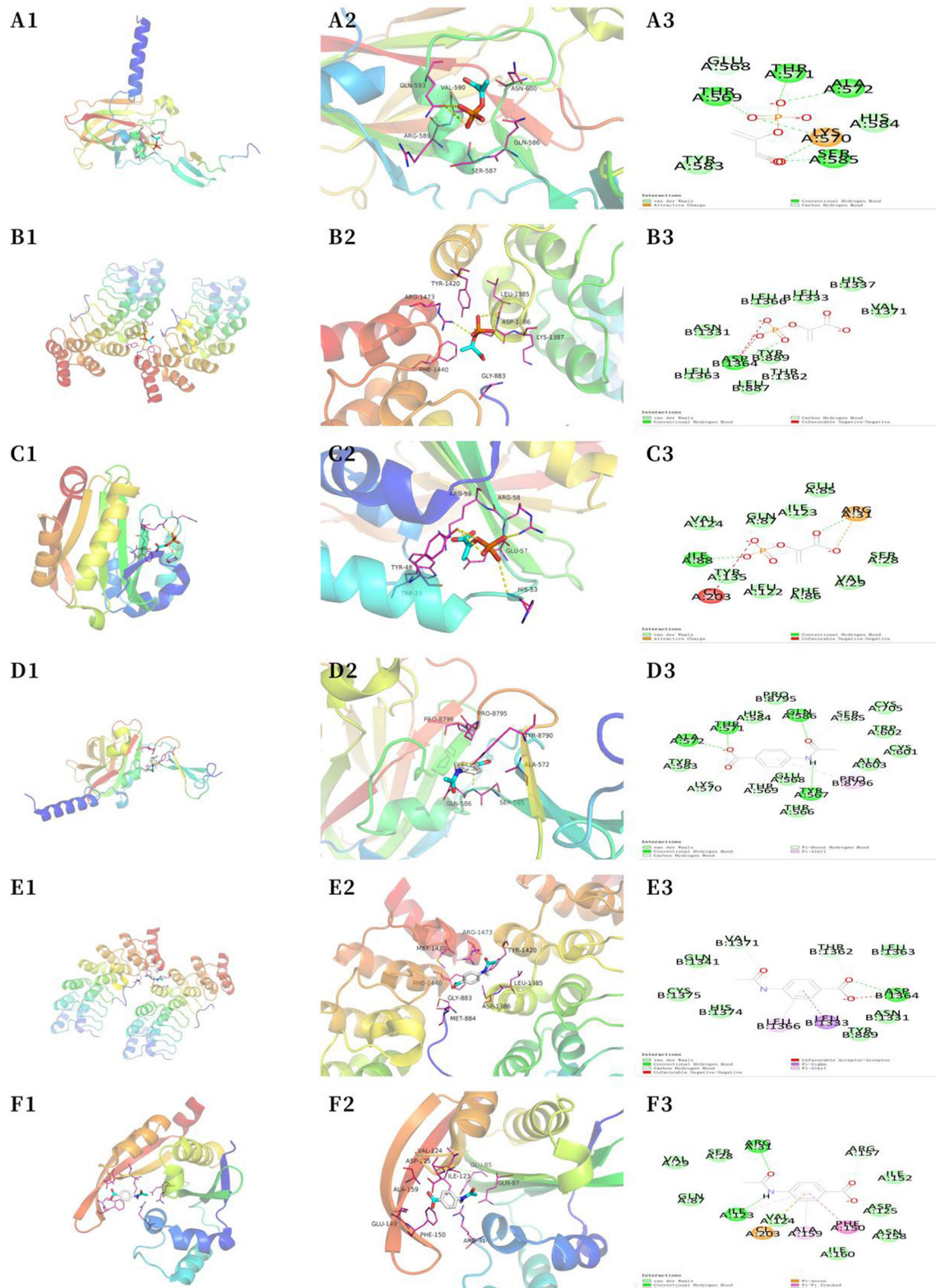


FIGURE 6

Molecular docking analysis. (A) SYNE1 phosphoenolpyruvate (macroscopic) (A1); SYNE1 phosphoenolpyruvate (microscopic) (A2); SYNE1 phosphoenolpyruvate (A3). (B) ANK2 phosphoenolpyruvate (macroscopic) (B1); ANK2 phosphoenolpyruvate (microscopic) (B2); ANK2

(Continued)

## FIGURE 6 (Continued)

phosphoenolpyruvate (B3). (C) SPEG phosphoenolpyruvate (macroscopic) (C1); SPEG phosphoenolpyruvate (microscopic) (C2); SPEG phosphoenolpyruvate (C3). (D) SYNE1 acetamidobenzoic acid (macroscopic) (D1); SYNE1 acetamidobenzoic acid (microscopic) (D2); SYNE1-acetamidobenzoic acid (D3). (E) ANK2-acetamidobenzoic acid (macroscopic) (E1); ANK2-acetamidobenzoic acid (microscopic) (E2); ANK2-acetamidobenzoic acid (E3). (F) SPEG-acetamidobenzoic acid (macroscopic) (F1); SPEG-acetamidobenzoic acid (microscopic) (F2); SPEG-acetamidobenzoic acid (F3).

hippocampus, thereby affecting autophagic homeostasis in the hippocampus, regulating the hippocampal-hypothalamic endocrine axis and eventually improving the diabetic and neurodegenerative disease states of patients with obesity.

## Data availability statement

The original contributions presented in the study are included in the article/Supplementary material, further inquiries can be directed to the corresponding author.

## Ethics statement

Ethical review and approval was not required for the study on human participants in accordance with the local legislation and institutional requirements. Written informed consent from the patients/participants or patients/participants' legal guardian/next of kin was not required to participate in this study in accordance with the national legislation and the institutional requirements.

## Author contributions

LP: conceptualization, methodology, software, investigation, formal analysis, and writing—original draft. YG: data curation, writing—original draft, methodology, software, investigation, and formal analysis. FD: visualization and investigation. NL: conceptualization, funding acquisition, resources, supervision, and writing—review and editing. All authors contributed to the article and approved the submitted version.

## Funding

This study was supported by the Chenzhou Science and Technology Project (lcy12021035): Clinical characteristics of early-onset type 2 diabetes mellitus and analysis of related risk factors.

## Acknowledgments

We would like to thank Shanghai Qiaoyidao Biotechnology Co Ltd and Hainan Superparameter Technology Co Ltd. for providing bioinformatics analysis services. We also thank Bullet Edits Limited for the linguistic editing and proofreading of the manuscript.

## Conflict of interest

The authors declare that the research was conducted in the absence of any commercial or financial relationships that could be construed as a potential conflict of interest.

## Publisher's note

All claims expressed in this article are solely those of the authors and do not necessarily represent those of their affiliated organizations, or those of the publisher, the editors and the reviewers. Any product that may be evaluated in this article, or claim that may be made by its manufacturer, is not guaranteed or endorsed by the publisher.

## Supplementary material

The Supplementary Material for this article can be found online at: <https://www.frontiersin.org/articles/10.3389/fneur.2022.1026904/full#supplementary-material>

## SUPPLEMENTARY FIGURE 1

(A) Heat map of differentially expressed methylation-related genes in the GSE62003 dataset. (B) Heat map of differentially expressed methylation-related genes in the GSE62003 dataset (the red color represents upregulated gene expression, and the green color represents downregulated gene expression).

## SUPPLEMENTARY FIGURE 2

(A) Quality control and data removal plots for the GSE163577 dataset. (B) Distribution of the top 10 most significant genes in the GSE163577 dataset. (C) Distribution of genes before and after normalization of data in the GSE163577 dataset.

## SUPPLEMENTARY FIGURE 3

(A) Principal component analysis distribution map. (B) t-SNE principal component distribution map.



## References

- Gregg EW, Shaw JE. Global health effects of overweight and obesity. *N Engl J Med.* (2017) 377:80–1. doi: 10.1056/NEJMe1706095
- Yang Z-J, Liu J, Ge J-P, Chen L, Zhao Z-G, Yang W-Y, et al. Prevalence of cardiovascular disease risk factor in the Chinese population: the 2007-2008 China national diabetes and metabolic disorders study. *Euro Heart J.* (2012) 33:213–20. doi: 10.1093/eurheartj/ehs205
- Medina-Remón A, Kirwan R, Lamuela-Raventós RM, Estruch R. Dietary patterns and the risk of obesity, type 2 diabetes mellitus, cardiovascular diseases, asthma, and neurodegenerative diseases. *Crit Rev Food Sci Nutr.* (2018) 58:262–96. doi: 10.1080/10408398.2016.1158690
- Saltiel AR, Olefsky JM. Inflammatory mechanisms linking obesity and metabolic disease. *J Clin Invest.* (2017) 127:1–4. doi: 10.1172/JCI92035
- Pugazhenth S, Qin L, Reddy PH. Common neurodegenerative pathways in obesity, diabetes, and Alzheimer's disease. *Biochim Biophys Acta.* (2017) 1863:1037–45. doi: 10.1016/j.bbdis.2016.04.017
- Tang G-Y, Yu P, Zhang C, Deng H-Y, Lu M-X, Le J-H. The neuropeptide-related HERC5/TAC1 interactions may be associated with the dysregulation of lncRNA GAS5 expression in gestational diabetes mellitus exosomes. *Dis Mark.* (2022) 2022:8075285. doi: 10.1155/2022/8075285
- Zhou S-P, Fei S-D, Han H-H, Li J-J, Yang S, Zhao C-Y. A prediction model for cognitive impairment risk in colorectal cancer after chemotherapy treatment. *BioMed Res Int.* (2021) 2021:6666453. doi: 10.1155/2021/6666453
- Liu Z, Li C. A predictive model for the risk of cognitive impairment in patients with gallstones. *BioMed Res Int.* (2021) 2021:3792407. doi: 10.1155/2021/3792407
- Bruce-Keller AJ, Keller JN, Morrison CD. Obesity and vulnerability of the CNS. *Biochim Biophys Acta.* (2009) 1792:395–400. doi: 10.1016/j.bbdis.2008.10.004
- Huynh MKQ, Kinyua AW, Yang DJ, Kim KW. Hypothalamic AMPK as a regulator of energy homeostasis. *Neural Plasticity.* (2016) 2016:2754078. doi: 10.1155/2016/2754078
- Chen Y, Luo Z, Sun Y, Li F, Han Z, Qi B, et al. Exercise improves choroid plexus epithelial cells metabolism to prevent glial cell-associated neurodegeneration. *Front Pharmacol.* (2022) 13:1010785. doi: 10.3389/fphar.2022.1010785
- Kullmann S, Kleinridders A, Small DM, Fritsche A, Häring H-U, Preissl H, et al. Central nervous pathways of insulin action in the control of metabolism and food intake. *Lancet Diabetes Endocrinol.* (2020) 8:524–34. doi: 10.1016/S2213-8587(20)30113-3
- Myers MG, Affinati AH, Richardson N, Schwartz MW. Central nervous system regulation of organismal energy and glucose homeostasis. *Nat Metab.* (2021) 3:737–50. doi: 10.1038/s42255-021-00408-5
- Béanger M, Allaman I, Magistretti PJ. Brain energy metabolism: focus on astrocyte-neuron metabolic cooperation. *Cell Metab.* (2011) 14:724–38. doi: 10.1016/j.cmet.2011.08.016
- Cavadas C, Avelaira CA, Souza GFP, Velloso LA. The pathophysiology of defective proteostasis in the hypothalamus — from obesity to ageing. *Nat Rev Endocrinol.* (2016) 12:723–33. doi: 10.1038/nrendo.2016.107
- Li C, Xu J-J, Hu H-T, Shi C-Y, Yu C-J, Sheng J-Z, et al. Amylin receptor insensitivity impairs hypothalamic POMC neuron differentiation in the male offspring of maternal high-fat diet-fed mice. *Mol Metab.* (2021) 44:101135. doi: 10.1016/j.molmet.2020.101135
- Biebermann H, Kühnen P, Kleinau G, Krude H. “The neuroendocrine circuitry controlled by POMC, MSH, and AGRP. In: Joost H-G, editor. *Appetite Control. Handbook of Experimental Pharmacology.* Berlin: Springer (2012). p. 47–75. doi: 10.1007/978-3-642-24716-3\_3
- Huisman C, Cho H, Brock O, Lim SJ, Youn SM, Park Y, et al. Single cell transcriptome analysis of developing arcuate nucleus neurons uncovers their key developmental regulators. *Nat Commun.* (2019) 10:3696. doi: 10.1038/s41467-019-11667-y
- Lizcano F, Arroyave F. Control of adipose cell browning and its therapeutic potential. *Metabolites.* (2020) 10:471. doi: 10.3390/metabo10110471
- Xu L, Sun X, Depoortere I, Lu J, Guo F, Peeters TL. Effect of motilin on the discharge of rat hippocampal neurons responding to gastric distension and its potential mechanism. *Peptides.* (2008) 29:585–92. doi: 10.1016/j.peptides.2007.12.002
- Feng H, Wang Q, Guo F, Han X, Pang M, Sun X, et al. Nesfatin-1 influences the excitability of gastric distension-responsive neurons in the ventromedial hypothalamic nucleus of rats. *Physiol Res.* (2017) 66:335–44. doi: 10.33549/physiolres.933347
- Cenquizca LA, Swanson LW. Analysis of direct hippocampal cortical field CA1 axonal projections to diencephalon in the rat. *J Comp Neurol.* (2006) 497:101–14. doi: 10.1002/cne.20985
- Boleti AP, Cardoso PH, Frihling BE, e Silva PS, de Moraes LF, Migliolo L. Adipose tissue, systematic inflammation, and neurodegenerative diseases. *Neural Regen Res.* (2023) 18:38. doi: 10.4103/1673-5374.343891
- Kino T. Stress, glucocorticoid hormones, and hippocampal neural progenitor cells: implications to mood disorders. *Front Physiol.* (2015) 6:230. doi: 10.3389/fphys.2015.00230
- Shohayeb B, Diab M, Ahmed M, Ng DCH. Factors that influence adult neurogenesis as potential therapy. *Transl Neurodegener.* (2018) 7:4. doi: 10.1186/s40035-018-0109-9
- Nguyen TD, Hållénus FF, Lin X, Nyman M, Prykhodko O. Monobutyrin and monovalerin affect brain short-chain fatty acid profiles and tight-junction protein expression in apoe-knockout rats fed high-fat diets. *Nutrients.* (2020) 12:E1202. doi: 10.3390/nu12041202
- Weitkunat K, Stuhlmann C, Postel A, Rumberger S, Fankhänel M, Woting A, et al. Short-chain fatty acids and inulin, but not guar gum, prevent diet-induced obesity and insulin resistance through differential mechanisms in mice. *Sci Rep.* (2017) 7:6109. doi: 10.1038/s41598-017-06447-x
- Nitta A, Imai S, Kajiyama S, Matsuda M, Miyawaki T, Matsumoto S, et al. Impact of dietitian-led nutrition therapy of food order on 5-year glycemic control in outpatients with type 2 diabetes at primary care clinic: retrospective cohort study. *Nutrients.* (2022) 14:2865. doi: 10.3390/nu14142865
- Al-Adwi ME, Al-Haswa ZM, Alhmmadi KM, Eissa YA, Hamdan A, Bawadi H, et al. Effects of different diets on glycemic control among patients with type 2 diabetes: a literature review. *Nutr Health.* (2022) 6:26010602211128. doi: 10.1177/02601060221112805
- Aune D, Norat T, Romundstad P, Vatten LJ. Whole grain and refined grain consumption and the risk of type 2 diabetes: a systematic review and dose-response meta-analysis of cohort studies. *Eur J Epidemiol.* (2013) 28:845–58. doi: 10.1007/s10654-013-9852-5
- Fulgioni VL, Brauchla M, Fleige L, Chu Y. Oatmeal-Containing breakfast is associated with better diet quality and higher intake of key food groups and nutrients compared to other breakfasts in children. *Nutrients.* (2019) 11:964. doi: 10.3390/nu11050964
- Cockburn DW, Koropatkin NM. Polysaccharide degradation by the intestinal microbiota and its influence on human health and disease. *J Mol Biol.* (2016) 428:3230–52. doi: 10.1016/j.jmb.2016.06.021
- Wang Y, LaPointe G. Arabinogalactan utilization by *Bifidobacterium longum* subsp. *longum* NCC 2705 and *Bacteroides caccae* ATCC 43185 in monoculture and coculture. *Microorganisms.* (2020) 8:1703. doi: 10.3390/microorganisms8111703
- Li S-C, Liu Y-H, Liu J-F, Chang W-H, Chen C-M, Chen C-YO. Almond consumption improved glycemic control and lipid profiles in patients with type 2 diabetes mellitus. *Metabolism.* (2011) 60:474–9. doi: 10.1016/j.metabol.2010.04.009
- Guess ND, Dornhorst A, Oliver N, Bell JD, Thomas EL, Frost GS. A randomized controlled trial: the effect of inulin on weight management and ectopic fat in subjects with prediabetes. *Nutr Metab.* (2015) 12:36. doi: 10.1186/s12986-015-0033-2
- Cuervo-Zanatta D, Syeda T, Sánchez-Valle V, Irene-Fierro M, Torres-Aguilar P, Torres-Ramos MA, et al. Dietary fiber modulates the release of gut bacterial products preventing cognitive decline in an alzheimer's mouse model. *Cell Mol Neurobiol.* (2022). doi: 10.1007/s10571-022-01268-7. [Epub ahead of print].
- Hamer HM, Jonkers D, Venema K, Vanhoutvin S, Troost FJ, Brummer R-J. Review article: the role of butyrate on colonic function: review: role of butyrate on colonic function. *Aliment Pharmacol Ther.* (2007) 27:104–19. doi: 10.1111/j.1365-2036.2007.03562.x
- Chambers ES, Viardot A, Psichas A, Morrison DJ, Murphy KG, Zac-Varghese SEK, et al. Effects of targeted delivery of propionate to the human colon on appetite regulation, body weight maintenance and adiposity in overweight adults. *Gut.* (2015) 64:1744–54. doi: 10.1136/gutjnl-2014-307913
- Kimura I, Ozawa K, Inoue D, Imamura T, Kimura K, Maeda T, et al. The gut microbiota suppresses insulin-mediated fat accumulation via the short-chain fatty acid receptor GPR43. *Nat Commun.* (2013) 4:1829. doi: 10.1038/ncomms2852
- Wang M, Yang F, Yan X, Chao X, Zhang W, Yuan C, et al. Anti-diabetic effect of banana peel dietary fibers on type 2 diabetic mellitus mice induced

by streptozotocin and high-sugar and high-fat diet. *J Food Biochem.* (2022) 46:e14275. doi: 10.1111/jfbc.14275

41. Ueno H, Haraguchi N, Azuma M, Shiiya T, Noda T, Ebihara E, et al. Active consumption of konjac and konjac products improves blood glucose control in patients with type 2 diabetes mellitus. *J Am Nutr Assoc.* (2021) 1–7. doi: 10.1080/07315724.2021.2002739

42. Lunnon K, Smith RG, Cooper I, Greenbaum L, Mill J, Beeri MS. Blood methylomic signatures of presymptomatic dementia in elderly subjects with type 2 diabetes mellitus. *Neurobiol Aging.* (2015) 36:1600.e1–4. doi: 10.1016/j.neurobiolaging.2014.12.023

43. Morris TJ, Butcher LM, Feber A, Teschendorff AE, Chakravarthy AR, Wojdacz TK, et al. ChAMP: 450k chip analysis methylation pipeline. *Bioinformatics.* (2014) 30:428–30. doi: 10.1093/bioinformatics/btt684

44. Tian Y, Morris TJ, Webster AP, Yang Z, Beck S, Feber A, et al. ChAMP: updated methylation analysis pipeline for illumina BeadChips. *Bioinformatics.* (2017) 33:3982–4. doi: 10.1093/bioinformatics/btx513

45. Pang Z, Chong J, Zhou G, de Lima Moraes DA, Chang L, Barrette M, et al. MetaboAnalyst 5.0: narrowing the gap between raw spectra and functional insights. *Nucleic Acids Res.* (2021) 49:W388–96. doi: 10.1093/nar/gkab382

46. Yang AC, Vest RT, Kern F, Lee DP, Agam M, Maat CA, et al. A human brain vascular atlas reveals diverse mediators of Alzheimer's risk. *Nature.* (2022) 603:885–92. doi: 10.1038/s41586-021-04369-3

47. Satija R, Farrell JA, Gennert D, Schier AF, Regev A. Spatial reconstruction of single-cell gene expression data. *Nat Biotechnol.* (2015) 33:495–502. doi: 10.1038/nbt.3192

48. Chen Y, Luo Z, Lin J, Qi B, Sun Y, Li F, et al. Exploring the potential mechanisms of melilotus officinalis (L.) Pall. in chronic muscle repair patterns using single cell receptor-ligand marker analysis and molecular dynamics simulations. *Dis Mark.* (2022) 2022:9082576. doi: 10.1155/2022/9082576

49. Luo Z, Qi B, Sun Y, Chen Y, Lin J, Qin H, et al. Engineering bioactive M2 macrophage-polarized, anti-inflammatory, miRNA-based liposomes for functional muscle repair: from exosomal mechanisms to biomaterials. *Small.* (2022) 18:2201957. doi: 10.1002/sml.202201957

50. Wu J, Qin J, Li L, Zhang K, Chen Y, Li Y, et al. Roles of the immune/methylation/autophagy landscape on single-cell genotypes and stroke risk in breast cancer microenvironment. *Oxid Med Cell Longev.* (2021) 2021:5633514. doi: 10.1155/2021/5633514

51. Lin W, Wang Q, Chen Y, Wang N, Ni Q, Qi C, et al. Identification of a 6-RBP gene signature for a comprehensive analysis of glioma and ischemic stroke: cognitive impairment and aging-related hypoxic stress. *Front Aging Neurosci.* (2022) 14:951197. doi: 10.3389/fnagi.2022.951197

52. Lin W, Wang Y, Chen Y, Wang Q, Gu Z, Zhu Y. Role of calcium signaling pathway-related gene regulatory networks in ischemic stroke based on multiple WGCNA and single-cell analysis. *Oxid Med Cell Longev.* (2021) 2021:8060477. doi: 10.1155/2021/8060477

53. The Gene Ontology Consortium. Gene ontology consortium: going forward. *Nucleic Acids Res.* (2015) 43:D1049–56. doi: 10.1093/nar/gku1179

54. Zhou Y, Zhou B, Pache L, Chang M, Khodabakhshi AH, Tanaseichuk O, et al. Metascope provides a biologist-oriented resource for the analysis of systems-level datasets. *Nat Commun.* (2019) 10:1523. doi: 10.1038/s41467-019-09234-6

55. Kang X, Sun Y, Yi B, Jiang C, Yan X, Chen B, et al. Based on network pharmacology and molecular dynamics simulations, baicalein, an active ingredient of yiqi qingre ziyin method, potentially protects patients with atrophic rhinitis from cognitive impairment. *Front Aging Neurosci.* (2022) 14:880794. doi: 10.3389/fnagi.2022.880794

56. Sun Y, Luo Z, Chen Y, Lin J, Zhang Y, Qi B, et al. si-Tgfb $\beta$ 1-loading liposomes inhibit shoulder capsule fibrosis via mimicking the protective function of exosomes from patients with adhesive capsulitis. *Biomater Res.* (2022) 26:39. doi: 10.1186/s40824-022-00286-2

57. Lin W-W, Xu L-T, Chen Y-S, Go K, Sun C, Zhu Y-J. Single-Cell transcriptomics-based study of transcriptional regulatory features in the mouse brain vasculature. *BioMed Res Int.* (2021) 2021:7643209. doi: 10.1155/2021/7643209

58. Luo Z, Sun Y, Qi B, Lin J, Chen Y, Xu Y, et al. Human bone marrow mesenchymal stem cell-derived extracellular vesicles inhibit shoulder stiffness via let-7a/Tgfb $\beta$ 1 axis. *Bioact Mater.* (2022) 17:344–59. doi: 10.1016/j.bioactmat.2022.01.016

59. Mering C. STRING: a database of predicted functional associations between proteins. *Nucleic Acids Res.* (2003) 31:258–61. doi: 10.1093/nar/gkg034

60. Sklarczyk D, Gable AL, Nastou KC, Lyon D, Kirsch R, Pyysalo S, et al. The STRING database in 2021: customizable protein–protein networks, and

functional characterization of user-uploaded gene/measurement sets. *Nucleic Acids Res.* (2021) 49:D605–12. doi: 10.1093/nar/gkaa1074

61. Feng W, Yang J, Song W, Xue Y. Crosstalk between heart failure and cognitive impairment via hsa-miR-933/RELB/CCL21 pathway. *BioMed Res Int.* (2021) 2021:2291899. doi: 10.1155/2021/2291899

62. Zhang Q, Yang J, Yang C, Yang X, Chen Y. *Eucommia ulmoides* Oliver-Tribulus terrestris L. drug pair regulates ferroptosis by mediating the neurovascular-related ligand-receptor interaction pathway- a potential drug pair for treatment hypertension and prevention ischemic stroke. *Front Neurol.* (2022) 13:833922. doi: 10.3389/fneur.2022.833922

63. Wang T, Liu G, Guo X, Ji W. Single-Cell analysis reveals the role of the neuropeptide receptor FPR2 in monocytes in kawasaki disease: a bioinformatic study. *Dis Mark.* (2022) 2022:1666240. doi: 10.1155/2022/1666240

64. Shannon P, Markiel A, Ozier O, Baliga NS, Wang JT, Ramage D, et al. Cytoscape: a software environment for integrated models of biomolecular interaction networks. *Genome Res.* (2003) 13:2498–504. doi: 10.1101/gr.1239303

65. Huang J, Liang X, Cai Z. A potential ceRNA network for neurological damage in preterm infants. *BioMed Res Int.* (2021) 2021:2628824. doi: 10.1155/2021/2628824

66. Goodsell DS, Morris GM, Olson AJ. Automated docking of flexible ligands: Applications of autodock. *J Mol Recognit.* (1996) 9:1–5. doi: 10.1002/(SICI)1099-1352(199601)9:1<1::AID-JMR241>3.0.CO;2-6

67. Zhang Y, Zhang J, Sun C, Wu F. Identification of the occurrence and potential mechanisms of heterotopic ossification associated with 17-beta-estradiol targeting MKX by bioinformatics analysis and cellular experiments. *PeerJ.* (2022) 9:e12696. doi: 10.7717/peerj.12696

68. Johansson-Persson A, Barri T, Ulmius M, Önnings G, Dragsted LO. LC-QTOF/MS metabolomic profiles in human plasma after a 5-week high dietary fiber intake. *Anal Bioanal Chem.* (2013) 405:4799–809. doi: 10.1007/s00216-013-6874-5

69. Wu J, Yang D, Gong H, Qi Y, Sun H, Liu Y, et al. Multiple omics analysis reveals that high fiber diets promote gluconeogenesis and inhibit glycolysis in muscle. *BMC Genomics.* (2020) 21:660. doi: 10.1186/s12864-020-07048-1

70. Rabanal-Ruiz Y, Korolchuk V. mTORC1 and nutrient homeostasis: the central role of the lysosome. *IJMS.* (2018) 19:818. doi: 10.3390/ijms19030818

71. Choi C, Son Y, Kim J, Cho YK, Saha A, Kim M, et al. TM4SF5 knockout protects mice from diet-induced obesity partly by regulating autophagy in adipose tissue. *Diabetes.* (2021) 70:2000–13. doi: 10.2337/db21-0145

72. Mattar P, Toledo-Valenzuela L, Hernández-Cáceres MP, Peña-Oyarzún D, Morselli E, Perez-Leighton C. Integrating the effects of sucrose intake on the brain and white adipose tissue: could autophagy be a possible link? *Obesity.* (2022) 30:1143–55. doi: 10.1002/oby.23411

73. Li Q, Zhang T, Wang J, Zhang Z, Zhai Y, Yang G-Y, et al. Rapamycin attenuates mitochondrial dysfunction via activation of mitophagy in experimental ischemic stroke. *Biochem Biophys Res Commun.* (2014) 444:182–8. doi: 10.1016/j.bbrc.2014.01.032

74. Castellazzi M, Patergnani S, Donadio M, Giorgi C, Bonora M, Bosi C, et al. Autophagy and mitophagy biomarkers are reduced in sera of patients with Alzheimer's disease and mild cognitive impairment. *Sci Rep.* (2019) 9:20009. doi: 10.1038/s41598-019-56614-5

75. Huang Y, Wang Y, Feng Y, Wang P, He X, Ren H, et al. Role of endoplasmic reticulum stress-autophagy axis in severe burn-induced intestinal tight junction barrier dysfunction in mice. *Front Physiol.* (2019) 10:606. doi: 10.3389/fphys.2019.00606

76. Xu J, Liang R, Zhang W, Tian K, Li J, Chen X, et al. *Faecalibacterium prausnitzii* -derived microbial anti-inflammatory molecule regulates intestinal integrity in diabetes mellitus mice via modulating tight junction protein expression. *J Diabetes.* (2020) 12:224–36. doi: 10.1111/1753-0407.12986

77. Eshraghi M, Ahmadi M, Afshar S, Lorzadeh S, Adlimoghaddam A, Rezvani Jalal N, et al. Enhancing autophagy in Alzheimer's disease through drug repositioning. *Pharmacol Ther.* (2022) 237:108171. doi: 10.1016/j.pharmthera.2022.108171

78. Moreau K, Fleming A, Imarisio S, Lopez Ramirez A, Mercer JL, Jimenez-Sanchez M, et al. PICALM modulates autophagy activity and tau accumulation. *Nat Commun.* (2014) 5:4998. doi: 10.1038/ncomms5998

79. Spooner HC, Derrick SA, Maj M, Manjarín R, Hernandez GV, Taylor DS, et al. High-Fructose, high-fat diet alters muscle composition and fuel utilization in a juvenile iberian pig model of non-alcoholic fatty liver disease. *Nutrients.* (2021) 13:4195. doi: 10.3390/nu13124195

80. Choi JW, Ohn JH, Jung HS, Park YJ, Jang HC, Chung SS, et al. Carnitine induces autophagy and restores high-fat diet-induced mitochondrial dysfunction. *Metabolism.* (2018) 78:43–51. doi: 10.1016/j.metabol.2017.09.005

81. Morales PE, Monsalves-Álvarez M, Tadinada SM, Harris MP, Ramírez-Sagredo A, Ortiz-Quintero J, et al. Skeletal muscle type-specific mitochondrial adaptation to high-fat diet relies on differential autophagy modulation. *The FASEB J.* (2021) 35:e21933. doi: 10.1096/fj.202001593RR
82. Akhtar A, Sah SP. Insulin signaling pathway and related molecules: role in neurodegeneration and Alzheimer's disease. *Neurochem Int.* (2020) 135:104707. doi: 10.1016/j.neuint.2020.104707
83. Georgousaki K, Tsfantakis N, Gumeni S, Lambrinidis G, González-Menéndez V, Tormo JR, et al. Biological evaluation and in silico study of benzoic acid derivatives from *Bjerkandera adusta* targeting proteostasis network modules. *Molecules.* (2020) 25:666. doi: 10.3390/molecules25030666
84. Pires KM, Ilkun O, Valente M, Boudina S. Treatment with a SOD mimetic reduces visceral adiposity, adipocyte death, and adipose tissue inflammation in high fat-fed mice. *Obesity.* (2014) 22:178–87. doi: 10.1002/oby.20465
85. Brestoff JR, Brodsky T, Sosinsky AZ, McLoughlin R, Stansky E, Fussell L, et al. Manganese [III] tetrakis [5,10,15,20]-Benzoic acid porphyrin reduces adiposity and improves insulin action in mice with pre-existing obesity. *PLoS ONE.* (2015) 10:e0137388. doi: 10.1371/journal.pone.0137388
86. Oh KK. A network pharmacology study to investigate bioactive compounds and signaling pathways of garlic (*Allium sativum* L.) husk against type 2 diabetes mellitus. *J Food Biochem.* (2022) 46:e14106. doi: 10.1111/jfbc.14106
87. Yang T, Zhang L, Shang Y, Zhu Z, Jin S, Guo Z, et al. Concurrent suppression of A $\beta$  aggregation and NLRP3 inflammasome activation for treating Alzheimer's disease. *Chem Sci.* (2022) 13:2971–80. doi: 10.1039/D1SC06071F
88. Hsieh C-M, Fukumoto S, Layne MD, Maemura K, Charles H, Patel A, et al. Striated muscle preferentially expressed genes  $\alpha$  and  $\beta$  are two serine/threonine protein kinases derived from the same gene as the aortic preferentially expressed gene-1. *J Biol Chem.* (2000) 275:36966–73. doi: 10.1074/jbc.M006028200
89. Lee K, Kim J, Köhler M, Yu J, Shi Y, Yang S-N, et al. Blocking Ca $^{2+}$  channel  $\beta$ 3 subunit reverses diabetes. *Cell Rep.* (2018) 24:922–34. doi: 10.1016/j.celrep.2018.06.086
90. Tsutsui Y, Hays FA. A link between alzheimer's and type II diabetes mellitus? Ca $^{2+}$ -mediated signal control and protein localization. *BioEssays.* (2018) 40:1700219. doi: 10.1002/bies.201700219
91. Quick AP, Wang Q, Philippen LE, Barreto-Torres G, Chiang DY, Beavers D, et al. SPEG (Striated muscle preferentially expressed protein kinase) is essential for cardiac function by regulating junctional membrane complex activity. *Circ Res.* (2017) 120:110–19. doi: 10.1161/CIRCRESAHA.116.309977
92. Karra E, O'Daly OG, Choudhury AI, Youssef A, Millership S, Neary MT, et al. A link between FTO, ghrelin, and impaired brain food-cue responsivity. *J Clin Invest.* (2013) 123:3539–51. doi: 10.1172/JCI44403
93. Takala J. Nutrition in acute renal failure. *Crit Care Clin.* (1987) 3:155–66. doi: 10.1016/S0749-0704(18)30566-9
94. Meng Y, Guan Y, Zhang W, Wu Y, Jia H, Zhang Y, et al. RNA-seq analysis of the hypothalamic transcriptome reveals the networks regulating physiopathological progress in the diabetic GK rat. *Sci Rep.* (2016) 6:34138. doi: 10.1038/srep34138



## OPEN ACCESS

EDITED BY  
Yuzhen Xu,  
Tongji University, China

REVIEWED BY  
Yildiz Degirmenci,  
Istanbul Medipol University, Türkiye  
Ren-Qiang Yu,  
Chongqing Medical University, China  
Huan Yang,  
Second Xiangya Hospital, Central South  
University, China

\*CORRESPONDENCE  
Ling Xiong  
✉ 504962348@qq.com  
Chunyan Huang  
✉ 48843432@qq.com

<sup>†</sup>These authors have contributed equally to this work and share first authorship

SPECIALTY SECTION  
This article was submitted to  
Neurological Biomarkers,  
a section of the journal  
Frontiers in Neurology

RECEIVED 22 November 2022  
ACCEPTED 30 December 2022  
PUBLISHED 30 January 2023

CITATION  
Wang Q, Gao Y, Zhang Y, Wang X, Li X, Lin H,  
Xiong L and Huang C (2023) Decreased degree  
centrality values as a potential neuroimaging  
biomarker for migraine: A resting-state  
functional magnetic resonance imaging study  
and support vector machine analysis.  
*Front. Neurol.* 13:1105592.  
doi: 10.3389/fneur.2022.1105592

COPYRIGHT  
© 2023 Wang, Gao, Zhang, Wang, Li, Lin, Xiong  
and Huang. This is an open-access article  
distributed under the terms of the [Creative  
Commons Attribution License \(CC BY\)](#). The use,  
distribution or reproduction in other forums is  
permitted, provided the original author(s) and  
the copyright owner(s) are credited and that  
the original publication in this journal is cited, in  
accordance with accepted academic practice.  
No use, distribution or reproduction is  
permitted which does not comply with these  
terms.

# Decreased degree centrality values as a potential neuroimaging biomarker for migraine: A resting-state functional magnetic resonance imaging study and support vector machine analysis

Qian Wang<sup>1†</sup>, Yujun Gao<sup>2†</sup>, Yuandong Zhang<sup>3†</sup>, Xi Wang<sup>4</sup>, Xuying Li<sup>4</sup>,  
Hang Lin<sup>5</sup>, Ling Xiong<sup>6,7,8\*</sup> and Chunyan Huang<sup>1\*</sup>

<sup>1</sup>Wuhan Third Hospital, Tongren Hospital of Wuhan University, Wuhan, China, <sup>2</sup>Department of Psychiatry, Renmin Hospital of Wuhan University, Wuhan, China, <sup>3</sup>Medical College of Wuhan University of Science and Technology, Wuhan, China, <sup>4</sup>Department of Sleep and Psychosomatic Medicine Center, Taihe Hospital, Affiliated Hospital of Hubei University of Medicine, Shiyan, China, <sup>5</sup>Clinical College of Wuhan University of Science and Technology, Wuhan, China, <sup>6</sup>Department of Anesthesia, Hubei Provincial Hospital of Traditional Chinese Medicine, Wuhan, China, <sup>7</sup>Department of Anesthesia, Affiliated Hospital of Hubei University of Traditional Chinese Medicine, Wuhan, China, <sup>8</sup>Department of Anesthesia, Hubei Province Academy of Traditional Chinese Medicine, Wuhan, China

**Objective:** Misdiagnosis and missed diagnosis of migraine are common in clinical practice. Currently, the pathophysiological mechanism of migraine is not completely known, and its imaging pathological mechanism has rarely been reported. In this study, functional magnetic resonance imaging (fMRI) technology combined with a support vector machine (SVM) was employed to study the imaging pathological mechanism of migraine to improve the diagnostic accuracy of migraine.

**Methods:** We randomly recruited 28 migraine patients from Taihe Hospital. In addition, 27 healthy controls were randomly recruited through advertisements. All patients had undergone the Migraine Disability Assessment (MIDAS), Headache Impact Test – 6 (HIT-6), and 15 min magnetic resonance scanning. We ran DPABI (RRID: SCR\_010501) on MATLAB (RRID: SCR\_001622) to preprocess the data and used REST (RRID: SCR\_009641) to calculate the degree centrality (DC) value of the brain region and SVM (RRID: SCR\_010243) to classify the data.

**Results:** Compared with the healthy controls (HCs), the DC value of bilateral inferior temporal gyrus (ITG) in patients with migraine was significantly lower and that of left ITG showed a positive linear correlation with MIDAS scores. The SVM results showed that the DC value of left ITG has the potential to be a diagnostic biomarker for imaging, with the highest diagnostic accuracy, sensitivity, and specificity for patients with migraine of 81.82, 85.71, and 77.78%, respectively.

**Conclusion:** Our findings demonstrate abnormal DC values in the bilateral ITG among patients with migraine, and the present results provide insights into the neural mechanism of migraines. The abnormal DC values can be used as a potential neuroimaging biomarker for the diagnosis of migraine.

## KEYWORDS

degree centrality, migraine, fMRI, support vector machine, biomarker



## 1. Introduction

Migraine is a nervous system disease characterized by high attack frequency and disability, which seriously endangers people's physical and mental health and quality of life (1). In recent years, the incidence of the disease has been increasing gradually, thereby affecting patients' normal life and work performance (2). The epidemiological survey of headaches in China in 2010 showed that the incidence of migraine in China was 9.3%. However, the pathophysiological mechanism of migraine is not completely understood, and the accuracy of its early diagnosis is low (3). In addition to symptomatic diagnosis, it is necessary to develop auxiliary diagnostic tools for migraine.

Resting-state functional magnetic resonance imaging (rs-fMRI) is a tool with the advantages of non-invasive and high repeatability, which can reveal the spontaneous activity of brain neurons at the resting state (4, 5). The most commonly used method to detect the spontaneous activity of brain regions is the measurement of blood oxygen level-dependent (BOLD) signals based on differences in magnetic properties of oxyhemoglobin (diamagnetic) and deoxyhemoglobin (paramagnetic). In the brain, blood flow and oxygenated hemoglobin fluctuate with the neuron activity, and thus changes in the BOLD signal can be recorded. Over the years, the BOLD-fMRI technology has been widely used to study neuropsychiatric brain diseases, such as temporal lobe epilepsy (6, 7), depression (8, 9), schizophrenia (10, 11), and mild cognitive impairment (12). Thus, fMRI can be used to study the potential imaging mechanisms of various neuropsychiatric diseases.

With the development of high-definition resolution magnetic resonance technology, it has been found that patients with migraine not only manifest organic changes in brain structure (13) but also show changes in functional connectivity after treatment (14). Recent studies have found that the topological properties of brain networks in patients with episodic migraine are altered (15, 16). Among such properties, the imbalance in the topological structure of brain networks in female migraine patients is the most pronounced (15, 17), but there are few studies that have explored the degree centrality of brain networks involved in migraine. Previous rs-fMRI studies revealed a significant difference in the communication between the brain Island, frontal cortex, and apex nucleus (18–20). Although the results are not consistent, it has been shown that migraines are highly communicative, but other studies found that the communication between migraines is low. To solve this problem, we used the intuitive index of the connection state of each spatial unit of the brain. The number of connections between the voxel in stationary fMRI and other voxels in the brain was calculated, and the pattern classification analysis was performed using the degree centrality (DC). A fully automatic program using 8 min of static fMRI can easily obtain DC and is not limited to the selection of priori region or the network definition. Therefore, it is reliable and can be obtained without the need for artificial estimation and image editing features and is widely used to quantify global connectivity. In recent years, researchers have applied DC to conduct clinical research on neuropsychiatric diseases, such as stroke, depression, schizophrenia, and epilepsy (6, 21–23). Three recent studies reported that migraine patients have abnormal DC values in the whole-brain network. Moreover, a significant between-group difference in DC was found using a data-driven

method. Using a data-driven method, Lee et al. found that patients with migraine have altered DC values (24). Other studies found that patients with migraines without aura exhibited significantly smaller DC values in the primary somatosensory cortex and right premotor cortex (25). Moreover, pain intensity is positively correlated with DC in the right amygdala (26). These findings demonstrate differences between migraine patients and bipolar disorder (BD) brain imaging. However, few studies have investigated indicators for the diagnosis, and there are no ideal neuroimaging biomarkers and predictive indicators for the clinical management of migraines. This can be ascribed due to the lack of strict selection of sample size, small sample size, and low sensitivity of analytical methods. Therefore, it is imperative to use DC patterns to explore potential biomarkers for neuroimaging of migraines. The innovation of our study lies in the combination of support vector machine (SVM) and DC analysis methods to identify migraine patients and healthy controls (HCs).

Based on previous studies, we constructed a resting-state brain function network by combining the DC with SVM analysis technology. The differences in DC between migraine patients and HCs were explored to reveal the characteristics of the migraine brain network and find a new method in order to improve the diagnosis of migraine.

## 2. Materials and methods

### 2.1. Subjects

In total, 30 patients with migraine were admitted to the outpatient department and ward of the Department of Psychology of Taihe Hospital in Shiyan from December 2018 to January 2022. The enrolled patients underwent neuropsychological scale assessment and brain resting-state functional magnetic resonance scanning. Among them, 1 patient refused magnetic resonance scanning, and 2 patients were excluded because their head movements were greater than 2 mm during the scanning. Therefore, 27 patients with migraine were enrolled in the study. Inclusion criteria for migraine patients were as follows: (1) The migraine diagnosis was confirmed by the Neurology Department according to the International Headache Society (IHS) criteria (27); (2) right handed; (3) aged 18–60 years; (4) migraine attack interval: no headache attack 3 days before the scan, the day of the scan, and the day after the scan; and (5) sign the relevant informed consent form and voluntarily agree to participate in the research. Exclusion criteria of migraine patients were as follows: (1) previous chronic physical diseases, including cardiovascular and cerebrovascular diseases, hypertension, hyperlipidemia, diabetes, tumors, other types of headache, and other chronic visceral or somatic pain; (2) having a history of chronic mental diseases, such as severe anxiety and depression disorder, sleep disorder, and schizophrenia; (3) history of heroin abuse, alcohol, and other drugs; (4) contraindication of MRI; and (5) pregnancy or lactation. For HCs, 30 healthy volunteers who were matched for the age and gender of migraine patients were enrolled, 2 of whom refused to undergo MRI scanning. Finally, 28 HCs were included in this study. The inclusion criteria of HCs were in line with items 2, 3, and 5 of the inclusion criteria for migraine patients, and the exclusion criteria were in line with items 1, 2, 3, 4, and 5 of the exclusion criteria for migraine patients.



## 2.2. Scale evaluation

Migraine Disability Assessment (MIDAS) and Headache Impact Test – 6 (HIT-6) were used to evaluate the headache and quality of life of all subjects. The MIDAS questionnaire was designed to assess headache-related disabilities and to improve migraine care. The headache patient answered five questions and scored the number of days with limited activity due to migraine in the past 3 months (28). The HIT-6 measures domains related to pain, social functioning, role functioning, vitality, cognitive functioning, and psychological distress (29). The evaluation was performed by two professionally trained graduate students. The study was approved by the ethics committee of the Taihe Hospital, Hubei Medical College, and all participants signed written informed consent forms.

## 2.3. Magnetic resonance imaging scanning procedures

Imaging data were recorded with the Philips 3.0T whole-body MRI scanner. During data acquisition, the participants were required to lie flat in the MRI scanner, relax, close their eyes, and keep their brains awake without any qualitative thinking. Earplugs and eye masks were used to reduce the impact of MRI noise, and foam pads were applied to minimize head movement. All participants were examined by a senior professional MRI technician. Rs-fMRI scanning parameters were as follows: TR = 3,000 ms, TE = 30 ms, matrix =  $64 \times 64$ , FOV =  $220 \times 220$  mm, turning angle  $90^\circ$ , slice thickness = 4 mm, slice spacing = 0, a total of 36 layers, scanning the whole brain for 8 min. T1-weighted fast scrambled phase gradient echo sequence was utilized to obtain structural images, with the following scanning parameters: TR = 7.1 ms, TE = 3.5 ms, FOV =  $220 \times 220$  mm, scanning layer thickness = 1 mm, turning angle  $8^\circ$ , matrix  $352 \times 352$ , scanning 176 layers. The whole-brain scanning time was 4.2 min.

## 2.4. Data processing

The software package DPABI (RRID: SCR\_010501) (30) was run on Matlab 2013a to pre-process the static data as follows: time layer correction, head motion correction, spatial standardization, linear drift, regression to remove covariates (head motion parameters, white matter signals, cerebrospinal fluid signals), and filtering. The images with head translation  $>2$  mm or rotation angle  $>2^\circ$  were rescanned on the same day until they met the scientific research needs. The  $6 \times 6 \times 6$  mm FWHM Gaussian filter was used to smoothen the image data spatially. Finally, in the REST (RRID: SCR\_009641) toolkit, the DC was employed to calculate the Z-valued DC distribution map.

## 2.5. Statistical analyses

Statistical analysis was performed using SPSS version 22.0. Gender differences among migraine patients and HCs were compared with the chi-square test; age was tested by two independent samples *t*-test, and a *p*-value of  $< 0.05$  was considered statistically significant. The measurement data were expressed as  $x \pm s$ . Using gender, age, and years of education as covariates, the REST tool was

used to analyze the DC values of migraine patients and HCs by two independent samples *t*-test, and brain regions with altered DC were identified ( $P < 0.01$ , cluster  $> 30$ , GRF correction). The DC values of patients with abnormal brain regions were extracted, and Pearson's correlation analysis was conducted for the neuropsychological scale ( $P < 0.05$ ).

## 2.6. Classification analyses

The SVM was conducted using a library for SVM (LIBSVM, RRID: SCR\_010243) software package in Matlab (RRID: SCR\_001622). The LIBSVM classifier is trained to learn differences between groups by providing examples in form of (xi, ci), where x represents the DC values of abnormal clusters and c standards for the class label. The grid search method and Gaussian radial basis function kernels were used for parameter optimization. The “leave-pair-out” cross-validation approach was applied using the LIBSVM software to achieve the highest sensitivity and specificity (31).

## 3. Results

### 3.1. Demographic data

A total of 28 migraine patients and 27 HCs were enrolled in the study. There was no significant difference in gender and age between migraine patients and HCs (Table 1).

### 3.2. DC analysis and correlation analysis

Compared with HCs, the DC value of the bilateral ITG in migraine patients was significantly lower and that of left ITG showed a positive linear correlation with MIDAS scores ( $r = -0.37$ ,  $P < 0.05$ ) (Figure 1 and Table 2).

### 3.3. Support vector machine results

The SVM analysis was conducted to determine whether DC values in bilateral ITG can be used to discriminate patients from HCs with optimal sensitivity and specificity (Figure 2). The best results were achieved for DC values in the left ITG. This showed a sensitivity of 85.71%, a specificity of 77.78%, and an accuracy of 81.82%.

## 4. Discussion

This study aimed to examine the DC between global network in patients with migraine and HCs. Reduced DC distribution primarily occurred in the bilateral ITG. We also observed that decreased DC in the left ITG was significantly correlated with MIDAS deficits. The SVM classification result suggested that the decreased DC in the left ITG may be an effective indicator for distinguishing patients with migraine from HCs with the highest sensitivity, specificity, and accuracy.

The results of the DC approach indicated that regions with aberrant cooperation were mainly located in the bilateral ITG.

TABLE 1 Demographic characteristics of the study groups.

| Characteristics      | Patients (n = 28) | Controls (n = 27) | x2 or T | P value           |
|----------------------|-------------------|-------------------|---------|-------------------|
| Gender (male/female) | 12/16             | 12/15             | 0.89    | 0.42 <sup>a</sup> |
| Age (years)          | 38.11 ± 6.49      | 37.37 ± 5.96      | 0.48    | 0.66 <sup>b</sup> |
| MIDAS (scores)       | 160.17 ± 26.45    |                   |         |                   |
| HIT-6 (scores)       | 61.54 ± 10.11     |                   |         |                   |

<sup>a</sup>The *p* value for gender distribution was obtained by chi-square test. <sup>b</sup>The *p* value were obtained by two sample *t*-tests. MIDAS, Migraine Disability Assessment; HIT-6, Headache Impact Test-6.

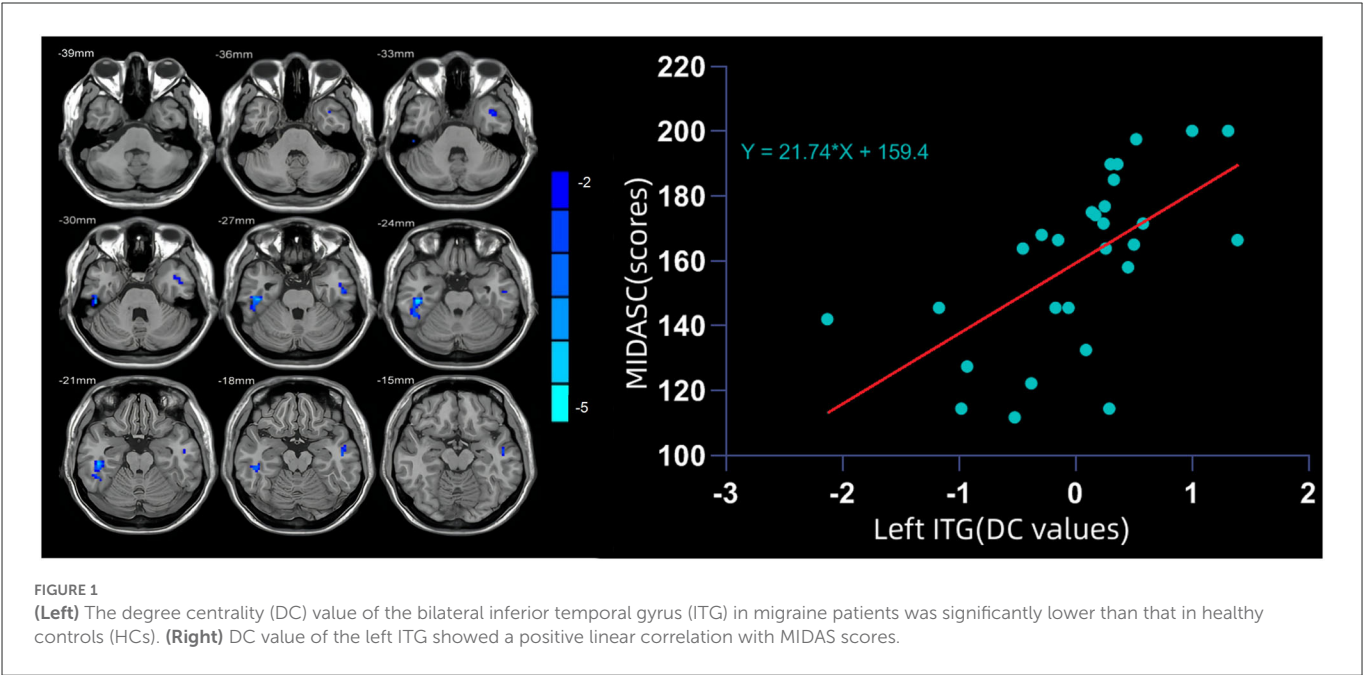


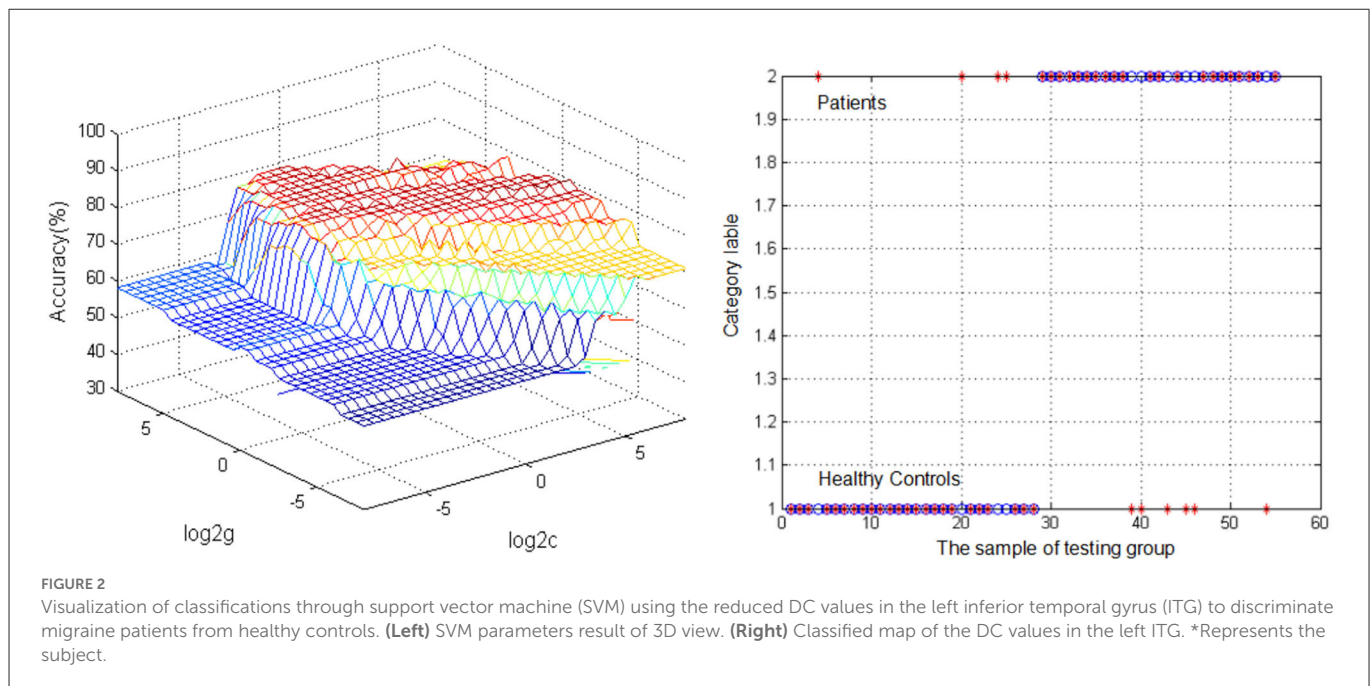
TABLE 2 Alterations of DC between patients and controls.

| Cluster location | Peak (MNI) |     |     | Number of voxels | T-value |
|------------------|------------|-----|-----|------------------|---------|
|                  | X          | Y   | Z   |                  |         |
| Left ITG         | -54        | -12 | -27 | 37               | -3.18   |
| Right ITG        | 45         | -24 | -24 | 87               | -4.49   |

DC, degree centrality; ITG, inferior temporal gyrus.

Previous studies reported that continuous pain stimulation can change the brain microstructure, and this outcome may be reversible (32). The anatomical distance of the pathway or the changes in connectivity across some brain regions may also gradually destroy the cerebral cortex, thereby affecting the entire brain network (33). A prospective study found that the frequency of migraine attacks in migraine patients increased yearly and that the density of gray matter in some brain regions, such as the hippocampus and supramarginal gyrus, decreased significantly compared with 1 year ago, suggesting that persistent pain can interfere with the brain's processing of information, leading to changes in brain structure (34). These findings demonstrate that patients with migraine manifest an abnormal brain structure and brain function to some extent. Furthermore, transcutaneous vagus nerve stimulation can increase the functional connectivity between the ITG and the anterior cingulate cortex/medial pre-frontal cortex and decrease the connectivity between the thalamus subregion and the precuneus (35).

Lai et al. found that the GM of the anterior cingulate cortex of chronic migraine (CM) patients after trauma decreased. During the 12 month follow-up, they found that when the pain disappeared, the gray matter of the thalamus and cerebellum increased, suggesting that the pain processing structure showed adaptive gray matter changes in terms of neuronal plasticity (36, 37). Among these regions, the dorsal anterior cingulate gyrus was significantly related to the course of the disease and was selected as the seed point to perform functional connections with other brain regions. A previous study uncovered the functional connection between the bilateral middle temporal gyrus and the seed regions was enhanced in patients with migraine (38). Although these findings are inconsistent, they can be explained by the following three reasons. First, the subtypes of participants in the studies were inconsistent, and the sample size selection process was different among the studies. Second, the analysis methods varied among the studies. Third, the brain is a complex organ, and thus scanning at different stages of the disease



will obtain different outcomes. Nevertheless, findings from these studies provide valuable information that the brain structure and function of migraine patients exhibit some abnormalities.

We also found that the DC values in the left ITG were positively correlated with MIDAS scores. Sequal and colleagues found that the ITG is abnormally activated in patients with migraine in both task-related and resting state (39–41). Therefore, the present findings demonstrated abnormal activity in the ITG and revealed new insights into the pathomechanisms of migraine patients. The reduced neural activity in the left ITG showed the potential to be an indicator for diagnostic neuroimaging of migraine with a high diagnostic accuracy of 81.82%, a sensitivity of 85.71%, and a specificity of 77.78%. This result implies that ITG may be involved in the pathophysiological mechanism of migraine.

## 5. Limitations

There are several limitations to this study. First, a small sample size was enrolled, and most patients were using drugs for symptomatic treatment. Such drugs may affect brain function and hence will affect the outcomes of this study (11, 42). In the future, we will enroll a large sample size and recruit participants who not using drugs to further validate the present findings. Second, the participants were enrolled at one hospital in one region. We plan to recruit participants from multiple centers in the future. Finally, we did not classify migraine patients into subtypes. Different subtypes of migraine may have different imaging mechanisms (43, 44). Therefore, the imaging mechanisms of different subtypes of migraines should be explored in the future.

## 6. Conclusion

This study reported the changes in the bilateral ITG of patients with migraine. The results suggest that normal DC values in the left ITG can be applied in the clinical diagnosis of migraine.

## Data availability statement

The raw data supporting the conclusions of this article will be made available by the authors, without undue reservation.

## Ethics statement

The study was approved by the Ethics Committee of the Taihe Hospital, Hubei Medical College, and all subjects signed the written informed consent. The patients/participants provided their written informed consent to participate in this study. Written informed consent was obtained from the individual(s) for the publication of any potentially identifiable images or data included in this article.

## Author contributions

QW and LX wrote the manuscript. XW, HL, XL, and YZ collected and analyzed the data. YG and CH conceived and critically reviewed the manuscript. All authors have read and approved the final manuscript.

## Funding

The study was supported by a grant from the Guided Scientific Research Project of Shiyang City (No. 21Y21).

## Acknowledgments

We thank all the participants and MJEEditor ([www.mjeditor.com](http://www.mjeditor.com)) for their linguistic assistance during the preparation of this

manuscript. We also thank all individuals who served as study subjects.

## Conflict of interest

The authors declare that the research was conducted in the absence of any commercial or financial relationships that could be construed as a potential conflict of interest.

## References

1. Attack Postdrome PAM. Migraine Episodes Can Be Divided into Several Phases: Prodrome (Also Known as Premonitory), Aura, Migraine Attack and Postdrome. *Nat Rev Dis Primer*. (2022) 8:1. doi: 10.1038/s41572-022-00335-z
2. Oie LR, Kurth T, Gulati S, Dodick DW. Migraine and risk of stroke. *J Neurol Neurosurg Psychiatry*. (2020) 91:593–604. doi: 10.1136/jnnp-2018-318254
3. Loder E. Migraine diagnosis and treatment. *Prim Care*. (2004) 31:277–92. doi: 10.1016/j.pop.2004.02.003
4. Bhattacharyya T, Gale D, Dewire P, Totterman S, Gale ME, McLaughlin S, et al. The clinical importance of meniscal tears demonstrated by magnetic resonance imaging in osteoarthritis of the knee. *J Bone Joint Surg Am*. (2003) 85:4–9. doi: 10.2106/00004623-200301000-00002
5. Gosseries O, Demertzi A, Noirhomme Q, Tshibanda J, Boly M, Op de Beeck M, et al. Functional Neuroimaging (fMRI, PET and MEg): what do we measure? *Rev Med Liege*. (2008) 63:231–7.
6. Gao Y, Xiong Z, Wang X, Ren H, Liu R, Bai B, et al. Abnormal degree centrality as a potential imaging biomarker for right temporal lobe epilepsy: a resting-state functional magnetic resonance imaging study and support vector machine analysis. *Neuroscience*. (2022) 487:198–206. doi: 10.1016/j.neuroscience.2022.02.004
7. Zhou S, Xiong P, Ren H, Tan W, Yan Y, Gao Y. Aberrant dorsal attention network homogeneity in patients with right temporal lobe epilepsy. *Epilepsy Behav*. (2020) 111:107278. doi: 10.1016/j.yebeh.2020.107278
8. Gao Y, Wang M, Yu R, Li Y, Yang Y, Cui X, et al. Abnormal default mode network homogeneity in treatment-naïve patients with first-episode depression. *Front Psychiatry*. (2018) 9:697. doi: 10.3389/fpsy.2018.00697
9. Guo W, Cui X, Liu F, Chen J, Xie G, Wu R, et al. Increased anterior default-mode network homogeneity in first-episode depression: a replication study. *J Affect Disord*. (2018) 225:767–72. doi: 10.1016/j.jad.2017.08.089
10. Gao Y, Tong X, Hu J, Huang H, Guo T, Wang G, et al. Decreased resting-state neural signal in the left angular gyrus as a potential neuroimaging biomarker of schizophrenia: an amplitude of low-frequency fluctuation and support vector machine analysis. *Front Psychiatry*. (2022) 13:949512. doi: 10.3389/fpsy.2022.949512
11. Cui X, Deng Q, Lang B, Su Q, Liu F, Zhang Z, et al. Less reduced gray matter volume in the subregions of superior temporal gyrus predicts better treatment efficacy in drug-naïve, first-episode schizophrenia. *Brain Imaging Behav*. (2021) 15:1997–2004. doi: 10.1007/s11682-020-00393-5
12. Gao Y, Zhao X, Huang J, Wang S, Chen X, Li M, et al. Abnormal regional homogeneity in right caudate as a potential neuroimaging biomarker for mild cognitive impairment: a resting-state fmri study and support vector machine analysis. *Front Aging Neurosci*. (2022) 14:979183. doi: 10.3389/fnagi.2022.979183
13. Petrovi F, Stojanov D, Aracki-Trenki A, Petrovi J, Petrovi M, Jankovi S. Brain Magnetic Resonance Spectroscopy in Migraine. *Acta Med Medianae*. (2021) 60:77–87. doi: 10.5633/amm.2021.0210
14. Zhang Y, Huang Y, Li H, Yan Z, Zhang Y, Liu X, et al. Transcutaneous auricular vagus nerve stimulation (tavns) for migraine: an fmri study. *Reg Anesth Pain Med*. (2021) 46:145–50. doi: 10.1136/rapm-2020-102088
15. Coppola G, Di Renzo A, Tinelli E, Di Lorenzo C, Scapecchia M, Parisi V, et al. Resting state connectivity between default mode network and insula encodes acute migraine headache. *Cephalalgia*. (2018) 38:846–54. doi: 10.1177/0333102417715230
16. Lee MJ, Park BY, Cho S, Park H, Kim ST, Chung CS. Dynamic functional connectivity of the migraine brain: a resting-state functional magnetic resonance imaging study. *Pain*. (2019) 160:2776–86. doi: 10.1097/j.pain.0000000000001676
17. Liu X, Huang L, Lei L, Xu WU, Zuneng LU, Xiao Z, et al. Advances in research of functional magnetic resonance imaging in migraine patients. *Med Recapitul*. (2019) 25:149–53. doi: 10.3969/j.issn.1006-2084.2019.01.029
18. Hadjikhani N, Ward N, Boshyan J, Napadow V, Maeda Y, Truini A, et al. The missing link: enhanced functional connectivity between amygdala and viscerosensitive cortex in migraine. *Cephalalgia*. (2013) 33:1264–8. doi: 10.1177/0333102413490344
19. Lei M, Zhang JJ, Neurology DO, Hospital Z, University W, Neurology DO. Advance of the correlation between insula and migraine. *Chin J Clin Neurosci*. (2017) 25:470–4. doi: 10.3969/j.issn.1008-0678.2017.04.019
20. Liu HY, Chou KH, Lee PL, Fuh JL, Niddam DM, Lai KL, et al. Hippocampus and amygdala volume in relation to migraine frequency and prognosis. *Cephalalgia*. (2017) 37:1329–36. doi: 10.1177/0333102416678624
21. Lin H, Xiang X, Huang J, Xiong S, Ren H, Gao Y. Abnormal degree centrality values as a potential imaging biomarker for major depressive disorder: a resting-state functional magnetic resonance imaging study and support vector machine analysis. *Front Psychiatry*. (2022) 13:960294. doi: 10.3389/fpsy.2022.960294
22. Guo X, Wang W, Kang L, Shu C, Bai H, Tu N, et al. Abnormal degree centrality in first-episode medication-free adolescent depression at rest: a functional magnetic resonance imaging study and support vector machine analysis. *Front Psychiatry*. (2022) 13:926292. doi: 10.3389/fpsy.2022.926292
23. Wang H, Chen N, Kun-Cheng LI, Duan XG, Radiology DO, Hospital X, et al. Degree centrality in the human functional connectome of basal ganglia stroke patients. *Chin J Magn Reson Imag*. (2016) 7:727–31. doi: 10.12015/issn.1674-8034.2016.10.002
24. Lee MJ, Park BY, Cho S, Kim ST, Park H, Chung CS. Increased connectivity of pain matrix in chronic migraine: a resting-state functional MRI study. *J Headache Pain*. (2019) 20:29. doi: 10.1186/s10194-019-0986-z
25. Zhang J, Su J, Wang M, Zhao Y, Zhang QT, Yao Q, et al. The sensorimotor network dysfunction in migraineurs without aura: a resting-state fMRI study. *J Neurol*. (2017) 264:654–63. doi: 10.1007/s00415-017-8404-4
26. Ke J, Yu Y, Zhang X, Su Y, Wang X, Hu S, et al. Functional alterations in the posterior insula and cerebellum in migraine without aura: a resting-state MRI study. *Front Behav Neurosci*. (2020) 14:567588. doi: 10.3389/fnbeh.2020.567588
27. Headache Classification Committee of the International Headache S. The International Classification of Headache Disorders, 3rd Edition (Beta Version). *Cephalalgia*. (2013) 33:629–808. doi: 10.1177/0333102413485658
28. Stewart WF, Lipton RB, Dowson AJ, Sawyer J. Development and testing of the migraine disability assessment (midas) questionnaire to assess headache-related disability. *Neurology*. (2001) 56:S20–8. doi: 10.1212/WNL.56.suppl\_1.S20
29. Kosinski M, Bayliss MS, Bjorner JB, Ware JE, Garber WH, Batenhorst A, et al. A six-item short-form survey for measuring headache impact: The Hit-6. *Qual Life Res*. (2003) 12:963–74. doi: 10.1023/A:1026119331193
30. Yan C, Zang Y. DPARSF: a MATLAB toolbox for “pipeline” data analysis of resting-state fMRI. *Front Syst Neurosci*. (2010) 4:13. doi: 10.3389/fnsys.2010.00013
31. Chang CC, Lin CJ. LIBSVM: a library for support vector machines. *ACM Trans Intell Syst Technol*. (2011) 2:1–27. doi: 10.1145/1961189.1961199
32. Niddam DM, Lai KL, Tsai SY, Lin YR, Chen WT, Fuh JL, et al. Neurochemical changes in the medial wall of the brain in chronic migraine. *Brain*. (2018) 141:377–90. doi: 10.1093/brain/awx331
33. Zhang X, Wang ZH, Geng ZJ, Zhang Y, Zhang L, Neurology DO. Functional abnormalities in migraine with aura patients: a resting-state fmri study. *J Brain Nerv Dis*. (2016) 24:7–11.
34. Wang Y, Zhang Y, Luo W. Effect of transcutaneous auricular vagus nerve stimulation on fractional amplitude of low-frequency fluctuation in migraine without aura. *J Clin Radiol*. (2019) 38:2010–4. doi: 10.13437/j.cnki.jcr.2019.11.002
35. Redgrave JN, Moore L, Oyekunle T, Ebrahim M, Falidas K, Snowden N, et al. Transcutaneous auricular vagus nerve stimulation with concurrent upper limb repetitive task practice for poststroke motor recovery: a pilot study. *J Stroke Cerebrovasc Dis*. (2018) 27:1998–2005. doi: 10.1016/j.jstrokecerebrovasdis.2018.02.056
36. Riederer F, Marti M, Luechinger R, Lanzenberger R, von Meyenburg J, Gantenbein AR, et al. Grey matter changes associated with medication-overuse headache: correlations

## Publisher's note

All claims expressed in this article are solely those of the authors and do not necessarily represent those of their affiliated organizations, or those of the publisher, the editors and the reviewers. Any product that may be evaluated in this article, or claim that may be made by its manufacturer, is not guaranteed or endorsed by the publisher.



with disease related disability and anxiety. *World J. Biol. Psychiatry*. (2012) 12:517–25. doi: 10.3109/15622975.2012.665175.

37. Lai TH, Chou KH, Fuh JL, Lee PL, Kung YC, Lin CP, et al. Gray matter changes related to medication overuse in patients with chronic migraine. *Cephalalgia*. (2016) 36:1324–33. doi: 10.1177/0333102416630593

38. Gomez-Beldarrain M, Oroz I, Zapirain BG, Ruanova BF, Fernandez YG, Cabrera A, et al. Right fronto-insular white matter tracts link cognitive reserve and pain in migraine patients. *J Headache Pain*. (2015) 17:4. doi: 10.1186/s10194-016-0593-1

39. Chen C, Yan M, Yu Y, Ke J, Xu C, Guo X, et al. Alterations in regional homogeneity assessed by fMRI in patients with migraine without aura. *J Med Syst*. (2019) 43:298. doi: 10.1007/s10916-019-1425-z

40. Schwedt TJ, Chiang CC, Chong CD, Dodick DW. Functional MRI of migraine. *Lancet Neurol*. (2015) 14:81–91. doi: 10.1016/S1474-4422(14)70193-0

41. Crowell GF, Stump DA, Biller J, McHenry LC, Toole JF. The transient global amnesia-migraine connection. *Arch Neurol*. (1984) 41:75–9. doi: 10.1001/archneur.1984.04050130081029

42. Guo W, Liu F, Chen J, Wu R, Li L, Zhang Z, et al. Olanzapine modulates the default-mode network homogeneity in recurrent drug-free schizophrenia at rest. *Aust N Z J Psychiatry*. (2017) 51:1000–9. doi: 10.1177/0004867417714952

43. Pisanu C, Lundin E, Preisig M, Gholam-Rezaee M, Castela E, Pistis G, et al. Major depression subtypes are differentially associated with migraine subtype, prevalence and severity. *Cephalalgia*. (2020) 40:347–56. doi: 10.1177/0333102419884935

44. Si N, Xu H, Mao JH, Li L, Gu W. Relationships of different migraine subtypes and severity of balance disorder. *China J Mod Med*. (2018) 28:104–8. doi: 10.3969/j.issn.1005-8982.2018.23.023





## OPEN ACCESS

## EDITED BY

Wen-Jun Tu,  
Chinese Academy of Medical Sciences and  
Peking Union Medical College, China

## REVIEWED BY

Raouf Hajji,  
University of Sousse, Tunisia  
Malgorzata Burek,  
Julius Maximilian University of  
Würzburg, Germany  
Thomas Webster,  
Interstellar Therapeutics, United States

## \*CORRESPONDENCE

Pan Huang  
✉ 1032857970@qq.com

## SPECIALTY SECTION

This article was submitted to  
Neurological Biomarkers,  
a section of the journal  
Frontiers in Neurology

RECEIVED 29 October 2022

ACCEPTED 20 January 2023

PUBLISHED 08 February 2023

## CITATION

Huang P (2023) Research progress on the  
protective mechanism of a novel soluble  
epoxide hydrolase inhibitor TPPU on ischemic  
stroke. *Front. Neurol.* 14:1083972.  
doi: 10.3389/fneur.2023.1083972

## COPYRIGHT

© 2023 Huang. This is an open-access article  
distributed under the terms of the [Creative  
Commons Attribution License \(CC BY\)](#). The use,  
distribution or reproduction in other forums is  
permitted, provided the original author(s) and  
the copyright owner(s) are credited and that  
the original publication in this journal is cited, in  
accordance with accepted academic practice.  
No use, distribution or reproduction is  
permitted which does not comply with these  
terms.

# Research progress on the protective mechanism of a novel soluble epoxide hydrolase inhibitor TPPU on ischemic stroke

Pan Huang\*

Department of Neurology, People's Hospital of Deyang City, Deyang, Sichuan, China

Arachidonic Acid (AA) is the precursor of cerebrovascular active substances in the human body, and its metabolites are closely associated with the pathogenesis of cerebrovascular diseases. In recent years, the cytochrome P450 (CYP) metabolic pathway of AA has become a research hotspot. Furthermore, the CYP metabolic pathway of AA is regulated by soluble epoxide hydrolase (sEH). 1-trifluoromethoxyphenyl-3(1-propionylpiperidin-4-yl) urea (TPPU) is a novel sEH inhibitor that exerts cerebrovascular protective activity. This article reviews the mechanism of TPPU's protective effect on ischemic stroke disease.

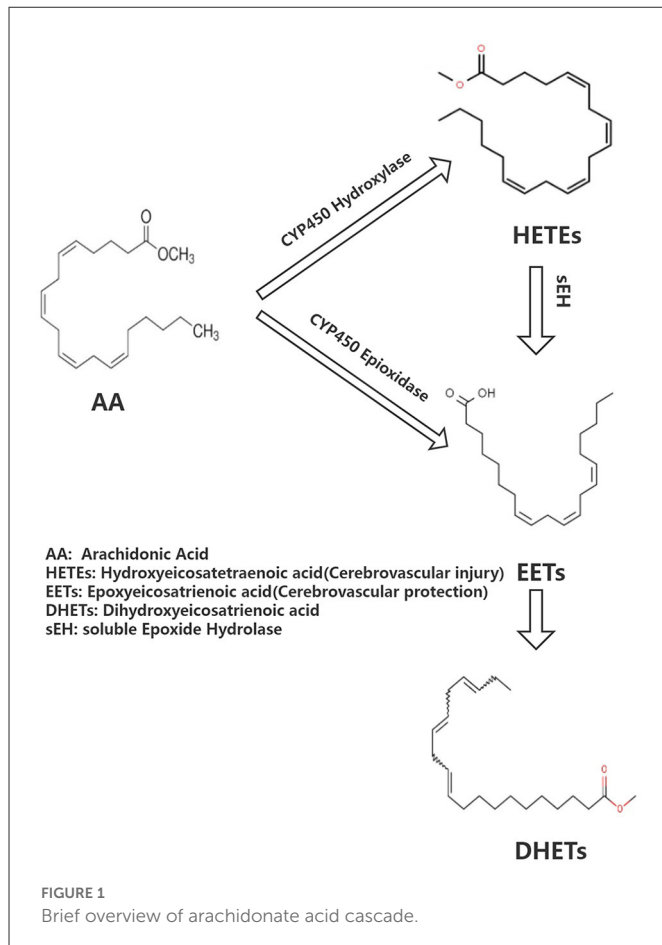
## KEYWORDS

TPPU, ischemic stroke, blood-brain barrier, ischemia reperfusion, arachidonic acid

## 1. Introduction

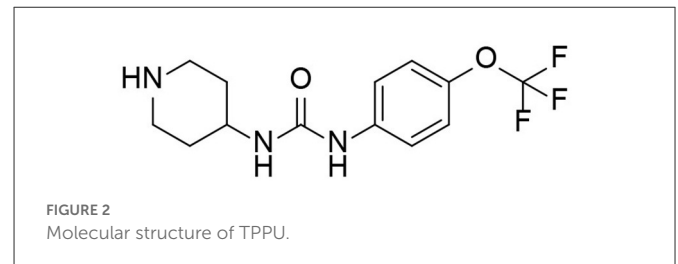
Ischemic stroke is a serious condition that endangers human health. The prevalence and incidence of stroke in China is rising faster than in other countries due to an aging population, the continued high prevalence of risk factors such as hypertension and diabetes and irregular management. Studies have shown that the prevalence of stroke among Chinese residents aged  $\geq 40$  years is 2.58%, or  $\sim 17.5$  million people. The prevalence of stroke in the adult population ( $\geq 18$  years) is  $\sim 1.29\%$ , with significantly higher increases in the male population and in urban areas (male vs. female: 18.1 vs. 7.3%; urban vs. rural: 18.6 vs. 9.9%), and overall China is facing the greatest stroke challenge in the world (1). Neuroprotective therapy has always been the primary choice in ischemic stroke treatment. In the past 30 years, various neuroprotective agents have been developed for the pathophysiology of cerebral ischemia, including antioxidants, calcium channel antagonists, excitatory amino acid receptor inhibitors, and neurotrophic factors. Experimental research and over 100 clinical studies, most of which are effective in animal experiments but ineffective in clinical trials, have resulted in clinical translation failure (2). Clinical guidelines have not yet suggested an effective neuroprotective agent; however, the exploration of an effective neuroprotective agent in humans continues (3).

Arachidonic acid (AA) is the precursor of cerebrovascular active substances in the human heart, and its metabolites are closely associated with the pathogenesis of cerebrovascular diseases (4). In recent years, the cytochrome P450 (CYP) metabolic pathway of AA has been a research hotspot (5). AA generates hydroxyeicosatetraenoic acid (HETEs) and epoxyeicosatrienoic acid (EETs) under the action of CYP hydroxylase and CYP epoxidase, respectively. Furthermore, EETs undergo the action of soluble epoxide hydrolase (sEH) to generate dihydroxyeicosatrienoic acids (DHETs) with weak biological activity (Figure 1). HETEs have potent cerebral vasoconstriction and pro-atherosclerotic effects. EETs possess various biological functions, including vasodilation, regulation of ion channels, and anti-atherosclerosis, as well as a protective effect on cardiovascular and cerebrovascular diseases. Previous studies have shown that the levels of CYP metabolic pathway metabolites (EETs and HETEs) of AA



are closely associated with the deterioration of neurological function following acute ischemic stroke, implying that they may have a role in cerebral ischemia (6).

sEH is a key rate-limiting enzyme regulating EETs. Previous research has shown that the reduction of peripheral blood EETs is not only closely associated with the deterioration of neurological function after ischemic stroke but also with the degree of carotid artery stenosis and plaque instability in patients with cerebral infarction and is regulated by the gene encoding sEH (epoxide hydrolase 2, EPHX<sub>2</sub>) (7–9). Another study has shown that EPHX<sub>2</sub> gene knockout can increase cerebral blood flow, reduce infarct volume in rats with middle-arterial artery occlusion, and has a protective effect on cerebral ischemia. sEH is considered a novel target for ischemic stroke prevention and treatment (10). 1-trifluoromethoxyphenyl-3-(1-propionylpiperidin-4-yl) urea (TPPU) is a novel sEH inhibitor that exerts a cerebrovascular protective effect. This article includes national and international basic original studies on TPPU intervention in ischaemic stroke, excluding: 1. studies that are more than 20 years old; 2. previous review studies on TPPU for ischaemic stroke. This paper provides a comprehensive understanding of the possible mechanisms of TPPU intervention in ischaemic stroke and hopefully contributes to the search for new targets for the treatment of ischaemic stroke.

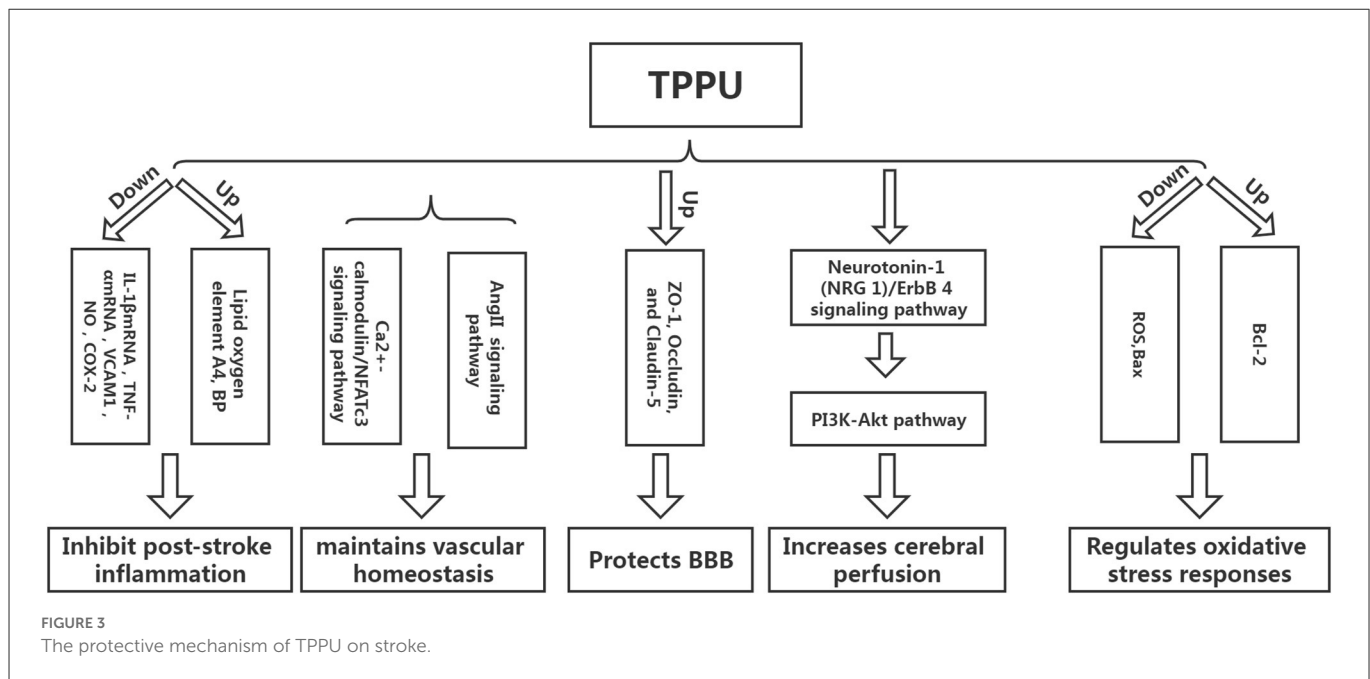


## 2. Research status of sEH inhibitors on cerebral ischemia protection

Neuroprotection against sEH has been a hot topic in recent years. Although EPHX2 gene knockout has a protective effect on experimental cerebral ischemia, it is still distant from clinical prevention and treatment of ischemic stroke. Therefore, sEH inhibitors R&D has attracted much attention. In 2005, the sEH inhibitor 12-(3-adamantan-1-yl-ureido)-dodecanoic acid (AUDA) was applied to the cerebral ischemic nerve. In protective experimental studies, it has been confirmed that AUDA has a protective effect on cerebral ischemia (11). Furthermore, in 2007, the sEH inhibitor, trans-4-[4-(3-adamantan-1-yl-ureido)-cyclohexyloxy]-benzoic acid (t-AUCB), improved the cerebral blood flow and had a protective effect on experimental cerebral ischemia. AUDA and t-AUCB have anti-apoptotic, anti-oxidative, and anti-inflammatory properties, inhibit Ca<sup>2+</sup> influx, protect mitochondria, and antagonize N-Methyl-D-Aspartate Receptor (NMDAR)-mediated excitotoxicity, among other mechanisms in brain protection (12). However, these two traditional sEH inhibitors have shown poor absorption and bioavailability from the gastrointestinal tract. The drug dose needed to obtain the effective blood concentration must be substantial enough because the drugs are easily accumulated in the body, the side effects are severe, and animal tolerance is poor. These traditional sEH inhibitors were found to have short half-lives and unstable blood concentrations *in vivo*, resulting in the failure of clinical translation of traditional sEH inhibitors.

## 3. Overview of TPPU

TPPU is a novel sEH inhibitor synthesized in 2012 by Professor Bruce from the Molecular Bioscience Center of the University of California Veterinary Medicine (13). Bruce Hamock is an entomologist whose research focuses on inhibitors of epoxides in rodents. In his basic research, Professor Bruce found that TPPU has therapeutic and protective effects against various diseases and may be a potential treatment for these diseases. TPPU has a molecular weight of 359.3, allowing it to easily cross the blood-brain barrier and bind to sEH in the central nervous system, inhibiting sEH activity (Figure 2). TPPU has also been proven in animal models of coronary atherosclerotic heart disease to prevent myocardial fibrosis following myocardial infarction and has various functions, including anti-apoptosis, anti-oxidation, and mitochondrial protection (14).



## 4. The protective mechanism of TPPU on stroke

### 4.1. TPPU inhibits inflammatory response after stroke

Inflammation can not only cause a cerebral infarction, but it can also further activate the inflammatory response, creating a vicious circle (15–18). Tu et al. developed a mouse model of cerebral infarction and found that TPPU could significantly promote the recovery of neurological function and reduce the infarct volume and the expression of inflammatory cytokines IL-1 $\beta$ mRNA and TNF- $\alpha$ mRNA, revealing that TPPU may reduce the inflammatory response after infarction and promote the recovery of neurological function (19). Yu et al. used endothelial human Nox4 dominant-negative (EDN) transgenic mice in an ApoE deficient background to mimic the dysfunction of endothelial Nox4 in atherosclerosis-prone conditions. sEH and the inflammatory marker vascular cell adhesion molecule 1 (VCAM1) were upregulated in EDN aortic endothelium. TPPU reduced atherosclerotic lesions in EDN mice. In EDN endothelial cells (ECs), the endoplasmic reticulum stress inhibitor, 4-phenyl butyric acid (4-PBA), downregulated the expression of sEH and VCAM1 and suppressed inflammation. Moreover, its application *in vivo* reduced atherosclerotic lesions of EDN mice (20). In a study by Schmelzer et al., lipopolysaccharide (LPS, 10 mg/kg) was injected into C57BL/6 mice to cause celiac inflammation 24 h before and after the subcutaneous TPPU injection (20 mg/kg) and at the same dose of processed palm in the control group. The findings revealed that all the mice in the experimental group survived, and their blood pressure was restored to pre-LPS levels 24 h later, while all the mice in the control group developed severe hypotension (systolic pressure <40 mmHg) and died within 4 days. Studies have shown that TPPU increases the EET indirect inhibition of nitric oxide synthase, reduces NO produce, hypotension due to reduce inflammation, and

inhibits non-specific inflammation index COX-2 (Cyclooxygenase-2) expression. Simultaneously, suppressing TNF alpha, IL-6, and monocyte chemotactic factor may reduce inflammation, improve lipid oxygen element A4 production, and increase inflammation abreaction (21). TPPU can simulate the role of EET in hemodynamics and anti-inflammatory activities and regulate growth, utility, and the forecast for new atherosclerosis compounds (22) (Figure 3).

### 4.2. TPPU maintains vascular homeostasis

Homeostasis of vascular structure and function is the basis of human physiological activities. If the vascular homeostasis is unbalanced, it may lead to the occurrence of various diseases (23). Vascular injury is one of the reasons for the imbalance of vascular homeostasis. After cerebral infarction, a vascular injury will inevitably occur, and the adventitia of blood vessels will undergo corresponding changes. Studies have shown that neutrophils can be detected in the adventitia 0.5 h following balloon stretch injury in the coronary arteries of the pig, while the intima-media can be detected later. The vascular endothelial growth factor can be detected in the adventitia at the earliest after balloon-stretch injury to the carotid artery of rats (24). The above findings suggest that the adventitia is the origin and active participant of vascular diseases and is one of the novel targets for treating abnormal vascular function. Protecting adventitia may reduce the imbalance of vascular homeostasis, thereby facilitating disease repair. Angiotensin II inhibitor competes with Ang II for AT1. Furthermore, it inhibits vasoconstriction, promotes aldosterone secretion, reverses hypertrophic cardiomyocytes, and lowers blood pressure. However, AngII-related preparations can result in vascular wall thickening and collagen deposition, affecting the remodeling of the vascular adventitia and causing an imbalance in vascular homeostasis. Researchers have found that TPPU

intervention in AngII model mice could significantly prevent AngII-induced vascular adventitia damage. Furthermore, *in vitro* studies have also found that TPPU may affect collagen synthesis *via* the  $\text{Ca}^{2+}$ -calmodulin/NFATc3 signaling pathway, suggesting that TPPU may be one of the novel ways to treat vascular adventitial injury (25).

### 4.3. TPPU protects the blood-brain barrier

Tight-junction proteins between endothelial cells, basement membrane, the foot process of astrocytes, and pericytes are the key structures that maintain the integrity of the blood-brain barrier (BBB). The main pathogenic changes in the early stages of cerebral ischemia are increased BBB permeability and damage of tight junction protein, which causes brain edema, directly or indirectly leading to neurological function damage. Hence, preventing ischemic stroke requires protecting the BBB, inhibiting increased permeability, and alleviating cerebral edema (26). Yi et al. found that TPPU can significantly reduce BBB damage in model rats following cerebral infarction by increasing the expression of ZO-1, Occludin, and Claudin-5, the subunits of tight junction proteins related to BBB (24). Claudin-5 regulates the normal and disturbed states of the BBB. The down-regulation of claudin-5 can directly cause an increase in BBB permeability. ZO-1, a regulator of tight junction proteins, plays an important role in maintaining cytoskeleton formation, cell polarity, and paracellular barrier (27). Multiple studies have reported that tight junction proteins are crucial in regulating BBB integrity and permeability, and the downregulation of tight junction protein expression is associated with increased BBB permeability (28, 29). Yi et al. found that a higher dose of TPPU (2 mg/kg) had a better protective effect on cerebral edema than a lower dose. However, the mechanism may be related to the pharmacokinetics of TPPU, as higher doses did not improve the protective effect (25). TPPU is readily absorbed and slowly eliminated, allowing it to remain in the bloodstream longer than other sEH inhibitors due to its metabolic stability. Previous studies have demonstrated that even at the lowest dose of 0.1 mg/kg, the concentration of TPPU *in vitro* is higher than the IC<sub>50</sub> value. When the TPPU dose exceeds 1 mg/kg, the EET/DHET ratio is lower than the TPPU dose of 1 mg/kg, indicating that TPPU should not be overused (13). Furthermore, studies have shown that TPPU can also reduce the damage to the BBB by reducing the damage to vascular endothelial cells. However, there are few studies on this aspect, and the detailed mechanism is unclear (30).

### 4.4. TPPU increases cerebral perfusion

The decrease in perfusion volume after cerebral infarction is the primary reason for the aggravation of neurological function. Low perfusion can not only stimulate the intensification of the local inflammatory response but also result in the activation of excessive oxygen free radicals, causing the aggravation of the disease (31). Hao et al. established a coil-type carotid artery stenosis model. They found that the neurological function of mice was significantly improved after TPPU intervention compared with the control group.

Furthermore, basic research has shown that the neuroprotective effect of TPPU on cerebral hypoperfusion may be associated with the activation of the Neuregulin-1 (NRG 1)/ErbB 4 signaling pathway, which can further trigger the PI3K-Akt pathway, implying that TPPU can play a multi-targeted protective effect and reduce the degree of nerve damage in mice with chronic cerebral hypoperfusion (32). However, the increase in cerebral perfusion after cerebral infarction is a reason for the deterioration of neurological function; hence, it is particularly important to explore the appropriate dose of TPPU to achieve a balance between the two. Currently, there are limited reports on TPPU improving ischemic stroke perfusion, and more studies are required to demonstrate the specific mechanism in the future.

### 4.5. TPPU regulates oxidative stress responses

Apoptosis is one of the primary reasons for brain injury after ischemic stroke, and oxidative stress is the main pathway of apoptosis. Studies have shown that TPPU can reduce the production of reactive oxygen species (ROS) after ischemic stroke, increase the expression of Bcl-2 protein, and decrease the expression of Bax protein, implying that TPPU can inhibit cell apoptosis after ischemic stroke (33). ROS production plays a key role in the breakdown of the blood-brain barrier during cerebral ischemia/reperfusion (34). After cerebral ischemia, the expression of ROS and inflammatory cytokines increases, causing mitochondrial damage, activation of pro-apoptotic protein Bax, and stimulation of cytochrome c cascade reaction. Moreover, the Bcl-2 protein can inhibit the downstream apoptotic cascade and block the release of cytochrome C (35).

## 5. TPPU future transformation

Due to the widespread existence of sEH in the human body, its metabolic pathway is involved in many diseases, including ischemic stroke, hypertension, heart disease, kidney disease, etc. In theory, the development of drugs that inhibit sEH would seem to reverse or treat the disease. Human drug exploration for sEH has never stopped. From the early discovery of epoxide sEH inhibitors to the design and synthesis of the third generation of urea human sEH inhibitors, the research on human sEH inhibitors has experienced more than 30 years of development. sEH inhibitors have progressed from the initial sEH inhibitors with only micromolar inhibitory activity *in vitro* and poor or no activity *in vivo* to the current sEH inhibitors with nanomolar activity *in vitro* and remarkable pharmacokinetic properties *in vivo* (36).

TPPU is a novel sEH with good activity *in vivo*. It has been used in basic research in various cardiovascular and cerebrovascular diseases. It can play a protective role through a variety of potential mechanisms. However, it has not yet entered the clinical research stage for cerebrovascular diseases. With the development of pharmacology, the effects and mechanisms of TPPU are constantly being discovered and clarified, further proving its rationality and effectiveness as a treatment for ischemic stroke. As the research



progresses, TPPU and its derivatives could be novel drugs for treating ischemic stroke-related diseases.

In conclusion, TPPU can intervene in ischemic stroke in various ways and may be one of the new targets for treating acute ischemic stroke. However, the treatment of acute ischemic stroke with TPPU is still in the exploratory stage, no clinical research has been carried out yet, and more trials are needed to confirm its potential.

## Author contributions

The author confirms being the sole contributor of this work and has approved it for publication.

## References

1. Tu WJ, Hua Y, Yan F, Bian H, Yang Y, Lou M, et al. Prevalence of stroke in China, 2013–2019: a population-based study. *Lancet Reg Health West Pac.* (2022) 28:100550. doi: 10.1016/j.lanwpc.2022.100550
2. Ward NC, Croft KD, Blacker D, Hankey GJ, Barden A, Mori TA, et al. Cytochrome P450 metabolites of arachidonic acid are elevated in stroke patients compared with healthy controls. *Clin Sci.* (2011) 121:501–7. doi: 10.1042/CS20110215
3. Dorrance AM, Rupp N, Pollock DM, Newman JW, Hammock BD, Imig JD. An epoxide hydrolase inhibitor, 12-(3-adamantan-1-yl-ureido)dodecanoic acid (AUDA), reduces ischemic cerebral infarct size in stroke-prone spontaneously hypertensive rats. *J Cardiovasc Pharmacol.* (2005) 46:842–8. doi: 10.1097/01.fjc.0000189600.74157.6d
4. Lee JS, Yaffe K, Lui LY, Cauley J, Taylor B, Browner W, et al. Prospective study of endogenous circulating estradiol and risk of stroke in older women. *Arch Neurol.* (2010) 67:195–201. doi: 10.1001/archneurol.2009.322
5. Huang H, Al-Shabraway M, Wang MH. Cyclooxygenase and cytochrome P450-derived eicosanoids in stroke. *Prostaglandins Other Lipid Media.* (2016) 122:45–53. doi: 10.1016/j.prostaglandins.2015.12.007
6. Yi X, Lin J, Li J, Zhou Q, Han Z. Epoxyeicosatrienoic acids are mediated by EPHX2 variants and CYP plasma metabolite levels in ischemic stroke. *J Atheroscler Thromb.* (2017) 24:1258–66. doi: 10.5551/jat.41145
7. Yi X, Wu L, Liao D, Wang C, Zhang B. Interactions among CYP2C8, EPHX2, and CYP4A11 variants and CYP plasma metabolite levels in ischemic stroke. *J Atheroscler Thromb.* (2016) 23:1286–93. doi: 10.5551/jat.35279
8. Yi X, Liao D, Wang C, Cheng W, Fu X, Zhang B. Cytochrome P450 genetic variants and their metabolite levels associated with plaque stability in ischemic stroke patients. *J Atheroscler Thromb.* (2016) 23:330–8. doi: 10.5551/jat.31120
9. Yi X, Liao D, Wu L, Chen H, Li J, Wang C. Genetic variants, CYP metabolite levels, and symptomatic carotid stenosis in ischemic stroke patients. *J Atheroscler Thromb.* (2016) 23:621–31. doi: 10.5551/jat.32714
10. Zuloaga KL, Zhang W, Roese NE, Alkayed N. Soluble epoxide hydrolase gene deletion improves blood flow and reduces infarct size after cerebral ischemia in reproductively senescent female mice. *Front Pharmacol.* (2015) 15:290. doi: 10.3389/fphar.2014.00290
11. O'Collins VE, Macleod MR, Donnan GA, Horky LL, van der Worp BH, et al. 1026 experimental treatments in acute stroke. *Ann Neurol.* (2006) 59:467–77. doi: 10.1002/ana.20741
12. Iliff JJ, Alkayed NJ. Soluble epoxide hydrolase inhibition: targeting multiple mechanisms of ischemic brain injury with a single agent. *Future Neurol.* (2009) 4:179–99. doi: 10.2217/14796708.4.2.179
13. Liu J, Lin YP, Qiu H, Morisseau C, Rose TE, Wang SH, et al. Substituted phenyl groups improve the pharmacokinetic profile and anti-inflammatory effect of urea-based soluble epoxide hydrolase inhibitors in murine models. *Eur J Pharm Sci.* (2013) 48:619–27. doi: 10.1016/j.ejps.2012.12.013
14. Sirish P, Li N, Liu JY, Lee Kin SS, Hwang SH, Qiu H, et al. Unique mechanistic insights into the beneficial effects of soluble epoxide hydrolase inhibitors in the prevention of cardiac fibrosis. *Proc Natl Acad Sci U S A.* (2013) 110:5618–23. doi: 10.1073/pnas.1221972110
15. Acar BA, Acar T, Vatan MB, Aras YG, Ulaş SB, Eryilmaz HA, et al. Predictive value of systemic immune-inflammation index for cerebral reperfusion and clinical outcomes

## Conflict of interest

The author declares that the research was conducted in the absence of any commercial or financial relationships that could be construed as a potential conflict of interest.

## Publisher's note

All claims expressed in this article are solely those of the authors and do not necessarily represent those of their affiliated organizations, or those of the publisher, the editors and the reviewers. Any product that may be evaluated in this article, or claim that may be made by its manufacturer, is not guaranteed or endorsed by the publisher.

- in patients with acute ischemic stroke undergoing endovascular treatment. *Eur Rev Med Pharmacol Sci.* (2022) 26:5718–28. doi: 10.26355/eurrev\_202208\_29507
16. Mosconi MG, Paciaroni M. Treatments in ischemic stroke: current and future. *Eur Neurol.* (2022) 85:349–66. doi: 10.1159/000525822
17. Welsh P, Lowe GD, Chalmers J, Campbell DJ, Rumley A, Neal BC, et al. Associations of proinflammatory cytokines with the risk of recurrent stroke. *Stroke.* (2008) 39:2226–30. doi: 10.1161/STROKEAHA.107.504498
18. Tuttolomondo A, Pecoraro R, Pinto A. Studies of selective TNF inhibitors in the treatment of brain injury from stroke and trauma: a review of the evidence to date. *Drug Des Devel Ther.* (2014) 8:2221–38. doi: 10.2147/DDDT.S67655
19. Tu R, Armstrong J, Lee KSS, Hammock BD, Sapirstein A, Koehler RC. Soluble epoxide hydrolase inhibition decreases reperfusion injury after focal cerebral ischemia. *Sci Rep.* (2018) 8:5279–93. doi: 10.1038/s41598-018-23504-1
20. Yu W, Li S, Wu H, Hu P, Chen L, Zeng C, et al. Endothelial Nox4 dysfunction aggravates atherosclerosis by inducing endoplasmic reticulum stress and soluble epoxide hydrolase. *Free Radic Biol Med.* (2021) 164:44–57. doi: 10.1016/j.freeradbiomed.2020.12.450
21. Schmelzer KR, Kubala L, Newman JW, Kim IH, Eiserich JP, Hammock BD. Soluble epoxide hydrolase is a therapeutic target for acute inflammation. *Proc Natl Acad Sci U S A.* (2018) 102:9772–7. doi: 10.1073/pnas.0503279102
22. Imig J. Aspects of soluble epoxide hydrolase inhibitors. *Cardiovas Ther.* (2010) 24:169–88. doi: 10.1111/j.1527-3466.2006.00169.x
23. Kim HS, Ullevig SL, Zamora D, Lee CF, Asmis R. Redox regulation of MAPK phosphatase 1 controls monocyte migration and macrophage recruitment. *Proc Natl Acad Sci USA.* (2012) 109:E2803–12. doi: 10.1073/pnas.1212596109
24. Yi XY, Xu CX, Huang P, Zhang LL, Qing T, Li J, et al. 1-Trifluoromethoxyphenyl-3-(1-Propionylpiperidin-4-yl) urea protects the blood-brain barrier against ischemic injury by upregulating tight junction protein expression, mitigating apoptosis and inflammation *in vivo* and *in vitro* model. *Front Pharmacol.* (2020) 11:1197. doi: 10.3389/fphar.2020.01197
25. Li XD, Chen J, Ruan CC, Zhu DL, Gao PJ. Vascular endothelial growth factor-induced osteopontin expression mediates vascular inflammation and neointima formation via Flt-1 in adventitial fibroblasts. *Arterioscler Thromb Vas.* (2012) 32:2250–8. doi: 10.1161/ATVBAHA.112.255216
26. Engelhardt S, Patkar S, Ogunshola OO. Cell-specific blood–brain barrier regulation in health and disease: a focus on hypoxia. *Br J Pharmacol.* (2014) 171:1210–30. doi: 10.1111/bph.12489
27. Park SY. Expression of E-cadherin in epithelial cancer cells increases cell motility and directionality through the localization of ZO-1 during collective cell migration. *Bioengineering.* (2021) 8:65. doi: 10.3390/bioengineering8050065
28. Lochhead JJ, McCaffrey G, Quigley CE, Finch J, DeMarco KM, Nametz N, et al. Oxidative stress increases blood-brain barrier permeability and induces alterations in occludin during hypoxia/reoxygenation. *J Cereb Blood Flow Metab.* (2010) 30:1625–36. doi: 10.1038/jcbfm.2010.29
29. Ye ZY, Xing HY, Wang B, Liu M, Yuan LP. DL-n-butylphthalide protects the blood-brain barrier against ischemia/hypoxia injury via upregulation of tight junction proteins. *Chin Med J.* (2019) 132:1344–53. doi: 10.1097/CM9.0000000000000232
30. Imig JD. Epoxides and soluble epoxide hydrolase in cardiovascular physiology. *Physiol Rev.* (2012) 92:101–30. doi: 10.1152/physrev.00021.2011



31. Ng CF, Churilov L, Yassi N, Kleinig JT, Thijs V, Wu YT, et al. Microvascular dysfunction in blood-brain barrier disruption and hypoperfusion within the infarct posttreatment are associated with cerebral edema. *Stroke*. (2022) 53:1597–605. doi: 10.1161/STROKEAHA.121.036104
32. Hao JH, Chen YX, Yao E, Liu XH. Soluble epoxide hydrolase inhibition alleviated cognitive impairments via NRG1/ErbB4 signaling after chronic cerebral hypoperfusion induced by bilateral carotid artery stenosis in mice. *Brain Res*. (2018) 1699:89–99. doi: 10.1016/j.brainres.2018.07.002
33. Chuang YC, Yang JL, Yang DI. Roles of sestrin 2 and ribosomal protein S6 in transient global ischemia-induced hippocampal neuronal injury. *Int J Mol Sci*. (2015) 16:26406–16. doi: 10.3390/ijms161125963
34. Jurcau A, Ardelean AI. Oxidative stress in ischemia/reperfusion injuries following acute ischemic stroke. *Biomedicines*. (2022) 10:574–574. doi: 10.3390/biomedicines10030574
35. Nhu NT, Li Q, Liu Y, Xu J, Xiao SY, Lee SD. Effects of Mdivi-1 on neural mitochondrial dysfunction and mitochondria-mediated apoptosis in ischemia-reperfusion injury after stroke: a systematic review of preclinical studies. *Front Mol Neurosci*. (2021) 14:778569. doi: 10.3389/fnmol.2021.778569
36. Yi XY, Han Z, Zhou Q, Lin J, Liu P. 20-hydroxyecosatetraenoic acid as a predictor of neurological deterioration in acute minor ischemic stroke. *Stroke*. (2016) 47:3045–7. doi: 10.1161/STROKEAHA.116.015146



## OPEN ACCESS

## EDITED BY

Wen-Jun Tu,  
Chinese Academy of Medical Sciences and  
Peking Union Medical College, China

## REVIEWED BY

Zhaohui He,  
First Affiliated Hospital of Chongqing Medical  
University, China  
Yuto Uchida,  
Johns Hopkins Medicine, United States

## \*CORRESPONDENCE

Anwen Shao  
✉ shaoanwen@zju.edu.cn  
Fengqiang Liu  
✉ 2311009@zju.edu.cn  
Jianmin Zhang  
✉ zjm135@zju.edu.cn

<sup>†</sup>These authors have contributed equally to this work

## SPECIALTY SECTION

This article was submitted to  
Neurological Biomarkers,  
a section of the journal  
Frontiers in Neurology

RECEIVED 18 December 2022

ACCEPTED 31 January 2023

PUBLISHED 23 February 2023

## CITATION

Zhou J, Wang R, Mao J, Gu Y, Shao A, Liu F and  
Zhang J (2023) Prognostic models for survival  
and consciousness in patients with primary  
brainstem hemorrhage.  
*Front. Neurol.* 14:1126585.  
doi: 10.3389/fneur.2023.1126585

## COPYRIGHT

© 2023 Zhou, Wang, Mao, Gu, Shao, Liu and  
Zhang. This is an open-access article  
distributed under the terms of the [Creative  
Commons Attribution License \(CC BY\)](#). The use,  
distribution or reproduction in other forums is  
permitted, provided the original author(s) and  
the copyright owner(s) are credited and that  
the original publication in this journal is cited, in  
accordance with accepted academic practice.  
No use, distribution or reproduction is  
permitted which does not comply with these  
terms.

# Prognostic models for survival and consciousness in patients with primary brainstem hemorrhage

Jingyi Zhou<sup>1†</sup>, Rui Wang<sup>1†</sup>, Jizhong Mao<sup>1†</sup>, Yichen Gu<sup>1</sup>,  
Anwen Shao<sup>1\*</sup>, Fengqiang Liu<sup>1\*</sup> and Jianmin Zhang<sup>1,2,3,4,5\*</sup>

<sup>1</sup>Department of Neurosurgery, Second Affiliated Hospital, School of Medicine, Zhejiang University, Hangzhou, Zhejiang, China, <sup>2</sup>Brain Research Institute, Zhejiang University, Hangzhou, Zhejiang, China, <sup>3</sup>Collaborative Innovation Center for Brain Science, Zhejiang University, Hangzhou, Zhejiang, China, <sup>4</sup>Stroke Research Center for Diagnostic and Therapeutic Technologies of Zhejiang Province, Hangzhou, China, <sup>5</sup>Clinical Research Center for Neurological Diseases of Zhejiang Province, Hangzhou, China

**Objectives:** Primary brainstem hemorrhage (PBSH) is one of the most catastrophic spontaneous intracerebral hemorrhage diseases, with a mortality rate of 70–80%. We explored the predictive factors for survival and consciousness in patients with PBSH (ClinicalTrials.gov ID: NCT04910490).

**Methods:** We retrospectively reviewed 211 patients with PBSH admitted to our institution between January 2014 and October 2020. Clinical outcomes included the 30-day survival rate and the 90-day consciousness rate as evaluated by the National Institutes of Health Stroke Scale score. Multiple logistic regression analysis was performed.

**Results:** The overall 30-day survival rate of 211 patients with PBSH was 70%. Several predictive factors including hematoma volume, hematoma location, activated partial thromboplastin time (APTT) upon admission, and therapeutic strategy were significantly related to 30-day survival. Compared with conservative treatment, stereotactic aspiration in our prediction model is strongly associated with improved 30-day survival (odds ratio, 6.67; 95% confidence interval, 3.13–14.29;  $P < 0.001$ ). The prognosis prediction model of 90-day consciousness including factors such as mydriasis, APTT value, hematoma location, and hematoma volume upon admission has a good predictive effect (AUC, 0.835; 95% confidence interval, 0.78–0.89;  $P < 0.001$ ).

**Conclusion:** In patients with PBSH, conscious state upon admission, coagulation function, hematoma volume, hematoma location, and therapeutic strategy were significantly associated with prognosis. Stereotactic aspiration could significantly reduce the 30-day mortality rate.

## KEYWORDS

primary brainstem hemorrhage, consciousness, multiple logistic regression, predictive factors, stereotactic aspiration

## 1. Introduction

Primary brainstem hemorrhage (PBSH) is one of the most catastrophic spontaneous intracerebral hemorrhage (ICH) diseases, which accounts for approximately 3.8–6.3% of ICH cases (1). PBSH is known to have a poor prognosis, with a mortality rate varying widely from 70 to 80% (2, 3), and the 30-day mortality rate for patients with a Glasgow

Coma Scale (GCS) score of  $< 5$  and a hematoma volume of  $>10$  ml even reaches 100% (4). Previous studies have found that the severity of initial neurological symptoms, hydrocephalus, hematoma volume, and GCS score may be predictors of poor outcomes for patients with PBSH (5, 6), but the conclusions of different studies are not uniform. Currently, there is no standard, widely accepted prognostic model or clinical grading scale for survival and consciousness outcomes, and there are no strong recommendations for clinical treatment strategies for PBSH.

Neurosurgical interventions continue to be controversial and have not been sufficiently investigated because ICH in the posterior fossa has been excluded from large ICH surgical intervention trials in the past (7, 8). The American Heart Association/American Stroke Association Guidelines clearly advise against the surgical evacuation of brainstem hematoma (9). However, others have advocated the efficacy of surgical treatment for PBSH or other brainstem diseases (10, 11). The number of patients with PBSH who underwent surgery enrolled in previous studies has been relatively small, and most studies date back to more than 20 years. Computed tomography (CT)-guided stereotactic hematoma puncture and drainage provided a potential treatment for PBSH, which showed a more favorable outcome than conservative therapy (12, 13). The option of PBSH treatments including conservative treatment or stereotactic surgery remains quite challenging for neurosurgeons. Accordingly, studies on PBSH treatments related to death or a better outcome are useful in clinical practice.

Here, we conducted a retrospective, observational, explorative, and single-center study to analyze the prognostic factors affecting the 30-day survival rate and the 90-day consciousness rate in 211 patients with PBSH undergoing conservative or stereotactic aspiration therapy. The present study aimed to identify chief predictors of survival and consciousness after PBSH.

## 2. Materials and methods

### 2.1. Study design

Using a retrospective, observational, explorative, and single-center study design, we aimed to explore the prognostic factors for survival and consciousness in patients with PBSH. This study was conducted with the approval of the Ethics Committee of the Second Affiliated Hospital Zhejiang University School of Medicine. Due to the retrospective, observational nature of this study and the anonymity of patients, the need for informed consent was waived. The objectives of this study were fully explained to patients or patients' families during follow-up. Moreover, this study tried to present the results of an explorative analysis without an *a priori* hypothesis for the prognostic factors.

### 2.2. Patient selection

We retrospectively reviewed the data of 211 patients with PBSH from 342 consecutive patients admitted to our institution between January 2014 and October 2020. The inclusion criteria were as follows: (1) a diagnosis of PBSH confirmed by CT and (2) complete clinical data (laboratory data, imaging data, and

other clinical data). The exclusion criteria were as follows: (1) secondary brainstem hemorrhage caused by trauma, thrombolytic therapy, cavernous hemangioma, or arteriovenous malformation, (2) surgical treatment of brainstem hemorrhage before admission to our hospital, (3) admission to our hospital more than 10 days after symptom onset, and (4) missed follow-up.

### 2.3. Clinical data

All patients' clinical data were reviewed including general characteristics (age, sex, smoking or drinking habits, previous functional status, and comorbidities), clinical characteristics upon admission (vital signs, blood pressure, pupillary abnormalities, GCS score, and emergency treatment), laboratory data, radiological findings upon admission or during hospitalization, treatment, and outcomes. Clinical data during hospitalization referred to the examination data from admission to hospital discharge when people have recovered sufficiently or can be appropriately rehabilitated elsewhere or died, except for the first data upon admission.

Upon admission to the emergency department, head CT plain scans were performed to assess the severity of the disease. The features evaluated on CT included the location and the extension of hemorrhage, hematoma volume, and the presence of hydrocephalus. Lesions located entirely within the cerebellum, the thalamus, the basal ganglia, or the ventricle were excluded, but lesions extending into these regions from the brainstem were included. Hemorrhage volume is calculated as follows: volume =  $(A \times B \times C)/2$  where A is the greatest hemorrhage diameter by CT, B is the diameter perpendicular to A, and C is the approximate number of CT slices with hemorrhage multiplied by the slice thickness (14), as shown in Figure 1. Hydrocephalus on CT was determined by enlarged ventricles or obstruction to the flow of cerebrospinal fluid within the ventricular system. Clinical data were reviewed, and radiological data were assessed by two trained neurosurgeons blinded to outcome.

### 2.4. Stereotactic aspiration treatment

The selection criteria for surgery were as follows: hematoma volume  $>5$  ml and GCS  $<8$ . All patients included in the study, who meet the selection criteria mentioned earlier and have no contraindications of surgery such as severe disorders of blood coagulation, were offered the option of surgery. Their relatives either agreed to surgical intervention or refused. Patients whose families consented to the surgery were allocated to the surgery group, and those patients whose families refused the surgery were put into the conservative treatment group.

### 2.5. Assessments of outcome

The 30-day survival rate and 90-day consciousness rate were chosen as the primary outcomes. Mortality data were obtained from medical records or by telephone contact with primary care

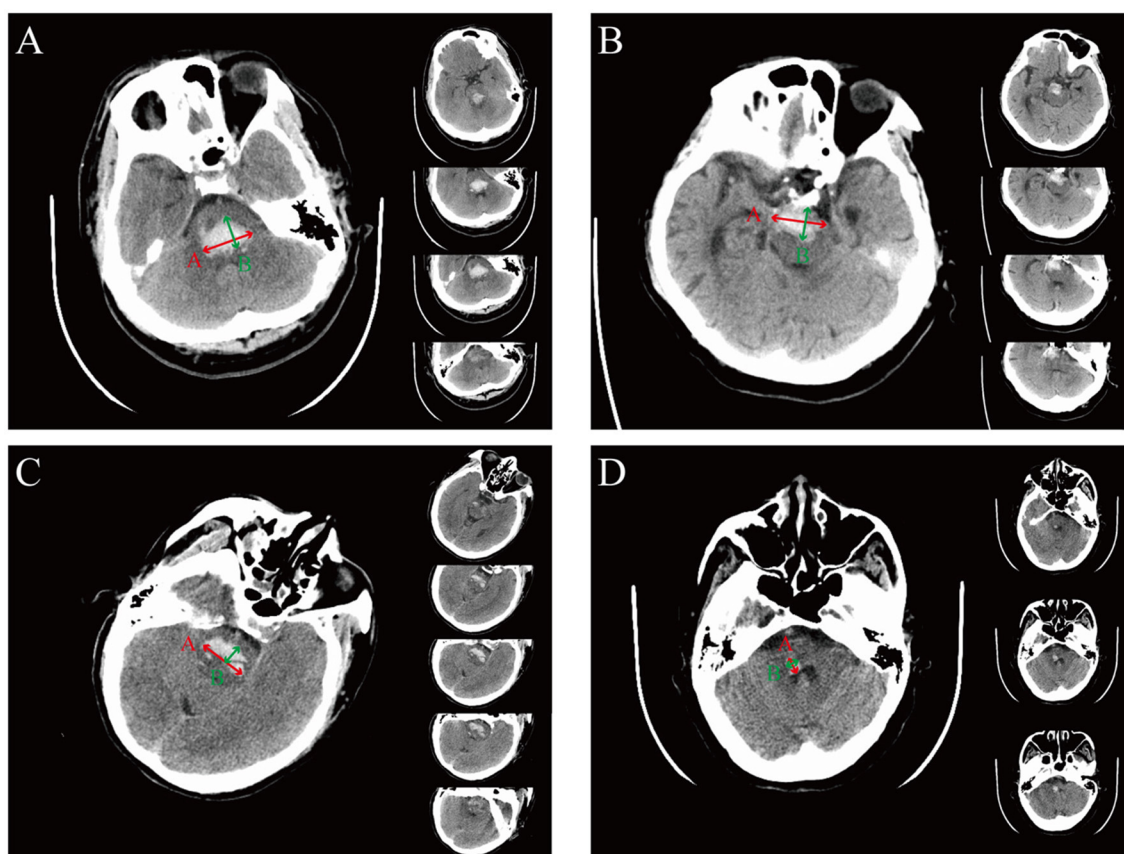


FIGURE 1

The representation of the ABC formula for calculating hemorrhage volume in different hemorrhagic locations. **(A)** Representative images of dorsal hematoma. The A value is defined as the longest segment (red arrow) in the largest hematoma slice, the B value is defined as the longest segment, which is perpendicular to the A segment on the same slice (green arrow), and the C value is defined as the approximate number of CT slices (right panel) with the slice thickness (being 0.5 cm in this example). For this example,  $(A \times B \times C)/2 = [3.2 \times 1.9 \times (4 \times 0.5)]/2 = 6.08 \text{ cm}^3$ . **(B)** Representative images of ventral hematoma. For this example,  $(A \times B \times C)/2 = [3.1 \times 1.5 \times (4 \times 0.5)]/2 = 4.65 \text{ cm}^3$ . **(C)** Representative images of hematoma crossing the midline. For this example,  $(A \times B \times C)/2 = [3.1 \times 1.1 \times (5 \times 0.5)]/2 = 4.26 \text{ cm}^3$ . **(D)** Representative images of hematoma without crossing the midline. For this example,  $(A \times B \times C)/2 = [0.9 \times 0.7 \times (3 \times 0.5)]/2 = 0.47 \text{ cm}^3$ .

physicians or family members. Consciousness was determined based on the National Institutes of Health Stroke Scale (NIHSS) (item 1a: value 0, 1, or 2 for consciousness, value 3 for unconsciousness), which was obtained from a clinic visit at 90-day follow-up or by telephone contact by two trained neurosurgeons blinded to research data.

## 2.6. Statistical analysis

R (version 4.0.3) and RStudio (version 1.4.1106) were used for statistical calculations. Normally distributed continuous variables are presented as mean  $\pm$  standard deviation (SD), and non-normally distributed continuous variables are presented as median with interquartile range (IQR). Normally distributed continuous variables were compared by the two-sided *t*-test, and non-normally distributed continuous variables and ordinal variables were compared by the Mann–Whitney–Wilcoxon test. Categorical variables were compared by the Pearson chi-square test, the continuity-corrected chi-square test, or Fisher's exact test (expected

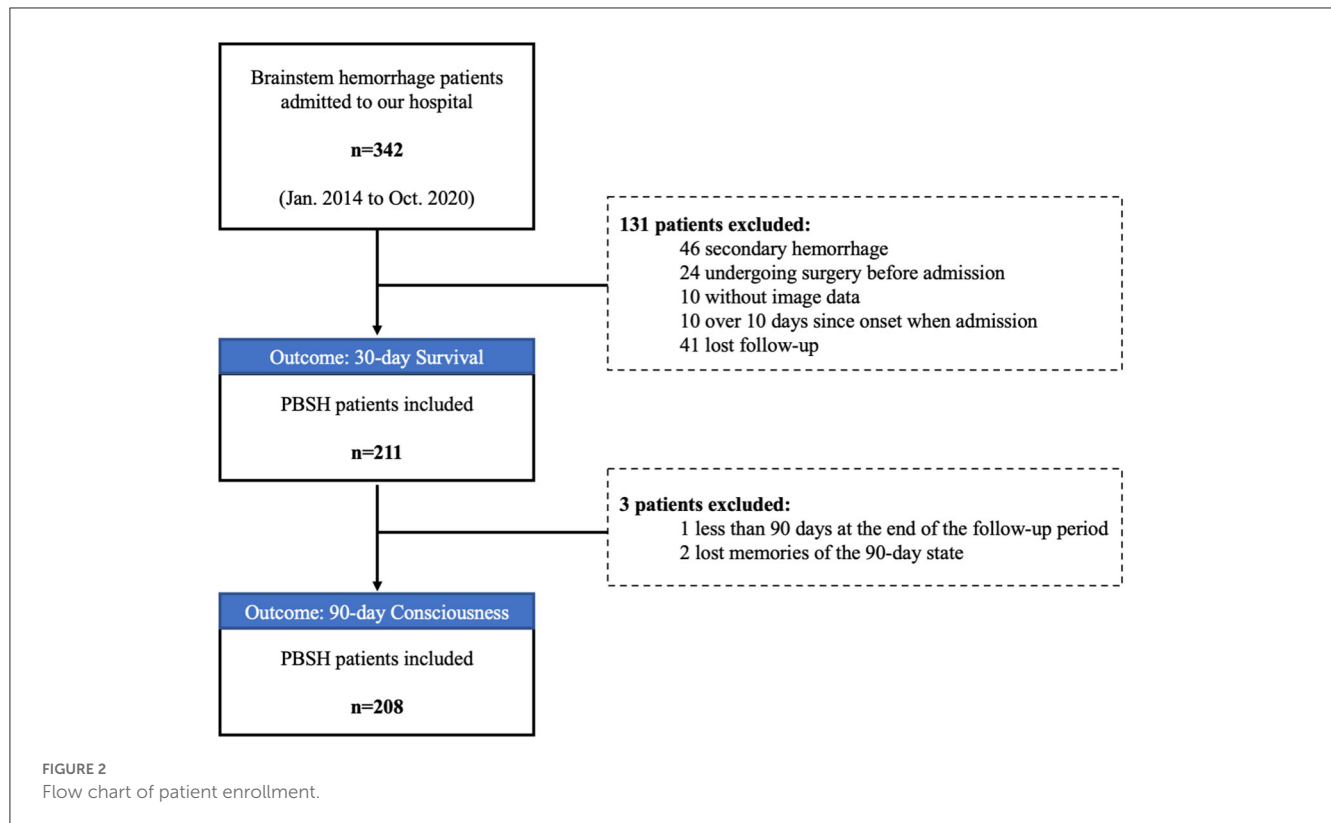
frequency  $<5$ ). Odds ratios (ORs) and 95% confidence intervals (CIs) were also reported.

Univariate analysis was used initially to identify possible relations between outcomes. Variables were only modeled using multiple logistic regression if they were statistically significant and biologically related to clinical outcomes. A pre-treatment prognosis prediction model including only admission indicators and a post-treatment prognosis prediction model including both admission and hospitalization indicators were established. The predictive effect was evaluated by the receiver operating curve (ROC) analysis. For the area under the ROC curve (AUC), a value of  $>0.8$  or  $0.7$ – $0.8$  represents an excellent or good prediction ability, respectively. The *p*-values of  $<0.05$  were regarded as statistically significant.

## 3. Results

### 3.1. Baseline characteristics

A total of 211 patients with PBSH were included in the final analysis (Figure 2). Table 1 shows the general characteristics of



included patients in the baseline and the variance data according to survival outcomes. The median age of the 211 patients was 49 years. Of the 175 (83%) male and 36 (17%) female patients, 153 (73%) had a history of hypertension, 26 (12%) had diabetes, and 21 (10%) had a history of stroke or myocardial infarction. The mean body mass index was  $24.9 \pm 4.4$ , suggesting a trend toward being overweight.

The mean blood pressure upon admission was  $166/95 \pm 31/19$  mmHg (Table 2), which was consistent with previous reports that hypertension was the most common risk factor of PBSH (15, 16). The median GCS score upon admission was 4 (IQR, 3–5), and 90% of patients were in a coma upon admission.

The mean hematoma volume on admission CT scans was  $11.3 \pm 7.9$  ml, and the median volume was 9.6 (IQR, 5.8–14.8) ml. A hematoma crossing the midline of the brainstem was found in 190 (90%) patients, and a dorsal location was found in 99 (47%) patients. Intraventricular hemorrhage was found in 125 (59%) patients, and hydrocephalus was observed in eight (4%) patients on emergency CT.

The median white blood cell count upon admission was  $11.3$  (IQR, 9.0–13.7)  $\times 10^{12}$  cells/L, and the median C-reactive protein level was 31 (IQR, 10–77) mg/L, indicating that inflammation may have appeared in the early course of PBSH.

### 3.2. Factors upon admission and during hospitalization influencing 30-day survival

The overall 30-day survival rate of 211 patients was 70%. The 30-day survival outcome was significantly related to the following

factors upon admission (Table 2): mydriasis ( $P = 0.004$ ; OR, 0.33; 95% CI, 0.16–0.68), pinpoint pupils ( $P = 0.015$ ; OR, 0.43; 95% CI, 0.23–0.82), hematoma volume ( $P = 0.006$ ; OR, 0.94; 95% CI, 0.91–0.98), dorsal brainstem hematoma ( $P = 0.011$ ; OR, 0.44; 95% CI, 0.24–0.81), extension into the thalamus ( $P = 0.047$ ; OR, 0.38; 95% CI, 0.16–0.91), blood creatinine ( $P < 0.001$ ; OR, 0.99; 95% CI, 0.98–0.99), troponin T (TnT,  $P < 0.001$ ; OR, 0.13; 95% CI, 0.03–0.52), and activated partial thromboplastin time (APTT,  $P = 0.045$ ; OR, 0.95; 95% CI, 0.90–0.99).

Among all 211 patients, 113 patients underwent stereotactic aspiration treatment and 98 patients underwent conservative treatment (Supplementary Table S1). Univariate analysis showed that stereotactic aspiration treatment ( $P < 0.001$ ; OR, 3.13; 95% CI, 1.67–5.88) and changes in blood sodium levels ( $P < 0.01$ ) during hospitalization were significantly related to 30-day survival.

We selected clinically related factors from the significant factors affecting 30-day survival upon admission and during hospitalization to construct a prognostic prediction model. In total, eight factors upon admission were found to be significantly associated with 30-day survival; of which, three factors were selected to build the pre-treatment prognosis prediction model: dorsal brainstem hematoma, showing a close relationship with survival outcome in previous reports (16, 17); extension into the thalamus, suggesting a vertically widespread extension of the hematoma; and APTT, reflecting the state of endogenous coagulation in the body. The post-treatment model incorporated four factors both upon admission and during hospitalization, including hematoma volume, dorsal brainstem hematoma, APTT, and treatment method. The pre-treatment model showed a



TABLE 1 General characteristics of study population.

| Characteristic                             | 211 patients | 30-day survival group (n = 147) | 30-day death group (n = 64) | P value |
|--|--------------|---------------------------------|-----------------------------|---------|
| Age (years)                                | 49 (42–57)   | 50 (42–57)                      | 48 (42–57)                  | 0.462   |
| Male                                       | 175 (83%)    | 119 (81%)                       | 56 (88%)                    | 0.335   |
| Hypertension                               | 153 (73%)    | 111 (76%)                       | 42 (66%)                    | 0.162   |
| Diabetes mellitus                          | 26 (12%)     | 19 (13%)                        | 7 (11%)                     | 0.860   |
| History of stroke or myocardial infarction | 21 (10%)     | 15 (10%)                        | 6 (9%)                      | 1       |
| Smoking habits (pack-years)                | 0 (0–14)     | 0 (0–11)                        | 0 (0–15)                    | 0.816   |
| Drinking habits (alcohol use)              | 0 (0–0)      | 0 (0–0)                         | 0 (0–8)                     | 0.311   |
| Hyperuricemia                              | 6 (3%)       | 3 (2%)                          | 3 (5%)                      | 0.540   |
| Anticoagulant drugs                        | 8 (4%)       | 5 (3%)                          | 3 (5%)                      | 0.954   |
| Antiplatelet drugs                         | 9 (3%)       | 9 (6%)                          | 0 (0%)                      | 0.097   |
| Lipid-lowering drugs                       | 5 (3%)       | 3 (2%)                          | 2 (3%)                      | 0.634   |
| Body mass index                            | 24.9 ± 4.4   | 24.9 ± 3.7                      | 24.9 ± 5.7                  | 0.997   |

Data are expressed as n (%), mean ± SD, median (IQR), as appropriate.

Body mass index = weight/height<sup>2</sup> (kg/m<sup>2</sup>).

Pack-years of cigarette smoking = Packs per day (one pack contains 20 cigarettes) × Years.

Alcohol use = Drink units of alcohol per week (one unit contains 12 grams of alcohol).

significant predictive effect (AUC, 0.680; 95% CI, 0.60–0.76;  $P < 0.001$ ; Figure 3A). The post-treatment model, which incorporated the treatment method as a factor, had a better predictive effect (AUC, 0.787; 95% CI, 0.71–0.85;  $P < 0.001$ ; Figure 3B). Compared with conservative treatment, stereotactic aspiration is strongly associated with 30-day survival (OR, 6.67; 95% CI, 3.13–14.29;  $P < 0.001$ ; Figure 3B). Larger admission hematoma volume (OR, 0.92; 95% CI: 0.88–0.97;  $P = 0.001$ ), higher APTT (OR, 0.94; 95% CI: 0.89–0.99;  $P = 0.036$ ), and dorsal brainstem hematoma (OR, 0.43; 95% CI: 0.21–0.87;  $P = 0.019$ ) upon admission are risk factors for 30-day death in the post-treatment model.

### 3.3. Factors upon admission and during hospitalization influencing 90-day consciousness

Among the 211 patients included in the present study, one patient had not yet reached 90 days at the end of the follow-up period, and two patients had lost their memory of the 90-day state. Therefore, we performed statistical analysis on the data of the remaining 208 patients. Univariate analysis of baseline data upon admission revealed that mydriasis ( $P = 0.017$ ; OR, 0.29; 95% CI, 0.11–0.78), abnormal light reflex ( $P = 0.002$ ; OR, 0.25; 95% CI, 0.11–0.57), GCS score ( $P < 0.001$ ; OR, 1.40; 95% CI, 1.22–1.61), emergency mechanical ventilation ( $P = 0.020$ ; OR, 0.31; 95% CI, 0.12–0.78), hematoma volume ( $P < 0.001$ ; OR, 0.85; 95% CI, 0.80–0.91), dorsal location ( $P < 0.001$ ; OR, 0.27; 95% CI, 0.14–0.51), hematoma across the midline ( $P = 0.011$ ; OR, 0.28; 95% CI, 0.11–0.71), hematoma expanding to the thalamus ( $P = 0.028$ ; OR, 0.27; 95% CI, 0.08–0.93), extension

into the basal ganglia ( $P = 0.037$ ; OR, 0.28; 95% CI, 0.08–0.99), the presence of intraventricular hemorrhage ( $P < 0.001$ ; OR, 0.34; 95% CI, 0.18–0.61), hydrocephalus signs ( $P = 0.047$ ), TnT ( $P < 0.001$ ; OR, 0.00; 95% CI, 0.00–0.01), and APTT ( $P < 0.001$ ; OR, 0.91; 95% CI, 0.85–0.97) upon admission were significantly associated with the 90-day consciousness outcome (Supplementary Table S2). Factors during hospitalization including high fever ( $P = 0.002$ ; OR, 0.46; 95% CI, 0.25–0.84), myocardial injury ( $P = 0.029$ ; OR, 0.31; 95% CI, 0.10–0.93), and blood potassium reduction ( $P = 0.042$ ; OR, 1.66; 95% CI, 1.01–2.71) were significantly associated with the 90-day consciousness outcome (Table 3).

As before, multiple logistic regression analysis was performed to construct a prognostic prediction model. We found that the prognosis prediction model upon admission was consistent with that during hospitalization, indicating no more risk factors during hospitalization for the 90-day consciousness outcome. According to our statistical analysis and potential biological links of the significant predictive factors with treatment outcome, we selected five factors out of 19 significant factors to build the prognosis prediction model: hematoma volume, dorsal brainstem hematoma, and extension into the thalamus, which may be associated with the impaired reticular activating system and its projections posteriorly to the thalamus; APTT, implying the possibility of rebleeding and imperceptible microbleeds during hospitalization; and mydriasis, involving the oculomotor nerve or oculomotor nuclei in the deep brainstem. The 90-day consciousness prognosis prediction model had an excellent predictive effect (AUC, 0.835; 95% CI, 0.78–0.89;  $P < 0.001$ ; Figure 4). Dorsal brainstem and thalamus involvement, higher APTT, and mydriasis upon admission are risk factors for 90-day unconsciousness in the prediction model.

TABLE 2 Associations of characteristics upon admission with 30-day survival.

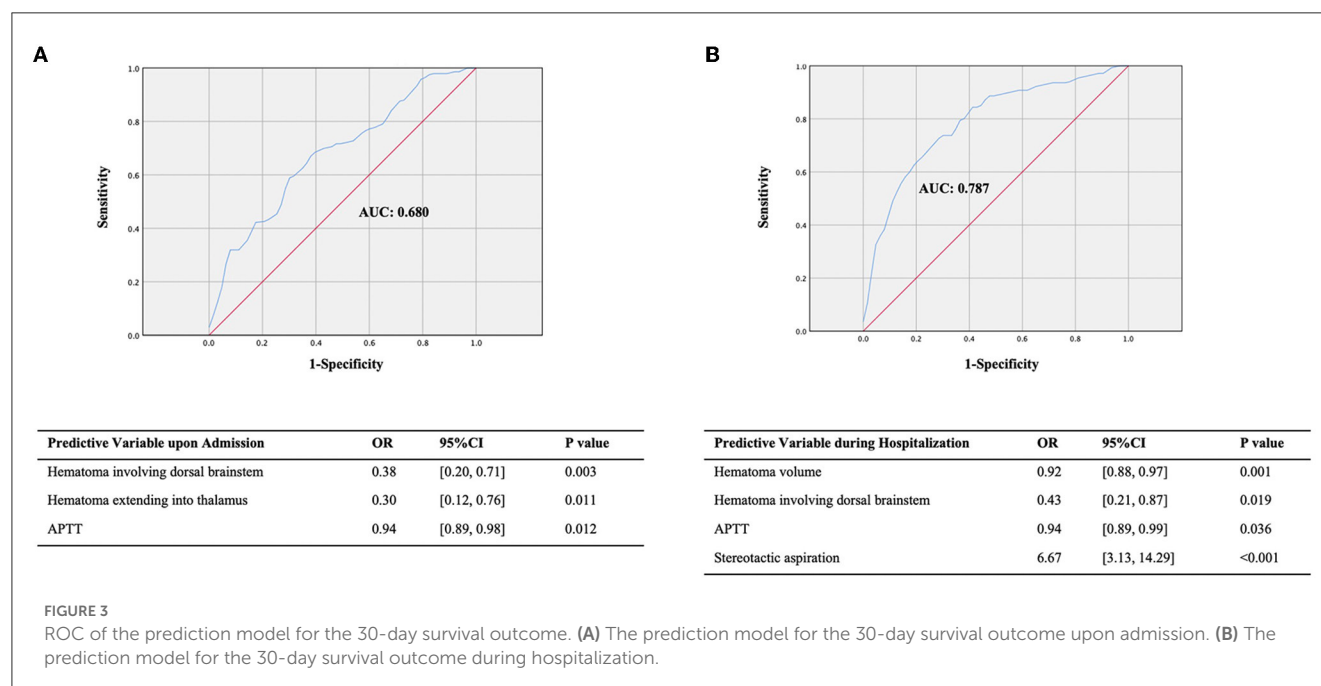
| Characteristic                                      | All patients<br>(n = 211) | Survivor<br>(n = 147) | Non-survivor<br>(n = 64) | P value   | OR (95% CI)      |
|---|---------------------------|-----------------------|--------------------------|-----------|------------------|
| <b>Clinical characteristics upon admission</b>      |                           |                       |                          |           |                  |
| Heart rate  | 84 (71–101)               | 82 (71–98)            | 89 (70–112)              | 0.149     | 0.99 (0.98–1.01) |
| Respiratory rate                                    | 12 (4–15)                 | 12 (3–15)             | 12 (4–15)                | 0.398     | 1.02 (0.97–1.06) |
| Systolic blood pressure (mmHg)                      | 166 ± 31                  | 164 ± 29              | 170 ± 35                 | 0.211     | 1.00 (0.99–1.02) |
| Diastolic blood pressure (mmHg)                     | 95 ± 19                   | 93 ± 18               | 99 ± 22                  | 0.069     | 0.98 (0.96–1.01) |
| Anisocoria  | 57 (27%)                  | 37 (25%)              | 20 (31%)                 | 0.456     | 0.74 (0.39–1.41) |
| Mydriasis   | 37 (18%)                  | 18 (12%)              | 19 (30%)                 | 0.004**   | 0.33 (0.16–0.68) |
| Pinpoint pupils                                     | 57 (27%)                  | 32 (22%)              | 25 (39%)                 | 0.015*    | 0.43 (0.23–0.82) |
| Abnormal light reflex                               | 182 (86%)                 | 122 (83%)             | 60 (94%)                 | 0.075     | 0.33 (0.11–0.98) |
| GCS score   | 4 (3–5)                   | 4 (3–5)               | 3 (3–5)                  | 0.099     | 1.14 (1.00–1.29) |
| Emergency hemostatic drugs                          | 78 (37%)                  | 60 (41%)              | 18 (28%)                 | 0.129     | 1.75 (0.93–3.33) |
| Emergency mechanical ventilation                    | 190 (90%)                 | 131 (89%)             | 59 (92%)                 | 0.664     | 0.69 (0.24–2.00) |
| Emergency decompression                             | 123 (58%)                 | 86 (59%)              | 37 (58%)                 | 1         | 1.03 (0.57–1.85) |
| Emergency external ventricular drainage             | 13 (6%)                   | 10 (7%)               | 3 (5%)                   | 0.783     | 1.49 (0.39–5.56) |
| <b>Image characteristics upon admission</b>         |                           |                       |                          |           |                  |
| Hematoma volume (ml)                                | 9.6 (5.8–14.8)            | 9.2 (5.3–14.0)        | 11.8 (7.7–17.7)          | 0.006**   | 0.94 (0.91–0.98) |
| <b>Location of hemorrhage</b>                       |                           |                       |                          |           |                  |
| Dorsal location                                     | 99 (47%)                  | 60 (41%)              | 39 (61%)                 | 0.011*    | 0.44 (0.24–0.81) |
| Crossing the midline                                | 190 (90%)                 | 128 (87%)             | 62 (97%)                 | 0.053     | 0.22 (0.05–0.96) |
| Midbrain  | 151 (72%)                 | 106 (72%)             | 45 (70%)                 | 0.920     | 1.09 (0.57–2.08) |
| Pons  | 207 (98%)                 | 143 (97%)             | 64 (100%)                | 0.434     | NA               |
| Medulla   | 12 (6%)                   | 7 (5%)                | 5 (8%)                   | 0.578     | 0.58 (0.18–1.92) |
| <b>Extension of hemorrhage</b>                      |                           |                       |                          |           |                  |
| Cerebellum  | 34 (16%)                  | 20 (14%)              | 14 (22%)                 | 0.194     | 0.56 (0.26–1.20) |
| Thalamus  | 24 (11%)                  | 12 (8%)               | 12 (10%)                 | 0.047*    | 0.38 (0.16–0.91) |
| Basal ganglia                                       | 23 (11%)                  | 13 (9%)               | 10 (16%)                 | 0.225     | 0.52 (0.22–1.27) |
| Ventricle   | 125 (59%)                 | 82 (56%)              | 43 (67%)                 | 0.162     | 0.62 (0.33–1.14) |
| Hydrocephalus                                       | 8 (4%)                    | 4 (3%)                | 4 (6%)                   | 0.399     | 0.42 (0.10–1.72) |
| <b>Laboratory blood examinations upon admission</b> |                           |                       |                          |           |                  |
| White blood cell count (10 <sup>12</sup> /L)        | 11.3 (9.0–13.7)           | 11.0 (8.8–13.5)       | 11.8 (9.5–15.7)          | 0.093     | 0.93 (0.87–1.00) |
| Hemoglobin (g/L)                                    | 133.2 ± 20.6              | 131.3 ± 16.7          | 137.6 ± 27.0             | 0.093     | 0.99 (0.97–1.00) |
| Platelet (10 <sup>9</sup> /L)                       | 179.8 ± 60.4              | 184.8 ± 57.0          | 168.4 ± 66.4             | 0.094     | 1.01 (1.00–1.01) |
| C-reactive protein (mg/L)                           | 31 (10–77)                | 33 (13–76)            | 24 (5–75)                | 0.199     | 1.00 (1.00–1.00) |
| Blood glucose (mmol/L)                              | 7.6 (6.5–8.9)             | 7.5 (6.4–8.8)         | 8.0 (6.9–9.3)            | 0.239     | 1.00 (0.94–1.07) |
| Blood creatinine (μmol/L)                           | 76 (62–108)               | 73 (58–96)            | 91 (70–134)              | <0.001*** | 0.99 (0.98–0.99) |
| TnT (ng/ml)   | 0.02 (0.01–0.05)          | 0.02 (0.01–0.04)      | 0.04 (0.02–0.18)         | <0.001*** | 0.13 (0.03–0.52) |
| APTT (s)  | 36.3 ± 6.0                | 35.7 ± 5.4            | 37.7 ± 7.1               | 0.045*    | 0.95 (0.90–0.99) |
| D-Dimer (μg/L)                                      | 2,045 (882–4,962)         | 1,860 (860–3,990)     | 2,410 (890–5,080)        | 0.492     | 1.00 (1.00–1.00) |

\*P &lt; 0.05, \*\*P &lt; 0.01, \*\*\*P &lt; 0.001.

Data are expressed as n (%), mean ± SD, median (IQR), OR (95% CI), as appropriate.

TnT, troponin T; APTT, activated partial thromboplastin time.

NA, not available.



## 4. Discussion

In the present study, we found that several factors are positively or negatively associated with 30-day survival and 90-day consciousness outcome, including clinical variables, radiological variables, and laboratory variables upon admission and during hospitalization, in a large database of 211 patients with PBSH.

### 4.1. Epidemiology

The incidence of ICH is higher among Chinese and men than among Caucasians and women, respectively (18). It is noteworthy that there is a prominent prevalence of male sex in the population with PBSH. For example, 202 (72%) out of 281 subjects and 59 (79%) out of 75 subjects were male in Korean and Chinese study populations, respectively (19, 20). In accordance with these results, the present study also showed a higher prevalence of men (83%). The reasons underlying the higher incidence of ICH and the higher risk of PBSH in men in the Chinese population are not clear but may be related to differences in the prevalence of vascular risk factors, personal living habits, and health conditions prior to their illness. Chinese people have been found to have higher rates of hypertension and higher susceptibility to micro-bleeding events and intracranial hemorrhage due to anticoagulation medication compared with other ethnic groups, which are more common in men (21, 22). Although men had a higher incidence, gender was not a prognostic factor in this study. A possible explanation could be that if a brainstem hemorrhage occurred, the clinical outcome does not differ significantly because of its high rate of mortality.

### 4.2. Radiological factors associated with primary outcomes

#### 4.2.1. Hematoma location

There is currently no unified classification for PBSH. In a study of 62 cases published in 1992, a close relationship was observed between overall survival and hematoma location, in which case, the survival rate is the highest in the small unilateral tegmental type and the lowest in the massive type with its bilateral spread into both the basis pontis and the tegmentum (21). Studies using another classification system emphasized the importance of the ventral and dorsal sides and reported that dorsal hematoma showed better recovery than ventral hematoma (6, 16). However, in the present study, the dorsal location of the hematoma is related to an unfavorable outcome. This might be explained by the fact that hematoma of the dorsal type is caused by rupture of the penetrating and long circumferential vessels that enter the tegmentum dorsally and course medially, resulting in rapid destruction of the brain stem as well as the reticular activating system in the pontine tegmentum.

#### 4.2.2. Hematoma extension associated with primary outcomes

Hematoma extension into the midbrain with or without the thalamus was shown to be independently associated with death (23, 24). Here, thalamic involvement could predict adverse outcomes, including death and unconsciousness, which might be caused by a vertically widespread extension of brainstem hematoma. Moreover, intraventricular extension and acute hydrocephalus were not correlated with death but were significantly more common in unconscious patients who survived, indicating a non-lethal but impaired functional outcome. The possible explanation may be

TABLE 3 Associations of characteristics during hospitalization with 90-day consciousness.

| Characteristic  | All patients<br>(n = 208) | Conscious<br>patients<br>(n = 67) | Unconscious<br>patients<br>(n = 141) | P value | OR (95% CI)          |
|---|---------------------------|-----------------------------------|--------------------------------------|---------|----------------------|
| <b>Laboratory blood examinations during hospitalization</b> |                           |                                   |                                      |         |                      |
| Blood creatinine increase (μmol/L)                          | 8 (−2 to 33)              | 4 (−2 to 18)                      | 10 (−1 to 44)                        | 0.156   | 1.00 (0.99 to 1.00)  |
| Blood sodium increase (μmol/L)                              | 4.8 (1.0 to 10.7)         | 4.2 (0.6 to 8.5)                  | 5.1 (1.1 to 11.8)                    | 0.097   | 0.96 (0.93 to 1.00)  |
| Blood sodium decrease (μmol/L)                              | −7.0 (−12.0 to −2.9)      | −7.0 (−10.0 to −4.0)              | −7.4 (−13.1 to −2.3)                 | 0.518   | 1.01 (0.97 to 1.05)  |
| Blood potassium increase (μmol/L)                           | 0.9 (0.4 to 1.4)          | 0.8 (0.4 to 1.2)                  | 0.9 (0.4 to 1.4)                     | 0.359   | 0.71 (0.48 to 1.06)  |
| Blood potassium decrease (μmol/L)                           | −0.4 (−0.9 to −0.1)       | −0.3 (−0.7 to −0.1)               | −0.4 (−1.0 to −0.1)                  | 0.042*  | 1.66 (1.01 to 2.71)  |
| <b>Treatment method</b>                                     |                           |                                   |                                      |         |                      |
| Stereotactic aspiration                                     | 112 (54%)                 | 35 (52%)                          | 77 (55%)                             | 0.864   | 0.91 (0.51 to 1.64)  |
| <b>Complications during hospitalization</b>                 |                           |                                   |                                      |         |                      |
| High fever  | 137 (66%)                 | 36 (54%)                          | 101 (72%)                            | 0.002** | 0.46 (0.25 to 0.84)  |
| Intracranial infection                                      | 3 (1%)                    | 0 (0%)                            | 3 (2%)                               | 0.229   | NA                   |
| Pneumonia   | 182 (88%)                 | 59 (88%)                          | 123 (87%)                            | 0.470   | 1.08 (0.44 to 2.63)  |
| Other infections  | 22 (11%)                  | 3 (4%)                            | 19 (13%)                             | 0.049*  | 0.30 (0.09 to 1.05)  |
| Deep venous thrombosis                                      | 12 (6%)                   | 4 (6%)                            | 8 (6%)                               | 0.932   | 1.05 (0.31 to 3.57)  |
| Myocardial injury   | 28 (14%)                  | 4 (6%)                            | 24 (17%)                             | 0.029*  | 0.31 (0.10 to 0.93)  |
| Bed sores   | 30 (14%)                  | 10 (15%)                          | 20 (14%)                             | 1       | 1.06 (0.46 to 2.44)  |
| Secondary epilepsy  | 10 (5%)                   | 1 (1%)                            | 9 (6%)                               | 0.123   | 0.22 (0.03 to 1.79)  |
| Digestive tract hemorrhage                                  | 3 (1%)                    | 1 (1%)                            | 2 (1%)                               | 0.967   | 1.05 (0.09 to 11.11) |

\*P &lt; 0.05, \*\*P &lt; 0.01.

Data are expressed as n (%), mean ± SD, median (IQR), OR (95% CI), as appropriate.

NA, not available.

that the primary brain injury to the vital structures within the brain parenchyma is more important than the secondary injury consisting of mass effect and toxic effect in the ventricular system, causing different clinical outcomes in the short and long term.

### 4.3. Laboratory evaluation

Abnormal coagulation function implies the possibility of rebleeding where APTT is the main indicator of endogenous coagulation status *in vivo* and it changes with coagulation status. Previous studies have found it to be an independent risk factor for cerebral micro-bleeding events in patients with ICH (25). Similarly, we found higher APTT was a significant predictor of death and unconsciousness in patients with PBSH. Therefore, for PBSH with prolonged APTT, further imaging examination should be advised for screening micro-bleeding events, which can further guide the treatment assessment.

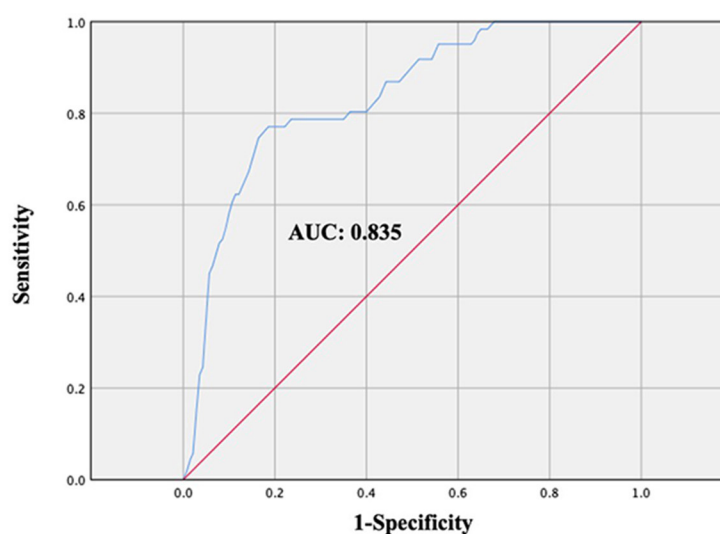
### 4.4. Surgical management and its impact on outcomes

Neurosurgical interventions such as hematoma evacuation remain controversial for PBSH because randomized clinical

studies have failed to demonstrate a clear benefit to surgical management. The efficacy and safety of surgery for patients with PBSH remain debatable. With the application of stereotactic equipment and anticoagulant urokinase, it is endowed with less invasive damage, higher precision, and a hematoma clearance rate than traditional surgical methods. Conceptually, in addition to reducing the space-occupying effect and intracranial pressure, the evacuation of the hematoma is also aimed at removing the hemorrhagic products that cause acute inflammation and degradation of the brain parenchyma. In the present study, stereotactic aspiration was found to be a strong protective factor for survival but not for consciousness. Hematoma clearance by stereotactic aspiration is effective in removing the lethal factors but does not prevent subsequent edema and arterial necrosis, which usually begin and exacerbate the symptoms 6 h after the initial hemorrhage in the brainstem, which may be the cause of the unimproved consciousness (26).

### 4.5. Indicators for short- and long-term clinical outcomes

In selecting the prognostic indicators, we aimed to cover both the short-term prognosis and the mid-term to long-term



| Predictive Variable                                | OR   | 95%CI        | P value |
|--|------|--------------|---------|
| Hematoma volume upon admission                     | 0.89 | [0.83, 0.95] | 0.001   |
| Hematoma involving dorsal brainstem upon admission | 0.20 | [0.09, 0.45] | <0.001  |
| Hematoma extending into thalamus upon admission    | 0.10 | [0.02, 0.47] | 0.004   |
| APTT upon admission                                | 0.87 | [0.81, 0.95] | 0.001   |
| Mydriasis upon admission                           | 0.19 | [0.05, 0.68] | 0.010   |

FIGURE 4  
ROC of the prediction model for the 90-day consciousness outcome.

prognoses of the patients. According to an epidemiological study based on 20 studies including 1,437 patients, the all-cause 30-day mortality rate among patients with pontine hemorrhage was  $\sim 48\%$  (6). These results generally seem to represent the natural course of the condition because surgery was seldom performed. Moreover, at our institute, we found that death after 30 days was often not directly caused by the brainstem hemorrhage itself but rather by complications (mainly infection), which led to many confounding factors (nursing level, treatment conditions for subsequent rehabilitation, etc.) that further affected the long-term survival rate. Therefore, the 30-day survival was chosen as a suitable short-term indicator.

Similarly, the 90-day consciousness outcome was selected as a mid-term to long-term prognostic indicator. Patients with PBSH are prone to early coma (90% of patients in this study were in a coma upon admission), and it takes a certain amount of time to become conscious. The reasons for not choosing a longer period of time were the lack of follow-up time for some patients and the smaller difference in the long-term consciousness rate than in the 90-day consciousness rate between groups.

## 4.6. Limitations

The present study had some limitations. First, this retrospective study was performed using data obtained at a single institute, so our results may not accurately represent the national situation. Second, it is debatable to conclude that surgical treatment is the more effective treatment modality in patients with PBSH due to the lack of randomization and the selection bias introduced by choosing treatment modalities. Although our indication for stereotactic aspiration (hematoma volume  $> 5$  ml and GCS  $< 8$ ) was much more stringent than the selection criteria for all 211 included patients, stereotactic aspiration was still found to be a strong protective factor for 30-day survival. Even so, such a selection bias has affected the generalizability of our findings. In the future, a prospective, randomized clinical trial with the involvement of multiple centers and other ethnicities is necessary for better evaluation of the effect of stereotactic aspiration in patients with PBSH. Third, the means of determining clinical outcomes differed from those used in similar studies. Important functional improvement may have been overlooked due to the inclusion of a simple primary outcome score to reduce recall bias.



To overcome these limitations, a more comprehensive, comparative, and prospective study is required, with detailed outcome measures such as functional improvement. Nevertheless, it is hoped that knowledge of the predictors of mortality and functional recovery identified in the present study will improve patient outcomes and individual patient management.

## Data availability statement

The raw data supporting the conclusions of this article will be made available by the authors, without undue reservation.

## Ethics statement

The studies involving human participants were reviewed and approved by the Ethics Committee of the Second Affiliated Hospital Zhejiang University School of Medicine. The patients/participants provided their written informed consent to participate in this study.

## Author contributions

All the authors participated in analyzing and discussing the literature, commenting on, and approving the manuscript. All authors read and approved the final manuscript.

## References

- Kittner SJ, Sekar P, Comeau ME, Anderson CD, Parikh GY, Tavarez T, et al. Ethnic and racial variation in intracerebral hemorrhage risk factors and risk factor burden. *JAMA Netw Open*. (2021) 4:e2121921. doi: 10.1001/jamanetworkopen.2021.21921
- Dziewas R, Kremer M, Ludemann P, Nabavi DG, Dräger B, Ringelstein B. The prognostic impact of clinical and CT parameters in patients with pontine hemorrhage. *Cerebrovasc Dis*. (2003) 16:224–9. doi: 10.1159/000071120
- Nilsson OG, Lindgren A, Brandt L, Säveland H. Prediction of death in patients with primary intracerebral hemorrhage: a prospective study of a defined population. *J Neurosurg*. (2002) 97:531–6. doi: 10.3171/jns.2002.97.3.0531
- Huang K, Ji Z, Sun L, Gao X, Lin S, Liu T, et al. Development and validation of a grading scale for primary pontine hemorrhage. *Stroke*. (2017) 48:63–9. doi: 10.1161/STROKEAHA.116.015326
- Takeuchi S, Suzuki K, Takasato Y, Masaoka H, Hayakawa T, Otani N, et al. Prognostic factors in patients with primary brainstem hemorrhage. *Clin Neurol Neurosurg*. (2013) 115:732–5. doi: 10.1016/j.clineuro.2012.08.022
- Behrouz R. Prognostic factors in pontine haemorrhage: a systematic review. *Eur Stroke J*. (2018) 3:101–9. doi: 10.1177/2396987317752729
- Morgenstern LB, Frankowski RF, Shedden P, Pasteur W, Grotta JC. Surgical treatment for intracerebral hemorrhage (STICH): a single-center, randomized clinical trial. *Neurology*. (1998) 51:1359–63. doi: 10.1212/WNL.51.5.1359
- Hanley DF, Thompson RE, Muschelli J, Rosenblum M, McBee N, Lane K, et al. Safety and efficacy of minimally invasive surgery plus alteplase in intracerebral haemorrhage evacuation (MISTIE): a randomised, controlled, open-label, phase 2 trial. *Lancet Neurol*. (2016) 15:1228–37. doi: 10.1016/S1474-4422(16)30234-4
- Hemphill JC 3rd, Greenberg SM, Anderson CS, Becker K, Bendok BR, Cushman M, et al. Guidelines for the management of spontaneous intracerebral hemorrhage: a guideline for healthcare professionals from the American Heart Association/American Stroke Association. *Stroke*. (2015) 46:2032–60. doi: 10.1161/STR.0000000000000069
- Ichimura S, Bertalanffy H, Nakaya M, Mochizuki Y, Moriwaki G, Sakamoto R, et al. Surgical treatment for primary brainstem hemorrhage to improve postoperative functional outcomes. *World Neurosurg*. (2018) 120:e1289–94. doi: 10.1016/j.wneu.2018.09.055
- Ramina R, Mattei TA, de Aguiar PHP, Meneses MS, Ferraz VR, Aires R, et al. Surgical management of brainstem cavernous malformations. *Neurol Sci*. (2011) 32:1013–28. doi: 10.1007/s10072-011-0477-8
- Takahama H, Morii K, Sato M, Sekiguchi K, Sato S. Stereotactic aspiration in hypertensive pontine hemorrhage: comparative study with conservative therapy. *No Shinkei Geka*. (1989) 17:733–9 (in Japanese).
- Hara T, Nagata K, Kawamoto S, Sashida J, Abe T, Wada A, et al. Functional outcome of primary pontine hemorrhage: conservative treatment or stereotactic surgery. *No Shinkei Geka*. (2001) 29:823–9 (in Japanese).
- Kothari RU, Brott T, Broderick JP, Barsan WG, Sauerbeck LR, Zuccarello M, et al. The ABCs of measuring intracerebral hemorrhage volumes. *Stroke*. (1996) 27:1304–5. doi: 10.1161/01.STR.27.8.1304
- Howard G, Howard VJ. Twenty years of progress toward understanding the stroke belt. *Stroke*. (2020) 51:742–50. doi: 10.1161/STROKEAHA.119.024155
- Wessels T, Möller-Hartmann W, Noth J, Klötzsch C. CT findings and clinical features as markers for patient outcome in primary pontine hemorrhage. *AJNR Am J Neuroradiol*. (2004) 25:257–60.
- Khoshnam SE, Winlow W, Farzaneh M, Farbood Y, Moghaddam HF. Pathogenic mechanisms following ischemic stroke. *Neurol Sci*. (2017) 38:1167–86. doi: 10.1007/s10072-017-2938-1
- Desai R, Patel U, Parekh T, Hanna B, Sitammagari K, Fong HK, et al. Nationwide trends in prevalent cardiovascular risk factors and diseases in young adults: differences by sex and race and in-hospital outcomes. *South Med J*. (2020) 113:311–9. doi: 10.14423/SMJ.000000000000001106
- Wu Z, Yao C, Zhao D, Wu G, Wang W, Liu J, et al. Sino-MONICA project: a collaborative study on trends and determinants in cardiovascular diseases in

## Funding

This work was supported by a grant from the Natural Science Foundation of Zhejiang Province (TGD23C040017).

## Conflict of interest

The authors declare that the research was conducted in the absence of any commercial or financial relationships that could be construed as a potential conflict of interest.

## Publisher's note

All claims expressed in this article are solely those of the authors and do not necessarily represent those of their affiliated organizations, or those of the publisher, the editors and the reviewers. Any product that may be evaluated in this article, or claim that may be made by its manufacturer, is not guaranteed or endorsed by the publisher.

## Supplementary material

The Supplementary Material for this article can be found online at: <https://www.frontiersin.org/articles/10.3389/fneur.2023.1126585/full#supplementary-material>

- China, Part i: morbidity and mortality monitoring. *Circulation*. (2001) 103:462–8. doi: 10.1161/01.CIR.103.3.462
20. Jang JH, Song YG, Kim YZ. Predictors of 30-day mortality and 90-day functional recovery after primary pontine hemorrhage. *J Korean Med Sci*. (2011) 26:100–7. doi: 10.3346/jkms.2011.26.1.100
21. Huang KB, Ji Z, Wu YM, Wang SN, Lin ZZ, Pan SY. The prediction of 30-day mortality in patients with primary pontine hemorrhage: a scoring system comparison. *Eur J Neurol*. (2012) 19:1245–50. doi: 10.1111/j.1468-1331.2012.03724.x
22. Wu S, Wu B, Liu M, Chen Z, Wang W, Anderson CS, et al. Stroke in China: advances and challenges in epidemiology, prevention, and management. *Lancet Neurol*. (2019) 18:394–405. doi: 10.1016/S1474-4422(18)30500-3
23. Chung CS, Park CH. Primary pontine hemorrhage: a new CT classification. *Neurology*. (1992) 42:830–4. doi: 10.1212/WNL.42.4.830
24. Weisberg LA. Primary pontine haemorrhage: clinical and computed tomographic correlations. *J Neurol Neurosurg Psychiatry*. (1986) 49:346–52. doi: 10.1136/jnnp.49.4.346
25. Zhang H, Deng J, Sun N, Zou L, Han J, Wei C, et al. Effect of coagulation function on cerebral microbleeds in intracerebral hemorrhage. *Brain Behav*. (2020) 10:e01634. doi: 10.1002/brb3.1634
26. Matsukawa H, Shinoda M, Fujii M, Takahashi O, Murakata A. Risk factors for mortality in patients with non-traumatic pontine hemorrhage. *Acta Neurol Scand*. (2015) 131:240–5. doi: 10.1111/ane.12312



## OPEN ACCESS

## EDITED BY

Wen-Jun Tu,  
Chinese Academy of Medical Sciences and  
Peking Union Medical College, China

## REVIEWED BY

Guixue Wang,  
Chongqing University, China  
Zun-Jing Liu,  
China-Japan Friendship Hospital, China  
Sasa R. Vasilijic,  
Stanford University, United States

## \*CORRESPONDENCE

Hengfang Liu  
✉ liuhf1965@163.com

## SPECIALTY SECTION

This article was submitted to  
Neurological Biomarkers,  
a section of the journal  
Frontiers in Neurology

RECEIVED 27 September 2022

ACCEPTED 06 February 2023

PUBLISHED 02 March 2023

## CITATION

Zhang Q, Liu H, Zhang M, Liu F and Liu T (2023)  
Identification of co-expressed central genes  
and transcription factors in  
atherosclerosis-related intracranial aneurysm.  
*Front. Neurol.* 14:1055456.  
doi: 10.3389/fneur.2023.1055456

## COPYRIGHT

© 2023 Zhang, Liu, Zhang, Liu and Liu. This is an  
open-access article distributed under the terms  
of the [Creative Commons Attribution License  
\(CC BY\)](https://creativecommons.org/licenses/by/4.0/). The use, distribution or reproduction  
in other forums is permitted, provided the  
original author(s) and the copyright owner(s)  
are credited and that the original publication in  
this journal is cited, in accordance with  
accepted academic practice. No use,  
distribution or reproduction is permitted which  
does not comply with these terms.

# Identification of co-expressed central genes and transcription factors in atherosclerosis-related intracranial aneurysm

Quan Zhang<sup>1</sup>, Hengfang Liu<sup>1\*</sup>, Min Zhang<sup>1</sup>, Fang Liu<sup>1</sup> and  
Tiantian Liu<sup>2</sup>

<sup>1</sup>Department of Neurology, Fifth Affiliated Hospital of Zhengzhou University, Zhengzhou, Henan, China,

<sup>2</sup>Department of Neurology, First Affiliated Hospital of Zhengzhou University, Zhengzhou, Henan, China

**Background:** Numerous clinical studies have shown that atherosclerosis is one of the risk factors for intracranial aneurysms. Calcifications in the intracranial aneurysm walls are frequently correlated with atherosclerosis. However, the pathogenesis of atherosclerosis-related intracranial aneurysms remains unclear. This study aims to investigate this mechanism.

**Methods:** The Gene Expression Omnibus (GEO) database was used to download the gene expression profiles for atherosclerosis (GSE100927) and intracranial aneurysms (GSE75436). Following the identification of the common differentially expressed genes (DEGs) of atherosclerosis and intracranial aneurysm, the network creation of protein interactions, functional annotation, the identification of hub genes, and co-expression analysis were conducted. Thereafter, we predicted the transcription factors (TF) of hub genes and verified their expressions.

**Results:** A total of 270 common (62 downregulated and 208 upregulated) DEGs were identified for subsequent analysis. Functional analyses highlighted the significant role of phagocytosis, cytotoxicity, and T-cell receptor signaling pathways in this disease progression. Eight hub genes were identified and verified, namely, CCR5, FCGR3A, IL10RA, ITGAX, LCP2, PTPRC, TLR2, and TYROBP. Two TFs were also predicted and verified, which were IKZF1 and SPI1.

**Conclusion:** Intracranial aneurysms are correlated with atherosclerosis. We identified several hub genes for atherosclerosis-related intracranial aneurysms and explored the underlying pathogenesis. These discoveries may provide new insights for future experiments and clinical practice.

## KEYWORDS

intracranial aneurysms, atherosclerosis, bioinformatics, differentially expressed genes, hub genes, transcription factor

## 1. Introduction

Intracranial aneurysm (IA) is a prevalent disease that affects ~3% of the population (1). The rupture of an IA leads to subarachnoid hemorrhage, with a high risk of morbidity and death. Although the pathogenesis of IA remains unclear, it may be closely related to atherosclerosis (AS). An increasing number of studies have found that IAs are frequently complicated by AS, resulting in a worse prognosis. Killer-Oberpfalzer et al. found atherosclerotic lesions in all their deaths from cystic IA (2). Evidence supports the hypothesis that atherosclerosis, inflammation, and degenerative changes in aneurysm walls play considerable roles in the development of IA, and the presence of atherosclerotic plaques in the aneurysm wall may contribute to the degeneration and rupture of IA (3, 4).

Aneurysm wall enhancement increases the instability of IA (5); it is related to an increased level of atherogenic proteins and a decreased level of anti-atherosclerotic proteins, and atherosclerosis can be detected when these enhanced arterial walls are observed *in vitro* (6, 7). In addition, inflammation-related atherosclerotic changes and neovascularization of the aneurysm wall have been found in larger unruptured IAs (4), and increased lipid infiltration was observed in the ruptured cerebral aneurysm wall (8). In summary, atherosclerosis-related intracranial aneurysms (AS-related IA) are more unstable and require further care in clinical practice.

Although atherosclerosis is considered one of the risk factors for IA, the pathogenic mechanism of the complication of IA and AS remains unknown but may be connected to inflammation, smooth muscle cell (SMC) proliferation, and macrophage phagocytosis (9). Currently, histological studies have demonstrated that the SMC phenotype, lipoprotein buildup, and production of foam cells in intracranial aneurysm walls are similar to the alterations in atherosclerotic artery walls (10–12), indicating that there may be some common mechanisms leading to the occurrence of these two diseases and triggering the onset of AS-related IA. The increased rupture risk of AS-related IA may be mainly caused by atherosclerosis-induced phenotypic modulation of SMC in the aneurysm media layer (13). The adventitia of intracranial aneurysms comprises collagen fibers, encasing the media layer primarily composed of the SMC and extracellular matrix (ECM), while the intima is the invasive site of atherosclerotic plaques. When atherosclerosis occurs on the wall of intracranial aneurysms, the SMC of the media layer transforms to the matrix remodeling phenotype, resulting in ECM dysfunctional remodeling and the destruction of elastic fibers (14). These pathological alterations reduce the stability of the media layer of the aneurysm wall, increasing the risk of AS-related IA rupture (Figure 1).

With the gradual revelation of the close association between IA and AS, there is still a lack of effective treatments, and new strategies are urgently required to prevent corresponding adverse prognoses. This study aimed to identify the transcriptome signature of AS-related IA. We retrieved differentially expressed genes (DEGs) of IA and AS from the Gene Expression Omnibus (GEO) database and used integrative bioinformatics tools to uncover functional pathways, potential hub genes, and transcription factors. Our findings are expected to shed new insights into the pathogenic mechanisms and treatments of IAs complicated with atherosclerosis.

## 2. Materials and methods

### 2.1. Data source

GEO (<http://www.ncbi.nlm.nih.gov/geo/>) is a vast online database containing various high-throughput sequencing data types. We downloaded sequencing datasets of IA (GSE75436) and atherosclerotic vascular specimens (GSE100927) from the GEO database. GSE75436 comprised 15 IA wall tissues and 15 matched control superficial temporal artery walls. GSE100927 comprised 69 atherosclerotic samples and 35 control arteries without atherosclerosis.

### 2.2. Differential expression analysis

First, the acquired data were normalized, background adjusted, and log2 transformed; the probes without gene annotation were removed, and the values of duplicate probes were averaged. We performed differential gene expression analysis on GSE75436 and GSE100927 using the “limma” R package (<https://www.bioconductor.org/packages/3.5/bioc/html/limma.html>) (15). DEGs were identified as genes with an adjusted *p*-value of <0.05 and a |logFC| of >1. Subsequently, we used Venny2.1 (<http://bioinfo.p.cn.b.csic.es/tools/venny/index.html>) to generate a Venn diagram of the intersection of the DEGs in these two datasets. Removing genes with opposite expression trends, we obtained the common DEGs (co-DEGs) in these two diseases.

### 2.3. Enrichment analyses of DEGs

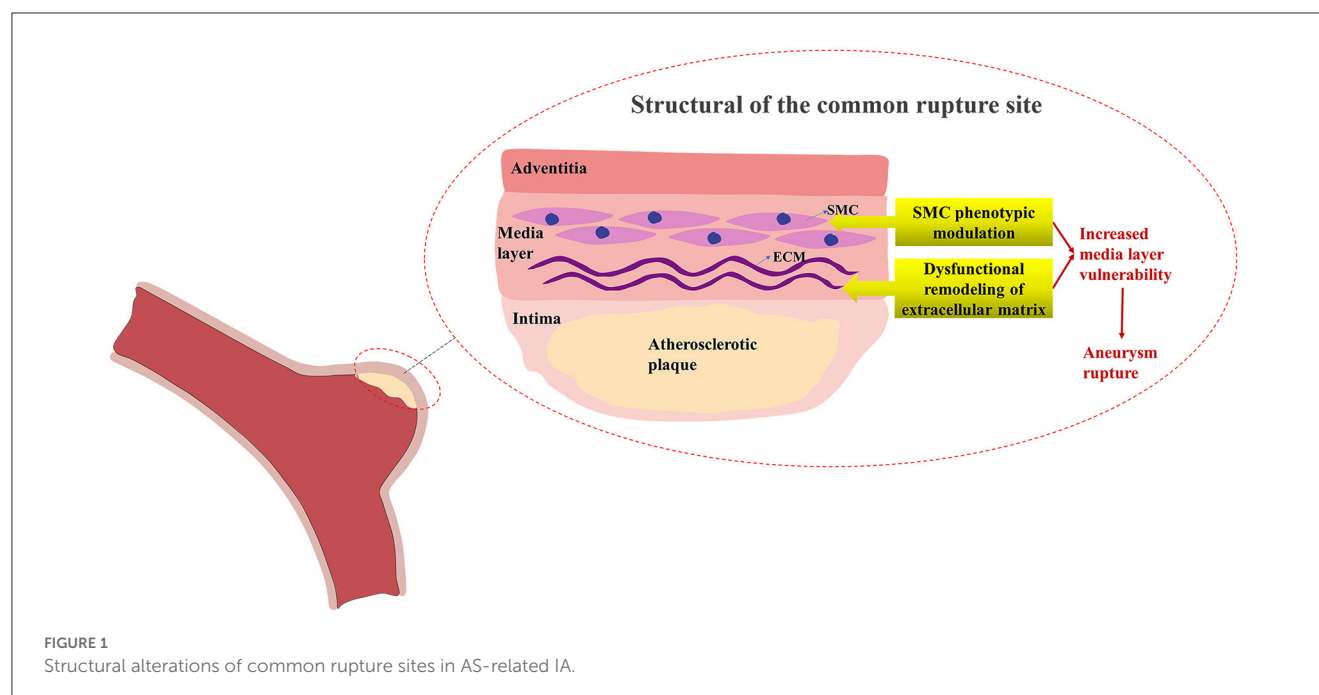
Gene Ontology (GO) is a database that describes the related biological processes, molecular functions, and cellular components for gene collections. Kyoto Encyclopedia of Genes and Genomes (KEGG) is supported by a database containing functional annotation and gene pathway enrichment across multiple species. The co-DEGs were submitted to enrichment analyses using the clusterProfiler package (16), with an adjusted *p*-value of <0.05 serving as the screening criteria. The results were displayed using the Ggplot2 package (<https://ggplot2.tidyverse.org/>).

### 2.4. Protein–protein interaction network construction and module analysis

The Search Tool for the Retrieval of Interacting Genes (STRING; <http://string-db.org>) is a database that can search for potential relationships between proteins (17) using the STRING database to construct a PPI network of co-DEGs with a combined score of >0.40 for meaningful interactions. To visualize the PPI network, we imported the results into Cytoscape (<http://www.cytoscape.org>) (18); subsequently, the MCODE plugin was used to find the potential meaningful gene modules in co-DEGs. Finally, we conducted an enrichment analysis on the most valuable gene modules.

### 2.5. Selection and analysis of candidate hub genes

Using the cytoHubba plugin in Cytoscape, we analyzed the entire PPI network. DEGs were analyzed in cytoHubba using 12 algorithms (MCC, DMNC, MNC, Degree, EPC, BottleNeck, Eccentricity, Closeness, Radiality, Betweenness, Stress, and ClusteringCoefficient), and each algorithm recorded the top 20 genes. Upset charts were constructed, calculating the frequency of gene registrations. Subsequently, we selected the genes reported six times or more as potential hub genes. GeneMANIA (<http://www.genemania.org/>) (19) is a dependable instrument for determining



gene correlations. Candidate hub genes were imported into GeneMANIA for analysis.

## 2.6. Verification and analysis of hub genes

Two external datasets, GSE43292 (AS) and GSE122897 (IA), were used to verify the expression of candidate hub genes. GSE43292 included 32 carotid atherosclerotic plaques paired with 32 distant macroscopic control tissue samples; GSE122897 included 44 IA samples and 16 control intracranial cortical arterials. Data between groups were compared using the mean *t*-test, with a *p*-value of <0.05 as the standard for significant differences. The candidate genes that passed the verification were considered hub genes, and enrichment analysis was performed on them.

## 2.7. Prediction and verification of transcription factors

ChEA3 (<https://maayanlab.cloud/chea3/>) is an internet transcription factor (TF) enrichment analysis instrument that can predict the regulatory relationship between TFs and their corresponding target genes (20). The ENCODE TF target library contains ChIP-seq experiments from humans and mice. We imported hub genes into the ChEA3 database, set library = "ENCODE", and predicted the top 10 TFs corresponding to them. Thereafter, we verified the expression levels of these TFs in GSE75436 and GSE100927.

## 3. Results

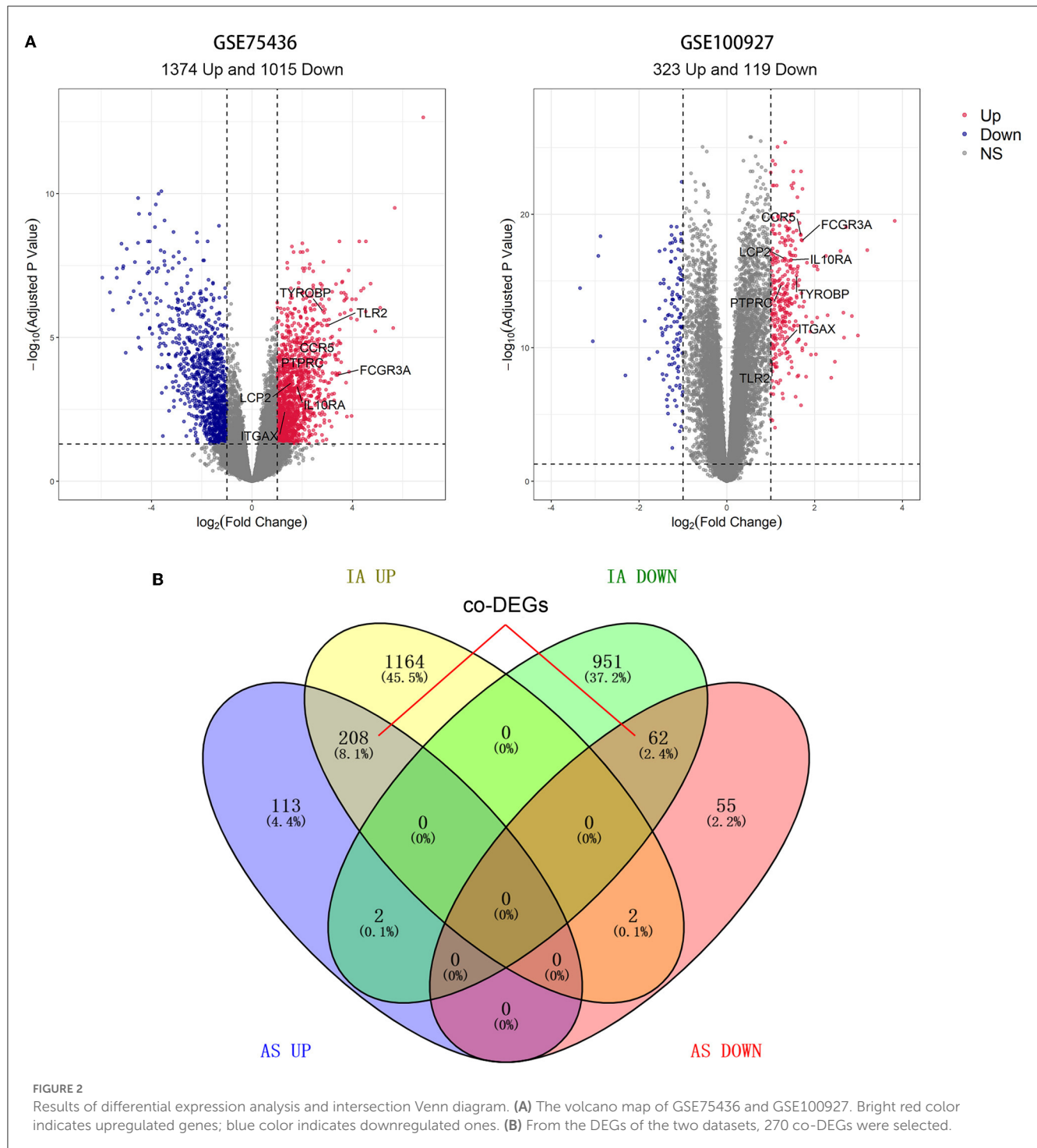
### 3.1. Differential expression analysis

Differential expression analysis revealed that GSE75436 included 2,389 DEGs comprising 1,374 upregulated DEGs and 1,015 downregulated DEGs; GSE100927 contained 442 DEGs consisting of 323 upregulated DEGs and 119 downregulated DEGs (Figure 2A). DEGs with the same expression trend in IA and AS were considered co-DEGs. Taking the intersection of DEGs and removing genes that had opposite expression trends in the two diseases, we obtained 208 upregulated co-DEGs and 62 downregulated co-DEGs (Figure 2B).

### 3.2. Enrichment analyses of DEGs

We performed enrichment analysis on 270 co-DEGs to explore their potential biological functions and pathways. According to GO analysis, these genes were primarily enriched in leukocyte-mediated immunity, leukocyte cell-cell adhesion, immune receptor activity, and endocytic vesicle, which were related to leukocyte immunity and cell phagocytosis (Figure 3B). Meanwhile, co-DEGs were substantially related to the phagosome, lipid, and atherosclerosis, and the B-cell receptor signaling pathway, as determined by KEGG analysis (Figure 3C). These results provide additional evidence that atherosclerosis induces the development of IA and reflect that immune response, phagocytosis, lipid accumulation, and other factors are implicated in the onset and progression of AS-related IA.

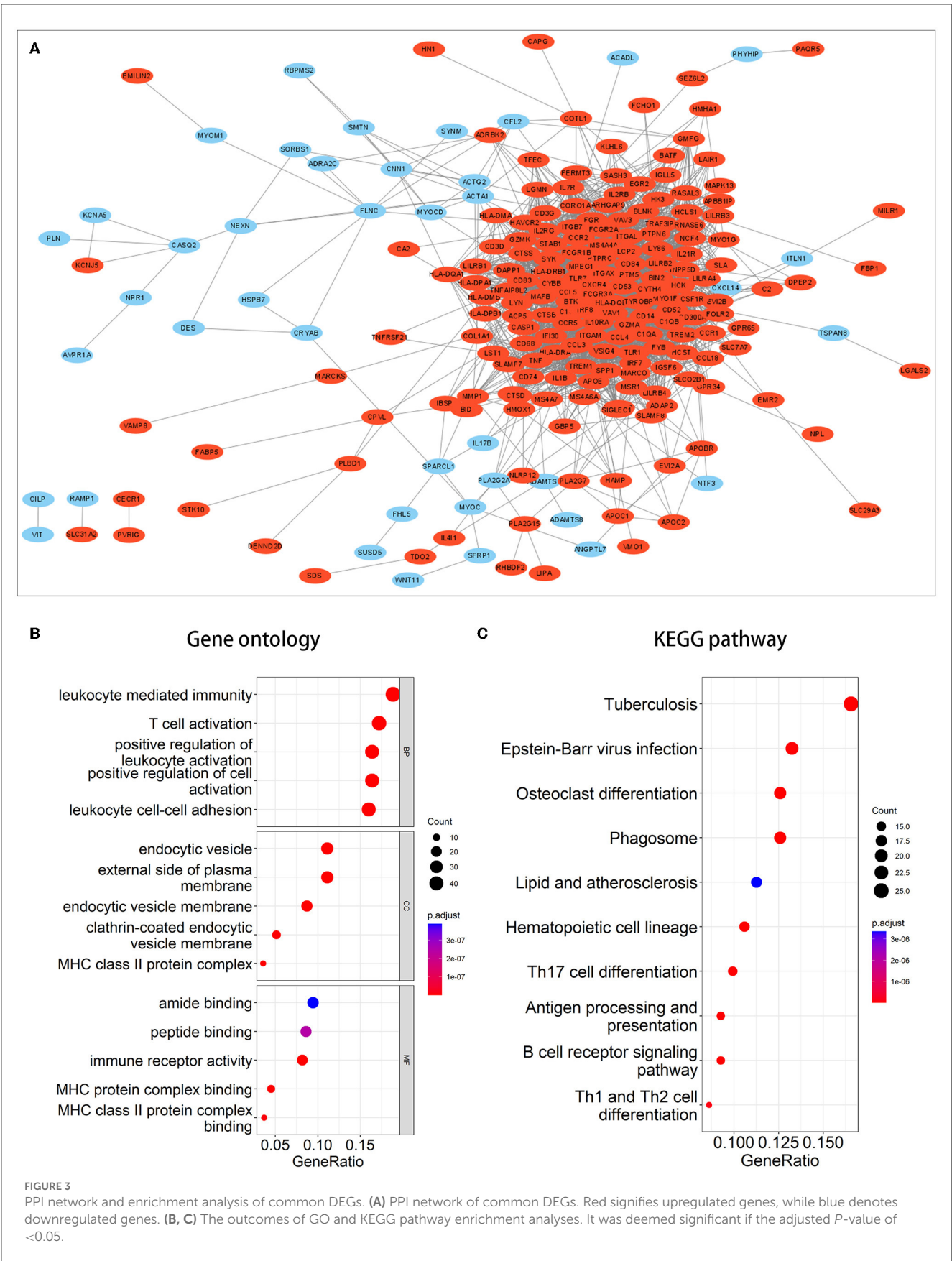




### 3.3. Construction and module analysis of the PPI network

A PPI network of co-DEGs with 227 nodes and 2,379 interaction pairings was established (Figure 3A). Using the MCODE plugin (set  $K$ -core = 2, degree cutoff = 2, max depth = 100, and node score cutoff = 0.2), we analyzed this network and identified the most significant gene module (score = 28.857, 36 genes, and 505 interaction pairs) (Figure 4A). Interestingly, all

genes in this module are upregulated co-DEGs, and heatmaps display their expression levels in GSE75436 (Figure 4B) and GSE100927 (Figure 4C). Moreover, we performed an enrichment analysis on this gene module. GO analysis revealed that these genes were predominantly engaged in immunologic inflammation and cell response regulation (Figure 4D), and KEGG analysis revealed their involvement in a toll-like receptor signaling pathway, a chemokine signaling route, lipid and atherosclerosis, and other pathways (Figure 4E).



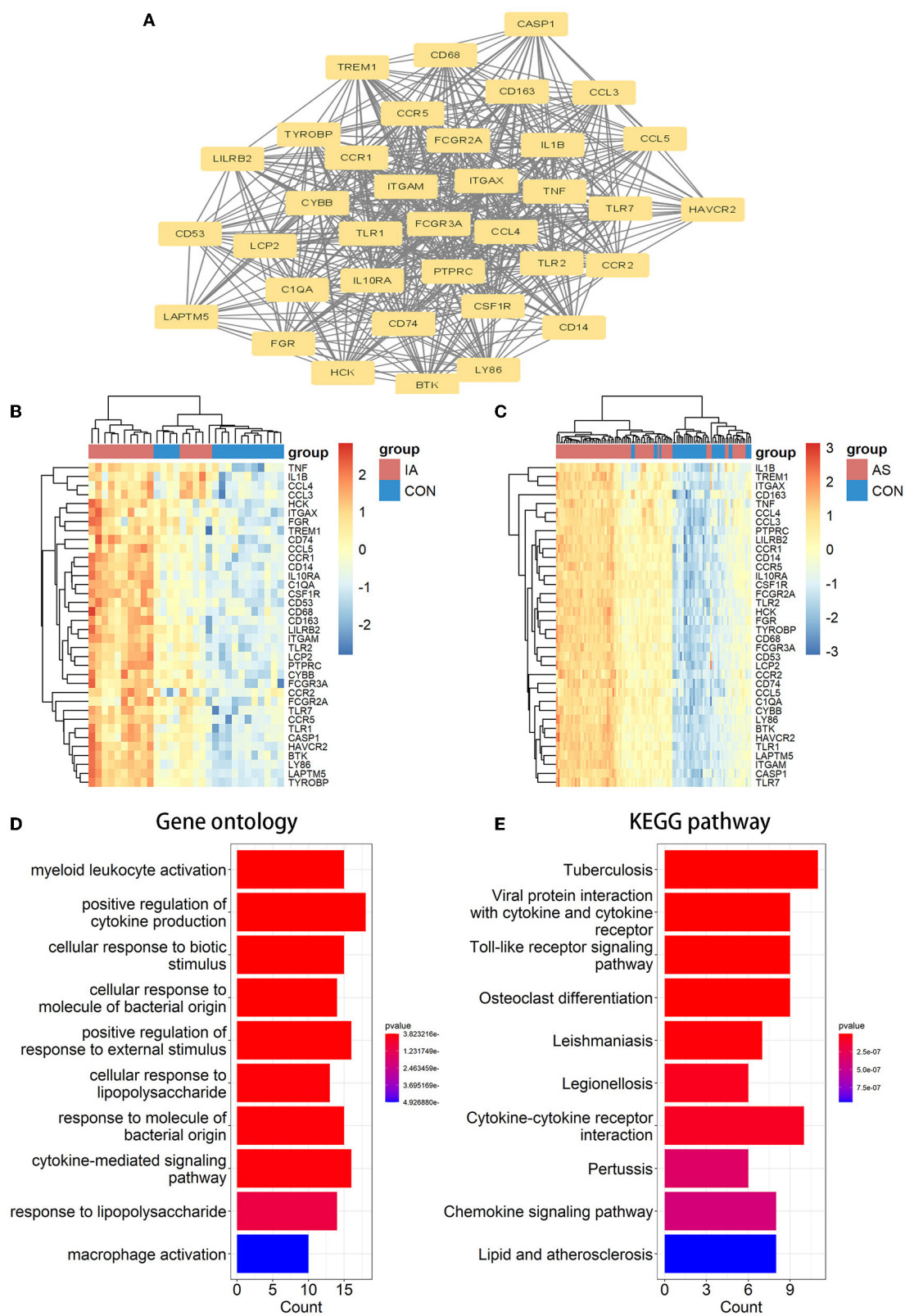
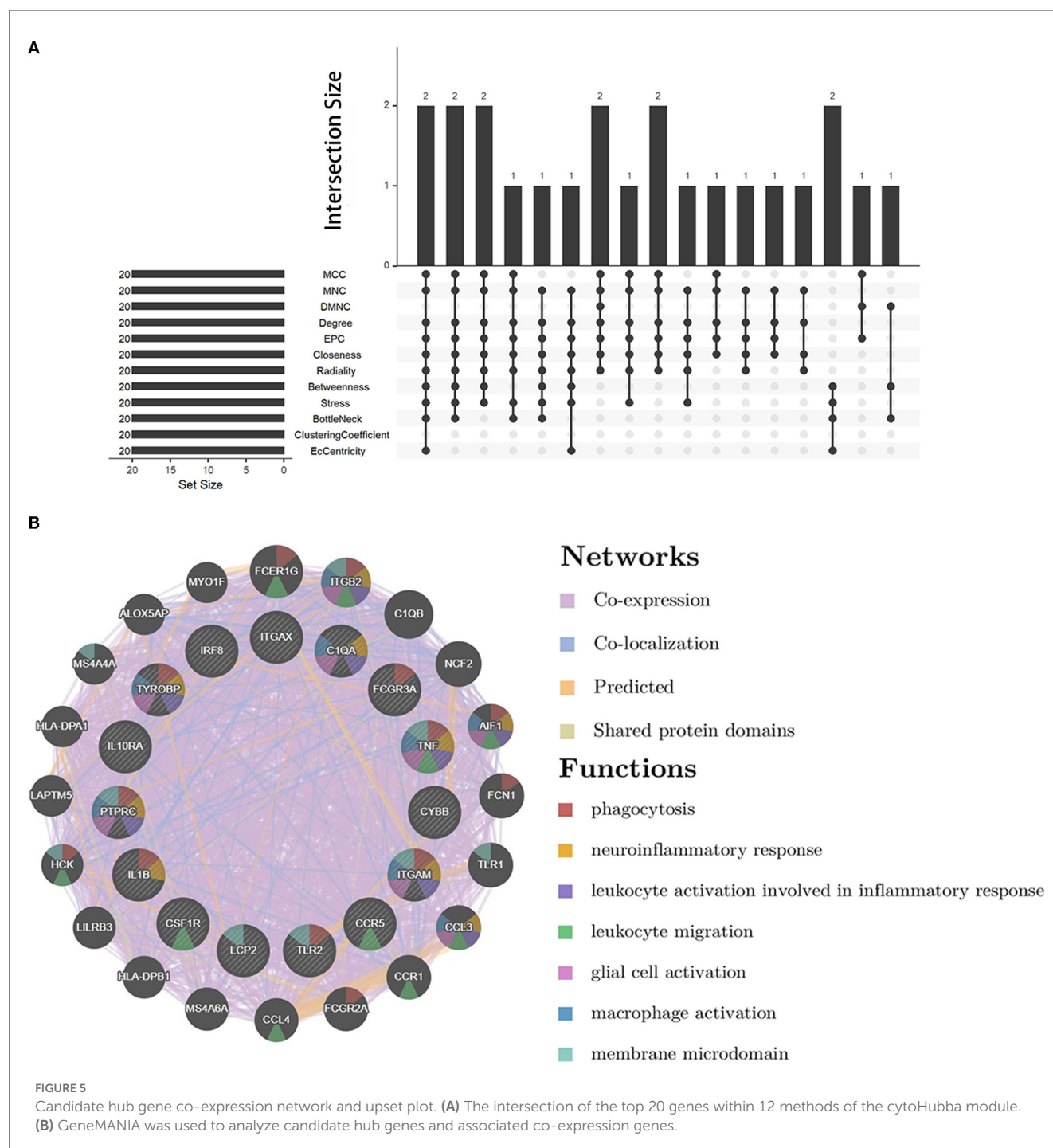


**FIGURE 4**  
MCODE-identified genes module and corresponding enrichment analysis results. **(A)** One essential module of gene clustering. **(B, C)** Distribution of gene expression levels in the module. **(D, E)** The genes module underwent GO and KEGG analysis. It was deemed significant if the adjusted *P*-value < 0.05.

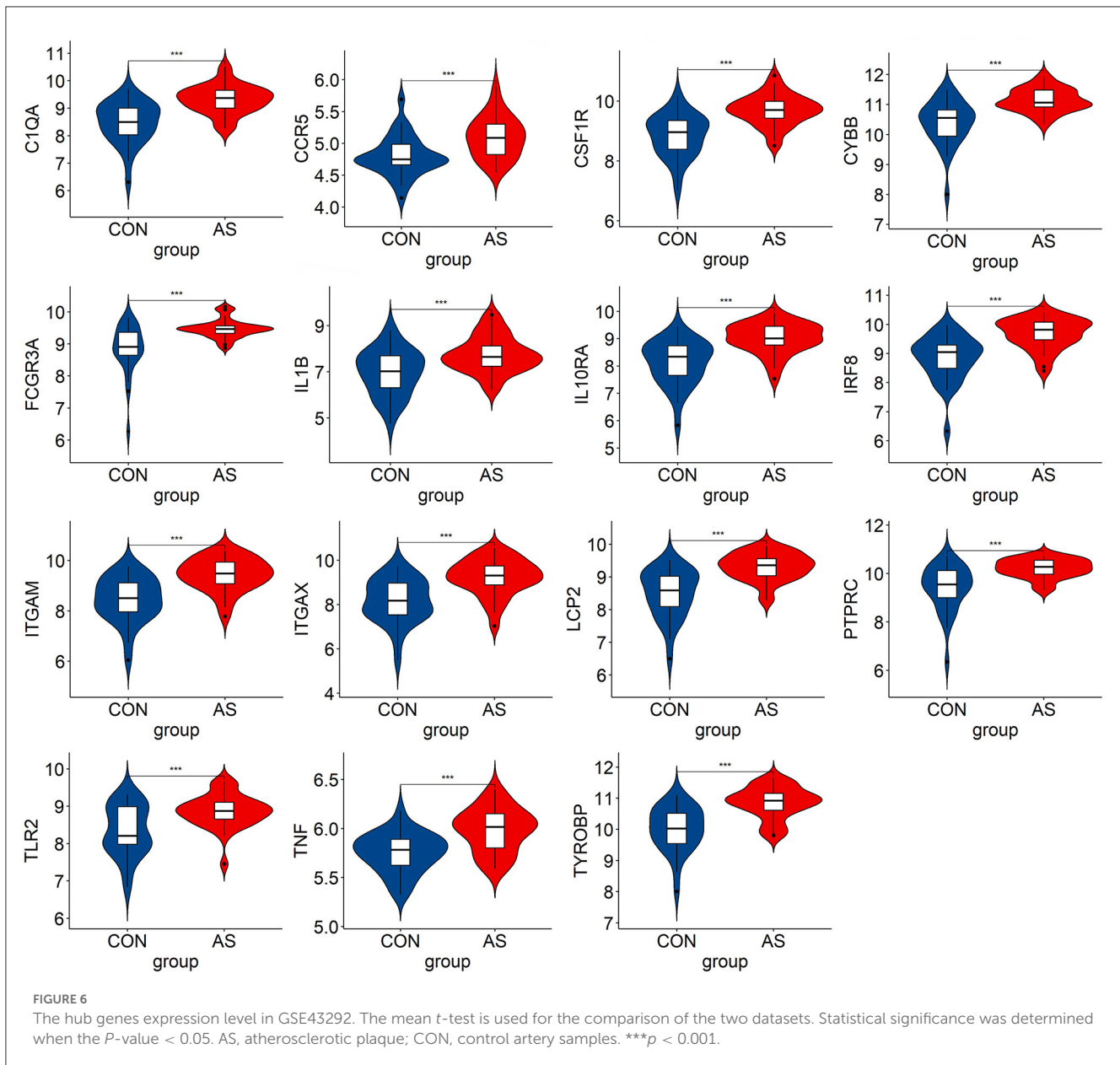


### 3.4. Selection and analysis of candidate hub genes

We analyzed the PPI network of co-DEGs using 12 algorithms in the cytoHubba plugin of Cytoscape software, and each algorithm obtained the top 20 candidate hub genes. According to the upset plot (Figure 5A), genes simultaneously selected by six or more algorithms were considered candidate hub

genes, namely, PTPRC, TNF, ITGAM, TYROBP, IL1B, CSF1R, FCGR3A, IRF8, LCP2, TLR2, CYBB, CCR5, ITGAX, IL10RA, and C1QA, which were all upregulated genes. Based on the GeneMANIA database, we created gene co-expression networks and demonstrated their associated functions. These genes exhibited a complicated PPI network with 88.81% co-expression, 7.24% co-localization, 2.45% prediction, and 1.51% shared protein domains (Figure 5B).





### 3.5. Verification and analysis of hub genes

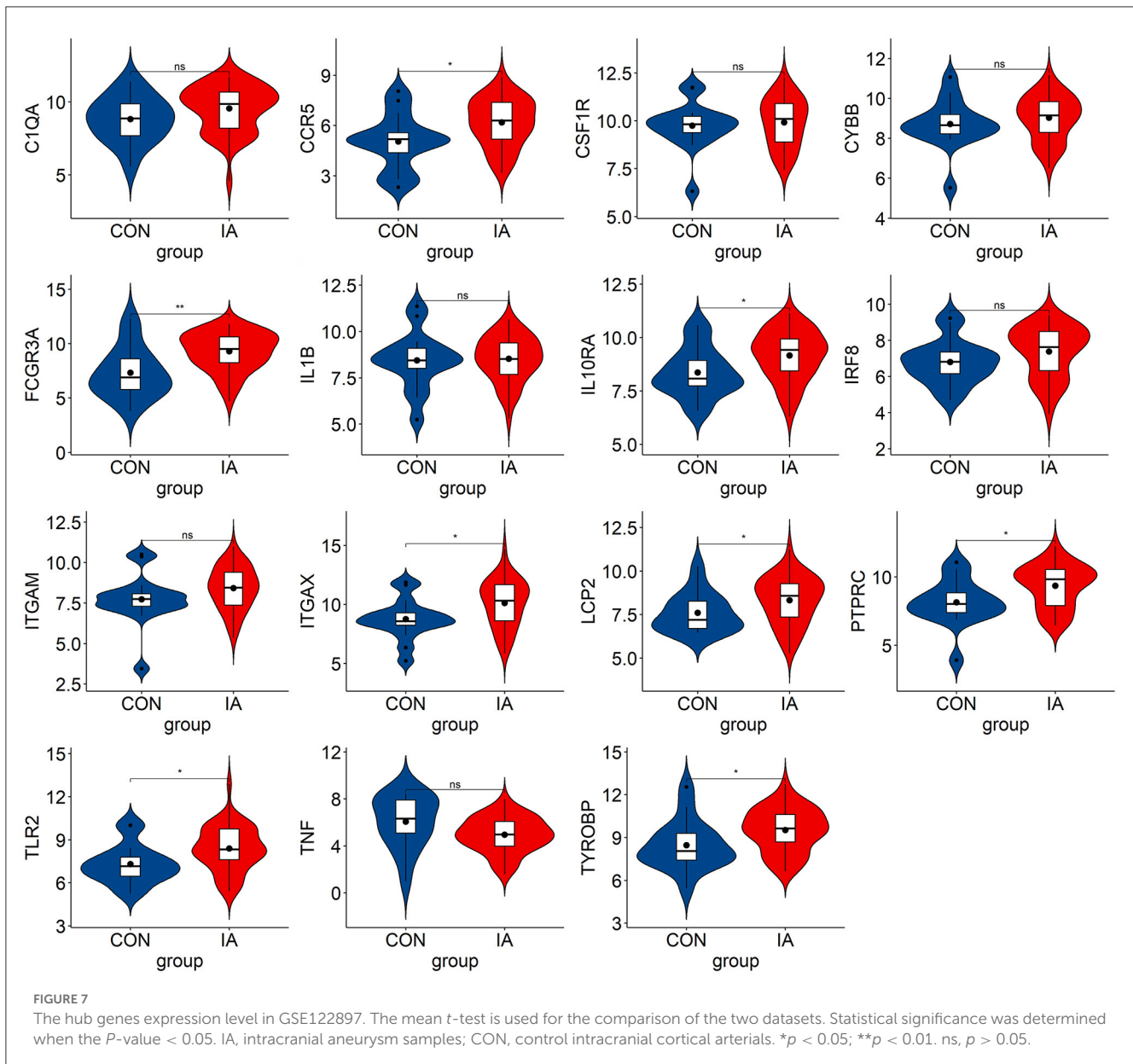
We verified the expression of 15 candidate hub genes with GSE43292 (AS) and GSE122897 (IA). All candidate hub genes were significantly upregulated in GSE43292 (Figure 6). While eight genes were remarkably upregulated in GSE122897, and the expression of candidate hub genes showed an overall upward trend in IA, except for IL1B and TNF (Figure 7). Eight genes were confirmed as hub genes of AS-related IA, namely, CCR5, FCGR3A, IL10RA, ITGAX, LCP2, PTPRC, TLR2, and TYROBP. Supported by the GeneCards database (<https://www.genecards.org/>), Table 1 displays their real names and associated functions. Interestingly, each hub gene corresponds to the MCODE algorithm's most significant gene module. Following the enrichment analysis of these genes, GO analysis demonstrated that they are mainly involved in the immune response, macrophage

phagocytic function, and cytotoxicity (Figure 8A). Subsequently, their involvement in natural killer cell-mediated cytotoxicity, FcR-mediated phagocytosis, and the T cell receptor (TCR) signaling pathway were revealed by KEGG analysis (Figure 8B).

### 3.6. Exploration and authentication of TFs

We predicted the top 10 TFs that may regulate hub gene expression using the ChEA3 database (Figure 9A). Thereafter, we verified the expression of these TFs in datasets. In total, two TFs, IKZF1 and SPI1, were significantly upregulated in GSE75436 (Figure 9B) and GSE100927 (Figure 9C). Subsequently, a network diagram of the TFs and hub genes was constructed. A total of five hub genes (CCR5, IL10RA, LCP2, TYROBP, and PTPRC) were coregulated by these two TFs (Figure 9D).





## 4. Discussion

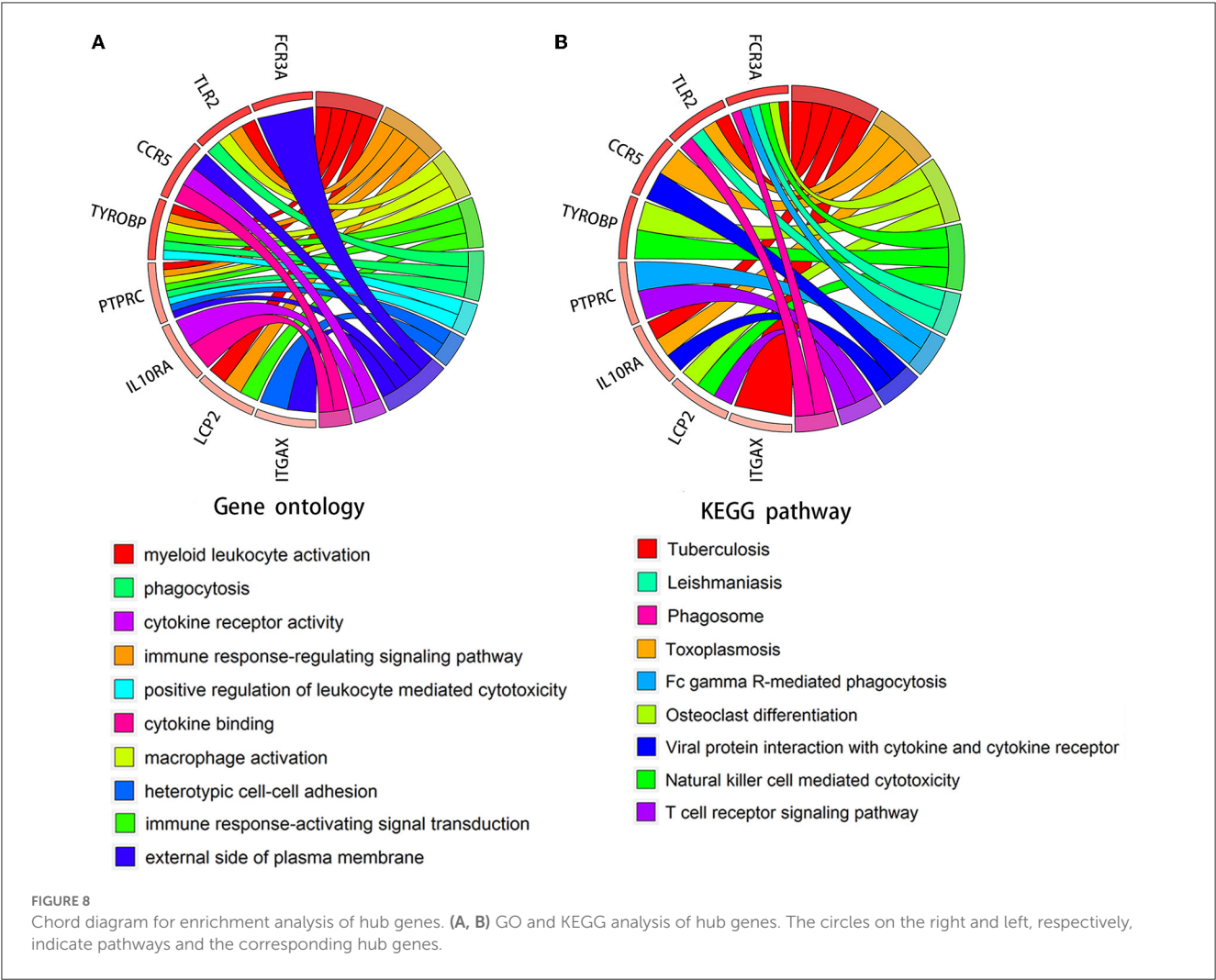
This study determined new targets for preventing and treating AS-related IA, revealing the potential biological mechanism in the pathogenesis. A total of 270 co-DEGs were identified, and then eight hub genes were selected and verified, namely, CCR5, FCGR3A, IL10RA, ITGAX, LCP2, PTPRC, TLR2, and TYROBP. After the enrichment analysis of hub genes, we found that these genes were principally enriched in cytotoxicity, phagocytosis, and TCR signaling pathways. SPI1 and IKZF1, two transcription factors, were discovered to be significant for the development of this disease, and they jointly regulate five hub genes, namely, CCR5, IL10RA, LCP2, TYROBP, and PTPRC.

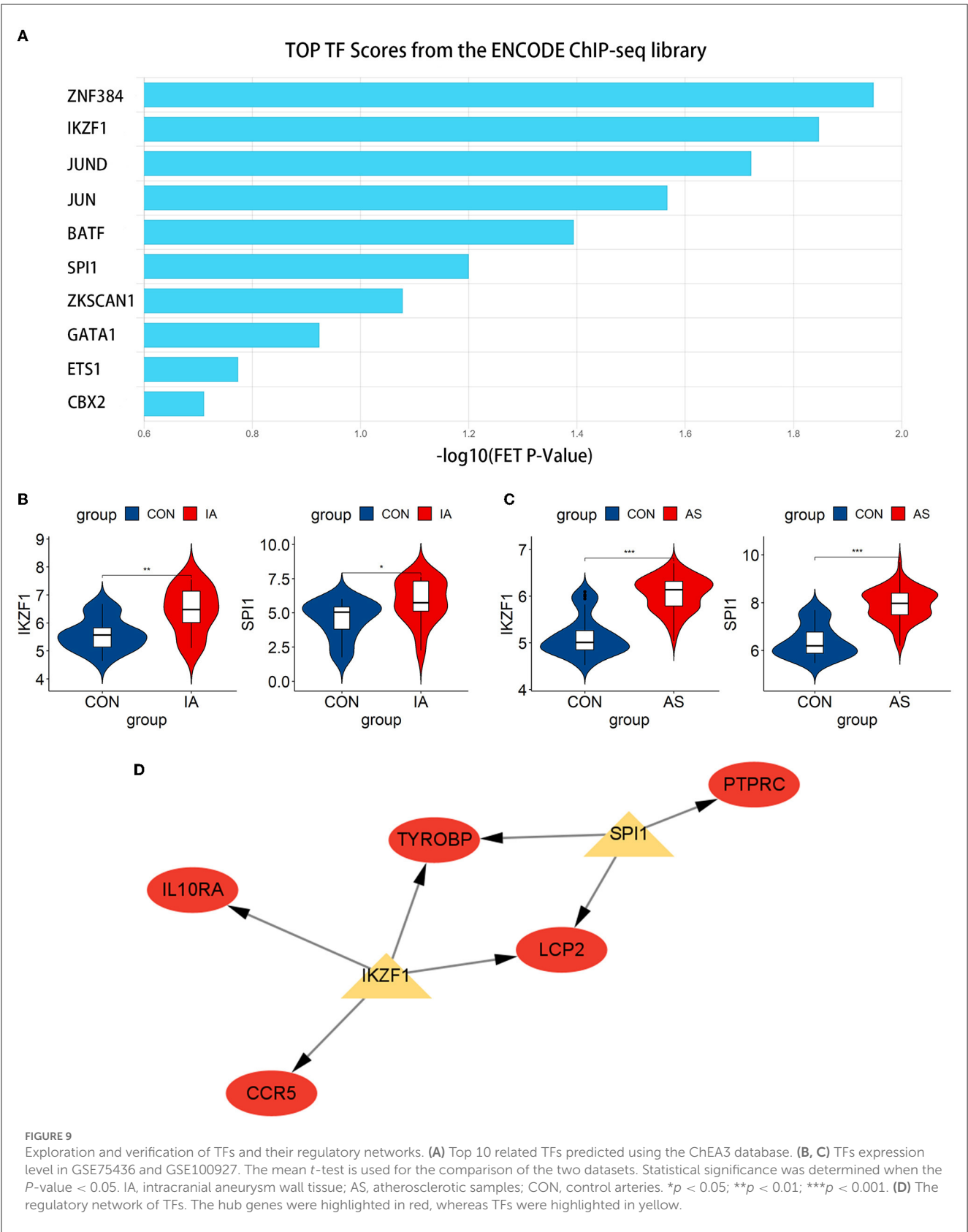
The enrichment analysis of hub genes showed that NK cell-mediated cytotoxicity, FcγR-mediated phagocytosis, and the TCR signaling pathway might play considerable roles in the pathogenesis

of AS-related IA. The atherosclerotic tissue is rich in NK cells that express many biomarkers, such as IFN-γ. NK cell activation may play a significant role in the exacerbation of AS (21), suggesting that the increased cytotoxicity mediated by NK cells may contribute to the development of AS. Moreover, the migration ability of NK cells in the peripheral blood of patients with IA is also enhanced (22). NK cells may aggregate and activate in the aneurysm wall during the pathogenesis, which mediates cytotoxicity to promote disease progression. In addition, phagocytosis appears to be activated during pathogenesis. FcγR is a receptor for the Fc portion of IgG, which activates the mitogen-activated protein kinase signaling pathway by mediating low-density lipoprotein immune complexes (LDL-ICs), thereby activating macrophages (23, 24). Subsequently, macrophage infiltration and its polarization toward the M1 phenotype increase the risk of IA pathogenesis and rupture (25). Inflammatory macrophages in the arterial wall can

TABLE 1 Specifics and functions of hub genes.

| No. | Gene symbol   | Full name  | Function  |
|-----|---------------|--|---|
| 1   | <i>PTPRC</i>  | Protein Tyrosine Phosphatase Receptor Type C         | PTPRC acts as a leukocyte antigen to regulate T- and B-cell immune signaling.   |
| 2   | <i>TYROBP</i> | Transmembrane Immune Signaling Adaptor <i>TYROBP</i> | TYROBP triggers the mobilization of intracellular calcium ions, activates transcription factors such as <i>NF-κB</i> , and promotes the occurrence of cellular inflammatory responses.  |
| 3   | <i>FCGR3A</i> | Fc Gamma Receptor IIIa                               | <i>FCGR3A</i> encodes the receptor for the Fc portion of immunoglobulin G and is involved in antibody-dependent biological processes such as mediating cytotoxicity.  |
| 4   | <i>LCP2</i>   | Lymphocyte Cytosolic Protein 2                       | LCP2 participates in the protein tyrosine kinase pathway activated by the T cell receptor, regulates helper T cell function, and promotes the activation of serine phosphorylation.   |
| 5   | <i>TLR2</i>   | Toll-Like Receptor 2                                 | TLR2 acts on MYD88 to activate NF-κB, activates inflammatory response and cytokine secretion, promotes apoptosis, and affects the lipid portion of lipoproteins.  |
| 6   | <i>CCR5</i>   | C-C Motif Chemokine Receptor 5                       | As a receptor of inflammatory CC-chemokines, CCR5 can increase the intracellular calcium ion level and transduce signals and can affect the inflammatory immune process by participating in the migration of T lymphocytes to the site of action. |
| 7   | <i>ITGAX</i>  | Integrin Subunit Alpha X                             | <i>ITGAX</i> encoded integrin α-X chain protein is involved in constituting leukocyte-specific integrins, mediates cell–cell interactions in inflammation, and plays a vital role in monocyte adhesion and chemotaxis.                            |
| 8   | <i>IL10RA</i> | Interleukin 10 Receptor Subunit Alpha                | IL10RA can mediate IL-10 to transmit immunosuppressive signals and reduce the synthesis of pro-inflammatory cytokines.  |





uptake LDL-ICs through FcγRI and transform them into foam cells (26), forming atherosclerotic plaques. FcγR may activate inflammatory macrophages and promote their phagocytosis to

induce the aggregation of foam cells, leading to the development of atherosclerotic plaque in the aneurysm wall, inducing the deterioration of IA. The activation of the TCR signaling pathway

will lead to the cascade reaction of the PKC $\theta$ -IKK-NF $\kappa$ B pathway (27), stimulating the NF $\kappa$ B-mediated inflammatory response and participating in the pathology process of AS-related IA.

As a receptor of inflammatory CC-chemokines, CCR5 can increase intracellular calcium ion levels to transduce signals. CCR5 transports blood monocytes to atherosclerotic plaques to promote disease progression (28). Cipriani et al. treated AS model mice with a CCR5 antagonist, which resulted in a 70% reduction in plaque volume and a 50% attenuation of monocyte/macrophage infiltration (29). T cells in the wall of IA express high levels of the chemokine receptor CCR5 (30). We speculate that CCR5 may promote disease progression by participating in the chemotactic process of inflammatory macrophages in the aneurysm wall. FCGR3A, also known as CD16, is involved in mediating cytotoxicity. Previous studies have found more CD16+ intermediate monocytes in patients with IA (31). Decreased CD16 monocyte subsets are also associated with a decrease in subclinical AS (32). Combined with our study, FCGR3A may induce disease development by promoting the cytotoxic effect of monocytes and macrophages. The protein encoded by IL10RA is a receptor for interleukin 10 (IL10); It can mediate immunosuppressive signals and reduce inflammatory responses. Patients with IA exhibit a decrease in IL-10, suggesting that the low IL-10 level *in vivo* may be associated with the development of IA (33). Moreover, the IL10RA was highly expressed in AS (34), indicating that the IL10RA-mediated inhibition of inflammation is similarly active in AS. Therefore, IL10RA may play a protective role in AS-related IAs by mediating the anti-inflammatory effect of IL-10, and activating the expression of IL10RA can effectively prevent the occurrence of AS-related IA. ITGAX, also known as CD11c, can mediate cell–cell interactions in inflammation, monocyte adhesion, and chemotaxis. The decrease in CD11c + cells can reduce the progression of abdominal aortic aneurysms (AAA) (35). According to our results, ITGAX may have a similar function in IA. Simultaneously, the high expression of ITGAX is a prominent feature of unstable carotid atherosclerotic plaques. CD11c + macrophages gather in vulnerable plaques, resulting in the deterioration of AS (36). The effect of ITGAX on AS-related IA may depend on affecting the adhesion and chemotaxis of monocytes.

PTPRC, also known as CD45, encodes a leukocyte antigen that regulates the immune response of T and B cells. PTPRC is involved in the progression of AS as a regulatory T cell-related gene (37). Hosaka et al. found the infiltration of CD45+ cells in IA walls (38), reflecting the involvement of PTPRC in the pathogenesis of IA. PTPRC may promote the inflammatory response of AS-related IA by regulating immune lymphocytes. TLR2 activates the inflammatory response and cytokine secretion by activating the TLR2-Myd88-NF- $\kappa$ B pathway and can also activate immune cells to promote apoptosis. Multiple studies have demonstrated that the TLR2-Myd88-NF- $\kappa$ B pathway is activated in IA and AS (39, 40). TLR2 may promote the pathogenesis of AS-related IA mainly by activating the inflammatory response mediated by the TLR2-Myd88-NF- $\kappa$ B pathway and apoptosis. TYROBP, also known as DAP12, encodes a protein that can activate TFs, such as NF- $\kappa$ B, and promote cellular inflammatory responses. Previous studies have found that the expression level of TYROBP is significantly

upregulated in the atherosclerotic tissue and AAA, and TYROBP promotes the pathogenesis of AAA through the activation of the NK cell-mediated cytotoxicity pathway (41, 42). Combined with our results, TYROBP may also have such a role in the progression of AS-related IA, which may lead to disease by activating NF- $\kappa$ B and affecting NK cell-mediated cytotoxicity. The association between LCP2 and AS-related IA is still unclear, and the underlying mechanism requires additional investigation.

Subsequently, we predicted and verified the TFs of hub genes. Among the top 10 TFs predicted from the ChEA3 database, IKZF1 and SPI1 passed the verification, and they jointly regulated five hub genes, namely, CCR5, IL10RA, LCP2, TYROBP, and PTPRC. IKZF1 is considered a transcriptional regulator of hematopoietic differentiation and participates in the development of lymphocytes, B cells, and T cells (43). IKZF1 can promote the production of the inflammatory cytokine INF- $\gamma$  by regulating the balance of Th1/Th2 (44). Increased INF- $\gamma$  levels can be observed in patients with IA, especially when the aneurysm ruptures (33). Moreover, the severity of AS is associated with genetic polymorphisms in the arterial INF- $\gamma$  gene (45). INF- $\gamma$  affects immune cells, endothelial cells, and SMCs (46, 47), leading to the progression of AS and may play a similar role in the pathogenesis of AS-related IA. IKZF1 is involved in regulating the expression of CCR5, IL10RA, LCP2, and TYROBP and can also promote the production of INF- $\gamma$  to affect the pathogenesis process. IKZF1 may become a new therapeutic target. Another TF, SPI1, regulates LCP2, PTPRC, and TYROBP. SPI1 was significantly upregulated in aortic atherosclerotic plaques in Tibetan minipigs (48). In addition, SPI1 was identified as a significant regulator in peripheral blood samples of patients with IA (49), which also corresponds to the results obtained in our study. Due to the lack of relevant studies, the relationship between SPI1 and AS-related IA still needs to be explored.

Our findings contribute to elucidating the mechanism of the link between IA and AS. However, there are still some flaws in our study. First, the findings of our retrospective study need to be further confirmed with external data. Second, hub genes need to be further verified experimentally in *in vitro* models. Complementing these shortcomings is the focus of our future study.

## 5. Conclusion

We identified and verified eight hub genes and two TFs for AS-related IA, providing new study directions and therapeutic targets for this disease. Eight genes, namely, CCR5, FCGR3A, IL10RA, ITGAX, LCP2, PTPRC, TLR2, and TYROBP, are considered hub genes, and their pathway enrichment results focus on phagocytosis, NK cell-mediated cytotoxicity, and the TCR signaling pathway. Moreover, IKZF1 and SPI1 were identified as the TFs of hub genes and jointly involved in regulating the expression of five genes, namely, CCR5, IL10RA, LCP2, TYROBP, and PTPRC.

## Data availability statement

The original contributions presented in the study are included in the article/supplementary material, further inquiries can be directed to the corresponding author.



## Ethics statement

Ethical review and approval was not required for the study on human participants in accordance with the local legislation and institutional requirements. Written informed consent from the patients/participants or patients/participants' legal guardian/next of kin was not required to participate in this study in accordance with the national legislation and the institutional requirements.

## Author contributions

QZ completed the data analysis and the writing of the manuscript. HL critically revised the manuscript. MZ checked for omissions in the study and provided comments. FL and TL participated in the formulation of the draft study design. The final manuscript has been read and approved by all authors.

## References

- Thompson BG, Brown RD Jr, Amin-Hanjani S, Broderick JP, Cockcroft KM, Connolly ES Jr, et al. Guidelines for the management of patients with unruptured intracranial aneurysms: a guideline for healthcare professionals from the American Heart Association/American Stroke Association. *Stroke*. (2015) 46:2368–400. doi: 10.1161/STR.0000000000000070
- Killer-Oberpfalzer M, Aichholzer M, Weis S, Richling B, Jones R, Virmani R, et al. Histological analysis of clipped human intracranial aneurysms and parent arteries with short-term follow-up. *Cardiovasc Pathol*. (2012) 21:299–306. doi: 10.1016/j.carpath.2011.09.010
- Hashimoto Y, Matsushige T, Shimonaga K, Hosogai M, Kaneko M, Ono C, et al. Vessel wall imaging predicts the presence of atherosclerotic lesions in unruptured intracranial aneurysms. *World Neurosurg*. (2019) 132:e775–82. doi: 10.1016/j.wneu.2019.08.019
- Matsushige T, Shimonaga K, Ishii D, Sakamoto S, Hosogai M, Hashimoto Y, et al. Vessel wall imaging of evolving unruptured intracranial aneurysms. *Stroke*. (2019) 50:1891–4. doi: 10.1161/STROKEAHA.119.025245
- Vergouwen MDI, Backes D, van der Schaaf IC, Hendrikse J, Kleinloog R, Algra A, et al. Gadolinium enhancement of the aneurysm wall in unruptured intracranial aneurysms is associated with an increased risk of aneurysm instability: a follow-up study. *Am J Neuroradiol*. (2019) 40:1112–6. doi: 10.3174/ajnr.A6105
- Ishii D, Matsushige T, Sakamoto S, Shimonaga K, Akiyama Y, Okazaki T, et al. Decreased antiatherogenic protein levels are associated with aneurysm structure alterations in MR vessel wall imaging. *J Stroke Cerebrovasc Dis*. (2019) 28:2221–7. doi: 10.1016/j.jstrokecerebrovasdis.2019.05.002
- Ishii D, Choi A, Piscopo A, Mehdi Z, Raghuram A, Zanaty M, et al. Increased concentrations of atherogenic proteins in aneurysm sac are associated with wall enhancement of unruptured intracranial aneurysm. *Transl Stroke Res*. (2022) 13:577–82. doi: 10.1007/s12975-021-00975-5
- Ou C, Qian Y, Zhang X, Liu J, Liu W, Su H, et al. Elevated lipid infiltration is associated with cerebral aneurysm rupture. *Front Neurol*. (2020) 11:154. doi: 10.3389/fneur.2020.00154
- Oka M, Shimo S, Ohno N, Imai H, Abekura Y, Koseki H, et al. Dedifferentiation of smooth muscle cells in intracranial aneurysms and its potential contribution to the pathogenesis. *Sci Rep*. (2020) 10:8330. doi: 10.1038/s41598-020-65361-x
- Coen M, Burkhardt K, Bijlenga P, Gabbiani G, Schaller K, Kövari E, et al. Smooth muscle cells of human intracranial aneurysms assume phenotypic features similar to those of the atherosclerotic plaque. *Cardiovasc Pathol*. (2013) 22:339–44. doi: 10.1016/j.carpath.2013.01.083
- Ollikainen E, Tulamo R, Lehti S, Lee-Rueckert M, Hernesniemi J, Niemelä M, et al. Smooth muscle cell foam cell formation, apolipoproteins, and ABCA1 in intracranial aneurysms: implications for lipid accumulation as a promoter of aneurysm wall rupture. *J Neuropathol Exp Neurol*. (2016) 75:689–99. doi: 10.1093/jnen/nlw041
- Frösen J, Tulamo R, Paetau A, Laaksamo E, Korja M, Laakso A, et al. Saccular intracranial aneurysm: pathology and mechanisms. *Acta Neuropathol*. (2012) 123:773–86. doi: 10.1007/s00401-011-0939-3
- Starke RM, Chalouhi N, Ding D, Raper DM, McKisic MS, Owens GK, et al. Vascular smooth muscle cells in cerebral aneurysm pathogenesis. *Transl Stroke Res*. (2014) 5:338–46. doi: 10.1007/s12975-013-0290-1
- Texakalidis P, Sweid A, Mouchtouris N, Peterson EC, Sioka C, Rangel-Castilla L, et al. Aneurysm formation, growth, and rupture: the biology and physics of cerebral aneurysms. *World Neurosurg*. (2019) 130:277–84. doi: 10.1016/j.wneu.2019.07.093
- Ritchie ME, Phipson B, Wu D, Hu Y, Law CW, Shi W, et al. Limma powers differential expression analyses for RNA-sequencing and microarray studies. *Nucleic Acids Res*. (2015) 43:e47. doi: 10.1093/nar/gkv007
- Yu G, Wang LG, Han Y, He QY. clusterProfiler: an R package for comparing biological themes among gene clusters. *OMICS*. (2012) 16:284–7. doi: 10.1089/omi.2011.0118
- Szklarczyk D, Gable AL, Lyon D, Junge A, Wyder S, Huerta-Cepas J, et al. STRING v11: protein-protein association networks with increased coverage, supporting functional discovery in genome-wide experimental datasets. *Nucleic Acids Res*. (2019) 47:D607–13. doi: 10.1093/nar/gky1131
- Smoot ME, Ono K, Ruscheinski J, Wang PL, Ideker T. Cytoscape 28: new features for data integration and network visualization. *Bioinformatics*. (2011) 27:431–2. doi: 10.1093/bioinformatics/btq675
- Warde-Farley D, Donaldson SL, Comes O, Zuberi K, Badrawi R, Chao P, et al. The GeneMANIA prediction server: biological network integration for gene prioritization and predicting gene function. *Nucleic Acids Res*. (2010) 38(Web Server issue):W214–20. doi: 10.1093/nar/gkq537
- Keenan AB, Torre D, Lachmann A, Leong AK, Wojciechowski ML, Utti V, et al. ChEA3: transcription factor enrichment analysis by orthogonal omics integration. *Nucleic Acids Res*. (2019) 47:W212–24. doi: 10.1093/nar/gkz446
- Bonaccorsi I, Spinelli D, Cantoni C, Barillà C, Pipitò N, De Pasquale C, et al. Symptomatic carotid atherosclerotic plaques are associated with increased infiltration of natural killer (NK) cells and higher serum levels of NK activating receptor ligands. *Front Immunol*. (2019) 10:1503. doi: 10.3389/fimmu.2019.01503
- Ge P, Liu C, Chan L, Pang Y, Li H, Zhang Q, et al. High-dimensional immune profiling by mass cytometry revealed the circulating immune cell landscape in patients with intracranial aneurysm. *Front Immunol*. (2022) 13:922000. doi: 10.3389/fimmu.2022.922000
- Virella G, Muñoz JF, Galbraith GM, Gissinger C, Chassereau C, Lopes-Virella MF. Activation of human monocyte-derived macrophages by immune complexes containing low-density lipoprotein. *Clin Immunol Immunopathol*. (1995) 75:179–89. doi: 10.1006/clin.1995.1069

## Funding

This research was supported by the Henan Province Medical Science and Technology Research Project (Project No. SB201901056).

## Conflict of interest

The authors declare that the research was conducted in the absence of any commercial or financial relationships that could be construed as a potential conflict of interest.

## Publisher's note

All claims expressed in this article are solely those of the authors and do not necessarily represent those of their affiliated organizations, or those of the publisher, the editors and the reviewers. Any product that may be evaluated in this article, or claim that may be made by its manufacturer, is not guaranteed or endorsed by the publisher.



24. Huang Y, Jaffa A, Koskinen S, Takei A, Lopes-Virella MF. Oxidized LDL-containing immune complexes induce Fc gamma receptor I-mediated mitogen-activated protein kinase activation in THP-1 macrophages. *Arterioscler Thromb Vasc Biol.* (1999) 19:1600–7. doi: 10.1161/01.ATV.19.7.1600
25. Muhammad S, Chaudhry SR, Dobrev G, Lawton MT, Niemelä M, Hänggi D. Vascular macrophages as therapeutic targets to treat intracranial aneurysms. *Front Immunol.* (2021) 12:630381. doi: 10.3389/fimmu.2021.630381
26. Lopes-Virella MF, Binzafar N, Rackley S, Takei A, La Via M, Virella G. The uptake of LDL-IC by human macrophages: predominant involvement of the Fc gamma RI receptor. *Atherosclerosis.* (1997) 135:161–70. doi: 10.1016/S0021-9150(97)00157-3
27. Shah K, Al-Haidari A, Sun J, Kazi JU. T cell receptor (TCR) signaling in health and disease. *Signal Transduct Target Ther.* (2021) 6:412. doi: 10.1038/s41392-021-00823-w
28. Tacke F, Alvarez D, Kaplan TJ, Jakubzick C, Spanbroek R, Llodra J, et al. Monocyte subsets differentially employ CCR2, CCR5, and CX3CR1 to accumulate within atherosclerotic plaques. *J Clin Invest.* (2007) 117:185–94. doi: 10.1172/JCI28549
29. Cipriani S, Francisci D, Mencarelli A, Renga B, Schiaroli E, D'Amore C, et al. Efficacy of the CCR5 antagonist maraviroc in reducing early, ritonavir-induced atherogenesis and advanced plaque progression in mice. *Circulation.* (2013) 127:2114–24. doi: 10.1161/CIRCULATIONAHA.113.001278
30. Joy MT, Ben Assayag E, Shabashov-Stone D, Liraz-Zaltsman S, Mazzitelli J, Arenas M, et al. CCR5 Is a therapeutic target for recovery after stroke and traumatic brain injury. *Cell.* (2019) 176:1143–57.e13. doi: 10.1016/j.cell.2019.01.044
31. Wang J, Cao Y. Characteristics of circulating monocytes at baseline and after activation in patients with intracranial aneurysm. *Hum Immunol.* (2020) 81:41–7. doi: 10.1016/j.humimm.2019.11.003
32. Poitou C, Dalmás E, Renovato M, Benhamo V, Hajduch F, Abdenour M, et al. CD14<sup>dim</sup>CD16<sup>+</sup> and CD14<sup>+</sup>CD16<sup>+</sup> monocytes in obesity and during weight loss: relationships with fat mass and subclinical atherosclerosis. *Arterioscler Thromb Vasc Biol.* (2011) 31:2322–30. doi: 10.1161/ATVBAHA.111.230979
33. Zhang HF, Zhao MG, Liang GB, Yu CY, He W, Li ZQ, et al. Dysregulation of CD4(+) T cell subsets in intracranial aneurysm. *DNA Cell Biol.* (2016) 35:96–103. doi: 10.1089/dna.2015.3105
34. Cagnin S, Biscuola M, Patuzzo C, Trabetti E, Pasquali A, Laveder P, et al. Reconstruction and functional analysis of altered molecular pathways in human atherosclerotic arteries. *BMC Genomics.* (2009) 10:13. doi: 10.1186/1471-2164-10-13
35. Okuno K, Cicalese S, Eguchi S. Depletion of CD11c<sup>+</sup> cell attenuates progression of abdominal aortic aneurysm. *Clin Sci.* (2020) 134:33–7. doi: 10.1042/CS20191083
36. Edsfeldt A, Swart M, Singh P, Dib L, Sun J, Cole JE, et al. Interferon regulatory factor-5-dependent CD11c<sup>+</sup> macrophages contribute to the formation of rupture-prone atherosclerotic plaques. *Eur Heart J.* (2022) 43:1864–77. doi: 10.1093/eurheartj/ehab920
37. Xia M, Wu Q, Chen P, Qian C. Regulatory T cell-related gene biomarkers in the deterioration of atherosclerosis. *Front Cardiovasc Med.* (2021) 8:661709. doi: 10.3389/fcvm.2021.661709
38. Hosaka K, Downes DP, Nowicki KW, Hoh BL. Modified murine intracranial aneurysm model: aneurysm formation and rupture by elastase and hypertension. *J Neurointerv Surg.* (2014) 6:474–9. doi: 10.1136/neurintsurg-2013-010788
39. Wang Y, Chen L, Tian Z, Shen X, Wang X, Wu H, et al. CRISPR-Cas9 mediated gene knockout in human coronary artery endothelial cells reveals a pro-inflammatory role of TLR2. *Cell Biol Int.* (2018) 42:187–93. doi: 10.1002/cbin.10885
40. Zhang X, Wan Y, Feng J, Li M, Jiang Z. Involvement of TLR2/4-MyD88-NF-κB signaling pathway in the pathogenesis of intracranial aneurysm. *Mol Med Rep.* (2021) 23:230. doi: 10.3892/mmr.2021.11869
41. Wang HM, Gao JH, Lu JL. Pravastatin improves atherosclerosis in mice with hyperlipidemia by inhibiting TREM-1/DAP12. *Eur Rev Med Pharmacol Sci.* (2018) 22:4995–5003. doi: 10.26355/eurev\_201808\_15640
42. Hinterseher I, Schworer CM, Lillis JH, Stahl E, Erdman R, Gatalica Z, et al. Immunohistochemical analysis of the natural killer cell cytotoxicity pathway in human abdominal aortic aneurysms. *Int J Mol Sci.* (2015) 16:11196–212. doi: 10.3390/ijms160511196
43. Georgopoulos K, Winandy S, Avitahl N. The role of the Ikaros gene in lymphocyte development and homeostasis. *Annu Rev Immunol.* (1997) 15:155–76. doi: 10.1146/annurev.immunol.15.1.155
44. Hu SJ, Wen LL, Hu X, Yin XY, Cui Y, Yang S, et al. IKZF1: a critical role in the pathogenesis of systemic lupus erythematosus? *Mod Rheumatol.* (2013) 23:205–9. doi: 10.3109/s10165-012-0706-x
45. Esperança JC, Miranda WR, Netto JB, Lima FS, Baumworcel L, Chimelli L, et al. Polymorphisms in IL-10 and INF-γ genes are associated with early atherosclerosis in coronary but not in carotid arteries: a study of 122 autopsy cases of young adults. *BBA Clin.* (2015) 3:214–20. doi: 10.1016/j.bbacli.2015.02.005
46. McLaren JE, Ramji DP. Interferon gamma: a master regulator of atherosclerosis. *Cytokine Growth Factor Rev.* (2009) 20:125–35. doi: 10.1016/j.cytogfr.2008.11.003
47. Tabas I, Lichtman AH. Monocyte-macrophages and T cells in atherosclerosis. *Immunity.* (2017) 47:621–34. doi: 10.1016/j.immuni.2017.09.008
48. Pan Y, Yu C, Huang J, Rong Y, Chen J, Chen M. Bioinformatics analysis of vascular RNA-seq data revealed hub genes and pathways in a novel Tibetan minipig atherosclerosis model induced by a high fat/cholesterol diet. *Lipids Health Dis.* (2020) 19:54. doi: 10.1186/s12944-020-01222-w
49. Zhao H, Li ST, Zhu J, Hua XM, Wan L. Analysis of peripheral blood cells' transcriptome in patients with subarachnoid hemorrhage from ruptured aneurysm reveals potential biomarkers. *World Neurosurg.* (2019) 129:e16–22. doi: 10.1016/j.wneu.2019.04.125



## OPEN ACCESS

## EDITED BY

Shenfeng Qiu,  
University of Arizona, United States

## REVIEWED BY

Renjun Gu,  
Nanjing University of Chinese Medicine, China  
Wenle Li,  
Xiamen University, China

## \*CORRESPONDENCE

Yuanzhen Chen  
✉ chen yuanzhen2011@163.com

## SPECIALTY SECTION

This article was submitted to  
Neurological Biomarkers,  
a section of the journal  
Frontiers in Neurology

RECEIVED 10 December 2022

ACCEPTED 13 February 2023

PUBLISHED 06 March 2023

## CITATION

Zhang Q, Li Z, Xie L, Cao S, Cui Z, Shi B and  
Chen Y (2023) Serum neutrophil  
gelatinase-associated lipocalin as a potential  
biomarker for cognitive decline in spinal cord  
injury. *Front. Neurol.* 14:1120446.  
doi: 10.3389/fneur.2023.1120446

## COPYRIGHT

© 2023 Zhang, Li, Xie, Cao, Cui, Shi and Chen.  
This is an open-access article distributed under  
the terms of the [Creative Commons Attribution  
License \(CC BY\)](https://creativecommons.org/licenses/by/4.0/). The use, distribution or  
reproduction in other forums is permitted,  
provided the original author(s) and the  
copyright owner(s) are credited and that the  
original publication in this journal is cited, in  
accordance with accepted academic practice.  
No use, distribution or reproduction is  
permitted which does not comply with these  
terms.

# Serum neutrophil gelatinase-associated lipocalin as a potential biomarker for cognitive decline in spinal cord injury

Qinghao Zhang<sup>1</sup>, Ziteng Li<sup>1,2</sup>, Liangyu Xie<sup>1</sup>, Shengnan Cao<sup>1</sup>,  
Zhonghao Cui<sup>1</sup>, Bin Shi<sup>1</sup> and Yuanzhen Chen<sup>1\*</sup>

<sup>1</sup>Bone Biomechanics Engineering Laboratory of Shandong Province, Shandong Medicinal Biotechnology Center (School of Biomedical Sciences), Neck-Shoulder and Lumbocurral Pain Hospital of Shandong First Medical University, Shandong First Medical University & Shandong Academy of Medical Sciences, Jinan, Shandong, China, <sup>2</sup>School of Acupuncture and Tuina, Shandong University of Traditional Chinese Medicine, Jinan, China

**Objective:** Neutrophil gelatinase-associated lipoprotein (NGAL), a protein encoded by the lipocalcin-2 (LCN2) gene, has been reported to be involved in multiple processes of innate immunity, but its relationship with spinal cord injury (SCI) remains unclear. This study set out to determine whether NGAL played a role in the development of cognitive impairment following SCI.

**Methods:** At the Neck-Shoulder and Lumbocurral Pain Hospital, a total of 100 SCI patients and 72 controls were enrolled in the study through recruitment. Through questionnaires, baseline data on the participants' age, gender, education level, lifestyle choices (drinking and smoking) and underlying illnesses (hypertension, diabetes, coronary heart disease, and hyperlipidemia) were gathered. The individuals' cognitive performance was evaluated using the Montreal Cognitive Scale (MoCA), and their serum NGAL levels were discovered using ELISA.

**Results:** The investigation included 72 controls and 100 SCI patients. The baseline data did not differ substantially between the two groups, however the SCI group's serum NGAL level was higher than the control group's ( $p < 0.05$ ), and this elevated level was adversely connected with the MoCA score ( $p < 0.05$ ). According to the results of the ROC analysis, NGAL had a sensitivity of 58.24% and a specificity of 86.72% for predicting cognitive impairment following SCI.

**Conclusions:** The changes in serum NGAL level could serve as a biomarker for cognitive impairment in SCI patients, and this holds true even after taking in account several confounding variables.

## KEYWORDS

neutrophil gelatinase-associated lipocalin, biomarker, cognitive, spinal cord injury, serum

## 1. Introduction

Spinal cord injury (SCI) can occur at any level of the spinal cord and can result in temporary or permanent functional changes (1, 2). Symptoms and prognosis vary depending on the location and severity of the injury (3, 4). In most cases, the injury comes from physical trauma, and more than half of all injuries affect the cervical spine (5). In the US, there are roughly 20,000 new instances of SCI each year, and the per-person lifetime economic cost can be as high as 3 million US dollars (6, 7). The annual socioeconomic impact of SCI is projected to be 2.67 billion US dollars (8). Therefore, early identification of potential biomarkers that can effectively predict disease severity and prognosis in SCI may be the key to treating cognitive decline after SCI.

Neutrophil gelatinase-associated lipocalin (NGAL), also known as lipocalcin-2 (LCN2) or oncogene 24p3 or, is an immune protein encoded by the LCN2 gene with a molecular weight of 25 kDa, and its immunomodulatory mechanism may be by limiting the utilization of iron by bacteria, it limits bacterial growth (9–11). *In vivo*, NGAL is mainly expressed in neutrophils, which is generally regarded as a biomarker of renal impairment (12, 13). In 1989, NGAL was first isolated from SV-40-infected mouse kidney cells by Hraba-Renevey et al. (14). Human NGAL contains a 20 amino acid signal peptide and a “lipidin” domain at the N-terminus of the protein, which exerts biological effects by binding to corresponding ligands (15). Human NGAL is up to 98% homologous to chimpanzees, but 62% and 63% homologous to mice and rats, respectively (15, 16).

The role of NGAL in neuroplasticity and its effects on cognitive function have been documented in recent years, but its precise mechanism is still poorly understood (17). Our purpose of this study is to further verify whether NGAL is involved in cognitive decline after SCI, in order to provide new biomarker targets for the prevention and treatment of cognitive impairment after SCI.

## 2. Methods

### 2.1. Study population

Patients with SCI and healthy controls who were hospitalized for Neck-Shoulder and Lumbocurral Pain Hospital between September 2020 and August 2022 made up the study population. The most recent recommendations provide the basis for SCI diagnosis. Congenital spinal abnormalities, severe systemic disorders, a history of spinal cord surgery, cognitive impairment, transfer to another hospital, and unwillingness to cooperate are the exclusion criteria for SCI. Additionally, a control group was drawn from the general population. All participants signed

informed consent, and our study was approved by the hospital ethics committee (No. 2022012). The detailed flowchart is shown in Figure 1.

### 2.2. Baseline data

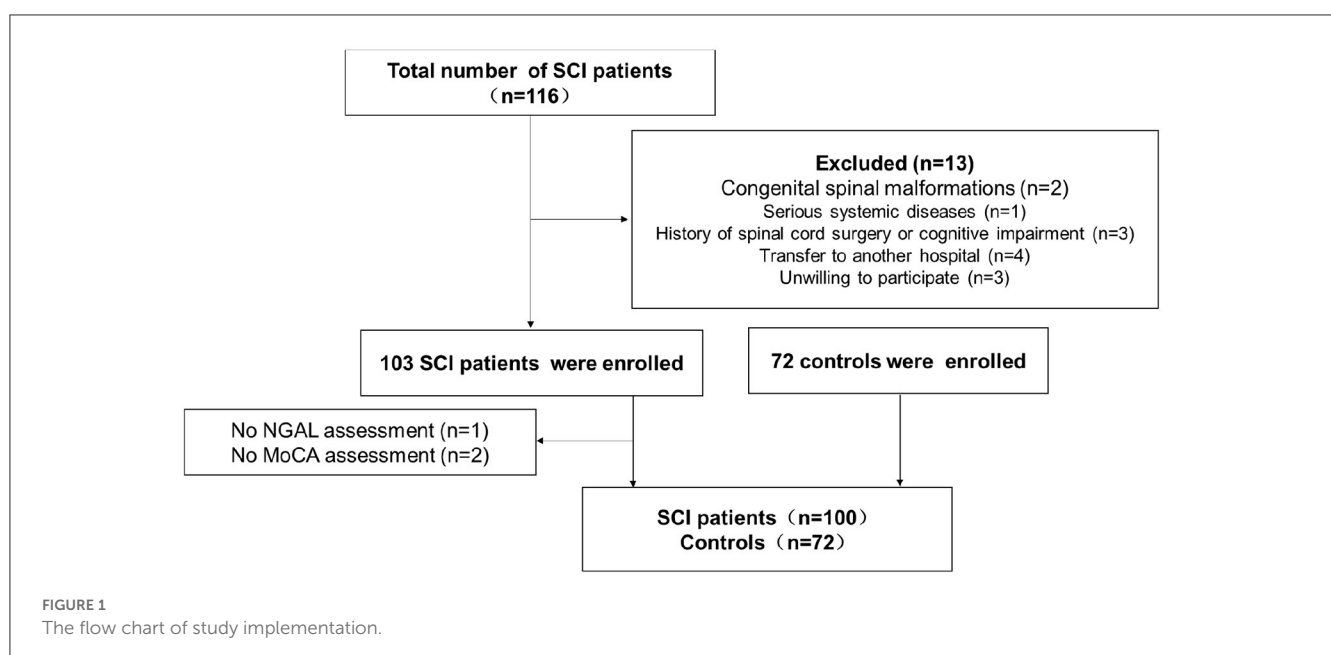
We collected baseline data including age, gender, education level, living habits (smoking and drinking), and underlying diseases (hypertension, diabetes, coronary heart disease, and hyperlipidemia). These data are obtained through questionnaires and recorded, counted and analyzed by specialized personnel.

### 2.3. Cognitive function

In this study, the MoCA scale, a popular measure for assessing cognitive function, was utilized to identify the cognitive function of SCI patients. The MoCA scale, developed by Montrealer Ziad Nasreddine, has been used by researchers and physicians worldwide since it was first released in 1996. It has been translated into 46 languages. For doctors, free. People were given 10 min to respond to 30 questions; the total score was 30, with one point deducted for each incorrect response, and a score of <26 being judged cognitively deficient (18). Our study was approved by MoCA Test Inc. The evaluators were specially trained and blinded to the baseline data of the test subjects.

### 2.4. Serum NGAL level

Venous blood was collected immediately after fasting for 8 h after enrollment in all participants. Venous blood was allowed to stand at room temperature for 10 min, then centrifuged at 1200 g for 15 min, and the upper serum was separated and aliquoted and



stored at  $-80^{\circ}\text{C}$  for future use (19). ThermoFisher, Wilmington, DE, USA, provided the ELISA kit that was utilized to measure the presence of NGAL in the serum of SCI patients.

## 2.5. Statistical analysis

The statistical analysis was performed using SPSS 26.0. The measurement data was represented by the mean  $\pm$  standard deviation (SD), while the enumeration data was represented by number (N). The link between serum NGAL and MoCA was discovered using P for trend. ROC analysis further evaluated the sensitivity and specificity of serum NGAL in predicting cognitive function in SCI. All statistical cutoffs were set at 0.05 and  $p < 0.05$  was considered statistically significant.

## 3. Results

### 3.1. Clinical baseline data of the study population

We recruited a total of 100 SCI patients and 72 healthy controls for this study. The baseline demographic and clinical information for the complete study population, stratified by clinical traits, is shown in Table 1. Age, sex, education level, smoking, drinking, hypertension, coronary heart disease, diabetes, and hyperlipidemia were not statistically significantly different between the two groups, as shown in the table ( $p > 0.05$ ).

### 3.2. Serum NGAL level and MoCA score

The serum NGAL level for the control group was ( $125.4 \pm 12.3$  pg/ml, as reported in Table 1, while it was ( $196.72 \pm 3.8$  pg/ml) for the SCI group. The SCI group's serum NGAL levels were noticeably greater than those of the control group ( $p < 0.001$ ). The SCI group's MoCA score was ( $24.6 \pm 1.7$ ) points, compared to the control group's ( $27.5 \pm 1.2$ ) points. When compared to the control group, the MoCA score of the SCI group was considerably lower ( $p < 0.001$ ). Figure 2 compares the MoCA ratings and serum NGAL concentrations between the two groups. The results showed that the serum NGAL level in SCI group was significantly higher than that in control group, while the MoCA score was significantly lower than that in control group.

### 3.3. Correlation analysis between serum NGAL level and MoCA assessment

We separated the SCI patients into 4 groups based on the quartile levels of the serum NGAL and looked at the connection between those groups and the MoCA score. Table 2 displays the correlation analysis between the serum NGAL level and MoCA score. From Q1 to Q4, MoCA scores were ( $25.8 \pm 1.9$ ), ( $24.9 \pm 1.8$ ), ( $24.2 \pm 1.5$ ) and ( $23.5 \pm 1.6$ ), respectively. The findings indicated that the MoCA score decreased as blood NGAL level increased ( $p$

TABLE 1 Demographic and clinical characteristics from the study population.

|                                      | Controls<br>( <i>n</i> = 72) | SCI<br>( <i>n</i> = 100) | <i>p</i> -value |
|--------------------------------------|------------------------------|--------------------------|-----------------|
| Age, years                           | $59.3 \pm 7.1$               | $60.6 \pm 7.8$           | 0.265           |
| Gender, male/female                  | 56/16                        | 88/12                    | 0.073           |
| Education level, <i>n</i> (%)        |                              |                          | 0.798           |
| Low                                  | 33                           | 51                       |                 |
| Middle                               | 26                           | 33                       |                 |
| High                                 | 13                           | 16                       |                 |
| Smoking, <i>n</i> (%)                |                              |                          | 0.520           |
| Never                                | 26                           | 38                       |                 |
| Former                               | 10                           | 17                       |                 |
| Current                              | 36                           | 45                       |                 |
| Drinking, <i>n</i> (%)               | 28                           | 42                       | 0.682           |
| Hypertension, <i>n</i> (%)           | 20                           | 32                       | 0.552           |
| Diabetes, <i>n</i> (%)               | 11                           | 14                       | 0.815           |
| Coronary heart disease, <i>n</i> (%) | 9                            | 13                       | 0.923           |
| Hyperlipidemia, <i>n</i> (%)         | 17                           | 28                       | 0.518           |
| NGAL, pg/ml                          | $125.4 \pm 12.3$             | $196.7 \pm 23.8$         | $<0.001$        |
| MoCA, points                         | $27.5 \pm 1.2$               | $24.6 \pm 1.7$           | $<0.001$        |

NGAL, Neutrophil gelatinase-associated lipocalin; MoCA, Montreal cognitive test.

$< 0.001$ ), indicating that a high serum NGAL level may be a sign of cognitive impairment.

### 3.4. Multiple model regression analysis

To explore the etiology affecting the MoCA score, we performed a multi-model regression analysis (Table 3). In model 1, after adjusting the confounding of age, sex and education level, it was suggested that serum NGAL was a risk factor for SCI-related cognitive impairment ( $p < 0.05$ ); in model 2, we further adjusted the Smoking and drinking suggest that serum NGAL is also a risk factor for SCI-related cognitive impairment ( $p < 0.05$ ); Serum NGAL was found to be an independent risk factor for cognitive impairment caused by SCI in model 3, which was based on model 2. After further adjusting for the underlying conditions (hypertension, diabetes, coronary heart disease, and hyperlipidemia), the same result was found ( $p = 0.047$ ).

### 3.5. ROC curve analysis

In order to further verify the accuracy of serum NGAL level in diagnosing cognitive impairment after SCI, we performed ROC curve analysis, and the results are shown in Figure 3. The sensitivity of serum NGAL in diagnosing cognitive impairment after SCI was 72.48%, and the specificity was 61.28%.

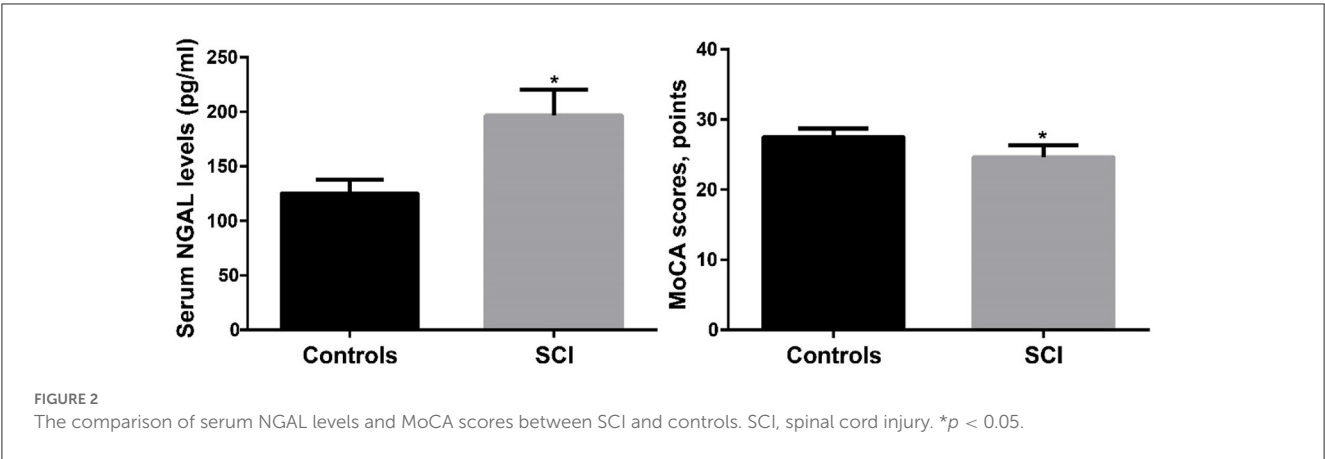


TABLE 2 Correlation analysis between serum NGAL levels and MoCA scores.

| Variable    | Q1         | Q2         | Q3         | Q4         | P-values |
|-------------|------------|------------|------------|------------|----------|
| MoCA scores | 25.8 ± 1.9 | 24.9 ± 1.8 | 24.2 ± 1.5 | 23.5 ± 1.6 | <0.001   |

NGAL, Neutrophil gelatinase-associated lipocalin; MoCA, Montreal cognitive test.

TABLE 3 Regression analysis of serum NGAL levels and MoCA scores.

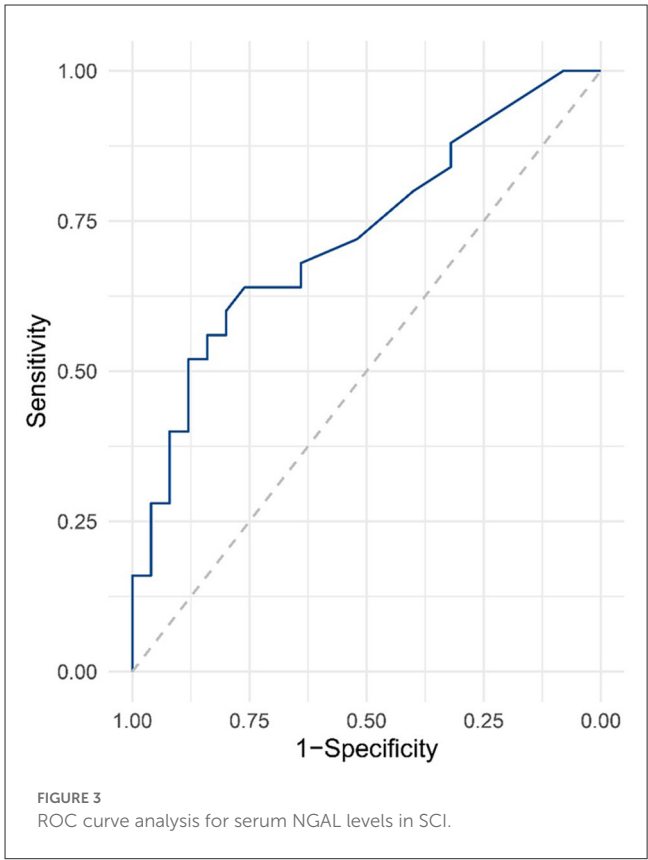
|         | MoCA scores            |          |
|---------|------------------------|----------|
|         | Regression coefficient | P-values |
| Model 1 | 0.352                  | <0.001   |
| Model 2 | 0.271                  | <0.001   |
| Model 3 | 0.218                  | 0.047    |

Model 1: adjusted for age, gender and education levels; Model 2: further adjusted for smoking and drinking; Model 3: further adjusted for Hypertension, Diabetes, Coronary heart disease and Hyperlipidemia. NGAL, Neutrophil gelatinase-associated lipocalin; MoCA, Montreal cognitive test.

#### 4. Discussion

This is the first study of the relationship between cognitive impairment and serum NGAL levels in patients after SCI. Our results showed that the blood level of NGAL in SCI patients was significantly higher than that in healthy controls, and the quartile level was negatively correlated with MoCA score. In multi-model regression analysis, serum NGAL levels were considered to be independent risk factors for SCI-related cognitive impairment after adjusting for multiple confounding. Subsequent ROC analysis further proved that the serum NGAL level has a high accuracy in diagnosing SCI-related cognitive impairment. Our study suggests that serum NGAL levels may serve as a potential biomarker of SCI-related cognitive function.

NGAL is mainly expressed and secreted by immune cells, liver cells or renal tubular cells, and it can capture and consume siderophore to play an antibacterial role (20, 21). In addition to antibacterial, NGAL can also be used as a factor regulating cell growth and differentiation, mediating the biological activity of iron inside and outside cells (22). Genomic studies have shown that NGAL is one of the most up-regulated genes in acute kidney injury, and it can regulate the secretion of a renal tubulin with a molecular



weight of 25KDa, which quickly enters the body fluid after the onset of renal injury (23). NGAL rises 24–48 h earlier than conventional serum creatinine, making it potentially a more effective biomarker. Studies have also shown that elevated levels of NGAL can predict the prognosis of acute kidney injury (24). All of the above make NGAL the focus of clinical translational research.

In addition to its involvement in acute kidney injury, a role for NGAL in neurological disorders has also been found. Zhao et al. (25) found that the expression of NGAL increased after traumatic brain injury, which was negatively correlated with the clinical score reflecting the severity of traumatic brain injury, and it has good sensitivity and specificity as a biomarker for diagnosing traumatic



brain injury (25). Peng et al. (26) found that the level of NGAL increases after cerebral ischemia, and the activation of EGF/EGFR can regulate the expression of NGAL by activating the JAK2/STAT3 pathway to improve neurological deficits (26). Serra et al. (27) discovered that plasma NGAL levels were significantly higher in aneurysm patients than in the control group, indicating that NGAL may be involved in the pathophysiological process of aneurysms and that NGAL may be used as an indicator for assessing aneurysm rupture and prognosis in the future (27).

In recent years, studies on the involvement of NGAL in cognitive impairment have been found. The Dutch research team found that low levels of NGAL in serum and cerebrospinal fluid can be used as potential biomarkers to predict the conversion of mild cognitive impairment to Alzheimer's disease (AD), and affect the pathophysiological process of AD accompanied by depression (28, 29). The same research team also found that NGAL was associated with cognitive impairment in patients with depression, and there were gender differences (30). In addition, NGAL is also considered to be associated with the pathogenesis of Down syndrome.

The research of NGAL in SCI has also come into the field of vision of researchers. Behrens, V found that NGAL was significantly increased in the spinal cord, brain, liver and serum in the SCI mouse model, while the absence of NGAL could significantly reduce the differentiation of glial cells, indicating that it may be involved in the inflammatory injury after SCI (31). Rathore et al. (32) found that Lcn2 can regulate the inflammatory response after SCI, while the lack of NGAL can reduce the secondary injury after SCI and improve the recovery of motor function (32). However, clinical studies of NGAL in SCI patients have not been reported.

The first study to reveal cognitive damage in patients following NGAL involvement in SCI is ours. However, our study has certain flaws. Our study is a single-center, small-sample investigation with Chinese participants. It is debatable if the findings of this study apply to other geographic or racial groups. There is an urgent need for large-sample multi-center research to confirm this study.

## 5. Conclusions

The results of the current study suggest that changes in serum NGAL could serve as a biomarker for cognitive impairment in SCI patients, and this finding holds true even after taking into account a number of confounding variables. To develop innovative methods for treating cognitive impairment caused by

SCI, future scientific and clinical research must further investigate the underlying mechanism.

## Data availability statement

The raw data supporting the conclusions of this article will be made available by the authors, without undue reservation.

## Ethics statement

The studies involving human participants were reviewed and approved by the Ethics Committee of Neck-Shoulder and Lumbocurral Pain Hospital. The patients/participants provided their written informed consent to participate in this study.

## Author contributions

QZ and YC designed this research and wrote the manuscript. ZL, LX, SC, ZC, and BS participated in data collection, experimental process, and data analysis. All authors contributed to the article and approved the submitted version.

## Acknowledgments

All authors are grateful to the Neck-Shoulder and Lumbocurral Pain Hospital.

## Conflict of interest

The authors declare that the research was conducted in the absence of any commercial or financial relationships that could be construed as a potential conflict of interest.

## Publisher's note

All claims expressed in this article are solely those of the authors and do not necessarily represent those of their affiliated organizations, or those of the publisher, the editors and the reviewers. Any product that may be evaluated in this article, or claim that may be made by its manufacturer, is not guaranteed or endorsed by the publisher.

## References

1. Li Z, Yu S, Hu X, Li Y, You X, Tian D. Fibrotic scar after spinal cord injury: crosstalk with other cells, cellular origin, function, and mechanism. *Front Cell Neurosci.* (2021) 15:720938. doi: 10.3389/fncel.2021.720938
2. Tran AP, Warren PM, Silver J. New insights into glial scar formation after spinal cord injury. *Cell Tissue Res.* (2021) 387:1–18. doi: 10.1007/s00441-021-03477-w
3. Fouad K, Popovich PG, Kopp MA, Schwab JM. The neuroanatomical-functional paradox in spinal cord injury. *Nat Rev Neurol.* (2021) 17:53–62. doi: 10.1038/s41582-020-00436-x
4. Krogh S, Aagaard P, Jønsson AB, Figlewski K, Kasch H. Effects of repetitive transcranial magnetic stimulation on recovery in lower limb muscle strength and gait function following spinal cord injury: a randomized controlled trial. *Spinal Cord.* (2022) 60:135–41. doi: 10.1038/s41393-021-00703-8
5. Ahuja CS, Wilson JR, Nori S, Kotter M, Druschel C, Curt A, et al. Traumatic spinal cord injury. *Nat Rev Dis Primers.* (2017) 3:1–21. doi: 10.1038/nrdp.2017.18

6. Liu FJ, Xu HH, Yin Y, Chen YZ, Xie LY, Li HZ. Decreased adiponectin levels are a risk factor for cognitive decline in spinal cord injury. *Disease Markers*. (2022). doi: 10.1155/2022/5389162
7. Castro-Marin F, Gaither JB, Rice AD, Blust R, Chikani V, Vossbrink A, et al. Prehospital protocols reducing long spinal board use are not associated with a change in incidence of spinal cord injury. *Prehospital Emerg Care*. (2020) 24:401–10. doi: 10.1080/10903127.2019.1645923
8. Cao Y, Krause JS. The association between secondary health conditions and indirect costs after spinal cord injury. *Spinal Cord*. (2021) 59:306–10. doi: 10.1038/s41393-020-00567-4
9. Ye Z, Wang S, Yang Z, He M, Zhang S, Zhang W, et al. Serum lipocalin-2, cathepsin S and chemerin levels and nonalcoholic fatty liver disease. *Mol Biol Rep*. (2014) 41:1317–23. doi: 10.1007/s11033-013-2977-5
10. Millar SA, Anderson SI, O'Sullivan SE. Osteokines and the vasculature: a review of the in vitro effects of osteocalcin, fibroblast growth factor-23 and lipocalin-2. *PeerJ*. (2019) 7:e7139. doi: 10.7717/peerj.7139
11. Zhang F, Liu E, Radaic A, Yu X, Yang S, Yu C, et al. Diagnostic potential and future directions of matrix metalloproteinases as biomarkers in gingival crevicular fluid of oral and systemic diseases. *Int J Biol Macromol*. (2021) 188:180–96. doi: 10.1016/j.ijbiomac.2021.07.165
12. Khawaja S, Jafri L, Siddiqui I, Hashmi M, Ghani F. The utility of neutrophil gelatinase-associated Lipocalin (NGAL) as a marker of acute kidney injury (AKI) in critically ill patients. *Biomarker Res*. (2019) 7:1–6. doi: 10.1186/s40364-019-0155-1
13. Mishra J, Dent C, Tarabishi R, Mitsnefes MM, Ma Q, Kelly C, et al. Neutrophil gelatinase-associated lipocalin (NGAL) as a biomarker for acute renal injury after cardiac surgery. *Lancet*. (2005) 365:1231–8. doi: 10.1016/S0140-6736(05)74811-X
14. Garay-Rojas E, Harper M, Hraba-Renevey S, Kress M. An apparent autocrine mechanism amplifies the dexamethasone- and retinoic acid-induced expression of mouse lipocalin-encoding gene 24p3. *Gene*. (1996) 170:173–80. doi: 10.1016/0378-1119(95)00896-9
15. Al Jaber S, Cohen A, D'Souza C, Abdulrazzaq YM, Ojha S, Bastaki S, et al. Lipocalin-2: structure, function, distribution and role in metabolic disorders. *Biomed Pharmacother*. (2021) 142:112002. doi: 10.1016/j.biopha.2021.112002
16. Kjeldsen L, Cowland JB, Borregaard N. Human neutrophil gelatinase-associated lipocalin and homologous proteins in rat and mouse. *BBA Protein Struct Mol Enzymol*. (2000) 1482:272–83. doi: 10.1016/S0167-4838(00)00152-7
17. Choi J, Lee H-W, Suk K. Increased plasma levels of lipocalin 2 in mild cognitive impairment. *J Neurol Sci*. (2011) 305:28–33. doi: 10.1016/j.jns.2011.03.023
18. Wang Q, Wang K, Ma Y, Li S, Xu Y. Serum galectin-3 as a potential predictive biomarker is associated with poststroke cognitive impairment. *Oxid Med Cell Longev*. (2021) 2021:5827812. doi: 10.1155/2021/5827812
19. Zhang F, Hou G, Hou G, Wang C, Shi B, Zheng Y. Serum irisin as a potential biomarker for cognitive decline in vascular dementia. *Front Neurol*. (2021) 12:755046. doi: 10.3389/fneur.2021.755046
20. Schmidt-Ott KM, Mori K, Li JY, Kalandadze A, Cohen DJ, Devarajan P, et al. Dual action of neutrophil gelatinase-associated lipocalin. *J Am Soc Nephrol*. (2007) 18:407–13. doi: 10.1681/ASN.2006080882
21. Yang J, Gan X, Song X, Yuan R, Xiang Y. Apamer-based sensitive and label-free electrochemical detection of neutrophil gelatinase-associated lipocalin via recycling amplification cascades. *Anal Chim Acta*. (2022) 1233:340515. doi: 10.1016/j.aca.2022.340515
22. Kim IY, Kim JH, Lee DW, Lee SB, Rhee H, Song SH, et al. Plasma neutrophil gelatinase-associated lipocalin is associated with iron status in anemic patients with pre-dialysis chronic kidney disease. *Clin Exp Nephrol*. (2018) 22:28–34. doi: 10.1007/s10157-017-1409-6
23. Virzi GM, Clementi A, De Cal M, Cruz DN, Ronco C. Genomics and biological activity of neutrophil gelatinase-associated lipocalin in several clinical settings. *Blood Purif*. (2013) 35:139–43. doi: 10.1159/000346100
24. Haase M, Bellomo R, Devarajan P, Schlattmann P, Haase-Fielitz A. Accuracy of neutrophil gelatinase-associated lipocalin (NGAL) in diagnosis and prognosis in acute kidney injury: a systematic review and meta-analysis. *Am J Kidney Dis*. (2009) 54:1012–24. doi: 10.1053/j.ajkd.2009.07.020
25. Zhao J, Chen H, Zhang M, Zhang Y, Qian C, Liu Y, et al. Early expression of serum neutrophil gelatinase-associated lipocalin (NGAL) is associated with neurological severity immediately after traumatic brain injury. *J Neurol Sci*. (2016) 368:392–8. doi: 10.1016/j.jns.2016.07.060
26. Peng D-H, Liu Y-Y, Chen W, Hu H-N, Luo Y. Epidermal growth factor alleviates cerebral ischemia-induced brain injury by regulating expression of neutrophil gelatinase-associated lipocalin. *Biochem Biophys Res Commun*. (2020) 524:963–9. doi: 10.1016/j.bbrc.2020.02.025
27. Serra R, Volpentesta G, Gallelli L, Grande R, Buffone G, Lavano A. Metalloproteinase-9 and neutrophil gelatinase-associated lipocalin plasma and tissue levels evaluation in middle cerebral artery aneurysms. *Br J Neurosurg*. (2015) 29:1–5. doi: 10.3109/02688697.2014.913777
28. Naudé PJ, Ramakers IH, van der Flier WM, Jiskoot LC, Reesink FE, Claassen JA, et al. Serum and cerebrospinal fluid Neutrophil gelatinase-associated lipocalin (NGAL) levels as biomarkers for the conversion from mild cognitive impairment to Alzheimer's disease dementia. *Neurobiol Aging*. (2021) 107:1–10. doi: 10.1016/j.neurobiolaging.2021.07.001
29. Dekens DW, Naudé PJ, Engelborghs S, Vermeiren Y, Van Dam D, Oude Voshaar RC, et al. Neutrophil gelatinase-associated lipocalin and its receptors in Alzheimer's disease (AD) brain regions: differential findings in AD with and without depression. *J Alzheimer's Dis*. (2017) 55:763–76. doi: 10.3233/JAD-160330
30. Naudé P, den Boer J, Comijs H, Bosker F, Zuidersma M, Groenewold N, et al. Sex-specific associations between neutrophil gelatinase-associated Lipocalin (NGAL) and cognitive domains in late-life depression. *Psychoneuroendocrinology*. (2014) 48:169–77. doi: 10.1016/j.psyneuen.2014.06.016
31. Behrens V, Voelz C, Müller N, Zhao W, Gasterich N, Clärner T, et al. Lipocalin 2 as a putative modulator of local inflammatory processes in the spinal cord and component of organ cross talk after spinal cord injury. *Mol Neurobiol*. (2021) 58:5907–19. doi: 10.1007/s12035-021-02530-7
32. Rathore KI, Berard JL, Redensek A, Chierzi S, Lopez-Vales R, Santos M, et al. Lipocalin 2 plays an immunomodulatory role and has detrimental effects after spinal cord injury. *J Neurosci*. (2011) 31:13412–9. doi: 10.1523/JNEUROSCI.0116-11.2011



## OPEN ACCESS

EDITED BY  
Yuzhen Xu,  
Tongji University, China

REVIEWED BY  
Tengyang Wang,  
Fujian Branch of Shanghai Children's Medical  
Center Affiliated to Shanghai Jiaotong  
University School of Medicine, China  
Luqian Li,  
Maoming People's Hospital, China  
Ning Zhang,  
General Hospital of Ningxia Medical  
University, China

\*CORRESPONDENCE  
Shizhong Fu  
✉ shioumo9@163.com;  
✉ 452770974@qq.com

SPECIALTY SECTION  
This article was submitted to  
Neurological Biomarkers,  
a section of the journal  
Frontiers in Neurology

RECEIVED 27 November 2022  
ACCEPTED 26 December 2022  
PUBLISHED 16 March 2023

CITATION  
Zhu D, Zhu Y, Liu L, He X and Fu S (2023)  
Metabolomic analysis of vascular cognitive  
impairment due to hepatocellular carcinoma.  
*Front. Neurol.* 13:1109019.  
doi: 10.3389/fneur.2022.1109019

COPYRIGHT  
© 2023 Zhu, Zhu, Liu, He and Fu. This is an  
open-access article distributed under the terms  
of the [Creative Commons Attribution License  
\(CC BY\)](https://creativecommons.org/licenses/by/4.0/). The use, distribution or reproduction  
in other forums is permitted, provided the  
original author(s) and the copyright owner(s)  
are credited and that the original publication in  
this journal is cited, in accordance with  
accepted academic practice. No use,  
distribution or reproduction is permitted which  
does not comply with these terms.

# Metabolomic analysis of vascular cognitive impairment due to hepatocellular carcinoma

Dan Zhu<sup>1</sup>, Yamei Zhu<sup>2</sup>, Lin Liu<sup>3</sup>, Xiaoxue He<sup>1</sup> and Shizhong Fu<sup>2\*</sup>

<sup>1</sup>Xinqiao Hospital, Army Medical University (Third Military Medical University), Chongqing, China,

<sup>2</sup>Department of Infectious Diseases, Wuhua Ward, 920th Hospital of Joint Logistics Support Force of Chinese PLA, Kunming, Yunnan, China, <sup>3</sup>Dalian Hunter Information Consulting Co. LTD, Dalian, China

**Introduction:** Screening for metabolically relevant differentially expressed genes (DEGs) shared by hepatocellular carcinoma (HCC) and vascular cognitive impairment (VCI) to explore the possible mechanisms of HCC-induced VCI.

**Methods:** Based on metabolomic and gene expression data for HCC and VCI, 14 genes were identified as being associated with changes in HCC metabolites, and 71 genes were associated with changes in VCI metabolites. Multi-omics analysis was used to screen 360 DEGs associated with HCC metabolism and 63 DEGs associated with VCI metabolism.

**Results:** According to the Cancer Genome Atlas (TCGA) database, 882 HCC-associated DEGs were identified and 343 VCI-associated DEGs were identified. Eight genes were found at the intersection of these two gene sets: NNMT, PHGDH, NR1H2, CYP2J2, PON1, APOC2, CCL2, and SOCS3. The HCC metabolomics prognostic model was constructed and proved to have a good prognostic effect. The HCC metabolomics prognostic model was constructed and proved to have a good prognostic effect. Following principal component analyses (PCA), functional enrichment analyses, immune function analyses, and TMB analyses, these eight DEGs were identified as possibly affecting HCC-induced VCI and the immune microenvironment. As well as gene expression and gene set enrichment analyses (GSEA), a potential drug screen was conducted to investigate the possible mechanisms involved in HCC-induced VCI. The drug screening revealed the potential clinical efficacy of A-443654, A-770041, AP-24534, BI-2536, BMS-509744, CGP-60474, and CGP-082996.

**Conclusion:** HCC-associated metabolic DEGs may influence the development of VCI in HCC patients.

## KEYWORDS

metabolomics, metabolic DEGs, prognostic model, biomarkers, neurovascular disease, hepatocellular carcinoma (HCC), vascular cognitive impairment (VCI)

## Introduction

Hepatocellular carcinoma (HCC) is one of the most common malignant tumors worldwide, characterized by the insidious and rapid onset, poor prognosis, and high metastasis rate. With an estimated 906,000 new cases of HCC in 2020, accounting for 4.7% of the overall cancer incidence, HCC is the sixth most common malignancy worldwide, after breast, lung, colorectal, prostate, and stomach cancers (1). It is the third most common cause of cancer-related death and patients generally have a poor prognosis as the onset is insidious and the tumor is often at an advanced stage at the time of diagnosis. In 2020, ~830,000 people died from HCC globally, accounting for 8.3% of cancer-related deaths (1). In recent years, with the popularization of hepatitis B vaccination and the improved efficacy of antiviral drug therapy, the incidence of virus-related HCC is on the decline, while non-alcoholic liver disease and metabolic syndrome-related HCC are increasing year by year due to lifestyle changes and dietary habits (2). The main treatment options for HCC include surgical resection, radiofrequency ablation, chemotherapy, liver-targeted

drugs, and liver transplantation. However, due to the insidious onset of the disease, the early stages may present with only non-specific symptoms such as weakness and dyspepsia, and progresses rapidly, resulting in the diagnosis of the tumor at an advanced stage, by when the opportunity for radical treatment had already passed (3). The late stage of HCC is often associated with complications such as gastrointestinal bleeding, infection, hepatic and renal syndrome, and hepatic encephalopathy. When complicated by hepatic encephalopathy, clinical manifestations may include behavioral abnormalities, cognitive impairment, altered consciousness, and even coma, which are often combined with liver dysfunction making the treatment more difficult and the patient's prognosis poor (4, 5). However, no extensive study has been conducted to determine whether other factors may contribute to cognitive impairment in patients with HCC.

Vascular cognitive impairment (VCI) is a syndrome of cognitive impairment secondary to bleeding, ischemic stroke, cerebrovascular injury, and other diseases. Patients may present with cognitive impairment such as memory problems, behavioral abnormalities, speech difficulties, and even dementia (6). Various mechanisms involving immune inflammatory response, oxidative stress, and damage to the blood-brain barrier are associated with the development of VCI (7–11). Some studies have also reported that a strong correlation between HCC and the changes in intestinal microbiota in Alzheimer's disease has been observed, indicating that HCC may promote cognitive impairment in Alzheimer's disease by affecting the intestinal microbial ecology (12). Furthermore, some studies have found common transcriptional changes between Alzheimer's disease and HCC and other cancers (13). Abnormal levels of circulating metabolites such as amino acids and fatty acids are associated with cognitive impairment caused by vascular dysfunction (14–16). Metabolomic analysis showed that dysregulation of various metabolites was closely related to HCC, suggesting its involvement in promoting the occurrence of HCC-related VCI (17). The circulating metabolites may, therefore, be affected by HCC, thereby resulting in cognitive impairment.

Metabolomics is the qualitative and quantitative analysis of the metabolites of an organism or cell during a specific period to deduce the relationship between different metabolites and the corresponding pathophysiological state. Metabolomics is now widely used in many fields such as disease diagnosis, drug toxicology, pharmaceutical development, and microbial metabolism (18, 19). Since abnormal metabolism is a common feature of cancer cells, metabolomics plays an important role in tumor prognosis, drug target research, and metabolic marker screening (20). The liver is the central organ of human metabolism and is involved in regulating the expression levels of many metabolites, which makes the metabolomic study of HCC particularly important (21, 22). Zoe Hall and other researchers found that the proliferation of HCC tumor cells is closely related to altered metabolic pathways such as adipogenesis and phosphatidylcholine production (23). Further, the serum bile acid levels were significantly higher and serum sphingolipid levels were lower in HCC patients, suggesting that the changes in these metabolites are closely related to the development of HCC (24). Metabolomic analysis of VCI showed that the disease-related biomarkers were mainly associated with homocysteine, folate, branched-chain amino acids, and lipid metabolism (16). Sphingolipids, cholesterol, phospholipids, and other lipids play an important role in the maintenance of the structure and function of neuronal structures. Therefore, some researchers

have suggested that disorders of lipid metabolism could be vital in the pathogenesis of VCI, but the exact mechanism is not yet clear (25). This suggests that HCC and VCI are associated with metabolomic changes, and related studies are needed.

The development of next generation sequencing (NGS) technologies and bioinformatic tools allows a large-scale analysis of each parameter involved in cancer and other systemic disease (26–32). In this study, the Gene Expression Omnibus (GEO) database and literature search were utilized to obtain metabolomic data on HCC and VCI, and Metaboanalyst 5.0 was used to obtain the metabolic differentially expressed genes (DEGs) as previous researches (33–36). In order to understand the possible mechanism of VCI caused by HCC and provide some theoretical basis for the clinical treatment of HCC, we conducted principal component analyses, functional enrichment analyses, immune function analyses, and tumor mutational burden (TMB) analyses of the above genes. We investigated possible mechanisms of VCI induction by HCC in this study.

## Methods

### Data acquisition

VCI clinical and transcriptomic (mRNA) data were downloaded from GEO database. The filter conditions were set to ① “vascular cognitive impairment”; ② human. This study was derived from 10 “normal cognitive patients” and 10 “patients with VCI” from the microarray dataset GSE201482 in 10 cases. DEGs of VCI were screened according to the criteria of  $P$ -value  $< 0.05$  and  $|\log_2FC| \geq 1.00$ . HCC clinical, transcriptomic (mRNA) data were downloaded from TCGA (<https://portal.gdc.cancer.gov/>) website, and their expression matrix was compiled and summarized by R. DEGs were screened by adjust  $P$ -value  $< 0.05$  and  $|\log_2FC| \geq 1.0$ , and heat maps were plotted. DEGs were categorized into up-regulated, down-regulated, and non-statistically significant groups, and then imported into R for volcano plots. Bioconductor R software's bioconductor R package was used to normalize and calculate expression values for microarray data. Based on the screened DEGs, heat maps and cluster analyses were performed using the heatmap package. We transformed DEG  $P$ -value to  $-\log_{10}$ , grouped them according to  $\log_2FC$ , and imported the processed data into R for volcano plotting. The HCC expression matrix data was downloaded from the Cancer Genome Atlas database. According to the pre-screened genes, the relative expression of the core genes in the HCC expression data was analyzed using “ggpubr” package and a relative expression box plot was drawn.

### Metabolomics matrix construction and multi-omics analyses

For multi-omics analysis, metabolically differentially expressed metabolites and DEGs were imported from HCC and VCI metabolomics into Metaboanalyst 5.0, while metabolomics genes associated with HCC and VCI were incorporated into Venny 2.1 software (<http://bioinfo.gp.cnb.csic.es/tools/venny/index.html>) for plotting Venn diagrams and obtaining metabolomic differential genes associated with HCC and VCI.



## Immuno-infiltration analysis and immunofunctional analysis

The HCC expression matrix data obtained above were subjected to a deconvolution algorithm using the CIBERSORT package, which allows estimation of the cellular composition of complex tissues based on normalized gene expression data, as well as quantification of specific cell types. The immune cell sorting perl script is used to sort the HCC-associated infiltrating immune cells. The limma R package in R was used to calculate expression values from the microarray data. HCC and paraneoplastic tissues were analyzed using the CIBERSORT package. With the CIBERSORT package, the composition of immune cells in each sample was further analyzed and histograms were plotted. Pheatmap was used to generate heat maps showing immune cell distribution. HCC immune cell infiltration co-expression map was plotted using corrrplot to analyse interactions between immune cell populations. Finally, the expression of each immune cell was analyzed using the vioplot package in HCC tissues and paracancerous tissues. In relation to immunofunctional analysis, we used the “limma,” “GSVA,” “gseabase,” “pheatmap,” and “reshape2” packages to perform immunofunctional analysis on HCC metabolomics-related genes to identify targets for precision therapy.

## VCI-associated HCC metabolic genes prognostic model

Standardized HCC metabolomics data were merged with HCC clinical data, and univariate and multifactorial Cox prognostic survival analyses on HCC differential genes were performed using the R language packages survival, caret, glmnet, survminer, and survroc to plot survival curves for closely related key metabolomics genes. In addition, 370 cases were randomly divided into testing group ( $n = 185$ ) and training group ( $n = 185$ ). R software was used to perform risk survival analysis on the pre-merged data, plotting risk survival curves and receiver operator characteristic (ROC) curves for testing group, training group, and total group as previous studies (37–40). On the general clinical data of HCC, the survival package was again used to perform clinical statistical analysis and risk prognostic analysis. To investigate the risk factors associated with HCC, forest plots, and histograms were plotted for single- and multi-factor independent prognostic analysis. Further model validation on clinical subgroups was performed using the “survival” and “survminer” packages.

## Principal component analysis and enrichment analysis of gene ontology (GO) and the Kyoto encyclopedia of genes and genomes (KEGG) for genes associated with HCC metabolomics

The scatterplot3d package was used for the principal component analysis of HCC metabolomics-related genes and HCC-related risk genes, and the clusterprofiler.R package in R (<https://www.r-project.org/>) software and Perl language were used for metabolomics-related HCC GO analysis for differential genes. KEGG pathway enrichment analysis was performed using the clusterprofilerkegg.R

package to analyze core pathway enrichment based on enrichment factor values and to investigate the biological functions and signaling pathways that may be associated with HCC.

## TMB analysis of HCC metabolism-related genes

TMB files were downloaded from the TCGA database and correlation tests between core genes and TMB were performed using functions, with correlation coefficients and *P*-values calculated. In addition, correlation analysis between metabolism-related genes and HCC tumor mutational load was performed using the survival and survminer software packages, and correlation coefficients and *P*-values were calculated.

## Gene set enrichment analysis (GSEA)

The GSEA website was used to download the GO/KEGG annotation files for the whole transcriptome genes, and GO and KEGG enrichment analyses of the core genes were performed using the limma, org, Hs, eg, db, clusterprofiler, and enrichplot packages as previous researches (41–43). Analyses of cellular component (CC), molecular function (MF), biological process (BP), and KEGG pathway enrichment were conducted for the core genes. Based on the enrichment factor values, we analyzed the core pathway enrichment and examined the potential biological functions and signaling pathways of the HCC core genes.

## Screening for potential therapeutic drugs

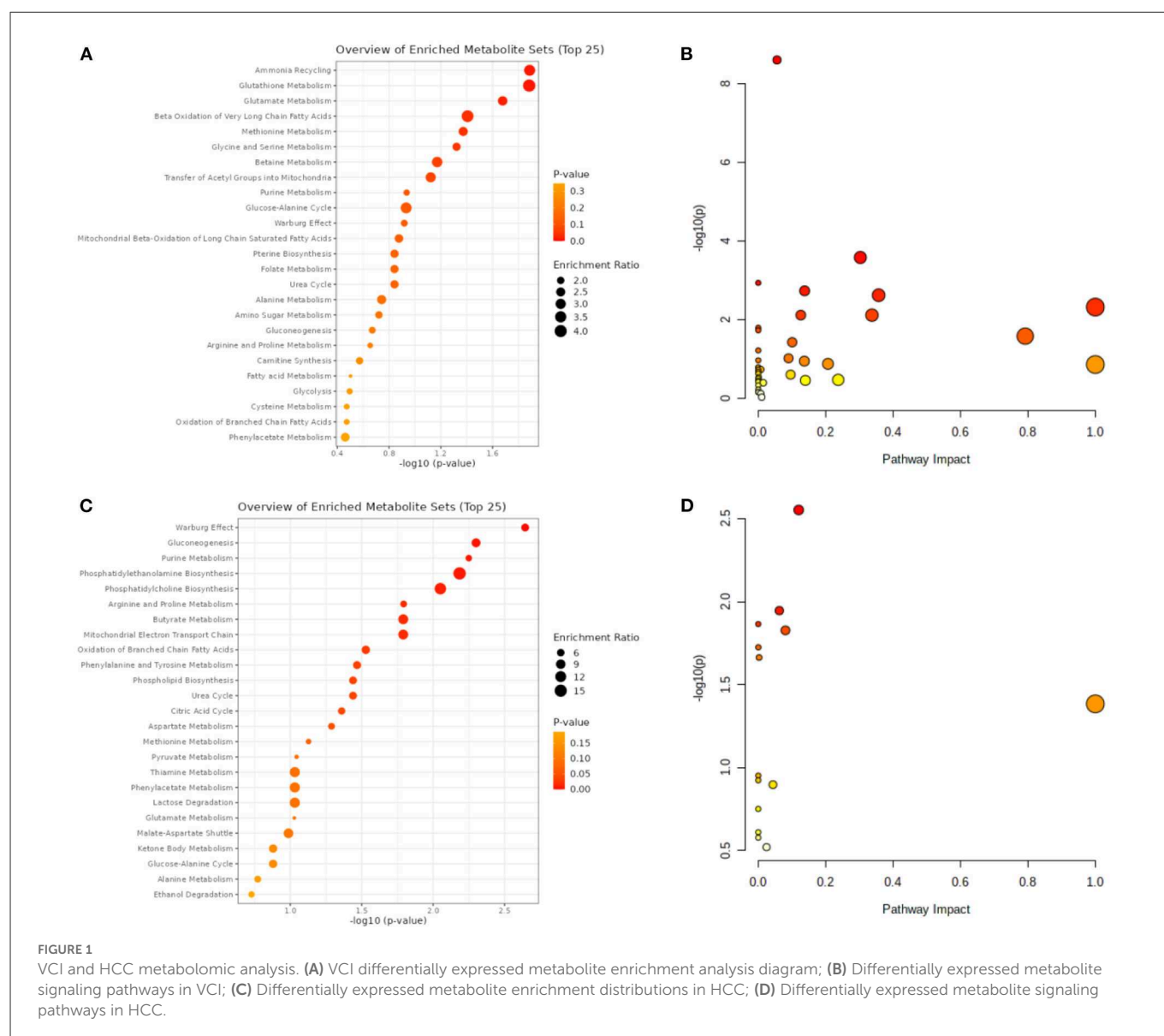
“pRRophetic” is a package that can be used to predict phenotypes from gene expression data, predict drug sensitivity in external cell lines, and predict clinical data. In order to determine the drug sensitivity of each sample from TCGA database, we used the R package “pRRophetic” to obtain HCC metabolism-related genes after prescreening.

## Results

### Metabolites with differential levels in patients with HCC and VCI

A total of 14 differentially expressed metabolites from HCC, including 2 up-regulated and 12 down-regulated metabolites, as well as 71 differentially expressed metabolites from VCI, including 32 up-regulated and 39 down-regulated metabolites, were identified by screening criteria of fold change (FC) >1.5 and *P*-value < 0.05. Data enrichment and metabolic pathway analysis were performed using Metabolanalyst 5.0. Ammonia recycling, glutathione metabolism, glutamate metabolism, and Beta A metabolism were enriched for differentially expressed metabolites of VCI (Figures 1A, B). As part of the metabolic signaling pathway enriched for aminoacyl-tRNA, glycine, serine, and threonine biosynthesis, valine, leucine, and isoleucine biosynthesis, glyoxylate and dicarboxylate metabolism, phenylalanine metabolism, phenylalanine, tyrosine, and tryptophan biosynthesis, etc





(Figures 1A, B). Among the metabolic functions enriched for differentially expressed metabolites of HCC are the Warburg effect, gluconeogenesis, purine metabolism, phosphatidylethanolamine biosynthesis, phosphatidylcholine biosynthesis, and arginine and proline metabolism (Figures 1C, D). The main enriched metabolic signaling pathways include glycerophospholipid metabolism, citrate cycle (TCA cycle), pyruvate metabolism, purine metabolism, glycolysis/gluconeogenesis, and the alanine, aspartate, and glutamate metabolism (Figures 1C, D). Based on the above, it is evident that metabolism-related genes may play a role in HCC and VCI.

## HCC and VCI transcriptome DEGs

The TCGA website (<https://portal.gdc.cancer.gov/>) was used to download clinical and transcriptomic expression data related to HCC, and a total of 424 transcriptomic and 377 clinical datasets were obtained according to the predefined screening criteria. Differential expression data were screened based on

adjusted  $P$ -values  $< 0.05$  and  $|\log_2FC| \geq 1.0$ . A total of 882 differentially expressed mRNAs were screened in the dataset, including 487 up-regulated mRNAs and 395 down-regulated mRNAs; DEGs were screened for differential analysis based on  $P$ -value. The top 100 most significant differentially expressed mRNAs were screened based on  $P$ -values and plotted as heat maps (Figure 2A). Following differential analysis,  $P$ -values were  $-\log_{10}$  transformed, grouped according to  $\log_2 FC$  (groups of up-regulated DEGs, down-regulated DEGs, and non-statistically significant DEGs), and imported into R for plotting volcanoes (Figure 2B). The GSE201482 dataset contained 343 differentially expressed mRNAs, including 179 up-regulated and 164 down-regulated mRNAs. The top 100 differentially expressed coding RNAs with the greatest significance were screened, and the heat map was created based on the  $P$ -value (Figure 2C). Further,  $-\log_{10}$  ( $P$ -value) was transformed from differential analysis microarray data,  $-\log_{10}$  ( $P$ -value) was grouped by  $\log_2 FC$  (groups of up-regulated DEGs, down-regulated DEGs, and non-statistically significant DEGs), and the processed data was imported into R to plot volcanoes (Figure 2D).

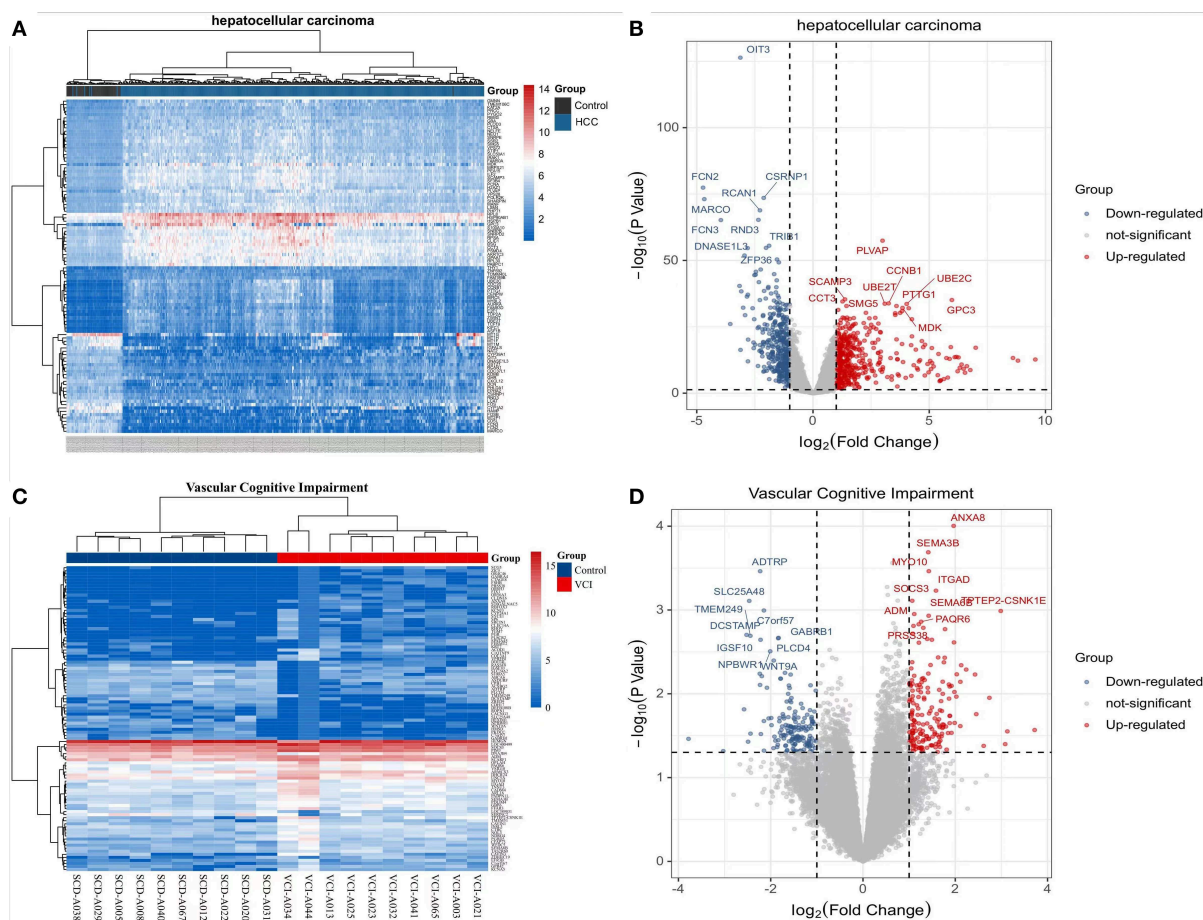


**FIGURE 2** Transcriptomic analysis of HCC and VCI. (A) Heat map of DEGs clustering for HCC transcriptomics; (B) Transcriptomics of DEGs volcanoes for HCC; (C) Heat map of DEGs clustering for VCI transcriptomics; (D) Volcano map for VCI transcriptomics based on DEGs.

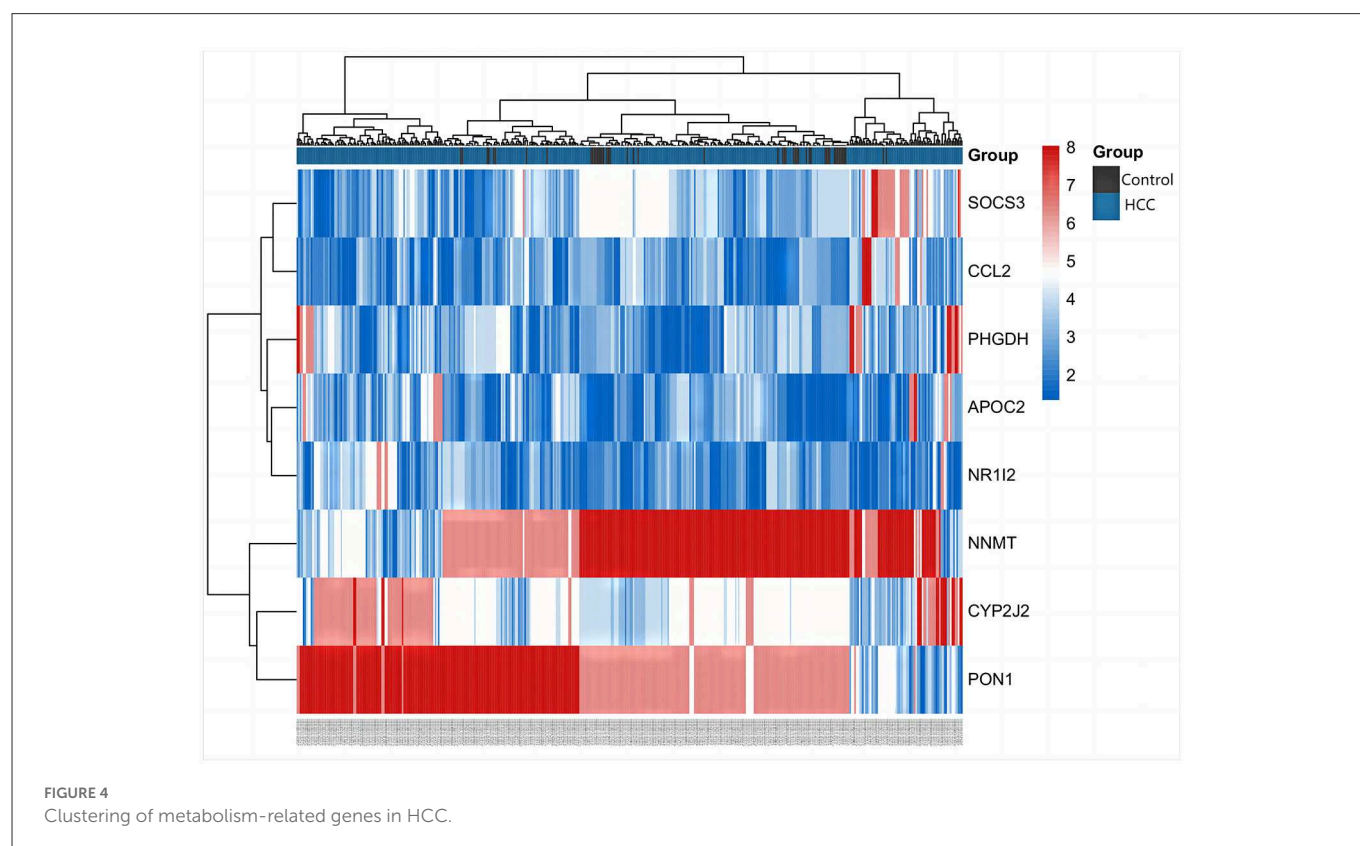
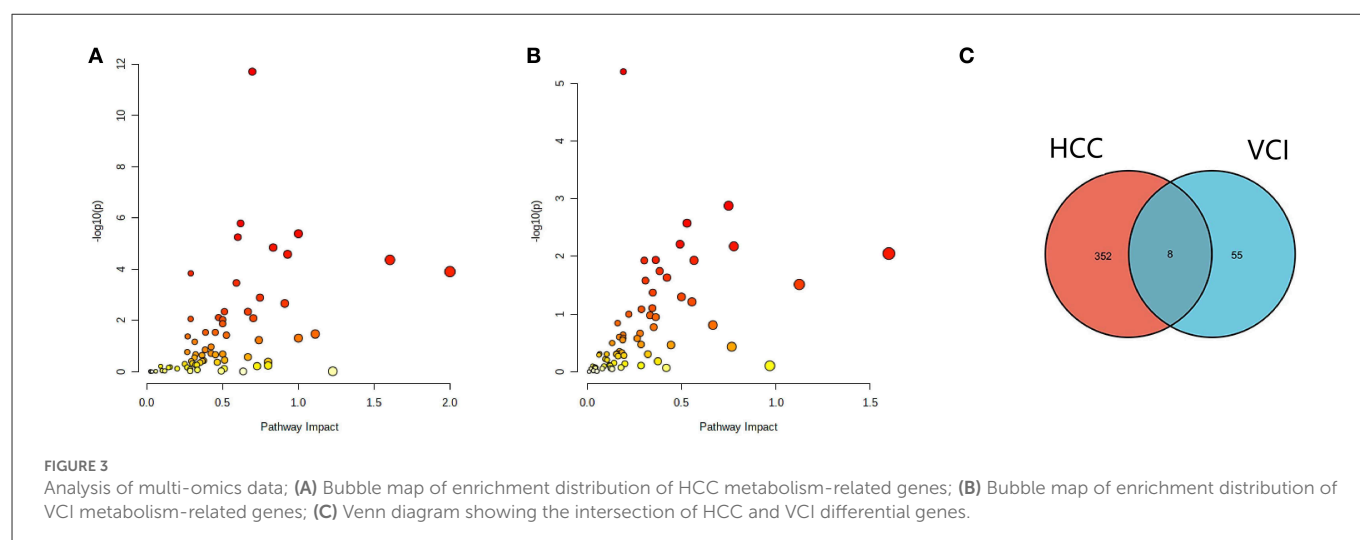
## Multi-omics analysis of HCC and VCI

The differentially expressed metabolites and DEGs of HCC and VCI obtained in the previous stage were imported into Metaboanalyst 5.0 for multi-omics analysis, and 360 metabolic DEGs associated with HCC and 63 metabolic DEGs associated with VCI were obtained (Figures 3A, B). To plot the Venn diagram, the above metabolomics genes associated with HCC and VCI were imported into Venny 2.1 software (<http://bioinfo.gp.cnb.csic.es/tools/venny/index.html>). Accordingly, 8 mRNAs were selected, including 1 up-regulated and 7 down-regulated mRNAs, namely: NNMT, PHGDH, NR1H2, CYP2J2, PON1, APOC2, CCL2, and SOCS3 (Figure 3C). Figure 4 shows a heat map of those differentially metabolized DEGs related to HCC and VCI.

## Prognostic models based on metabolic genes related to HCC and VCI

The 377 clinical cases were randomly divided into a test group and a training group, for clinical and statistical analysis.

No significant differences were found between the two groups in terms of age, gender, and tumor stage ( $P$ -value  $> 0.05$ ), and the data from the two groups were comparable, as shown in [Supplementary Table 1](#). Based on a multifactorial regression model, we composed these six genes (NNMT, PHGDH, NR1H2, CYP2J2, PON1, APOC2, CCL2, and SOCS3) into a risk factor model called riskScore. In the COX survival prognostic model, survival time decreased with increasing riskScore in the test group and the training group ( $P$ -value  $< 0.05$ ) (Figures 5A, B). Independent prognostic analyses by univariate and multifactorial regression showed that the tumor stage and riskScore were significantly associated with prognosis in HCC patients (Figures 5C, D). For prognosis prediction of HCC patients at 1, 3, and 5 years, the area under the curve (AUC) of the subject working characteristic (ROC) curve exceeded 0.59 (Figure 5E). Among the ROC curves for all HCC risk factors, the AUC of riskScore for metabolic genes related to HCC and VCI was the largest and  $> 0.6$  (Figure 5F), indicating a good sensitivity of the established survival prognostic model. Based on HCC and VCI-related metabolic genes, a nomogram prognostic model was constructed, and the test results showed survival rates of 0.929, 0.86, and 0.81 after 1 year ( $P$ -value  $< 0.05$ ) (Figure 5G).



## Principal component analysis, GO, and KEGG enrichment analysis of metabolism-related genes of HCC

Principal component analysis of HCC metabolism-related genes and HCC-associated genes was performed using the scatterplot3d package (Figures 6A, B). GO and KEGG pathway enrichment analysis of those eight differentially metabolized DEGs related to HCC and VCI were done using Bioconductor package and clusterprofiler package in R language. The GO analysis of those eight differentially metabolized DEGs showed that their biological processes were mainly enriched in response to a drug

or an exogenous drug catabolic process (Figures 7A–F). The cellular components that were mainly enriched included high-density lipoprotein particles and plasma lipoprotein particles. The molecular functions including phospholipase activator activity, lipase activator activity, and phospholipase binding were also enriched. The enriched KEGG pathways included TNF signaling pathway, Influenza A lipid and atherosclerosis pathway, linoleic acid metabolism, nicotinate and nicotinamide metabolism, glycine, serine, and threonine metabolism, and so on (Figures 7G, H). This indicates that the pathways and functions of these DEGs enrichment may be connected to the immune microenvironment and metabolism.

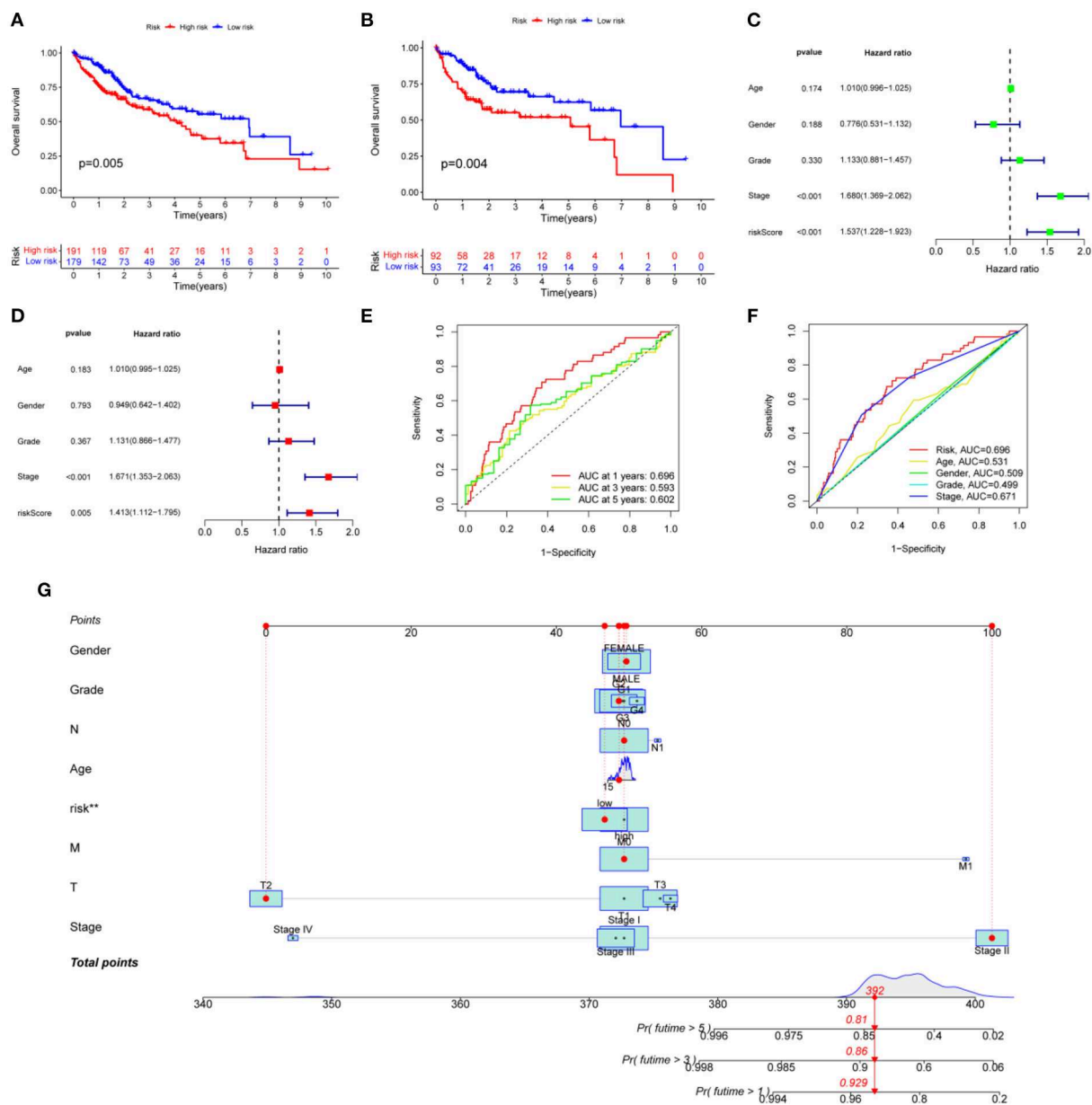


FIGURE 5

Developing a prognosis model for HCC. (A) Prognostic curves for the overall sample group; (B) The survival prognosis curve for the training group; (C) Analysis of independent prognostic factors based on single-factor regression; (D) Analysis of independent prognostic factors based on multi-factor regression; (E) HCC 5-year survival ROC curves; (F) HCC risk factor ROC curves; (G) Nomograph of metabolomic prognostic models for HCC.

## Immuno-infiltration and immunofunctional analysis of metabolized DEGs related to HCC and VCI

The obtained HCC expression matrix data were background corrected and normalized and expression values for the microarray data were calculated using the limma R package in R. The immune cell composition of each sample was further analyzed using the CIBERSORT package and histograms were plotted (Figure 8A). The immune cell distribution heat map was plotted using the pheatmap package (Figure 8B). The interaction of immune cell populations in HCC was then analyzed using the corrplot package and co-expression maps of immune cell infiltration in HCC were plotted

(Figure 8C). Finally, the expression matrix data were analyzed using the Vioplot package to investigate the expression of each immune cell in HCC tissues as well as paracancerous tissues, and further plotted (Figure 8D).

Immunological functions of HCC metabolism-related genes were analyzed using limma, Gene Set Variation Analysis (GSVA), gseabase, pheatmap, and reshape2 packages. The immune functions were mainly focused on antigen-presenting cells (APC) co-inhibition, APC co-stimulation, cytokine-cytokine receptor interaction (CCR), checkpoint, cytolytic activity, human leukocyte antigens (HLA), inflammation-promoting, MHC\_class\_I, and parainflammation (Figure 9). This study reveals and visualizes immune infiltration and immune function associated with metabolic DEGs of HCC and VCI.



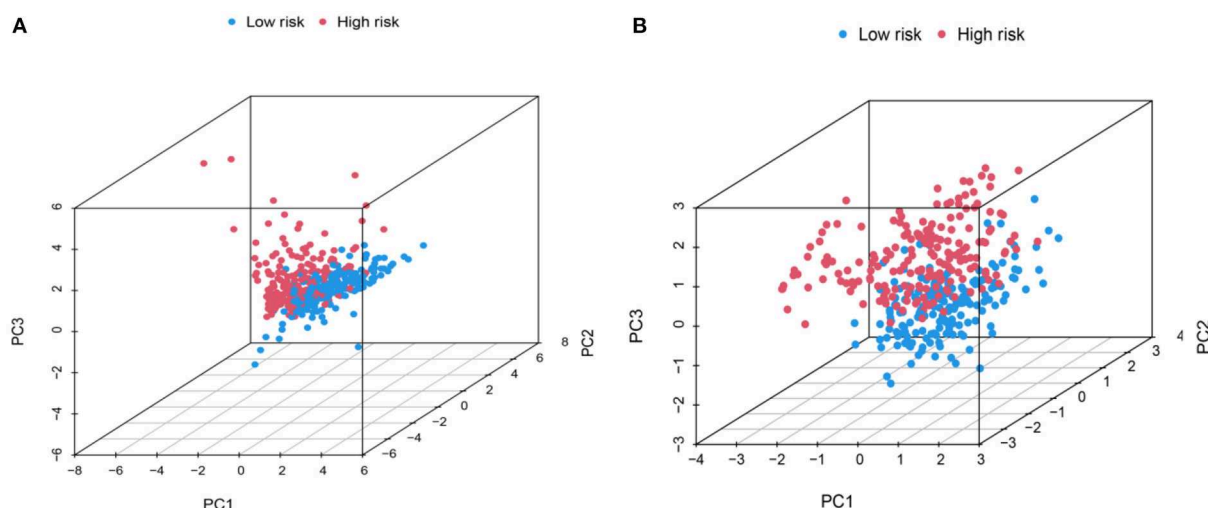


FIGURE 6  
PCA distribution map. (A) Metabolic-related genes PCA distribution map; (B) Genes related to HCC PCA distribution map.

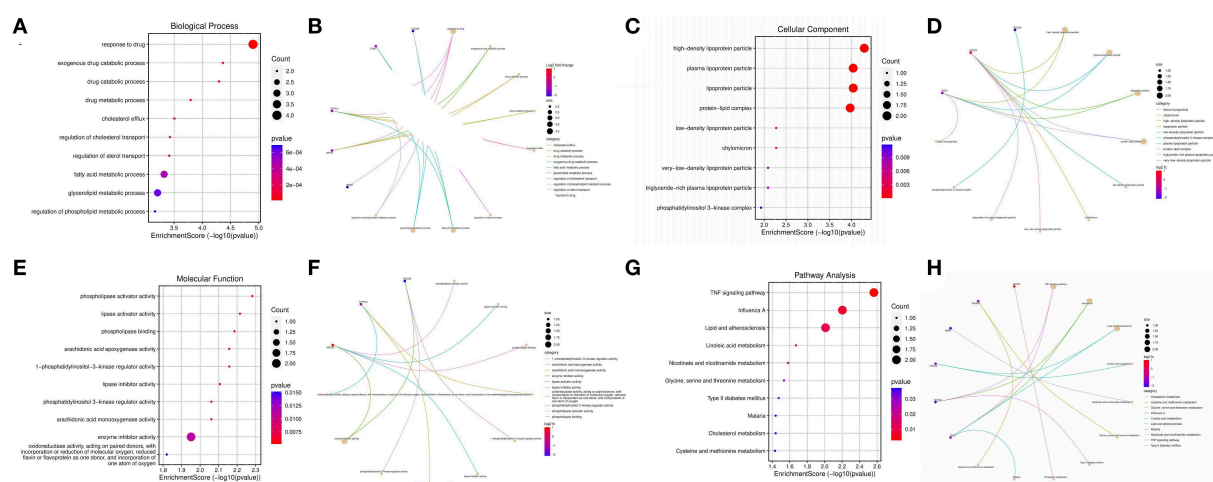


FIGURE 7  
Enrichment analysis; (A) BP enrichment bubble plot; (B) BP enrichment plot; (C) CC enrichment bubble plot; (D) CC enrichment plot; (E) MF enrichment bubble plot; (F) MF enrichment plot; (G) KEGG enrichment bubble plot; (H) KEGG enrichment plot.

## TMB analysis of metabolized DEGs related to HCC and VCI

The HCC expression data and TMB files were imported into R, and the correlation between DEGs related to HCC and tumor mutation load was calculated by using the function, and the waterfall plots of high and low-risk groups were drawn according to the correlation results (Figures 10A, B). The differential analysis results suggested that the tumor mutation load in the low-risk group was significantly higher than that in the high-risk group (Figure 10C). Survival analysis of the tumor mutation load of HCC metabolism-related genes showed that the survival period of the low tumor mutation load group was significantly longer than that of the high tumor mutation load group ( $P$ -value  $< 0.05$ ) (Figure 10D). In addition, combining tumor mutation load characteristics and

metabolism-related genetic factors, the low-risk group with low tumor mutation load had the highest probability of survival while the high-risk group with low tumor mutation load had the lowest probability of survival (Figure 10E).

## Relative expression of PHGDH, NR1I2, and APOC2

After obtaining the core genes PHGDH, NR1I2, and APOC2 from the previous differential expression analysis and survival prognosis analysis, we further investigated their relative expression in HCC. The transcriptome data of HCC were downloaded from the TCGA and the ggpubr package was used to analyze the relative expression of the identified core genes and to draw box expression



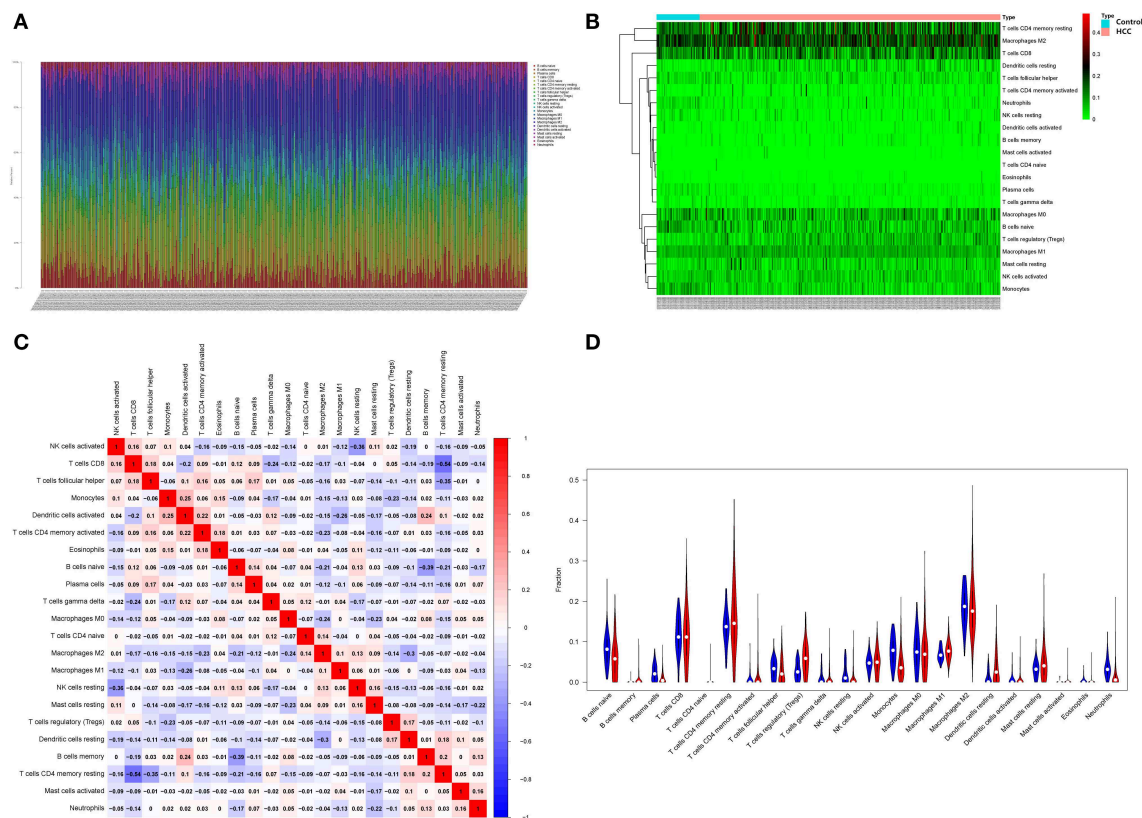


FIGURE 8

Infiltration analysis of immune cells. (A) Distribution of immune cells in HCC; (B) HCC immune cell distribution heat map; (C) HCC immune cell interaction heat map; (D) Image showing the relative amount of immune cells in HCC.

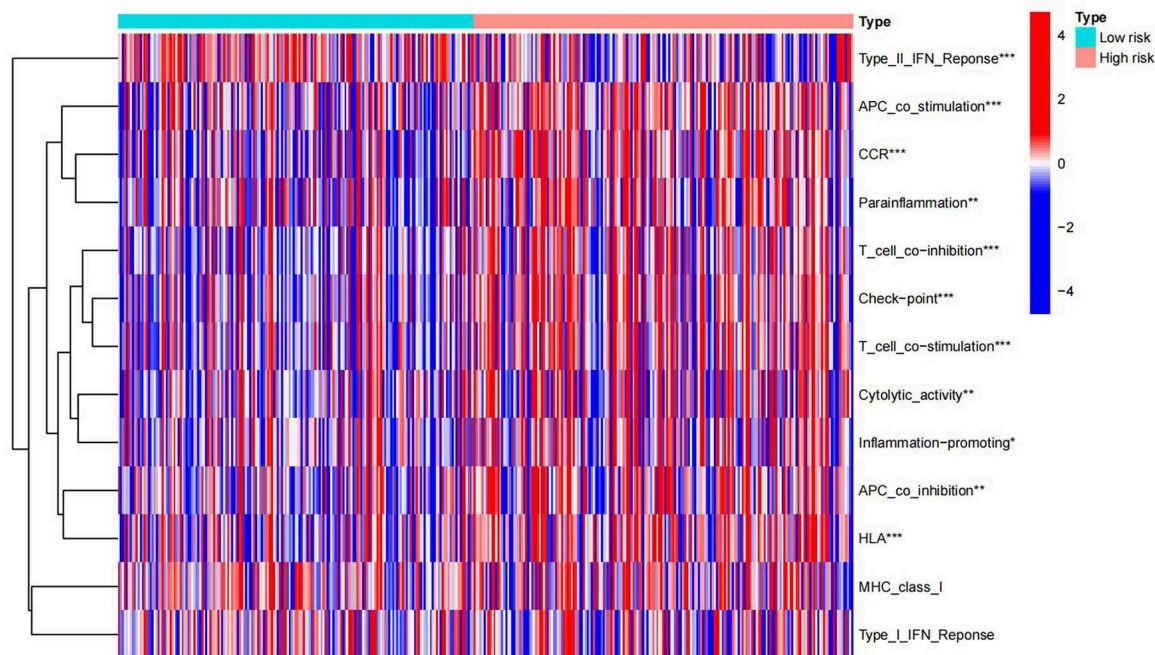
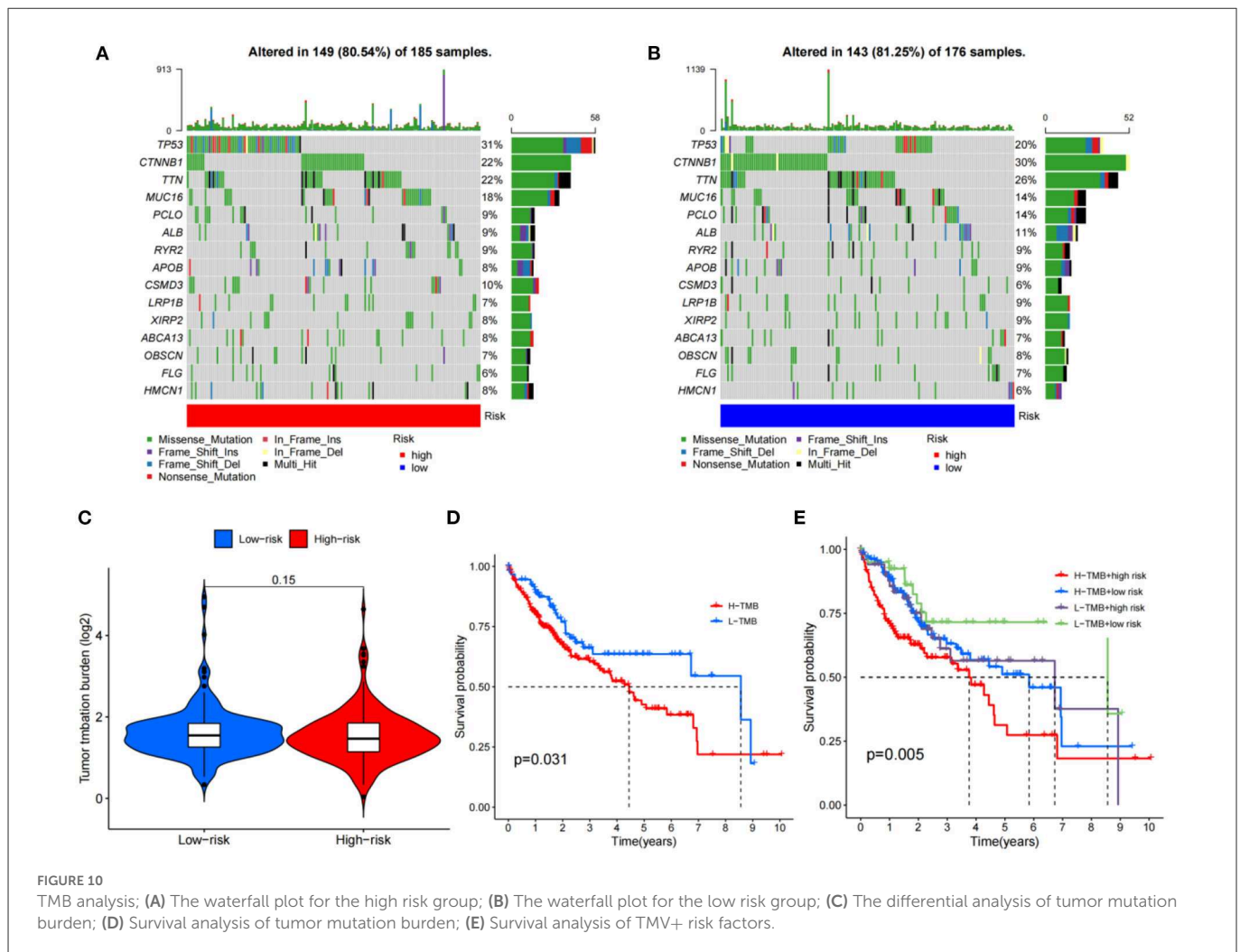


FIGURE 9

Immune enrichment analysis heat map.



maps (Figures 11A–C). The results revealed that *PHGDH* and *NR1I2* genes exhibited low expression in HCC tumor tissues ( $P$ -value < 0.001) while *APOC2* genes were highly expressed in HCC tumor tissues ( $P$ -value < 0.01).

## Single-gene GSEA enrichment analysis

The GO/KEGG annotation file downloaded from the GSEA website and the HCC tumor data file were read into R. Analytical operations were performed, and it was found that: the GO of gene *PHGDH* at HCC was enriched in CHROMATIN REMODELING, DNA PACKAGING, and PROTEIN DNA COMPLEX SUBUNIT ORGANIZATION functions (Figure 12A). The GO function of gene *NR1I2* was enriched in ACTIVATION OF IMMUNE RESPONSE, ADAPTIVE IMMUNE RESPONSE BASED ON SOMATIC RECOMBINATION OF IMMUNE RECEPTORS BUILT FROM IMMUNOGLOBULIN SUPERFAMILY DOMAINS, and ALPHA BETA T CELL ACTIVATION (Figure 12B). The gene *APOC2* was functionally enriched in CHROMATIN ASSEMBLY OR DISASSEMBLY, EPIDERMAL CELL DIFFERENTIATION, and INFLAMMATORY RESPONSE TO ANTIGENIC STIMULUS (Figure 12C); The main *PHGDH* gene-enriched KEGG pathways are OLFACTORY TRANSDUCTION, CIRCADIAN RHYTHM

MAMMAL, GRAFT VS. HOST DISEASE signaling pathways (Figure 12D); The *NR1I2* gene enriched KEGG pathways are mainly ANTIGEN PROCESSING AND PRESENTATION, CYTOKINE RECEPTOR INTERACTION, and CYTOSOLIC DNA SENSING signaling pathways (Figure 12E). The main KEGG pathways enriched by the *APOC2* gene are OLFACTORY TRANSDUCTION, CYTOSOLIC DNA SENSING PATHWAY, and REGULATION OF AUTOPHAGY signaling pathway (Figure 12F).

## Potential drug screening

To evaluate therapeutically effective drugs against DEGs related to HCC and VCI, we used the limma, ggpubr, prophetic, and ggplot2 packages. Drugs with potential clinical efficacy against HCC metabolism-related genes include A-443654, A-770041, AP-24534, BI-2536, BMS-509744, CGP-60474, CGP-082996, CMK, cyclopamine, dasatinib, doxorubicin, etoposide, gemcitabine, GW843682X, HG-6-64-1, and JW-7-52-1 (Figures 13A–P).

## Discussions

VCI is an acquired mental impairment syndrome, which is characterized by cognitive impairment, memory difficulties, and

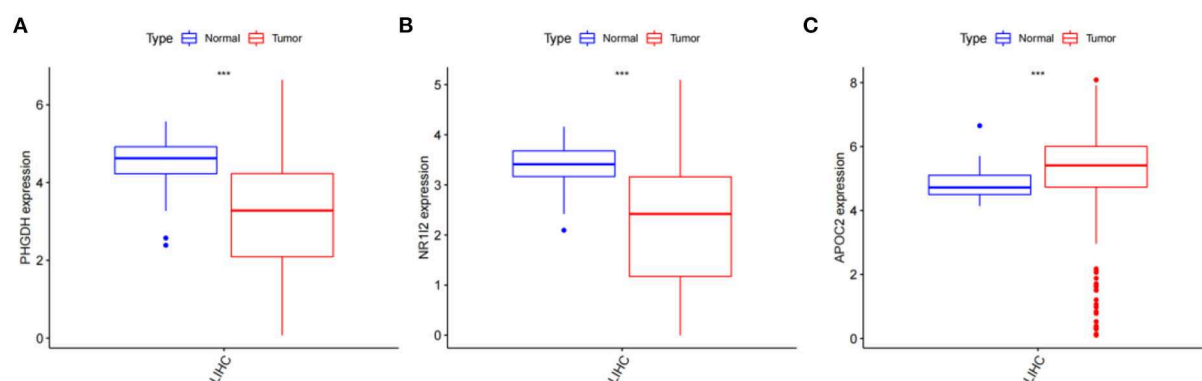


FIGURE 11

Analysis of the relative expression of target genes; (A) Relative expression of PHGDH ( $p < 0.001$ ); (B) Relative expression of NR1I2 ( $p < 0.001$ ); (C) Relative expression of APOC2 ( $p < 0.001$ ).

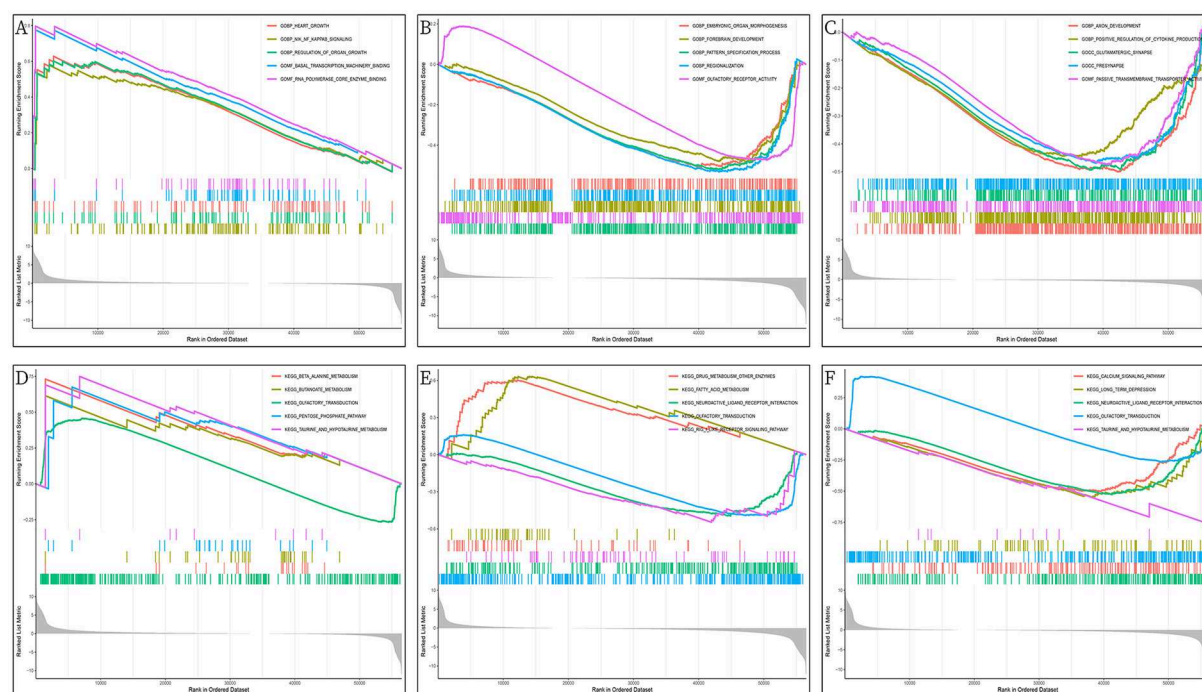


FIGURE 12

GSEA enrichment analysis of DEGs (PHGDH, NR1I2, and APOC2); (A) GO enrichment analysis of PHGDH in HCC; (B) GO enrichment analysis of NR1I2 in HCC; (C) GO enrichment analysis of APOC2 in HCC; (D) KEGG enrichment analysis of PHGDH in HCC; (E) KEGG enrichment analysis of NR1I2 in HCC; (F) KEGG enrichment analysis of APOC2 in HCC.

neurodegenerative lesions (44). Previous studies have pointed out that HCC may be associated with cognitive disorders of the brain such as hepatic encephalopathy, but the specific mechanisms by which HCC induces VCI are unclear (45). Metabolomic studies have shown that the pathogenesis of VCI may involve various mechanisms such as impaired myelin synthesis caused by glucolipid metabolism disorders and related metabolites leading to blood-brain barrier disruption and vascular endothelial damage (46–48). HCC may affect metabolic disorders promoting the development of VCI. According to the current studies, the possible mechanisms of cognitive impairment due to HCC include impaired blood ammonia and bile acid metabolism, oxidative stress injury and inflammatory

response, impaired blood-brain barrier, neurotransmission disorders, neurotoxic accumulation, and disturbance of cerebral energy metabolism (49–51). Therefore, in this study, we propose that HCC may influence the body's metabolism to promote the occurrence of VCI. In this study, we obtained the 8 significant HCC-VCI DEGs by metabolomic analysis, which are NNMT, PHGDH, NR1I2, CYP2J2, PON1, APOC2, CCL2, and SOCS3. Previous literature indicated that the above eight genes are mostly involved in the development of VCI.

NNMT encodes proteases involved in the metabolism of various substances and drugs *in vivo* and is highly expressed in a variety of tumors, correlating with tumor infiltration, distant metastasis, and malignancy (52, 53). NNMT encodes neuronal proteins

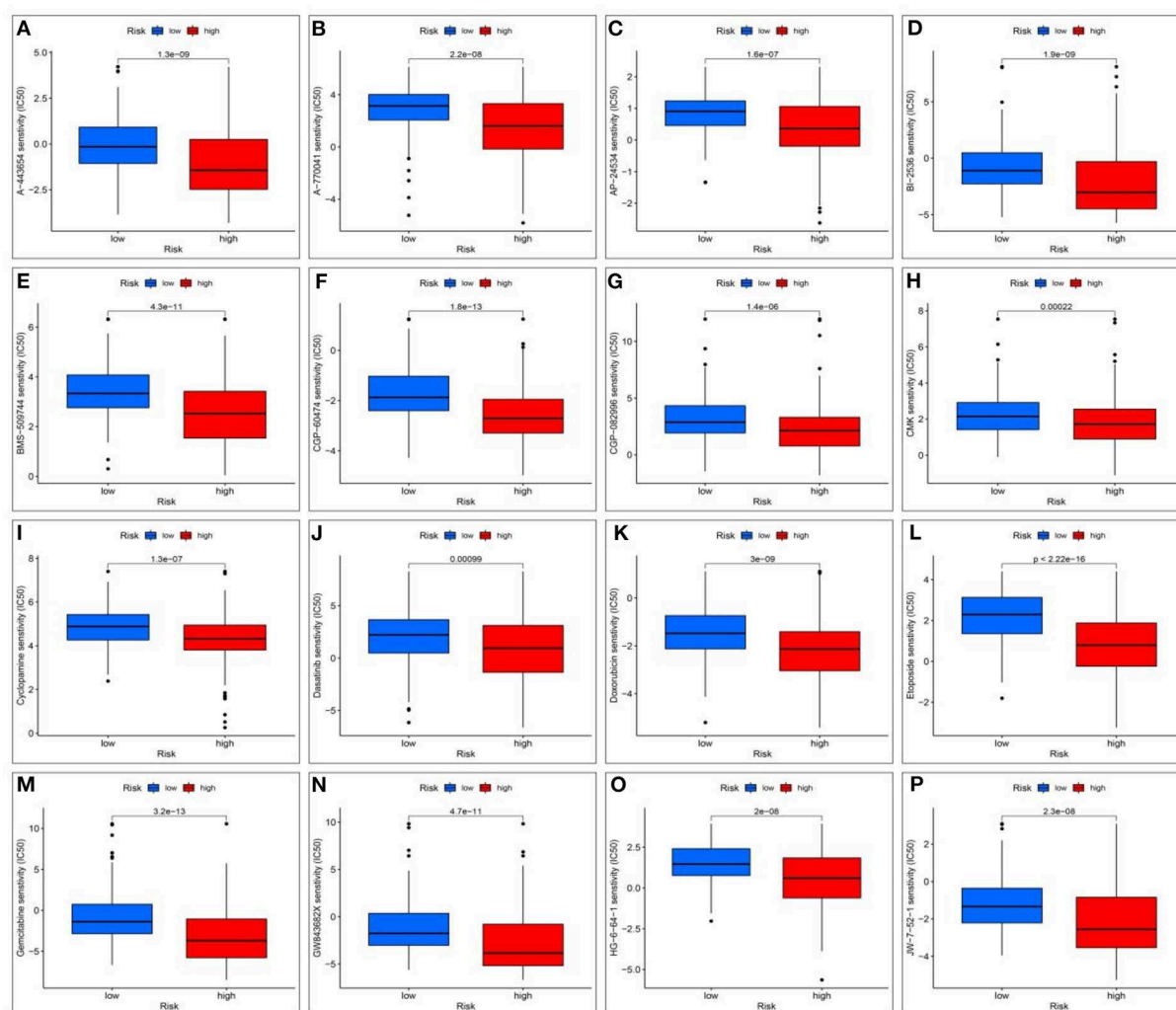


FIGURE 13

Screening for potential drugs; (A) The therapeutic effect of the drug A-443654; (B) The therapeutic effect of the drug A-770041; (C) The therapeutic effect of the drug AP-24534; (D) The therapeutic effect of the drug BI-2536; (E) The therapeutic effect of the drug BMS-509744; (F) The therapeutic effect of the drug CGP-60474; (G) The therapeutic effect of the drug CGP-082996; (H) The therapeutic effect of the drug RSK2 kinase inhibitor (CMK); (I) Cyclopamine drug's therapeutic effects; (J) The therapeutic effect of the drug Dasatinib; (K) The therapeutic effect of the drug Doxorubicin; (L) The therapeutic effect of the drug Etoposide; (M) The therapeutic effect of the drug Gemcitabine; (N) The therapeutic effect of the drug GW843682X; (O) The therapeutic effect of the drug HG-6-64-1; (P) The therapeutic effect of the drug HG-6-64-1.

whose increased expression is associated with stress responses in the brain microenvironment and can be involved in promoting cognitive impairment (54–56). PHGDH encodes a phosphoglycerate dehydrogenase involved in the synthesis of L-serine, a regulator of synaptic plasticity and an essential product for T-cell expansion (57, 58). PHGDH mutants can result in neurological symptoms such as impaired motor function, and its overexpression can promote proliferation and invasion of cancer cells such as HCC (59–61). Further, PHGDH has been found to contribute to the development of cognitive impairment (62). NR1I2 is a member of the nuclear receptor superfamily and is involved in encoding a transcriptional regulator that regulates cytochrome P450 (CYP) enzymes. Previous studies suggest that NR1I2 may regulate bile acid metabolism involved in promoting the progression of cognitive impairment (63). CYP2J2 is a cyclooxygenase that is involved in regulating the body's inflammatory response, cell proliferation, and other physiological functions, and plays an important role in the homeostasis (64).

CYP2J2 variants are involved in promoting cerebrovascular disease and their polymorphisms are associated with susceptibility to cognitive impairment (65, 66). CYP2J2 increases the production of eets and enhances HIF-1 alpha stability and promotes the development of HCC (67). PON1 encodes calcium-dependent high-density lipoprotein-related lipase, which can reduce reactive oxygen species, reduce LDL oxidative stress, enhance HDL antioxidant capacity, and participate in anti-inflammatory and antioxidant activities in neurodegenerative diseases, neuroinflammation, and other neurological diseases (68, 69). Studies have pointed out that reduced PON1 activity may affect lipid metabolism, promote vascular endothelial damage, and contribute to the development of cognitive impairment (69–72). PON1 levels were negatively correlated with HCC vascular invasion, probably due to its anti-inflammatory activity and its role in the maintenance of normal vascular endothelial function (73). APOC2 encodes a lipid-binding protein belonging to the apolipoprotein family, which is involved



in the composition of very low-density lipoproteins and in promoting the hydrolysis of triglycerides (74, 75). High serum levels of APOC2 are associated with cognitive impairment, and the exact underlying mechanism of action is unclear (76, 77). CCL2 or MCP-1 is a member of the CC chemokine family, and abnormally expressed CCL2 is closely associated with CNS diseases, neoplastic diseases, and inflammatory diseases. The CCL2/CCR2 axis activates the Hedgehog pathway involved in the induction of HCC invasion and epithelial-mesenchymal transition (78). Further, CCL2 may be involved in promoting the progression of cognitive impairment through enhancing excitotoxicity, oxidative stress-induced inflammatory damage, and apoptosis in neuronal cells, affecting glutamate metabolism and inducing microglia activation in the local microenvironment (79–82). SOCS3 is an important negative feedback regulatory protein in the JAK/STAT signaling pathway, a key physiological regulator in natural and acquired immunity, T-lymphocyte differentiation, and immune regulation, and plays a negative feedback regulatory role in immune/inflammatory diseases (83–85). The SOCS3 signaling pathway is also involved in the development of HCC (86, 87). Thus, the above genes may be associated with the occurrence of HCC-induced VCI.

The developed HCC metabolomics prognostic model based on HCC-VCI DEGs has a good prognostic effect. Principal component analysis, functional enrichment analysis, immune function analysis, and TMB analysis suggested that HCC-VCI DEGs may affect the immune microenvironment and thus result in the occurrence and development of VCI in HCC. Therefore, the immune-related effects of the above genes were probed, and it was observed that several of these genes were associated with immunity. PHGDH can promote liver ceramide synthesis to maintain lipid homeostasis, and participate in the maintenance of mitochondrial REDOX homeostasis and cellular homeostasis in the immune microenvironment (88, 89). NR1H2 is involved in the regulation of T-cell differentiation and plays an important role in the regulation of immune homeostasis (90, 91). APOC2 may play a protective role in the immune microenvironment of atherosclerotic disease by inhibiting foam cell formation, in addition to participating in lipid metabolism (74, 92, 93). CCL2 plays an important role in immune regulation by recruiting chemotactic monocytes/macrophages to the site of inflammation, mediating the inflammatory response to limit pathogen invasion, and participating in the repair of damaged tissues (94, 95).

In summary, our study revealed that the HCC-associated metabolic DEGs such as NNMT and PHGDH may influence the occurrence and progression of VCI in HCC patients by affecting the immune microenvironment. Further by establishing a prognostic model and screening potential targeted drugs, we found that the above genes had a good prognostic effect on HCC. Finally, drugs that may target HCC-VCI DEGs were screened, namely A-443654, A-770041, AP-24534, BI-2536, BMS-509744, CGP-60474, and CGP-082996, and are expected to have good potential clinical efficacy in patients with HCC-induced VCI. Therefore, this study provides theoretical support and potential therapeutic strategies for the pathogenesis and clinical treatment of VCI in HCC patients. However, the current study also has some limitations. On the one hand, a larger sample of data is needed to verify the conclusions while

on the other, relevant biological experiments are needed to clarify the specific regulatory mechanisms.

## Conclusion

HCC metabolism-related DEGs such as NNMT and PHGDH may lead to the occurrence of VCI in HCC patients by affecting the immune microenvironment. Further by establishing a prognostic model and screening the potential targeted drugs, we found that the above genes had a good prognostic effect on HCC. A-443654, A-770041, AP-24534, BI-2536, BMS-509744, CGP-60474, and CGP-082996 could be potential candidates with good clinical efficacy for treating VCI in HCC patients.

## Data availability statement

The original contributions presented in the study are included in the article/Supplementary material, further inquiries can be directed to the corresponding author.

## Author contributions

DZ, YZ, LL, XH, and SF contributed to conception and design of the study and organized the database. DZ and SF performed the statistical analysis and wrote sections of the manuscript. DZ wrote the first draft of the manuscript. All authors contributed to manuscript revision, read, and approved the submitted version.

## Conflict of interest

LL was employed by Dalian Hunter Information Consulting Co. LTD, Dalian, China.

The remaining authors declare that the research was conducted in the absence of any commercial or financial relationships that could be construed as a potential conflict of interest.

## Publisher's note

All claims expressed in this article are solely those of the authors and do not necessarily represent those of their affiliated organizations, or those of the publisher, the editors and the reviewers. Any product that may be evaluated in this article, or claim that may be made by its manufacturer, is not guaranteed or endorsed by the publisher.

## Supplementary material

The Supplementary Material for this article can be found online at: <https://www.frontiersin.org/articles/10.3389/fneur.2022.1109019/full#supplementary-material>



## References

- Sung H, Ferlay J, Siegel RL, Laversanne M, Soerjomataram I, Jemal A, et al. Global cancer statistics 2020: GLOBOCAN estimates of incidence and mortality worldwide for 36 cancers in 185 countries. *CAA Cancer J Clin.* (2021) 71:209–49. doi: 10.3322/caac.21660
- Cheng A-L, Kang Y-K, Chen Z, Tsao C-J, Qin S, Kim JS, et al. Efficacy and safety of sorafenib in patients in the Asia-Pacific region with advanced hepatocellular carcinoma: a phase III randomised, double-blind, placebo-controlled trial. *Lancet Oncol.* (2009) 10:25–34. doi: 10.1016/S1470-2045(08)70285-7
- Tang B, Zhu J, Zhao Z, Lu C, Liu S, Fang S, et al. Diagnosis and prognosis models for hepatocellular carcinoma patient's management based on tumor mutation burden. *J Adv Res.* (2021) 33:153–65. doi: 10.1016/j.jare.2021.01.018
- Osui N, Shiba S, Shibuya K, Okazaki S, Miyasaka Y, Okamoto M, et al. Carbon-ion radiotherapy subsequent to balloon-occluded retrograde transvenous obliteration for hepatocellular carcinoma with hepatic encephalopathy: a multidisciplinary approach. *Clin J Gastroenterol.* (2021) 14:852–7. doi: 10.1007/s12328-021-01395-6
- Surjan RCT, Santos ES, dos Silveira SP, Makdissi FF, Machado MAC. Fibrolamellar hepatocellular carcinoma-related hyperammonemic encephalopathy: up to now and next steps. *Clin Mol Hepatol.* (2020) 26:231–2. doi: 10.3350/cmh.2019.0084
- van der Flier WM, Skoog I, Schneider JA, Pantoni L, Mok V, Chen CLH, et al. Vascular cognitive impairment. *Nat Rev Dis Primers.* (2018) 4:18003. doi: 10.1038/nrdp.2018.3
- Arvanitakis Z, Capuano AW, Leurgans SE, Buchman AS, Bennett DA, Schneider JA. The relationship of cerebral vessel pathology to brain microinfarcts: cerebral vessel pathology and microinfarcts. *Brain Pathol.* (2017) 27:77–85. doi: 10.1111/bpa.12365
- Dudvarski Stankovic N, Teodorczyk M, Ploen R, Zipp F, Schmidt MHH. Microglia-blood vessel interactions: a double-edged sword in brain pathologies. *Acta Neuropathol.* (2016) 131:347–63. doi: 10.1007/s00401-015-1524-y
- Burrows F, Haley MJ, Scott E, Coutts G, Lawrence CB, Allan SM, et al. Systemic inflammation affects reperfusion following transient cerebral ischaemia. *Exp Neurol.* (2016) 277:252–60. doi: 10.1016/j.expneurol.2016.01.013
- Faraco G, Sugiyama Y, Lane D, Garcia-Bonilla L, Chang H, Santisteban MM, et al. Perivascular macrophages mediate the neurovascular and cognitive dysfunction associated with hypertension. *J Clin Invest.* (2016) 126:4674–89. doi: 10.1172/JCI86950
- Cai Z, Liu Z, Xiao M, Wang C, Tian F. Chronic cerebral hypoperfusion promotes amyloid-beta pathogenesis via activating  $\beta/\gamma$ -secretases. *Neurochem Res.* (2017) 42:3446–55. doi: 10.1007/s11064-017-2391-9
- Zhang W, Zhang X, Zhang Y, Wu H, Liu Q, Zhou X, et al. Analysis of changes of intestinal flora in elderly patients with Alzheimer's Disease and liver cancer and its correlation with abnormal gastrointestinal motility. *J Oncol.* (2021) 2021:1–5. doi: 10.1155/2021/7517379
- Forés-Martos J, Boullousa C, Rodrigo-Domínguez D, Sánchez-Valle J, Suay-García B, Climent J, et al. Transcriptomic and genetic associations between Alzheimer's disease, Parkinson's disease, and cancer. *Cancers.* (2021) 13:2990. doi: 10.3390/cancers13122990
- Snyder HM, Corriveau RA, Craft S, Faber JE, Greenberg SM, Knopman D, et al. Vascular contributions to cognitive impairment and dementia including Alzheimer's disease. *Alzheimer's Dement.* (2015) 11:710–7. doi: 10.1016/j.jalz.2014.10.008
- Lee SJ, Teunissen CE, Pool R, Shipley MJ, Teuner A, Chouraki V, et al. Circulating metabolites and general cognitive ability and dementia: evidence from 11 cohort studies. *Alzheimer's Dement.* (2018) 14:707–22. doi: 10.1016/j.jalz.2017.11.012
- Qureshi MI, Vorkas PA, Coupland AP, Jenkins IH, Holmes E, Davies AH. Lessons from metabolomics on the neurobiology of stroke. *Neuroscientist.* (2017) 23:374–82. doi: 10.1177/1073858416673327
- Yang C, Huang X, Liu Z, Qin W, Wang C. Metabolism-associated molecular classification of hepatocellular carcinoma. *Mol Oncol.* (2020) 14:896–913. doi: 10.1002/1878-0261.12639
- Mayo R, Crespo J, Martínez-Arranz I, Banales JM, Arias M, Mincholé I, et al. Metabolomic-based noninvasive serum test to diagnose nonalcoholic steatohepatitis: results from discovery and validation cohorts. *Hepatol Commun.* (2018) 2:807–20. doi: 10.1002/hep4.1188
- Chen B, Garmire L, Calvisi DF, Chua M-S, Kelley RK, Chen X. Harnessing big 'omics' data and AI for drug discovery in hepatocellular carcinoma. *Nat Rev Gastroenterol Hepatol.* (2020) 17:238–51. doi: 10.1038/s41575-019-0240-9
- Fitian AI, Nelson DR, Liu C, Xu Y, Ararat M, Cabrera R. Integrated metabolomic profiling of hepatocellular carcinoma in hepatitis C cirrhosis through GC/MS and UPLC/MS-MS. *Liver Int.* (2014) 34:1428–44. doi: 10.1111/liv.12541
- Zeng J, Yin P, Tan Y, Dong L, Hu C, Huang Q, et al. Metabolomics Study of hepatocellular carcinoma: discovery and validation of serum potential biomarkers by using capillary electrophoresis-mass spectrometry. *J Proteome Res.* (2014) 13:3420–31. doi: 10.1021/pr500390y
- Wang B, Chen D, Chen Y, Hu Z, Cao M, Xie Q, et al. Metabonomic profiles discriminate hepatocellular carcinoma from liver cirrhosis by ultraperformance liquid chromatography-mass spectrometry. *J Proteome Res.* (2012) 11:1217–27. doi: 10.1021/pr2009252
- Hall Z, Chiarugi D, Charidemou E, Leslie J, Scott E, Pellegrinet L, et al. Lipid remodeling in hepatocyte proliferation and hepatocellular carcinoma. *Hepatology.* (2021) 73:1028–44. doi: 10.1002/hep.31391
- Banables JM, Iñarrairaegui M, Arbelaz A, Milkiewicz P, Muntané J, Muñoz-Bellvis L, et al. Serum metabolites as diagnostic biomarkers for cholangiocarcinoma, hepatocellular carcinoma, and primary sclerosing cholangitis. *Hepatology.* (2019) 70:547–62. doi: 10.1002/hep.30319
- Qin Q, Yin Y, Xing Y, Wang X, Wang Y, Wang F, et al. Lipid metabolism in the development and progression of vascular cognitive impairment: a systematic review. *Front Neurol.* (2021) 12:709134. doi: 10.3389/fneur.2021.709134
- Holtsträter C, Schrörs B, Bukur T, Löwer M. Bioinformatics for cancer immunotherapy. In: Boegel S, editor. *Bioinformatics for Cancer Immunotherapy. Methods in Molecular Biology.* New York, NY: Springer (2020). p. 1–9. doi: 10.1007/978-1-0716-0327-7\_1
- Xuan Z, Ma T, Qin Y, Guo Y. Role of ultrasound imaging in the prediction of TRIM67 in brain metastases from breast cancer. *Front Neurol.* (2022) 13:889106. doi: 10.3389/fneur.2022.889106
- Fan Y, Xu H, Lv M, Li N. Preoperative serum calcitonin level and ultrasonographic characteristics predict the risk of metastatic medullary thyroid carcinoma: functional analysis of calcitonin-related genes. *Dis Mark.* (2022) 2022:1–14. doi: 10.1155/2022/9980185
- Sun Y, Sun X, Liu S, Liu L, Chen J. The overlap between regeneration and fibrosis in injured skeletal muscle is regulated by phosphatidylinositol 3-kinase/Akt signaling pathway: a bioinformatic analysis based on lncRNA microarray. *Gene.* (2018) 672:79–87. doi: 10.1016/j.gene.2018.06.001
- Zhang Q, Yang J, Yang C, Yang X, Chen Y. Eucommia ulmoides Oliver-Tribulus terrestris L. drug pair regulates ferroptosis by mediating the neurovascular-related ligand-receptor interaction pathway: a potential drug pair for treatment hypertension and prevention ischemic stroke. *Front Neurol.* (2022) 13:98. doi: 10.3389/fneur.2022.833922
- Luo Z, Qi B, Sun Y, Chen Y, Lin J, Qin H, et al. Engineering bioactive M2 macrophage-polarized, anti-inflammatory, miRNA-based liposomes for functional muscle repair: from exosomal mechanisms to biomaterials. *Small.* (2022) 18:2201957. doi: 10.1002/smll.202201957
- Lin W, Wang Q, Chen Y, Wang N, Ni Q, Qi C, et al. Identification of a 6-RBP gene signature for a comprehensive analysis of glioma and ischemic stroke: cognitive impairment and aging-related hypoxic stress. *Front Aging Neurosci.* (2022) 14:951197. doi: 10.3389/fnagi.2022.951197
- Pang Z, Chong J, Zhou G, de Lima Morais DA, Chang L, Barrette M, et al. MetaboAnalyst 50: narrowing the gap between raw spectra and functional insights. *Nucl Acids Res.* (2021) 49:W388–96. doi: 10.1093/nar/gkab382
- Chong J, Wishart DS, Xia J. Using MetaboAnalyst 40 for comprehensive and integrative metabolomics data analysis. *Curr Protocols Bioinform.* (2019) 68:86. doi: 10.1002/cpbi.86
- Chen Y, Luo Z, Sun Y, Li F, Han Z, Qi B, et al. Exercise improves choroid plexus epithelial cells metabolism to prevent glial cell-associated neurodegeneration. *Front Pharmacol.* (2022) 13:1010785. doi: 10.3389/fphar.2022.1010785
- Li T, Zhang W, Hu E, Sun Z, Li P, Yu Z, et al. Integrated metabolomics and network pharmacology to reveal the mechanisms of hydroxysafflower yellow A against acute traumatic brain injury. *Comput Struct Biotechnol J.* (2021) 19:1002–13. doi: 10.1016/j.csbj.2021.01.033
- van Houwelingen HC, Putter H. Comparison of stopped Cox regression with direct methods such as pseudo-values and binomial regression. *Lifetime Data Anal.* (2015) 21:180–96. doi: 10.1007/s10985-014-9299-3
- Sun C, Chen Y, Kim NH, Lowe S, Ma S, Zhou Z, et al. Identification and verification of potential biomarkers in gastric cancer by integrated bioinformatic analysis. *Front Genet.* (2022) 13:911740. doi: 10.3389/fgene.2022.911740
- Kang X, Chen Y, Yi B, Yan X, Jiang C, Chen B, et al. An integrative microenvironment approach for laryngeal carcinoma: the role of immune/methylation/autophagy signatures on disease clinical prognosis and single-cell genotypes. *J Cancer.* (2021) 12:4148–71. doi: 10.7150/jca.58076
- Chen Y, Sun Y, Luo Z, Lin J, Qi B, Kang X, et al. Potential mechanism underlying exercise upregulated circulating blood exosome miR-215-5p to prevent necroptosis of neuronal cells and a model for early diagnosis of Alzheimer's Disease. *Front Aging Neurosci.* (2022) 14:860364. doi: 10.3389/fnagi.2022.860364
- Subramanian A, Tamayo P, Mootha VK, Mukherjee S, Ebert BL, Gillette MA, et al. Gene set enrichment analysis: a knowledge-based approach for interpreting genome-wide expression profiles. *Proc Natl Acad Sci USA.* (2005) 102:15545–50. doi: 10.1073/pnas.0506580102
- Huang J, Liang X, Cai Z. A potential ceRNA network for neurological damage in preterm infants. *Biomed Res Int.* (2021) 2021:2628824. doi: 10.1155/2021/2628824
- Zhao B, Jiang X. Hsa-miR-518-5p/hsa-miR-3135b regulates the REL/SOD2 pathway in Ischemic cerebral infarction. *Front Neurol.* (2022) 13:852013. doi: 10.3389/fneur.2022.852013

44. Smith EE. Clinical presentations and epidemiology of vascular dementia. *Clin Sci*. (2017) 131:1059–68. doi: 10.1042/CS20160607
45. Rose CF, Amodio P, Bajaj JS, Dhiman RK, Montagnese S, Taylor-Robinson SD, et al. Hepatic encephalopathy: novel insights into classification, pathophysiology and therapy. *J Hepatol*. (2020) 73:1526–47. doi: 10.1016/j.jhep.2020.07.013
46. Teruya T, Chen Y-J, Kondoh H, Fukui Y, Yanagida M. Whole-blood metabolomics of dementia patients reveal classes of disease-linked metabolites. *Proc Natl Acad Sci USA*. (2021) 118:e2022857118. doi: 10.1073/pnas.2022857118
47. González-Domínguez R, Javier Rupérez F, García-Barrera T, Barbas C, Luis Gómez-Ariza J. Metabolomic-driven elucidation of serum disturbances associated with Alzheimer's disease and mild cognitive impairment. *CAR*. (2016) 13:641–53. doi: 10.2174/1567205013666160129095138
48. Le Douce J, Maudard M, Veran J, Matos M, Jégo P, Vigneron P-A, et al. Impairment of glycolysis-derived L-Serine production in astrocytes contributes to cognitive deficits in Alzheimer's disease. *Cell Metabol*. (2020) 31:503–17.e8. doi: 10.1016/j.cmet.2020.02.004
49. Hadjihambi A, Harrison IF, Costas-Rodríguez M, Vanhaecke F, Arias N, Gallego-Durán R, et al. Impaired brain glymphatic flow in experimental hepatic encephalopathy. *J Hepatol*. (2019) 70:40–9. doi: 10.1016/j.jhep.2018.08.021
50. Lu K, Zimmermann M, Görg B, Bidmon H-J, Biermann B, Klöcker N, et al. Hepatic encephalopathy is linked to alterations of autophagic flux in astrocytes. *EBioMedicine*. (2019) 48:539–53. doi: 10.1016/j.ebiom.2019.09.058
51. Nho K, Kueider-Paisley A, MahmoudianDehkordi S, Arnold M, Risacher SL, Louie G, et al. Altered bile acid profile in mild cognitive impairment and Alzheimer's disease: relationship to neuroimaging and CSF biomarkers. *Alzheimer's Dement*. (2019) 15:232–44. doi: 10.1016/j.jalz.2018.08.012
52. Geng F, Liu J, Guo Y, Li C, Wang H, Wang H, et al. Persistent exposure to porphyromonas gingivalis promotes proliferative and invasion capabilities, and tumorigenic properties of human immortalized oral epithelial cells. *Front Cell Infect Microbiol*. (2017) 7:57. doi: 10.3389/fcimb.2017.00057
53. Yin H, He Q, Chen J, Li Z, Yang W, Hu X. Drug metabolism-related eight-gene signature can predict the prognosis of gastric adenocarcinoma. *J Clin Lab Anal*. (2021) 35:85. doi: 10.1002/jcla.24085
54. Liu KY, Mistry RJ, Aguirre CA, Fasouli ES, Thomas MG, Klamt F, et al. Nicotinamide N-methyltransferase increases complex I activity in SH-SY5Y cells via sirtuin 3. *Biochem Biophys Res Commun*. (2015) 467:491–6. doi: 10.1016/j.bbrc.2015.10.023
55. Parsons RB, Aravindan S, Kadampeswaran A, Evans EA, Sandhu KK, Levy ER, et al. The expression of nicotinamide N-methyltransferase increases ATP synthesis and protects SH-SY5Y neuroblastoma cells against the toxicity of Complex I inhibitors. *Biochem J*. (2011) 436:145–55. doi: 10.1042/BJ20101685
56. Yan Z, Zhou Z, Wu Q, Chen ZB, Koo EH, Zhong S. Presymptomatic increase of an extracellular RNA in blood plasma associates with the development of Alzheimer's disease. *Curr Biol*. (2020) 30:1771–82.e3. doi: 10.1016/j.cub.2020.02.084
57. Guercio GD, Panizzutti R. Potential and challenges for the clinical use of d-Serine as a cognitive enhancer. *Front Psychiatry*. (2018) 9:14. doi: 10.3389/fpsy.2018.00014
58. Ma EH, Bantug G, Griss T, Condotta S, Johnson RM, Samborska B, et al. Serine is an essential metabolite for effector T cell expansion. *Cell Metabol*. (2017) 25:345–57. doi: 10.1016/j.cmet.2016.12.011
59. Liu S, Sun Y, Jiang M, Li Y, Tian Y, Xue W, et al. Glyceraldehyde-3-phosphate dehydrogenase promotes liver tumorigenesis by modulating phosphoglycerate dehydrogenase: hepatology. Vol. XX, No. X, 2017 Liu et al. *Hepatology*. (2017) 66:631–45. doi: 10.1002/hep.29202
60. Rossi M, Altea-Manzano P, Demicco M, Doglioni G, Bornes L, Fukano M, et al. PHGDH heterogeneity potentiates cancer cell dissemination and metastasis. *Nature*. (2022) 605:747–53. doi: 10.1038/s41586-022-04758-2
61. Tan Y, Zhou X, Gong Y, Gou K, Luo Y, Jia D, et al. Biophysical and biochemical properties of PHGDH revealed by studies on PHGDH inhibitors. *Cell Mol Life Sci*. (2022) 79:27. doi: 10.1007/s00018-021-04022-2
62. Chen X, Calandrelli R, Girardini J, Yan Z, Tan Z, Xu X, et al. expression increases with progression of Alzheimer's disease pathology and symptoms. *Cell Metabol*. (2022) 34:651–3. doi: 10.1016/j.cmet.2022.02.008
63. Predecki M, Kowalska M, Toton E, Kozubski W. Genetic editing and pharmacogenetics in current and future therapy of neurocognitive disorders. *CAR*. (2020) 17:238–58. doi: 10.2174/1567205017666200422152440
64. Das A, Weigle AT, Arnold WR, Kim JS, Carnevale LN, Huff HC. CYP2J2 molecular recognition: a new axis for therapeutic design. *Pharmacol Therapeut*. (2020) 215:107601. doi: 10.1016/j.pharmthera.2020.107601
65. Yao M, Lv D, Huo J, Sun Z. Cerebral small vessel disease is associated with genetic variations in CYP2J. *CNR*. (2018) 14:378–84. doi: 10.2174/1567202614666171017151128
66. Yan H, Kong Y, He B, Huang M, Li J, Zheng J, et al. CYP2J2 rs890293 polymorphism is associated with susceptibility to Alzheimer's disease in the Chinese Han population. *Neurosci Lett*. (2015) 593:56–60. doi: 10.1016/j.neulet.2015.03.024
67. Gui L, Xu Q, Huang J, Wu G, Tang H, Hui L, et al. CYP2J2 promotes the development of hepatocellular carcinoma by increasing the EETs production to improve HIF-1 $\alpha$  stability. *Am J Transl Res*. (2020) 12:7923–37.
68. Cervellati C, Trentini A, Romani A, Bellini T, Bosi C, Otolani B, et al. Serum paraoxonase and arylesterase activities of paraoxonase-1 (PON-1), mild cognitive impairment, and 2-year conversion to dementia: a pilot study. *J Neurochem*. (2015) 135:395–401. doi: 10.1111/jnc.13240
69. Castellazzi M, Trentini A, Romani A, Valacchi G, Bellini T, Bonaccorsi G, et al. Decreased arylesterase activity of paraoxonase-1 (PON-1) might be a common denominator of neuroinflammatory and neurodegenerative diseases. *Int J Biochem Cell Biol*. (2016) 81:356–63. doi: 10.1016/j.biocel.2016.06.008
70. Cervellati C, Romani A, Bergamini CM, Bosi C, Sanz JM, Passaro A, et al. PON-1 and ferroxidase activities in older patients with mild cognitive impairment, late onset Alzheimer's disease or vascular dementia. *Clin Chem Lab Med*. (2015) 53:803. doi: 10.1515/cclm-2014-0803
71. Perla-Kaján J, Włoczkowska O, Ziola-Frankowska A, Frankowski M, Smith AD, de Jager CA, et al. Paraonase 1, B vitamins supplementation, and mild cognitive impairment. *JAD*. (2021) 81:1211–29. doi: 10.3233/JAD-210137
72. Bednarz-Misa I, Berdowska I, Zboch M, Misiak B, Zieliński B, Placzkowska S, et al. Paraonase 1 decline and lipid peroxidation rise reflect a degree of brain atrophy and vascular impairment in dementia. *Adv Clin Exp Med*. (2020) 29:71–8. doi: 10.17219/acem/111377
73. Ding G-Y, Zhu X-D, Ji Y, Shi G-M, Shen Y-H, Zhou J, et al. Serum PON1 as a biomarker for the estimation of microvascular invasion in hepatocellular carcinoma. *Ann Transl Med*. (2020) 8:204–204. doi: 10.21037/atm.2020.01.44
74. Gao M, Yang C, Wang X, Guo M, Yang L, Gao S, et al. ApoC2 deficiency elicits severe hypertriglyceridemia and spontaneous atherosclerosis: a rodent model rescued from neonatal death. *Metabolism*. (2020) 109:154296. doi: 10.1016/j.metabol.2020.154296
75. Groenendijk M. The apoAI-CIII-AIV gene cluster. *Atherosclerosis*. (2001) 157:1–11. doi: 10.1016/S0021-9150(01)00539-1
76. Ma C, Li J, Bao Z, Ruan Q, Yu Z. Serum levels of ApoA1 and ApoA2 are associated with cognitive status in older men. *BioMed Res Int*. (2015) 2015:1–10. doi: 10.1155/2015/481621
77. Cervantes S, Samaranch L, Vidal-Taboada JM, Lamet I, Bullido MJ, Frank-García A, et al. Genetic variation in APOE cluster region and Alzheimer's disease risk. *Neurobiol Aging*. (2011) 32:2107.e7. doi: 10.1016/j.neurobiolaging.2011.05.023
78. Zhuang H, Cao G, Kou C, Liu T. CCL2/CCR2 axis induces hepatocellular carcinoma invasion and epithelial-mesenchymal transition *in vitro* through activation of the Hedgehog pathway. *Oncol Rep*. (2017) 39:21–30. doi: 10.3892/or.2017.6069
79. Zhou Y, Chen J, Sapkota K, Long J, Liao Y, Jiang J, et al. Panax notoginseng saponins attenuate CCL2-induced cognitive deficits in rats via anti-inflammation and anti-apoptosis effects that involve suppressing over-activation of NMDA receptors. *Biomed Pharmacother*. (2020) 127:110139. doi: 10.1016/j.bioph.2020.110139
80. Naziroglu M, Taner AN, Balbay E, Çig B. Inhibitions of anandamide transport and FAAH synthesis decrease apoptosis and oxidative stress through inhibition of TRPV1 channel in an *in vitro* seizure model. *Mol Cell Biochem*. (2019) 453:143–55. doi: 10.1007/s11010-018-3439-0
81. Xu J, Dong H, Qian Q, Zhang X, Wang Y, Jin W, et al. Astrocyte-derived CCL2 participates in surgery-induced cognitive dysfunction and neuroinflammation via evoking microglia activation. *Behav Brain Res*. (2017) 332:145–53. doi: 10.1016/j.bbr.2017.05.066
82. Chen J, Tan L, Liao Y, Long J, Zhou Y, Wei J, et al. Chemokine CCL2 impairs spatial memory and cognition in rats via influencing inflammation, glutamate metabolism and apoptosis-associated genes expression- a potential mechanism for HIV-associated neurocognitive disorder. *Life Sci*. (2020) 255:117828. doi: 10.1016/j.lfs.2020.117828
83. Qin H, Holdbrooks AT, Liu Y, Reynolds SL, Yanagisawa LL, Benveniste EN. SOCS3 deficiency promotes M1 macrophage polarization and inflammation. *JL*. (2012) 189:3439–48. doi: 10.4049/jimmunol.1201168
84. Zhang X, He B, Li H, Wang Y, Zhou Y, Wang W, et al. SOCS3 Attenuates GM-CSF/IFN- $\gamma$ -mediated inflammation during spontaneous spinal cord regeneration. *Neurosci Bull*. (2020) 36:778–92. doi: 10.1007/s12264-020-00493-8
85. Gao Y, Liu R, He C, Basile J, Vesterlund M, Wahren-Herlenius M, et al. SOCS3 expression by thymic stromal cells is required for normal T cell development. *Front Immunol*. (2021) 12:642173. doi: 10.3389/fimmu.2021.642173
86. Lin J. C1QTNF1-AS1 regulates the occurrence and development of hepatocellular carcinoma by regulating miR-221-3p/SOCS3. *Hepatol Int*. (2021) 15:526–526. doi: 10.1007/s12072-021-10152-3
87. Liu Z-K, Li C, Zhang R-Y, Wei D, Shang Y-K, Yong Y-L, et al. EYA2 suppresses the progression of hepatocellular carcinoma via SOCS3-mediated blockade of JAK/STAT signaling. *Mol Cancer*. (2021) 20:79. doi: 10.1186/s12943-021-01377-9
88. Kang YP, Falzone A, Liu M, González-Sánchez P, Choi B-H, Colloff JL, et al. supports liver ceramide synthesis and sustains lipid homeostasis. *Cancer Metab*. (2020) 8:6. doi: 10.1186/s40170-020-00212-x
89. Samanta D, Park Y, Andrabi SA, Shelton LM, Gilkes DM, Semenza GL. PHGDH expression is required for mitochondrial redox homeostasis, breast cancer stem cell maintenance, and lung metastasis. *Cancer Res*. (2016) 76:4430–42. doi: 10.1158/0008-5472.CAN-16-0530

90. Elentner A, Schmuth M, Yannoutsos N, Eichmann TO, Gruber R, Radner FPW, et al. Epidermal overexpression of xenobiotic receptor PXR impairs the epidermal barrier and triggers Th2 immune response. *J Invest Dermatol.* (2018) 138:109–20. doi: 10.1016/j.jid.2017.07.846
91. Dubrac S, Elentner A, Ebner S, Horejs-Hoeck J, Schmuth M. Modulation of T lymphocyte function by the pregnane X receptor. *Jl.* (2010) 184:2949–57. doi: 10.4049/jimmunol.0902151
92. Rensen PC, Voshol PJ, Havekes LM. The role and mode of action of apolipoproteins CIII and AV: synergistic actors in triglyceride metabolism? *Curr Opin Lipidol.* (2004) 15:239–46. doi: 10.1097/00041433-200406000-00002
93. Li L, Xu W, Fu X, Huang Y, Wen Y, Xu Q, et al. Blood miR-1275 is associated with risk of ischemic stroke and inhibits macrophage foam cell formation by targeting ApoC2 gene. *Gene.* (2020) 731:144364. doi: 10.1016/j.gene.2020.144364
94. Lv L-L, Feng Y, Wen Y, Wu W-J, Ni H-F, Li Z-L, et al. Exosomal CCL2 from tubular epithelial cells is critical for albumin-induced tubulointerstitial inflammation. *JASN.* (2018) 29:919–35. doi: 10.1681/ASN.2017050523
95. Sierra-Filardi E, Nieto C, Domínguez-Soto Á, Barroso R, Sánchez-Mateos P, Puig-Kroger A, et al. CCL2 shapes macrophage polarization by GM-CSF and M-CSF: identification of CCL2/CCR2-dependent gene expression profile. *Jl.* (2014) 192:3858–67. doi: 10.4049/jimmunol.1302821



## OPEN ACCESS

## EDITED BY

Pradeep Kumar,  
All India Institute of Medical Sciences, India

## REVIEWED BY

Sabrina Reinehr,  
Ruhr-University Bochum, Germany  
Prabhakar Mujagond,  
Southern Medical University, China  
Sandhya Gazare,  
Gulbarga University, India

## \*CORRESPONDENCE

Huiya Fan  
✉ fanghuiya2022@163.com

## SPECIALTY SECTION

This article was submitted to  
Neurological Biomarkers,  
a section of the journal  
Frontiers in Neurology

RECEIVED 07 November 2022

ACCEPTED 20 February 2023

PUBLISHED 22 March 2023

## CITATION

Zhou L, Lin D, Xu G, Wang X, Chen Z, Wang D  
and Fan H (2023) Alteration of neurofilament  
heavy chain and its phosphoforms reveals early  
subcellular damage beyond the optic nerve  
head in glaucoma. *Front. Neurol.* 14:1091697.  
doi: 10.3389/fneur.2023.1091697

## COPYRIGHT

© 2023 Zhou, Lin, Xu, Wang, Chen, Wang and  
Fan. This is an open-access article distributed  
under the terms of the [Creative Commons  
Attribution License \(CC BY\)](#). The use,  
distribution or reproduction in other forums is  
permitted, provided the original author(s) and  
the copyright owner(s) are credited and that  
the original publication in this journal is cited, in  
accordance with accepted academic practice.  
No use, distribution or reproduction is  
permitted which does not comply with these  
terms.

# Alteration of neurofilament heavy chain and its phosphoforms reveals early subcellular damage beyond the optic nerve head in glaucoma

Lan Zhou<sup>1,2</sup>, Dongyue Lin<sup>2</sup>, Guihua Xu<sup>1</sup>, Xiaoyi Wang<sup>1</sup>, Zilin Chen<sup>1</sup>,  
Dingding Wang<sup>1</sup> and Huiya Fan<sup>1\*</sup>

<sup>1</sup>Ophthalmological Center of Huizhou Central People's Hospital, Huizhou, Guangdong, China, <sup>2</sup>State Key Laboratory of Ophthalmology, Zhongshan Ophthalmic Center, Sun Yat-sen University, Guangzhou, Guangdong, China

**Background:** Retinal ganglion cells (RGCs) axon loss at the site of optic nerve head (ONH) is long believed as the common pathology in glaucoma since different types of glaucoma possessing different characteristic of intraocular pressure, and this damage was only detected at the later stage.

**Methods:** To address these disputes and detect early initiating events underlying RGCs, we firstly detected somatic or axonal change and compared their difference in acute and chronic phase of primary angle-closed glaucoma (PACG) patient using optical coherence tomography (OCT), then an axonal-enriched cytoskeletal protein neurofilament heavy chain and its phosphoforms (NF-H, pNF-H) were utilized to reveal spatio-temporal undetectable damage insulted by acute and chronic ocular hypertension (AOH, COH) in two well characterized glaucoma mice models.

**Results:** In clinic, we detected nonhomogeneous changes such as ONH and soma of RGCs presenting edema in acute phase but atrophy in chronic one by OCT. In AOH animal models, an increase expression of NF-H especially its phosphorylation modification was observed as early as 4 h before RGCs loss, which presented as somatic accumulation in the peripheral retina and at the sites of ONH. In contrast, in microbeads induced COH model, NF-H and pNF-H reduced significantly, these changes firstly occurred as NF-H or pNF-H disconnection at ONH and optic nerve after 2 weeks when the intraocular pressure reaching the peak; Meanwhile, we detected aqueous humor pNF-H elevation after AOH and slight reduction in the COH.

**Conclusion:** Together, our data supports that early alteration of NF-H and its phosphoforms would reveal undetectable subcellular damage consisting of peripheral somatic neurofilament compaction, impaired axonal transport and distal axonal disorganization of cytoskeleton beyond the ONH, and identifies two distinct axonal degeneration which were Wallerian combination with retrograde degeneration in acute PACG and retrograde degeneration in the chronic one.

## KEYWORDS

neurofilament heavy chain, optic nerve head, retinal ganglion cells, axon degeneration, acute angle closed glaucoma, chronic angle closed glaucoma



## Introduction

Glaucoma is the leading cause of irreversible blindness worldwide. It consists of different subtypes, including primary angle-closed glaucoma (PACG) and primary open-angle glaucoma (POAG), and among these subtypes, In China, PACG is the most prevalent subtype and is highly deleterious to visual function (1, 2). Elevated intraocular pressure (IOP) is a well-known risk factor of PACG, which leads to an elevated pressure gradient across the lamina cribrosa, predisposing the retinal ganglion cell (RGC) axon to damage at the sites of the optic nerve head (ONH) (3, 4). Clinically, structural measurements of the retinal nerve fiber layer (RNFL) at the ONH are widely used to assess RGC damage (5). However, these structural changes are only detected by current methods when the visual field is seriously damaged (6). The early pathogenesis underlying RGC damage still remains poorly understood. A better understanding of early glaucomatous axon damage is, therefore, essential to develop effective methods, as well as therapeutic agents for the diagnosis and treatment of glaucoma.

To date, evidence from experimental glaucoma models has demonstrated axonal transport deficit at the site of the ONH and the distal visual central system occurs preceding structural loss (7, 8). However, the axonal transport is visualized mostly by virtue of an exogenous anterograde or retrograde tracer; therefore, evidence supporting axonal transport failure at the ONH is circumstantial. The normal function of axonal transport depends on the intact organization of the axonal cytoskeleton, including neurofilaments, microtubules, and their associated proteins, which provides the molecular tracks for the bidirectional movement of motor proteins and their associated cargo (9). Aberrations in several cytoskeletal proteins, such as neurofilament and tau, have been proven to potentially act as surrogate markers for axonal injury and transport damage (10). Among them, neurofilament heavy chain and its phosphoforms have been gaining more and more attention because of their deep involvement in maintaining the integrity of the neuronal cytoskeleton and the important role of revealing early uneasily detectable damage in neurodegeneration diseases (11–14). In glaucoma, the changes in neurofilaments have been investigated in animal models but have remained controversial, as some bodies of research have observed a reduction in neurofilament heavy chain (NF-H) at the ONH in AOH (15, 16); conversely, the elevation of dephosphorylation or phosphorylated NF-H (pNF-H) has been demonstrated in some acute and chronic ocular hypertension (AOH, COH) models (17, 18). This suggests that the changes in NF-H and pNF-H may be different when insulted by different patterns of elevated IOP, and whether alteration of them would indicate early and undetected damage beyond ONH needs further study.

To address these questions, we first evaluated and compared the differences in RGC axonal and somatic changes after an AOH attack and a COH insult in angle-closed glaucoma through an optical coherence tomography (OCT) RNFL and a ganglion cell layer (GCL) scan. Then, from clinic to the basic pathological damage, using two well-characterized glaucoma mice models that mimicked acute and chronic primary angle-closed glaucoma (APACG, CPACG), we attempted to reveal the truths underlying RGC damage through the molecular marker NF-H. In clinic, RNFL and GCL often presented as edema after the acute attack of ocular hypertension in APACG but reduced significantly in

CPACG. Our experimental data showed that acute elevated IOP would cause an early increase in phosphorylated NF-H and NF-H and that the accumulation was primarily observed in the soma of peripheral RGCs, while intra-axon swellings and beadings of pNF-H at the ONH site were observed as well. Unlike these features, the expression of pNF-H and NF-H markedly decreased in COH, and these changes first occurred at the ONH and the optic nerve, presenting as local NF-H or pNF-H disconnection. Importantly, we detected a correspondingly significant elevation and a slight reduction in the aqueous humor of both AOH and COH models. Together, our data support the evidence that early alteration of NF-H and its phosphoforms would not only explain the current changes detected by the OCT but also reveal undetectable damage beyond an axonal loss at the ONH, and we identified two distinct characteristics of axonal degeneration that were a retrograde combination with Wallerian degeneration in APACG and chronic dying back degeneration in CPACG.

## Methods

### Classification of patients with glaucoma

Acute primary angle-closed glaucoma (APACG) and CPACG were defined using the International Society of Geographical and Epidemiological Ophthalmology classification (19). The acute attack of APACG is defined by the presence of the following aspects: (1) at least two of the symptoms by the acute episode of IOP increase, which are nausea and/or vomiting, decreased vision, ocular pain or headache, and rainbow-colored halos around lights; (2) IOP  $\geq 45$  mmHg by the Goldmann applanation tonometry; (3) signs such as corneal epithelial edema, conjunctival injection, shallow anterior chamber, or a mid-dilated unreactive pupil at the first presentation; (4) closed angles in at least three quadrants by a gonioscopic examination; and (5) the start of the symptoms only recently, which were relieved by local or systematic IOP-lowering drugs during hospitalization.

Chronic primary angle-closed glaucoma is demonstrated by the following criteria: (1) visual function damage; (2) at least three quadrants of the posterior trabecular meshwork being invisible on gonioscopy; and (3) gradually elevated IOP without signs of acute angle-closure attack.

The exclusion criteria of the present study were as follows: (1) a previous laser or an intraocular surgery performed on either eye; (2) patients with a subluxated lens or intumescent cataract; (3) patients with uveal effusion; (4) patients with retinal detachment or macular pathology on ocular examination; (5) patients with AL  $< 19$  mm in either eye; (6) both eyes were involved; (7) the pictures or data did not meet the standard for analysis; and (8) basic diseases, such as hypertension or diabetes, are affecting the patient.

### RNFL and ganglion cell layer evaluation through optical coherence tomography

A total of 35 patients with APACG and 30 patients with CPACG aged 50–80 years who visited the glaucoma service of our hospital between January 2020 and December 2021 were recruited



for analysis. All patients were administered local or systematic IOP-lowering drugs to eliminate pain and edema, and then, they underwent routine glaucomatous examinations, including the Humphrey visual field, A/B scan and OCT. The RNFL and GCL evaluation was performed by optical coherence tomography angiography (Carl Zeiss AG, Oberkochen, Germany) with two scan models, which were the peripapillary retinal nerve fiber layer and the macular ganglion cell layer. RNFL thickness was measured by reference to a circle scan with a diameter of  $\sim 3.45$  mm, which was divided into four focal sectors: superior, inferior, temporal, and nasal. GCL thickness was acquired with a  $6 \times 6$ -mm scanning area centered on the macula. Informed consent was obtained from all patients.

## Animals

We used female or male adult C57BL/6J (6–8 weeks) mice (Vital River, China) for the experiments conducted during the study. All mice were housed under a 12-h light/dark cycle at  $22 \pm 2^\circ\text{C}$ , with free access to food and water. The animals were habituated in the experimental environment for 1 week before each experimental procedure. All animal experiments were conducted in accordance with the National Institutes of Health Guide for the Care and Use of Laboratory Animals approved by the Institutional Animal Care and Use Committee of Guang Dong Medical University and Zhongshan Ophthalmic Center.

## Acute ocular hypertension and microbead-induced chronic ocular hypertension model

The induction of AOH was performed on the right eye as previously reported (20). Briefly, animals were anesthetized by an intraperitoneal injection of a 1:1 mixture (1.0 ml/kg) of ketamine (100 mg/ml, Fujian Gutian Pharmaceutical Co., Ltd., China) and xylazine (20 mg/ml, Sigma, Germany), the cornea was topically anesthetized with 0.5% tetracaine hydrochloride, and the pupil was dilated with 1% tropicamide. Next, the anterior chamber of the right eye was perfused with a 30-gauge needle connected to a normal saline reservoir, which was elevated to a height of 80 cm  $\text{H}_2\text{O}$  (60 mmHg) for 2 h. The same operation was performed on the eyes of the sham control group but without increasing the pressure. IOP was confirmed by a tonometer (Tono-Lab; ICARE, Finland). Three different time points, including 4, 6, and 12 h after AOH, were set for histological and molecular studies, while 30 mice were used for analysis ( $n = 5$  mice per experiment at each time point) and 4 mice were excluded because of cataract or intra-ocular hemorrhage.

A microbead-induced chronic ocular hypertension model was established as described in earlier sections (21, 22). Before a microbead injection, baseline IOP was acquired using the tonometer (Tono-Lab; ICARE, Finland) in mice anesthetized with 2.5% isoflurane (Minrad Inc., Bethlehem, PA, USA) for at least two consecutive days prior to surgery. Next, 2  $\mu\text{l}$  of 3- $\mu\text{m}$  magnetic microbeads (Bangs Laboratories, Inc, IN, USA) was injected into

the anterior chamber angle of the experimental mice anesthetized with 2.5% isoflurane, and the same volume of sterile saline was injected into the anterior chamber of control mice. After the surgery, antibiotic drops (0.5% ofloxacin hydrochloride ophthalmic solution; Alcon Laboratories, Inc., USA) were applied in the surgery eye, and the animal recovered for 24 h prior to IOP measurements. IOP was measured every 2 days for 10 days and then every 5 days for 20 days. Thirty-six mice were prepared for the experiment; six mice with inadequate IOP elevation and infection were excluded. Finally, 20 mice were used for the IOP measurement: nine mice at 2 weeks and the remaining 11 mice housed for 4 weeks were used for a further study.

## Tissue collection

Tissues such as retinal wholemount, sections, and the optic nerve were collected at a certain time point of AOH and COH animal models. A 20-mm cryostat section was acquired from the eye cups embedded in Optimal Cutting Temperature compound (OCT, Tissue-Tek, USA) after being fixed in 4% paraformaldehyde (PFA) for 30 min and dehydrated in 20% sucrose dissolved in PBS overnight. To obtain the retinal wholemount and the optic nerve, mice were transcardially perfused with cold saline followed by 4% paraformaldehyde for 30 min. Their eyes were enucleated, the cornea and the lenses were removed, and the eye cups were postfixed in 4% PFA for 10 min. The retinas or the retinal nerve were then dissected from the eye cups for further study.

## Western blot analysis

The retinas and the optic nerve head from AOH and COH models were harvested at a certain time point and then homogenized in RIPA lysis buffer (Millipore, Germany). Then, the sample was separated on SDS-PAGE and electroblotted onto a PVDF membrane (Bio-Rad, USA). Primary antibodies against phosphorylated neurofilament-H (1:500; Millipore, Germany), neurofilament-H or L (1:1,000; Millipore, Germany), neurofilament-M (1:1,000; Cell Signaling Technology, USA) followed by incubation with a HRP-conjugated secondary antibody were used. Antibody-reactive bands were visualized using an Immobilon Western Chemiluminescent HRP Substrate (Millipore, Germany) and a G-BOX (Syngene, USA) image capture system. Relative protein expression level was measured by calculating the band density with ImageJ software (NIH, USA), followed by normalization to the GAPDH loading control.

## Collection of the aqueous humor from mice

The aqueous humor was collected from the experiment and control eyes of AOH or COH using a syringe with a 35-gauge needle (Hamilton). A total of 3  $\mu\text{l}$  of AH was collected from each mouse, and 15 samples were pooled for ELISA. The aqueous humor was collected 6 h after AOH and 2 weeks after COH.

## Immunofluorescence staining of retinal wholemount and retinal and optic nerve cryostat sections

To analyze the spatial distribution of NF-H and its phosphoforms, we performed immunofluorescence staining in retinal wholemount and the retinal and optic nerve cryostat sections. After drying and rehydration in PBS, the samples were permeabilized in 0.5% Triton X-100 for 30 min, blocked in 5% donkey serum for 1 h at room temperature (RT), and incubated overnight at 4°C with primary antibody, which was followed by incubation with an Alexa Fluor-labeled secondary antibody (Cell Signaling Technology, Beverly, MA, USA) for 1 h at RT after three washes with PBS. Primary antibodies against phosphorylated neurofilament-H (1:500, Millipore, Germany), Neurofilament-H (1:1,000, Millipore, Germany), Brn3a (1:200, Millipore, Germany), and NeuN (1:500, Millipore, Germany) were used for IF staining. The samples were finally examined under a confocal microscope (LSM710; Carl Zeiss, Germany). Retinal wholemount was dissected into four quadrants, three different eccentricities away from the optic disk in each quadrant: central (0.5 mm), middle (2 mm), and peripheral (4 mm) were chosen for quantification analysis with a 20× objective (500 × 500 μm for each image, 12 images per retina). Five histological sections (400 × 400 μm) through the optic nerve head (centered at ~0.4 mm from the scleral margin) or the optic nerve (centered ~1.2 mm away from the scleral margin) of each IOP elevation and the control eye were examined with a 10× objective by two masked observers.

## Analysis of neurofilament score

The analysis of neurofilament disconnection was performed using an established scoring system ranging from 0 to 2, which was graded as follows: 0 = intact structure and no retraction bulbs, 1 = shortened axons and some retraction bulbs, and 2 = loss of structural integrity and plenty of retraction bulbs and holes (23). The score was averaged for the final statistical analysis.

## ELISA measurement of the aqueous humor

The aqueous humor collected from AOH and COH models was used for quantifying pNF-H through an enzyme-linked immunosorbent assay (ELISA) kit (Phosphorylated Neurofilament Sandwich ELISA Kit, Merck KGaA, Germany), and the analysis was carried out according to the manufacturer's protocols. The samples were diluted at a ratio of 1:6 with a sample diluent. pNF-H antibody-coated strip wells were incubated with 50 μl of standards or samples at room temperature (RT) for 1 h with gentle shaking. Plates were washed six times with diluted wash buffer provided in the kit; then, 100 μl of detection antibody was added to all wells and incubated for 1 h at RT. Plates were washed six times and 100 μl of the diluted alkaline phosphatase-conjugated goat anti-rabbit polyclonal antibody was added to each well and incubated for 1 h. After six washes, 100 μl of freshly diluted 1× pNPP alkaline phosphatase substrate was added to each well and incubated in the

dark at RT for 30–60 min. Stop solution (3N NaOH) was added and plates were read at 405 nm on an Infinite 200 PRO NanoQuant Plate reader (Tecan, Switzerland) using i-control analytical software.

## Statistical analysis

IBM SPSS Statistics 22 (IBM Corp: Armonk, NY, USA) was used for all statistical analyses. For the comparison of clinical data between the glaucoma eye and the contralateral unaffected eye, a two-tailed *t*-test, the Mann–Whitney rank sum test, and Pearson's chi-square ( $\chi^2$ ) test were used to obtain for a variety of data. Differences in IOP throughout the 4-week experimental time course between the COH and the control groups were statistically analyzed using a one-way repeated-measures analysis of variance (ANOVA). For neurofilament expression, a comparison between all experimental groups at each time point was carried out using one-way analysis of variance (ANOVA) followed by a Dunnett's test for normally distributed data and equal variances; otherwise, it was analyzed using the Kruskal–Wallis analysis followed by the Dunn–Bonferroni *post hoc* method. Differences in pNF-H accumulation, neurofilament disconnection between glaucoma and the control eye were assessed with a two-tailed *t*-test. Graphical representations of the data were made with scatter diagrams or box-and-whisker plots. A *P*-value of < 0.05 was considered significant.

## Results

### In clinic, RGC axon and soma exhibited signs of edema after acute attack in APACG but presented a significant degeneration insulted by chronic IOP elevation in CPACG

Retinal nerve fiber layer and GCL thickness in OCT are taken as important tools to evaluate RGC damage in clinic. To determine the changes in RGCs insulted by acute or chronic ocular hypertension in clinic, RNFL and GCL scans of OCTA were performed in APACG and CPACG. Thirty-five patients with APACG and 30 patients with CPACG were included in the analysis. The contralateral eyes of each group without glaucoma were set as control. Demographic data for APACG and CPACG are shown in Table 1. There were no significant differences in age or sex between the two groups (Table 1). Peripapillary RNFL thickness localized at the four sectors in APACG eyes increased significantly compared to control eyes (inferior: 168.54 ± 37.08 vs. 138.11 ± 18.94 μm, superior: 154.74 ± 37.45 vs. 124.74 ± 14.59 μm, nasal: 85.57 ± 22.71 vs. 68.37 ± 8.64 μm, and temporal: 86.43 ± 15.17 vs. 75.8 ± 10.28 μm; *P* < 0.05, Figures 1A, C) after an acute attack. The average thickness of GCL also showed to be slightly elevated in APACG vs. control (84.16 ± 5.19 vs. 81.32 ± 7.30 μm, *P* = 0.067, Figures 1A, D). By contrast, RNFL thickness maps and thickness deviation maps in CPACG vs. control eyes showed an obvious loss of RNFL within four sectors of the optic disk (inferior: 71.80 ± 25.07 vs. 127.97 ± 18.23 μm, superior: 76.97 ± 24.30 vs. 120.77 ± 16.39 μm, nasal: 65.17 ± 14.95 vs. 72.13 ± 14.45 μm, and temporal: 51.23 ± 14.64 vs. 72.13 ± 14.45 μm, *P* < 0.05, Figures 1B, E). The GCL thickness also reduced significantly in CPACG vs. control

TABLE 1 Demographics and basic clinical data of recruited eyes.

|            |           | APACG        |                   |                     | CPACG        |                   |                     | P-value           |
|------------|-----------|--------------|-------------------|---------------------|--------------|-------------------|---------------------|-------------------|
|            |           | Affected eye | Contralateral eye | P-value             | Affected eye | Contralateral eye | P-value             |                   |
| Age        | Mean ± SD | 62.3 ± 7.1   |                   | -                   | 60.1 ± 7.8   |                   | -                   | 0.23 <sup>a</sup> |
|            | Range     | 46–84        |                   |                     | 43–76        |                   |                     |                   |
| Sex        | Male      | 7            |                   | -                   | 11           |                   | -                   | 0.13 <sup>c</sup> |
|            | Female    | 28           |                   |                     | 19           |                   |                     |                   |
| IOP (mmHg) | Mean ± SD | 51.0 ± 7.6   | 15.4 ± 3.5        | <0.001 <sup>a</sup> | 34.7 ± 6.5   | 15.5 ± 3.8        | <0.001 <sup>a</sup> | -                 |
|            | Range     | 34–62        | 10–25             |                     | 26–54        | 9–24              |                     |                   |
| VA, LogMAR | Median    | 0.5          | 0.2               | <0.001 <sup>b</sup> | 0.5          | 0.1               | <0.001 <sup>b</sup> | -                 |
|            | Range     | 0.2–3.3      | 0–0.5             |                     | 0.2–3.6      | 0–0.5             |                     |                   |

Values are mean  $\pm$  SD for continuous factors, median for visual acuity (VA).

<sup>a</sup>Student's t-test.

<sup>b</sup>Mann–Whitney U-test.

<sup>c</sup>Pearson  $\chi^2$  test.

(57.55  $\pm$  9.32 vs. 81.91  $\pm$  7.37  $\mu$ m,  $P$  < 0.001, [Figures 1B, F](#)). Taken together, the data from clinical patients indicated that RGC axon and soma presented edema after the acute attack in APACG but degeneration in CPACG, which suggested that two types of RGC damage existed between them.

## Anterior chamber perfusion with normal saline in mice to mimic acute attack of APACG and a microbead injection in the anterior chamber angle to mimic chronic IOP elevation of CPACG

Next, to uncover what lies beneath the aforementioned clinical observations, two animal models were set to mimic the acute attack of APACG and chronic IOP elevation of CPACG. In AOH animal models, the IOP immediately increased to 60 mmHg by perfusion with normal saline into the anterior chamber, which well-simulated the state of onset in APACG ([Figure 2A](#)). In the microbead-induced models, the IOP began to increase at 2 days (average IOP, 17.43  $\pm$  3.06 mmHg vs. control 10.13  $\pm$  1.12 mmHg;  $P$  < 0.01) and reached the peak at 2 weeks (28.10  $\pm$  5.42 mmHg vs. control 10.30  $\pm$  1.02 mmHg,  $P$  < 0.001) after the microbead injection into the anterior chamber angle ([Figures 2B, C](#)). The elevation of IOP sustained for 1 month and began to decrease ([Figure 2C](#)).

## Acute ocular hypertension caused early elevation of phosphorylated NF-H in the retina and the ONH, and an evident neurofilament increase in the retina

Neurofilaments are major proteins synthesized by RGCs and conveyed along the ON by fast axonal transport. Alterations in neurofilaments, especially NF-H and its phosphoforms, had been proven as biomarkers of axonal transport failure in some

neurodegenerative diseases ([24, 25](#)). However, other studies from traumatic brain injury showed that intra-axonal neurofilaments' compaction may occur independent of axonal transport failure and not evoke axonal swelling ([11](#)). Since our clinical observation from APACG only showed neuronal swelling, which encouraged us to question whether it was caused by neurofilaments' compaction or transport failure, we performed the spatiotemporal analysis in the aforementioned animal models.

Our previous study has demonstrated that apoptotic RGCs and axon loss were first visualized as early as 6 h after AOH ([20](#)). Based upon these, we detected the expression of neurofilament and its phosphoforms in the retina and ONH, respectively, from 4 h after AOH preceding RGC apoptosis and axon loss. Neurofilament subunit including NF-H, M, and L increased significantly in the retina after 6 h; among them, NF-H was elevated by almost two-fold compared to control, which was the most obvious one (1.92  $\pm$  0.26 vs. control 1.12  $\pm$  0.16,  $P$  < 0.001, [Figures 3A, C](#)). More importantly, retinal pNF-H levels showed a significant increase as early as 4 h after AOH (pNF-H/NF-H, 1.16  $\pm$  0.16 vs. control 0.68  $\pm$  0.11,  $P$  < 0.001) when the neurofilament did not change ([Figures 3A, D](#)). For the tissues of ONH, we did not detect significant changes in neurofilament subunits at an early time (4 h) when the retinal pNF-H began to increase; however, we detected a nearly two-fold increase of pNF-H at 6 h after AOH (pNF-H/NF-H, 1.94  $\pm$  0.53 vs. control 1.04  $\pm$  0.27,  $P$  < 0.05, [Figures 3B, E](#)). Thus, our data showed an early elevation of NF-H and its pNF-H in the retina and only a significant increase of pNF-H in the ONH.

## NF-H and its phosphoforms accumulated in the soma of peripheral RGCs after AOH

Based on the changes in NF-H and its phosphoforms' expression in the Western blot, the retinal wholemounts were collected to study their distribution through immunofluorescence staining. In the retina, an abnormal increase of NF-H and its pNF-H presented as a character of protein deposits or accumulations

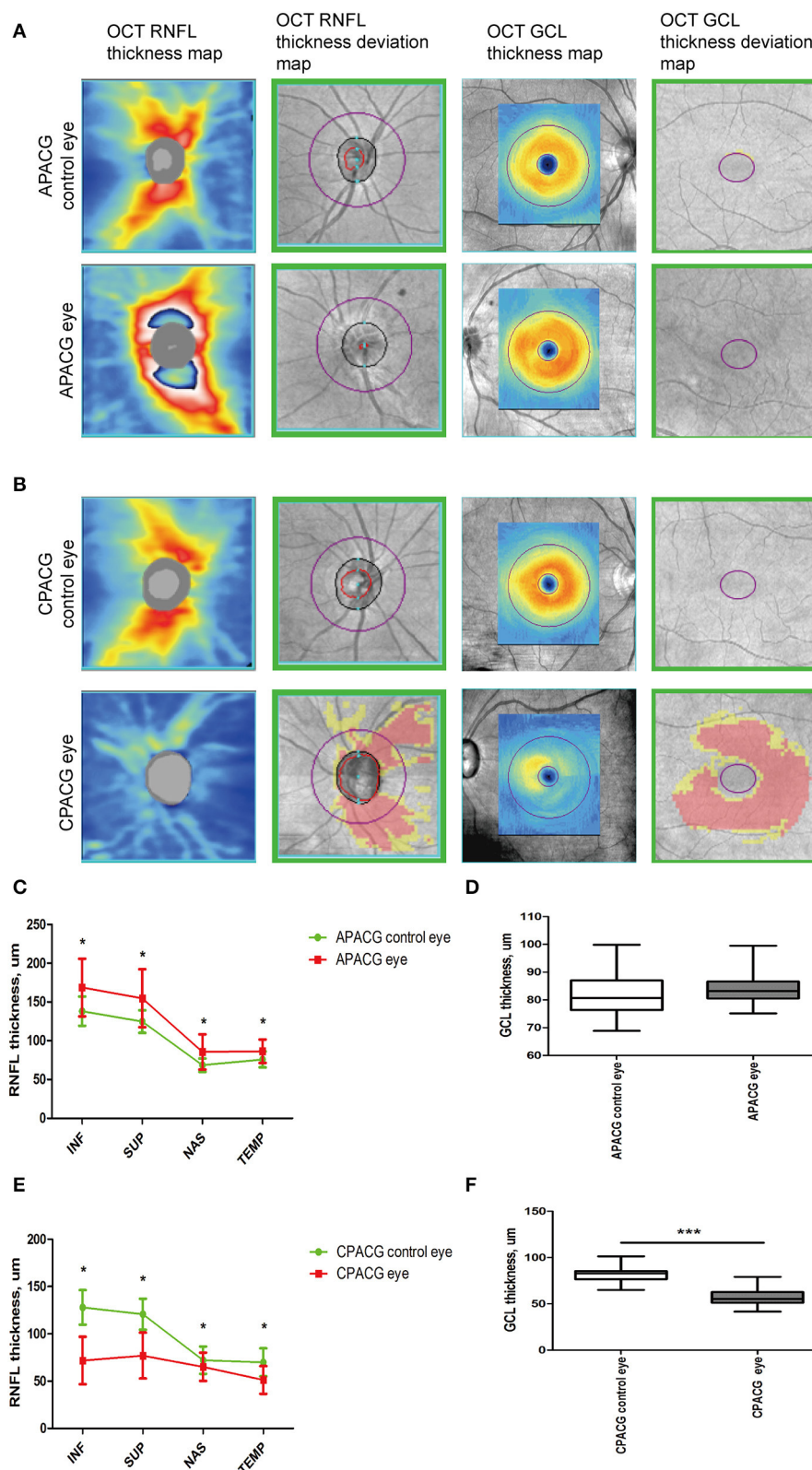


FIGURE 1

Heterogeneity such as RGC axon and soma presenting edema insulted by acute damage but atrophy in chronic glaucoma evaluated by OCT. **(A)** OCT RNFL thickness maps, OCT RNFL thickness deviation maps, OCT GCL thickness maps, and OCT GCL thickness deviation maps are presented, which show that the thickness of RNFL and GCL increased significantly after an acute attack. The warm colors on the thickness maps represent a thicker RNFL or GCL and cooler colors represent a thinner one. **(B)** OCT imaging showed an obvious loss of RNFL and GCL loss insulted by chronic damage in CPACG. The cooler colors in thickness maps suggested RNFL and GCL thickness reduction. Areas coded in red and yellow in deviation

(Continued)



FIGURE 1 (Continued)

maps represent measurements below the 99th and 95th percentile ranges, respectively. (C) Peripapillary RNFL thickness was quantified in four regions, including the inferior (INF), superior (SUP), nasal (NAS), and temporal (TEP) regions. The line graph indicates that the detailed RNFL thickness of patients with APACG (colored in red) reduced significantly, with the contralateral unaffected eyes as the control group.  $*P < 0.05$ . (D) The bar graph shows the average GCL thickness in patients with APACG. GCL thickness increased slightly. Data are presented as mean  $\pm$  SD. (E) The line graph shows that the RNFL thickness in patients with CPACG reduced significantly, and a Mann–Whitney rank sum test was used to analyze the data,  $*P < 0.05$ . (F) Macular GCL thickness in CPACG was obviously reduced. Data are presented as box-and-whisker plots, where the “box” delineates the median and the 25th and 75th quartiles and the “whiskers” show the minimum and maximum values. A two-tailed  $t$ -test was used to analyze the data,  $***P < 0.001$ .

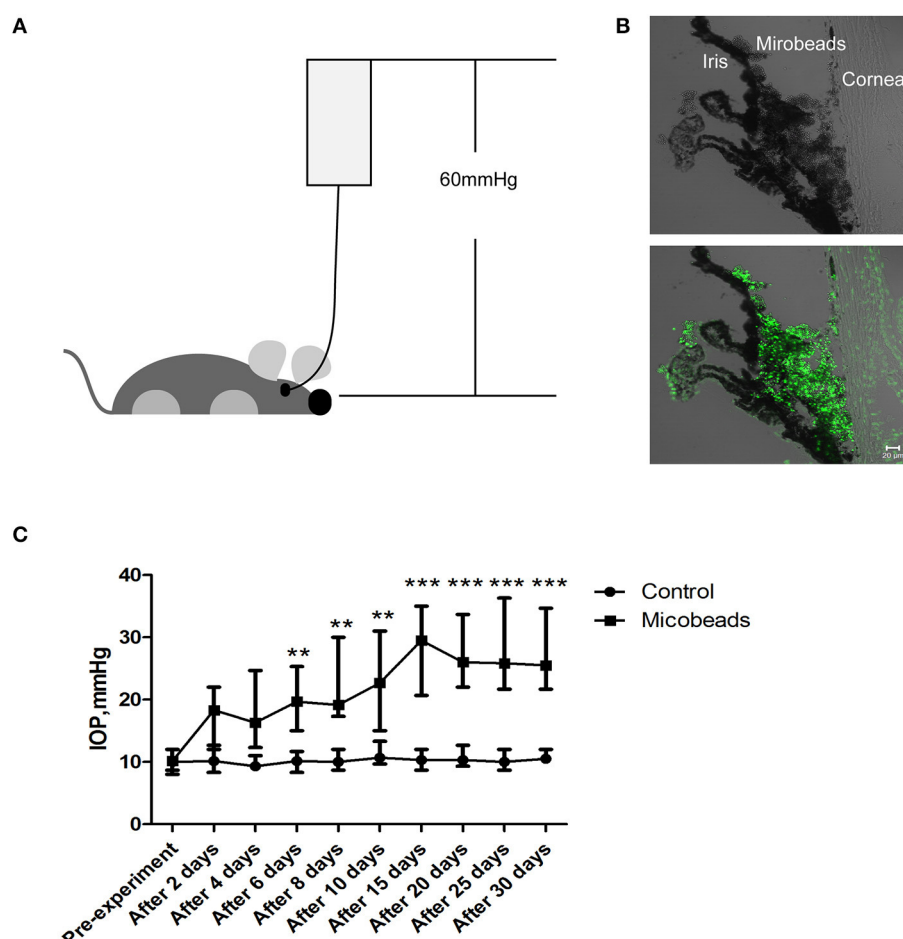


FIGURE 2

Two well-established glaucoma animal models were set to mimic acute attack of APACG and chronic damage of CPACG. (A) Acute ocular hypertension model: IOP acutely increased to 60 mmHg by perfusion with normal saline into the anterior chamber, and the ocular hypertension was sustained for 2 h. (B) Three-micrometer magnetic microbeads were injected into the anterior chamber after 2 days to mimic chronic ocular hypertension. The microbeads showed autofluorescence (bottom). Scale bars: 20  $\mu$ m. (C) IOP began to increase after 2 days and reached the peak 2 weeks after the injection. IOP was measured at pre-treatment, 2, 4, 6, 8, and 10 days, and then every 5 days for 1 month after the surgery.  $n = 20$  mice,  $**P < 0.01$ ,  $***P < 0.001$ .

in the cell bodies along the axon, which first appeared at 4 h after AOH in the peripheral retina (asterisk, Figure 4A). After 6 h of AOH, the NF-H also began to accumulate, and the accumulation of pNF-H and NF-H was highly overlapped (Figure 4C). The number of somatic pNF-H deposits was then counted, and we found that it increased remarkably in the AOH group ( $53 \pm 14$  vs. control  $14 \pm 7$  per field,  $P < 0.001$ , Figure 4B). Then, to confirm that pNF-H accumulation was located in the soma of RGCs, several cell markers, including Brn3a and NeuN, were used for immunofluorescence staining. pNF-H deposits were highly co-labeled with these two markers (Figure 4D),

indicating that pNF-H and NF-H accumulated in the soma of peripheral RGCs.

### At the sites of ONH, pNF-H exhibited a sign of intra-axon plaque and vacuolization after acute attack

Optic nerve cryostat sections were harvested to study the spatial distribution of pNF-H since we found that its expression increased



at the ONH. The ONH has been considered as the primary site of early axonal cytoskeleton damage. However, the neurofilament including NF-H, M, and L here did not show significant change at an early time (Figure 3B). At 6 h after AOH, NF-H phosphoforms began to accumulate at the ONH, which exhibited a sign of intra-axon plaque (Figure 5, arrows) and vacuolization (Figure 5, arrowheads) different from their accumulation in RGC soma.

## Chronic ocular hypertension led to a marked reduction in pNF-H and NF-H at an early time

The accumulation of pNF-H at the site of peripheral RGCs and ONH induced by AOH prompted us to observe the changes induced by the COH insult. Therefore, the expression of pNF-H and NF-H had been analyzed in different tissues of the COH model. However, unlike the alteration in AOH, a chronic IOP elevation caused a significant reduction in neurofilament and NF-H phosphoforms at the ONH as early as 2 weeks when the IOP reached the peak after a microbead injection (NF-H/GAPDH:  $1.03 \pm 0.20$  vs. control  $2.21 \pm 0.21$ ,  $P < 0.001$ , Figures 6A, C). In the tissues of the retina, the expression of neurofilament, especially NF-H or pNF-H, did not change till 4 weeks, after which it began to reduce (NF-H/GAPDH:  $1.88 \pm 0.29$  vs. control  $3.51 \pm 0.77$ ,  $P < 0.001$ , Figures 6B, D). In general, the data here suggested that axonal cytoskeleton damage occurred first in the ONH in COH.

## Neurofilament degeneration first occurred at ONH and the optic nerve presented as local NF-H or pNF-H disconnection

To further confirm the characteristic of neurofilament damage, we performed immunofluorescence staining of NF-H and pNF-H in the longitudinal ONH and optic nerve cryostat sections. The pattern of NF-H at the sites of ONH showed a significant filament disconnection where the neurofilaments were disrupted and detected retraction bulbs or loss of structural integrity by COH (Figure 7A). The extent of ONH NF-H disconnection was calculated using an established scoring system. The results revealed that COH caused almost four-fold greater damage compared to the control by 2 weeks ( $1.7 \pm 0.4$  vs.  $0.2 \pm 0.1$ ,  $P < 0.001$ , Figures 7A, C). Of particular concern was the NF-H disconnection at the optic nerve, whereby it dispersed into granular ones after COH (asterisk, Figure 7B) and the NF-H score increased significantly compared to the control ( $1.4 \pm 0.3$  vs.  $0.3 \pm 0.1$ ,  $P < 0.001$ , Figure 7C). For pNF-H immunofluorescence staining, besides a presentation of general reduction at the ONH and the optic nerve, it also showed a local vessel-like structural debris disconnection in the degenerated axon. Therefore, the data here suggested that COH caused early neurofilament damage at the ONH and that the optic nerve presented as local NF-H or pNF-H disconnection.

## pNF-H was elevated in the aqueous humor of AOH but reduced in the aqueous humor of COH

The phosphorylated forms of NF-H have been proven to be released from damaged and diseased axons and are particularly resistant to proteolytic cleavage (12, 13, 26). Therefore, to evaluate the pNF-H change released from damaged RGCs of the aforementioned experimental glaucoma models, we measured the pNF-H concentration by ELISA in the aqueous humor collected from AOH and COH animal models. The results showed that pNF-H was significantly elevated in the aqueous humor of AOH vs. control ( $37.03 \pm 5.71$  vs.  $11.06 \pm 2.15$  ng/ml,  $P < 0.001$ , Figure 8A). By contrast, in COH, the concentration of NF-H in the aqueous humor reduced slightly ( $3.93 \pm 0.95$  vs.  $8.17 \pm 1.66$  ng/ml,  $P < 0.05$ , Figure 8B). Our results here showed that pNF-H change in the aqueous humor took place corresponding to its alterations in the damaged RGCs insulted by AOH and COH.

## Discussion

In the current study, we introduced the molecular marker NF-H and its phosphoforms to study early subcellular damage in glaucoma and explain the heterogeneity detected in patients with clinical glaucoma. Our results suggested that the ONH was not the only primary damage site when insulted by different durations and degrees of elevated IOP in angle-closed glaucoma. When attacked by AOH, beside NF-H and pNF-H intra-axonal plaque or vacuolization at the ONH, their accumulation in the peripheral RGC soma was demonstrated to be early damage, which was also the potential pathological damage beneath RNFL or GCL edema in a patient with APACG. Furthermore, after being insulted by COH, focal intra-axonal NF-H and its phosphoforms' loss or disconnection at the site of ONH and the optic nerve proved to be the primary damage event, which also explained why the axonal degeneration often occurred in the ONH. Meanwhile, the two different types of damage suggested here that the neurons in AOH were degenerated by Wallerian and retrograde degeneration, while those in COH were degenerated by retrograde degeneration.

The lamina cribrosa of the ONH has long been believed to be the primary site of RGC damage in glaucoma. Pioneering basic research performed on monkeys (27–29) and pigs (30) insulted by AOH and COH has demonstrated axonal transport failure preceding axonal loss at the lamina cribrosa. Rodents lack a true lamina cribrosa, but their ONH owns a similar function as the lamina cribrosa. Similar operations performed on rodents have revealed that the ONH is the site of early axonal transport disruption and cytoskeleton damage (7, 31, 32). In clinic, it is difficult to monitor the changes in axonal transport directly. With the use of OCT, the peripapillary RNFL analysis is considered as one important tool for detecting the changes in the entire RGC axon at the ONH, and RNFL reduction is considered as one of the necessary criteria for the diagnosis of glaucoma (33). However, the RNFL analysis only represents the structural changes in the ONH. Furthermore, the point of emphasis too much on the pathological changes of ONH would exclude the subcellular

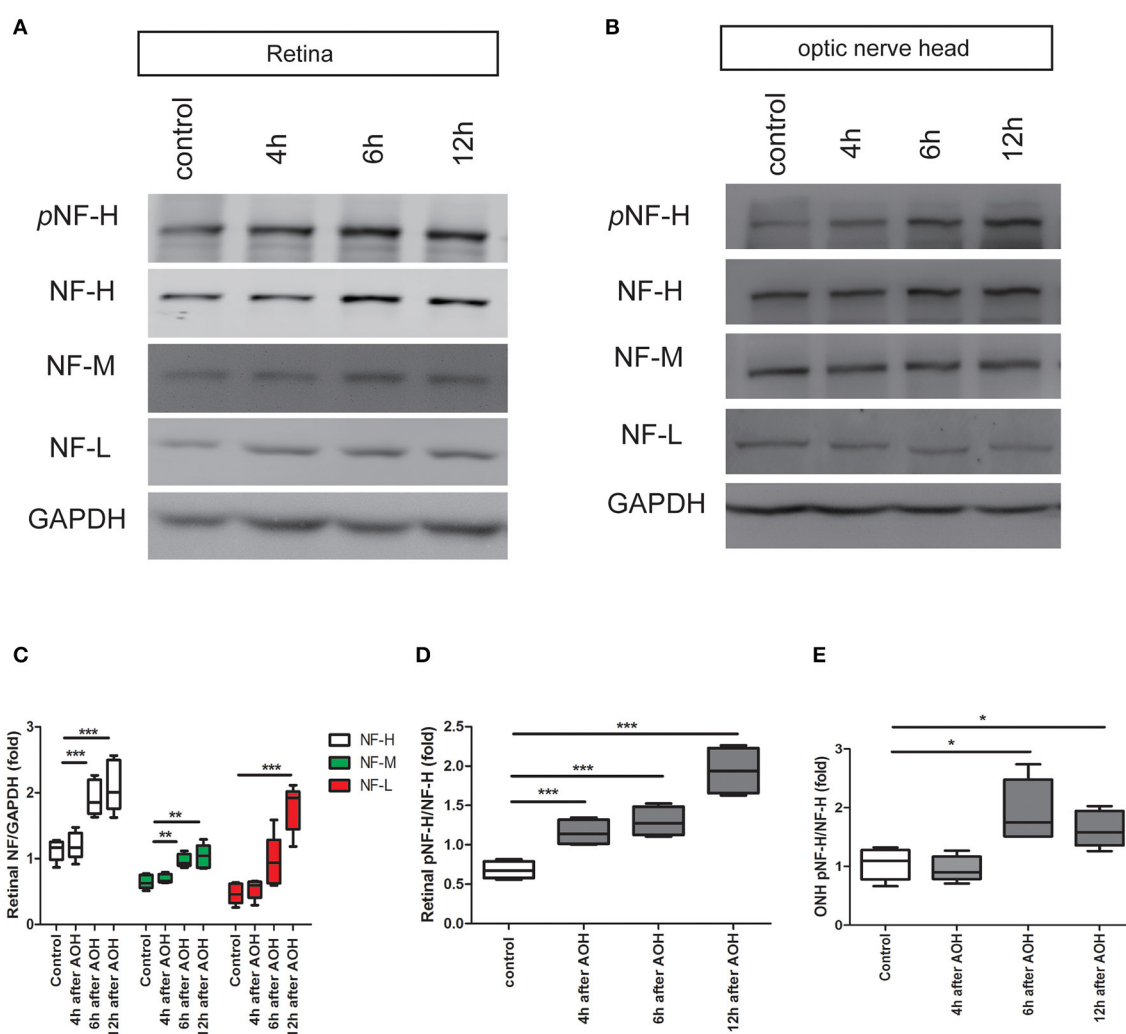


FIGURE 3

Early elevation of pNF-H expression observed in the retina and ONH following induction of AOH. An obvious elevation of the neurofilament was also observed in the retina. (A) Representative blots of NF-H, M, L, and pNF-H from AOH and the control retinas at 4, 6, and 12 h are shown. In the retina, the bands of the neurofilament three subunits were more visible at 6 and 12 h, while the band of pNF-H was more visible as early as 4 h. pNF-H, NF-H was recognized at 200 kDa, NF-M was visible at 160 kDa, and NF-L was at 70 kDa. GAPDH was used as an internal control. (B) The expression of neurofilament subunits and pNF-H in the ONH was traced at 4, 6, and 12 h after AOH, but western blotting of the ONH showed that NF-H, NF-M, and NF-L were unchanged, while the pNF-H band increased significantly at 6 h. (C) Densitometry measurements of three neurofilament subunits in the retina (normalized for GAPDH and expressed relative to the control) are provided in the box-and-whisker plots,  $n = 5$  mice for each group,  $**P < 0.01$ ,  $***P < 0.001$ . (D, E) Quantification of pNF-H expression from the retina at 4 h and ONH at 6 h is shown as box-and-whisker plots, respectively.  $n = 5$  mice for each group,  $*P < 0.05$ ,  $***P < 0.001$ .

changes in RGCs at other sites. Homogeneity or variability of RNFL changes in the ONH was also found in our clinical data, whereby even when insulted by an acute elevated IOP (above 50 mmHg) for hours or days, we did not detect classical RNFL atrophy in these patients. Conversely, RNFL thickness and somatic atrophy were often observed simultaneously in patients suffering from chronic elevated IOP. It thus raised two questions: Is ONH the common primary damage site in glaucoma? What happens when intra-RGCs are insulted by different degrees and durations of elevated IOP? In fact, recent studies increasingly focused on cellular changes beyond ONH (6). A proteomic analysis of the experimental glaucoma retinas demonstrated that the cytoskeletal protein is the most obvious and earliest changed molecule (34, 35). Urged by these facts, we performed a histological study using a major

cytoskeletal protein neurofilament in different tissues of glaucoma animal models. Our study revealed that the primary damage site in angle-closed glaucoma varies depending on the character of the initial stressor (elevated IOP); in AOH, accumulation of pNF-H and NF-H in the peripheral RGC soma suggests that the peripheral retina would be affected as well; in COH, the early disconnection of NF-H in the ONH and the optic nerve indicated that damage first appears in the distal optic nerve and progresses to the proximal retina. Therefore, our study helps to strengthen an important viewpoint that the primary damage site in glaucoma is not limited to the ONH.

Neurofilament is one of the dominant proteins of the axonal cytoskeleton in RGCs, which is composed of triplet subunits, a light (NF-L), a medium (NF-M), and a heavy (NF-H) chain.

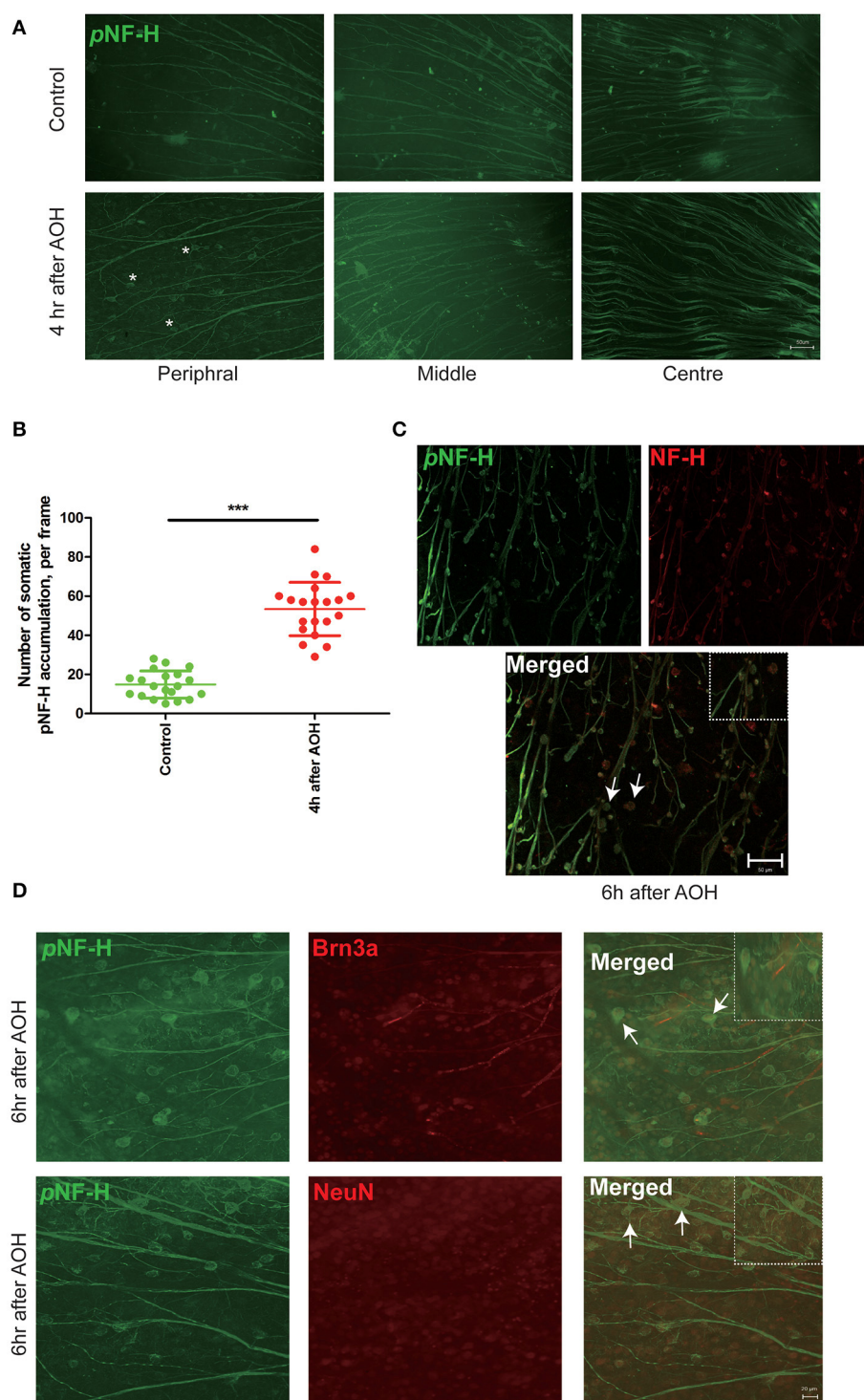


FIGURE 4

NF-H and its phosphoforms accumulated in the soma of peripheral RGCs after AOH. **(A)** Immunofluorescence of the pNF-H marker, SMI31, in the retinal wholemount 4 h after AOH; retinal wholemount was observed from peripheral to central regions. Asterisk indicates pNF-H accumulation in the peripheral retina. Scale bars: 50  $\mu$ m. **(B)** Quantification of pNF-H accumulation in the peripheral retina. The data are presented as a scatter diagram. Mean  $\pm$  SD is shown,  $n = 5$  for each group,  $***P < 0.001$ . **(C)** Immunofluorescence of pNF-H and NF-H in the retinal wholemount of AOH after 6 h. Micrographs show that most of the pNF-H accumulations were overlapped with NF-H, with arrows indicating examples of co-expression, and the high magnification image is also shown (top right of the third picture). Scale bars: 50  $\mu$ m. **(D)** Immunofluorescence of pNF-H and the RGC markers Brn3a and NeuN in the retinal wholemount of AOH after 6 h. pNF-H accumulations were highly overlapped with an RGC marker, and the high magnification images are also shown (top right of the third picture and sixth picture). Scale bars: 20  $\mu$ m.



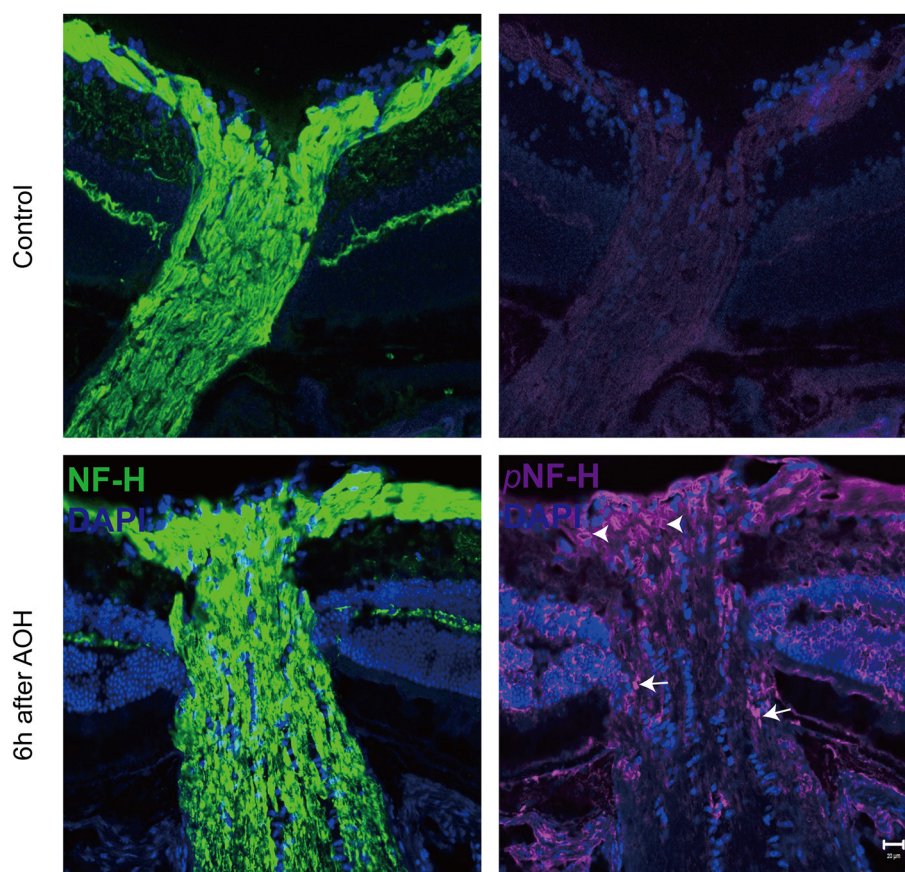


FIGURE 5

Phosphorylated neurofilament heavy chain (pNF-H) presented as intra-axon plaque and vacuolization at the site of ONH after an acute attack. Immunofluorescence of pNF-H and NF-H in the ONH 6 h after AOH. The arrowhead shows the vacuolization, while the arrows show the plaque. Scale bars: 20  $\mu$ m.

Neurofilaments are first generated in the soma of RGC and concentrated in the axon, where they play an important role in maintaining the extreme morphology of RGCs (12). Among them, the protein of NF-H has aroused great interest because of its very unusual properties. First, it contains 50–60 back-to-back hexa, hepta, or octapeptide repeats, each containing the sequence Lysine-Serine-Proline (KSP); the serine residues in these peptide repeats can be highly phosphorylated after the protein is transported from the neuronal cell soma to the axon (12, 36). Second, the phosphorylated forms of NF-H are quite resistant to proteases. Once this protein is hyperphosphorylated, it would lead it to accumulate and form aggregates that ultimately block axonal transport (24, 37). The properties of this protein suggest that it would be used as a sensitive marker to indicate early change of damaged or diseased axons. As recently shown, accumulation of pNF-H has been observed in a range of neurodegenerative diseases, including amyotrophic lateral sclerosis (ALS) (38), Parkinson's disease (PD), Alzheimer's disease (AD) (39, 40), and so on. More interestingly, NF-H phosphoforms can be detected in the cerebrospinal fluid (CSF) and blood following experimental spinal cord and brain injury in rats (41). Consistent with the study of neurodegenerative diseases, our data from the AOH model showed early pNF-H accumulation in the soma of RGCs and ONH and the

corresponding elevation of pNF-H in the aqueous humor. Unlike these data, the data from the COH model demonstrated that NF-H and its phosphoforms manifested general reduction and local disconnection in damaged axons. Hence, through a thorough study of the neurofilament reaction to acute and chronic damage, we enrich the pathology of glaucoma and creatively suggest both pNF-H accumulation and disconnection as biomarkers of RGC damage. However, limitations do exist in our study. First, although we observed a pathological change in NF-H same like tau in AD, we do not relate them together in current glaucoma models; since tau accumulation has been proven to promote neuronal degeneration in glaucoma (42), it is strongly believed that current neurofilament changes associated with glaucoma may share the same mechanism in AD. Second, the changes in pNF-H in the aqueous humor of a patient with glaucoma have been not further studied, so the role of pNF-H as a marker for disease progression remains unknown.

The histological study of the neurofilament in experimental glaucoma models truly helps us to learn more about the underlying damage of RGCs, but it poses a very practical question: can these be visualized *in vivo* by current techniques? Indeed, our clinical OCT imaging from patients with glaucoma indirectly demonstrates the different characteristics of the neurofilament between AOH and COH, but fails to provide many more detailed cellular changes.

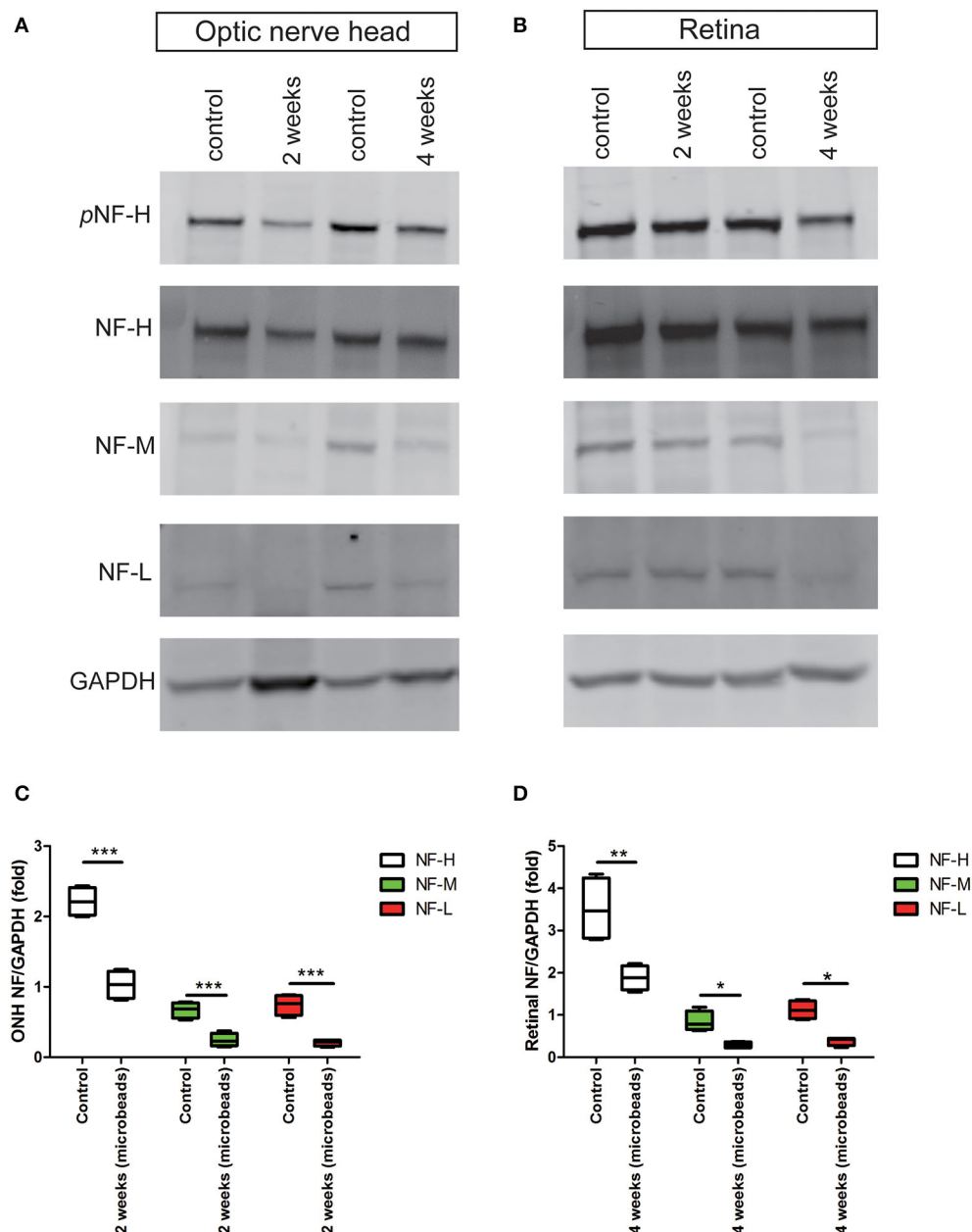


FIGURE 6

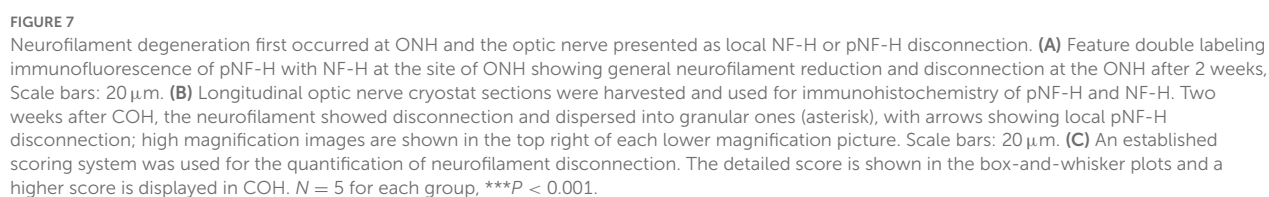
Early reduction in pNF-H and NF-H expression in the ONH after chronic ocular hypertension. (A) Western blot showing control and treated ONH 2 and 4 weeks after COH occurred. pNF-H and NF-H was recognized at 200 kDa, NF-M was visible at 160 kDa, and NF-L was visible at 70 kDa, with GAPDH as the internal control. The density of pNF-H and neurofilament subunit reduce to 2 weeks. (B) Representative blots from control and treated retinas 2 and 4 weeks after COH occurred. The density of pNF-H and NF-H began to reduce 4 weeks after COH occurred. (C, D) Densitometry measurements of three neurofilament subunits in the ONH and the retina (normalized for GAPDH and expressed relative to the control) are provided in the box-and-whisker plots,  $N = 4$  for each group,  $*P < 0.05$ ,  $**P < 0.01$ ,  $***P < 0.001$ .

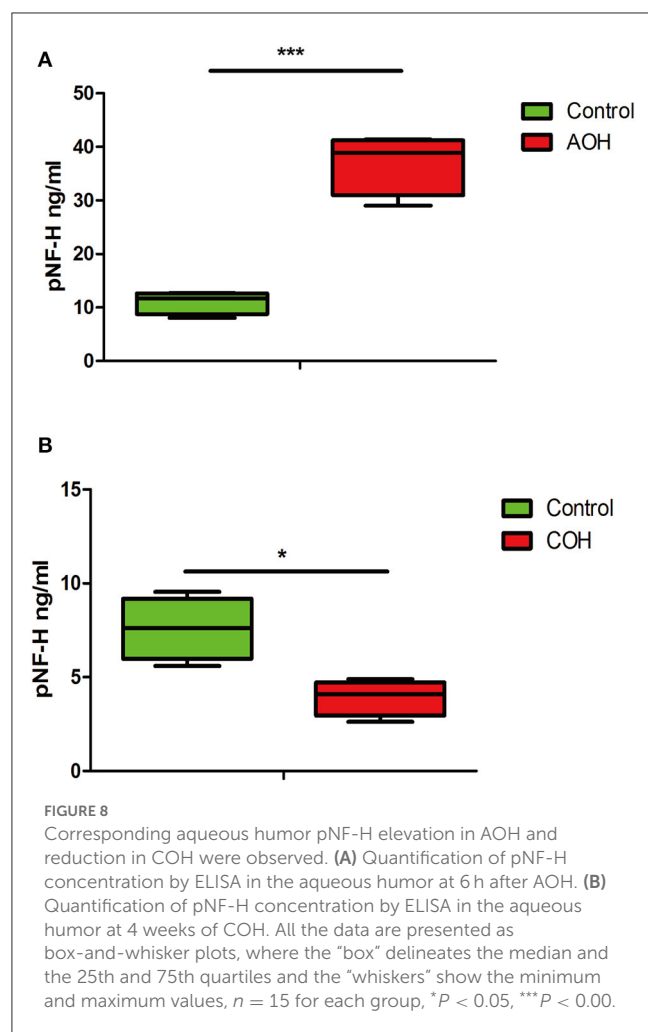
Benefit from the advance of ophthalmic imaging technology and labeling techniques, recently cellular-level RGC imaging, such as adaptive optics-optical coherence tomography (AO-OCT), has enabled the resolution of many cellular and subcellular structures (43, 44). Recent studies from AO-OCT in a patient with glaucoma have demonstrated subcellular changes, including enlarged RGC somas and nuclear hyporeflectivity, which is quite similar to the images of somatic NF-H or pNF-H accumulation in our study. Additionally, cytoskeleton alteration, including the neurofilament

is found to be the major element contributing to the change in retinal nerve fiber layer birefringence, which serves as an early biomarker of glaucomatous damage prior to losses in thickness (45, 46). So, our experimental data have advanced our understanding of the latest findings observed in new techniques.

Combined with experimental and clinical data, our study revealed two distinct types of axonal degeneration. Insulted by acute damage, both proximal RGC cell bodies and the distal axon in the ONH are affected, which is characterized







as intra-somatic and intra-axonal neurofilament compaction followed by fragmentation or degradation. While in COH, the neurofilament disconnection first begins distally and spreads toward the retina. Axonal degeneration is a common pathological event that occurs in various neurological diseases, but the cellular and molecular processes underlying different types of damage are highly variable. There are at least four forms of axonal degeneration in neurological diseases, the most common and classical two examples are Wallerian degeneration and dying back degeneration (retrograde degeneration) (47, 48). Wallerian degeneration is classically defined as the distal axons and cell body rapidly undergoing breaking down insult by an acute injury; dying back disorder is a neurodegenerative disorder in which axons die before cell bodies and/or in a retrograde pattern that begins with their distal ends. The damaged axons in our acute glaucoma seem like Wallerian degeneration; however, studies from some neurodegenerative diseases suggest that axonal degeneration associated with the accumulation of neurofilaments is distinct from a typical Wallerian degeneration (14). Importantly, studies of an RGC axotomy model showed that Wallerian and retrograde degeneration occurred synchronously, in which the neurofilament accumulated as well (49). Therefore, we believed that, in our AOH study, a combination of Wallerian and retrograde degeneration also presented. Conversely, the axons in COH degenerated like

dying back degeneration. For the detailed reasons contributing to these phenomena, several proposed mechanisms including axonal transport failure, neurotrophic factors' deprivation, and ischemic and reperfusion damage would be used for explaining (50). Considering the degree and duration of elevated IOP in APACG, the reasons for acute damage would be a mixture of the aforementioned mechanisms, and neurotrophic factors' deprivation in the distal optic nerve may play the major role in chronic glaucoma.

The overall results of this study revealed early glaucomatous damage beyond the ONH, including peripheral RGC somatic NF-H, pNF-H aggregation in AOH, and distal optic nerve neurofilament disconnection in COH. These results also indicated the role of NF-H and pNF-H as biomarkers of glaucomatous damage. Furthermore, the two distinct neural degenerations existing between AOH and COH provide a concept that different neuroprotection strategies should be adopted in an angle-closed glaucoma treatment.

## Data availability statement

The original contributions presented in the study are included in the article/Supplementary material, further inquiries can be directed to the corresponding author.

## Ethics statement

The animal study was reviewed and approved by the Institutional Animal Care and Use Committee of Guang Dong Medical University and Zhongshan Ophthalmic Center. The studies involving human participants were reviewed and approved by the Ethics Committee of Huizhou Central People's Hospital. The patients/participants provided their written informed consent to participate in this study.

## Author contributions

Study design and drafting of the manuscript: LZ and HF. Acquisition of photographs: LZ and DL. Analysis and interpretation of data: GX and LZ. Critical revision of the manuscript: DW and LZ. Statistical analysis: LZ, ZC, and HF. All authors contributed to the article and approved the submitted version.

## Conflict of interest

The authors declare that the research was conducted in the absence of any commercial or financial relationships that could be construed as a potential conflict of interest.

## Publisher's note

All claims expressed in this article are solely those of the authors and do not necessarily represent those of

their affiliated organizations, or those of the publisher, the editors and the reviewers. Any product that may be evaluated in this article, or claim that may be made by its manufacturer, is not guaranteed or endorsed by the publisher.

## References

- Sun X, Dai Y, Chen Y, Yu DY, Cringle SJ, Chen J, et al. Primary angle closure glaucoma: what we know and what we don't know. *Prog Retin Eye Res.* (2017) 57:26–45. doi: 10.1016/j.preteyeres.2016.12.003
- Tham YC, Li X, Wong TY, Quigley HA, Aung T, Cheng CY, et al. Global prevalence of glaucoma and projections of glaucoma burden through 2040: a systematic review and meta-analysis. *Ophthalmology.* (2014) 121:2081–90. doi: 10.1016/j.ophtha.2014.05.013
- Jonas JB, Aung T, Bourne RR, Bron AM, Ritch R, Panda-Jonas S, et al. Glaucoma. *Lancet.* (2017) 390:2183–93. doi: 10.1016/S0140-6736(17)31469-1
- Stein JD, Khawaja AP, Weizer JS. Glaucoma in adults—screening, diagnosis, management: a review. *JAMA.* (2021) 325:164–74. doi: 10.1001/jama.2020.21899
- Smith CA, Vianna JR, Chauhan BC. Assessing retinal ganglion cell damage. *Eye.* (2017) 31:209–17. doi: 10.1038/eye.2016.295
- Ban N, Siegfried CJ, Apte RS. Monitoring neurodegeneration in glaucoma: therapeutic implications. *Trends Mol Med.* (2018) 24:7–17. doi: 10.1016/j.molmed.2017.11.004
- Crish SD, Sappington RM, Inman DM, Horner PJ, Calkins DJ. Distal axonopathy with structural persistence in glaucomatous neurodegeneration. *Proc Natl Acad Sci U S A.* (2010) 107:5196–201. doi: 10.1073/pnas.0913141107
- Crish SD, Dapper JD, MacNamee SE, Balaran P, Sidorova TN, Lambert WS, et al. Failure of axonal transport induces a spatially coincident increase in astrocyte BDNF prior to synapse loss in a central target. *Neuroscience.* (2013) 229:55–70. doi: 10.1016/j.neuroscience.2012.10.069
- Hirokawa N, Takemura R. Molecular motors and mechanisms of directional transport in neurons. *Nat Rev Neurosci.* (2005) 6:201–14. doi: 10.1038/nrn1624
- Sleigh JN, Rossor AM, Fellows AD, Tosolini AP, Schiavo G. Axonal transport and neurological disease. *Nat Rev Neurol.* (2019) 15:691–703. doi: 10.1038/s41582-019-0257-2
- Stone JR, Singleton RH, Povlishock JT. Intra-axonal neurofilament compaction does not evoke local axonal swelling in all traumatically injured axons. *Exp Neurol.* (2001) 172:320–31. doi: 10.1006/exnr.2001.7818
- Petzold A. Neurofilament phosphoforms: surrogate markers for axonal injury, degeneration and loss. *J Neurol Sci.* (2005) 233:183–98. doi: 10.1016/j.jns.2005.03.015
- Natori A, Ogata T, Sumitani M, Kogure T, Yamauchi T, Yamauchi H, et al. Potential role of pNF-H, a biomarker of axonal damage in the central nervous system, as a predictive marker of chemotherapy-induced cognitive impairment. *Clin Cancer Res.* (2015) 21:1348–52. doi: 10.1158/1078-0432.CCR-14-2775
- Vickers JC, Kirkcaldie MT, Phipps A, King AE. Alterations in neurofilaments and the transformation of the cytoskeleton in axons may provide insight into the aberrant neuronal changes of Alzheimer's disease. *Brain Res Bull.* (2016) 126:324–33. doi: 10.1016/j.brainresbull.2016.07.012
- Taniguchi T, Shimazawa M, Hara H. Alterations in neurofilament light in optic nerve in rat kainate and monkey ocular hypertension models. *Brain Res.* (2004) 1013:241–8. doi: 10.1016/j.brainres.2004.04.023
- Balaratnasingam C, Morgan WH, Bass L, Cringle SJ, Yu DY. Time-dependent effects of elevated intraocular pressure on optic nerve head axonal transport and cytoskeleton proteins. *Invest Ophthalmol Vis Sci.* (2008) 49:986–99. doi: 10.1167/iovs.07-1090
- Kashiwagi K, Ou B, Nakamura S, Tanaka Y, Suzuki M, Tsukahara S, et al. Increase in dephosphorylation of the heavy neurofilament subunit in the monkey chronic glaucoma model. *Invest Ophthalmol Vis Sci.* (2003) 44:154–9. doi: 10.1167/iovs.02-0398
- Wilson GN, Smith MA, Inman DM, Dengler-Crish CM, Crish SD. Early cytoskeletal protein modifications precede overt structural degeneration in the DBA/2J mouse model of glaucoma. *Front Neurosci.* (2016) 10:494. doi: 10.3389/fnins.2016.00494
- Foster PJ, Buhrmann R, Quigley HA, Johnson GJ. The definition and classification of glaucoma in prevalence surveys. *Br J Ophthalmol.* (2002) 86:238–42. doi: 10.1136/bjo.86.2.238
- Zhou L, Chen W, Lin D, Hu W, Tang Z. Neuronal apoptosis, axon damage and synapse loss occur synchronously in acute ocular hypertension. *Exp Eye Res.* (2019) 180:77–85. doi: 10.1016/j.exer.2018.12.006
- Liu H, Ding C. Establishment of an experimental glaucoma animal model: a comparison of microbead injection with or without hydroxypropyl methylcellulose. *Exp Ther Med.* (2017) 14:1953–60. doi: 10.3892/etm.2017.4728
- Morgan JE, Tribble JR. Microbead models in glaucoma. *Exp Eye Res.* (2015) 141:9–14. doi: 10.1016/j.exer.2015.06.020
- Noristani R, Kuehn S, Stute G, Reinehr S, Stellbogen M, Dick HB, et al. Retinal and optic nerve damage is associated with early glial responses in an experimental autoimmune glaucoma model. *J Mol Neurosci.* (2016) 58:470–82. doi: 10.1007/s12031-015-0707-2
- Gafson AR, Barthélemy NR, Bomont P, Carare RO, Durham HD, Julien JP, et al. Neurofilaments: neurobiological foundations for biomarker applications. *Brain.* (2020) 143:1975–98. doi: 10.1093/brain/awaa098
- Zmira O, Halpern AI, Drori T. Anti-neurofilament antibodies and neurodegeneration: markers and generators. *J Neuroimmunol.* (2020) 344:577248. doi: 10.1016/j.jneuroim.2020.577248
- Ueno T, Ohori Y, Ito J, Hoshikawa S, Yamamoto S, Nakamura K, et al. Hyperphosphorylated neurofilament NF-H as a biomarker of the efficacy of minocycline therapy for spinal cord injury. *Spinal Cord.* (2011) 49:333–6. doi: 10.1038/sc.2010.116
- Anderson DR, Hendrickson A. Effect of intraocular pressure on rapid axoplasmic transport in monkey optic nerve. *Invest Ophthalmol.* (1974) 13:771–83.
- Minckler DS, Bunt AH, Johanson GW. Orthograde and retrograde axoplasmic transport during acute ocular hypertension in the monkey. *Invest Ophthalmol Vis Sci.* (1977) 16:426–41.
- Quigley HA, Addicks EM. Chronic experimental glaucoma in primates. II Effect of extended intraocular pressure elevation on optic nerve head and axonal transport. *Invest Ophthalmol Vis Sci.* (1980) 19:137–52.
- Balaratnasingam C, Morgan WH, Bass L, Matich G, Cringle SJ, Yu DY, et al. Axonal transport and cytoskeletal changes in the laminar regions after elevated intraocular pressure. *Invest Ophthalmol Vis Sci.* (2007) 48:3632–44. doi: 10.1167/iovs.06-1002
- Chidlow G, Ebner A, Wood JP, Casson RJ. The optic nerve head is the site of axonal transport disruption, axonal cytoskeleton damage and putative axonal regeneration failure in a rat model of glaucoma. *Acta Neuropathol.* (2011) 121:737–51. doi: 10.1007/s00401-011-0807-1
- Maddineni P, Kasetti RB, Patel PD, Millar JC, Kiehlbauch C, Clark AF, et al. CNS axonal degeneration and transport deficits at the optic nerve head precede structural and functional loss of retinal ganglion cells in a mouse model of glaucoma. *Mol Neurodegener.* (2020) 15:48. doi: 10.1186/s13024-020-00400-9
- Huo YJ, Thomas R, Li L, Cao K, Wang HZ, Wang NL, et al. Comparison of peripapillary retinal nerve fiber layer thickness, functional subzones, and macular ganglion cell-inner plexiform layer in differentiating patients with mild, moderate, and severe open-angle glaucoma. *J Glaucoma.* (2020) 29:761–6. doi: 10.1097/IJG.0000000000001598
- Funk S, Perumal N, Bell K, Pfeiffer N, Grus FH. The potential impact of recent insights into proteomic changes associated with glaucoma. *Expert Rev Proteomics.* (2017) 14:311–34. doi: 10.1080/14789450.2017.1298448
- Cao L, Wang L, Cull G, Zhou A. Alterations in molecular pathways in the retina of early experimental glaucoma eyes. *Int J Physiol Pathophysiol Pharmacol.* (2015) 7:44–53.
- Yuan A, Rao MV, Veeranna, Nixon RA. Neurofilaments and neurofilament proteins in health and disease. *Cold Spring Harbor Perspect Biol.* (2017) 9:a018309. doi: 10.1101/cshperspect.a018309
- Khalil M, Teunissen CE, Otto M, Piehl F, Sormani MP, Gatteringer T, et al. Neurofilaments as biomarkers in neurological disorders. *Nat Rev Neurol.* (2018) 14:577–89. doi: 10.1038/s41582-018-0058-z

## Supplementary material

The Supplementary Material for this article can be found online at: <https://www.frontiersin.org/articles/10.3389/fneur.2023.1091697/full#supplementary-material>

38. Ganesalingam J, An J, Bowser R, Andersen PM, Shaw CE. pNfH is a promising biomarker for ALS. *Amyotroph Lateral Scler Frontotemporal Degener.* (2013) 14:146–9. doi: 10.3109/21678421.2012.729596
39. Su JH, Cummings BJ, Cotman CW. Plaque biogenesis in brain aging and Alzheimer's disease. I Progressive changes in phosphorylation states of paired helical filaments and neurofilaments. *Brain Res.* (1996) 739:79–87. doi: 10.1016/S0006-8993(96)00811-6
40. Su JH, Cummings BJ, Cotman CW. Plaque biogenesis in brain aging and Alzheimer's disease. II Progressive transformation and developmental sequence of dystrophic neurites. *Acta Neuropathol.* (1998) 96:463–71. doi: 10.1007/s004010050920
41. Shaw G, Yang C, Ellis R, Anderson K, Parker Mickle J, Scheff S, et al. Hyperphosphorylated neurofilament NF-H is a serum biomarker of axonal injury. *Biochem Biophys Res Commun.* (2005) 336:1268–77. doi: 10.1016/j.bbrc.2005.08.252
42. Chiasseu M, Cueva Vargas JL, Destroismaisons L, Vande Velde C, Leclerc N, Di Polo A, et al. Tau accumulation, altered phosphorylation, and missorting promote neurodegeneration in glaucoma. *J Neurosci.* (2016) 36:5785–98. doi: 10.1523/JNEUROSCI.3986-15.2016
43. Jonnal RS, Kocaoglu OP, Zawadzki RJ, Liu Z, Miller DT, Werner JS, et al. A review of adaptive optics optical coherence tomography: technical advances, scientific applications, and the future. *Invest Ophthalmol Vis Sci.* (2016) 57:51–68. doi: 10.1167/iovs.16-19103
44. Burns SA, Elsner AE, Sapoznik KA, Warner RL, Gast TJ. Adaptive optics imaging of the human retina. *Prog Retin Eye Res.* (2019) 68:1–30. doi: 10.1016/j.preteyeres.2018.08.002
45. Huang XR, Knighton RW, Spector YZ, Feuer WJ. Cytoskeletal alteration and change of retinal nerve fiber layer birefringence in hypertensive retina. *Curr Eye Res.* (2017) 42:936–47. doi: 10.1080/02713683.2016.1262043
46. Huang XR, Knighton RW, Spector YZ, Qiao J, Kong W, Zhao Q, et al. Reflectance spectrum and birefringence of the retinal nerve fiber layer with hypertensive damage of axonal cytoskeleton. *Invest Ophthalmol Vis Sci.* (2017) 58:2118–29. doi: 10.1167/iovs.16-20553
47. Raff MC, Whitmore AV, Finn JT. Axonal self-destruction and neurodegeneration. *Science.* (2002) 296:868–71. doi: 10.1126/science.1068613
48. Coleman MP, Freeman MR. Wallerian degeneration, wld(s), and nmnat. *Annu Rev Neurosci.* (2010) 33:245–67. doi: 10.1146/annurev-neuro-060909-153248
49. Kanamori A, Catrinescu M-M, Belisle JM, Costantino S, Levin LA. Retrograde and wallerian axonal degeneration occur synchronously after retinal ganglion cell axotomy. *Am J Pathol.* (2012) 181:62–73. doi: 10.1016/j.ajpath.2012.03.030
50. Almasieh M, Wilson AM, Morquette B, Cueva Vargas JL, Di Polo A. The molecular basis of retinal ganglion cell death in glaucoma. *Prog Retin Eye Res.* (2012) 31:152–81. doi: 10.1016/j.preteyeres.2011.11.002





## OPEN ACCESS

## EDITED BY

Wen-Jun Tu,  
Chinese Academy of Medical Sciences and  
Peking Union Medical College, China

## REVIEWED BY

Lin Zhang,  
Renmin Hospital of Wuhan University, China  
Yuto Uchida,  
Johns Hopkins Medicine, United States

## \*CORRESPONDENCE

Li Chen  
✉ chenliqfk@163.com

RECEIVED 08 December 2022

ACCEPTED 26 April 2023

PUBLISHED 17 May 2023

## CITATION

Qin R-X, Yang Y, Chen J-F, Huang L-J, Xu W,  
Qin Q-C, Liang X-J, Lai X-Y, Huang X-Y,  
Xie M-S and Chen L (2023) Transcriptomic  
analysis reveals the potential biological  
mechanism of AIS and lung adenocarcinoma.  
*Front. Neurol.* 14:1119160.  
doi: 10.3389/fneur.2023.1119160

## COPYRIGHT

© 2023 Qin, Yang, Chen, Huang, Xu, Qin, Liang,  
Lai, Huang, Xie and Chen. This is an  
open-access article distributed under the terms  
of the [Creative Commons Attribution License  
\(CC BY\)](https://creativecommons.org/licenses/by/4.0/). The use, distribution or reproduction  
in other forums is permitted, provided the  
original author(s) and the copyright owner(s)  
are credited and that the original publication in  
this journal is cited, in accordance with  
accepted academic practice. No use,  
distribution or reproduction is permitted which  
does not comply with these terms.

# Transcriptomic analysis reveals the potential biological mechanism of AIS and lung adenocarcinoma

Rong-Xing Qin<sup>1</sup>, Yue Yang<sup>1</sup>, Jia-Feng Chen<sup>1</sup>, Li-Juan Huang<sup>1</sup>,  
Wei Xu<sup>1</sup>, Qing-Chun Qin<sup>1</sup>, Xiao-Jun Liang<sup>1</sup>, Xin-Yu Lai<sup>2</sup>,  
Xiao-Ying Huang<sup>1</sup>, Min-Shan Xie<sup>1</sup> and Li Chen<sup>1,3\*</sup>

<sup>1</sup>Department of Neurology, The First Affiliated Hospital, Guangxi Medical University, Nanning, Guangxi Zhuang Autonomous Region, China, <sup>2</sup>Collaborative Innovation Centre of Regenerative Medicine and Medical BioResource Development and Application Co-constructed by the Province and Ministry, Guangxi Medical University, Nanning, Guangxi Zhuang Autonomous Region, China, <sup>3</sup>Guangxi Key Laboratory of Regenerative Medicine and Guangxi Collaborative Innovation Center for Biomedicine, Guangxi Medical University, Nanning, Guangxi Zhuang Autonomous Region, China

**Introduction:** Acute ischemic stroke (AIS) and lung adenocarcinoma (LUAD) are associated with some of the highest morbidity and mortality rates worldwide. Despite reports on their strong correlation, the causal relationship is not fully understood. The study aimed to identify and annotate the biological functions of hub genes with clinical diagnostic efficacy in AIS and LUAD.

**Methods:** Transcriptome and single-cell datasets were obtained from the Gene Expression Omnibus (GEO) and The Cancer Genome Atlas (TCGA). We identified the differentially expressed genes (DEGs) upregulated in AIS and LUAD and found 372 genes intersecting both datasets. Hub genes were identified using protein-protein interaction (PPI) networks, and the diagnostic and prognostic utility of these hub genes was then investigated using receiver operating characteristic (ROC) curves, survival analysis, and univariable Cox proportional hazard regression. Single-cell analysis was used to detect whether the hub genes were expressed in tumor epithelial cells. The immune microenvironment of AIS and LUAD was assessed using the CIBERSORT algorithm. The protein expression of these hub genes was tracked using the Human Protein Atlas (HPA). We calculated the number of positive cells using the digital pathology software QuPath. Finally, we performed molecular docking after using the Enrichr database to predict possible medicines.

**Results:** We identified the molecular mechanisms underlying hub genes in AIS and LUAD and found that *CCNA2*, *CCNB1*, *CDKN2A*, and *CDK1* were highly expressed in AIS and LUAD tissue samples compared to controls. The hub genes were mainly involved in the following pathways: the cell cycle, cellular senescence, and the HIF-1 signaling pathway. Using immunohistochemical slices from the HPA database, we confirmed that these hub genes have a high diagnostic capability for AIS and LUAD. Further, their high expression is associated with poor prognosis. Finally, curcumin was tested as a potential medication using molecular docking modeling.

**Discussion:** Our findings suggest that the hub genes we found in this study contribute to the development and progression of AIS and LUAD by altering the cellular senescence pathway. Thus, they may be promising markers for diagnosis and prognosis.

## KEYWORDS

lung adenocarcinoma, acute ischemic stroke, transcriptome, cellular senescence, bioinformatics



## 1. Introduction

Human health is in peril from conditions like cancer and stroke (1). Over 795,000 acute ischemic stroke (AIS) occurrences are reported each year in the United States alone, making it the second most frequent cause of mortality and long-term disability worldwide (2). A study found that in 2020, the incidence and mortality rates of stroke in China were 505.2 and 343.4 per 100,000 person-years, respectively (3). The proportions of acute ischemic stroke due to atherosclerosis and cardiogenic embolism were 39% and 22%, respectively (4). AIS is a multifactorial disease influenced by atherosclerosis, hypertension, alcohol consumption, smoking, and D-dimer levels. In many low-income and middle-income nations, stroke incidence and fatality rates have increased in recent decades (5). Genetic variables, which are essential for determining the etiology of AIS, are suggested by epidemiological research to be connected to the prevalence of stroke (6).

One of the molecular mechanisms of AIS includes immune activation, which can lead to both neuroprotective and neurotoxic effects (7, 8). Thrombolysis and antiplatelet therapy are currently the main treatment methods for stroke, but it is unclear whether these treatments improve prognosis in patients (9). Lung cancer is the leading cause of cancer-related deaths globally. Additionally, lung cancer has a terrible prognosis (10, 11). The most common histological subtype of malignant lung cancer is lung adenocarcinoma (LUAD). Deaths are mostly attributed to cancer cell invasion and distant metastasis (12). Gene abnormalities are the initial factors that influence the biological behavioral changes of heterogenic cancer cells, including cell signaling and the immune microenvironment. According to reports, several genes play a role in the development of LUAD tumors (13–15). During tumor progression, changes in genes that mediate important biological processes can occur, resulting in the rapid proliferation of malignant cells. However, the mechanism by which this process occurs is still unclear (16). As a result of studies on the molecular basis of lung cancer, programmed death ligand 1 and epidermal growth factor receptor tyrosine kinase inhibitors are two newly emerging treatment targets. Even though lung cancer treatment choices have increased thanks to genetic testing, novel targeted therapy, and immunotherapy, its 5-year survival rate is as low as 20% in many nations (10, 17), and the recurrence rate remains high (18). Recently, an increasing number of reports have documented AIS caused by malignant tumors (19) and demonstrated that patients with lung cancer and metastatic cancer display a higher risk of stroke. Notably, the cumulative incidence of stroke among lung cancer patients was 5.1% (20). The connection between lung cancer and stroke significantly decreased the patients' life longevity and quality (19). LUAD may lead to multiple acute cerebral infarction lesions involving multiple arterial blood supply areas (21). *CCNB2* may be a possible target against lung cancer and AIS, according to earlier research (22). Moreover, the stroke is the second most frequent neurological condition associated with death in cancer patients. Risk factors for cancer-related AIS include high levels of D-dimer, fibrinogen breakdown products, and C-reactive protein (23). LUAD and AIS are closely associated with the occurrence of gene abnormalities. However, the regulatory mechanisms of the genes involved have not yet been elucidated.

Therefore, it is crucial to comprehend how they interact and find relevant indicators to provide a plan for diagnosis and treatment. In this study, we used bioinformatics to identify hub genes in AIS and LUAD, investigated their biological functions, and determined their clinical significance.

## 2. Materials and methods

### 2.1. Data sources

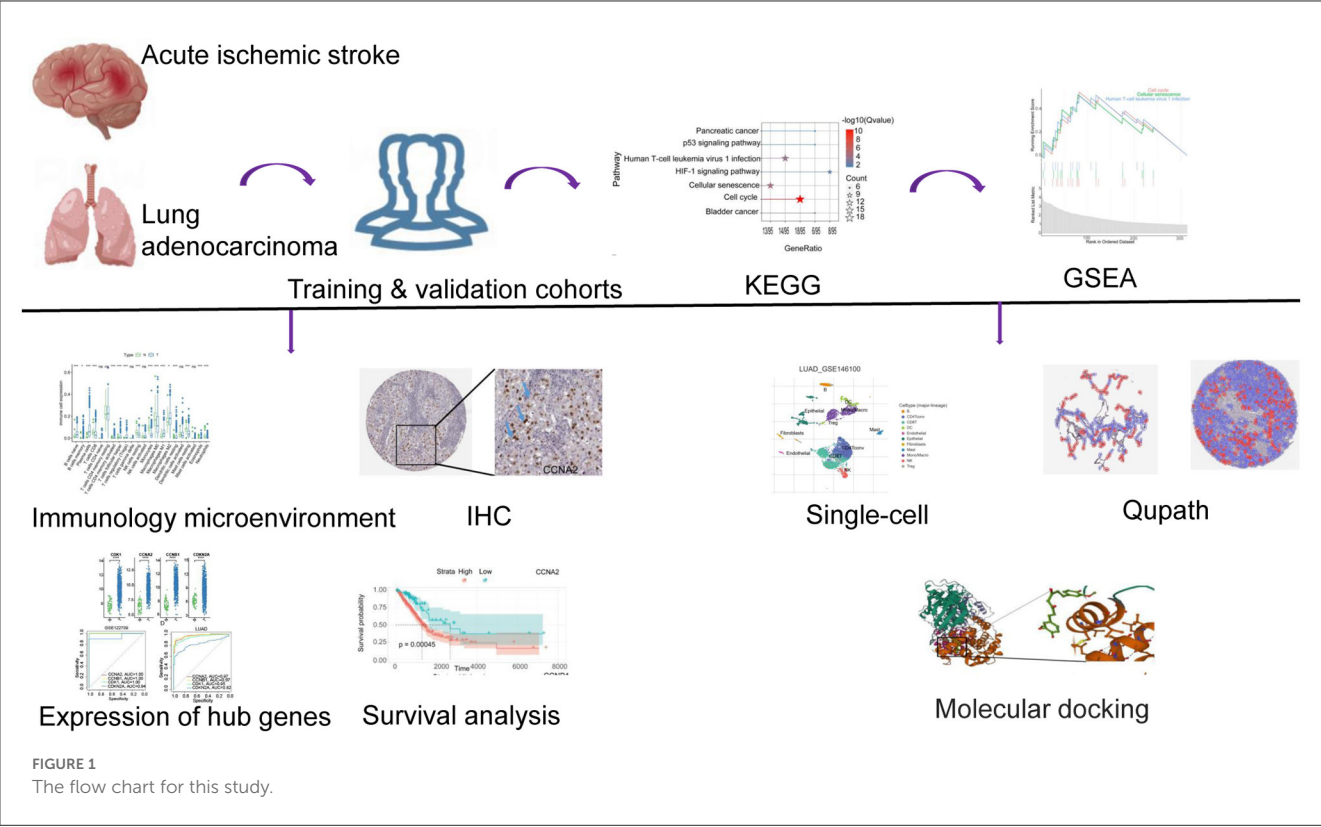
Using the expression data of AIS in the GEO database, we discovered the expression data and clinical details about LUAD on the Xena platform. The inclusion criteria were as follows: (i) case and control groups, (ii) microarray data of mRNA, (iii) the specimen was a peripheral blood sample or tissue, and (iv) *Homo sapiens*. The GSE122709 dataset was included according to the above criteria, including five control peripheral blood samples and 10 AIS peripheral blood samples. The Cancer Genome Atlas (TCGA)-LUAD array from the Xena platform was selected, which included 59 surrounding normal samples and 524 tumor samples. Furthermore, we also downloaded LUAD validation datasets GSE42127, GSE68465, GSE50081, GSE13231, and GSE31210. In addition, we downloaded the validation datasets of AIS (GSE58294 and GSE140275) from GEO. All of these datasets met the above inclusion criteria. Datasets obtained were subjected to logarithmic-scale conversion and other data processing. We downloaded the single-cell dataset GSE146100 and then did quality assurance and data filtering.

### 2.2. Differential gene expression analysis

We performed a difference analysis using the R package “limma”. Differential genes were defined as those with a *P*-value < 0.05 and  $|\log_2FC$  (fold change)  $\geq 1$  values. The number of 372 differentially expressed genes (DEGs) was found after using a Venn diagram to find the intersecting genes.

### 2.3. Functional analysis

We examined the Gene Ontology (GO) and Kyoto Encyclopedia of Genes and Genomes (KEGG) of the elevated DEGs using the R package “clusterProfiler.” *P*-values < 0.05 were used to determine whether an enrichment function was significant. Cellular components, molecular functions, and biological processes are all included in the GO category. The top 10 GO biological processes were chosen in ascending order of *P*-values. Ten significant KEGG in total were found. The increased DEGs were annotated using the disease ontology (DO) analysis R package “DOSE”. Gene set enrichment analysis (GSEA) was used to define hub genes to pinpoint the signaling pathways connected to AIS and LUAD. Patients were split into two groups (control and case group) based on the levels of expression of the four hub genes. GSEA analysis reveals differences in signaling pathways. The gene sets with a significant enrichment were then sorted.



GSEA was used to investigate the relationship between illness categories and biological processes. The cutoff was established at  $P < 0.05$ .

2.4. Building a protein-protein interaction (PPI) network and choosing hub genes

We chose DEGs from the KEGG pathway for cellular senescence for the PPI network. Using the STRING internet database (<http://stringdb.org>), we looked for connections between proteins. We constructed a PPI network for genes with a rating scale  $>0.4$  using Cytoscape.

2.5. Immune infiltration analysis

CIBRSORT was used to estimate the proportion of immune cells in the AIS gene expression matrix. We use the R package “ggplot2” to draw the boxplots. Statistics were deemed significant at  $P < 0.05$ .

2.6. Receiver operating characteristic (ROC) analysis

We investigated the mRNA expression levels of the hub genes in patients with AIS and LUAD using ROC curves

TABLE 1 The sample information of AIS and LUAD.

| Accession | Controls | Patients | Upregulated genes |
|-----------|----------|----------|-------------------|
| GSE122709 | 5        | 10       | 4,452             |
| TCGA-LUAD | 59       | 524      | 2,013             |

and boxplots. To create the ROC curves, we utilized the R package “pROC”.

2.7. Survival analysis

TCGA-LUAD expression data and clinical data were used to conduct a survival analysis using the R packages “survminer” and “survival”. The prognosis of LUAD patients was examined using Kaplan-Meier (KM) analysis. The time-dependent ROC curve (timeROC) method was applied to assess the hub genes prediction accuracy at 1, 3, and 5 years.

2.8. Analysis of single-cell data and identification of cell subpopulations

We downloaded the scRNA-seq dataset GSE146100 of LUAD. We used the TISCH database (<http://tisch.comp-genomics.org>) and Maestro analysis for quality control, clustering and cell type annotation, making the expression of four hub genes in the epithelial cell type comparable.

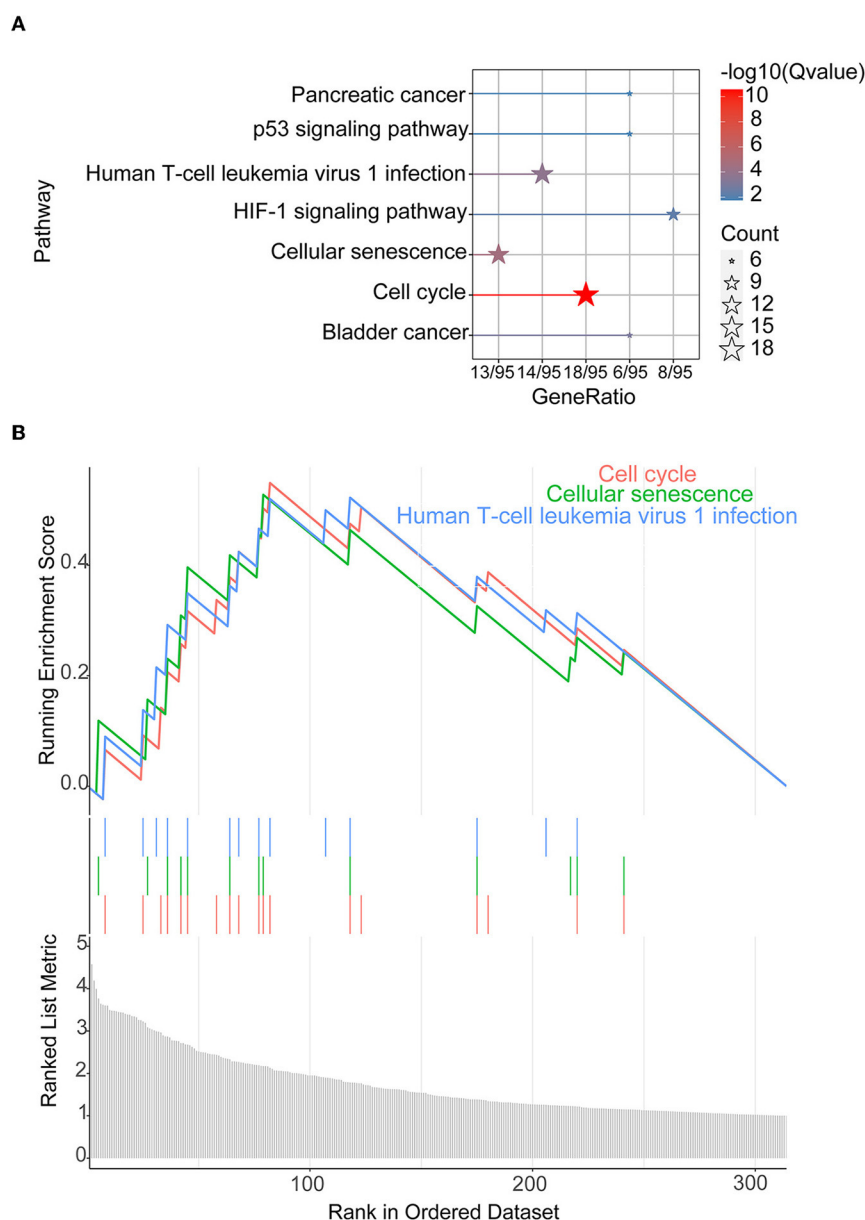


FIGURE 2  
KEGG and GSEA. (A) KEGG of 372 upregulated DEGs in AIS and LUAD. (B) We conducted GSEA on 372 upregulated DEGs in LUAD.

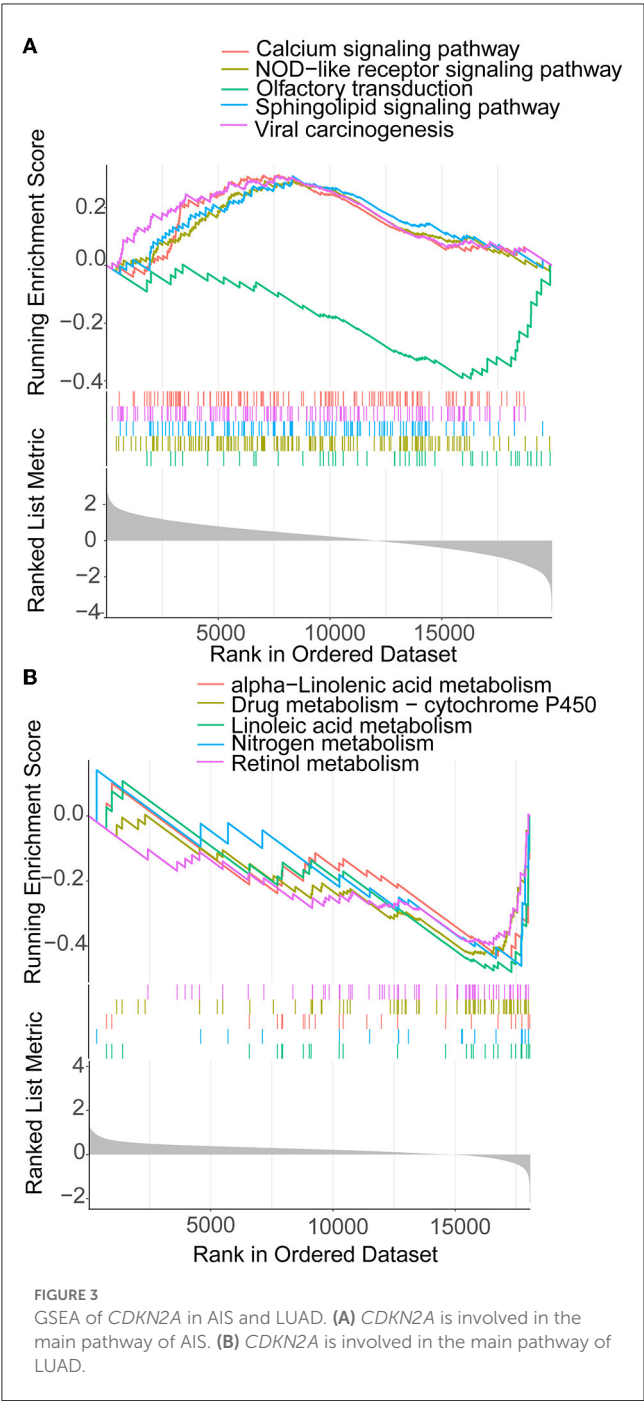
## 2.9. Protein expression and validation

Information about the distribution of proteins in human organs and cells can be found in the HPA database (<https://www.proteinatlas.org>). We acquired immunohistochemistry (IHC) pictures of LUAD tissues and investigated the differential protein expression of hub genes in matched HPA normal tissues. QuPath, a program for digital pathology, was utilized to count the positive cells. We analyzed The Clinical Proteomic Tumor Analysis Consortium (CPTAC) dataset using the UALCAN tool (<https://ualcan.path.uab.edu>). The protein

levels of the four hub genes were compared between LUAD and normal tissues.

## 2.10. Drug prediction and molecular docking

We used the DSigDB dataset in Enrichr (<http://amp.pharm.mssm.edu/Enrichr>) for drug prediction of hub genes. Structural information of curcumin was downloaded from the pubChem compound database



(<https://pubchem.ncbi.nlm.nih.gov>). The 3D structures of the proteins of the four hub genes were downloaded using the PDB database (<https://www.rcsb.org>). “Dockeasy” (<https://www.dockeasy.cn/>) was used to achieve molecular docking.

### 2.11. Statistical analysis

All data were analyzed using R version 4.2.1. Statistics were deemed significant at  $P < 0.05$ .

**TABLE 2** The top 10 genes in the PPI network for LUAD and AIS.

| Rank | Node          |
|------|---------------|
| 1    | <i>CCNA2</i>  |
| 1    | <i>CCNB1</i>  |
| 1    | <i>CDKN2A</i> |
| 1    | <i>CDK1</i>   |
| 5    | <i>CCNE2</i>  |
| 5    | <i>CCNB2</i>  |
| 5    | <i>FOXM1</i>  |
| 5    | <i>E2F1</i>   |
| 9    | <i>MYBL2</i>  |
| 9    | <i>CHEK2</i>  |

## 3. Results

### 3.1. Differently expressed genes (DEGs) in AIS and LUAD

The flowchart of our study is as follows (Figure 1). The GEO database provided the AIS-related GSE122709 dataset. Expression data for LUAD were obtained from the Xena database. The specific sample information for the two datasets is listed below (Table 1). Using the standard of  $|\log_2FC| > 1$  and  $P < 0.05$ , 4452 and 2013 upregulated DEGs were identified in the AIS and TCGA-LUAD datasets, respectively. We found 372 upregulated DEGs intersecting the two datasets, which may be connected to the pathophysiology of AIS and LUAD.

### 3.2. Functional analyses

The 372 elevated DEGs were examined to seek into the shared biological processes and signaling pathways. The GO analysis revealed that these genes were mainly enriched in nuclear, organic fission, and mitotic nuclear divisions. The main KEGG enrichment pathways were the cell cycle, cellular senescence, and the HIF-1 signaling pathway in AIS and LUAD (Figure 2A). DO analysis revealed that the DEGs were linked to many malignancies. These results imply that LUAD and AIS development and incidence may be caused by the differential expression of these genes. These pathways were primarily enriched in the cell cycle, cellular senescence, and human T-cell leukemia virus 1 infection in LUAD, according to the 372 elevated DEGs discovered by GSEA (Figure 2B). In contrast, no related pathways were enriched in the 372 upregulated DEGs in AIS. In AIS, *CDKN2A* is mainly localized in the calcium signaling pathway, NOD-like receptor signaling pathway and olfactory transduction pathway (Figure 3A). In LUAD, *CDKN2A* was mostly implicated in alpha-linolenic acid metabolism, drug

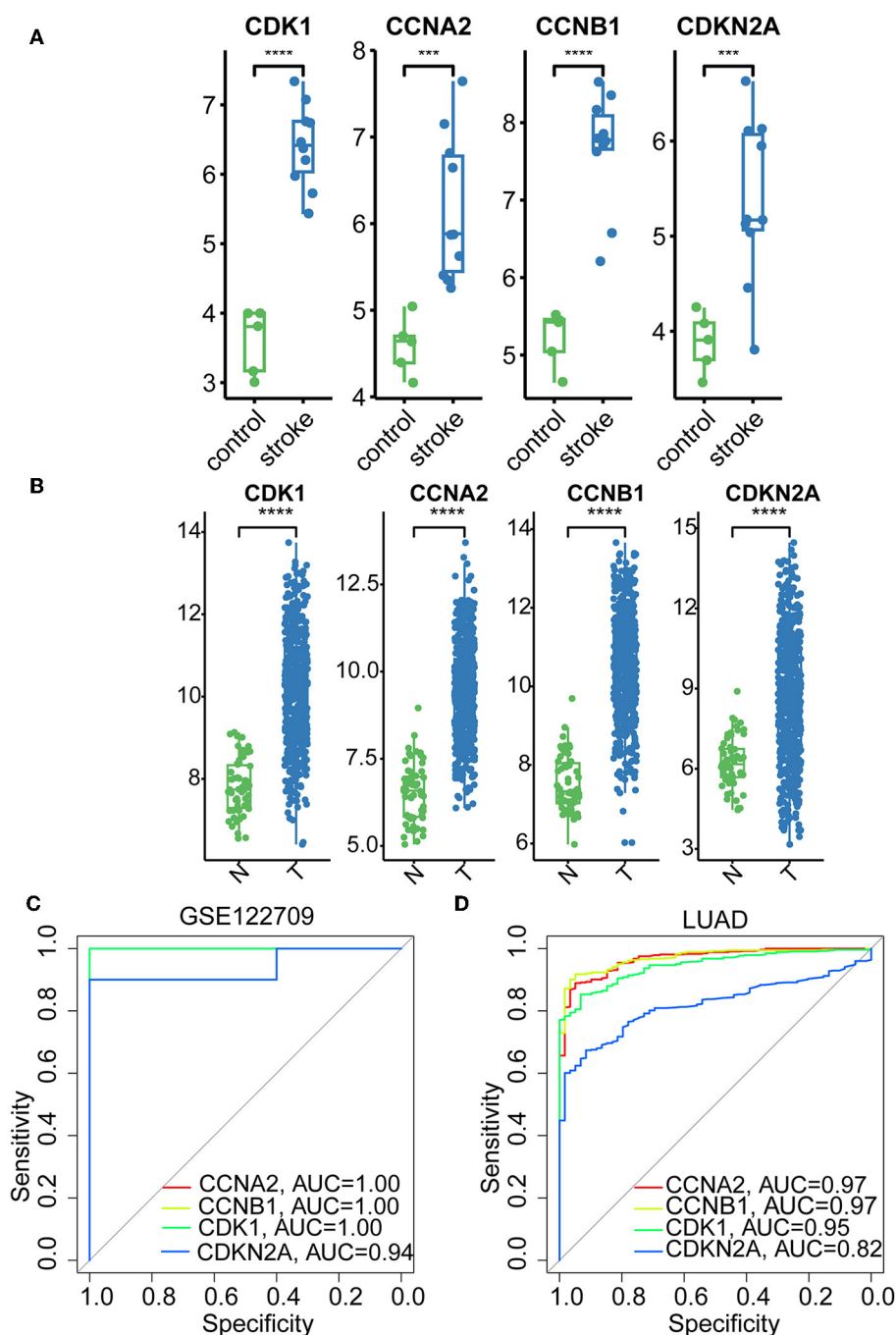


FIGURE 4

Boxplots and ROC curves of four hub genes in AIS and LUAD. **(A)** Boxplots of the four hub genes in AIS. **(B)** Boxplots of the four hub genes in LUAD. **(C)** ROC curves of the four hub genes in AIS. **(D)** ROC curves of the four hub genes in LUAD (\*\*\*,  $p < 0.001$ ; \*\*\*\*,  $p < 0.0001$ ; N, normal; T, tumor).

metabolism-cytochrome P450, and Linoleic acid metabolism (Figure 3B). We selected DEGs in the cellular senescence pathway using KEGG for analysis. We discovered hub genes and elucidated the potential link between DEG-encoded proteins. Using the STRING database, we built a PPI network and identified the top 10 genes (Table 2), and then we defined four hub genes *CCNA2*, *CCNB1*, *CDKN2A*, and *CDK1* from the top 10 genes using Cytoscape.

### 3.3. Validation of hub genes expression and assessment of diagnostic value

The hub genes displayed considerably higher expression in LUAD and AIS patients compared to the control group. In addition, we checked the expression of four hub genes in AIS using the validation datasets (GSE58294 and GSE140275). According to our findings, AIS patients had higher levels of



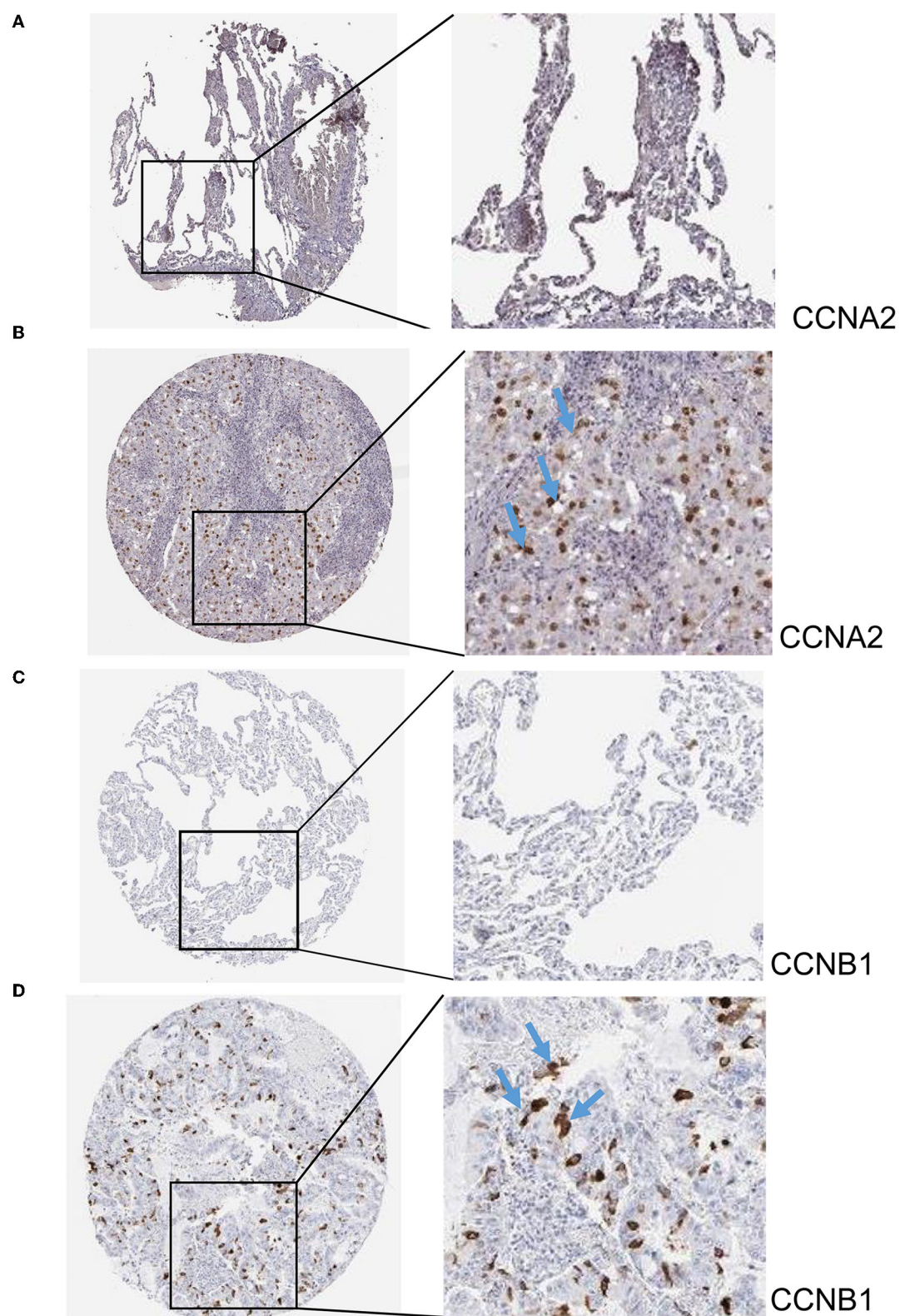


FIGURE 5

Immunohistochemistry slices of *CCNA2* and *CCNB1*. (A) Immunohistochemistry slices of normal lung tissues of *CCNA2*. (B) Immunohistochemistry slices of LUAD of *CCNA2*. (C) Immunohistochemistry slices of normal lung tissues of *CCNB1*. (D) Immunohistochemistry slices of LUAD of *CCNB1*.

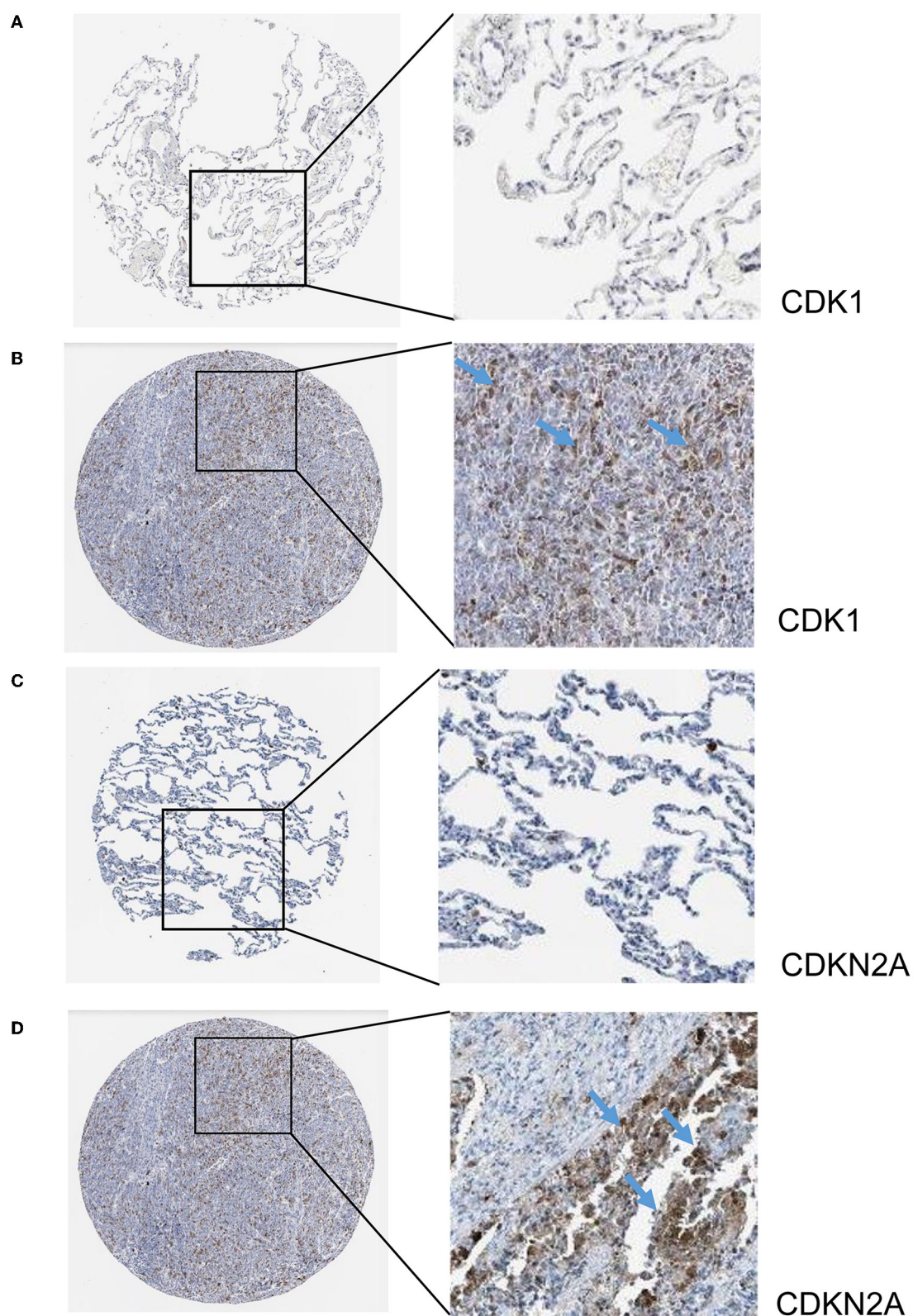
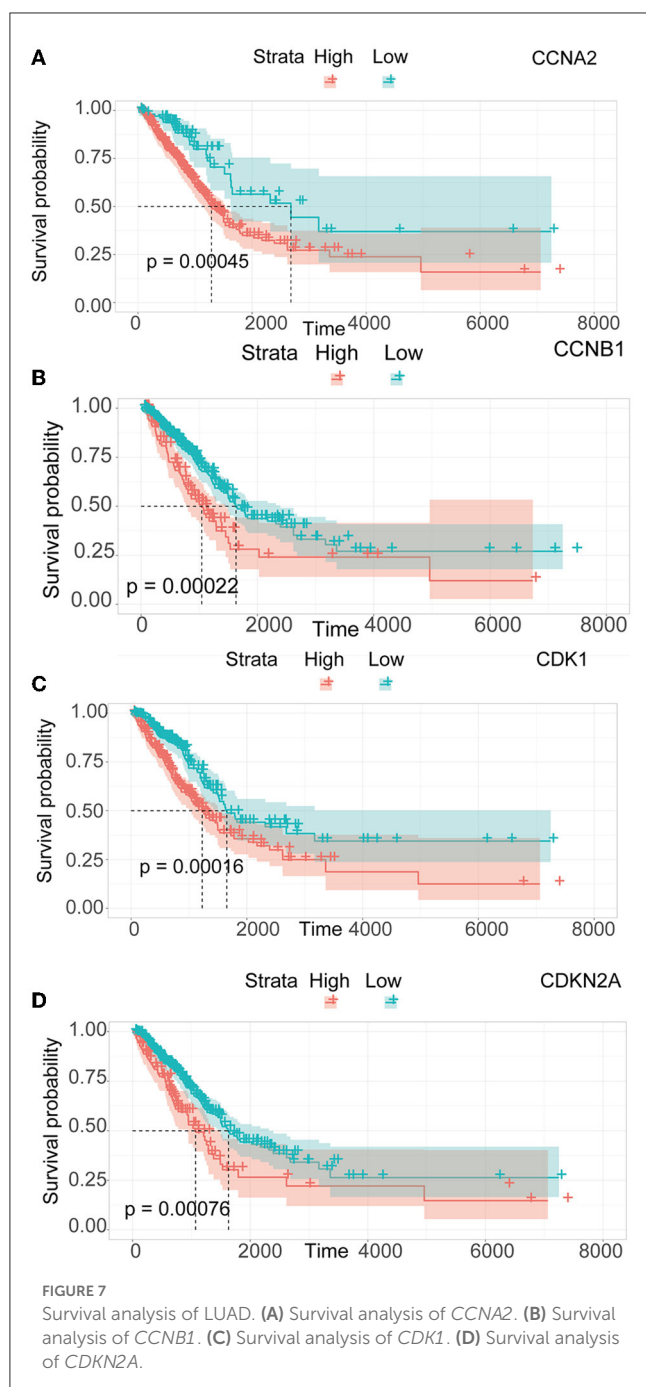


FIGURE 6

Immunohistochemistry slices of *CDK1* and *CDKN2A*. (A) Immunohistochemistry slices of normal lung tissues of *CDK1*. (B) Immunohistochemistry slices of LUAD of *CDK1*. (C) Immunohistochemistry slices of normal lung tissues of *CDKN2A*. (D) Immunohistochemistry slices of LUAD of *CDKN2A*.





*CCNA2*, *CCNB1*, and *CDK1* expression compared to the control group (Supplementary Figure 1). However, the four hub genes are insignificant in the GSE140275 dataset, which would account for the limited sample size. Single-cell data analysis revealed that 10996 cells were divided into 11 clusters. The results indicated that *CCNA2*, *CCNB1*, *CDK1* and *CDKN2A* were expressed in cancer epithelial cells (Supplementary Figure 2). The diagnostic effectiveness of these hub genes was further investigated using ROC curves, which revealed that these genes have great diagnostic efficacy for LUAD and AIS (Figure 4). This work analyzed immunohistochemistry slices from LUAD patients and typical tissues from healthy people. The four hub genes' protein expression

levels were higher in LUAD tissues than those in healthy tissues (Figures 5, 6). We used the digital pathology software QuPath to count the number of positive cells in LUAD and normal lung tissue figures. As a result, we observed that there were more positive cells overall in the LUAD field than there were in the normal lung tissue (Supplementary Figure 3). It's showed that four hub genes had higher protein levels in LUAD compared with normal tissues (Supplementary Figure 4).

### 3.4. Survival analysis and validation

We performed a survival study where patients were classified into high-risk and low-risk groups depending on their gene expression level to confirm the prognosis of the four hub genes in LUAD. The findings revealed that hub genes with high expression have a poor prognosis in LUAD (Figure 7). It was revealed that the OS time of patients with a high risk score was significantly shorter than that of patients with a low risk score. The AUC values of 1, 3 and 5 years of four hub genes were about 0.5–0.6 (Figure 8). By plotting KM curves and univariate Cox regression analysis, we obtained 5-year AUC, HR and 95% CI (Supplementary Table 1).

### 3.5. Immune infiltration analysis in LUAD and AIS

Immune infiltration is essential for the onset, prognosis, and treatment of numerous disorders. While the control group had higher levels of neutrophils, AIS patients had higher levels of resident memory  $CD4^+$  T cells, monocytes, and eosinophils (Figure 9A). As seen in the image, several immune cells are involved in the formation of LUAD (Figure 9B). In AIS patients, only *CDK1* is associated with  $CD8^+$  T cells (Figure 10A). In LUAD patients, infiltration levels of resident memory  $CD4^+$  T cells, and activated dendritic cells were positively linked with *CDKN2A* overexpression. The immunological infiltration of resident memory  $CD4^+$  T cells, macrophage, activated dendritic cells, mast cells resting, activated NK cells and neutrophils were favorably connected with *CDK1* and *CCNA2* overexpression. However, it was not discovered that *CCNB1* was connected to immune cells (Figure 10B).

### 3.6. Molecular docking of curcumin with hub genes

Potential medicines were identified based on transcriptome features in the DSigDB database of Enrichr. Curcumin is considered as a potential drug for AIS treatment and later analysis. Moreover, we predicted the binding mechanism of curcumin with four hub genes using molecular docking. It is commonly accepted that the likelihood of action increases with decreasing ligand and receptor binding energies. The binding energies of curcumin with four hub genes (*CCNA2*, *CCNB1*, *CDK1*, *CDKN2A*) were  $-6.999$  kcal/mol,  $-5.87$  kcal/mol,  $-7.1$  kcal/mol,  $-5.366$  kcal/mol, respectively. These findings demonstrate the highly stable binding of curcumin to four hub genes (Figure 11).

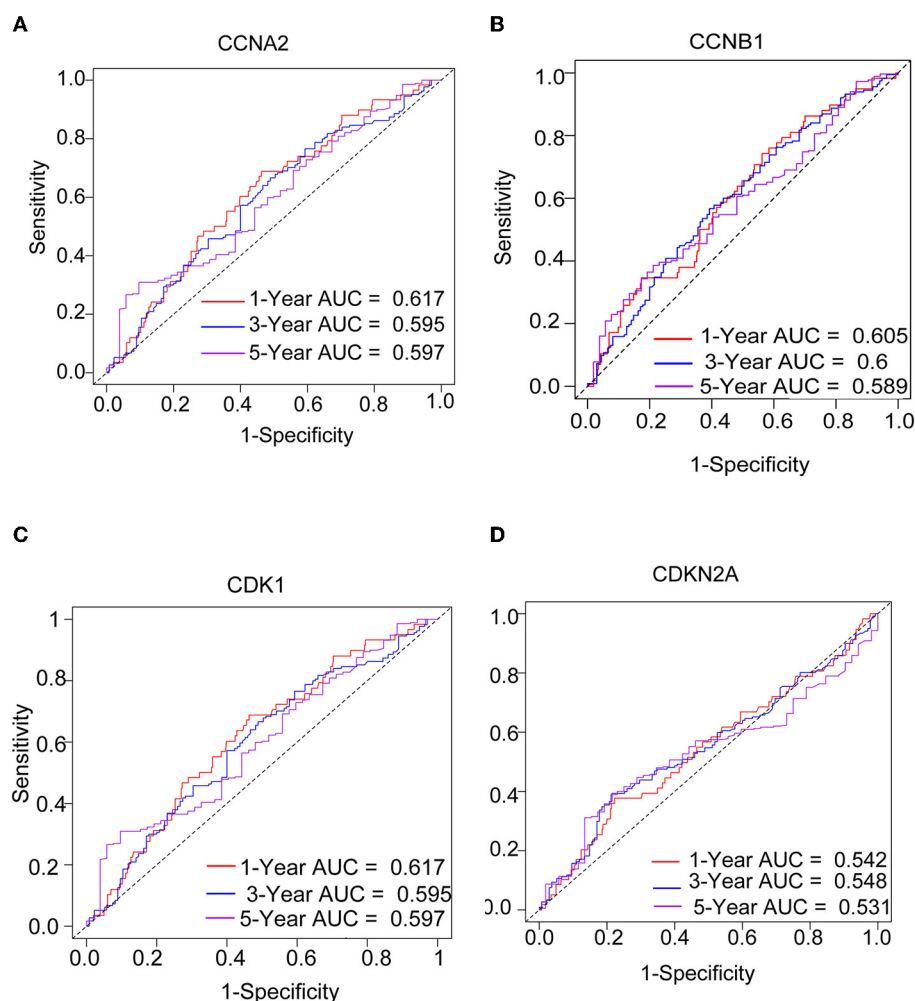


FIGURE 8

The ROC curves of four hub genes for predicting 1, 3, and 5-year mortality risk in the TCGA-LUAD dataset. (A) *CCNA2*. (B) *CCNB1*. (C) *CDK1*. (D) *CDKN2A*.

### 3.7. DEGs of different etiologies of AIS

According to the analysis above, *CCNA2*, *CCNB1*, *CDK1*, *CDKN2A* are the hub genes for AIS and LUAD. Results of DEGs of AIS caused by atherosclerosis and cardiac embolism shown by heatmaps (Supplementary Figure 5).

## 4. Discussion

The leading cause of adult disability and the second leading cause of death globally, behind ischemic heart disease, is stroke (24). Nearly 85% of lung cancer cases are non-small cell lung cancer (NSCLC), with the most prevalent histological subtype, LUAD, having a high mortality and recurrence rate (25). Stroke patients have an increased incidence of cancer, including lung cancer (26). A previous clinical study indicated that AIS may be a unique precursor to LUAD. In patients with LUAD combined with AIS, LUAD occurs due to the occurrence of AIS. The prevalence of lung cancer in the stroke cohort was 5.3 per 1000 person-years

(27, 28). Lung cancer patients are most likely to experience a stroke within one year after diagnosis. The risk of stroke occurring in lung cancer patients is more than two times higher than that in people without cancer (HR 2.40, 95% CI 1.53–3.78) (23, 29). However, the causal relationship, genetic mechanisms, and their interactions between LUAD and AIS are still unclear. It is crucial to study the biological processes that underlie AIS and LUAD. The cerebral atherosclerosis-related gene *PITX2*, *RGS7*, *NKX2-5*, *NKX2-5*, and *ZFHX3* are involved in AIS. The genes of AIS brought on by cardiogenic embolism are *TM4SF4-TM4SF1*, *EDNRA*, *HDAC9-TWIST1*, and *LINC01492* (30). Our study shows that the hub genes of AIS with LUAD are *CCNA2*, *CCNB1*, *CDK1*, and *CDKN2A*. Meanwhile, our findings suggest that LUAD-induced AIS is distinct from AIS produced by large artery atherosclerosis and cardiac embolism in terms of genes. These genes' prognostic and diagnostic capabilities in LUAD were examined, and their mRNA levels were significantly elevated in AIS and LUAD. Herein, we investigated the link between AIS and LUAD using our four hub genes and explored the underlying biological mechanisms shared between these two diseases.





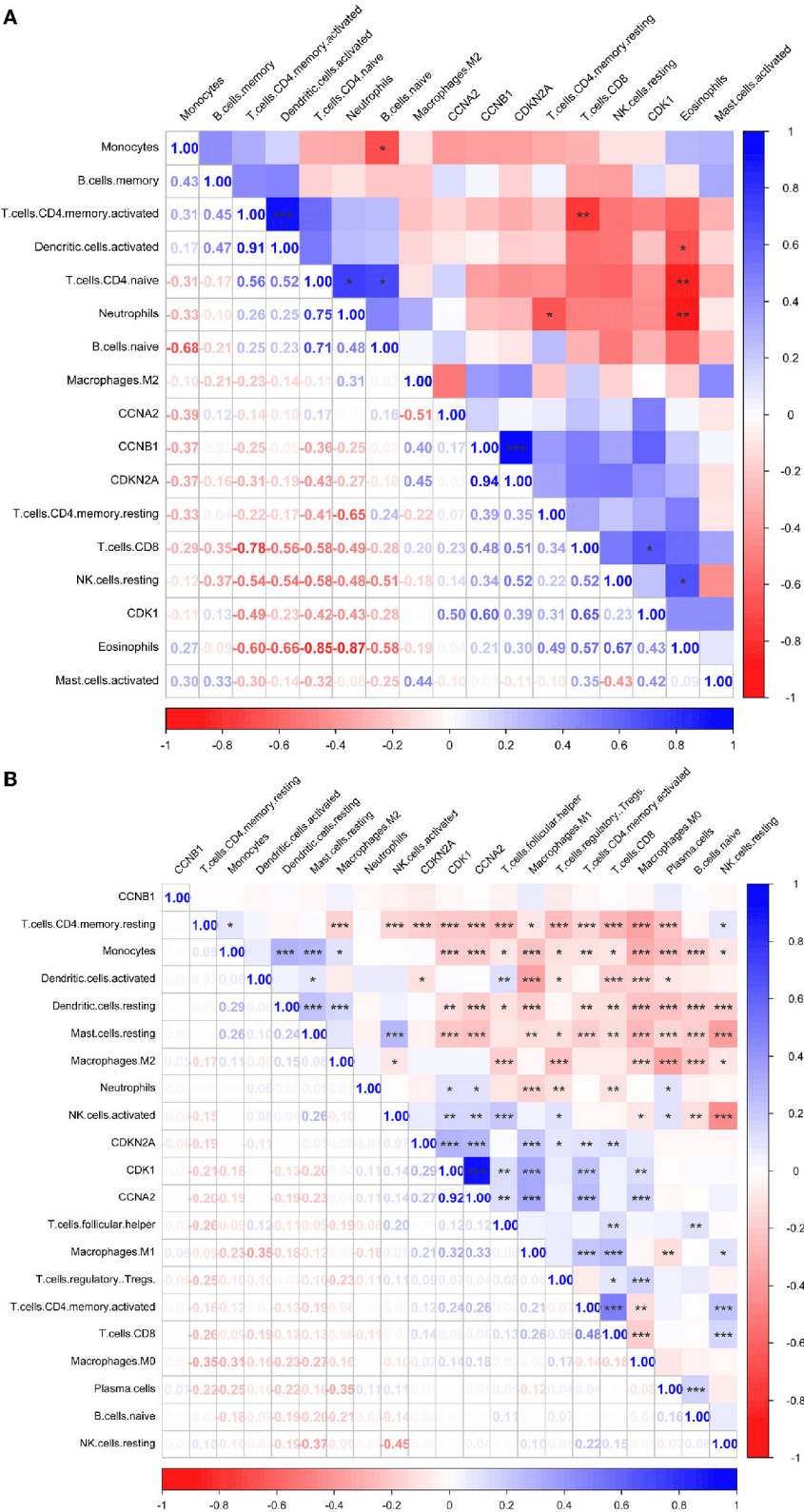


FIGURE 10 Immune correlation heatmaps of four hub genes in AIS and LUAD. (A) AIS. (B) LUAD (\*,  $P < 0.05$ ; \*\*,  $P < 0.01$ ; \*\*\*,  $P < 0.001$ ).

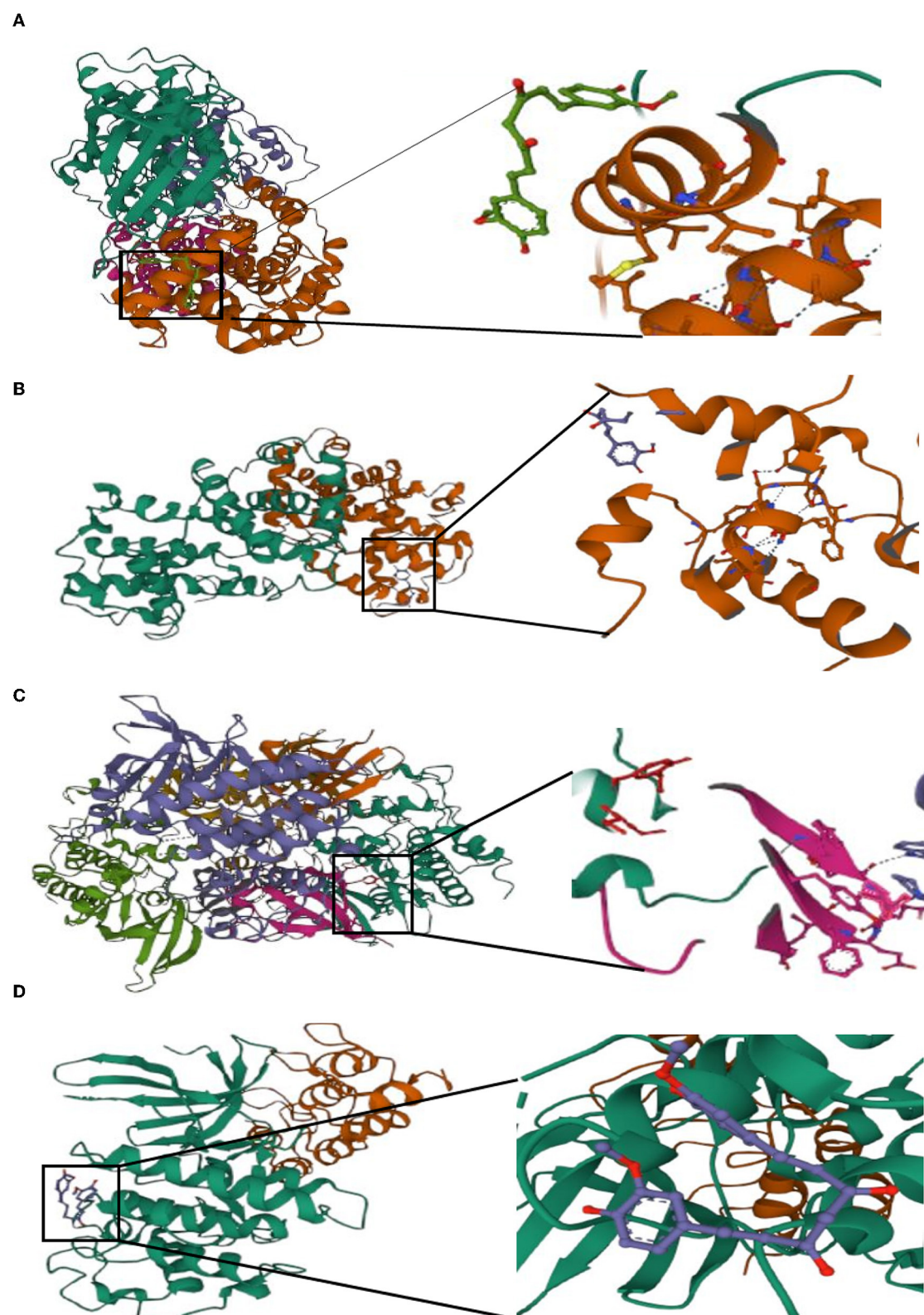


FIGURE 11  
Molecular docking of curcumin with four hub genes. (A) *CCNA2*. (B) *CCNB1*. (C) *CDK1*. (D) *CDKN2A*.

GO, KEGG, and DO enrichment analyses were performed on the 372 DEGs that intersecting both datasets. DEGs are mainly enriched in nuclear division, organelle fission and mitotic nuclear division, and they are associated with the biological behavior of LUAD and the neuroprotective inhibition observed in AIS. The primary enriched pathways in KEGG are the cell cycle, cellular senescence, and the HIF-1 signaling pathway. The cellular senescence pathway was highlighted as the main contributor of this study, and the overexpression of four cellular senescence-related genes was closely related to AIS and LUAD. HIF-1 was found to have a positive connection with infarct size in AIS (31). However, HIF's impact on neuronal survival following a stroke is still debatable (32). HIF-1- $\alpha$  is associated with aggressiveness in lung cancer (33). Our investigation revealed that the DEGs were linked to many malignancies.

According to one definition, cellular senescence is an ongoing proliferative arrest brought on by various stressors. Furthermore, senescence and hyperplastic pathology are both related to a type of stress response known as cellular senescence (34). Numerous neurological diseases, including neurodegenerative conditions like Alzheimer's disease, Parkinson's disease, and stroke, are linked to cellular senescence (35). Cellular senescence of the cells happens as AIS, which develops and progresses (36). AIS and neurological damage are impacted by the senescence-associated secretory phenotype (SASP) (37). Cellular senescence is considered the new hallmark of cancer, as malignant and non-malignant tumor cells develop a SASP that stimulates cancer recurrence and metastasis (38). However, it was once believed that cellular senescence contributed to the prevention of tumors; therefore, the mechanism of cellular senescence in cancer is not welldefined and should be further explored (39). Recently, it was demonstrated that a high expression of cellular senescence genes correlates with a poor LUAD prognosis (40). This is in line with our study, where our four hub genes *CCNA2*, *CCNB1*, *CDKN2A*, and *CDK1* were related to cellular senescence pathways. We investigated genes that were highly expressed in LUAD and that were linked to poor prognosis. It is crucial to deepen our understanding of how cellular senescence in AIS and LUAD functions, how it interacts with the immune system, and how it affects prognosis because the mechanism underlying these diseases has not yet been fully uncovered.

*CCNB1* combines with *CDK1* to form a complex that enables cells to enter the G2/M phase to promote mitosis (41, 42). Numerous malignancies have high *CCNB1* expression (43), increase apoptosis and cell death via controlling the p53 signaling pathway (44), accumulate in the degenerating brain regions of stroke patients, and can participate in neuronal death (45). The regulation of the mitotic cell cycle is influenced by *CDK1* (46). According to studies, *CDK1* may contribute to stroke through an oxidative mode of damage (47) and may also be a potential biomarker for NSCLC (48). *CDK1* is upregulated in patients with LUAD and accelerates tumor progression (49). *CCNB1* and *CDK1* enable the sustained proliferation of NSCLC by regulating the pRb protein (50). In our study, survival analysis showed that LUAD and AIS patients with overexpression of *CCNA2*,

*CCNB1*, and *CDK1* had a poor prognosis and that these genes can be used as predictors of prognosis. In addition, these genes have high diagnostic abilities in patients with LUAD and AIS and could later serve as biomarkers for predicting these two diseases.

The cell cycle is regulated by *CDKN2A*, a cyclin-dependent kinase inhibitor that encodes the p16 protein (51). *CDKN2A* is a ferroptosis and cuproptosis gene (52, 53). When iron-dependent lipid hydroperoxides build up to deadly amounts, controlled cell death known as ferroptosis occurs (54). Cuproptosis is another type in which excess copper leads to cell death by aggregation of mitochondrial proteins (55). According to reports, *CDKN2A* is a locus for AIS risk. It has been linked to an elevated risk of AIS in the Han Chinese population and in native West African men. Genetic variation at the *CDKN2A* locus also predicts stroke in hypertensive patients (56–58). Lung cancer is associated with genetic mutations in *CDKN2A*, such as genomic deletions (59). The high expression of *CDKN2A* in LUAD is correlated with a bad prognosis. High *CDKN2A* expression may be associated with increased immune cell numbers, immune checkpoint enhancement, and elevated chemokine levels (60). *CDKN2A* is often regarded as a tumor suppressor gene; however, hypermethylated *CDKN2A* may be responsible for poor cancer prognosis (61). These four hub genes were verified in the HPA database and discovered to be related to LUAD prognosis, indicating they are crucial to the onset and development of LUAD. Curcumin has been shown to have neuroprotective and neuroregenerative properties. It can also be utilized as a drug for the treatment of ischemic stroke (62). This is in line with our findings, which shows that curcumin has a strong affinity to four hub genes. Curcumin might be a potential therapeutic target for the therapy of AIS, according to our drug prediction and molecular docking results.

This research has several restrictions. First, this study only employed a few samples. Second, we did not confirm the hub genes discovered in this study based on data from earlier experiments. However, their expression levels were validated.

According to our research, *CCNA2*, *CCNB1*, *CDKN2A*, and *CDK1* are significant components in AIS and LUAD. With multiple analyses, we explored AIS and LUAD pathogenesis as well as their common molecular mechanisms and observed high expression of these four hub genes, high diagnostic power in patients, and poor prognosis. Our results shed new light on improving AIS and LUAD prognosis. Further research into early intervention and treatment using our identified hub genes is warranted. Overall, this study identified *CCNA2*, *CCNB1*, *CDKN2A*, and *CDK1* as hub genes involved in the cellular senescence pathway and may serve as diagnostic and prognostic indicators for AIS and LUAD.

## Data availability statement

The original contributions presented in the study are included in the article/Supplementary material, further inquiries can be directed to the corresponding author.



## Author contributions

LC and R-XQ conceived the study. R-XQ, YY, and J-FC contributed to the data analysis and interpretation of the results. L-JH, WX, Q-CQ, X-JL, X-YL, X-YH, and M-SX wrote the manuscript. LC, R-XQ, YY, J-FC, L-JH, WX, Q-CQ, X-JL, X-YL, X-YH, and M-SX contributed to its editing. All authors contributed to the article and approved the submitted version.

## Funding

This study was supported by grants from the National Natural Science Foundation of China (82271371 and 82260367), the High-Level Medical Expert Training Program of Guangxi 139 Plan Funding, the Guangxi Medical and Health Appropriate Technology Development and Application Project (S2021107), the Clinical Research Climbing Program of the First Affiliated Hospital of Guangxi Medical University (YYZS2021002), and Advanced Innovation Teams and Xinghu Scholars Program of Guangxi Medical University, 2023 Guangxi Postgraduate Innovation Project (YCSW2023242).

## References

- Li R, Cheng X, Schwebel DC, Yang Y, Ning P, Cheng P, et al. Disability-adjusted life years associated with population ageing in China, 1990–2017. *BMC Geriatr*. (2021) 21:369. doi: 10.1186/s12877-021-02322-7
- Barthels D, Das H. Current advances in ischemic stroke research and therapies. *Biochimica et biophysica acta Mol Basis Dis*. (2020) 1866:165260. doi: 10.1016/j.bbdis.2018.09.012
- Tu WJ, Zhao Z, Yin P, Cao L, Zeng J, Chen H, et al. Estimated burden of stroke in China in 2020. *JAMA Netw Open*. (2023) 6:e231455. doi: 10.1001/jamanetworkopen.2023.1455
- Chung JW, Park SH, Kim N, Kim WJ, Park JH, Ko Y, et al. Trial of ORG 10172 in Acute Stroke Treatment (TOAST) classification and vascular territory of ischemic stroke lesions diagnosed by diffusion-weighted imaging. *J Am Heart Assoc*. (2014) 3:4. doi: 10.1161/JAHA.114.001119
- Feigin VL, Krishnamurthi RV, Parmar P, Norrving B, Mensah GA, Bennett DA, et al. Update on the global burden of ischemic and hemorrhagic stroke in 1990–2013: The GBD 2013 study. *Neuroepidemiology*. (2015) 45:161–76. doi: 10.1159/000441085
- Kumar A, Misra S, Sagar R, Kumar P, Yadav AK, Talwar P, et al. Relationship between factor V Leiden Gene variant and risk of ischemic stroke: a case-control study. *Ann Indian Acad Neurol*. (2017) 20:284–8.
- Iadecola C, Anrather J. The immunology of stroke: from mechanisms to translation. *Nat Med*. (2011) 17:796–808. doi: 10.1038/nm.2399
- Iadecola C, Buckwalter MS, Anrather J. Immune responses to stroke: mechanisms, modulation, and therapeutic potential. *J Clin Invest*. (2020) 130:2777–88. doi: 10.1172/JCI135530
- Campbell BC. Thrombolysis and thrombectomy for acute ischemic stroke: strengths and synergies. *Semin Thromb Hemost*. (2017) 43:185–90. doi: 10.1055/s-0036-1585078
- Sung H, Ferlay J, Siegel RL, Laversanne M, Soerjomataram I, Jemal A, et al. Global cancer statistics 2020: GLOBOCAN estimates of incidence and mortality worldwide for 36 cancers in 185 countries. *CA Cancer J Clin*. (2021) 71:209–49. doi: 10.3322/caac.21660
- Qi SA, Wu Q, Chen Z, Zhang W, Zhou Y, Mao K, et al. High-resolution metabolomic biomarkers for lung cancer diagnosis and prognosis. *Sci Rep*. (2021) 11:11805. doi: 10.1038/s41598-021-91276-2
- Behera M, Owonikoko TK, Gal AA, Steuer CE, Kim S, Pillai RN, et al. Lung Adenocarcinoma Staging using the 2011 IASLC/ATS/ERS classification: a pooled analysis of adenocarcinoma in situ and minimally invasive adenocarcinoma. *Clin Lung Cancer*. (2016) 17:e57–64. doi: 10.1016/j.clcc.2016.03.009
- de Sousa VML, Carvalho L. Heterogeneity in lung cancer. *Pathobiol J Immunopathol Mol Cell Biol*. (2018) 85:96–107. doi: 10.1159/000487440
- Dai X, Lu L, Deng S, Meng J, Wan C, Huang J, et al. USP7 targeting modulates anti-tumor immune response by reprogramming tumor-associated macrophages in lung cancer. *Theranostics*. (2020) 10:9332–47. doi: 10.7150/thno.47137
- Fan Y, Liu B, Chen F, Song Z, Han B, Meng Y, et al. Hepcidin upregulation in lung cancer: a potential therapeutic target associated with immune infiltration. *Front Immunol*. (2021) 12:612144. doi: 10.3389/fimmu.2021.612144
- Garnis C, Buys TP, Lam WL. Genetic alteration and gene expression modulation during cancer progression. *Mol Cancer*. (2004) 3:9. doi: 10.1186/1476-4598-3-9
- Sibilia M, Kroismayr R, Lichtenberger BM, Natarajan A, Hecking M, Holcman M. The epidermal growth factor receptor: from development to tumorigenesis. *Differentiation*. (2007) 75:770–87. doi: 10.1111/j.1432-0436.2007.00238.x
- Yang G, Wang W, Han S, Xu S, Liu H. Effect of microRNA-181b on the biological characteristics and clinical drug resistance of small-cell lung cancer by targeting angiotensin converting enzyme 2. *Thoracic Cancer*. (2022) 13:742–9. doi: 10.1111/1759-7714.14313
- Salazar-Camelo RA, Moreno-Vargas EA, Cardona AF, Bayona-Ortiz HF. Ischemic stroke: a paradoxical manifestation of cancer. *Crit Rev Oncol Hematol*. (2021) 157:103181. doi: 10.1016/j.critrevonc.2020.103181
- Chen PC, Muo CH, Lee YT, Yu YH, Sung FC. Lung cancer and incidence of stroke: a population-based cohort study. *Stroke*. (2011) 42:3034–9. doi: 10.1161/STROKEAHA.111.615534
- Yuan T, Wang J. [Clinical and Imaging Features of Acute Cerebral Infarction in Non-small Cell Lung Cancer Patients with Trousseau Syndrome]. *Zhongguo Fei Ai Za Zhi*. (2021) 24:13–8. doi: 10.3779/j.issn.1009-3419.2021.102.01
- Li MJ, Yan SB, Chen G, Li GS, Yang Y, Wei T, et al. Upregulation of CCNB2 and its perspective mechanisms in cerebral ischemic stroke and all subtypes of lung cancer: a comprehensive study. *Front Integr Neurosci*. (2022) 16:854540. doi: 10.3389/fnint.2022.854540
- Zhang J, Zhao J. Clinical characteristics and analysis of lung cancer-associated acute ischemic stroke. *J Stroke Cerebrovascul Dis Off J Nat Stroke Assoc*. (2020) 29:105164. doi: 10.1016/j.jstrokecerebrovasdis.2020.105164
- Koton S, Schneider AL, Rosamond WD, Shahar E, Sang Y, Gottesman RF, et al. Stroke incidence and mortality trends in US communities, 1987 to 2011. *Jama*. (2014) 312:259–68. doi: 10.1001/jama.2014.7692
- Bajbouj K, Al-Ali A, Ramakrishnan RK, Saber-Ayad M, Hamid Q. Histone modification in NSCLC: molecular mechanisms and therapeutic targets. *Int J Mol Sci*. (2021) 22:21. doi: 10.3390/ijms222111701

## Conflict of interest

The authors declare that the research was conducted in the absence of any commercial or financial relationships that could be construed as a potential conflict of interest.

## Publisher's note

All claims expressed in this article are solely those of the authors and do not necessarily represent those of their affiliated organizations, or those of the publisher, the editors and the reviewers. Any product that may be evaluated in this article, or claim that may be made by its manufacturer, is not guaranteed or endorsed by the publisher.

## Supplementary material

The Supplementary Material for this article can be found online at: <https://www.frontiersin.org/articles/10.3389/fneur.2023.1119160/full#supplementary-material>



26. Selvik HA, Thomassen L, Logallo N, Næss H. Prior cancer in patients with ischemic stroke: the Bergen NORSTROKE study. *J Stroke Cerebrovascul Dis Off J Nat Stroke Assoc.* (2014) 23:919–25. doi: 10.1016/j.jstrokecerebrovasdis.2013.07.041
27. Lin J, Wu S, Xu R, Shi Q, Tian C, Cui F, et al. Clinical characteristics and risk factors of lung cancer-associated acute ischemic stroke. *Biomed Res Int.* (2019) 2019:6021037. doi: 10.1155/2019/6021037
28. Babore AD, Tybjerg AJ, Andersen KK, Olsen TS. Occult lung cancer manifesting within the first year after stroke. *J Stroke Cerebrovascul Dis Off J Nat Stroke Assoc.* (2020) 29:105023. doi: 10.1016/j.jstrokecerebrovasdis.2020.105023
29. Florido R, Daya NR, Ndumele CE, Koton S, Russell SD, Prizment A, et al. Cardiovascular disease risk among cancer survivors: the atherosclerosis risk in communities (ARIC) study. *J Am Coll Cardiol.* (2022) 80:22–32. doi: 10.1016/j.jacc.2022.04.042
30. Ilinca A, Samuelsson S, Piccinelli P, Soller M, Kristoffersson U, Lindgren AG, et al. stroke gene panel for whole-exome sequencing. *Euro J Hum Genet EJHG.* (2019) 27:317–24. doi: 10.1038/s41431-018-0274-4
31. Xue L, Chen H, Lu K, Huang J, Duan H, Zhao Y. Clinical significance of changes in serum neuroglobin and HIF-1 $\alpha$  concentrations during the early-phase of acute ischemic stroke. *J Neurol Sci.* (2017) 375:52–7. doi: 10.1016/j.jns.2017.01.039
32. Bartczek P, Li L, Ernst AS, Böhrer LI, Marti HH, Kunze R. Neuronal HIF-1 $\alpha$  and HIF-2 $\alpha$  deficiency improves neuronal survival and sensorimotor function in the early acute phase after ischemic stroke. *J Cerebr Blood Flow Metabol Off J Int Soc Cerebr Blood Flow Metabol.* (2017) 37:291–306. doi: 10.1177/0271678X15624933
33. Hao S, Li F, Jiang P, Gao J. Effect of chronic intermittent hypoxia-induced HIF-1 $\alpha$ /ATAD2 expression on lung cancer stemness. *Cell Mol Biol Lett.* (2022) 27:44. doi: 10.1186/s11658-022-00345-5
34. Sharpless NE, Sherr CJ. Forging a signature of in vivo senescence. *Nat Rev Cancer.* (2015) 15:397–408. doi: 10.1038/nrc3960
35. Wyss-Coray T. Ageing, neurodegeneration and brain rejuvenation. *Nature.* (2016) 539:180–6. doi: 10.1038/nature20411
36. Baixauli-Martin J, Aliena-Valero A, Castelló-Ruiz M, Burguete MC, López-Morales MA, Muñoz-Espin D, et al. Brain Cell Senescence: A New Therapeutic Target for the Acute Treatment of Ischemic Stroke. *J Neuropathol Exp Neurol.* (2022) 81:614–20. doi: 10.1093/jnen/nlnc048
37. Torres-Querol C, Torres P, Vidal N, Portero-Otin M, Arque G, Purroy F. Acute ischemic stroke triggers a cellular senescence-associated secretory phenotype. *Sci Rep.* (2021) 11:15752. doi: 10.1038/s41598-021-95344-5
38. Faget DV, Ren Q, Stewart SA. Unmasking senescence: context-dependent effects of SASP in cancer. *Nat Rev Cancer.* (2019) 19:439–53. doi: 10.1038/s41568-019-0156-2
39. Hanahan D. Hallmarks of cancer: new dimensions. *Cancer Discov.* (2022) 12:31–46. doi: 10.1158/2159-8290.CD-21-1059
40. Lin W, Wang X, Wang Z, Shao F, Yang Y, Cao Z, et al. Comprehensive analysis uncovers prognostic and immunogenic characteristics of cellular senescence for lung adenocarcinoma. *Front Cell Develop Biol.* (2021) 9:780461. doi: 10.3389/fcell.2021.780461
41. Nam HJ, van Deursen JM. Cyclin B2 and p53 control proper timing of centrosome separation. *Nat Cell Biol.* (2014) 16:538–49. doi: 10.1038/ncb2952
42. Chiu HC, Huang WR, Liao TL, Chi PI, Nielsen BL, Liu JH, et al. Mechanistic insights into avian reovirus p17-modulated suppression of cell cycle CDK-cyclin complexes and enhancement of p53 and cyclin H interaction. *J Biol Chem.* (2018) 293:12542–62. doi: 10.1074/jbc.RA118.002341
43. Ding K, Li W, Zou Z, Zou X, Wang C. CCNB1 is a prognostic biomarker for ER+ breast cancer. *Med Hypotheses.* (2014) 83:359–64. doi: 10.1016/j.mehy.2014.06.013
44. Zhang H, Zhang X, Li X, Meng WB, Bai ZT, Rui SZ, et al. Effect of CCNB1 silencing on cell cycle, senescence, and apoptosis through the p53 signaling pathway in pancreatic cancer. *J Cell Physiol.* (2018) 234:619–31. doi: 10.1002/jcp.26816
45. Maestre C, Delgado-Esteban M, Gomez-Sanchez JC, Bolaños JP, Almeida A. Cdk5 phosphorylates Cdh1 and modulates cyclin B1 stability in excitotoxicity. *EMBO J.* (2008) 27:2736–45. doi: 10.1038/emboj.2008.195
46. Malumbres M, Barbacid M. Cell cycle, CDKs and cancer: a changing paradigm. *Nat Rev Cancer.* (2009) 9:153–66. doi: 10.1038/nrc2602
47. Cobelens PM, Kavelaars A, Heijnen CJ, Ribas C, Mayor F. Jr., Penela P. Hydrogen peroxide impairs GRK2 translation via a calpain-dependent and cdk1-mediated pathway. *Cell Signall.* (2007) 19:269–77. doi: 10.1016/j.cellsig.2006.06.009
48. Zhang L, Peng R, Sun Y, Wang J, Chong X, Zhang Z. Identification of key genes in non-small cell lung cancer by bioinformatics analysis. *PeerJ.* (2019) 7:e8215. doi: 10.7717/peerj.8215
49. Xue J, Song Y, Xu W, Zhu Y. The CDK1-Related lncRNA and CXCL8 mediated immune resistance in lung adenocarcinoma. *Cells.* (2022) 11(17). doi: 10.3390/cells11172688
50. Arora S, Singh P, Rahmani AH, Almatroodi SA, Dohare R, Syed MA. Unravelling the Role of miR-20b-5p, CCNB1, HMGA2 and E2F7 in development and progression of non-small cell lung cancer (NSCLC). *Biology.* (2020) 9(8). doi: 10.3390/biology9080201
51. Chan SH, Chiang J, Ngeow J. CDKN2A germline alterations and the relevance of genotype-phenotype associations in cancer predisposition. *Hered Cancer Clin Pract.* (2021) 19:21. doi: 10.1186/s13053-021-00178-x
52. Shi J, Wu P, Sheng L, Sun W, Zhang H. Ferroptosis-related gene signature predicts the prognosis of papillary thyroid carcinoma. *Cancer Cell Int.* (2021) 21:669. doi: 10.1186/s12935-021-02389-7
53. Tsvetkov P, Coy S, Petrova B, Dreishpoon M, Verma A, Abdusamad M, et al. Copper induces cell death by targeting lipoylated TCA cycle proteins. *Science (New York, NY).* (2022) 375:1254–61. doi: 10.1126/science.abf0529
54. Stockwell BR, Friedmann Angeli JP, Bayir H, Bush AI, Conrad M, Dixon SJ, et al. Ferroptosis: a regulated cell death nexus linking metabolism, redox biology, and disease. *Cell.* (2017) 171:273–85. doi: 10.1016/j.cell.2017.09.021
55. Kahlson MA, Dixon SJ. Copper-induced cell death. *Science (New York, NY).* (2022) 375:1231–2. doi: 10.1126/science.abo3959
56. Wahlstrand B, Orho-Melander M, Delling L, Kjeldsen S, Narkiewicz K, Almgren P, et al. The myocardial infarction associated CDKN2A/CDKN2B locus on chromosome 9p21 is associated with stroke independently of coronary events in patients with hypertension. *J Hypertens.* (2009) 27:769–73. doi: 10.1097/HJH.0b013e328326f7eb
57. Akinyemi R, Arnett DK, Tiwari HK, Ovbiagele B, Sarfo F, Srinivasasainagendra V, et al. Interleukin-6 (IL-6) rs1800796 and cyclin dependent kinase inhibitor (CDKN2A/CDKN2B) rs2383207 are associated with ischemic stroke in indigenous West African Men. *J Neurol Sci.* (2017) 379:229–35. doi: 10.1016/j.jns.2017.05.046
58. Hu WL, Li SJ, Liu DT, Wang Y, Niu SQ, Yang XC, et al. Genetic variants on chromosome 9p21 and ischemic stroke in Chinese. *Brain Res Bull.* (2009) 79:431–5. doi: 10.1016/j.brainresbull.2009.04.001
59. Ulivi P, Urbini M, Petracci E, Canale M, Dubini A, Bartolini D, et al. Wide next-generation sequencing characterization of young adults non-small-cell lung cancer patients. *Cancers.* (2022) 14(10). doi: 10.3390/cancers14102352
60. Cheng T, Wu Y, Liu Z, Yu Y, Sun S, Guo M, et al. CDKN2A-mediated molecular subtypes characterize the hallmarks of tumor microenvironment and guide precision medicine in triple-negative breast cancer. *Front Immunol.* (2022) 13:970950. doi: 10.3389/fimmu.2022.970950
61. Xing X, Cai W, Shi H, Wang Y, Li M, Jiao J, et al. The prognostic value of CDKN2A hypermethylation in colorectal cancer: a meta-analysis. *Br J Cancer.* (2013) 108:2542–8. doi: 10.1038/bjc.2013.251
62. Zhu T, Wang L, Wang LP, Wan Q. Therapeutic targets of neuroprotection and neurorestoration in ischemic stroke: applications for natural compounds from medicinal herbs. *Biomed Pharmacother.* (2022) 148:112719. doi: 10.1016/j.biopha.2022.112719

# Frontiers in Neurology

Explores neurological illness to improve patient care

The third most-cited clinical neurology journal explores the diagnosis, causes, treatment, and public health aspects of neurological illnesses. Its ultimate aim is to inform improvements in patient care.

## Discover the latest Research Topics

[See more →](#)

### Frontiers

Avenue du Tribunal-Fédéral 34  
1005 Lausanne, Switzerland  
[frontiersin.org](https://frontiersin.org)

### Contact us

+41 (0)21 510 17 00  
[frontiersin.org/about/contact](https://frontiersin.org/about/contact)

